

**YMP Milestone Report SP2224M3**

**EVALUATION OF  
FLOW AND TRANSPORT MODELS  
OF YUCCA MOUNTAIN,  
BASED ON CHLORINE-36 STUDIES FOR FY97**

by

**J. T. Fabryka-Martin<sup>1</sup>, A. L. Flint<sup>2</sup>, D. S. Sweetkind<sup>2</sup>, A.V. Wolfsberg<sup>1</sup>, S. S. Levy<sup>1</sup>,  
G. J. C. Roemer<sup>1</sup>, J. L. Roach<sup>1</sup>, L. E. Wolfsberg<sup>1</sup>, and M. C. Duff<sup>1</sup>**

**September 29, 1997**

---

<sup>1</sup> Los Alamos National Laboratory, Los Alamos, NM.

<sup>2</sup> U.S. Geological Survey, Denver, CO.

## **Evaluation of Flow and Transport Models of Yucca Mountain, based on Chlorine-36 Studies for FY97**

**J. T. Fabryka-Martin<sup>1</sup>, A. L. Flint<sup>2</sup>, D. S. Sweetkind<sup>2</sup>, A.V. Wolfsberg<sup>1</sup>, S. S. Levy<sup>1</sup>,  
G. J. C. Roemer<sup>1</sup>, J. L. Roach<sup>1</sup>, L. E. Wolfsberg<sup>1</sup>, and M. C. Duff<sup>1</sup>**

---

<sup>1</sup> Los Alamos National Laboratory, Los Alamos, NM.

<sup>2</sup> U.S. Geological Survey, Denver, CO.

## TABLE OF CONTENTS

	Page
Abstract .....	x
1. Introduction .....	1-1
1.1 Background .....	1-1
1.2 Objectives and organization of this report .....	1-2
2. Geologic and Hydrologic Setting .....	2-1
2.1 Geologic framework .....	2-1
2.2 Conceptual model of surface infiltration .....	2-3
2.3 Conceptual model of subsurface fluxes .....	2-6
2.3.1 Hydrologic Framework .....	2-6
2.3.2 Distribution of Hydrologic Properties .....	2-6
2.3.3 Conceptual Model of Percolation .....	2-7
2.3.4 Unresolved Flow and Transport Issues .....	2-8
2.4 Caveats about Infiltration and Percolation Processes .....	2-9
3. Chlorine-36 as a Hydrologic Tracer .....	3-1
3.1 Radiometric Dating of Water using Atmospheric Chlorine-36 .....	3-1
3.1.1 Principles of Dating using Chlorine-36 .....	3-1
3.1.2 Past Variations in the Atmospheric <sup>36</sup> Cl/Cl Signal .....	3-2
3.1.3 Evaluation of Franklin Lake Playa as a Local Source of Cl Deposition .....	3-3
3.2 Global Fallout of Atmospheric Radionuclides .....	3-5
3.3 Local Sources .....	3-7
3.4 Production of <sup>36</sup> Cl in Rocks and Soil Minerals .....	3-8
3.4.1 Deep Subsurface Production in Rocks .....	3-8
3.4.2 Cosmogenic Production in Surface Rocks .....	3-9
3.4.3 Cosmogenic Production in Soil Calcites .....	3-9
4. Experimental Design .....	4-1
4.1 Analytical Methods .....	4-1
4.1.1 Chlorine Isotopic Analysis .....	4-1
4.1.2 Pore-water Extraction .....	4-3
4.1.3 Ion Chromatography Analysis .....	4-4
4.2 ESF Rock Samples .....	4-5
4.2.1 Sample Collection .....	4-5
4.2.2 ESF Construction Water .....	4-8
4.2.3 Analytical Data for ESF Rock Samples .....	4-11
4.2.4 Statistical Analysis for the Presence of Bomb-Pulse <sup>36</sup> Cl .....	4-13
4.2.5 Replicate Analyses .....	4-15
4.3 Soil Samples .....	4-17

**TABLE OF CONTENTS (continued)**

	Page
4.4 Borehole Samples .....	4-22
4.4.1 Shallow Surface-based Boreholes .....	4-22
4.4.2 Deep Surface-based Boreholes .....	4-24
4.4.3 Characterization of in-situ SO <sub>4</sub> /Cl Ratios in Paintbrush Tuffs .....	4-29
4.5 Water Samples .....	4-32
4.5.1 Surface Waters .....	4-32
4.5.2 Unsaturated-zone Waters .....	4-33
4.5.3 Saturated-zone Water .....	4-35
5. Surface Infiltration Rates .....	5-1
5.1 Application of the Cl Mass Balance Method .....	5-1
5.1.1 Overview of Method and its Limitations .....	5-1
5.1.2 Summary of Previous Report Results .....	5-3
5.1.3 Input to Flow and Transport Models .....	5-6
5.2 Penetration of Bomb-Pulse <sup>36</sup> Cl into Soil Profiles .....	5-6
6. Subsurface Flow Paths and Travel Times .....	6-1
6.1 Subsurface Distribution of <sup>36</sup> Cl at Yucca Mountain .....	6-1
6.1.1 Samples with elevated <sup>36</sup> Cl/Cl ratios .....	6-1
6.1.2 Samples with Low <sup>36</sup> Cl/Cl Ratios .....	6-3
6.1.3 Samples with Intermediate <sup>36</sup> Cl/Cl Ratios .....	6-4
6.1.4 Comparison of <sup>36</sup> Cl Results for ESF and Borehole Samples .....	6-7
6.2 Comparison with other Environmental Tracers .....	6-9
6.2.1 Tritium, <sup>14</sup> C, and Major Ion Chemistry of Porewaters .....	6-9
6.2.2 Cesium-137, plutonium, and technetium-99 .....	6-12
6.2.3 Strontium isotopic ratios .....	6-13
6.2.4 Uranium-series disequilibrium studies of fracture mineral ages in the ESF ..	6-15
6.3 Surface infiltration controls on subsurface distribution of Cl and <sup>36</sup> Cl .....	6-18
6.3.1 Surface infiltration controls on the subsurface distribution of Cl .....	6-18
6.3.2 Surface infiltration controls on the subsurface distribution of Cl .....	6-20
6.4 Structural controls on subsurface distribution of <sup>36</sup> Cl .....	6-21
6.4.1 Structural characterization of ESF sample sites .....	6-21
6.4.2 Recognition of syngenetic features .....	6-21
6.4.3 Fault characteristics .....	6-22
6.4.4 Fracture characteristics .....	6-24
6.4.5 Local structural control .....	6-25
6.4.6 Summary of structural controls .....	6-26
6.5 Predicted distribution of fast paths containing bomb-pulse <sup>36</sup> Cl in the planned East-West Drift .....	6-27

**TABLE OF CONTENTS (continued)**

	Page
<b>7. Petrologic and Mineralogic Characteristics of Flow Paths</b> .....	7-1
7.1 Rationale for Petrologic Characterization .....	7-1
7.2 History of Secondary Mineral Deposition .....	7-5
7.3 Distributions of Secondary Minerals .....	7-6
7.3.1 Calcite .....	7-6
7.3.2 Opal .....	7-7
7.3.3 Clays .....	7-7
7.3.4 Transported Particulates .....	7-8
7.3.5 Feldspar, Crystalline Silicas, and Fe-Ti oxides .....	7-10
7.3.6 Manganese Minerals .....	7-10
7.4 Textural Studies of Breccia/Wall Rock Paired Samples .....	7-11
7.5 Discussion and Conclusions about Petrologic and Mineralogic Trends .....	7-15
<b>8. Solute Transport Simulations of <sup>36</sup>Cl Migration and Distribution to Test Alternative Conceptual Models</b> .....	8-1
8.1 Introduction .....	8-1
8.2 Implications .....	8-2
8.3 Background .....	8-3
8.3.1 Previous <sup>36</sup> Cl Modeling Studies at Yucca Mountain .....	8-3
8.3.2 Significant Previous Findings .....	8-4
8.4 Flow and Transport Model .....	8-5
8.4.1 Numerical Flow and Transport Model: FEHM .....	8-5
8.4.2 <sup>36</sup> Cl Input .....	8-5
8.4.3 Simulated Systems .....	8-6
8.4.4 Domain and Boundary Conditions .....	8-6
8.4.5 Material Properties .....	8-7
8.5 Two-Dimensional <sup>36</sup> Cl Simulation Results .....	8-8
8.6 Three-Dimensional <sup>36</sup> Cl Simulation Results .....	8-9
8.6.1 Simulated <sup>36</sup> Cl/Cl Ratios .....	8-9
8.6.2 Travel Time Summary .....	8-10
8.6.3 PTn Thickness/ Flux/ Bomb-Pulse <sup>36</sup> Cl Arrival Study .....	8-10
8.7 Carbon-14, Chloride, and other Conservative Tracers .....	8-11
8.7.1 Chloride and other Conservative Tracers .....	8-11
8.7.2 Carbon-14 .....	8-12
8.8 One-Dimensional Process Level Modeling .....	8-13
8.8.1 Column Descriptions .....	8-13
8.8.2 One-Dimensional Modeling Approach .....	8-14
8.8.3 One-Dimensional Modeling Results .....	8-14
8.9 Conclusions .....	8-18

**TABLE OF CONTENTS (continued)**

	<b>Page</b>
<b>9. Conclusions</b> .....	<b>9-1</b>
9.1 Data collection and analysis .....	9-1
9.2 Conceptual model of flow and transport .....	9-2
9.3 Conceptual model of fast paths .....	9-4
9.4 Numerical modeling results .....	9-5
9.5 Mineralogic characteristics of flow paths .....	9-8
9.6 Open issues and the need for additional work .....	9-9
 <b>Acknowledgments</b> .....	 <b>9-10</b>
 <b>10. References</b> .....	 <b>10-1</b>
 <b>Appendix A. ESF Samples Collected for <sup>36</sup>Cl analysis, February 1995 to August 1997</b> .....	 <b>A-1</b>
 <b>Appendix B. Halide, sulfate and <sup>36</sup>Cl analyses of ESF rock samples, sorted by ESF station</b> ..	 <b>B-1</b>
 <b>Appendix C. Structural and petrologic characterization of ESF sampling sites</b> .....	 <b>C-1</b>
C-1. Characterization of sample sites with elevated <sup>36</sup> Cl/Cl ratios .....	C-2
C-2. Characterization of sample sites with low <sup>36</sup> Cl/Cl ratios .....	C-30
C-3. Petrologic characterization of other sample sites .....	C-45
 <b>Appendix D. Description of surface and subsurface geology</b> .....	 <b>D-1</b>
D1. Scope of Appendix D .....	D-1
D2. Geologic setting and coverage of detailed maps .....	D-1
D3. Azreal Ridge area .....	D-3
D4. Drill Hole Wash and Diabolus Ridge area .....	D-5
D5. Vicinity of the Sundance Fault .....	D-7
D6. Antler Ridge-Whale Back Ridge area .....	D-8
D7. Ghost Dance Wash-Dune Wash area .....	D-9
D8. Boundary Ridge area .....	D-11
 <b>Appendix E. QA status and traceability of new or revised data cited in this report</b> .....	 <b>E-1</b>
E1. Traceability of analytical and field data .....	E-2
E2. Traceability of the solute transport code, FEHM .....	E-3
E3. Description of milestone completion criteria and a summary of their location for the U.S. Department of Energy .....	 E-4

**LIST OF TABLES**

	Page
2-1. Generalized lithostratigraphy of Yucca Mountain area and ages .....	2-2
3-1. Field and laboratory descriptions of soil samples used to evaluate <sup>36</sup> Cl production in soil calcites .....	3-11
3-2. Mineralogic analyses (wt%) of soils .....	3-12
3-3. Measured <sup>36</sup> Cl/Cl ratios for soil calcites .....	3-13
4-1. Summary of ESF samples collected, by collection criterion .....	4-6
4-2. Analyses of J-13 well water and ESF construction water .....	4-9
4-3. Summary of ESF samples analyzed, by collection criterion .....	4-12
4-4. Summary of <sup>36</sup> Cl/Cl analyses for ESF samples, by magnitude of measured ratio .....	4-14
4-5. Replicate analyses of ESF samples .....	4-16
4-6. Chloride and chlorine-36 analyses of soils collected from depths within 0.5 m of the surface .....	4-19
4-7. Sulfate and chloride analyses of surface soils .....	4-20
4-8. Measured <sup>36</sup> Cl/Cl and anion concentration profiles for NRSF-TP-19 and MWV-P31 ..	4-21
4-9. List of boreholes for which measured <sup>36</sup> Cl/Cl ratios are available .....	4-23
4-10. <sup>36</sup> Cl/Cl ratios measured for cuttings from nonwelded units .....	4-25
4-11. Halide, sulfate and <sup>36</sup> Cl/Cl analyses of cuttings from boreholes SD-12 and ONC#1 ...	4-27
4-12. Sulfate/chloride ratios measured for Paintbrush tuffs by step-leaching to remove meteoric salts .....	4-31
4-13. Measured <sup>36</sup> Cl/Cl ratios and anion concentrations for surface runoff .....	4-34
4-14. Measured halide and sulfate concentrations of porewater samples from boreholes ...	4-34
4-15. Halide and sulfate concentrations for Ptn porewater samples from the ESF, listed in order of stratigraphic sequence .....	4-36
4-16. Measured <sup>36</sup> Cl/Cl ratios and anion concentrations for perched water samples .....	4-37
4-17. Measured <sup>36</sup> Cl/Cl ratios and anion concentrations for water samples from the saturated zone .....	4-38
5-1. Apparent infiltration rates calculated for soil and alluvial profiles >2 m, based on the Cl mass balance method .....	5-4
5-2. Effective infiltration rates calculated from pore-water Cl concentrations, based on the Cl mass balance method .....	5-5
6-1. Overall distribution of <sup>36</sup> Cl in the unsaturated zone at Yucca Mountain .....	6-2
6-2. Measured <sup>36</sup> Cl/Cl ratios for borehole cuttings from the TSw unit, adjusted for dilution by rock Cl .....	6-10
7-1. Lithostratigraphic and structural settings, <sup>36</sup> Cl/Cl values, and secondary mineralogy of ESF sample sites .....	7-2
7-2. Quantitative and qualitative X-ray powder diffraction results for mineralogy samples from the ESF .....	7-9
7-3. Paired anion and chlorine-36 analyses of ESF rock sample .....	7-12
8-1. Infiltration Maps Used in Environmental Isotope Simulations .....	8-7
8-2. Parameter Sets for Environmental Isotope Simulations .....	8-7
8-3. Transient Infiltration Rate Models .....	8-16

## LIST OF FIGURES

**Note: Figures for each section are found at the end of the text for that section.**

- 1-1. Map showing the location of boreholes for which chlorine-36 analyses are available
- 2-1a. Geologic map of Yucca Mountain
- 2-1b. Explanation of map units shown on Figure 2-2a.
- 2-2. Conceptual model of infiltration for Yucca Mountain
- 2-3. Conceptual model of hydrologic pathways at Yucca Mountain
- 3-1. Reconstructed  $^{36}\text{Cl}/\text{Cl}$  ratio in the atmosphere, (A) for the past million years, and (B) for the past 50 ka, as a function of variations in the geomagnetic field intensity and chloride deposition rates
- 3-2. Reconstructed atmospheric  $^{36}\text{Cl}/\text{Cl}$  ratio
- 3-3. Comparison of input functions for bomb-pulse nuclides at Yucca Mountain
- 4-1. Analytical results for 67 process blanks prepared alongside Yucca Mountain samples, 1992-1997
- 4-2. Results of replicate analyses of an internal standard, 1994-1997
- 4-3. Plan view of central Yucca Mountain, showing the ESF
- 4-4. Distribution of  $^{36}\text{Cl}/\text{Cl}$  ratios measured for rock samples, as a function of distance along the ESF as measured from the North Ramp Portal
- 4-5. Frequency distribution of  $^{36}\text{Cl}/\text{Cl}$  ratios measured in ESF rock samples
- 4-6. Application of Chauvenet's criterion to establish the cutoff  $^{36}\text{Cl}/\text{Cl}$  ratio for identifying the presence of bomb-pulse  $^{36}\text{Cl}$  in ESF rock samples
- 4-7. Measured  $^{36}\text{Cl}/\text{Cl}$  profiles for boreholes located in large channel bottoms and terraces
- 4-8. Measured  $^{36}\text{Cl}/\text{Cl}$  profiles for boreholes located in sideslopes and ridgetops
- 4-9. Sulfate/chloride ratios in water samples
- 5-1. Schematic diagram illustrating the underlying basis of the chloride mass balance method
- 6-1. Faults and distribution of  $^{36}\text{Cl}/\text{Cl}$  ratios measured for rock samples in the ESF
- 6-2. Three-dimensional profile of  $^{36}\text{Cl}/\text{Cl}$  ratios measured for rock samples in the ESF
- 6-3. Simplified geologic map and diagrammatic cross section of Diabolus Ridge
- 6-4. Surface infiltration rates above the ESF, compared to  $^{36}\text{Cl}/\text{Cl}$  ratios of ESF samples
- 6-5. Fault density and measured  $^{36}\text{Cl}/\text{Cl}$  ratios for rock samples in the ESF
- 6-6. Fracture frequency and measured  $^{36}\text{Cl}/\text{Cl}$  ratios for rock samples in the ESF
- 6-7. Areas for which the infiltration rate exceeds 2 mm/yr above a mapped fault at the surface
- 6-8. Areas for which the infiltration rate exceeds 5 mm/yr above a mapped fault at the surface
- 6-9. Areas for which the infiltration rate exceeds 10 mm/yr above a mapped fault at the surface
- 7-1. Analytical results for paired size separates

**LIST OF FIGURES (continued)**

- 8-1. Reconstructed  $^{36}\text{Cl}/\text{Cl}$  ratio in infiltrating water, a) last 500,000 years, b) last 50,000 years, c) last 50 years
- 8-2. Plan view of three-dimensional model domain with locations of ESF, ESF stations, two-dimensional east-west model transect, north-south transect, and one-dimensional vertical column studies
- 8-3. Two-dimensional cross section at Antler Ridge. Northing location in NSP coordinates is 232100 m.
- 8-4. Infiltration rates extracted from Flint et al. (1996) map along Antler Ridge cross section.
- 8-5. Plan view of three-dimensional domain outline on top of Flint et al. (1996) infiltration map.
- 8-6. Simulated  $^{36}\text{Cl}/\text{Cl}$  ratios in Antler Ridge 2-D cross section with 6541a material property set and Flint et al. (1996) infiltration map
- 8-7. Simulated  $^{36}\text{Cl}/\text{Cl}$  ratios in Antler Ridge 2-D cross section with 6541b material property set (no weighting of fracture-matrix connection in PTn) and Flint et al. (1996) infiltration map.
- 8-8. Simulated saturations in Antler Ridge 2-D cross section with 6541a material property set and Flint et al. (1996) infiltration map
- 8-9. Simulated saturations in Antler Ridge 2-D cross section with 6541b material property set and Flint et al. (1996) infiltration map
- 8-10. Difference in simulated saturations for property sets 6541a and 6541b
- 8-11. Three-dimensional simulation of  $^{36}\text{Cl}/\text{Cl}$  ratios using property set 6541a and infiltration map of Flint et al. (1996)
- 8-12. Simulated  $^{36}\text{Cl}/\text{Cl}$  ratios at ESF horizon with three-dimensional transport model.
- 8-13. PTn thickness for bomb-pulse arrival study
- 8-14. Infiltration map for bomb-pulse arrival study
- 8-15. Predicted bomb-pulse arrivals at potential repository horizon using property set 6541a
- 8-16. Predicted bomb-pulse arrivals at potential repository horizon using modified property set 6541b
- 8-17. Scatter plot of bomb-pulse indicators for infiltration rate vs. PTn thickness above monitored location.
- 8-18. Scatter plot of bomb-pulse indicators for infiltration rate vs. PTn thickness above monitored location
- 8-19. Chloride concentration(mg/L) predicted in the three-dimensional model.
- 8-20. Reconstructed  $^{14}\text{C}$  and  $^{36}\text{Cl}$  activities for the last 50 ka
- 8-21. Reconstructed  $^{14}\text{C}$  and  $^{36}\text{Cl}$  activities in the atmosphere for the last 20 ka
- 8-22. Simulated flux variation responses at potential repository in repository column model for 10-5-10 and 50-5-10 transient infiltration models.
- 8-23. Simulated flux variation responses at ESF in Station 57 model for 10-5-10 and 50-5-10 transient infiltration models.

### LIST OF FIGURES (continued)

- 8-24. Simulated flux variation responses in fault zones at potential repository elevation with the Repository Column model and Station 57 model for 10-5-10 and 50-5-10 transient infiltration rate models.
- 8-25. Simulated flux variation responses in faults at potential repository horizon with the Repository Column model and the Station 57 model for 50-1-10 and 50-5-10 transient infiltration rate models.
- 8-26. Simulated flux distributions in Repository Column model and Station 57 model for parameter sets 6541a and 6541b during 10-5-50 transient infiltration simulation.

### LIST OF APPENDIX FIGURES

**Note:** Figures for Appendix D are found at the end of the text for that appendix.

- D-1. Plan view of central Yucca Mountain, showing the ESF
- D-2. Explanation of stratigraphic units and map symbols
- D-3a. Geologic map of Azreal Ridge area
- D-3b. Surface infiltration map of Azreal Ridge area
- D-3c. Soil thickness map of Azreal Ridge area
- D-4a. Geologic map of Drill Hole Wash/Diabolus Ridge area
- D-4b. Surface infiltration map of Drill Hole Wash/Diabolus Ridge area
- D-4c. Soil thickness map of Drill Hole Wash/Diabolus Ridge area
- D-5a. Geologic map in the vicinity of the Sundance Fault
- D-5b. Surface infiltration map in the vicinity of the Sundance Fault
- D-5c. Soil thickness map in the vicinity of the Sundance Fault
- D-6a. Geologic map of the Antler Ridge/Whale Back Ridge area
- D-6b. Surface infiltration map of the Antler Ridge/Whale Back Ridge area
- D-6c. Soil thickness map of the Antler Ridge/Whale Back Ridge area
- D-7a. Geologic map of the vicinity of Ghost Dance Wash
- D-7b. Surface infiltration map of the vicinity of Ghost Dance Wash
- D-7c. Soil thickness map of the vicinity of Ghost Dance Wash
- D-8a. Geologic map of the Boundary Ridge area
- D-8b. Surface infiltration map of the Boundary Ridge area
- D-8c. Soil thickness map of the Boundary Ridge area

**Evaluation of Flow and Transport Models of Yucca Mountain,  
based on Chlorine-36 Studies for FY97**

by

J. T. Fabryka-Martin<sup>1</sup>, A. L. Flint<sup>2</sup>, D. S. Sweetkind<sup>2</sup>, A.V. Wolfsberg<sup>1</sup>, S. S. Levy<sup>2</sup>,  
G. J. C. Roemer<sup>1</sup>, J. L. Roach<sup>1</sup>, L. E. Wolfsberg<sup>1</sup>, and M. C. Duff<sup>1</sup>

**ABSTRACT**

The objective of the Water Movement Test activity is to acquire geochemical and isotopic data relevant to the development and testing of conceptual flow and transport models of the unsaturated zone at Yucca Mountain. More than 600 samples have been analyzed for <sup>36</sup>Cl from deep and shallow boreholes, soil profiles, ground water, and the Exploratory Studies Facility (ESF). These data have been used to establish lower bounds on infiltration rates, estimate ground-water ages, establish bounding values for hydrologic flow parameters governing fracture transport, and develop a conceptual model for the distribution of fast flow paths.

The most extensive set of <sup>36</sup>Cl data for Yucca Mountain is from the ESF. The signals in the northern part of the ESF are highly variable and elevated above present background levels. At several locations, the measured signals are high enough to be unambiguous indicators of at least a small component of bomb-pulse <sup>36</sup>Cl, implying that some fraction of the water at the ESF level arrived there during the past 50 years. In the southern part of the ESF, the <sup>36</sup>Cl signals are less variable and at levels equal to or slightly below present-day background. Detailed characterization of the structural settings of the <sup>36</sup>Cl sample locations and of their relationships to structural features and infiltration rates has generally supported the proposed conceptual model for fast pathways at Yucca Mountain. In order to transmit bomb-pulse <sup>36</sup>Cl to the sampled depth within 50 years, the model requires the presence of faults that cut the PTn unit and increase its fracture conductivity, sufficiently high infiltration to initiate and sustain fracture flow through the PTn, and a less than 3 meters of soil cover. The model was used to predict the distribution of bomb-pulse <sup>36</sup>Cl for the study area, including the planned East-West drift. A case-by-case evaluation of the model's ability to account for the presence or absence of bomb-pulse <sup>36</sup>Cl concluded that the model successfully predicted the presence of bomb-pulse <sup>36</sup>Cl in most cases but did not adequately account for the apparent lack of bomb-pulse <sup>36</sup>Cl in the southern part of the ESF.

Cl concentrations measured in porewater from the PTn in the North Ramp range from 15 to 45 mg/L and, based on their low Br/Cl ratios, have not been influenced by ESF construction water. These low Cl concentrations are consistent with the Flint et al. (1996) infiltration model. Their uniformity suggests that the flux through the PTn matrix is on the order of 5 mm/yr at this location. Also, because the lower values approach those measured in perched water at Yucca

---

<sup>1</sup> Los Alamos National Laboratory, Los Alamos, NM.

<sup>2</sup> U.S. Geological Survey, Denver, CO.

Mountain, these results support a conceptual model that does not need to invoke fracture flow through the PTn to explain the perched water chemistry.

The  $^{36}\text{Cl}$  data are consistent with  $^{14}\text{C}$  data and with the results of solute-transport simulations suggesting that groundwater travel times are less than 10,000 years everywhere in the unsaturated zone at Yucca Mountain. Low  $^{36}\text{Cl}/\text{Cl}$  ratios measured for some samples from the southern part of the ESF require further evaluation in order to assess whether or not these ratios provide evidence for longer groundwater travel times.

Some discrepancies exist between the  $^{36}\text{Cl}$  data, the conceptual model for flow and transport, and the numerical solute transport simulations. Actions needed to resolve these discrepancies include a re-assessment of PTn hydrologic properties, the incorporation of porewater Cl concentrations into the flow-model calibration process, independent evidence to confirm the infiltration model, corroborating evidence to confirm the bomb-pulse  $^{36}\text{Cl}$  results, and an expanded data base of porewater Cl measurements.

## 1. INTRODUCTION

### 1.1 Background

Yucca Mountain, Nevada, is under investigation as a potential site at which to host the Nation's first repository for commercial high-level radioactive waste. The investigation is sponsored by the U.S. Department of Energy and conducted by several Federal agencies and laboratories. The site is in the northern Mojave Desert and lies 150 km northwest of Las Vegas in southern Nevada. The landform is composed of alternating layers of interbedded welded and nonwelded tuffs that have been uplifted and tilted, fractured and faulted. About 500 to 750 meters of unsaturated rock are present at the site. An understanding of the rates and pathways of water movement at a potential repository site is critical in order to assess its probable performance in isolating these wastes from the accessible environment. Such a task at the Yucca Mountain site is complicated by the extremely low moisture fluxes, the great thickness of the unsaturated zone, the heterogeneity of the rock units, and uncertainties about past and future climatic variations.

In the 1980s, the Yucca Mountain Site Characterization Project (YMP) began drilling a series of deep and shallow boreholes to permit access by investigators to characterize hydrologic, geologic and material properties of the unsaturated and saturated zones at Yucca Mountain (Figure 1-1). Early in 1995, construction began on the Exploratory Studies Facility (ESF), a 8-km long tunnel, to study relevant properties of the potential repository horizon. Construction was completed by mid-1997. In contrast with surface-based drill-hole studies, examination of the tunnel exposures allows detailed characterization of the petrologic and structural settings of sample sites. The silicic tuffs exposed in the ESF include three main stratigraphic units of the Miocene Paintbrush Group: the mostly welded Tiva Canyon Tuff, an underlying interval of variably welded pyroclastic deposits, and the mostly welded Topopah Spring Tuff, in order of increasing age and depth. The stratigraphic interval within the Paintbrush Group at Yucca Mountain that extends from the base of the densely welded and devitrified portion of the Tiva Canyon Tuff downward to the top of the densely welded portion of the underlying Topopah Spring Tuff corresponds to the Paintbrush nonwelded (PTn) hydrologic unit (Montazer and Wilson, 1984; Ortiz et al., 1985), used in flow and transport modeling efforts.

The particular technique that is the focus of this report is the application of chlorine-36 ( $^{36}\text{Cl}$ ) and halide analyses to the evaluation of alternative conceptual models for flow and transport processes in the unsaturated zone at Yucca Mountain. Chlorine-36 is a radioactive isotope produced in the atmosphere and carried underground with percolating groundwater. Where the residence time of groundwater is of the same order of magnitude as the  $^{36}\text{Cl}$  half-life of 301 ka (ka, thousand years), bounding limits can be established for the age of the groundwater based on the extent of decay of the meteoric  $^{36}\text{Cl}$ . High concentrations of this isotope were also added to meteoric water during a period of global fallout from atmospheric testing of nuclear devices, primarily in the 1950s. This bomb-pulse signal can be used to test for the presence of fast transport paths. Because of the variable influence of evapotranspiration, the  $^{36}\text{Cl}$  concentration is generally reported relative to the concentration of stable chloride (Cl) in a given sample.

Because its concentration is assumed to be directly proportional to loss of water by evapotranspiration, Cl by itself is also useful as an independent indicator of surface infiltration rates. Working in conjunction with its USGS colleagues, Los Alamos National Laboratory (LANL) has analyzed soil, rock and water samples from boreholes and the ESF in order to identify fast flow paths and to estimate residence times for groundwater at this site based upon measurements of Cl, bromide (Br) and  $^{36}\text{Cl}$  concentrations in salts in rock and soil porespaces and on fracture surfaces.

## 1.2 Objectives and organization of this report

The objectives of this report are: (1) to summarize the available data about the subsurface distribution of  $^{36}\text{Cl}$ , and (2) to assess alternative conceptual models about flow and transport through the unsaturated zone at Yucca Mountain, based on their consistency with the subsurface distribution of  $^{36}\text{Cl}$  and other environmental tracers. The current report incorporates data and discussion from a number of recent reports on this subject (Fabryka-Martin et al., in press [a]; Fabryka-Martin et al., in press [b]; Levy et al., 1997; Sweetkind et al., 1997a; Robinson et al., 1997), as well as presenting new data. This report summarizes sample collection, analytical data, and transport calculations for  $^{36}\text{Cl}$  as of September 1997. It updates reports prepared in previous years on this subject (Fabryka-Martin et al., 1993; Fabryka-Martin and Liu, 1995) and also incorporates much of the work in a companion report on sampling, analysis and transport simulations of  $^{36}\text{Cl}$  in the ESF as an indication of infiltration processes at the depth of the potential repository horizon (Fabryka-Martin et al., in press [b]). Because some aspects of the data interpretation remain inconclusive at the present time, this document should be viewed as an interim status report.

This report is organized as follows:

- Section 2 provides an overview of issues about surface infiltration rates and processes at Yucca Mountain, and about the redistribution of these percolating fluids in the deeper unsaturated zone.
- Section 3 reviews the various sources of  $^{36}\text{Cl}$  in the hydrologic environment: atmospheric production by cosmic rays, global fallout from nuclear weapons testing, local sources from Nevada Test Site activities, and production in rocks and soils by cosmogenic and nucleogenic processes.
- Section 4 describes the analytical methods used to process and analyze samples for anion and  $^{36}\text{Cl}$  concentrations, and presents data for soils, boreholes, ESF rocks, and waters. Statistical analysis of the extensive ESF data set is used to establish the threshold for identifying the presence of bomb-pulse  $^{36}\text{Cl}$ .
- Section 5 summarizes  $^{36}\text{Cl}$  and halide distributions in soils and shallow boreholes, and their implications for shallow infiltration rates and processes, based on the Cl mass balance

method and the distribution of bomb-pulse  $^{36}\text{Cl}$ .

- Section 6 summarizes the available data on  $^{36}\text{Cl}$  signals in deeper samples from the ESF and deep surface-based boreholes. Alternative hypotheses are presented for interpreting the data, each with different implications for deep percolation rates, flowpaths, and groundwater travel times. The data are examined relative to their relationship to infiltration rates, soil thicknesses, and structural features. Trend analyses of specific structural parameters, such as fault density and joint orientation, provide an evaluation of the significance of each in controlling the distribution of bomb-pulse  $^{36}\text{Cl}$  in the ESF.
- Section 7 provides an overview of the origin and timing of fracture mineral coatings and examines the extent to which these minerals may provide a guide to the recognition of fast paths, stagnant zones, and connected fracture paths.
- Section 8 summarizes a comparison between the measured  $^{36}\text{Cl}/\text{Cl}$ ,  $\text{Cl}$  and  $^{14}\text{C}$  signals to those predicted by solute transport calculations using the flow and transport model FEHM. These simulations illustrate how the environmental data are used to bound the range of hydrologic parameters, evaluate alternative conceptual models of flow and transport at the site, and develop estimates of groundwater travel times.
- Section 9 summarizes the observations and conclusions in this report, and presents conceptual models for the unsaturated flow system at Yucca Mountain, the distribution of fast paths, and the origin of perched water. Aspects which would benefit from additional work are noted.
- Appendices to this report contain:
  - A) a listing of ESF samples collected for  $^{36}\text{Cl}$  analysis,
  - B)  $^{36}\text{Cl}$  analytical results for ESF samples,
  - C) detailed structural and mineralogic characterization of ESF sampling sites, and
  - D) a case-by-case evaluation of the distribution of  $^{36}\text{Cl}$  in the ESF, based on a set of  $\sim 1 \text{ km}^2$  maps showing the relationship of  $^{36}\text{Cl}$  analytical results to faults, surface geology, surface infiltration rates, and soil thicknesses.
- Appendix E tabulates the Q-status of new and revised data appearing in this report.

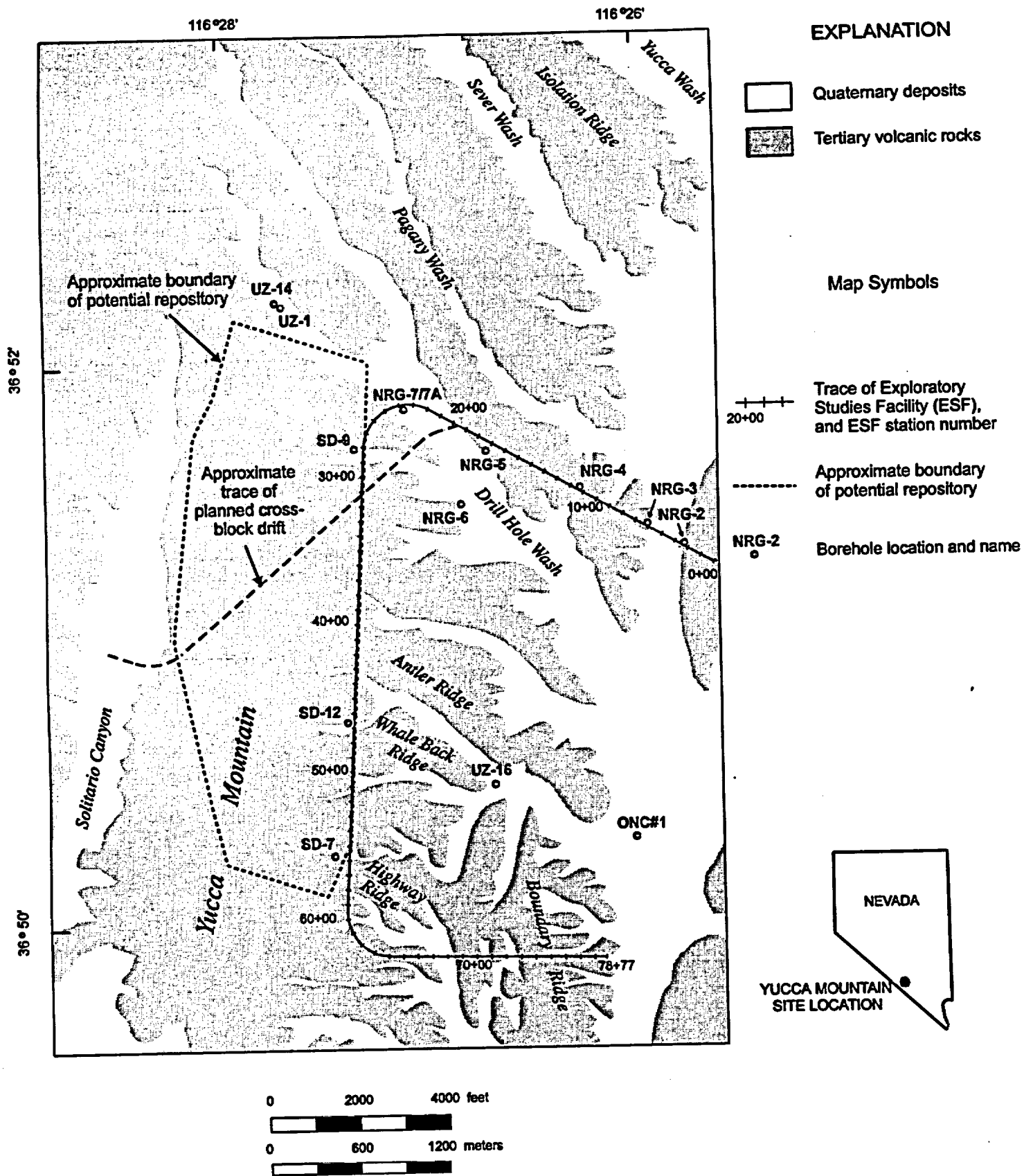


Figure 1-1. Index map of Yucca Mountain, Nevada, showing the trace of the ESF and locations of selected boreholes.

## 2. GEOLOGIC AND HYDROLOGIC SETTING

This section describes the geologic framework at Yucca Mountain and provides overviews of the conceptual models for surface infiltration at the site and for redistribution of these percolating fluids in the deeper unsaturated zone. Caveats about infiltration and percolation processes presented at the end of this section are intended to correct common misconceptions that can lead to misinterpretation or inaccurate representation of data and flow models.

### 2.1 Geologic framework

Yucca Mountain is located within the southern portion of the southwestern Nevada volcanic field in an area where a thick section of Tertiary volcanic rocks overlie Paleozoic sedimentary strata (Byers et al., 1976). These strata record the evolution of at least seven calderas that compose the Timber Mountain-Oasis Valley caldera complex (Sawyer et al., 1994). The study area consists of a series of north-trending, eastward-dipping structural blocks that are bounded by mostly west-dipping normal faults (Carr et al., 1986). These fault blocks are composed principally of thick, welded ash-flow tuff deposits that are separated by thinner, silicic lavas, and tuffaceous sedimentary units. Formations of the Paintbrush Group (Table 2-1) erupted from 12.8 to 12.7 Ma and form most of the exposures in the study area (Sawyer et al., 1994; Christiansen and Lipman, 1965; Scott and Bonk, 1984). Yucca Mountain is underlain by two densely welded and devitrified ash-flow tuffs (the Tiva Canyon and Topopah Spring Tuffs) that are separated by a comparatively thin interval of mostly nonwelded, vitric pyroclastic deposits referred to as the PTn (Paintbrush Tuff nonwelded). These deposits include the Yucca Mountain and Pah Canyon Tuffs, which are negligible to the south of the study area, nonwelded within the study area, and relatively thick to the north, where portions can be densely welded (Moyer et al., 1996). Underlying the Topopah Spring Tuff is the rhyolitic Calico Hills Formation (nonwelded and referred to as CHn), and the Prow Pass and Bullfrog Tuffs of the Crater Flat Group. These rocks are primarily zeolitized with relatively thin zones of increased welding and devitrification and are separated by thin bedded tuff units (Moyer and Geslin, 1995).

Throughout this report, certain stratigraphic intervals will be referred to by using hydrogeologic and thermal-mechanical unit nomenclature as informally defined by Montazer and Wilson (1984) and Ortiz et al. (1985). Montazer and Wilson (1984) originally subdivided subsurface geological units into five major hydrogeological units on the basis of degree of welding as follows:

- 1) The Tiva Canyon welded unit (TCw) including the moderately to densely welded portions of the Tiva Canyon Tuff of the Paintbrush Group (Sawyer et al., 1994) (Table 2-1). In this definition, lithostratigraphic units overlying the moderately to densely welded portions of the Tiva Canyon Tuff, including uppermost nonwelded, vitric Tiva Canyon Tuff and younger tuffs and tuffaceous sedimentary units, are referred to as undifferentiated overburden (UO, Table 2-1).
- 2) The Paintbrush nonwelded unit (PTn) consisting of the stratigraphic interval within the Paintbrush Group that extends from the base of the densely welded portion of the Tiva Canyon Tuff downward to the top of the densely welded portion of the underlying

Table 2-1. Generalized lithostratigraphy of Yucca Mountain area and ages

Lithostratigraphic Nomenclature <sup>1</sup>	Age (Ma)	Hydrogeologic unit <sup>2</sup>
<b>TIMBER MOUNTAIN GROUP (Tm)</b>		
Rainier Mesa Tuff (Tmr)	11.6	
<b>PAINTBRUSH GROUP</b>		UO
Tiva Canyon Tuff (Tpc)	12.7	
crystal-rich member (Tpcr)		
vitric zone (Tpcrv)		
nonlithophysal zone (Tpcrn)		
lithophysal zone (Tpcrl)		
crystal-poor member (Tpcp)		TCw
upper lithophysal zone (Tpcpul)		
middle nonlithophysal zone (Tpcpmn)		
lower lithophysal zone (Tpcpll)		
lower nonlithophysal zone (Tpcpln)		
vitric zone (Tpcpv)		
Pre-Tiva Canyon Tuff bedded tuff (Tpbt4)		
Yucca Mountain Tuff (Tpy)		
Pre-Yucca Mountain Tuff bedded tuff (Tpbt3)		PTn
Pah Canyon Tuff (Tpp)		
Pre-Pah Canyon Tuff bedded tuff (Tpbt2)		
Topopah Spring Tuff (Tpt)	12.8	
crystal-rich member (Tptr)		
vitric zone (Tptrv)		
nonlithophysal zone (Tptrn)		
lithophysal zone (Tptrl)		
crystal-poor member (Tptp)		TSw
upper lithophysal zone (Tptpul)		
middle nonlithophysal zone (Tptpmn)		
lower lithophysal zone (Tptpll)		
lower nonlithophysal zone (Tptpln)		
vitric zone (Tptpv)		
Pre-Topopah Spring Tuff bedded tuff (Tpbt1)		
<b>CALICO HILLS FORMATION (Tac)</b>	12.9	
Bedded tuff (Tacbt)		
Basal sandstone (Tacbs)		CHn
<b>WAHMONIE FORMATION (Tw)</b>	13.0	
<b>CRATER FLAT GROUP</b>		
Prow Pass Tuff (Tep)		
Pre-Prow Pass bedded tuff (Tepbt)		
Bullfrog Tuff (Teb)	13.5	
Tram Tuff (Tet)		CFu

<sup>1</sup> Group and Formation names, shown in bold type, are formal stratigraphic nomenclature after Sawyer et al. (1994). Member designations, zonal subdivisions, and unit abbreviations are informal and follow the usage of Buesch et al. (1996).

<sup>2</sup> Following the usage of Montazer and Wilson (1984) and Ortiz et al. (1985).

Topopah Spring Tuff (Buesch et al., 1996). This interval includes parts or all of four formations (the Tiva Canyon Tuff, the Yucca Mountain Tuff, the Pah Canyon Tuff, and the Topopah Spring Tuff) and three informally designated interstratified bedded tuff units (Moyer et al., 1996) (Table 2-1).

- 3) The Topopah Spring welded unit (TSw) consisting of the moderately to densely welded portions of the Topopah Spring Tuff of the Paintbrush Group (Sawyer et al., 1994), including the densely welded basal vitrophyre (Buesch et al., 1996) (Table 2-1).
- 4) The Calico Hills nonwelded unit (CHn) includes the stratigraphic interval that extends from the base of the densely welded portion of the Topopah Spring Tuff downward to the top of the welded portion of the Bullfrog Tuff of the Crater Flat Group (Sawyer et al., 1994). This interval includes parts or all of four formations and various interstratified nonwelded tuffaceous units, including: the basal vitric portion of the Topopah Spring Tuff; the Calico Hills Formation; the Prow Pass Tuff of the Crater Flat Group (Sawyer et al., 1994); and the non- to partially-welded upper portion of the Bullfrog Tuff of the Crater Flat Group (Sawyer et al., 1994) (Table 2-1).
- 5) The Crater Flat undifferentiated unit (CFu), consisting of the lower Bullfrog and Tram Tuffs of the Crater Flat Group (Sawyer et al., 1994), and interbedded tuffs (Table 2-1).

The central part of Yucca Mountain that includes the potential repository occupies a relatively undeformed block, called the central block, bounded by major, or block-bounding, faults (Figure 2-1a). Block-bounding faults within the vicinity of this central block of Yucca Mountain include the Solitario Canyon, Bow Ridge, and Dune Wash faults. All of these major faults dip 60° to 70° to the west and commonly have experienced hundreds of meters of Tertiary displacement of Miocene Paintbrush Group tuffs, with subordinate amounts of strike-slip motion (Scott and Bonk, 1984; Day et al., in press). In some places, Quaternary offset has been documented on these faults (Simonds et al., 1995). Faults that lie entirely within the structural blocks defined by the block-bounding faults may be described as intrablock faults. Intrablock faults are nearly vertical, have 1-30 m of displacement, and typical mapped lengths of less than 1 km (Day et al., in press). The largest intrablock fault, the Ghost Dance fault (Figure 1-1), has up to 25 m of stratigraphic offset. Other important intrablock faults include the Sundance fault, faults in the hanging-wall of the Bow Ridge fault (part of the "imbricate fault zone" of Scott, 1990), and the Drill Hole Wash fault.

## 2.2 Conceptual model of surface infiltration

A conceptual model of the spatial distribution of net infiltration was developed by Flint et al. (1996). The model describes the effect that observed processes of precipitation, runoff, evapotranspiration, and redistribution of water in the shallow unsaturated zone have on net infiltration. Field measurements of water content profiles from neutron probes at the soil-bedrock interface indicate that periodic fracture flow is initiated when the soil becomes saturated, or nearly saturated, at the interface. The amount and timing of precipitation, combined with soil thickness, soil properties, and bedrock properties, determine if infiltrated precipitation can percolate below the zone dominated by evapotranspiration to the soil/bedrock interface to

become potential recharge. The spatial and temporal distribution of precipitation and the spatial distribution of soil thickness are the most important factors in determining if net infiltration would occur (slope, aspect, and bedrock properties being secondary controlling factors). The hydrologic properties of the bedrock underlying shallow soils (the mappable bedrock in Figure 2-1a) control the amount of net infiltration at a given location, once the conditions exist that would allow net infiltration to occur (high saturation at the tuff/alluvium contact).

In arid environments, deep (greater than 3 meters) soils and alluvial fill in washes have small net infiltration (at the soil-bedrock interface) due to low average annual precipitation, high storage capacity, deep root zones, and high evapotranspiration (Flint and Flint, 1995; Flint et al., 1996). The presence of faults or fractures in bedrock underlying deep soil has little effect on the magnitude of deeper infiltration because the thicker soils store more water, retarding the percolation of the wetting front and allowing for evapotranspiration to occur before fracture flow can be initiated (Hevesi et al., 1996). Infiltration rates in upland areas with shallow (less than 3 m) soils are much more sensitive to the hydrologic properties of the underlying bedrock because the soils have low storage capacity and shallow root zones, allowing water to contact the underlying bedrock following long-duration, low-intensity winter storms or short-duration, high-intensity summer storms (Flint and Flint, 1995). Topographically high areas with thin soil cover underlain by fractured or porous bedrock, such as the vapor-phase altered upper portion of the crystal-rich member of the Tiva Canyon Tuff, are settings considered most favorable for high net infiltration (Flint and Flint, 1995). Faults underlying thin soils in such locations may be the most likely areas for initiating fast flow paths for surface infiltration (Flint et al., 1996).

A big caveat to the above conditions for initiation of a fast path is that they may not adequately account for enhanced infiltration due to channel runoff events. A channel is the small part of a wash, generally no more than a few meters wide, that actively collects and concentrates surface runoff. Water can be concentrated in channels during episodic runoff events and wetting fronts can penetrate to depths of 10 m or more, well below the root zone, in less than a year. This mechanism probably does not contribute significantly to net infiltration on a site-wide scale because of the infrequency of runoff events and because the channels comprise only a small percentage of the watershed (Flint and Flint, 1995). Nonetheless, it may be important for initiating fast paths. If the channel alluvium is shallow (less than about 3 m), the storage capacity may be exceeded by the runoff such that saturated or near-saturated conditions will occur at the alluvium/tuff interface and initiate fracture flow. On the other hand, paleosols or cemented carbonate horizons often develop within several meters of the surface at Yucca Mountain. These conditions may cause lateral redistribution of the infiltration such that the occurrence of channel flow does not necessarily indicate enhanced infiltration rates along its full length. Under deeper soil (>10 m), the wetting front is diffuse and would not increase saturations at the tuff/alluvial contact to the extent necessary to initiate fracture flow into the bedrock.

The conceptual model described above provided the basis for the development of a site-scale numerical model, in which net infiltration is predicted for over 250,000 30-m grid cells in the study area as a function of spatially and temporally variable precipitation (Figure 2-2) (Flint et

al., 1996). For precipitation during an average year (~170 mm), net infiltration estimates range from zero for a soil thickness of 6 m or more, to over 50 mm/yr for a thin soil on north-facing slopes and at high elevations overlying highly-permeable bedrock. Infiltration averages 3.8 mm/yr for the site over the potential repository area and approximately 6 mm/yr for the area shown in Figure 2-2. On a year-to-year basis, the site-wide average net infiltration ranges from zero for dry years, to over 20 mm/yr when annual precipitation exceeds 300 mm (Flint et al., 1996).

In general, average annual infiltration is reported but it should be noted that the temporal distribution of this infiltration is significant within any given year (Flint et al., 1996). Net infiltration generally occurs in the winter over a 3- to 4-week period, with one to two significant infiltration events occurring in a single year. Three out of the last 17 years have produced significant runoff, whereas five or six out of the last 17 years are estimated to have produced significant net infiltration over the potential repository area. Portions of the site-scale infiltration map for an average precipitation year are shown in Appendix D for the purpose of characterizing infiltration conditions above the ESF and selected boreholes. Each of the eight partial maps covers an area of about 1 km by 1 km, corresponding to companion maps on surficial geology and structural features and on alluvial depth.

The numerical model for infiltration is based upon the results of detailed mapping of surface soils, bedrock and precipitation (Flint et al., 1996). Detailed field and laboratory measurements of soil and rock properties are used to develop the necessary spatially distributed model properties. The measured properties were used to define the average property for each surface map unit, both surficial material and underlying bedrock. For each grid cell, the model assigns slope, aspect, soil thickness, soil water holding capacity, and the hydraulic conductivity and water retention functions of both the soil and the underlying bedrock (including fractures). A detailed elevation model was used in conjunction with the surficial material and bedrock maps to spatially distribute estimated properties. Spatially distributed infiltration is determined, at a minimum, by the spatial distribution of the above listed properties, including precipitation. Modeling is done using daily time steps to account for daily precipitation and evapotranspiration.

Although the numerical infiltration model captures most of the spatial variability in these properties, there is some concern about missing the surface runoff events and subsurface (down slope) flow. In determining average annual net infiltration, surface runoff is accounted for by adding approximately 10 mm/yr to the calculated infiltration in the channels, which is consistent with neutron probe data collected after runoff events (Flint and Flint, 1995). Accounting for subsurface flow is more difficult. Saturated subsurface lateral flow could be sustained for at most 45 meters, in general, before evapotranspiration would stop the process (this estimate is based on saturating a 0.5 m thick soil cover, assuming a 2 mm/day evapotranspiration rate, with no additional input of water, and a 45 degree sloping surface). The typical slope lengths of 200 to 300 meters at Yucca Mountain would have continuous lateral flow both in and out of each down-slope grid square. The 30-m spacing used for the grid squares in the model is generally large enough so that lateral flow is self-contained. The one-dimensional assumption for

infiltration, therefore, would only cause slight errors, and only at the base of slopes. For the first approximation of spatially distributed infiltration, these errors are assumed to be minimal.

### **2.3 Conceptual model of subsurface fluxes**

A detailed conceptual model of unsaturated zone hydrology at Yucca Mountain continues to be refined (Kwicklis et al., 1997, in preparation). Early conceptual models of the unsaturated zone were developed by Winograd (1981), Scott et al. (1983) and Montazer and Wilson (1984). These concepts are now being revised in light of recent hydrochemical data bases (Fabryka-Martin et al., 1996; Flint et al., 1996; Bodvarsson et al., 1997; Levy et al., 1997; Yang et al., 1996, 1997; Paces et al., 1996; Robinson et al., 1997) as well as updated laboratory and field observations from hydrologic, mineralogic, and structural studies. The challenge is to integrate these diverse data sets and to develop self-consistent and testable conceptual models of flow and transport based on them. This section provides a general, simplified overview of the conceptual flow model as it is currently envisioned by the authors of this report (Figure 2-3). The issues of alternate conceptual models are addressed in section 6.1 in this report.

#### ***2.3.1 Hydrologic Framework***

Data collection has been an integral part of the characterization of the hydrologic framework and the conceptual model of the unsaturated zone at Yucca Mountain. The analysis of hydrologic properties and surface infiltration data has led to the development of a conceptual and numerical model of infiltration (Flint et al., 1996). Subsurface hydrologic properties and results of the infiltration model have formed a basis for the development of a conceptual and numerical model of subsurface flow (Bodvarsson et al., 1997). The combination of the surface and subsurface hydrologic and geologic data, when combined with geochemical data, provide the basis for our current understanding of the unsaturated zone at Yucca Mountain.

#### ***2.3.2 Distribution of Hydrologic Properties***

The surface exposures over the study area incorporate rocks with a large range of properties leading to varying degrees of infiltration of surface water. Over the potential repository area, the rocks are generally the fractured welded rocks from the crystal-poor member of the Tiva Canyon Tuff, and the crest of the mountain is composed of higher porosity, less fractured rocks of the crystal-rich member of the Tiva Canyon Tuff. Several exposures of high-porosity, relatively unfractured PTn rocks are scattered around the study area, particularly in downcut washes to the south and north of the potential repository area. Ridgetops to the north of the potential repository area are composed of highly-fractured vitric rocks that form the uppermost part of the crystal-rich member of the Tiva Canyon Tuff. Matrix properties, including porosity, bulk density, particle density, saturated-hydraulic conductivity ( $K_s$ ) and moisture retention characteristics (Flint, 1996) of volcanic tuffs, have been specifically determined for the rocks of the Tiva Canyon, Yucca Mountain, Pah Canyon, and Topopah Spring Tuffs and interlayered bedded tuffs, as well as the Calico Hills Formation and Prow Pass Tuff. These properties have been

associated with each of the lithostratigraphic units mapped by Scott and Bonk (1984) and were combined with estimates of fracture densities and fracture apertures to estimate hydraulic conductivities (Flint et al., 1996).

### *2.3.3 Conceptual model of percolation*

The following discussion constitutes one conceptual view of water that has moved below the zone of evapotranspiration (discussed in section 2.2). Water can percolate through the unsaturated zone through a variety of pathways:

- Downward migration through the TCw occurs via rapid fracture flow to the top of the PTn. This aspect of the conceptual model is supported by neutron hole data presented by Flint and Flint (1995) and the extensive presence of bomb pulse <sup>36</sup>Cl data in virtually all TCw samples retrieved from boreholes (Fabryka-Martin et al., in press [b]). TCw permeabilities are on the order of 2 mm/yr with 10 fractures per meter (f/m) (Flint et al., 1996). Groundwater ages in the TCw are young with the exception that porewater in the matrix, although a small component of the total flow may be very old due to low matrix permeabilities.
- A transition from fracture-dominated flow to matrix-dominated flow occurs when the flow enters the PTn, under low infiltration rates and with the exception of discrete fracture flow paths associated with faulting. Under high infiltration rates, fracture flow through the PTn may be more predominant but is still far less than half of the total water flux through this unit. The PTn matrix material has relatively high permeabilities (20,000 mm/yr) and porosities (approximately 30%) and low fracture densities (2 f/m, Flint et al., 1996). The young water entering the PTn ages as it flows through the matrix. With current properties, PTn thickness variability, and flux variability, the ages of matrix water at the bottom of the PTn should generally be between 500 and 20,000 years. Under zones of very low infiltration, the ages will even be larger.
- The transition process from fracture to matrix flow in the PTn is expected to damp out most of the climate variability that occurs seasonally and even on the scale of decades, if not the extreme events with recurrence intervals of a century. Fault zones that provide continuous fracture pathways through the PTn may only slightly damp climate variability.
- The matrix-dominated flow in the PTn must then transition to fracture-dominated flow as it enters the underlying TSw. In the repository area, the TSw permeability is on the order of 2 mm/yr but with fracture densities of 20 f/m. The fracture-dominated flow in the TSw allows for fast travel times from the base of PTn to the top of the vitrophyre at the base of the TSw regardless of the travel time through the PTn. Thus, water ages at the bottom of the Tsw should be similar to those at the bottom of the PTn. As we the
- Lateral diversion is possible and can lead to formation of perched water bodies on the down-dropped sides of large normal faults at the level of the TSw basal vitrophyre, particularly under flux rates greater than 1 to 2 mm/yr (Robinson et al., 1997). Exceptions are where the vitrophyre is missing or where it is disrupted by complex tectonic breaks at intersecting faults. Lateral flow from high-percolation zones, combined with fast vertical flow component, leads to mixed perched-water chemistry with low Cl on top of the vitrophyre.
- Relatively slow seepage from perched water bodies, as well as seepage along the lateral-flow

path, occurs through fractures in the vitrophyre and these waters mix with CHn porewaters (Robinson et al., 1997). At low percolation rates or where the vitrophyre does not present a barrier to local vertical flow, the vertical component of the water flux is unimpeded such that flow reaches the top of the CHn. Complex flow in CHn occurs due to interlayered vitric and zeolitized rocks. Where the TSw basal vitrophyre is non-existent or bypassed by fracture flow, a permeability barrier may occur in the zeolitic CHn unit and lead to the formation of perched water and lateral flow with a small component of seepage via fractures and matrix flow from base of CHn to the saturated zone.

#### *2.3.4 Unresolved flow and transport issues*

Some of the key questions that are still under evaluation about flow and transport processes in the unsaturated zone at Yucca Mountain are as follows:

- Is there evidence that a significant amount of lateral flow occurs at contacts between welded and nonwelded units, such as the TCw and the underlying nonwelded PTn, due to possible capillary or permeability barriers occurring between these two units? Does lateral flow occur within the nonwelded units because of the significant difference between vertical and horizontal hydraulic conductivities? Does it take place at the Calico Hills zeolitic unit, the TSw basal vitrophyre, or other units? Could lateral diversion result in flow paths that bypass the Calico Hills unit to the saturated zone?
- How should fast paths be modeled? Is their distribution predictable? What fraction of flow occurs in these pathways? Do the pathways change with time? Are fast paths important to the occurrence of future seeps in subsurface excavations?
- How important are short-term and long-term transient flow processes?
- Is there evidence that infiltrating water reaches the Calico Hills nonwelded (CHn) unit via fractures or faults in the TSw unit? Could fracture flow result in flow paths that bypass the Calico Hills unit to the saturated zone?
- What is the nature of matrix/fracture interactions?
- What is the origin and stability of perched water bodies encountered at Yucca Mountain? How extensive are they? What does the chemistry of the perched water as compared to UZ matrix water imply about matrix/fracture interactions?
- What range of matrix and fracture properties should be used in flow and transport simulations? Do these vary spatially, e.g., are they different in faulted zones?
- What types of data are suitable for flow and transport model calibration?

Future work on gathering and interpreting additional geochemical and isotopic data for Yucca Mountain, such as those data presented in this and other reports, should focus on their implications for resolving these issues.

## 2.4 Caveats about infiltration and percolation processes

The following points are made in order to correct common misconceptions about flow and transport processes.

*Velocity vs flux.* The presence of a fast path, e.g., as indicated by the detection of bomb-pulse  $^{36}\text{Cl}$ , does not necessarily mean a high flux. The presence of bomb-pulse  $^{36}\text{Cl}$  can not by itself indicate the magnitude of the flux, but only that a portion of the flux is moving along a fast path consisting of a continuous fracture pathway extending from the surface to the sample location. In other words, the  $^{36}\text{Cl}/\text{Cl}$  signal is a function of travel time—which is determined by both flux and by the nature of the flowpath, and not by flux alone. As shown by solute transport modeling in Fabryka-Martin et al. (in press [a]), bomb-pulse  $^{36}\text{Cl}$  signals can result even if the component of the total flux that occurs as fracture flow is a small fraction ( $\ll 1\%$ ) of the total flux. Conversely, the same simulation approach shows that high fluxes can be consistent with long travel times to the ESF, without carrying any bomb-pulse  $^{36}\text{Cl}$  to-depth, if there are no continuously connected fracture paths present (particularly through the PTn).

*Channels vs washes:* Active channels constitute a relatively small areal coverage over Yucca Mountain, generally 1 to 2 percent (Flint et al., 1996). On the other hand, alluvial-filled washes cover a much larger area. During large precipitation events, only the portion of the wash that is an active channel carries runoff and therefore has the potential to enhance infiltration rates; this mechanism is one example of "focused recharge." The remainder of the relatively flat alluvial washes only receive precipitation, not runoff, and hence do not have the potential to enhance infiltration.

*Fast flow paths vs preferential flow paths:* A fast flow path is simply a flow path that conducts water at a rate higher than the mean travel time of water. The rate selected is arbitrary in that a fast flow path could be defined as that with travel times in 60<sup>th</sup>, 70<sup>th</sup>, 80, or 90<sup>th</sup> percentiles. In the case of this work, a fast flow path is defined as a flow path that conducts a measurable component of bomb-pulse  $^{36}\text{Cl}$ , which means that a component of the flow was conducted to the sampled depth with a travel time of 50 years or less. It is not known whether this age is in the 99<sup>th</sup>, 90<sup>th</sup> or any other percentile because the age distribution of all of the flow pathways is not known. It is probably true, for any sample collected below the TCw unit, that the mean flow pathway travel time is always greater than 50 years. In contrast, preferential flow pathways are coalescing pathways in that several pathways come together, abandoning initially independent pathways. Examples are multiple independent fracture networks that eventually feed a single fracture, or multiple independent pathways that terminate at a flow boundary, flow laterally, then flow vertically down a fault zone.

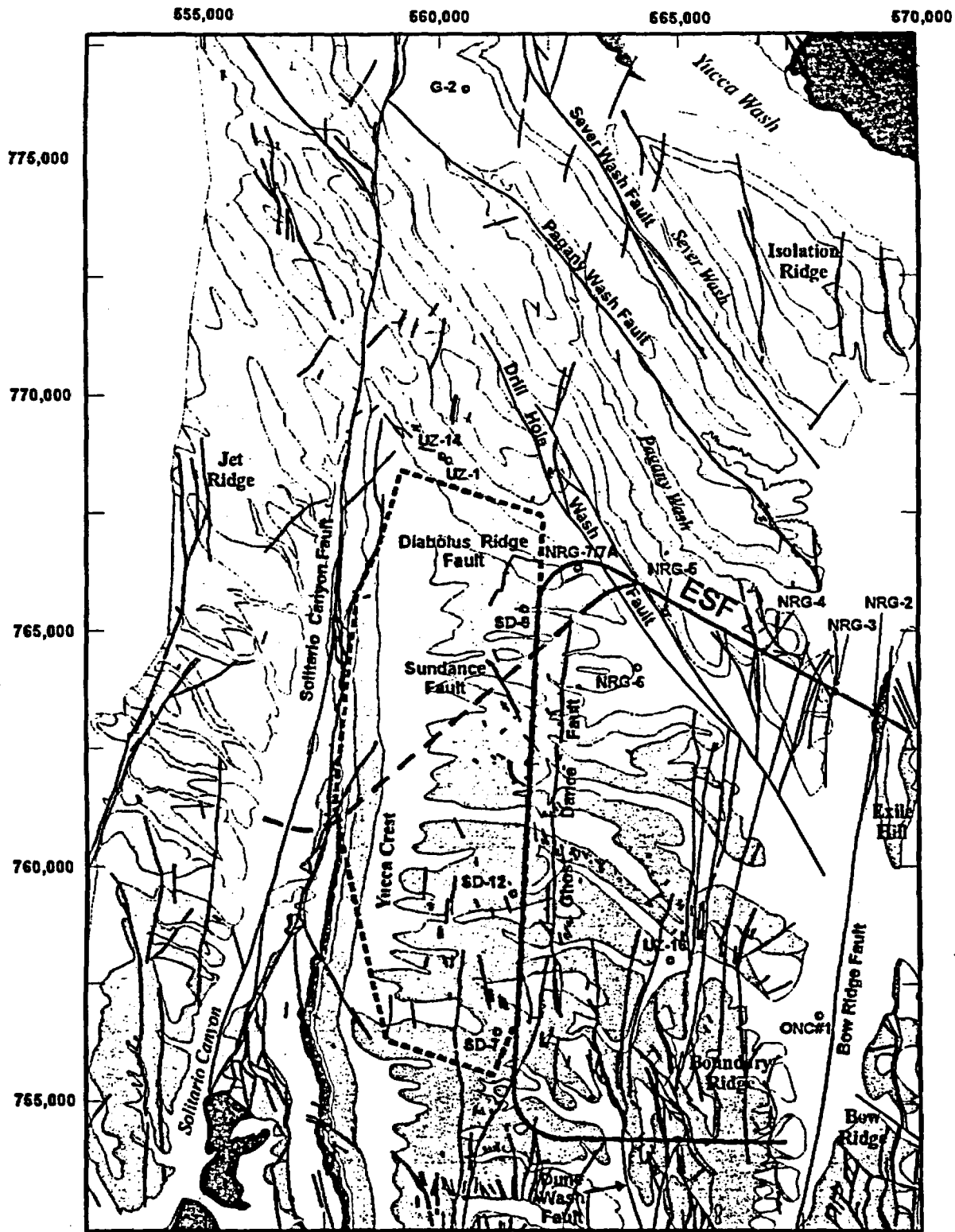


Figure 2-1a. Geologic map of Yucca Mountain, simplified from Day et al. (in press). The area depicted corresponds to the area shown on the Day et al. (in press) 1:6,000-scale geologic map of the central block of Yucca Mountain. The reference coordinates correspond to the Nevada State Plane coordinate system, in feet.

## Explanation

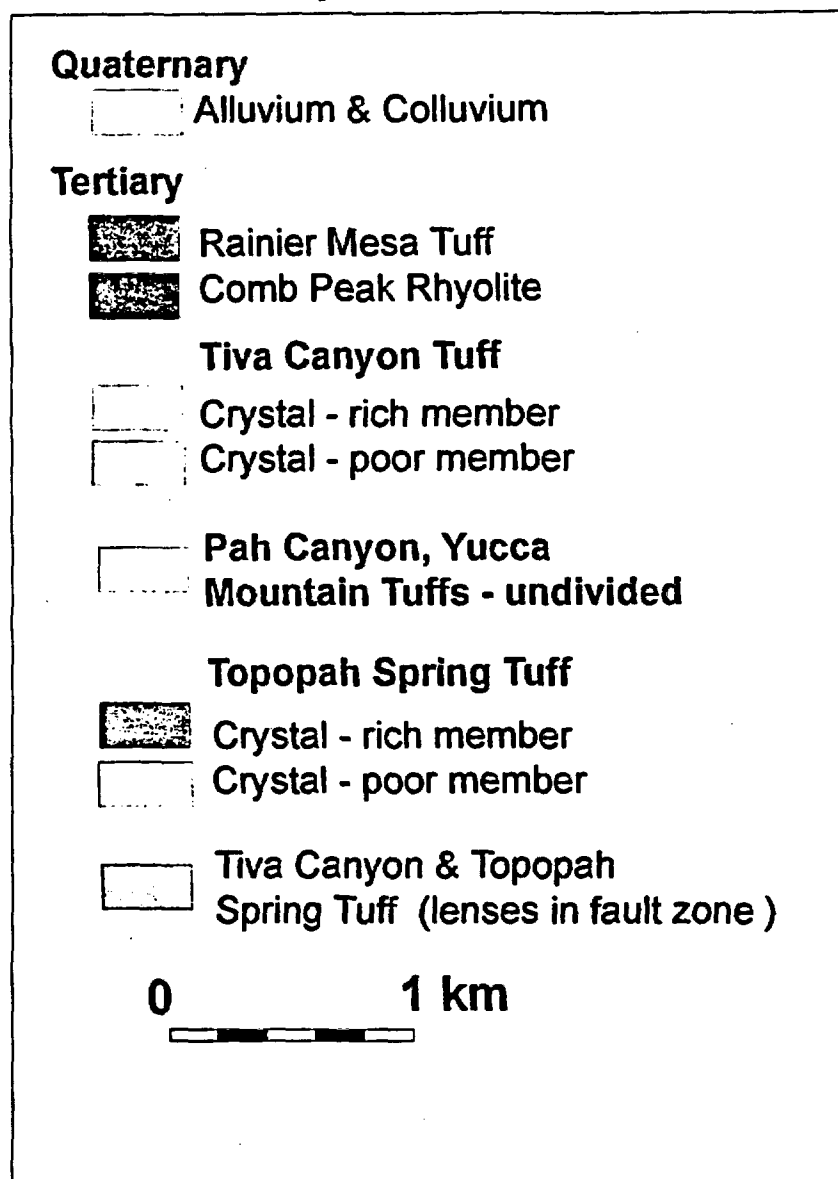


Figure 2-1b. Explanation of map units shown on Figure 2-1a. Geologic units are simplified from Day et al. (in press).



Figure 2-2. Conceptual model of infiltration for Yucca Mountain. Numerical model of infiltration, using average annual precipitation, from Flint et al. (1996). The area depicted corresponds to the area shown on Figure 2-2. The reference coordinates correspond to the Nevada State Plane coordinate system, in feet.

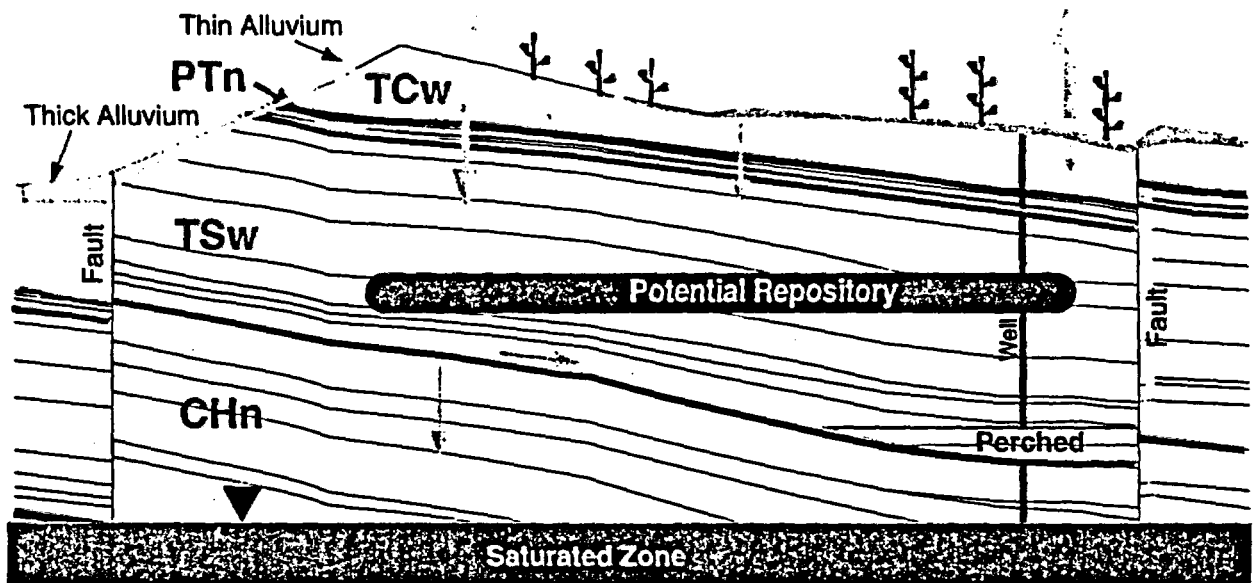


Figure 2-3. Conceptual model of hydrologic pathways at Yucca Mountain (not to scale, vertical scale is exaggerated).

### 3. CHLORINE-36 AS A HYDROLOGIC TRACER

A number of YMP studies are designed to test specific aspects of the UZ flow conceptual model by independent approaches: moisture profiling, physical properties, fracture characteristics, climate and water-budget modeling. The Cl mass balance approach, which compares Cl pore-water concentrations to rainwater concentrations as a measure of water loss by evapotranspiration, provides qualitative and quantitative information on fluxes and flow paths (section 5.1). Detection of bomb-pulse levels of atmospheric tritium,  $^{14}\text{C}$ , and  $^{36}\text{Cl}$  carried underground by percolating water provides valuable data on the types of hydrogeologic situations in which episodic fracture flow may be occurring (sections 5.2 and 5.3). Finally, the ideal indicator of long-term water movement is the spatial distribution of water travel times in the subsurface. Radiometric methods, which are based on measurements of atmospheric tritium,  $^{14}\text{C}$ , and  $^{36}\text{Cl}$ , provide a means for obtaining estimates or establishing limits on travel time as a function of location (section 6). These methods also intrinsically average many large-scale geologic heterogeneities as well as short- and long-term climatic, vegetal and geomorphic variations (Davis and Murphy, 1987). Data from this activity are being used as corroborating evidence for defining hydrologic boundary conditions, for developing and assessing alternative conceptual models, and for evaluating the travel time results of various site-scale hydrologic and solute transport models (section 8). The present activity focuses on the distribution of  $^{36}\text{Cl}$  which has a half-life of 301 ka; other YMP studies have addressed the collection and interpretation of tritium and  $^{14}\text{C}$  data (e.g., Yang et al., 1996, 1997).

About 300 soil samples, 250 water samples, 50 pack-rat midden samples, and over 1000 rock samples have been collected from the Yucca Mountain area for Cl and  $^{36}\text{Cl}$  analyses as part of site-characterization activities. Most of the groundwater samples, some of the surface soil samples, and all of the pack-rat midden samples, were collected by YMP investigators for other characterization studies such as shallow infiltration, local and regional flow systems, and climate reconstruction. Thus far, over 600 samples have been analyzed for  $^{36}\text{Cl}$  (plus numerous blanks and replicates). These data were largely summarized in Fabryka-Martin et al. (in press [b]), and the current report includes earlier data only to the extent necessary to make this document self-contained, or to update a particular data set. Appendix E lists the data tracking numbers associated with the new or revised analytical results cited in this report.

#### 3.1 Radiometric dating of water using atmospheric chlorine-36

##### 3.1.1 Principles of dating using chlorine-36

Chlorine-36 is produced naturally in the atmosphere as a result of high-energy cosmogenic nucleons (protons and neutrons) bombarding isotopes of argon and stable chlorine-35. Infiltrating rainwater carries the radioactive nuclide into the subsurface. In order to address the effects of variable amounts of evapotranspiration,  $^{36}\text{Cl}$  concentrations are typically discussed relative to the concentration of stable chlorine. The present-day (pre-bomb)  $^{36}\text{Cl}/\text{Cl}$  ratio for Cl being deposited on the surface at Yucca Mountain is estimated to be on the order of  $500 \times 10^{-15}$ .

(Fabryka-Martin et al., in press [b]). This value is based largely on measurements of samples from soil profiles and is consistent with theoretical calculations for present-day conditions (Fabryka-Martin et al., in press [b]).

In the simplest case, the measured  $^{36}\text{Cl}/\text{Cl}$  ratios can be used to estimate upper limits for average water residence time at the sampled locations. Water-age estimates based upon the measured  $^{36}\text{Cl}/\text{Cl}$  ratio for a sample assume that the initial meteoric  $^{36}\text{Cl}/\text{Cl}$  ratio in infiltrating water is known throughout the period of interest. For old water (ages on the order of  $10^5$  yr), the buildup of  $^{36}\text{Cl}$  as a result of the subsurface neutron flux must also be taken into account. The secular equilibrium  $^{36}\text{Cl}/\text{Cl}$  ratio for Paintbrush tuffs is on the order of  $20 \times 10^{-15}$  to  $60 \times 10^{-15}$  (section 3.4.1). An age estimate is obtained by applying the standard equation for radioactive decay with correction for ingrowth (Bentley et al., 1986),

$$t = -\frac{1}{\lambda_{36}} \ln \left[ \frac{(R_x)_{36} - (R_r)_{36}}{(R_0)_{36} - (R_r)_{36}} \right] \quad (3-1)$$

where  $\lambda_{36}$  is the decay constant for  $^{36}\text{Cl}$ ,  $2.30 \times 10^{-6} \text{ yr}^{-1}$ , and  $(R_x)_{36}$ ,  $(R_r)_{36}$  and  $(R_0)_{36}$  are the measured, secular equilibrium, and initial meteoric  $^{36}\text{Cl}/\text{Cl}$  ratios, respectively.

### 3.1.2 Past variations in the atmospheric $^{36}\text{Cl}/\text{Cl}$ signal

Interpretation of measured  $^{36}\text{Cl}/\text{Cl}$  signals in terms of water residence times is complicated by uncertainties about the variations in the initial  $^{36}\text{Cl}/\text{Cl}$  signal  $(R_0)_{36}$  in meteoric water. Analytical measurements of  $^{36}\text{Cl}/\text{Cl}$  ratios in fossil packrat urine and in deep alluvial profiles at the Nevada Test Site, as well as theoretical modeling of atmospheric physics, indicates that the atmospheric  $^{36}\text{Cl}/\text{Cl}$  value has not been constant over time and in fact was higher by a factor of approximately 11,000 years ago (Plummer et al., 1997; Tyler et al., 1996; Fabryka-Martin et al., in press [b]). Several hypotheses to account for the variations are proposed by Plummer et al. (1997):

- **Variations in geomagnetic field intensity.** Production of  $^{36}\text{Cl}$  in the atmosphere is a function of atmospheric cosmic-ray intensity, which is in turn controlled by temporal variations in the earth's geomagnetic field intensity. The  $^{36}\text{Cl}$  production rate is high when the geomagnetic field intensity is low, and *vice versa*. The geomagnetic field intensity was considerably lower prior to the past 10,000 years, contributing to a higher production rate of  $^{36}\text{Cl}$  during that time.
- **Shifting of the jet stream.** An additional hypothesis proposed by Plummer et al. (1997) is that deposition of stratospheric  $^{36}\text{Cl}$  was greater during the last glacial period. Atmospheric mixing across the tropopause is strongest at the jet stream, such that southward migration of the jet stream during the glacial period would have moved the latitude of maximum  $^{36}\text{Cl}$  fallout southward, increasing it by as much as 30% in southern Nevada.
- **Changes in Cl deposition rates.** The fact that the observed decrease in the  $^{36}\text{Cl}/\text{Cl}$  ratio is coincident with the climate transition at the end of the last glacial period suggests the

possibility that local Cl deposition—and hence greater dilution of the  $^{36}\text{Cl}$  signal—may have increased due to aridification of pluvial lakes and subsequent deflation of the saline surface salts during the Holocene. Possible sources include Franklin Lake Playa and Death Valley, ~50 km south and ~100 km southwest of Yucca Mountain, respectively (see section 3.1.3).

The effect of geomagnetic variations on  $^{36}\text{Cl}$  production using the model by Blinov (1988) is combined with the assumption of a present-day  $^{36}\text{Cl}/\text{Cl}$  ratio of  $500 \times 10^{-15}$  and a decreased stable Cl input during the Pleistocene to reconstruct  $^{36}\text{Cl}/\text{Cl}$  ratios for the Yucca Mountain region during the past 2 Ma (Fabryka-Martin et al., in press [b]). Figure 3-1 shows the reconstructed input signal (solid line), and its present-day signal (dotted line) under the influence of radioactive decay. The basis for this reconstruction is described in Fabryka-Martin et al. (in press [b]). This reconstructed  $^{36}\text{Cl}/\text{Cl}$  signal indicates that the value of the undecayed atmospheric  $^{36}\text{Cl}/\text{Cl}$  ratio at Yucca Mountain during the past 500 ka may have ranged from as low as  $440 \times 10^{-15}$  at 2.7 ka, to a peak of  $1100 \times 10^{-15}$  at 40 ka, averaging about  $900 \times 10^{-15}$  throughout the Pleistocene.

A comparison of the reconstructed  $^{36}\text{Cl}/\text{Cl}$  ratio against that for atmospheric  $^{14}\text{C}$  (Figure 3-2a) shows that both nuclides had higher activities 25,000 years ago as compared to the past 10,000 years but the changes in the two signals do not parallel one another (Plummer et al., 1997). The dependence of the  $^{36}\text{Cl}$  production rate on changes in the geomagnetic field strength is similar to that of  $^{14}\text{C}$ . However, the dissimilar response is probably a consequence of differences in their chemical behaviors and geochemical cycles. Plummer et al. (1997) points out that Cl is rapidly removed from the atmosphere by precipitation and dry fallout, while  $^{14}\text{C}$  shows a lag in its response to production rate changes due to exchange of  $\text{CO}_2$  between the ocean and atmosphere.

In order to verify the timing and magnitude of the reconstructed  $^{36}\text{Cl}/\text{Cl}$  signal,  $^{36}\text{Cl}/\text{Cl}$  ratios have been measured in fossil urine from packrat middens (Fabryka-Martin et al., in press [b]) collected by the Desert Research Institute (Reno, NV) from various locations in the vicinity of the Nevada Test Site and dated by the  $^{14}\text{C}$  method. The packrat data set agrees fairly well with the theoretical reconstruction for Yucca Mountain for the past 30 ka (Figure 3-2b).

### *3.1.3 Evaluation of Franklin Lake Playa as a local source of Cl deposition*

We have explored the possibility that eolian Cl deposition from drying pluvial lakes contributed to lower  $^{36}\text{Cl}/\text{Cl}$  ratios during the last ~11,000 years by studying surficial samples collected along a 20-km transect between Franklin Lake Playa and Owl Canyon, ~50 km SSE of Yucca Mountain. Owl Canyon is one of the collection sites for packrat midden data used to reconstruct  $^{36}\text{Cl}/\text{Cl}$  ratios of the past 40,000 years (Plummer et al., 1997). With prevailing wind directions from the southwest (Reheis and Kihl, 1995), Owl Canyon is downwind from Franklin Lake Playa.

The objective of our exploratory study was to search for elemental or mineral constituents of surficial deposits that could serve as tracers for playa-derived eolian deposition. Samples of surface crusts, subsoils, and dust were collected at Franklin Lake Playa. Owl Canyon samples

included surface materials from a sand ramp composed of local colluvium and eolian material in a high-angle deposit against the canyon wall. Bedrock from the canyon wall above the sand ramp and dust deposits from an adjacent boulder field were also collected. Surface soils were collected along a transect between the playa and the canyon. Additional samples of playa crusts and subsoils and desert pavement were collected south and west of the transect.

The only direct evidence we have found for eolian Cl transport is the presence of ~1 wt. % NaCl in a dust sample collected from a dry stream channel cut into the surface of the playa. The leachable SO<sub>4</sub> content of the dust is higher than in the adjacent playa crusts but similar to values for crusts and subsoils further south. The Cl content is lower in the dust than in either adjacent or southern playa samples, possibly indicating that Cl is more readily removed by dissolution as the dust is blown to the northeast.

Leachable Ca, K, Mg, Na, Cl, Br, SO<sub>4</sub>, and H<sub>4</sub>BO<sub>4</sub> contents generally show trends of decreasing values northward from the playa, compatible with a conceptual model of lessening playa-derived eolian input with distance from the source. However, similar trends are observed in the Na, Cl, and SO<sub>4</sub> concentrations in the shallow ground water within the valley fill of the Amargosa River further north of the playa (Claassen, 1983). We must consider the possibility that the compositional evolution of ground water as it flows south and the input of playa dust blowing north may both contribute to the composition of soil leachates.

Similarly, our efforts to use mineralogy and elemental composition as indicators of sources for eolian material are complicated by evidence that surficial materials at both the source sites and the potential depositional sites are of hybrid origin. By way of the Amargosa River system, the playa and transect sampling locations to the north have received input of alluvium derived from Paleozoic rocks like those exposed at Owl Canyon. The transect locations between the playa and Owl Canyon are also close to Pliocene carbonate rocks, Mg clays, zeolites, and K-feldspars, some of which are products of alteration in saline, alkaline waters (Hay et al., 1986). As an example, with so many potential source areas, calcite in the dust at Owl Canyon could include components from local Paleozoic bedrock, from Paleozoic alluvium transported by wind from the playa, from Pliocene exposures north of the playa as sources of eolian dust, from Pliocene alluvium transported by wind from the playa, or from calcite precipitated in the playa and transported by the wind.

Our results suggest that eolian deposition of playa-derived Cl is an unknown but potentially fundamental factor affecting long-term variations in the <sup>36</sup>Cl/Cl value. Analyses of lofted dust and newly deposited dust during and after dust storms at the playa could be used to estimate how much halite travels as discrete particles and as coatings on other grains during the initial episodes of eolian transport. Analysis of new surface deposits of eolian dust could provide data on the distance, direction, and amount of Cl transport.

### 3.2 Global fallout of atmospheric radionuclides

Measured and reconstructed records of the global fallout of bomb-pulse nuclides over the past 50 years are being used by site-scale hydrologic and solute transport modelers for comparing predicted and measured concentration profiles in the ESF and deep boreholes (e.g., Robinson et al., 1996, 1997; Bodvarsson et al., 1997). Detection of elevated concentrations of these nuclides in deep samples is generally taken as evidence for fast transport of water during the past 50 years. This section summarizes estimated input functions for tritium,  $^{14}\text{C}$  and  $^{36}\text{Cl}$  for the time period from the mid-1950s to the 1980s. Derivations and tabulations of these functions are presented in Fabryka-Martin et al. (in press [b]). Input functions for  $^{14}\text{C}$  and  $^{36}\text{Cl}$  are based on measured data that are assumed to be applicable to Yucca Mountain. Reconstruction of tritium concentrations in local atmospheric moisture is based largely upon measurements made in Albuquerque, New Mexico.

*Reconstructed Global Fallout Signal for Chlorine-36.* Chlorine-36 is present at high concentrations (relative to its natural background) in young infiltrating waters as global fallout from more than 70 nuclear-weapons tests conducted primarily in the Pacific Proving Grounds between 1952 and 1958. The annual deposition rate of bomb-pulse  $^{36}\text{Cl}$  at Yucca Mountain is assumed to be similar in timing and magnitude to that measured in Greenland ice core by Synal et al. (1990). The input function is expressed as a  $^{36}\text{Cl}/\text{Cl}$  ratio in order to allow a more direct comparison against field data. The reconstructed ratio is calculated by assuming a constant annual Cl deposition rate of  $106 \text{ mg Cl m}^{-2}$  (section 5.1). By this approach, the peak in the bomb-pulse signal would have occurred in 1957, with a  $^{36}\text{Cl}/\text{Cl}$  ratio of  $217,000 \times 10^{-15}$ , about 400 times greater than the present-day value of  $500 \times 10^{-15}$ . All samples measured thus far at Yucca Mountain have been far lower than this peak, probably because the  $^{36}\text{Cl}/\text{Cl}$  ratio of Cl transported into successively deeper parts of the profile is a function of the average residence time of Cl in the overlying material, and hence has been diluted by Cl with lower  $^{36}\text{Cl}$  contents that had entered the system before or after the bomb-pulse. Figure 3-3a plots the reconstructed bomb-pulse  $^{36}\text{Cl}/\text{Cl}$  ratio assuming Cl residence times of one and ten years in the zone of evapotranspiration before being carried into the underlying bedrock. The effect of longer residence time is not only to lower the peak ratio, but also to shift to later years the time at which the peak is reached. For a residence time of 10 years, for example, the peak ratio of  $119,000 \times 10^{-15}$  would have occurred in 1963. Also for the latter case, the  $^{36}\text{Cl}/\text{Cl}$  ratio for Cl entering the unsaturated-zone flow system at the present day would still be elevated above meteoric background. This expectation is borne out by the ratios measured for soils collected from depths within 0.5 m of the surface (Table 4-6), as well as by ratios measured for surface runoff (Table 4-13). Only two of the 27 samples in these two tables are near background levels; the vast majority of the ratios are on the order of  $2000 \times 10^{-15}$  to  $3000 \times 10^{-15}$ . However, it would be useful to obtain additional analyses of surface soils to test for spatial variations, particularly at locations directly above the ESF, in order to assess more thoroughly the possibility that the signal entering the bedrock at the present time has returned to background levels.

*Annual Concentration of Atmospheric  $^{14}\text{C}$ , 1945 - 1984.* Reconstruction of the input function for

bomb-pulse  $^{14}\text{C}$  is simplified by the fact that the atmospheric reservoir is well-mixed for this isotope, such that adjustments do not need to be made for local variations. Atmospheric concentrations are plotted in Figure 3-3b. The peak activity occurred in 1963, at 200 pmC (percent modern carbon). In contrast with the other two atmospheric radionuclides, the modern value is still elevated about 20% above natural background due to the comparatively long residence time of carbon in the atmosphere.

*Reconstructed Record of Tritium in Atmospheric Moisture, 1953 - 1985.* Reconstruction of the bomb-pulse tritium signal is more complicated than for the previous two cases because its concentration is strongly influenced by a variety of factors such that it varies considerably from one location to another, and from one rain event to another. Therefore, an accurate reconstruction of tritium concentration at Yucca Mountain is not possible. Very few historical data of tritium are available for Yucca Mountain or for nearby communities such as Las Vegas, Nevada. However, tritium concentrations at various locations in the northern hemisphere generally show similar trends with time. Consequently, a crude approximation can be made by assuming that the tritium record for Yucca Mountain is represented by that for Albuquerque, New Mexico, which is at nearly the same latitude, has a similar climate to that at Yucca Mountain, and is the closest station with an extensive published monitoring record of monthly and quarterly values. The reconstructed record is plotted in Figure 3-3c.

*Disparities among Bomb-pulse Nuclides.* Although all three radiometric species were present in global fallout of bomb-pulse nuclides, bomb-pulse levels of all three will not always be observed in the same sample. This apparent discrepancy is inevitable and can be attributed to many factors, such as those presented below (Liu et al., 1995). Factors governing  $^{14}\text{C}$  activities in pore waters are contrasted with those for  $^{36}\text{Cl}$  in the list below; similar examples could be given using tritium (Liu et al., 1995; Fabryka-Martin et al., in press [b]):

- (1) *Different transport mechanisms for carbon and Cl.* Chloride is only transported in the liquid phase, while carbon can be transported in both the liquid phase (as  $\text{HCO}_3^-$  or  $\text{CO}_3^{2-}$ ) and gas phase (as  $\text{CO}_2$ ). Subsequent  $\text{CO}_2$  exchange between the liquid and gas phases could shift  $^{14}\text{C}$ -based water ages to younger or older ages.
- (2) *Different magnitudes and timing of bomb-pulse signals.* The bomb-pulse  $^{36}\text{Cl}$  peak exceeds the natural meteoric  $^{36}\text{Cl}$  signal by at least a factor of 100, while the bomb-pulse  $^{14}\text{C}$  peak is higher than the natural level only by a factor of 2. Therefore,  $^{36}\text{Cl}$  can be a more sensitive indicator for a fast aqueous transport path than is  $^{14}\text{C}$ . In addition, the timing of the bomb pulses in the atmosphere are quite different: the bomb-pulse  $^{36}\text{Cl}$  peak preceded the  $^{14}\text{C}$  peak by about 10 years, and largely returned to pre-bomb background levels by the early 1980s, whereas  $^{14}\text{C}$  concentrations are still elevated at the present day by about 20% above the pre-bomb background. On the other hand, in arid regions the  $^{36}\text{Cl}$  signal in infiltrating water can remain at bomb-pulse levels long after the atmospheric component has returned to background, due to mixing in the soil zone (Figure 3-3a).

- (3) *Mixing of waters from different flow paths.* Due to the hydrogeological complexity of Yucca Mountain, one-dimensional downward matrix flow is unlikely to be characteristic of water movement in the unsaturated zone. Rather, mixing of waters with different hydraulic ages from different flow paths is probably a dominant phenomenon. Disparate radiometric ages based on  $^{36}\text{Cl}$  and  $^{14}\text{C}$  are inevitable whenever mixing of waters containing fluids of markedly-different ages occurs, particularly if a small component of water containing bomb-pulse nuclides is present in the mixture.
- (4) *Inadequate methods for correcting for the effect of sample contamination by carbon or chloride from sources other than that in the infiltrating water.* Chloride leached from a rock sample may contain a significant component of rock Cl that serves to dilute the  $^{36}\text{Cl}$  signal of the meteoric Cl, making it appear older than its true average age. Methods to quantify the effect of sample dilution by rock Cl are being investigated, such as those based on distinctive Br/Cl ratios in the meteoric and rock end-members (section 6.1.5). However, these methods are not yet well established. Similarly, carbon extracted from water can also be diluted by "dead" carbon from carbonate or enriched by circulating young  $\text{CO}_2$  gas. In the former case, the uncorrected  $^{14}\text{C}$  ages will be older than the true water age while in the latter case the  $^{14}\text{C}$  ages will be younger than the true water age.

### 3.3 Local sources

Nevada Test Site (NTS) activities also produced  $^{36}\text{Cl}$  and, in some cases, released it to the atmosphere. The following is a summary of a more extensive discussion of NTS activities in Fabryka-Martin et al. (in press [b]).

*Atmospheric testing of nuclear-weapon devices* was conducted at the NTS from 1951 to 1958. The NTS weapons tests emitted neutrons which produced  $^{36}\text{Cl}$  by irradiating Cl in surface soils. The zone of influence, or the zone in which the  $^{36}\text{Cl}/\text{Cl}$  ratio of Cl in surface soil would have been elevated by at least an order of magnitude above background, would be a function of the burst height but could conceivably have extended to several km in some cases. Most of the NTS tests which may have produced significant quantities of  $^{36}\text{Cl}$  in surface soils were conducted near Frenchman Flat in Area 5 about 45 to 50 km east of Yucca Mountain, and in Yucca Flat about 40 to 55 km ENE from Yucca Mountain. These sources could have contributed to the elevated signals measured at Yucca Mountain through atmospheric lofting of dust, either during the event or even years later as a result of dust storms. However, the general trend of air movement is most commonly eastward, away from Yucca Mountain.

*Project Plowshare* involved a series of low-yield nuclear detonations on the NTS and in Colorado from the late 1950s through 1970. The project was designed to explore peaceful uses of nuclear technology while also providing information about post-detonation effects of nuclear explosions. The generally low yields of these tests in combination with trajectories for the main and surge clouds heading away from Yucca Mountain make it unlikely for these events to have contributed significant quantities of  $^{36}\text{Cl}$  to the signals seen at Yucca Mountain.

*The Rover Nuclear Rocket Program* conducted nuclear-reactor engine tests at Test Cells A and C in Area 25, about 10 km east of the ESF North Portal, from 1959 to 1969. High cumulative neutron fluxes from these tests produced  $^{36}\text{Cl}$  in the surface soil through neutron-capture by stable  $^{35}\text{Cl}$ . The highest fluxes were generated by the Test Cell C tests, which would have produced  $^{36}\text{Cl}/\text{Cl}$  ratios in soil salts as high as  $1 \times 10^{-8}$  within 20 meters of the reactor, decreasing exponentially with distance to a level of  $1 \times 10^{-12}$  at a distance of 600 m. Although subsequent deposition of atmospheric Cl has diluted these signals, and precipitation has transported some of it further down into the profile, these calculated production rates have been confirmed by the measurement of ratios of  $10^{-10}$  in soil samples collected about 60 m from the reactor site at Test Cell C. The most likely route by which this source could contribute to that at Yucca Mountain would be via contaminated equipment and materials moving through this area.

It is difficult to assess the extent to which these potential sources of extraneous  $^{36}\text{Cl}$  may have contributed to the distribution of this nuclide at Yucca Mountain. However, it is important to bear in mind that the timing of these sources is sufficiently similar to that of global fallout  $^{36}\text{Cl}$  that the presence of elevated  $^{36}\text{Cl}$  in a subsurface sample would be interpreted the same regardless of the source of the  $^{36}\text{Cl}$ , i.e., that some component of the water at the sampled location was transported there in less than 50 years. The exception to this rule would be the introduction of  $^{36}\text{Cl}$  into the subsurface via the use of contaminated equipment, but there is no evidence that such has been the case.

### **3.4 Production of $^{36}\text{Cl}$ in rocks and soil minerals**

Atmospheric  $^{36}\text{Cl}$  from natural and global fallout sources is expected to dominate the  $^{36}\text{Cl}$  component of most Yucca Mountain samples collected for this activity. However, under some circumstances, other sources may also contribute a significant component to the subsurface. These are cosmogenic production in surface rocks and surface calcites, and deep subsurface production as a consequence of a low but ubiquitous neutron flux. The following is summarized from Fabryka-Martin et al. (in press [b]), with the addition of recently-acquired analyses of the  $^{36}\text{Cl}$  content of soil calcites (section 3.4.3).

#### **3.4.1 Deep Subsurface Production in Rocks**

Chlorine-36 is produced at low levels in subsurface rocks at Yucca Mountain due to a low but ubiquitous neutron flux resulting from the radioactive decay of uranium and thorium isotopes. A small proportion of these neutrons are captured by stable  $^{35}\text{Cl}$  in the rocks, producing  $^{36}\text{Cl}$ . Theoretical calculations based on measured chemical compositions of Yucca Mountain tuff samples predict  $^{36}\text{Cl}/\text{Cl}$  ratios on the order of  $20 \times 10^{-15}$  to  $40 \times 10^{-15}$  from this mechanism (Fabryka-Martin et al., 1993). Norris et al. (1990) reported a measured value of  $25 \times 10^{-15}$  for a sample from USW UZ-1 (depth, 76-78 m). Analyses of this component for four TSw samples from the ESF showed ratios averaging  $40 \times 10^{-15}$  (Fabryka-Martin et al., in press [b]).

### 3.4.2 *Cosmogenic Production in Surface Rocks*

Chlorine-36 is produced at even higher rates in rocks and minerals in the uppermost 10 meters of the earth's surface. In the top few meters, the dominant production mechanisms are spallation of potassium-39 ( $^{39}\text{K}$ ) and calcium-40 ( $^{40}\text{Ca}$ ) by high-energy cosmogenic neutrons, and capture of low-energy neutrons by  $^{35}\text{Cl}$ . Surface production rates for the approximate latitude and elevation of Yucca Mountain are on the order of 190 atoms  $^{36}\text{Cl yr}^{-1} \text{ g}^{-1} \text{ }^{39}\text{K}$ , and 152 atoms  $^{36}\text{Cl yr}^{-1} \text{ g}^{-1} \text{ }^{40}\text{Ca}$  (rates measured by Zreda et al., 1991, as re-evaluated by Stone et al., 1996). The production rate by neutron-capture on  $^{35}\text{Cl}$  is a function of the Cl concentration at the surface. Cosmogenic neutrons, however, do not penetrate deeply into the subsurface, dropping off exponentially with a half-length of about  $155 \text{ g cm}^{-2}$  (i.e., the flux of cosmogenic neutrons is reduced by a factor of  $\ln(2)$  for each 155 grams of material transected in a  $1\text{-cm}^2$  column; the equivalent depth for a soil with a bulk density of  $1.5 \text{ g cm}^{-3}$  would be 1.0 m) (Zreda et al., 1991). In the range of 2 to 10 meters beneath the surface, production by muon-capture by  $^{40}\text{Ca}$  is the dominant source. A representative rock composition of welded tuff from Yucca Mountain is 0.5% Ca, 5% K and 200 ppm Cl. The predicted rate of  $^{36}\text{Cl}$  production would be  $56 \text{ atoms g}^{-1} \text{ yr}^{-1}$ , with a steady-state concentration of  $2.4 \times 10^7 \text{ atoms g}^{-1}$ , corresponding to a  $^{36}\text{Cl}/\text{Cl}$  ratio of  $7200 \times 10^{-15}$  (calculations based on method of Zreda et al., 1991, using elemental compositions from Broxton et al., 1986, and Vaniman et al., 1995). Under the slow weathering conditions that prevail at Yucca Mountain, the rate of transfer to infiltrating water of  $^{36}\text{Cl}$  produced in the rock and its fluid inclusions should be generally negligible relative to the rate of deposition of  $^{36}\text{Cl}$  from atmospheric sources.

### 3.4.3 *Cosmogenic Production in Surface Calcite*

For the most part, the contribution of *in-situ* produced  $^{36}\text{Cl}$  to that being transported in pore water is assumed to be negligible relative to atmospheric sources of this nuclide. A possible exception may be the special case in which  $^{36}\text{Cl}$  is produced in calcites or caliche deposited or formed near the surface (Fabryka-Martin et al., in press [b]). An upper limit for the contribution of  $^{36}\text{Cl}$  from this source can be estimated as follows. At a production rate of  $152 \text{ atoms (g Ca)}^{-1} \text{ yr}^{-1}$ , one gram of calcite exposed at the surface would contain about  $2.6 \times 10^7 \text{ atoms } ^{36}\text{Cl}$  at equilibrium (i.e., for a minimum surface exposure age of three  $^{36}\text{Cl}$  half-lives or about 1 Ma). Calcite solubility in an open system with a typical soil  $P_{\text{CO}_2}$  of  $10^{-2} \text{ atm}$  would be  $0.15 \text{ g L}^{-1}$  at  $25^\circ\text{C}$ ; infiltrating water in equilibrium with such calcite would contain  $3.9 \times 10^6 \text{ atoms } ^{36}\text{Cl L}^{-1}$ . For typical pore-water concentrations of 10 to  $100 \text{ mg Cl L}^{-1}$ , this would correspond to  $^{36}\text{Cl}/\text{Cl}$  ratios of  $2 \times 10^{-15}$  to  $20 \times 10^{-15}$ , less than 5% of the present-day atmospheric ratio.

It could be argued that the above does not provide a true bounding calculation. Higher  $^{36}\text{Cl}$  concentrations could conceivably derive from calcite through multiple wetting and drying cycles (Fabryka-Martin et al., in press [b]). For example, calcite could be dissolved in response to several consecutive storms, releasing its  $^{36}\text{Cl}$  content. The  $^{36}\text{Cl}$  would stay in the soil as highly soluble salt while the calcite would reprecipitate as the soil dried out. Eventually, a storm would occur under conditions conducive to leading to net infiltration, which would carry the

accumulated  $^{36}\text{Cl}$  into the subsurface, below the zone of evapotranspiration. A counterbalancing argument is that atmospheric Cl would also be accumulating in the soil throughout the wetting and drying cycles, thereby continuing to swamp out the contribution of in-situ produced  $^{36}\text{Cl}$ . In addition, it is probable that the calcites being actively dissolved at the surface are not even close to 1 Ma exposure ages but are probably considerably younger. The calcite being dissolved by each storm event is most likely that which was most recently precipitated following soil dry-out after the previous storm event, and hence with a negligible  $^{36}\text{Cl}$  content. A final argument against soil calcites as a dominating source of  $^{36}\text{Cl}$  in infiltrating waters is that fossil urine samples from pack-rat middens discussed in section 3.1.2 show no indication of highly elevated  $^{36}\text{Cl}/\text{Cl}$  signals. Presumably, Cl in pack-rat urine is derived from that in plants which in turn is extracted from the root zone, which should be sensitive to a calcite-enhanced signal.

Soil samples were collected from three locations at Yucca Mountain in 1996 in order to evaluate the magnitude of the calcite source term in the Yucca Mountain environment. Based on U-series dating of the calcite, the three locations span a wide range of soil ages, from a fairly young soil profile in Coyote Wash, to old profiles on Whaleback Ridge and Yucca Crest (Swadley et al., 1984; Lundstrom et al., 1995; Paces et al., 1995). The samples were collected within the top meter. The four samples that were subsequently analyzed are described in Table 3-1. Mineralogic analyses showed that the proportion of calcite varied from <1% in the young Coyote Wash profile, to as much as 55% in the Yucca Crest profile (Table 3-2).

In order to remove the meteoric Cl component, the soils were washed repeatedly with deionized water until the wash contained less than 0.5 ppm Cl. The  $^{36}\text{Cl}/\text{Cl}$  ratio of this meteoric component was elevated well above background ( $680 \times 10^{-15}$  to  $3200 \times 10^{-15}$ ) and probably contains bomb-pulse  $^{36}\text{Cl}$  based on the shallow depth of these samples. The values measured for this component are similar to those measured for Cl leached from surface soils (section 4.3, Table 4-6) and for Cl in surface runoff (section 4.5.1, Table 4-13). The isotopic composition of the calcite was determined after digesting the washed soil in nitric acid. The measured Ca concentration of this acid solution was assumed to indicate the mass of calcite dissolved from the soil sample and releasing its *in-situ*  $^{36}\text{Cl}$  content. Data in Table 3-3 show that the  $^{36}\text{Cl}/\text{Cl}$  ratios of Cl trapped in these calcite samples range over an order of magnitude, from  $800 \times 10^{-15}$  to  $9800 \times 10^{-15}$ . However, a more relevant measure is the  $^{36}\text{Cl}$  concentration, which averages  $2 \times 10^6$  atoms per gram of calcite, roughly 10% of the maximum concentration one would estimate assuming secular equilibrium at the sampled depth. For comparison, Table 3-3 also shows the  $^{36}\text{Cl}$  concentration attributable to meteoric Cl in the soil. Taking into account the proportion of calcite in each sample, these data support the contention that the  $^{36}\text{Cl}$  content of calcareous soil attributable to *in-situ* production in calcite would generally be at least an order of magnitude less than that from the atmosphere.

Table 3-1. Field and laboratory descriptions of soil samples used to evaluate  $^{36}\text{Cl}$  production in soil calcites

*Coyote Wash Cross Trench (Lundstrom et al., 1995; Paces et al., 1995)*

**Sample CWXT-CI-1:**

- Collected sample of fine-grained soil from surface down to ~ 0.6 m from west wall of trench (near TL-52 site reported in Paces et al., 1995).
- Fine sand mixed with granules to pebbles < 4 cm. Abundant root fragments, mostly with no visible calcite coatings. ~1-2% of the root fragments have soil carbonate, including root casts, ~ 0.5-3 mm across. Sand is predominantly unconsolidated silicate and oxide mineral grains, some very well-rounded and polished. Pebbles are densely welded devitrified tuff, probably mostly Tpc. Essentially all pebbles have carbonate coatings, < 0.5 mm thick, but none have complete carbonate coats.

**Sample CWXT-CI-2:**

- Gravel and cobble fraction from the same horizon as CWXT-CI-1.
- Gravel/cobble fraction is ~5-15 cm. Carbonate coatings are common. Coatings are very fine-grained on undersides, ~ 0.3 mm thick; sand and cement on topsides. Root fragments are common. Fe-Mn spots on and under calcite coatings. Cobbles are densely welded devitrified tuff.

*Whaleback Ridge, Trench exposing Ghost Dance Fault on east side of Yucca Mountain (Paces et al., 1995)*

**Sample WBR-CI-1:**

- Collected sample of laminar calcrete with silica at top of calcrete K horizon, ~ 0.6 m below original pre-trench ground surface, ~ 10 cm west of HD1722 sample site and immediately below the vesicular A horizon.
- Dense, hard to very hard, laminar calcrete with scattered clasts of moderately to densely welded Tpc tuff < 5 cm across. Matrix is mostly a mixture of very fine-grained calcite and silica. Silica occurs in silica-rich scattered mm-scale patches. Numerous < 1-mm diameter powdery white plant casts, a few with residual root cores. Mm-scale pores in a tuff clast contain < 1mm globular aggregates and knobby needles of silica, some with very thin calcite overgrowths.

*Yucca Crest, near Trench 1 site (Swadley et al., 1984)*

**Sample YC-CI-1:**

- Collected sample of ~ 0.8 m below original top of A horizon at surface. Note that the eolian A horizon has been stripped here by erosion and excavation (~15 years ago).
- Laminar to platy K horizon. Individual plates are hard, up to ~10 across and 1-4 cm thick. Carbonate-rich (fluoresces blue and white in short-wave uv) with local ooidal texture. Irregular 1-2 mm thick laminae of brown silica-rich material. Silica also occurs as < 1 mm thick linings of ~1/2 cm diameter root casts running parallel to platy fabric. Root casts have residual root cores and some have sandy infillings.

Table 3-2. Mineralogic analyses (wt %) of soils

Mineral	CWXT-CI-1	CWXT-CI-2	WBR-CI-1	YC-CI-1
Smectite	5 ± 2	---	3 ± 1	2 ± 1
Clinoptilolite	2 ± 1	---	1 ± 1	---
Tridymite	10 ± 1	24 ± 2	3 ± 1	---
Cristobalite	5 ± 2	6 ± 3	2 ± 1	---
Quartz	17 ± 1	Trace	Trace	1 ± 1
Feldspar	60 ± 9	70 ± 10	26 ± 4	4 ± 1
Glass/amorphous silica	---	---	20 ± 5	38 ± 3
Calite	1 ± 1	---	44 ± 2	55 ± 3
Chlorite/kaolinite	Trace	---	---	---
Hematite	1 ± 1	1 ± 1	Trace	---
Hornblende	1 ± 1	---	---	---
Mica	1 ± 1	Trace	1 ± 1	---
Gypsum	Trace	---	---	---
Total	103 ± 10	101 ± 11	100 ± 5	100 ± 3

Note: XRD analyses conducted by S. Chipera (LANL/EES-1)

Table 3-3. Measured  $^{36}\text{Cl}/\text{Cl}$  ratios for soil calcites

Sample description and pretreatment	Meteoric component (Notes 1 and 2)			Calcite component (Note 3)		
	mg Cl kg <sup>-1</sup>	$^{36}\text{Cl}/\text{Cl}$ $\times 10^{-15}$	$10^6$ $^{36}\text{Cl}$ atoms per g soil	% cal- cite	$10^6$ $^{36}\text{Cl}$ atoms per g calcite	$^{36}\text{Cl}/\text{Cl}$ $\times 10^{-15}$
<i>Coyote Wash Cross Trench</i> CWXT-CI-1-2: fraction passing 1 mm sieve CWXT-CI-2-2: fraction > 5 cm	352 0.2	2807 ± 150 3177 ± 162	17 0.01	1% <1%	1.7 3.3	941 ± 60 816 ± 71
<i>Whaleback Ridge Trench</i> WBR-CI-1-2: fraction passing 2 mm sieve	467	2317 ± 70 2299 ± 97 (Note 1)	18	44%	1.0	9772 ± 547
<i>Yucca Crest Trench 1 site</i> YC-CI-1-2: crushed and used fraction passing 2 mm sieve	25	679 ± 26 677 ± 27	0.3	55%	0.9	5067 ± 204

Notes:

1. Soil samples were repeatedly leached with deionized water until the Cl content of the decanted leachate was less than 0.5 mg/L (i.e., after about seven leaches). The isotopic composition of the meteoric component was determined on Cl removed during the third leach. For samples WBR-CI-1-2 and YC-CI-1-2, it was also measured for Cl removed by the fourth leach to test the homogeneity of the isotopic signature of the Cl being removed.
2. The concentration of Cl leached from the sample is only a qualitative indicator of the sample's Cl content and is probably an underestimate of the true value. The meteoric Cl content of the samples was measured by leaching them for 48 hours in deionized water using a water:soil weight ratio of 1:1. Because the focus of this activity is on determining isotopic ratios, no attempt was made to maximize the yield of the leaching process, which is probably quite variable.
3. The isotopic composition of the *in-situ* Cl in the calcite was determined after digesting the washed soil in nitric acid. The measured Ca concentration of this acid solution was assumed to indicate the mass of calcite dissolved from the soil sample and releasing its *in-situ*  $^{36}\text{Cl}$  content.

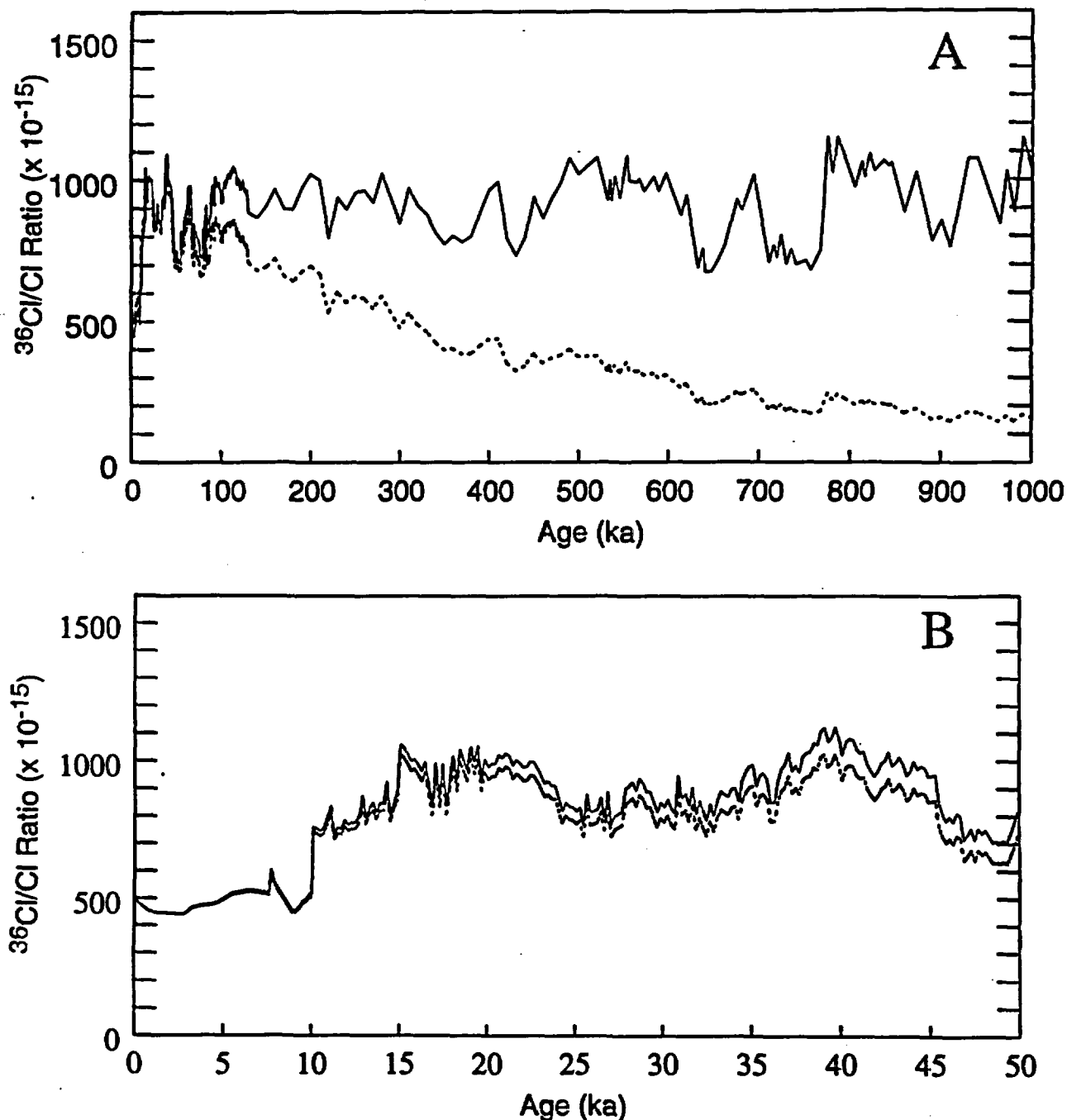


Figure 3-1. Reconstructed  $^{36}\text{Cl}/\text{Cl}$  ratio in the atmosphere, (A) for the past million years, and (B) for the past 50,000 years (50 ka), as a function of variations in the geomagnetic field intensity and chloride deposition rates. The reconstructed ratio shown by the solid line assumes that the deposition rate of stable chloride was constant at present-day rates during the Holocene (i.e., ages less than 10 ka) but 33% lower throughout the Pleistocene. The dashed line includes radioactive decay to present-day ratios.

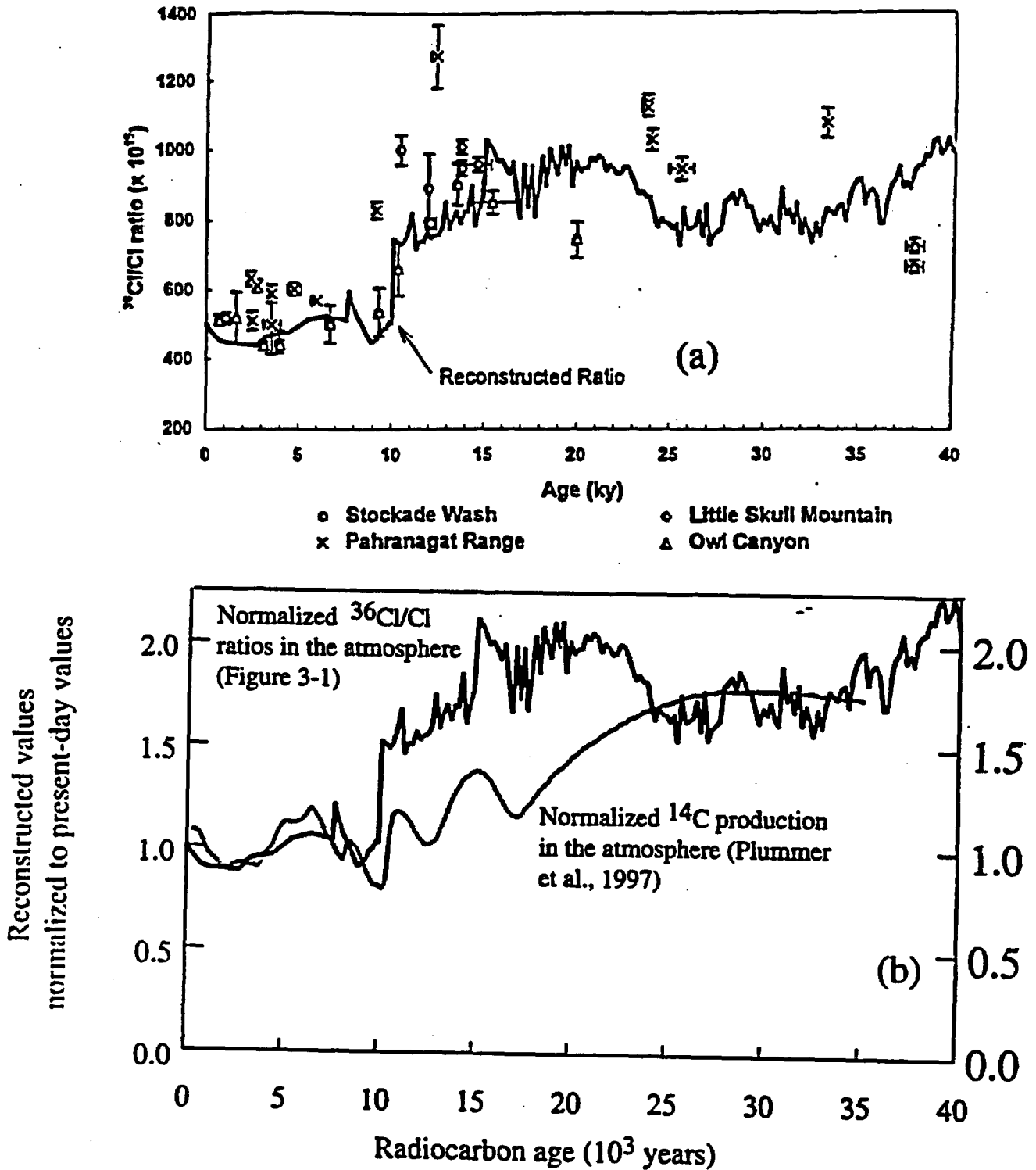


Figure 3-2. Reconstructed atmospheric  $^{36}\text{Cl}/\text{Cl}$  ratio. (a) Comparison of reconstructed  $^{36}\text{Cl}/\text{Cl}$  ratio to measured  $^{36}\text{Cl}/\text{Cl}$  ratios for fossilized packrat urine from southern Nevada (Plummer et al., 1997). (b) Comparison of reconstructed  $^{36}\text{Cl}/\text{Cl}$  ratio (normalized to present-day value of  $500 \times 10^{-15}$ ) to the reconstructed  $^{14}\text{C}$  activity of Plummer et al. (1997).

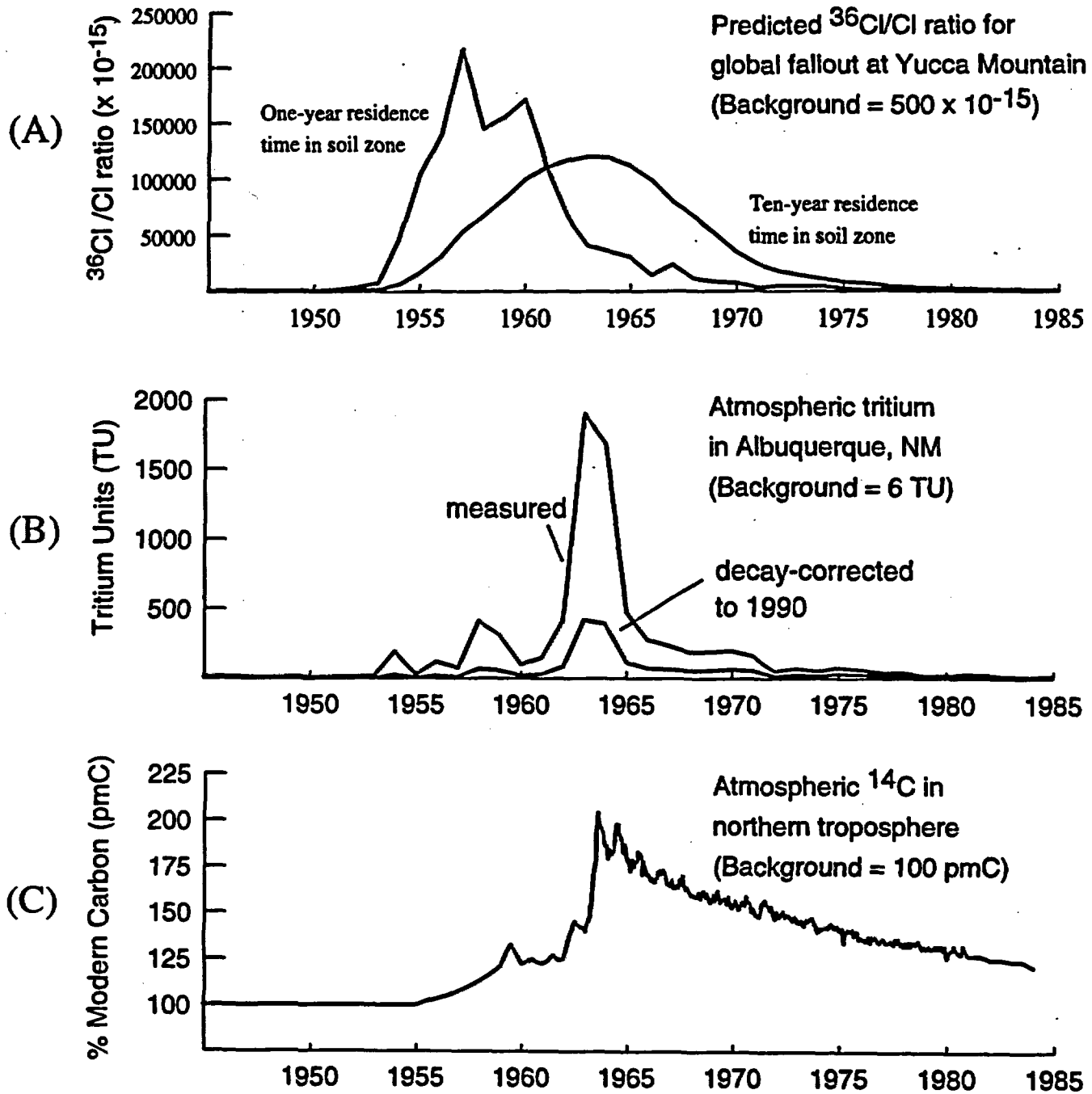


Figure 3-3 Comparison of input functions for bomb-pulse nuclides at Yucca Mountain. (A) Estimated  $^{36}\text{Cl}/\text{Cl}$  ratio for global fallout at Yucca Mountain, as a function of average residence time in the soil zone, (B) tritium in atmospheric moisture in Albuquerque, NM, and (C) atmospheric concentrations of bomb-pulse  $^{14}\text{C}$  for the northern hemisphere (Fabryka-Martin et al., in press [b]).

## 4. EXPERIMENTAL DESIGN

Geochemical and isotopic analyses have been conducted on a variety of sample matrices for this study, including soils, borehole cuttings and drillcore, rocks collected by hand from ESF tunnel walls, and surface and subsurface waters at the site. Sample preparation involves leaching of soil and rock samples with deionized water to extract soluble salts, or direct extraction of pore fluids from drill core by high-speed centrifugation. Mass spectrometry is used to measure the  $^{36}\text{Cl}/\text{Cl}$  ratios for these samples, and ion chromatography is used to measure the anion concentrations. This section describes the analytical methods, including quality control measures (section 4.1), and presents data obtained for ESF rocks (section 4.2), surface soils and soil profiles (section 4.3), borehole samples (section 4.4), and waters (section 4.5). Statistical analysis of the extensive data set for ESF rock samples is used to establish the threshold  $^{36}\text{Cl}/\text{Cl}$  ratio for identifying the presence of bomb-pulse  $^{36}\text{Cl}$  in subsurface samples.

### 4.1 Analytical methods

#### 4.1.1 Chlorine isotopic analysis

Analysis of chlorine isotopes in a sample requires 2 to 5 mg Cl. To prepare soil or rock samples for Cl isotopic analysis, Cl is extracted from 1 to 5 kg of material by leaching it with an equal mass of deionized water for 48 hours. The Cl of interest is on the outer surfaces of particles or fractures. Loose or poorly consolidated material is leached without further size reduction, but other samples are generally gently crushed to 1- to 2-cm size fragments prior to leaching in order to increase the efficiency of extracting porewater salts. An unfortunate but unavoidable side-effect of such treatment is to increase also the efficiency of extracting fluid inclusion salts, and the magnitude of this effect is estimated from the Br/Cl and  $\text{SO}_4/\text{Cl}$  ratios of the extracted salts. An aliquot of the leachate is therefore analyzed for Cl, Br and  $\text{SO}_4$  by ion chromatography to estimate the contribution of Cl from sources other than meteoric salts (e.g., rock fluid inclusion salts, or Cl in ESF construction water which is traced with lithium bromide). It is important to note that the concentrations of salts leached from soil and rock samples for this study provide only a qualitative indication of the sample's actual soluble salt content. Because the focus of the activity is generally on determining anion ratios and isotopic ratios, no attempt has been made to maximize the yield of the leaching process, which is probably quite variable as well as probably quite low for consolidated material. Hence, it is inappropriate to use salt concentrations leached from rock samples in combination with known or estimated moisture contents to estimate *in-situ* porewater concentrations.

The leachate is decanted, acidified to promote settling of particulates, and filtered. Water samples are also analyzed by ion chromatography to ensure sufficient Cl for analysis, then acidified and filtered. A known quantity of isotopically pure  $^{35}\text{Cl}$  is added to the leachate or water sample if its total Cl concentration is less than 2 mg. Silver nitrate is added to the aqueous solution to precipitate silver chloride, AgCl. The AgCl is purified of sulfur, which has an interfering isobar at mass 36, by multiple cycles of dissolution in ammonium hydroxide with

Table 4-2. Analyses of J-13 well water and ESF construction water

LANL ID	Collection date	Source	Concentrations, mg/L			Weight ratios		<sup>36</sup> Cl/Cl x 10 <sup>-15</sup>
			Cl	Br	SO <sub>4</sub>	Br/Cl	SO <sub>4</sub> /Cl	
J-13 well water (source used to prepare ESF construction water)								
W101	22-Mar-95	J-13 well water	7.02	0.051	18.5	0.007	2.6	505 ± 9
W148	10-Mar-97	J-13 well water	7.19	0.051	18.7	0.007	2.6	---
W149	10-Mar-97	J-13 well water	7.14	0.050	18.6	0.007	2.6	---
ESF construction water samples, from makeup tank								
W112	31-Jan-96	Makeup tank	6.72	19.9	---	3.0	---	532±15
W123	09-Feb-96	Makeup tank	6.67	21.5	---	3.2	---	---
W126	23-Feb-96	Makeup tank	6.87	18.9	19.3	2.8	2.8	---
W128	05-Mar-96	Makeup tank	7.03	21.1	---	3.0	---	---
W143	13-Aug-96	Makeup tank	6.83	14.5	---	2.1	---	---
W150	05-Mar-97	Makeup tank	7.08	20.9	18.5	3.0	2.6	---
W152	06-Mar-97	Makeup tank	7.61	26.4	22.5	3.5	3.0	---
W153	17-Mar-97	Makeup tank	7.46	20.3	22.3	2.7	3.0	---
W154	02-Apr-97	Makeup tank	7.10	21.2	19.4	3.0	2.7	---
W155	30-Apr-97	Makeup tank	7.05	21.8	18.5	3.1	2.6	---
ESF construction water samples, from water outlets at point of use								
W096	27-Apr-95	Water jet	8.90	19.5	---	2.2	---	493±13
W114	31-Jan-96	Outlet @ CS35+89	6.67	19.9	---	3.0	---	---
W116	31-Jan-96	Supplem'l drill deck @CS40+17	6.67	19.9	---	3.0	---	---
W117	31-Jan-96	TBM Deck 14 @CS40+17	6.71	20.0	---	3.0	---	---
W118	31-Jan-96	TBM Primary drill deck, CS40+17	6.71	20.1	---	3.0	---	---
W119	31-Jan-96	Water outlet, Alcove #2	6.68	19.9	---	3.0	---	---
W120	31-Jan-96	Water outlet @CS28+66	6.79	20.6	---	3.0	---	---
W121	31-Jan-96	Water outlet, Alcove #3	6.67	19.7	---	3.0	---	---
W122	31-Jan-96	Water outlet, Alcove #4	6.64	21.1	---	3.2	---	---
W137	13-Aug-96	Thermal Test Facility @ CS0+83	7.13	17.9	15.3	2.5	2.2	---
W138	13-Aug-96	Water outlet @ CS19+66	7.19	18.5	---	2.6	---	---
W140	13-Aug-96	Water outlet @ CS01+49	7.06	18.2	18.7	2.6	2.6	---
W142	13-Aug-96	Water outlet @ CS10+90	7.07	18.4	---	2.6	---	---
W144	13-Aug-96	Water outlet @ CS29+48	7.03	16.6	---	2.4	---	---

several forms:

- interlaboratory comparisons in the early phase of the project (1992-93), in which aliquots of several samples were submitted to three different analytical facilities,
- blind duplicates submitted to the analytical facility by the user under different sample identifiers, and
- internal duplicates. The latter is a standard QA/QC practice for PRIME Laboratory and involves re-analysis of previously-analyzed silver chloride samples for which sufficient material still exists.

Results of these QA/QC checks indicate a degree of precision that is more than adequate for the intended purpose.

*Replicate analyses of environmental samples.* A final type of quality control measure involves re-analysis of environmental samples starting from the raw material and independently processing different aliquots of the same sample. Such analyses show that signals measured in Cl extracted from homogeneous samples such as waters and soils are reproducible. However, signals measured for fractured rock samples are often difficult to reproduce, presumably because of variable degrees of dilution of the meteoric component by other sources of Cl. Differences are particularly large—by as much as a factor of 2— if bomb-pulse  $^{36}\text{Cl}$  is present in the sample. This issue is discussed in section 4.2.5, which presents data for several replicates of ESF rock samples and discusses how Br/Cl and  $\text{SO}_4/\text{Cl}$  ratios might serve to identify extraneous sources of Cl.

Another type of replicate analysis involves resampling of a particular location. Again, the signal is generally reproducible for homogeneous matrices such as water (e.g., perched water, section 4.5). Data are still being collected to evaluate the reproducibility of signals for rock samples when a given location is resampled, but the few data available so far for ESF samples indicate that reproducibility is difficult if the sample consists of fractured rock containing a component of bomb-pulse  $^{36}\text{Cl}$ , presumably because of the heterogeneous distribution of construction water and water containing bomb-pulse  $^{36}\text{Cl}$  in the fractured rock.

#### 4.1.2 Pore-water extraction

We recently began extracting pore water from unsaturated drillcore using a high-speed centrifuge, for the purpose of measuring *in-situ* anion concentrations (see Yang et al., 1990, for a discussion of this method). Direct extraction, as opposed to leaching crushed rock, is much preferable when feasible because it provides data on the *in-situ* anion concentrations and  $^{36}\text{Cl}/\text{Cl}$  ratios and minimizes uncertainties arising from the problem of salts released from broken fluid inclusions. Although the efficiency of water extraction is less using a centrifuge than it is using the alternative method of high-pressure compression (Mower et al., 1994), the centrifuge may be preferable to the compression system for some applications because the latter applies a body force that acts unequally on various points within the system, dependent on the rock's physical properties; consequently, the high pressures used in a compression system run the risk of inducing fracturing or grain rearrangements that could cause subtle changes to the concentrations

of trace elements such as Br. These effects were discussed in detail by Mower et al. (1994), who provided quantitative data for the changes in pore size distributions and fractures caused by the compression method, as a function of tuff lithology and maximum axial stress applied to the sample. The authors concluded that the effects of uniaxial compression on pore-water chemistry were not sufficiently understood at that time. The effect of fluid inclusion salts is probably negligible in samples with relatively high porosities or water contents, but could conceivably be significant for rocks with low porosity or low water content in which the release of salts from larger fluid inclusions could significantly shift anion ratios, which we are using as *in-situ* tracers of mixing processes.

The high-speed centrifuge that is being used for this effort is a Beckman L8-UFA ultracentrifuge capable of operating at 10,000 rpm by running in a vacuum chamber. The samples are derived from dry-drilled drillholes and are sealed in Lexan Protecure in the field. These are stored under cool conditions until ready for analysis. About 100 grams of the drillcore is gently broken to the minimum extent necessary to fit pieces into the centrifuge specimen holder. Effluent is collected in a cup at the bottom of the specimen assembly. Thus far, only PTn samples have been analyzed, and typical yields have been 0.4 to 5 mL per 70-g sample after an extraction period of about 24 hours. Results are reported in section 4.5.2.

#### 4.1.3 Ion chromatography analysis

Aqueous solutions are analyzed for Cl, Br and SO<sub>4</sub> using a customized ion chromatography system. In this system, eluent solution carries the aqueous sample through an anion exchange column where the various anionic species are separated based on their relative affinities for the fixed exchange sites. Anions are detected using a conductivity detector. Detector response is recorded as peaks in a chromatogram which is integrated by a chromatography software program. Anion concentrations in the sample are determined by comparison of sample peak areas with the peak areas in a calibration curve prepared from a suite of standards. The LANL system routinely achieves detection limits of 2 ppb Br and 0.1 ppm Cl with precisions better than 5%. Each of the system's individual components play a critical and necessary role in ensuring this level of performance:

- Dionex IP-20 pump: Dual pump heads reduce pulsation, thereby minimizing baseline noise.
- Thermo Separation AS3500 autosampler: The autosampler contains no metal parts in the sample delivery system, thereby decreasing background conductivity.
- Dionex 2 mm AS4A-SC column: The small bore of this anion-exchange column allows for increased sensitivity because samples are eluted by a smaller volume of eluent, thus decreasing sample dilution in the column.
- Dionex 2 mm ASRS1 suppressor with pressurized regenerant. The use of pressure to control the regenerant flow removes pump noise from the baseline. The regenerant decreases background conductivity, thereby increasing the detector's response to the analyte.
- Dionex CDM-III conductivity detector: An 18-bit processor smooths the baseline by increasing the rate of data acquisition.
- Dionex AI-450 computer software. This software permits precise and reproducible marking of

chromatogram peaks, resulting in more accurate integration of the peak areas.

The acceptability of data collected using this system is determined by following strict quality assurance guidelines:

- A blank of deionized water is analyzed, at a minimum, at the beginning and end of each day's run to monitor for the presence of contamination. Sample data are discarded if the analyte concentration of the blank exceeds 5% of the sample concentration.
- A calibration check standard is analyzed after every fifth sample.
- Samples are always analyzed in duplicate, with results rejected if the duplicates do not agree within 10%.
- Calibration curves must have a minimum  $r^2$  value of 0.99. The precision and accuracy of the curve throughout its range is tested by comparing the nominal concentration of each standard to its concentration calculated from its measured peak area. The calibration curve is valid for use only if the calculated concentrations agree with the nominal ones within 10%.

## 4.2 ESF rock samples

### 4.2.1 Sample collection

The ESF is a 8-km long tunnel at Yucca Mountain immediately east of the approximate boundary of the potential repository (Figure 4-3). ESF locations are specified as a function of position along the tunnel, called stationing. Each station represents 100 m, measured from the north portal (Figure 4-3). For example, a location 1115 m inward is designated as Station (abbreviated Sta.) 11+15. Appendix A lists the 234 samples collected in the ESF for  $^{36}\text{Cl}$  analysis from November 1995 to August 1997. Additional samples were also collected before and during this period of time but have been omitted from the appendix because there are currently no plans to analyze them in the near future. Reasons for their low priority for analysis include excessive contamination with construction water, inadequate quantity, a matrix requiring the development of new sample-processing techniques, or adequate coverage of an area by other samples which have been analyzed. Although the excavation of the ESF tunnel was completed between April and June of 1997, sample collection is still ongoing for this activity in the South Ramp, in Niches #1 and #2, and in Alcoves 6 and 7. Sample collection involving drilling equipment was temporarily halted in July 1997 due to concerns about the generation of rock dust during drilling and due to a lack of available miners and safety escorts for this activity.

Table 4-1 summarizes the 234 samples according to the criterion used to guide their collection and according to the approximate location within the ESF, as plotted in the series of detailed maps of surface geology, infiltration and soil thickness contained in Appendix D. The samples are classified in two general categories: systematic samples and feature-based samples (Fabryka-Martin et al., in press [a]). Systematic samples comprise 20% of the sample inventory and were collected at fixed intervals along the ESF tunnel: every 200 m from Station 5+00 to 59+00, increasing in frequency to every 100 m from Station 59+00 to 69+00 and from 69+50 to 76+50. The increase in frequency of systematic sampling was adopted in response to informal

Table 4-1. Summary of ESF samples collected, by collection criterion

Appendix figure	General geographic area	ESF stations		Sample collection criterion <sup>1</sup>				
		From	To	Systematic	Feature-based			Total
					Subunit contact	Feature <sup>2</sup>	Other <sup>3</sup>	
D-3	Azreal Ridge	0+00	18+00	8	22	34	3	67
D-4	Drill Hole Wash / Diabolus Ridge	18+00	30+00	6	0	20	0	26
D-5	Sundance Fault	30+00	40+00	4	0	29	0	33
D-6	Antler Ridge / Whale Back Ridge	40+00	54+00	7	0	20	0	27
D-7	Ghost Dance Wash	54+00	69+00	13	2	29	2	46
D-8	Boundary Ridge	69+00	77+10	8	4	23	0	35
Subtotal				46	28	155	5	234
% of total				20%	12%	66%	2%	100%

<sup>1</sup> This table is only intended to provide an approximate picture of the type of number of samples collected. At many locations, sample fractions were collected in separate bags (e.g., fault gouge and adjacent wall rock) but were only counted as a single sample in the above table.

<sup>2</sup> Feature: This category includes samples collected from specific fractures, faults, lithophysal cavities, breccia zones, or zones of broken rock.

<sup>3</sup> Other: This sampling category includes intact rock collected next to a fracture or fault, wet zone, or intact matrix

discussion with the Advisory Committee on Nuclear Waste because of the concern that the 200-m spacing was inadequate for characterization of the frequency of fast paths. The systematic sampling was designed to acquire isotopic data unbiased by any other selection criteria. These samples represent the rock matrix and whatever fracture fabric typifies the collection site.

All samples collected that are not systematic samples are considered feature-based samples. The 188 feature-based samples listed in Appendix A comprise 80% of the sample inventory. The selection of feature-based sample localities in the ESF followed criteria designed to address key aspects of flow variability and permeability differences and to test conceptual models of subsurface percolation. The following general types of criteria and sampling objectives were used in selecting feature-based samples in the ESF; in many cases, the same sample fulfilled more than one objective.

- *Zones of high moisture content* are areas that are notably damper than the surrounding rock. For example, three locations along the South Ramp between stations 67+00 and 68+00 were noticeably damp at time of sampling, as well as the back of Niche #1 near station 37+37. Such areas could represent one or more of the following: fast paths, preferential paths, perched water, fracture-matrix interaction, or lateral diversion. Chlorine-36 analysis may help distinguish among these alternatives.
- Sampling of *faults* was undertaken to establish the role of faults in percolation in the unsaturated zone and to investigate the existence and distribution of fast pathways. Faults and fractures (discussed below) were the single most common target for sampling, together accounting for about 66% of the samples in Appendix A. Faults sampled included ESF exposures of large faults known to correlate with faults mapped at the surface, as well as minor offsets of only local extent. ESF exposures of faults that cut across the top and base of the PTn hydrogeologic unit were sampled to study how such faults modify the flow across or along these boundaries.
- The role of *fractures, breccias, and broken zones* in percolation includes the distribution of flow paths away from faults and the contribution of fracture flow to the overall unsaturated zone percolation budget.
- *Stagnant zones* are conceived of as zones where water movement has been the slowest. Such zones may be expected where fractures and faults are absent or have the least connectivity across units. The locations and existence of stagnant zones may also be related to low net infiltration. These form a subset of the systematic and fracture categories.
- Coordination with *uranium-series and <sup>14</sup>C studies* was a criterion for sampling some deposits of calcite and opal. The existence of these secondary-mineral deposits in fractures, breccia zones, and lithophysal cavities indicates that these features have received infiltration. The deposits have been extensively sampled by the U.S. Geological Survey for geochronology studies (e.g. Paces et al., 1996). Although the kilogram-size samples collected for <sup>36</sup>Cl/Cl analysis are not physically equivalent to the small (tens of mg) samples collected for uranium-series and <sup>14</sup>C geochronology, the parallel sampling provides some basis for comparison between estimates of infiltrating water ages inferred from all three techniques.
- *Lateral diversion of flow* at unit and subunit contacts and subhorizontal fractures is a process

invoked by many conceptual models of infiltration. Changes in matrix hydrologic properties or fracture frequency associated with contacts between different lithostratigraphic units may cause infiltration to move laterally along the contacts. These conditions are most likely to exist within, and just above, the PTn hydrogeologic unit. Subhorizontal fractures that intersect steeply dipping transmissive faults and fractures may also cause lateral diversion of flow.

- *Fracture-matrix interaction* includes the movement of percolating water from fractures into the rock matrix. In some damp zones, such movement may be self-evident and can be used to guide the selection of sample sites. The more common situation is for sampling to be based solely on the textural differences between highly fractured rock and adjacent less fractured matrix. Breccia zones represent a special case of interaction between the bounding fractures of the breccia zones and the broken-up breccia matrix. In all cases, isotopic evidence of differences between paired fracture and matrix samples is more readily detected at sites where bomb-pulse  $^{36}\text{Cl}/\text{Cl}$  values are present (section 7.4).
- *Representative background values* of  $^{36}\text{Cl}/\text{Cl}$  typical of matrix pore fluids are required for comparison with isotopic data from faults and fractures. Most of the systematic samples serve this purpose, but additional matrix samples may be collected to represent specific lithologies or locations of interest.
- The role of *PTn matrix flow* is a key factor modulating the downward movement of percolating water from the surface, even without additional factors such as lateral diversion at lithologic contacts.

#### 4.2.2 *ESF construction water*

Construction water is used for numerous routine operations in the ESF, including wetting the Tunnel Boring Machine cutter head, wet-drilling for installation of rock bolts, providing dust control on the muck belt, and spraying tunnel ribs to facilitate fracture mapping. It is prepared from UE25 J#13 wellwater traced with lithium bromide salt to a bromide concentration of 20 mg/L, about 400 times its background level. ESF construction water has been sampled periodically over the past two years from a variety of locations in order to provide data needed to evaluate the extent to which this source could be contributing Cl to the rock samples. Water samples were collected by the Test Coordination Office (TCO) from various locations including the mixing tank where the LiBr tracer is added, multiple water outlets within the ESF, and the return flow from the ESF. Halide and  $^{36}\text{Cl}/\text{Cl}$  analyses of selected samples and of well J-13 source water are reported in Table 4-2. Based on the 24 samples from the makeup tank and water outlets, these data confirm that the construction water is usually traced with appropriate precision and accuracy, to a Br concentration of  $20 \pm 2$  mg/L. The Cl concentration in these samples varies slightly, with an average value of  $7.0 \pm 0.5$  mg/L. The Br/Cl ratio, which is the parameter most relevant to the  $^{36}\text{Cl}$  activity, has an average value of  $2.8 \pm 0.3$ , which is about 400 times greater than the Br/Cl ratio of J-13 water.

Increased Cl concentrations in the used water, as much as 4 times the concentration in the original water, presumably result from a combination of evaporation and addition of salts released from the rock during drilling (Table 4-2, "ESF construction water samples after use").

Table 4-2. Analyses of J-13 well water and ESF construction water

LANL ID	Collection date	Source	Concentrations, mg/L			Weight ratios		<sup>36</sup> Cl/Cl x 10 <sup>-15</sup>
			Cl	Br	SO <sub>4</sub>	Br/Cl	SO <sub>4</sub> /Cl	
J-13 well water (source used to prepare ESF construction water)								
W101	22-Mar-95	J-13 well water	7.02	0.051	18.5	0.007	2.6	505 ± 9
W148	10-Mar-97	J-13 well water	7.19	0.051	18.7	0.007	2.6	---
W149	10-Mar-97	J-13 well water	7.14	0.050	18.6	0.007	2.6	---
ESF construction water samples, from makeup tank								
W112	31-Jan-96	Makeup tank	6.72	19.9	---	3.0	---	532±15
W123	09-Feb-96	Makeup tank	6.67	21.5	---	3.2	---	---
W126	23-Feb-96	Makeup tank	6.87	18.9	19.3	2.8	2.8	---
W128	05-Mar-96	Makeup tank	7.03	21.1	---	3.0	---	---
W143	13-Aug-96	Makeup tank	6.83	14.5	---	2.1	---	---
W150	05-Mar-97	Makeup tank	7.08	20.9	18.5	3.0	2.6	---
W152	06-Mar-97	Makeup tank	7.61	26.4	22.5	3.5	3.0	---
W153	17-Mar-97	Makeup tank	7.46	20.3	22.3	2.7	3.0	---
W154	02-Apr-97	Makeup tank	7.10	21.2	19.4	3.0	2.7	---
W155	30-Apr-97	Makeup tank	7.05	21.8	18.5	3.1	2.6	---
ESF construction water samples, from water outlets at point of use								
W096	27-Apr-95	Water jet	8.90	19.5	---	2.2	---	493±13
W114	31-Jan-96	Outlet @ CS35+89	6.67	19.9	---	3.0	---	---
W116	31-Jan-96	Supplem'l drill deck @CS40+17	6.67	19.9	---	3.0	---	---
W117	31-Jan-96	TBM Deck 14 @CS40+17	6.71	20.0	---	3.0	---	---
W118	31-Jan-96	TBM Primary drill deck, CS40+17	6.71	20.1	---	3.0	---	---
W119	31-Jan-96	Water outlet, Alcove #2	6.68	19.9	---	3.0	---	---
W120	31-Jan-96	Water outlet @CS28+66	6.79	20.6	---	3.0	---	---
W121	31-Jan-96	Water outlet, Alcove #3	6.67	19.7	---	3.0	---	---
W122	31-Jan-96	Water outlet, Alcove #4	6.64	21.1	---	3.2	---	---
W137	13-Aug-96	Thermal Test Facility @ CS0+83	7.13	17.9	15.3	2.5	2.2	---
W138	13-Aug-96	Water outlet @ CS19+66	7.19	18.5	---	2.6	---	---
W140	13-Aug-96	Water outlet @ CS01+49	7.06	18.2	18.7	2.6	2.6	---
W142	13-Aug-96	Water outlet @ CS10+90	7.07	18.4	---	2.6	---	---
W144	13-Aug-96	Water outlet @ CS29+48	7.03	16.6	---	2.4	---	---

LANL ID	Collection date	Source	Concentrations, mg/L			Weight ratios		<sup>36</sup> Cl/Cl x 10 <sup>-15</sup>
			Cl	Br	SO <sub>4</sub>	Br/Cl	SO <sub>4</sub> /Cl	
<b>ESF construction water samples after use</b>								
W115	31-Jan-96	Belt water near Alcove #1	26.6	43.8	---	1.6	---	---
W113	31-Jan-96	Recovery tank	13.1	27.5	---	2.1	---	---
W124	09-Feb-96	Recovery tank	11.5	28.3	---	2.5	---	---
W127	23-Feb-96	Return water	10.9	23.6	---	2.2	---	---
W129	05-Mar-96	Return water	9.1	22.1	21.9	2.4	2.4	---
W139	13-Aug-96	Return water	12.2	26.5	---	2.2	---	---
W151	05-Mar-97	Recovery tank	10.5	24.1	21.9	2.3	2.1	---
<b>Other sources of water in the ESF</b>								
W110	27-Dec-95	Dripping rock bolt, Alcove #3	7.87	22.7	---	2.9	---	---
W111	27-Dec-95	Dripping rock bolt, Alcove #3	9.59	29.1	---	3.0	---	---
W145	25-Nov-96	Water from SHT Hole #16	2.19	0.029	1.6	0.001	0.7	334±16

Note: Samples were collected by the YMP Test Coordination Office and prepared for analysis at LANL. <sup>36</sup>Cl/Cl ratios were analyzed by the PRIME Laboratory at Purdue University.

Br concentrations increase to a lesser extent. Because of the negligibly low concentration of Br in the rock, increases in Br concentrations in the traced water after use should reflect the effects of evaporation only, provided there is no contribution from unintended sources of contamination.

One problem encountered with the use of Br/Cl ratios for estimating the extent to which Cl from construction water is present in a sample is that any release of rock Cl (e.g., from fluid inclusions) will dilute this ratio and lead to an underestimate of the construction water contribution. Consequently,  $\text{SO}_4/\text{Cl}$  ratios are presently being evaluated as an independent check for the presence of rock Cl. Although the  $\text{SO}_4/\text{Cl}$  ratio in construction water (average 2.7, Table 4-2) is indistinguishable from that of meteoric water, this signal is distinctly different and generally lower by one to two orders of magnitude in salts extracted from the different tuff units (section 4.4.4, Table 4-12). The effect of adding a small component of rock-derived salts to porewater containing meteoric salts (as represented by ESF construction water) is illustrated by the slight decrease observed in the Br/Cl and  $\text{SO}_4/\text{Cl}$  ratios measured in the ESF water after use (Table 4-2, compare ratios for the makeup water to those for the water after use). In this case, the original ratios of the construction water from the makeup tank (in which the tracer is added to J-13 well water) are slightly diluted by the lower Br/Cl and  $\text{SO}_4/\text{Cl}$  ratios of the rock component released during the mining operation. Application of  $\text{SO}_4/\text{Cl}$  ratios to the evaluation of the  $^{36}\text{Cl}$  analyses for ESF rock samples is discussed further in section 4.2.5.

#### 4.2.3 Analytical data for ESF rock samples

Based on Br/Cl ratios in the salts leached from the rocks, measured  $^{36}\text{Cl}/\text{Cl}$  ratios are adjusted for the presence of Cl from construction water. The proportion of Cl contributed by construction water has been estimated using a two-component mixing equation and known or estimated Br/Cl ratios of the construction water and percolating waters (see notes 2 and 3, Appendix B, page B-1). It is important to note that the  $^{36}\text{Cl}/\text{Cl}$  ratio of the construction water ( $500 \times 10^{-15}$ ) is equal to the atmospheric background  $^{36}\text{Cl}/\text{Cl}$  level, such that any  $^{36}\text{Cl}$  levels above background cannot be attributed to this source. The measured Br and Cl concentrations and the corrected  $^{36}\text{Cl}/\text{Cl}$  ratios for ESF rock samples are presented in Appendix B. Recently, we also began to measure  $\text{SO}_4$  concentrations in the rock leachates in order to evaluate the extent to which the assumption of only two components may be an over-simplification. This aspect is discussed in section 4.2.5.

The last progress report for the Water Movement Test activity (Levy et al., 1997) reported 189 analytical results for 173 sample locations up to Station 67+90; the present report increases the number of analyses to 247 results for 224 locations (Appendix B). The data are plotted as a function of station in Figure 4-4. Table 4-3 summarizes these analyses according to the sampling criterion under which they were classified, and according to their spatial location as shown on the geology, infiltration and soil thickness maps presented in Appendix D. About 67% of the analyses are for samples collected from faults, fractures, lithophysal cavities, breccia zones, and broken rock. Forty-nine analyses of systematic samples compose 20% of the analytical data base, 11% of the analyses (28 sample results) are subunit contacts in and above the PTn unit, and

Table 4-3. Summary of ESF samples analyzed, by collection criterion

Appen figure	General geographic area	ESF stations		Sample collection criterion <sup>1</sup>				
		From	To	Systematic	Feature-based			Total
					Subunit contact	Feature <sup>2</sup>	Other <sup>3</sup>	
D-3	Azreal Ridge	0+00	18+00	10	22	36	3	71
D-4	Drill Hole Wash / Diabolus Ridge	18+00	30+00	6	0	22	0	28
D-5	Sundance Fault	30+00	40+00	4	0	30	0	34
D-6	Antler Ridge / Whale Back Ridge	40+00	54+00	7	0	22	0	29
D-7	Ghost Dance Wash	54+00	69+00	15	3	31	1	50
D-8	Boundary Ridge	69+00	77+10	7	3	25	0	35
Subtotal				49	28	166	4	247
% of total				20%	11%	67%	2%	100%

Notes

- <sup>1</sup> This table is meant to provide an approximate picture of the type and number of samples analyzed. Many samples were analyzed more than once, generally to assess the reproducibility of a result or to compare the results of different aliquots of a given sample (e.g., fracture fill versus the adjacent intact matrix). All analyses have been included in the sample count above.
- <sup>2</sup> Feature: This category includes samples collected from specific fractures, faults, lithophysal cavities, breccia zones, or zones of broken rock.
- <sup>3</sup> Other: This sampling category includes intact rock collected next to a fracture or fault, wet zone, or intact matrix

the remaining 2% (4 samples) are for damp zones or other categories not covered by the previous set.

Table 4-4 summarizes the analyses according to the magnitude of the  $^{36}\text{Cl}/\text{Cl}$  ratio, and according to their location in the ESF, corresponding to the areas covered by the detailed maps in Appendix D. The  $^{36}\text{Cl}/\text{Cl}$  data fall clearly into two distinct populations (Figures 4-4 and 4-5). The majority of the samples (77%) have corrected  $^{36}\text{Cl}/\text{Cl}$  ratios ranging between  $350 \times 10^{-15}$  and  $1000 \times 10^{-15}$ , or 0.7 to 2 times the present-day background value of  $500 \times 10^{-15}$ . These results fall well within the range over which the atmospheric  $^{36}\text{Cl}/\text{Cl}$  signal has varied during the past 30 ka or more (section 3.1.2, Figure 3-2b). However, at a few locations, ratios extend well above this range, to a maximum of  $4100 \times 10^{-15}$  measured for a sample from station 34+28. These high ratios are interpreted as indicating the presence of a component of bomb-pulse  $^{36}\text{Cl}$  at these locations. In addition, a small number of samples extend significantly below the range of meteoric background values ( $^{36}\text{Cl}/\text{Cl}$  ratios  $< 350 \times 10^{-15}$ ). One possible interpretation that is being evaluated for this set of samples is whether or not these provide evidence for stagnant zones with travel times sufficiently long for radioactive decay of meteoric  $^{36}\text{Cl}$  to have occurred (i.e., water ages on the order of  $10^5$  years). Appendix C contains detailed characterization of structural and petrologic characteristics of these samples with ratios outside the range of meteoric background values. Interpretation of the distribution of  $^{36}\text{Cl}$  in ESF samples, with respect to the implications for conceptual model of unsaturated-zone flow and transport at Yucca Mountain, is discussed in detail in Appendix D and section 6.

#### 4.2.4 *Statistical analysis for the presence of bomb-pulse $^{36}\text{Cl}$*

Chauvenet's criterion for identifying outliers is the basis of the statistical test used to establish the cutoff ratio above which a sample result is considered to be elevated above natural background (Bevington and Robinson, 1992). The approach taken in this report is to rank the 247 data points (Appendix B) from lowest to highest value, and to calculate a cumulative average and standard deviation for each step of the ranking. One then calculates the number of standard deviations that the highest-value data point lies above the mean as each new data point is included in the cumulative average. These standard deviations are plotted in Figure 4-6, in which they are compared against Chauvenet's criterion for identifying outliers (solid line) as a function of ranking. This criterion states that a data point is an outlier of a Gaussian (normal) distribution if the probability of such a value being that far from the cumulative mean of the ranked data set is less than 0.5% (Bevington and Robinson, 1992).

The plot of sample standard deviations versus sample rank (Figure 4-6) varies smoothly within the region of background values but shows an abrupt jump between samples ranked 215 and 216, with  $^{36}\text{Cl}/\text{Cl}$  ratios of  $1202 \times 10^{-15}$  and  $1292 \times 10^{-15}$  for samples E196-2 and E195-2, which are samples above and within a PTn subunit contact at station 10+56, respectively. For the latter sample, the calculated number of standard deviations (3.44) exceeds Chauvenet's criterion for identifying statistical outliers. Hence, all subsequent values at or above that measured for sample

Table 4-4. Summary of  $^{36}\text{Cl}/\text{Cl}$  analyses for ESF rock samples, by magnitude of measured ratio

Appendix figure	General geographic area	ESF stations		Range of Corrected $^{36}\text{Cl}/\text{Cl}$ Ratios ( $\times 10^{-15}$ )					Total
		From	To	< 350	350-600	600-1000	1000-1250	> 1250	
D-3	Azreal Ridge	0+00	18+00	0	18	37	4	12	71
D-4	Drill Hole Wash / Diabolus Ridge	18+00	30+00	0	7	11	3	7	28
D-5	Sundance Fault	30+00	40+00	0	14	7	2	11	34
D-6	Antler Ridge / Whale Back Ridge	40+00	54+00	2	14	9	1	3	29
D-7	Ghost Dance Wash	54+00	69+00	6	35	8	1	0	50
D-8	Boundary Ridge	69+00	77+10	4	31	0	0	0	35
Subtotal				12	119	72	11	33	247
% of total				5%	48%	29%	4%	13%	100%

E195-2 are also considered to lie clearly outside the range of the population of background samples. The cutoff value is a ratio of about  $1250 \times 10^{-15}$ . This value also marks the upper limit of the normal distribution of the background samples in a frequency, or histogram, plot of these data (Figure 4-5). Figure 4-5 also shows that the background data do not follow a truly Gaussian distribution but rather are moderately to strongly skewed, with a Pearsonian coefficient of skewness of 0.90 (Pearsonian coefficient of skewness =  $3 \text{ (mean - median) / standard deviation}$ ). This deviation from ideal conditions is not expected to significantly affect the test results with respect to identifying samples with an unambiguous component of bomb-pulse, although it probably results at least in part from the presence of a small component of bomb-pulse  $^{36}\text{Cl}$  in many of the samples with ratios less than  $1250 \times 10^{-15}$ . In the future, more sophisticated statistical analyses will be used in the next stage of data evaluation to address this shortcoming of the current approach.

Based on a cutoff ratio of  $1250 \times 10^{-15}$ , 33 analyses (13%) indicate the presence of bomb-pulse  $^{36}\text{Cl}$ . It can be seen from the profile in Figure 4-4 that the fast paths identified by this approach are not distributed evenly throughout the ESF, but rather that they cluster at distinct locations in the north half of the ESF, along the North Ramp and the Main Drift as far south as station 45+00. No samples containing unambiguous levels of bomb-pulse  $^{36}\text{Cl}$  have yet been detected in any of the 103 samples analyzed beyond Station 45+00, although the distinct peaks in the profile at station 56+93 (near the Ghost Dance fault) and station 68+00 (near the Dune Wash fault) are suggestive of its presence at these locations.

#### 4.2.5 Replicate analyses

The reproducibility of analytical results for a given sample, and the validity of the method for correcting the ratios for construction water, were tested by processing different aliquots from the same raw material (Table 4-5). The measured ratio for each case was corrected using the two-component mixing model described in section 4.2.2 and Appendix B, i.e., assuming the absence of any significant rock Cl, and assuming that the Br/Cl ratios of construction water and meteoric water could each be adequately characterized by distinctive values.

- Results for the two aliquots of E300 and E326 (stations 69+68 and 76+31, respectively) are statistically indistinguishable, suggesting homogeneity of the signal at these locations, with negligible contribution of Cl from sources other than meteoric water. These two samples do not appear to contain any component of bomb-pulse  $^{36}\text{Cl}$ , nor a significant proportion of Cl derived from construction water.
- Differences among the  $^{36}\text{Cl}/\text{Cl}$  results for the three aliquots of E249 (station 11+00) are slightly greater. Based on the Br/Cl ratio, this sample contains a large proportion (26%) of Cl from construction water. The slightly elevated and variable ratios suggest a possible small component of bomb-pulse  $^{36}\text{Cl}$ , implying heterogeneity of the signal in the fractured rock at this location.
- The differences between  $^{36}\text{Cl}/\text{Cl}$  ratios are extreme for E046 (by a factor of 2) and E160 (factor

Table 4-5. Replicate analyses of ESF samples

Sample ID (Note 1)	Aliquot	ESF station	Lithologic unit (Note 2)	Leached salts (Note 3)			% Cl from construction water (Note 4)	Corrected $^{36}\text{Cl}/\text{Cl}$ $\times 10^{-15}$ (Note 5)
				Leached mg Cl $\text{kg}^{-1}$	Br/Cl $\times 10^{-3}$	$\text{SO}_4/\text{Cl}$		
E046-1	Representative	22+71	Tptpul	0.97	586	1.4	9	862 ± 43
E046-4*	Representative	22+71		1.05	278	4.7	3	458 ± 24
E160-1	Representative	35+45	Tptpmn	0.25	802	1.6	27	3329 ± 166
E160-4*	Representative	35+45		1.77	64	1.0	2	388 ± 17
E249-1	Representative	11+00	Tptrv1	0.46	815	2.4	27	655 ± 37
E249-3	Coarse fraction	11+00		0.35	771	2.1	25	674 ± 47
E249-4	Fine fraction	11+00		0.93	781	3.2	26	910 ± 58
E300-1	Representative	69+68	Tptrn	2.49	176	1.1	6	354 ± 13
E300-3	Representative	69+68		2.27	181	1.0	6	376 ± 16
E326-1	Representative	76+31	Tpcpln	4.65	62	1.4	2	423 ± 9
E326-3	Representative	76+31		3.35	29	0.9	1	419 ± 11

Notes:

1. An asterisk (\*) denotes samples that were processed at PRIME Laboratory. The ultimate objective of this particular set of analyses was to determine the *in-situ*  $^{36}\text{Cl}/\text{Cl}$  ratio for the tuff. Consequently, samples were crushed and ground before leaching them to extract Cl. The analyses reported above are for the first leach, in which the proportion of meteoric Cl would be maximized but in which a significant component of rock Cl would also be present.
2. Hydrogeologic and lithostratigraphic units are defined in Table 2-1.
3. Analytical data from Appendix B. The concentration of Cl leached from the sample is only a qualitative indicator of the sample's Cl content. Rock samples were leached for 48 hours in deionized water using a water:rock weight ratio of 1:1. Because the focus of this activity is generally on determining anion ratios and isotopic ratios, no attempt is made to maximize the yield of the leaching process, which is probably quite variable.
4. The Br/Cl ratio of the leached salts is used to estimate the proportion of Cl derived from construction water, assuming that meteoric salts and construction water are the only two significant sources of Cl in a sample. See footnotes to Appendix B.
5. Analytical data from Appendix B.  $^{36}\text{Cl}/\text{Cl}$  ratios reported in this table have been adjusted for the assumed presence of construction water using this correction approach. The shortcomings of this approach as a result of its inability to account for shifts in the Br/Cl ratio as the result of salts released from the rock itself are readily apparent from the disparate ratios obtained for the two first pairs of samples, in which the second sample in each pair is known to contain a sizable proportion of rock-derived Cl.

of 9) (stations 22+71 and 35+45, respectively). Such differences were expected because the second aliquot of each pair was ground before leaching, thereby releasing fluid inclusion salts that diluted the  $^{36}\text{Cl}/\text{Cl}$  ratio, while the first aliquot was processed following the normal method in which crushing the sample is minimized in order to minimize the release of rock Cl during leaching.

The data for the last two pairs of samples in particular illustrate the critical but difficult need to replicate identical conditions during sample preparation. Cl in any ESF rock sample will be a mixture of 3 sources: meteoric water, fluid inclusions in the rock, and construction water. The measured  $^{36}\text{Cl}/\text{Cl}$  ratio in a given aliquot of a sample is thus very sensitive to the proportion of fracture surfaces (which would be influenced to the greatest extent by construction water, if present, as well as by bomb-pulse  $^{36}\text{Cl}$ ) and to the extent to which the sample has been crushed, thereby releasing rock Cl from fluid inclusions. For ground sample E160-4, the release of rock Cl is clearly suggested by the observation of much higher Cl concentrations in its leachate relative to that in the leachate from sample E160-1, which was not finely ground. However, the amount of Cl itself in the leachate is not a reliable indicator for the presence of rock Cl as shown by the identical concentrations measured for E046-1 and E046-4. Likewise, for this extreme case, in which the release of rock salts was knowingly induced, the Br/Cl ratio by itself is shown to be an inadequate indicator of the proportion of rock Cl present because it is overwhelmed by the Br content of the construction water. We are currently investigating the possible use of  $\text{SO}_4/\text{Cl}$  ratios for distinguishing rock Cl in the presence of construction water in ESF rock samples.

Also in progress is a test of the reproducibility of analytical results by resampling a given location. Several locations containing bomb-pulse levels of  $^{36}\text{Cl}$  have been resampled. However, results of this resampling were not available at the time of this report.

#### 4.3 Soil samples

Soil profiles have been collected from Midway Valley (near the ESF North Portal), the NRG-5 drillpad, and Test Cell C and analyzed for Cl, Br and  $^{36}\text{Cl}$  in order to address the following issues:

- to estimate infiltration rates in areas of alluvial cover,
- to evaluate conditions under which fracture flow may be initiated into the underlying bedrock,
- to provide data suitable for estimating meteoric  $^{36}\text{Cl}/\text{Cl}$ , Br/Cl and  $\text{SO}_4/\text{Cl}$  ratios as a basis for correcting borehole and ESF data for dilution by rock Cl, and
- to evaluate potential sources of contamination (i.e., Test Cell C in NTS Area 25, section 3.3),

Halide results were also obtained for surface soils that were collected throughout the site area in order to evaluate variability in the meteoric Br/Cl ratios. Additional surface soil samples were

collected by the USGS for analysis of bulk density, particle size, and other physical characteristics; these were also made available for the present effort for the same purpose. Most of the available data were discussed in Fabryka-Martin et al. (in press [b]). Recently,  $\text{SO}_4$  concentrations have also been analyzed in soil leachates in order to provide data for characterizing the meteoric  $\text{SO}_4/\text{Cl}$  ratio as a basis for correcting borehole and ESF data for dilution by rock Cl. New data contained in the present report include  $\text{SO}_4$  concentrations and  $^{36}\text{Cl}/\text{Cl}$  and  $\text{SO}_4/\text{Cl}$  ratios measured for surface soil samples, and an additional profile of Cl,  $\text{SO}_4$ , and  $^{36}\text{Cl}/\text{Cl}$  variations for one of the Midway Valley soil pits.

*$^{36}\text{Cl}/\text{Cl}$  ratios in surface soils (Table 4-6).* Data in this table are significant, in conjunction with the ratios reported for surface runoff in section 4.5, as corroborative evidence that the  $^{36}\text{Cl}/\text{Cl}$  ratio for Cl entering the unsaturated-zone flow system at the present day is—for the most part—still elevated above meteoric background despite the fact that the  $^{36}\text{Cl}/\text{Cl}$  ratio in precipitation probably returned to background levels several years ago (Synal et al., 1990). Only two of the 27 surface soil and surface runoff samples listed in Tables 4-6 and 4-16 are near background levels; the vast majority of the ratios are on the order of  $2000 \times 10^{-15}$  to  $3000 \times 10^{-15}$ . This continued elevated signal in Cl entering the bedrock is a result of mixing with residual bomb-pulse  $^{36}\text{Cl}$  still in the soil (section 3.3).

*Sulfate/chloride ratios in surface soils (Table 4-7).* Nine surface-soil samples had soluble  $\text{SO}_4$  concentrations ranging from 1 to 5 mg/kg, plus one sample containing 15 mg/kg. The  $\text{SO}_4/\text{Cl}$  ratios for these samples ranged from 1.3 to 3.2, averaging 2.2 and showing no correlation with Cl content.

*Sulfate/chloride ratios in soil profiles (Table 4-8).* Sulfate, Cl and Br profiles were measured for two soil pits at the North Portal in Midway Valley, about 160 m apart: MWV-P31, extending to a depth of 2.2 m, and NRSF-TP-19, extending to a depth of 3.3 m. Samples were collected in 1992. Selected intervals of the NRSF-TP-19 profile were also analyzed for  $^{36}\text{Cl}/\text{Cl}$ . Cl and  $\text{SO}_4$  concentrations were extremely low throughout the NRSF-TP-19 profile, averaging about 0.5 mg/kg for Cl and with a maximum concentration of 2 mg/kg at about 2.7 m.  $\text{SO}_4/\text{Cl}$  ratios ranged from 1.3 to 3.7, averaging 2.3. The MWV-P31 profile was similarly low in Cl and  $\text{SO}_4$ , except for the deepest sample, with 236 mg/kg Cl and 358 mg/kg  $\text{SO}_4$ . The  $\text{SO}_4/\text{Cl}$  ratios for MWV-P31 were about 3 times those for NRSF-TP-19, ranging from 3 to 14 and averaging 8. The deepest sample in each pit had nearly identical  $\text{SO}_4/\text{Cl}$  ratios (1.4) despite the fact that the Cl and  $\text{SO}_4$  concentrations in the bottom of MWV-P31 were greater than those in the bottom of NRSF-TP-19 by a factor of about 300.

*Cl and  $^{36}\text{Cl}/\text{Cl}$  profiles in NRSF-TP-19 (Table 4-8).* The  $^{36}\text{Cl}/\text{Cl}$  ratio was essentially uniform at an average value of  $924 \times 10^{-15}$  in the 7 intervals for which it was measured between 0.5 and 3.3 m depth. This smeared profile of bomb-pulse  $^{36}\text{Cl}$  is consistent with the extremely low Cl concentrations and suggests a fairly high infiltration rate for this alluvial setting. The profile also illustrates the persistence of the bomb-pulse  $^{36}\text{Cl}$  signal in the soil zone, despite evidence for

Table 4-6. Chloride and chlorine-36 analyses of soils collected from depths within 0.5 m of the surface

Location	LANL ID (Note 1)	Depth (cm)	Leached mg Cl/kg (Note 2)	<sup>36</sup> Cl/Cl x 10 <sup>-15</sup>
~ 200 m north of UZ-N55	SMO-001-1	0-15	2.1	1662 ± 46
	SMO-003-1	~20	1.4	1860 ± 80
Near UZ-N55	SMO-006-1	0-15	2.2	701 ± 113
	SMO-007-1	15-30	2.9	518 ± 26
Near UZ-N54	SMO-010-1	0-15	---	610 ± 70
	SMO-011-1	15-30	2.6	710 ± 70
~ 42 m south of UZ-N54 (roughly halfway between UZ-N54 and UZ-N53)	SMO-012-1	0-15	1.8	2270 ± 90
	SMO-013-1	15-30	1.7	2300 ± 90
Near UZ-N53	SMO-015-1	15-30	---	2163 ± 315
Soil exposed at rockcut for NRG5 drillpad	ST094-1	0-40	2.2	5690 ± 230
	ST098-1	0-50	4.2	3850 ± 70
	ST101-1	0-40	8.2	2150 ± 90
	ST107-1	0-6	1.5	2800 ± 110
	ST108-1	0-3	8.2	3810 ± 130
	ST109-1	0-30	1.2	3100 ± 140
Midway Valley soil pits • MWV-P2 • MWV-P2 • NRSF-TP-19	ST024-2	45-50	4.8	2439 ± 55
	ST022-2	35-40	4.7	2950 ± 120
	ST066-2	45-50	0.7	938 ± 43

Notes

6. Samples within LANL identifiers beginning with SMO are non-Q because they were not collected according to an approved YMP/QA procedure. Sample with LANL identifiers beginning with ST are Q-data.
7. The concentration of Cl leached from the sample is only a qualitative indicator of the sample's Cl content. Soil samples were leached for 48 hours in deionized water using a water:soil weight ratio of 1:1. Because the focus of this activity is generally on determining anion ratios and isotopic ratios, no attempt is made to maximize the yield of the leaching process, which is probably quite variable.

Table 4-7. Sulfate and chloride analyses of surface soils

LANL ID	Leachable salts, mg/kg		SO <sub>4</sub> /Cl
	Cl	SO <sub>4</sub>	
SP030	1.1	3.5	3.2
SP031	6.1	15.5	2.6
SP032	1.0	1.6	1.6
SP033	0.84	2.3	2.8
SP034	0.83	2.4	3.0
SP035	3.1	4.9	1.6
SP036	0.89	1.9	2.2
SP037	0.95	1.3	1.3
SP038	1.1	1.4	1.3
SP039	1.6	3.6	2.3

**Note:** The concentration of Cl leached from the sample is only a qualitative indicator of the sample's Cl content. Soil samples were leached for 48 hours in deionized water using a water:soil weight ratio of 1:1. Because the focus of this activity is on determining anion ratios, no attempt is made to maximize the yield of the leaching process, which is probably quite variable.

Table 4-8. Measured <sup>36</sup>Cl/Cl and anion concentration profiles for NRSF-19 and MWV-P31

LANL ID	Depth (m)	Leached salts, mg/kg (Note)		SO <sub>4</sub> /Cl	<sup>36</sup> Cl/Cl x 10 <sup>-15</sup>
		Cl	SO <sub>4</sub>		
<i>NRSF-TP-19</i>					
ST058	0.05 - 0.10	0.25	0.83	3.3	---
ST059	0.10 - 0.15	0.37	0.69	1.9	---
ST060	0.15 - 0.20	0.35	0.68	1.9	---
ST061	0.20 - 0.25	0.25	0.55	2.2	---
ST062	0.25 - 0.30	0.51	0.86	1.7	---
ST063	0.30 - 0.35	0.53	1.18	2.2	---
ST064	0.35 - 0.40	1.45	1.85	1.3	---
ST065	0.40 - 0.45	0.50	1.50	3.0	---
ST066	0.45 - 0.50	0.66	1.08	1.6	938 ± 43
ST067	0.50 - 0.55	0.47	1.17	2.5	954 ± 44
ST068	0.55 - 0.60	0.52	1.05	2.0	969 ± 48
ST069	0.60 - 0.65	0.52	1.25	2.4	845 ± 40
ST070	0.65 - 0.70	0.51	1.87	3.7	982 ± 51
ST071	0.70 - 0.75	0.79	2.77	3.5	---
ST072	0.75 - 0.80	1.27	2.98	2.3	---
ST073	0.80 - 0.85	2.25	5.12	2.3	---
ST074	1.25 - 1.4	1.64	3.98	2.4	---
ST075	1.8 - 2.0	1.06	3.39	3.2	---
ST076	2.55 - 2.8	1.28	14.0	10.9	898 ± 40
ST077	3.1 - 3.3	0.79	1.03	1.3	882 ± 32
<i>MWV-P31</i>					
SM038	0.00 - 0.05	0.32	5.74	17.8	---
SM039	0.05 - 0.10	0.27	1.52	5.6	---
SM040	0.10 - 0.15	0.20	2.51	12.8	---
SM042	0.15 - 0.20	0.38	5.31	13.8	---
SM043	0.20 - 0.25	0.39	2.12	5.4	---
SM044	0.25 - 0.30	0.34	2.81	8.4	---
SM045	0.30 - 0.35	0.64	5.38	8.4	---
SM046	0.35 - 0.40	0.28	2.91	10.3	---
SM047	0.40 - 0.45	1.44	3.26	2.6	---
SM048	0.45 - 0.50	0.57	7.11	12.5	---
SM049	0.50 - 0.55	0.47	2.69	5.8	---
SM050	0.55 - 0.60	0.41	1.34	3.3	---
SM051	0.60 - 0.65	0.69	3.51	5.1	---
SM052	0.65 - 0.70	1.18	5.13	4.3	---
SM053	0.70 - 0.75	1.10	6.35	5.8	---
SM054	0.75 - 0.80	1.51	8.21	5.4	---
SM055	0.80 - 0.86	2.37	11.28	4.8	---
SM056	0.86 - 1.03	1.33	13.5	10.2	---
SM057	1.70 - 1.74	4.22	13.5	3.2	---
SM058	2.00 - 2.22	236	358	1.5	---

Table 4-8 footnote:

The concentration of Cl leached from the sample is only a qualitative indicator of the sample's Cl content. Soil samples were leached for 48 hours in deionized water using a water:soil weight ratio of 1:1. Because the focus of this activity is generally on determining anion ratios and isotopic ratios, no attempt is made to maximize the yield of the leaching process, which is probably quite variable.

considerable flushing of the profile. The porewater Cl concentration estimated based on the measured moisture content is about 11 mg/L at the bottom of the profile. (The true concentration is probably somewhat higher, assuming that the leaching process is not completely effective at recovering all porewater Cl.) This concentration corresponds to a maximum infiltration rate of 10 mm/yr at this depth by the Cl mass balance method described in section 5.

#### 4.4 Borehole samples

Borehole samples available for this activity were collected as ream-bit cuttings by Sample Management Facility staff during dry-drilling operations. Table 4-9 lists the boreholes for which measured  $^{36}\text{Cl}/\text{Cl}$  ratios are available. The full suite of halide and  $^{36}\text{Cl}$  analyses of ream-bit cuttings were reported in Fabryka-Martin et al. (in press [b]). These results are summarized below, with new or revised data presented for selected intervals from boreholes ONC#1 and SD-12 in section 4.4.2.

##### 4.4.1 Shallow surface-based boreholes

Fifteen of the sampled boreholes are shallow infiltration monitoring boreholes (UZ-N holes) which were sited by the USGS with the objective of evaluating topographic controls on surface infiltration rates (Flint and Flint, 1995). The depths of the boreholes range from 18 to 83 m. Most of these holes extend into the TCw or PTn; only one (UZ-N55) extends into the top of the TSw. The upper parts of the profiles for deep holes UZ-14 and UZ#16 are also included in this discussion because of its focus on infiltration rates and processes above the TSw. Most of the borehole locations are plotted on the set of maps in Appendix D to show their relation to surface geology, estimated infiltration rates, and soil thickness. The following general qualitative observations are made on halide distributions in this set of samples. A quantitative discussion of these data for the shallow zone is contained in section 5.

- Five of the holes are in a channel or on a terrace with more than 5 m of alluvial cover (UZ-N37, UZ-N39, UZ-N54, UZ-14, UZ#16), and UZ-N61 is on a sideslope with 3 m of alluvial cover. Bomb-pulse  $^{36}\text{Cl}$  does not appear to have penetrated to the underlying bedrock at any of these five locations, but rather has remained within the alluvium (Figure 4-7). Cl concentrations are also about an order of magnitude higher in the alluvium of these boreholes than in any other part of the unsaturated zone. Both of these characteristics reflect the effectiveness of the alluvial cover and its associated vegetation in promoting moisture loss by

Table 4-9. List of boreholes for which measured  $^{36}\text{Cl}/\text{Cl}$  ratios are available

Borehole	Range of depths sampled	Thickness of alluvial cover (m)	Lithologic unit at bottom of sampled interval (see note)	# of $^{36}\text{Cl}$ analyses
<i>Shallow neutron-monitoring boreholes</i>				
• UZ-N11	0 - 26 m	1.2	PTn	6
• UZ-N15	0 - 17 m	0.7	TCw	4
• UZ-N16	0 - 18 m	1.5	TCw	3
• UZ-N17	0 - 18 m	0.8	TCw	3
• UZ-N27	0 - 62 m	0.9	TCw	5
• UZ-N36	0 - 18 m	0.8	TCw	3
• UZ-N37	0 - 83 m	11.1	TCw	20
• UZ-N38	0 - 29 m	5.5	TCw	3
• UZ-N39	0 - 18 m	18.1+	QTac	4
• UZ-N53	0 - 64 m	0.8	PTn	8
• UZ-N54	0 - 75 m	5.8	PTn	24
• UZ-N55	0 - 78 m	0.7	TSw	19
• UZ-N61	0 - 36 m	3.1	TCw	4
• UZ-N62	0 - 18 m	0.7	TCw	3
• UZ-N64	0 - 18 m	0.8	TCw	3
<i>Deep surface-based boreholes</i>				
• UZ-14	0 - 427 m	12	CHn	18
• UZ#16	0 - 495 m	12	Tcp	46
• SD-12	199 - 258, 402 - 592 m	Not known	Tcp	10
• NRG-4	174 - 177 m	Not known	Tptrn	1
• NRG-6	125 - 210 m	<1	Tptpul	1
• NRG-7A	174 - 256 m	Not known	Tptpmn	1
• ONC#1	3 - 438 m	29	CHn	10

Note: Hydrogeologic and lithostratigraphic units are defined in Table 2-1. Analytical data are reported in Fabryka-Martin et al. (in press [b]), except for SD-12 and ONC#1, for which data are reported in Table 4-11.

evapotranspiration, thereby minimizing infiltration at such locations.

- Most of the remaining shallow boreholes are on ridgetops, sideslopes or terraces on which the alluvial cover is less than 2 m and usually less than 1 m. Bomb-pulse  $^{36}\text{Cl}$  has been transmitted well into the underlying fractured bedrock at all but one of these sites (Figure 4-8).

#### 4.4.2 Deep Surface-Based Boreholes

The following summary of results for deep surface-based boreholes is taken from Fabryka-Martin et al. (in press [b]). To aid in the discussion that follows, isotopic ratios for samples from nonwelded units in UZ-14, UZ#16 and the neutron holes are shown in Table 4-10. Results from these stratigraphic units are believed to be representative of porewater values and not unduly diluted by Cl released from the rock during drilling or sample processing. The underlying basis for this assumption is discussed in Fabryka-Martin et al. (in press [b], their section 6.2.2). Table 4-11 presents revised data for SD-12, because only preliminary data were reported in the August 1996 review draft of Fabryka-Martin et al. (in press [b]). New data are also presented for selected intervals in ONC#1 in that table.

*UE-25 UZ#16* is located on a terrace at the mouth of WT-2 Wash, about 200 m NE of UZ-N54 (Appendix Figure D-6a to D-6c). The hole extends to a total depth of 514 m, and penetrates the water table. Data for the alluvium are interpreted in section 5.2, and data for the deeper part of the profile are discussed in section 6.1.4. The  $^{36}\text{Cl}/\text{Cl}$  profile for UZ#16 extends from the surface, through 12 m of alluvial cover, to a total depth of 495 m. Although bomb-pulse  $^{36}\text{Cl}$  is not unambiguously evident anywhere in the alluvial cover, it is not certain how much of the original soil cover was removed during construction of the drillpad. No bomb-pulse is evident in the underlying TCw or PTn (Figure 4-7). Chlorine-36 signals in the CHn unit are elevated by 15 to 30% over the present-day meteoric signal, and those in the underlying Prow Pass (PP) unit (depths of 452 to 495 m) have  $^{36}\text{Cl}/\text{Cl}$  signals ranging from 20% to 70% of the modern meteoric signal (Table 4-10). Br/Cl ratios in the CHn unit are distinctly higher than in any other part of the profile, including the alluvial cover. Both Br/Cl and  $^{36}\text{Cl}/\text{Cl}$  ratios in the CHn samples from UZ#16 are close to those measured for cuttings from these units in SD-12 as well as for perched water samples from UZ-14 and SD-7 (Table 4-16), and may indicate similar origins and groundwater travel times.

*USW UZ-14* is located in the channel in the upper part of Drillhole Wash (Appendix Figure D-4). Twelve meters of alluvium cover the underlying PTn bedrock. Norris et al. (1990) reported bomb-pulse levels of  $^{36}\text{Cl}$  in USW UZ-1, which is within a hundred meters of UZ-14, at depths of 30, 53, and 152 m. In the profile measured in the present study, the bomb-pulse  $^{36}\text{Cl}$  peak is clearly preserved in the shallow alluvium (Figure 4-7). However, bomb-pulse  $^{36}\text{Cl}$  is not evident in any of the samples below 3.4 m. Chloride concentrations range from 2 to 330 mg kg<sup>-1</sup> in the alluvium with a distinct bulge for the interval of 3 to 5.5 m. Br/Cl ratios show a systematic trend from high values ( $19 \times 10^{-3}$  to  $25 \times 10^{-3}$ ) in the topmost 1.5 m, through intermediate values ( $7 \times$

Table 4-10. <sup>36</sup>Cl/Cl ratios measured for cuttings from nonwelded units

Borehole	LANL ID	Depth (m)	Hydrologic unit (Note 1)	Lithostratigraphic unit (Note 1)	Uncorrected <sup>36</sup> Cl/Cl x 10 <sup>-15</sup> (Note 2)
UZ-N11	R152	9	PTn	Tpcpv1	690 ± 23
	R154	12		Tpcpv1	917 ± 13
	R157	17		Tpbt4	1076 ± 37
	R159	20		Tpy	13060 ± 250
	R162	24		Tpy	10100 ± 700
UZ-N37	R285	34	PTn	Tpcpv2	498 ± 22
	R288	38		Tpcpv1/Tpbt4	247 ± 10
	R293	45		Tpp	321 ± 6
	R298	53		Tpp	841 ± 12
	R301	58		Tpp	575 ± 124
	R307	66		Tpp/Tpbt2	850 ± 105
	R312	74		Tptrv3	263 ± 6
	R314	77		Tptrv2	1394 ± 111
UZ-N38	R497	26	PTn	Tpcpv2	1590 ± 40
UZ-N53	R361	56	PTn	Tpbt3	2363 ± 34
	R364	60		Tpbt2	710 ± 36
	R366	63		Tpbt2	516 ± 17
	R366	63		Tpbt2	496 ± 15
UZ-N54	R114	46	PTn	Tpcpv2	376 ± 25
	R117	50		Tpcpv1/Tpy	381 ± 10
	R117	50		Tpcpv1/Tpy	391 ± 20
	R121	56		Tpbt3	480 ± 16
	R125	62		Tpbt2	594 ± 71
	R125	62		Tpbt2	367 ± 67
	R125	62		Tpbt2	471 ± 25
	R128	66		Tptrv2	352 ± 13
	R129	68		Tptrv2	1300 ± 60
	R130	69		Tptrv2/m	332 ± 16
UZ-N55	R075	55	PTn	Tpcpv2	11885 ± 746
	R075	55		Tpcpv2	13240 ± 190
	R078	58		Tpcpv2/pv1	1413 ± 57
	R081	62		Tpcpv1/Tpy	32406 ± 2625
	R081	62		Tpcpv1/Tpy	22120 ± 350
	DC005	63		Tpy	1088 ± 85
	R084	66		Tpbt3/bt2	17168 ± 1202
	R087	71		Tptrv3	6580 ± 364
	R088	72		Tptrv3/rv2	8184 ± 140

Borehole	LANL ID	Depth (m)	Hydrologic unit (Note 1)	Lithostratigraphic unit (Note 1)	Uncorrected $^{36}\text{Cl}/\text{Cl}$ $\times 10^{-15}$ (Note 2)
UZ-14	R419	81	PTn	Tptrv3	440 ± 9
	R420	84		Tptrv3	485 ± 26
	R420	84		Tptrv3	420 ± 30
	R421	86		Tptrv2	202 ± 6
UZ-14	R428	427	CHn	Tptpv1	443 ± 13
UZ#16	R184	48	PTn	Tpcpv1	329 ± 24
	R185	50		Tpbt	338 ± 20
	R186	55		Tpbt	306 ± 21
	R187	67		Tptrv3	434 ± 26
UZ#16	R224	355	CHn	Tptpv1/2	272 ± 19
	R225	357		Tptpv1/2	363 ± 34
	R376	395		Tac	508 ± 16
	R383	426		Tac	616 ± 12
	R386	435		Tac	579 ± 19
	R387	437		Tac	620 ± 14
	R388	440		Tac	648 ± 15
UZ#16	R392	453	Prow Pass	PP-npw	354 ± 7
	R394	462		PP-npw	327 ± 11
	R398	481		PP-npw	266 ± 13

Notes:

1. Hydrogeologic and lithostratigraphic units are defined in Table 2-1.
2. Reported  $^{36}\text{Cl}/\text{Cl}$  ratios have not been corrected for the presence of any rock Cl, which is assumed to be negligible in samples prepared by leaching nonwelded tuffs.

Table 4-11. Halide, sulfate and <sup>36</sup>Cl/Cl analyses of cuttings from boreholes SD-12 and ONC#1

Sample	Ave. depth (m)	Lithology	Hydrogeologic unit	Cl mg kg <sup>-1</sup>	Br/Cl x 10 <sup>-3</sup>	SO <sub>4</sub> mg kg <sup>-1</sup>	SO <sub>4</sub> /Cl	<sup>36</sup> Cl/Cl x 10 <sup>-15</sup>
SD-12								
R625-2	199	Tptpul	TSw	3.5	2.5	29	8.3	224 ± 12
R627-2	229	Tptpmn	TSw	5.7	1.8	2.2	0.4	77 ± 6
R629-2	258	Tptpll	TSw	2.3	3.8	3.3	1.4	180 ± 9
R571-2	402	Tptpv2	TSw	1.6	3.0	12.4	7.6	285 ± 11
R577-2	431	Tac-unit4	CHn	1.2	6.8	5.5	4.7	390 ± 19
R582-2	462	Tac-unit3	CHn	1.7	6.0	6.1	3.5	370 ± 16
R588-2	494	Tacbt	CHn	1.8	5.3	5.8	3.2	812 ± 45
R593-2	525	Tcp-unit3	CHn	0.7	9.9	0.8	1.2	719 ± 28
R598-2	561	Tcp-unit3	CHn	0.6	17.4	1.3	2.1	426 ± 15
R602-2	591	Tcp-unit2	CHn	0.8	8.3	2.4	3.2	843 ± 34
ONC#1								
R518	3.4	Qal	UO	12.2	3.5	26.5	2.2	---
R519	6.4	Qal	UO	40.5	4.2	28.3	0.7	556 ± 16
R520	9.9	Qal	UO	32.2	4.3	20.0	0.6	---
R521	12.3	Qal	UO	17.0	5.0	17.2	1.0	468 ± 12
R522	15.4	Qal	UO	19.0	4.3	13.0	0.7	---
R523	18.4	Qal	UO	13.1	4.7	10.0	0.8	---
R524	21.5	Qal	UO	6.8	9.7	10.3	1.5	459 ± 18
R526	24.5	Qal	UO	6.3	6.0	7.0	1.1	429 ± 21
R527	26.1	Qal	UO	2.8	5.8	3.8	1.4	---
R528	27.6	Qal	UO	4.4	4.4	6.4	1.5	---
R529	29.1	Qal	UO	3.1	4.5	3.9	1.3	386 ± 31
R530	30.6	Tmr	UO	2.1	5.1	2.4	1.2	---
R532	61.1	Tmbt, Tpkbt, or Tpbt5	UO	2.0	7.0	---	---	455 ± 33
R535	65.7	Tmbt, Tpkbt, or Tpbt5	UO	0.6	6.9	---	---	367 ± 37
R538	70.3	Tpc (specific unit unknown)	TCw	0.8	7.4	---	---	385 ± 37
R542	184.5	Tpbt3	PTn	3.4	10.0	---	---	475 ± 13
R546	190.6	Tpbt2	PTn	2.0	6.3	---	---	---
R551	353.7	Tptpll-tpv2	TSw-CHn(z)	0.9	7.8	---	---	410 ± 11
R552	355.2	Tptpll-tpv2	TSw-CHn(z)	1.1	4.6	---	---	---
R553	356.8	Tptpll-tpv2	TSw-CHn(z)	0.9	5.0	---	---	---
R554	358.3	Tptpll-tpv2	TSw-CHn(z)	3.2	11.3	---	---	---
R555	359.8	Tptpll(?) -tpv2	TSw(?) -CHn(z)	1.5	13.2	---	---	---
R556	361.3	Tptpv2	CHn(z)	1.4	7.9	---	---	---
R561	384.2	Tpbt1	CHn(z)	2.1	4.1	---	---	---
R562	390.3	Tac	CHn(z)	2.6	4.1	---	---	---

Table 4-11 notes:

1. SD-12 lithology from L. Flint (pers. commun., 1997)
2. Preliminary ONC#1 lithology from D. Buesch (pers. commun., 1997). A relatively high-angle fault between 351 and 359 m juxtaposes Tptpl1 and Tptpv2; therefore samples R551 to R555 are probably mixtures of these two units. Hydrogeologic and lithostratigraphic units are defined in Table 2-1.
3. The concentration of Cl leached from the sample is only a qualitative indicator of the sample's Cl content. Rock samples were leached for 48 hours in deionized water using a water:rock weight ratio of 1:1. Because the focus of this activity is generally on determining anion ratios and isotopic ratios, no attempt is made to maximize the yield of the leaching process, which is probably quite variable.

$10^{-3}$  to  $11 \times 10^{-3}$ ) down to 3.3 m, to a low of  $4 \times 10^{-3}$  at the base of the alluvium. The high values are similar to those for rainwater; the intermediate values are typical of surface soils; and the low values are typical of deeper soil samples below the root zone (Fabryka-Martin et al., in press [b], their section 6.2.3). This distribution supports the hypothesis that the Br/Cl ratio may be fractionated from its initial meteoric value as a function of residence time of the water in the plant root zone.

The top three of four samples from the PTn (depth interval, 81 to 86 m) as well as the single sample analyzed from the CHn (depth, 427 m) have ratios that range from 84% to 98% of the modern signal (Figure 4-7, Table 4-10). Four samples from the overlying TSw unit have ratios that are 22% to 60% of the modern signal. However, Br/Cl ratios for the TSw samples indicate significant dilution of the  $^{36}\text{Cl}/\text{Cl}$  ratio of the meteoric component by Cl released from the rock (e.g., from fluid inclusion) during drilling (section 6.1.).

*USW SD-7* is situated on a ridgetop on Highway Ridge, south of the perimeter of the potential repository (Appendix Figure D-7). This hole is of particular interest because it is about 140 m west of ESF Station 56+00 and hence provides an opportunity to compare halide and  $^{36}\text{Cl}$  data obtained from the ESF to those from borehole cuttings collected from the same horizon. Such a comparison is important in order to judge the consistency of ESF and borehole results because each type of sample has its own disadvantages that contribute to the overall uncertainty in the correction and interpretation of the data. Chlorine-36 results were not available for samples from this hole at the time that this report was written. The samples have low priority for analysis because the finely crushed consistency of the cuttings indicated that the results would probably be significantly affected by rock Cl.

*USW SD-12* is at the base of a steep sideslope on the north side of Whaleback Ridge, offset by less than 100 m from the ESF tunnel at approximately Station 46+50 (Appendix Figure D-6). Samples from the TSw, CHn and PP units were analyzed for halides and  $^{36}\text{Cl}$  (Table 4-12). The lowest  $^{36}\text{Cl}/\text{Cl}$  ratios in the profile were those measured for the TSw unit and ranged from  $77 \times 10^{-15}$  to  $285 \times 10^{-15}$ . However, Br/Cl and  $\text{SO}_4/\text{Cl}$  ratios for these samples indicate the presence of rock Cl, particularly in the first sample, which serves to dilute the  $^{36}\text{Cl}/\text{Cl}$  ratio to a low value.

Six samples from the underlying nonwelded units ranged from  $390 \times 10^{-15}$  at 431 m to  $843 \times 10^{-15}$  at 591 m, showing a distribution similar to the UZ#16 profile in these same units.

UE-25 ONC#1 is at the eastern end of Antler Ridge (Figure 1-1), slightly west of the surface projection of the Bow Ridge Fault. This hole was hammer-drilled by Nye County and was not constructed following YMP quality assurance procedures. Hence, samples collected from this borehole are not qualified for YMP use except as corroborative data. Nonetheless, samples were analyzed from ONC#1 because the deep alluvium at this location offered a rare opportunity to extend the data base of  $^{36}\text{Cl}/\text{Cl}$  results representative of the pre-bomb meteoric ratio (Table 4-11). Four samples analyzed between depths of 6 to 24 m showed no signs of bomb-pulse and had  $^{36}\text{Cl}/\text{Cl}$  ratios ranging from 429 to  $556 \times 10^{-15}$ , consistent with the range of signals expected for the past 10 ka as discussed in section 3.1. Br/Cl ratios for the 11 intervals from the alluvial cover (3-29 m) were similar for those measured in the same intervals in UZ-14, averaging  $4.8 \times 10^{-3}$ . Excluding the top interval (3.4 m), the average  $\text{SO}_4/\text{Cl}$  ratio for the remaining 10 alluvial samples is 1.3. For comparison, the  $\text{SO}_4/\text{Cl}$  ratio for water from this borehole was 4.4, with a Cl concentration of 7.9 mg/L (section 4.5).

Also of interest was to examine the ONC#1 borehole data for evidence of fast transport of water along the Bow Ridge Fault. Samples from depths ranging from 60 to 355 m had ratios ranging from  $367 \times 10^{-15}$  to  $475 \times 10^{-15}$ . All of these are within the range of past meteoric  $^{36}\text{Cl}/\text{Cl}$  ratios (section 3.1).

UE-25 NRG-4, UE-25 NRG-5, UE-25 NRG-6, and UE-25 NRG-7A are located along the trace of the ESF North Ramp, with less than a 100-m horizontal offset from that facility (Figure 1-1; Appendix Figure D-3a). As is for the case for SD-7, these holes are of particular interest because of the opportunity to compare halide and  $^{36}\text{Cl}$  data obtained from the ESF to those from borehole cuttings collected from the same horizon. The measured  $^{36}\text{Cl}/\text{Cl}$  ratios for depths similar to that of the ESF at these locations were  $724 \times 10^{-15}$  (NRG-4, 175 m),  $395 \times 10^{-15}$  (NRG-6, 165 m), and  $486 \times 10^{-15}$  (NRG-7A, 208 m). Br/Cl ratios indicate that the  $^{36}\text{Cl}/\text{Cl}$  ratios in these samples may have been diluted to some extent by rock Cl. In section 6.1.5, corrected ratios are calculated for these samples based on the measured Br/Cl ratios. The corrected ratios suggest the presence of bomb-pulse  $^{36}\text{Cl}$  in the NRG-4 and NRG-6 samples, although the proportion of rock Cl present is so large as to make the corrected ratios highly uncertain. However, the measured ratio for the NRG-4 sample is so high that almost any reasonable correction method would probably reach the same conclusion: that bomb-pulse  $^{36}\text{Cl}$  is present here. Bomb-pulse  $^{36}\text{Cl}$  was also measured in several ESF samples at stations 10+56 and 10+62, which are very near NRG-4 (Appendix Figure D-3b).

#### 4.4.3 Characterization of in-situ $\text{SO}_4/\text{Cl}$ ratios in Paintbrush tuffs

Reported  $^{36}\text{Cl}/\text{Cl}$  ratios for the ESF rock samples have been corrected for contributions of Cl from the construction water based on the Br/Cl ratio. The contribution of Cl from the rock's

fluid inclusions, although obviously significant for welded tuff samples from boreholes (section 6.1.5), has been assumed to be generally negligible for the ESF samples because the manual method of collection used in the ESF does not pulverize the rock as does the ream bit. However, the limited data for replicate samples in section 4.2.5 illustrates that it is possible to have a large contribution of rock Cl present in a sample, and yet not to be able to detect it using the Br/Cl ratio as an indicator because of the construction water. Consequently, an independent indicator is needed for the presence of rock Cl in a sample, that is insensitive to the presence of construction water, and the  $SO_4/Cl$  ratio is being investigated for this purpose.

Characterization of the meteoric  $SO_4/Cl$  ratio is described for precipitation, surface runoff, perched water and porewaters in section 4.5, for surface soils and soil profiles in section 4.3, and for borehole alluvium in section 4.4. For characterization of the rock  $SO_4/Cl$  ratio, a step-leaching method is used. This method was developed at LANL for determining the Br/Cl ratio of rocks at Yucca Mountain (Fabryka-Martin et al., in press [b]), and these same samples were also analyzed for  $SO_4$ . The method involves repeated grinding and leaching of the rock sample, thereby decreasing the meteoric component and increasing the rock component of  $SO_4$ , Br and Cl (presumably released from fluid inclusions and groundmass glass) with each step. A total of 37 samples have been processed in duplicate by this procedure in order to build a data base of  $SO_4/Cl$  ratios and to look for stratigraphic and spatial trends. The results of these experiments are summarized in Table 4-12 and represent the final leach step. The data show the following trends:

- **Welded TCw unit.** The step-leaching experiment provided a tight estimate for the rock  $SO_4/Cl$  ratio for all TCw subunits tested (average,  $0.2 \pm 0.1$ ) except for samples from Tpcrn, the crystal-rich nonlithophysal unit. The latter samples had variably larger ratios as a consequence of the extremely low Cl content of these samples (generally  $< 1$  mg/kg).
- **Welded TSw unit.** Excluding the basal vitrophyre, all 12 TSw samples had  $SO_4/Cl$  ratios less than unity. Those from the lower and middle nonlithophysal units had the lowest average of any category,  $0.04 \pm 0.01$ . These units are exposed between stations 35+00 and 63+00 in the ESF. Samples from the crystal-rich nonlithophysal unit (Tptrn) had an average  $SO_4/Cl$  ratio of  $0.7 \pm 0.3$ .
- **Nonwelded PTn units.** The  $SO_4/Cl$  ratios measured for these 18 samples were highly variable, ranging up to 200 in the Tptrv2 unit, in which  $SO_4$  concentrations were as high as 600 mg/kg.  $SO_4/Cl$  ratios were less than 1 in the Tpy and Tptrn samples.

In summary, measured  $SO_4/Cl$  ratios vary between units as well as within units. Welded units generally have less variability than nonwelded units and generally have  $SO_4/Cl$  ratios  $< 1$ . The intra-unit variability is greatest in the nonwelded subunits within the PTn and in the TSw basal vitrophyre. The variability for the PTn unit may be attributable to the numerous thin welded and nonwelded subunits in the PTn. Additional geologic reasons for variability in the Cl and  $SO_4$  contents of rock leachates may include the following:

Table 4-12. Sulfate/chloride ratios measured for Paintbrush tuffs by step-leaching to remove meteoric salts

Hydrologic unit (see note)	Lithostratigraphic units (see note)	Number of analyses	Range of SO <sub>4</sub> /Cl ratios	Average (± 1 std dev)
TCw (upper)	Tpcrn	4	5 - 16	10 ± 5
TCw, excluding Tpcrn	Tpcpul, Tpcpll, Tpcplnh, Tpcplnc, Tpcpv3	22	0.1 - 0.7	0.2 ± 0.1
PTn	Tpcpv2, Tpy, Tptrv3, Tptrv2	18	0.5 - 200	35 ± 60
TSw	Tptrn	6	0.4 - 1.0	0.7 ± 0.3
TSw	Tptpmn, Tptpln	6	0.02 - 0.06	0.04 ± 0.01
TSw	Tptpv3	6	0.3 - 164	68 ± 69
CHn	Tptpv1, Tptpv2, Tac	4	0.7 - 0.8	0.7 ± 0.0
CHn	Tcp: non-, partially, and moderately welded	8	0.2 - 0.7	0.4 ± 0.2

Note: Hydrogeologic and lithostratigraphic units are defined in Table 2-1.

- Differences in adsorption and retention of SO<sub>4</sub> and Cl on silicate ash particles in the volcanic eruption column (Smith et al., 1982). Densely welded vitric tuff might be most likely to retain SO<sub>4</sub> and Cl from this source.
- Differences in the content of phenocrysts with high-temperature magmatic fluid inclusions. Phenocryst content varies from almost zero to about 25% (Buesch et al., 1994).
- Changes in SO<sub>4</sub> and Cl contents and distributions in the rock matrix associated with devitrification, leading to differences in SO<sub>4</sub>/Cl ratios between glassy and devitrified rocks.
- Differences in smectite and zeolite contents, with their associated salts. Generally, these minerals are most abundant in nonwelded glassy tuffs and just below the lower devitrified-vitric transitions in the Tiva Canyon (Tpcplnc-Tpcpv2) and Topopah Spring Tuffs (Tptpln-Tptpv3) (Bish and Chipera, 1989; Levy and Chipera, 1997).

An additional source of variability in the SO<sub>4</sub>/Cl ratios may be due to differences in the length of time that the samples were leached. Variable leaching times were not a concern for the determination of the Br/Cl ratios because any mineral phases containing these halides would be expected to be highly soluble and immediately dissolve in the presence of water. The same cannot be assumed for soluble SO<sub>4</sub>-bearing minerals.

Despite the variability of the SO<sub>4</sub>/Cl ratio in some of the units, it appears that the ratio for most of the TSw has a sufficiently small variability and is sufficiently different from those for the various meteoric sources as to be worth pursuing as a correction method.

#### 4.5 Water samples

Water samples were collected from the surface, unsaturated zone and saturated zone in the vicinity of Yucca Mountain, generally by USGS investigators as part of other YMP activities. These samples were provided to LANL for characterization of Cl, Br, and SO<sub>4</sub> concentrations, and of <sup>36</sup>Cl/Cl ratios. Data which were not included in the previous summary reports by Fabryka-Martin and Liu (1995) and Fabryka-Martin et al. (in press [b]) are included here. The new or revised data are described below.

##### 4.5.1 Surface waters

**Precipitation.** Rainwater samples were collected from precipitation monitoring stations at Yucca Mountain during the early part of 1995 (Fabryka-Martin et al., in press [b]). The objective was to characterize Cl concentrations and Br/Cl ratios; recently, these samples were reanalyzed for SO<sub>4</sub>. Cl concentrations ranged from 0.2 to 3 mg/L, with a geometric average of 0.5 mg/L. An independent estimate based on <sup>36</sup>Cl/Cl ratio resulted in an effective concentration of 0.62 mg/L, including the dry fallout component (section 5.1). SO<sub>4</sub> concentrations in the Yucca Mountain rain samples ranged from 0.9 to 9 mg/L, with a geometric average of 2.1 mg/L. SO<sub>4</sub>/Cl ratios ranged from 1.0 to 13, with a geometric average of 3.3. The distribution of the ratios is plotted in Figure 4-9, in which the data are compared to those measured for precipitation in Red Rock

Canyon, Nevada (NADP, 1997). This record of 115 analyses for 1987-1996 shows geometric average Cl and SO<sub>4</sub> concentrations of 0.2 mg/L and 1.0 mg/L, respectively, and an average SO<sub>4</sub>/Cl ratio of 4.5. These data are considered only qualitative indicators of the characteristics of the anion chemistry of water infiltrating into Yucca Mountain. They may be adequate for their intended purpose, but the user should be aware of their shortcomings: (a) the limited time frame, particularly for the Yucca Mountain set; (b) the Red Rock Canyon data set only includes only wet fallout but dry fallout comprises a source of salts of roughly equal magnitude; and (c) the data have not been weighted by the amount of precipitation associated with each analysis. No <sup>36</sup>Cl analyses have been conducted for local precipitation samples.

*Surface runoff.* Seven samples of surface runoff were collected by USGS investigators in 1995 to provide a measure of initial Cl, Br and SO<sub>4</sub> concentrations and <sup>36</sup>Cl/Cl ratio of surface infiltration at the present-day. These data are presented in Table 4-13. The average Cl concentration is 3.8 mg/L, enriched about 6 times over the average effective concentration for precipitation at Yucca Mountain. The average SO<sub>4</sub> concentration is 10 mg/L, showing a similar degree of enrichment as did the Cl; and the average SO<sub>4</sub>/Cl ratio is 2.7, similar to that measured for Yucca Mountain precipitation. This ratio is also similar to those measured for salts leached from surface soils (Tables 4-6 and 4-7) and for the NRSF-TP-19 soil profile (Table 4-8). The seven surface runoff samples all had <sup>36</sup>Cl/Cl ratios elevated by factors of 2 to 6 times above present-day background, presumably attributable to leaching of residual bomb-pulse <sup>36</sup>Cl from the surface soil.

#### 4.5.2 *Unsaturated-zone waters*

*Unsaturated-zone pore waters.* A small number of pore-water samples extracted from core by the tri-axial compression method have been provided in the past by I.C. Yang (USGS/Denver) to allow characterization of the Br/Cl ratios and, in one case, to permit analysis of the <sup>36</sup>Cl/Cl ratio in a pore-water sample to compare against that obtained by leaching the corresponding ream-cuttings (Fabryka-Martin et al., in press [b]). Some of these samples were also analyzed for their SO<sub>4</sub> concentrations, as reported in Table 4-14. The SO<sub>4</sub>/Cl ratios range from 0.1 to 1.0, similar to ratios calculated for Yucca Mountain pore waters from data in Yang et al. (1988, 1990, 1996, 1997) (Figure 4-9). Only one porewater sample has been analyzed thus far for <sup>36</sup>Cl, a combined sample extracted by I.C. Yang (USGS) from UZ#16 drill core from depths of 414 m and 440 m. This porewater sample had a <sup>36</sup>Cl/Cl ratio of 824 x 10<sup>-15</sup> (see Table 4-14 footnote).

Recently, LANL began extracting porewaters from drillcore samples using an ultracentrifuge (section 4.1.2). The 10 analyzed drillcore samples are from a suite of 2-m deep holes that sample stratigraphic units ranging from the base of the TCw, through the PTn, to the top of the TSw where these units are exposed in the North Ramp between stations 7+27 and 10+70 and in Alcove #4. Cl concentrations range from 15 to 45 mg/L, on the average being nearly twice as high in the fractured rocks at the base of the TCw (Tpcplnc and Tpcpv2) than in the comparatively unfractured PTn samples from lower in the stratigraphic sequence. The average

Table 4-13. Measured  $^{36}\text{Cl}/\text{Cl}$  ratios and anion concentrations of surface runoff

LANL ID	Location	Cl, mg L <sup>-1</sup>	Br, μg L <sup>-1</sup>	SO <sub>4</sub> , mg L <sup>-1</sup>	Br/Cl x 10 <sup>-3</sup>	SO <sub>4</sub> /Cl	$^{36}\text{Cl}/\text{Cl}$ x 10 <sup>-15</sup>
W055	Overland flow	3.44	9.7	8.2	2.8	2.4	1302 ± 37
W056	Overland flow	3.52	10.3	8.5	2.9	2.4	1363 ± 35
W059	Overland flow	2.69	7.4	10.4	2.8	3.9	2510 ± 110
W060	Wren Wash	6.81	18.1	19.3	2.7	2.8	2770 ± 100
W061	Upper Split Wash	3.86	12.6	11.1	3.3	2.9	3240 ± 120
W062	Yucca Wash	2.29	4.0	5.5	1.8	2.4	3350 ± 100
W063	Pah Canyon tributary	4.31	9.9	9.8	2.3	2.3	3290 ± 80

Note: Samples were collected from the vicinity of Yucca Mountain by C. Savard (USGS) in January 1995.

Table 4-14. Measured halide and sulfate concentrations of porewater samples from boreholes<sup>1</sup>

LANL ID	Borehole	Lithologic unit <sup>2</sup>	Hydrogeologic unit <sup>2</sup>	Average depth (m)	Concentration, mg/L			Br/Cl x 10 <sup>-3</sup>	SO <sub>4</sub> /Cl
					Cl	Br	SO <sub>4</sub>		
W077	UZ#16	Tac	CHn	372	49.4	0.171	27.9	3.5	0.6
W080	UZ#16	Tac	CHn	395	37.1	0.107	13.0	2.9	0.4
W036 <sup>3</sup>	UZ#16	Tac	CHn	414	11.6	—	—	—	—
W037 <sup>3</sup>	UZ#16	Tac	CHn	440	6.73	—	—	—	—
W079	NRG-6	Tpbt4	PTn	49	134.	0.571	162.	4.2	1.2
W076	NRG-6	Tptrv3	PTn	78	78.1	0.504	1116	6.5	14.3
W081	NRG-7/7A	Tpbt1	CHn	455	32.1	0.098	15.1	3.1	0.5
W078	UZ-14	Not known	PTn	14	228.	0.533	36.3	2.3	0.2
W075	UZ-14	Tpbt3	PTn	26	60.1	0.225	68.0	3.8	1.1
W049	UZ-14	Tpbt3	PTn	57	112.	0.349	141.	3.1	1.3
W048	UZ-14	Tcp	CHn	483	10.6	0.066	—	6.2	—
W082	UZ-14	Tcp	CHn	517	21.7	0.083	20.4	3.8	0.9

Notes:

- <sup>1</sup> These porewater samples were extracted from dry-drilled core using tri-axial compression, by I.C. Yang (USGS/Denver).
- <sup>2</sup> Hydrogeologic and lithostratigraphic units are defined in Table 2-1. Borehole stratigraphy is from Geslin et al. (1994), Moyer et al. (1996), and Geslin and Moyer (1994).
- <sup>3</sup> Samples W036 and W037 were combined to provide sufficient sample mass for  $^{36}\text{Cl}$  analysis; the measured  $^{36}\text{Cl}/\text{Cl}$  ratio was  $824 \pm 107 \times 10^{-15}$ . For comparison, ratios measured for Cl leached from UZ#16 drill cuttings within this depth range were  $587 \pm 16 \times 10^{-15}$  (R386-2, 435 m depth),  $618 \pm 12 \times 10^{-15}$  (R387-4, 437 m depth), and  $653 \pm 16 \times 10^{-15}$  (R388-2, 440 m depth).

Cl concentration for these latter PTn samples is 17 mg/L, and these are by far the lowest Cl concentrations measured to-date in this unit (Table 4-15). The uniformity of the Cl concentrations throughout this part of the PTn implies matrix-dominated flow because more variable Cl concentrations—more like those in the fractured TCw—would be expected if fracture flow were significant.

The low Br/Cl ratio of 0.01 indicates the absence of construction water in these samples, as well as the probable absence of Cl released from rock fluid inclusions. Moisture profiles measured in these holes using a neutron probe indicate that the drying front resulting from ESF operations has not penetrated more than about a meter at this location, and hence the measured concentrations are believed to be representative of *in-situ* conditions. SO<sub>4</sub>/Cl ratios are 1.7, which is slightly less than that measured for precipitation but not as low as the ratios for the samples extracted using tri-axial compression (Table 4-14). The North Ramp Cl data are also discussed in section 5, in which the low concentrations are shown to be consistent with the predicted surface infiltration rate for this location.

*Perched water.* Perched water has been collected from 5 deep boreholes:

- UZ-1, UZ-14, NRG-7A in Drill Hole Wash, with NRG-7A immediately south of ESF station 24+00 (Figure 1-1; Appendix Figure D-4a),
- SD-9 in Wren Wash, immediately south of Drill Hole Wash and just west of ESF station 28+00 (Figure 1-1; Appendix Figure D-4a), and
- SD-7 on Highway Ridge just west of ESF station 56+00 (Figure 1-1; Appendix Figure D-7a).

In addition, samples of perched water were collected from the bottom of two shallow neutron holes (UZN#2 and UZN#91) shortly after rain events. Anion and <sup>36</sup>Cl data for these perched waters are reported in Table 4-16; the SO<sub>4</sub> data are new. The high Br concentrations in the UZN#2 water samples were due to a Br tracer salt that had been spread on the surface at that location. Section 5 discusses the use of these Cl data to estimate effective infiltration rates.

#### 4.5.3 Saturated-zone water

*Water samples from the saturated zone.* Table 4-17 presents halide, SO<sub>4</sub> and <sup>36</sup>Cl data for water samples from boreholes tapping the tuff aquifer in the vicinity of Yucca Mountain. New data are reported for G-2, ONC#1, C#3, WT-10, and WT-12. All of these waters are similar with respect to Cl, SO<sub>4</sub> and <sup>36</sup>Cl/Cl ratios. The Br concentrations for water samples from the C#3 wells are elevated above natural background due to the lingering presence of a Br tracer used in flow and transport tests at the C-wells complex. The Cl concentration averages about 7 mg/L in the 7 wells for which data are reported (excluding the non-Q sample from ONC#1), and appears to be independent of depth over the 260-m range for which samples were available from G-2. The SO<sub>4</sub> concentration is about 20 mg/L, with an average SO<sub>4</sub>/Cl ratio of 3; and these parameters likewise do not show any spatial trend. The average <sup>36</sup>Cl/Cl ratio is about 510 x 10<sup>-15</sup>, identical to the present-day (pre-bomb) background ratio. Assuming that the meteoric ratio was much higher for times older than 10,000 years ago than at the present-day, then these ratios suggest that the

Table 4-15. Halide and sulfate concentrations measured for PTn porewater samples from the ESF, listed in order of stratigraphic sequence<sup>1</sup>

North Ramp bore-hole	ESF station	Hydro-geologic unit <sup>2</sup>	Litho-logic unit <sup>2</sup>	Frax den-sity <sup>5</sup> (per 10 m)	Sample ID	Ave. depth from wall <sup>3</sup> , m	Concentrations <sup>4</sup> , mg/L			Br/Cl	SO <sub>4</sub> /Cl
							Cl	Br	SO <sub>4</sub>		
NR#1a	7+27	TCw	Tpcplnc	40	EDC011	1.8	29	0.40	36	0.014	1.2
NR#2	7+50	TCw	Tpcplnc /mw	50	EDC013	1.5	20	0.23	31	0.016	1.6
NR#3	7+70	TCw	Tpcplnc /mw	35	EDC017	1.7	35	0.26	45	0.008	1.3
NR#4	7+72	PTn	Tpcpv2	35	EDC020	1.8	45	0.36	58	0.008	1.3
NR#5	7+83	PTn	Tpcpv2	28	EDC023	1.7	In process				
NR#6	8+21	PTn	Tpcpv1	10	EDC025	1.4	In process				
NR#7	8+67	PTn	Tpbt4	11	EDC027	1.4	16	0.16	26	0.010	1.6
NR#8	8+70	PTn	Tpy	11	EDC029	1.4	15	0.19	22	0.013	1.5
NR#10	8+80	PTn	Tpbt3	7	EDC035	1.7	In process				
NR#11	8+92	PTn	Tpp	3	EDC038	1.7	In process				
NR#13	10+08	PTn	Tpp	16	EDC041	1.7	In process				
LCPA#2	Ale #4 middle	PTn	Tpbt2 argillic	6	EDC055	1.8	17	0.26	34	0.016	2.0
LCPA#3	Ale #4 upper	PTn	Tpbt2	6	EDC058	1.7	15	0.20	37	0.014	2.5
NR#15	10+54	PTn	Tptrv3/ rv2	15	EDC045	1.2	23	0.20	40	0.009	1.8
NR#16	10+69	PTn	Tptrv2	25	EDC048	1.5	16	0.15	26	0.009	1.6
NR#17	10+70	TSw	Tptrv1	33	EDC051	1.6	No water extracted after 24 hours of centrifuging				

Table 4-15 footnotes:

- <sup>1</sup> Porewaters were extracted from dry-drilled core by centrifuging core chips for at least 24 hours at 10,000 rpm. Units are listed in order of stratigraphic sequence, transitioning from the base of the TCw to the top of the TSw.
- <sup>2</sup> Hydrogeologic and lithostratigraphic units are defined in Table 2-1.
- <sup>3</sup> In addition to the samples listed above, samples were also collected from each drillhole from locations closer to the tunnel wall, for the purpose of evaluating the extent to which the drying front has penetrated into the bedrock as a function of its hydrologic properties.
- <sup>4</sup> Extraction of porewater from sample E048 was still in progress at the time that this report was prepared. The data were obtained for the water extracted after centrifuging the core for only 3 hours.
- <sup>5</sup> Fracture densities are from detailed line surveys (data packages listed in Sweetkind et al., 1997, their Appendix C).

Table 4-16. Measured  $^{36}\text{Cl}/\text{Cl}$  ratios and anion concentrations for perched water samples (See note)

LANL ID	Borehole	Collection date	Concentration, mg/L			Weight ratio		$^{36}\text{Cl}/\text{Cl}$ $\times 10^{15}$
			Cl	Br	$\text{SO}_4$	Br/Cl	$\text{SO}_4/\text{Cl}$	
W003	UZN#2	09-Apr-91	20.5	5.85	---	285	---	2012 ± 166
W069	UZN#2	22-Feb-95	5.90	0.24	---	40.5	---	3150 ± 110
W005	UZN#91	05-Mar-92	19.5	0.13	---	6.6	---	880 ± 83
W041	NRG7A	04-Mar-94	9.37	0.081	9.9	8.6	1.1	518 ± 15
W043	NRG7A	07A-Mar-94	9.96	0.085	7.1	8.5	0.7	491 ± 14
W042	NRG7A	07B-Mar-94	8.93	0.078	5.8	8.8	0.7	---
W038	NRG7A	7,14-Mar-94	9.78	0.082	6.9	8.4	0.7	474 ± 9
W083	SD-7	08-Mar-95	4.83	0.048	10.0	9.9	2.1	511 ± 14
W084	SD-7	08-Mar-95	4.88	0.049	10.1	10.0	2.1	---
W085	SD-7	08-Mar-95	4.98	0.049	---	9.8	---	---
W087	SD-7	16-Mar-95	4.38	0.047	---	10.7	---	---
W086	SD-7	16-Mar-95	4.37	0.046	---	10.5	---	---
W090	SD-7	17-Mar-95	4.41	0.047	---	10.6	---	---
W091	SD-7	17-Mar-95	4.41	0.048	---	10.8	---	---
W089	SD-7	17-Mar-95	4.46	0.046	---	10.4	---	657 ± 34
W092	SD-7	20-Mar-95	4.39	0.047	---	10.7	---	---
W093	SD-7	20-Mar-95	4.39	0.047	9.5	10.7	2.2	---
W095	SD-7	21-Mar-95	4.46	0.047	---	10.6	---	609 ± 15
W094	SD-7	21-Mar-95	4.43	0.047	9.8	10.7	2.2	---
W100	SD-7	21-Mar-95	3.95	0.048	---	12.1	---	635 ± 35
W044	SD-9	07-Mar-94	6.67	0.070	---	10.6	---	449 ± 17
W001	UZ-1 (note)	21-Jul-83	---	---	---	---	---	999 ± 80
W029	UZ-14 A1	02-Aug-93	7.59	0.188	---	24.8	---	566 ± 6
W028	UZ-14 A2	02-Aug-93	7.94	0.124	---	15.6	---	538 ± 20
W031	UZ-14 A	02-Aug-93	7.58	0.188	---	24.8	---	559 ± 67
W032	UZ-14 B	04-Aug-93	7.66	0.098	---	12.8	---	566 ± 27
W030	UZ-14 C	05-Aug-93	15.6	0.114	---	7.3	---	389 ± 10
W033	UZ-14 PT1	17-Aug-93	6.86	0.076	---	11.1	---	644 ± 12
W034	UZ-14 PT2	19-Aug-93	6.73	0.073	---	10.9	---	656 ± 15
W027	UZ-14 PT4	27-Aug-93	6.86	0.077	---	11.2	---	675 ± 12
W035	UZ-14 D	01-Sep-93	6.80	0.075	---	11.0	---	690 ± 24
W039	UZ-14	10-Mar-94	6.76	0.056	---	8.2	---	---
W040	UZ-14	10-Mar-94	6.13	0.054	---	8.8	---	---

--- Not measured

Note: Samples were collected by, or under the supervision of, J. Czarnecki, W. Steinkampf, or I.C. Yang (USGS/Denver) as part of other YMP activities. Data for UZ-1 are non-Q because borehole drilling and sample collection were not conducted under the YMP QA program. However, all analyses of this sample were conducted following YMP/QA procedures.

Table 4-17. Measured  $^{36}\text{Cl}/\text{Cl}$  ratios and anion concentrations for water samples from the saturated zone

LANL ID	Source	Collection date	Concentrations, mg/L			Weight ratios		$^{36}\text{Cl}/\text{Cl}$ $\times 10^{-15}$
			Cl	Br	$\text{SO}_4$	Br/Cl	$\text{SO}_4/\text{Cl}$	
Saturated zone, tuff aquifer, vicinity of Yucca Mountain								
W101	J-13	22-Mar-95	7.02	0.051	18.5	7.2	2.6	506 ± 9
W148	J-13	10-Mar-97	7.19	0.051	18.7	7.1	2.6	---
W149	J-13	10-Mar-97	7.14	0.050	18.6	7.0	2.6	---
W004	JF-3	05-Mar-92	---	---	---	---	---	511 ± 63
W097	C#3	31-May-95	6.40	0.052	20.6	8.1	3.2	475 ± 20
W098	C#3	22-May-95	6.70	0.051	21.5	7.7	3.2	486 ± 12
W099	C#3	23-May-95	6.45	0.050	20.5	7.8	3.2	496 ± 11
W146	C#3	04-Dec-96	6.17	0.698	22.4	113	3.6	501 ± 21
W147	C#3	19-Feb-97	6.02	0.151	20.0	25.1	3.3	542 ± 20
W156	C#3	12-Jun-97	6.81	0.151	21.4	22.2	3.1	---
W064	G-2 / 1761 ft	02-Feb-95	7.43	0.050	14.5	6.7	1.9	457 ± 20
W065	G-2 / 2130 ft	02-Feb-95	6.93	0.051	16.5	7.3	2.4	524 ± 13
W066	G-2 / 2601 ft	02-Feb-95	6.94	0.049	16.4	7.1	2.4	509 ± 10
W130	G-2	08-Feb-96	5.96	0.039	14.6	6.5	2.4	531 ± 17
W131	G-2	30-Jan-96	6.04	0.045	12.8	7.4	2.1	525 ± 15
W135	G-2	12-Apr-96	6.44	0.043	---	6.6	---	---
W136	G-2	23-Apr-96	6.35	0.044	15.6	7.0	2.5	---
W045	SD-9	12-Sep-94	7.05	0.059	---	8.3	---	497 ± 19
W006	VH-1	30-Jul-92	8.83	---	---	---	---	540 ± 11
W132	WT-10	18-Jan-96	7.17	0.050	31.9	7.0	4.5	526 ± 39
W108	WT-12	22-Aug-95	6.92	0.049	---	7.1	---	---
W133	WT-12	19-Aug-95	6.62	0.054	24.2	8.2	3.6	563 ± 13
W134	WT-12	21-Aug-95	6.52	0.052	23.8	7.9	3.6	568 ± 14
W109	ONC#1 (note)	15-Dec-94	7.88	0.139	34.9	17.6	4.4	---
Saturated zone, carbonate aquifer								
W002	UE#25-P1	06-Jun-90	25.6	---	---	---	---	132 ± 10
Saturated zone, Pahute Mesa, north of Yucca Mountain								
W074	ER30-1-L	31-Jan-95	6.58	0.090	13.2	13.6	2.0	453 ± 17
W070	ER30-1-U	07-Feb-95	6.42	0.169	14.2	26.3	2.2	460 ± 15
W102	U-20 WW	31-May-95	11.6	0.065	30.0	5.6	2.6	523 ± 15

Note: Samples were collected by USGS investigators and prepared for analysis at LANL.  $^{36}\text{Cl}/\text{Cl}$  ratios were analyzed by the PRIME Laboratory at Purdue University and by the NRSL at University of Rochester. Some data may differ slightly from those reported previously due to inclusion of additional analyses in the average measured concentrations, or due to slight changes in the protocol used to estimate uncertainties and calculate weighted averages of the isotopic ratios. Data for ONC#1 are non-Q because borehole drilling and sample collection were not conducted under the YMP QA program. However, all analyses of this sample were conducted following YMP/QA procedures.

average age for all of these waters is less than 10 ka.

Also in Table 4-17 are halide and  $^{36}\text{Cl}$  data for a borehole tapping the carbonate aquifer and for boreholes on Pahute Mesa, a recharge area for the groundwater underlying Yucca Mountain.

Data for other saturated-zone samples have been reported elsewhere:

- *ESF construction water* data are presented in section 4.2.2.
- Data for *shallow water table samples from the Amargosa Desert* were reported in Fabryka-Martin and Liu (1995), and no new data are available.
- Data for *spring discharges*, mostly from Death Valley, were also reported in Fabryka-Martin and Liu (1995), and no new data are available.

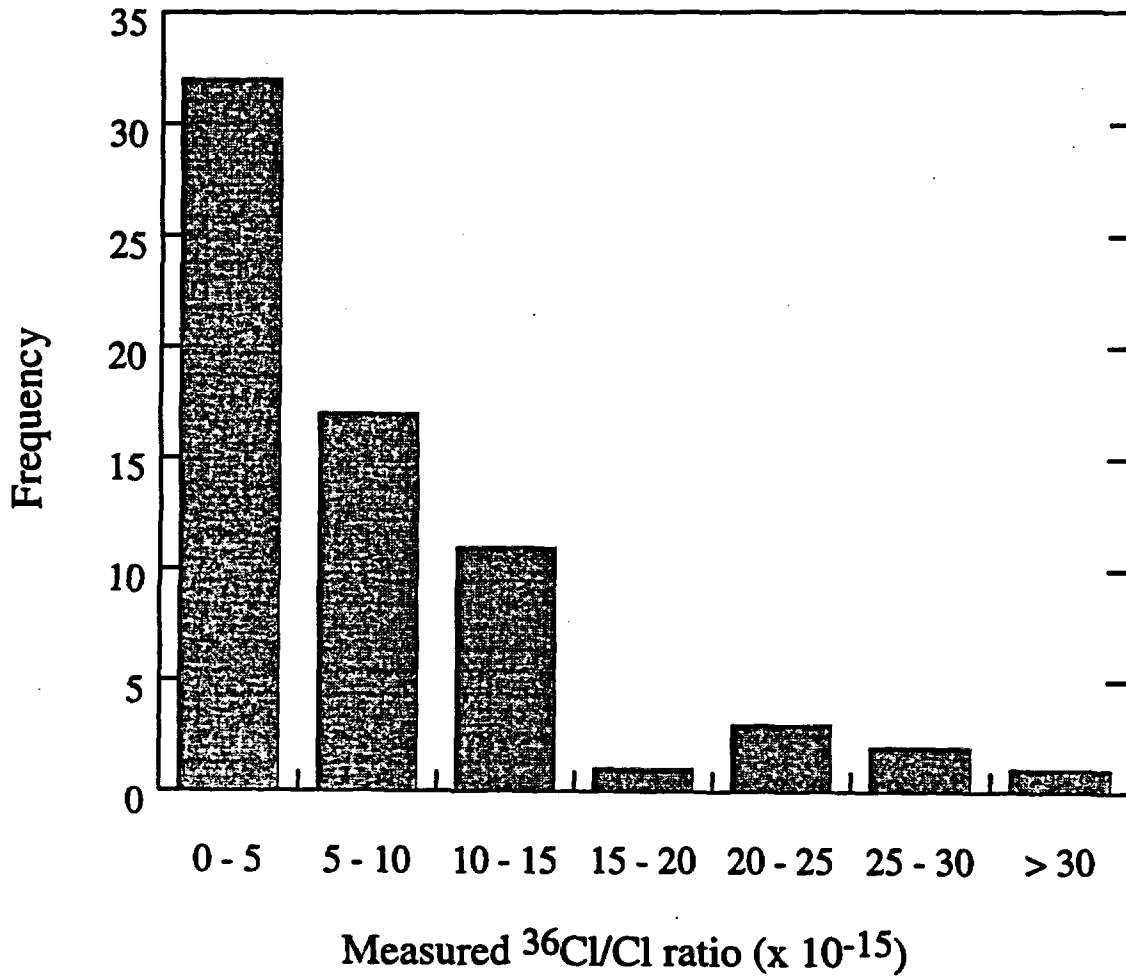


Figure 4-1. Analytical results for 67 process blanks prepared alongside Yucca Mountain samples, 1992 - 1997. The maximum ratio measured had a value of  $65 \pm 4 \times 10^{-15}$ . Because of large error bars at these low levels, most of the results were indistinguishable from zero.

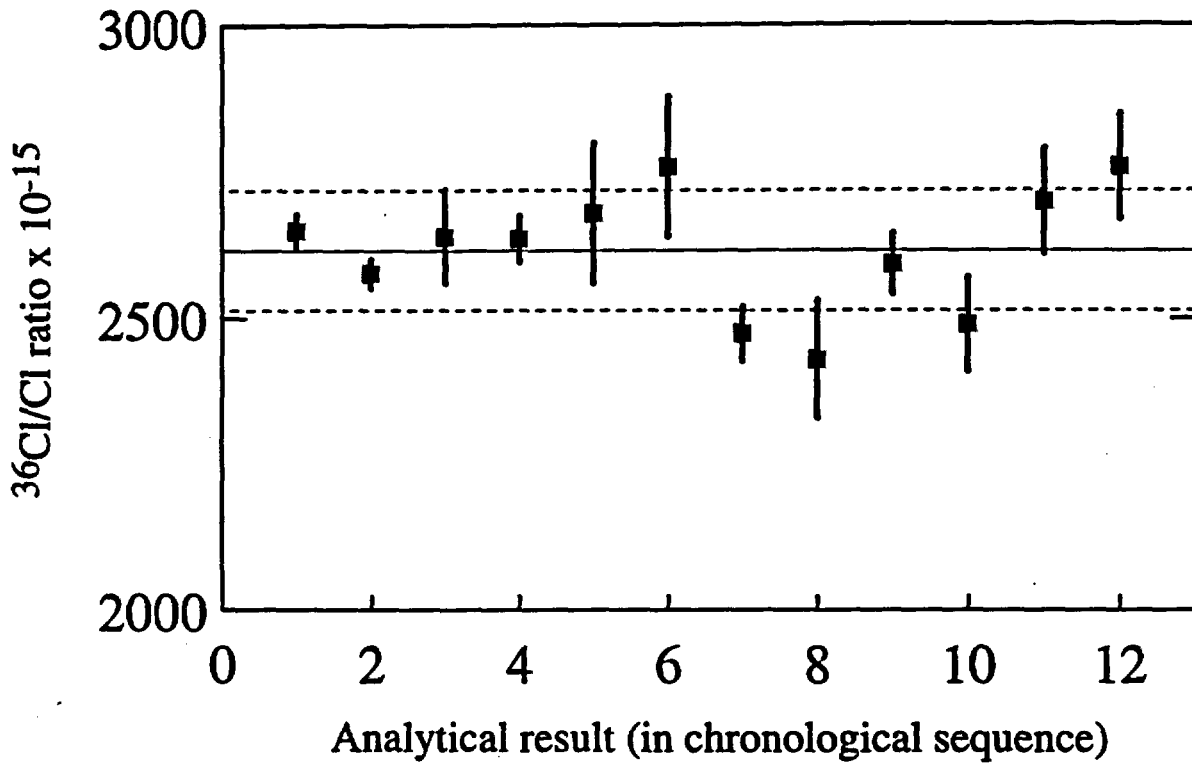


Figure 4-2. Results of replicate analyses of an internal standard, 1994 - 1997. The average measured ratio was  $2616 \pm 103 \times 10^{-15}$  (one standard deviation).

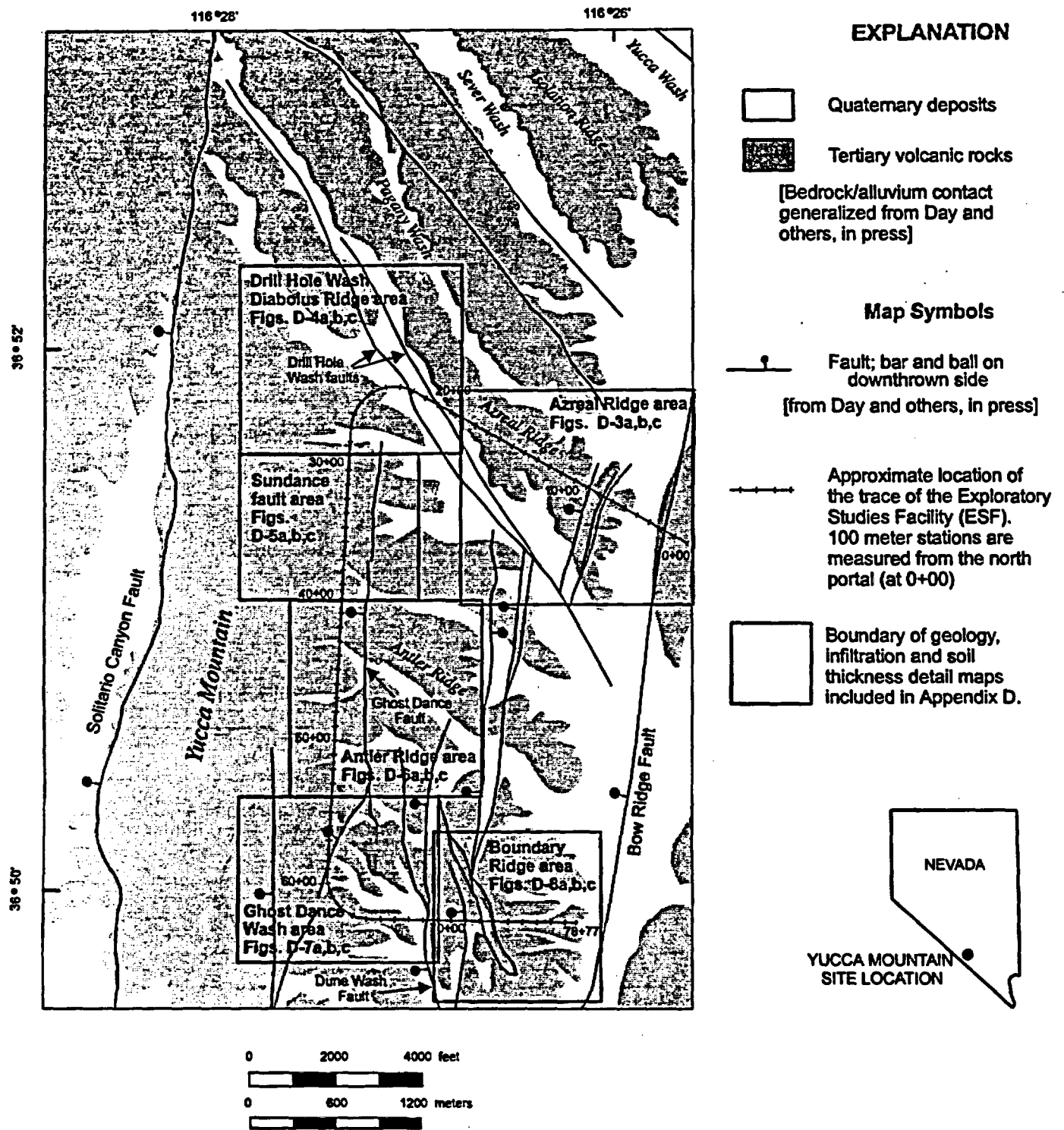


Figure 4-3. Index map of central Yucca Mountain. Outlines of the detail maps in Appendix D are shown.

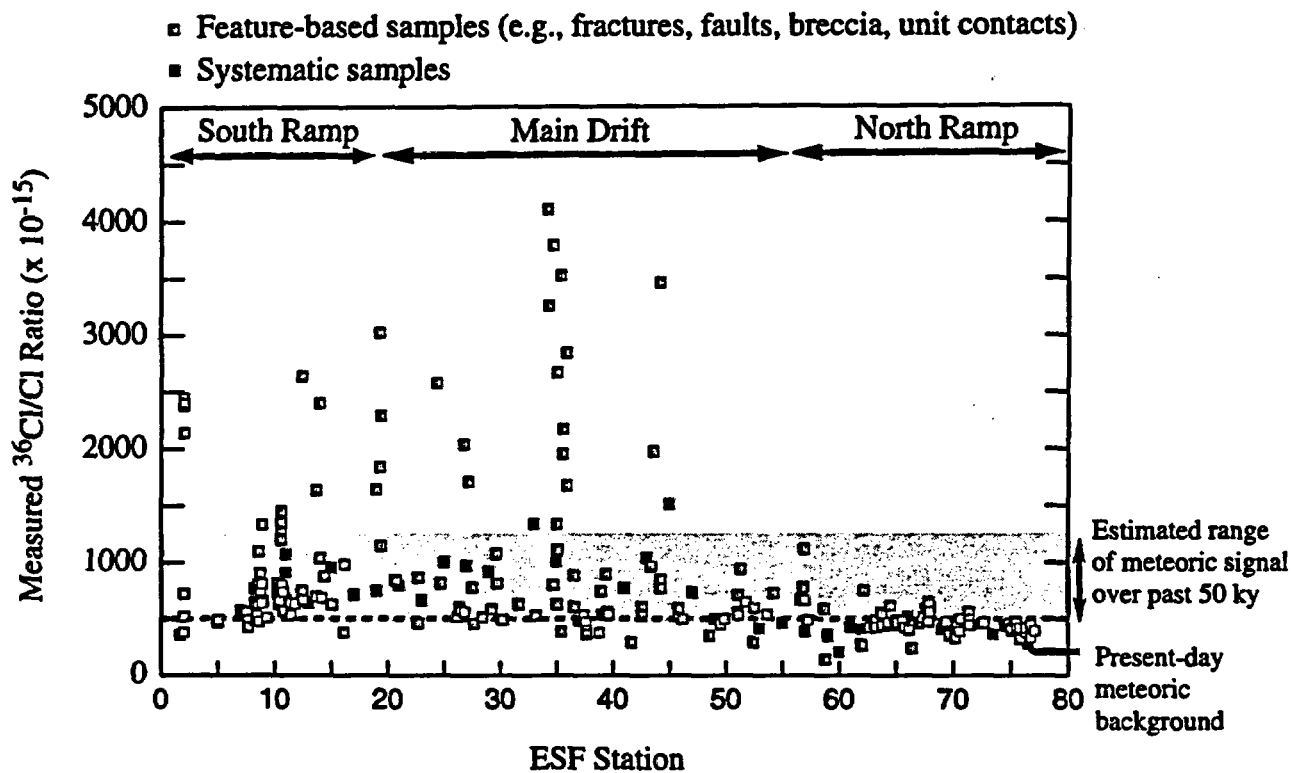


Figure 4-4. Distribution of  $^{36}\text{Cl}/\text{Cl}$  ratios measured for rock samples, as a function of distance along the ESF as measured from the North Ramp Portal. ESF stations are marked in 100-m increments. Samples with ratios exceeding  $1250 \times 10^{-15}$  are considered to contain a component of bomb-pulse  $^{36}\text{Cl}$ . Data from Appendix B.

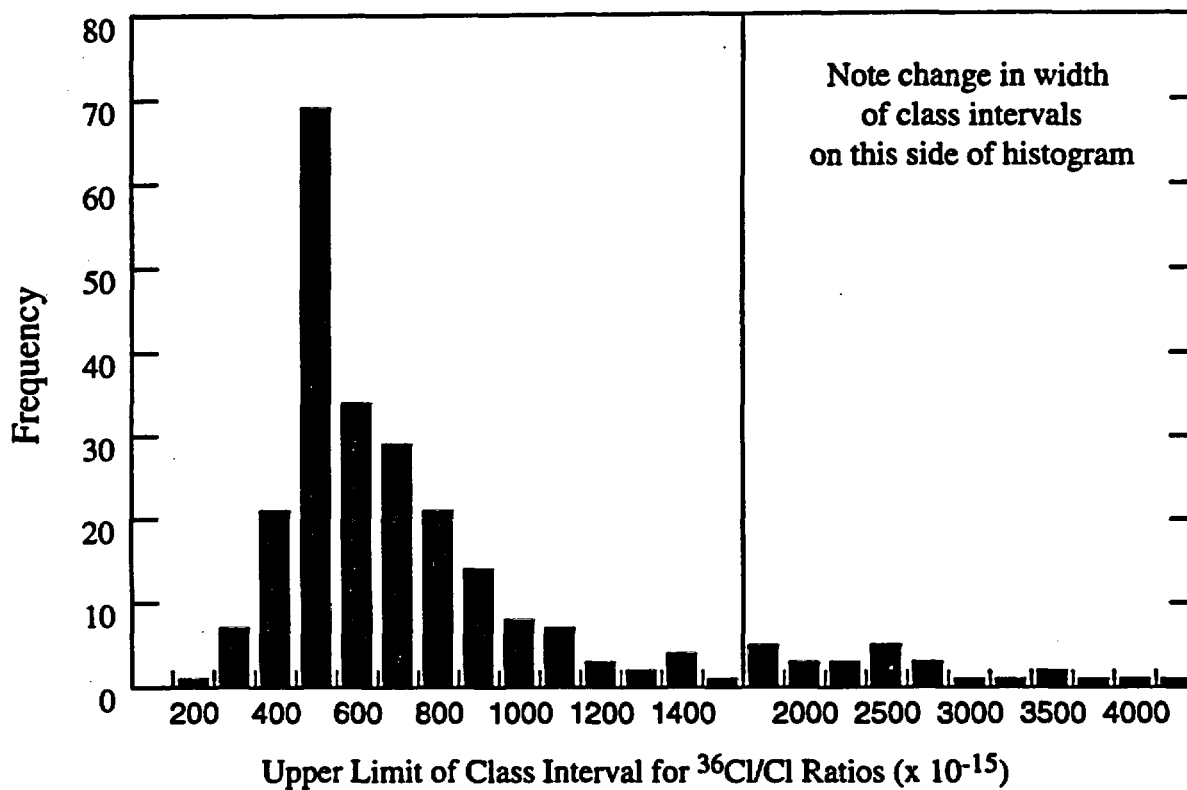


Figure 4-5. Frequency distribution of  $^{36}\text{Cl}/\text{Cl}$  ratios measured in ESF rock samples. Data from Appendix B.

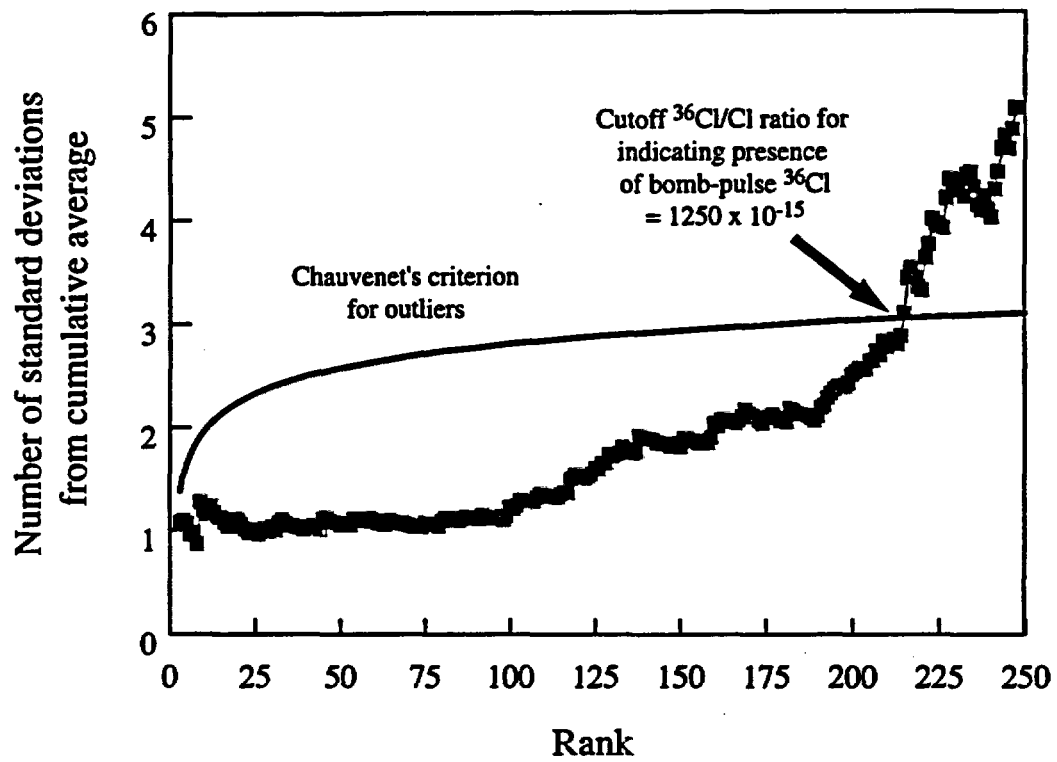


Figure 4-6. Application of Chauvenet's criterion to establish the cutoff  $^{36}\text{Cl}/\text{Cl}$  ratio for identifying the presence of bomb-pulse  $^{36}\text{Cl}$  in ESF rock samples. Data from Appendix B.

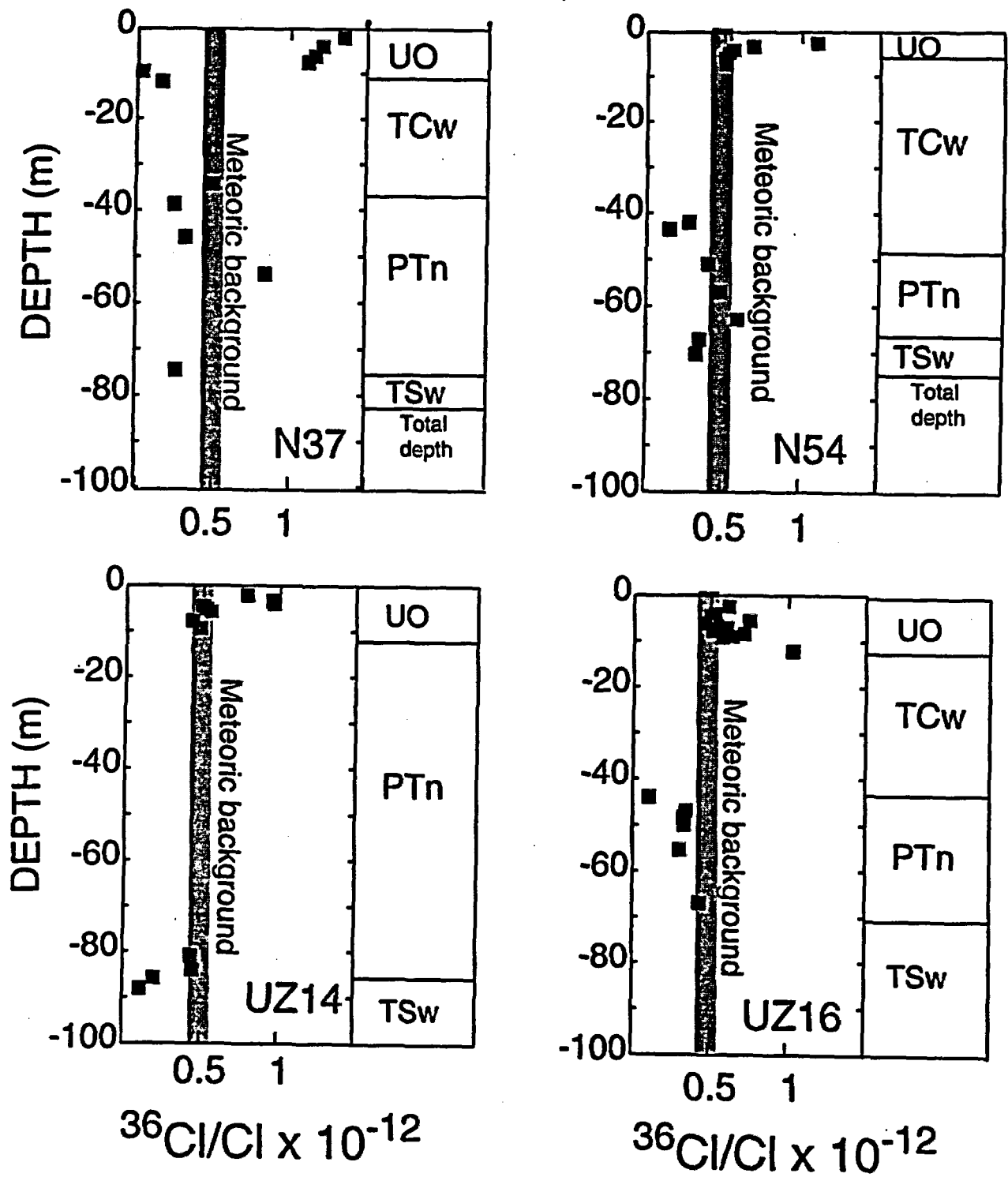


Figure 4-7. Measured  $^{36}\text{Cl}/\text{Cl}$  profiles for boreholes located in large channel bottoms and terraces (Fabryka-Martin et al., in press [b]).

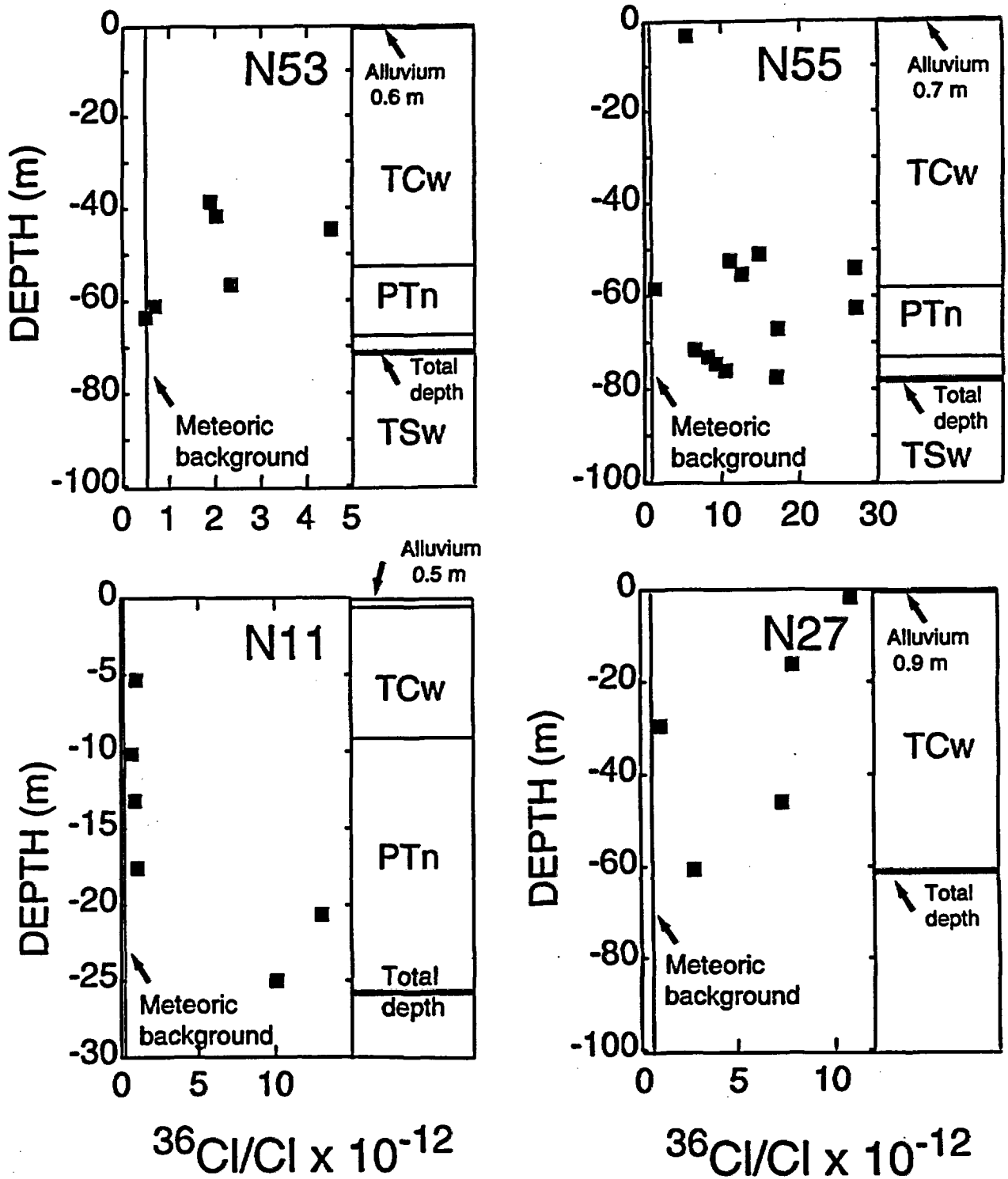


Figure 4-8. Measured  $^{36}\text{Cl}/\text{Cl}$  profiles for boreholes located in sideslopes and ridgetops (Fabryka-Martin et al., in press [b]).

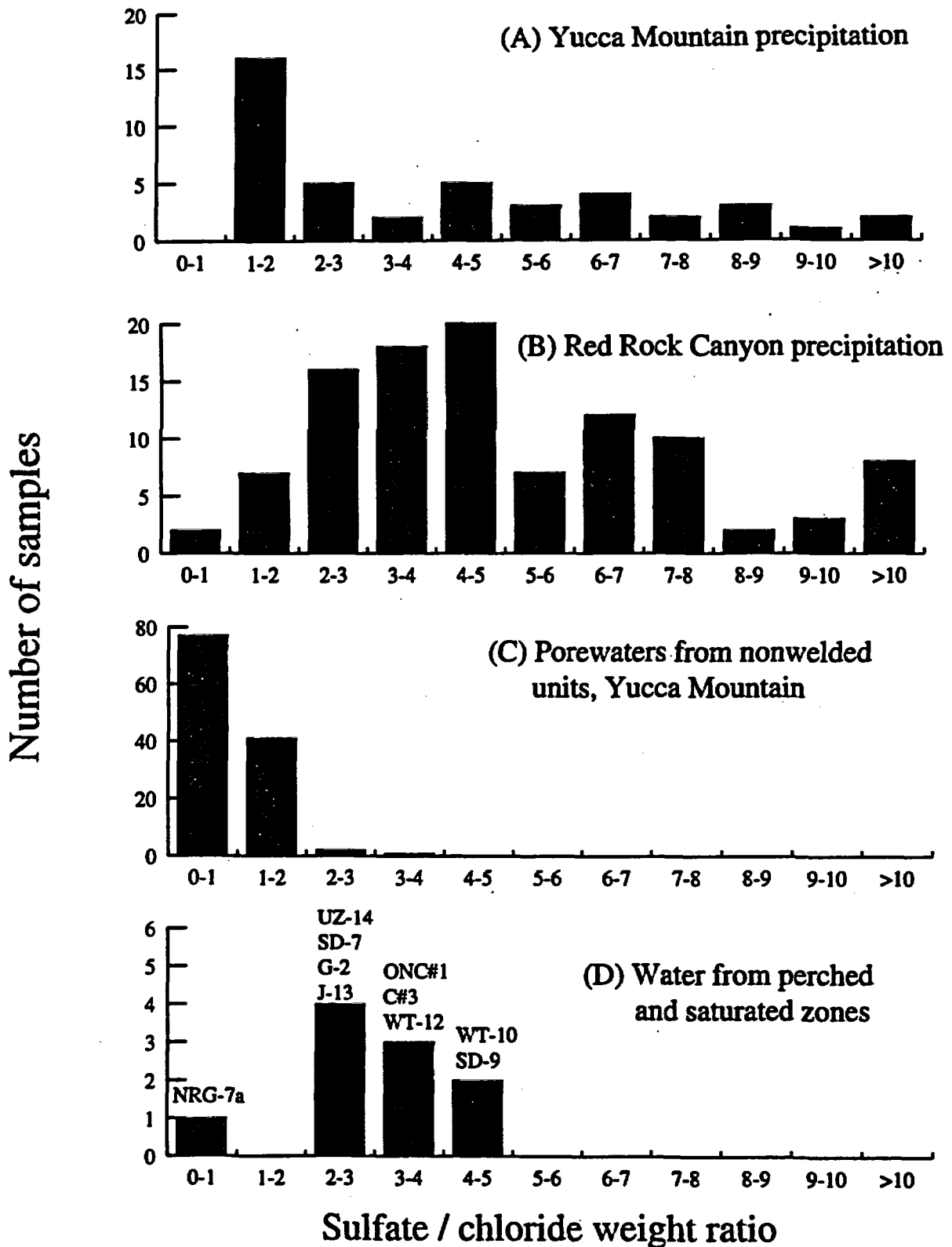


Figure 4-9. Sulfate/chloride ratios in water samples. (A) Yucca Mountain precipitation, March 1995 (this report), (b) Red Rock Canyon, Nevada, precipitation (NADP, 1997), (C) porewaters extracted from nonwelded units at Yucca Mountain (Yang et al., 1988, 1990, 1996, 1997), (d) water from perched and saturated zones (Tables 4-16 and 4-17).

## 5. SURFACE INFILTRATION RATES

Two approaches were used in Fabryka-Martin et al. (in press [b]) to derive information about shallow infiltration processes from Cl and  $^{36}\text{Cl}$  data. These are summarized below and include the Cl mass balance method (section 5.1) and distribution of bomb-pulse  $^{36}\text{Cl}$  (sections 5.2 and 5.3). There are few new data which are relevant to these applications so the following is mostly a summary of information and data discussed in Fabryka-Martin et al. (in press [b]).

### 5.1 Application of the Cl Mass Balance (CMB) Method

#### 5.1.1 Overview of method and its limitations

The Cl mass balance method proposes that the infiltration flux can be estimated as a proportion of precipitation based upon the extent of enrichment of Cl in pore water relative to its concentration in precipitation. The underlying assumption for this approach is that pore-water concentrations provide a direct measure of the extent of water loss by evapotranspiration in the root zone. Hence, pore-water concentrations will increase, and apparent infiltration rates will decrease proportionally, as water moves downward through the root zone (Figure 5-1). A commonly observed variation of this simplistic view is the presence of a bulge of higher Cl concentrations near the base of the root zone, with somewhat lower concentrations observed below the root zone. Such variations in Cl concentrations are assumed to reflect past climatic variations, variations in infiltration rates, or evidence for fast flow bypassing the root zone (e.g., Allison et al., 1994).

This approach has been widely used to estimate water transport rates in alluvial profiles through the unsaturated zone (Matthias et al., 1986; Phillips et al., 1988; Scanlon, 1991, 1992; Sharma and Hughes, 1985; Tyler et al., 1996). In these studies, the average water flux in the unsaturated zone is calculated by assuming that the flux of Cl deposited at the surface ( $P C_0$ ) equals the flux of Cl carried beneath the root zone by infiltrating water ( $I C_p$ ) (e.g., Allison and Hughes, 1978; Gardner, 1967; Stone, 1984):

$$P C_0 = I C_p \quad (5-1)$$

Equation (5-1) can be rearranged to solve for the infiltration rate, I:

$$I = \frac{P C_0}{C_p} \quad (5-2)$$

$$= P C_0 \frac{\sum \theta_i z_i}{\sum \rho_i C_{l_i} z_i} \quad (5-3)$$

where

- P = average annual precipitation (cm yr<sup>-1</sup>),  
C<sub>0</sub> = average Cl concentration in precipitation (mg L<sup>-1</sup>), including the contribution from dry fallout,  
C<sub>p</sub> = average Cl concentration in pore water (mg L<sup>-1</sup>),  
θ<sub>i</sub> = volumetric soil water content in the interval i (m<sup>3</sup> water m<sup>-3</sup> soil),  
z<sub>i</sub> = thickness of depth interval i (m),  
ρ<sub>i</sub> = dry bulk density (kg m<sup>-3</sup>) in interval i,  
C<sub>l<sub>i</sub></sub> = Cl concentration in bulk dry soil in interval i (mg kg<sup>-1</sup>), and  
l = conversion factor for g m<sup>-3</sup> to mg L<sup>-1</sup>.

The summation term  $\sum_i (\rho_i C_{l_i} z_i)$  is the cumulative total mass of Cl from the surface to depth z<sub>i</sub> (g Cl m<sup>-2</sup>). Assumptions underlying the CMB method are:

- one-dimensional, downward piston flow (i.e., matrix or piston-displacement flow),
- constant average annual precipitation rate,
- constant average annual Cl deposition rate,
- no run-on or run-off
- no Cl source other than precipitation (e.g., Cl brought in by surface runoff and Cl released from weathering of surface rocks are assumed to be negligible), and
- no Cl sink (e.g., removal of Cl through the formation of halite is assumed negligible).

Section 6.3 discusses conditions under which these assumptions may not be valid at Yucca Mountain.

Even in the absence of water content data, the CMB method can be used to estimate Cl accumulation time (t, yr) in the unsaturated zone, a qualitative indicator of rates of water movement:

$$t_i = \frac{\sum (\rho_i C_{l_i} z_i)}{P C_0} \quad (5-4)$$

The Cl deposition rate (C<sub>l<sub>0</sub></sub>) is a key parameter in the CMB method. This parameter can be estimated by dividing the natural <sup>36</sup>Cl fallout at the site by the product of mean annual

precipitation and the natural (prebomb)  $^{36}\text{Cl}/\text{Cl}$  ratio for that site (Phillips et al., 1988; Scanlon et al., 1990). For the vicinity of Yucca Mountain, the estimated Cl deposition rate ( $P \text{ Cl}_0$ ) is  $106 \text{ mg m}^{-2} \text{ yr}^{-1}$ , with a corresponding concentration in precipitation  $C_0$  of  $0.62 \text{ mg L}^{-1}$ . This estimate is based on an average annual precipitation rate of  $17 \text{ cm yr}^{-1}$  (Hevesi et al., 1992), a prebomb  $^{36}\text{Cl}/\text{Cl}$  ratio of  $500 \times 10^{-15}$ , and a natural  $^{36}\text{Cl}$  fallout of  $28 \text{ atoms } ^{36}\text{Cl m}^{-2} \text{ s}^{-1}$  (Bentley et al., 1986).

The validity of the estimated Cl deposition rate at Yucca Mountain can be checked by two independent methods. One method is to compare the effective concentration in precipitation,  $0.62 \text{ mg L}^{-1}$ , against actual measured concentrations. For example, the concentration of Cl in 111 samples collected from Yucca Mountain for the present study during the Spring of 1995 ranged from  $0.3$  to  $1.8 \text{ mg L}^{-1}$ , averaging  $0.5 \text{ mg L}^{-1}$ . Similarly, 17 monthly rain samples collected from 1989 to 1992 from Kawich Peak, about  $130 \text{ km}$  due north of Yucca Mountain, ranged from  $0.2$  to  $1.7 \text{ mg L}^{-1}$ , also averaging  $0.5 \text{ mg L}^{-1}$  (McKinley and Oliver, 1994, 1995). A 10-year record of rain chemistry data from Red Rock Canyon, Nevada, showed an average Cl concentration of  $0.2 \text{ mg/L}$  (section 4.5.1). These latter data sets only include the wet component of Cl fallout and would tend to underestimate the total deposition rate.

A second method is to compare the deposition rate of  $106 \text{ mg m}^{-2} \text{ yr}^{-1}$  against deposition rates estimated by other investigators at other sites in the arid southwestern U.S. Total deposition rates estimated by Phillips (1994) for sites in Arizona, New Mexico and Nevada, range from  $75$  to  $150 \text{ mg m}^{-2} \text{ yr}^{-1}$ .

### *5.1.2 Summary of previous report results*

The CMB method was applied to soil profiles and alluvial profiles from boreholes (Fabryka-Martin et al., in press [b]). Apparent infiltration rates for three Midway Valley soil profiles for depths of  $2 \text{ m}$  or more are  $0.1$  to  $0.2 \text{ mm yr}^{-1}$ . Comparable calculations for the base of the deep alluvial profiles in UZ-N37, UZ-N54, UZ-14 and UZ#16 range from a low of  $0.1 \text{ mm yr}^{-1}$  for UZ#16 and UZ-N54, a marginally higher rate of  $0.2 \text{ mm yr}^{-1}$  for UZ-14, and a high of  $0.5 \text{ mm yr}^{-1}$  for UZ-N37 (Table 5-1). These low fluxes are consistent with the infiltration estimates (for matrix flow only) proposed for this part of Yucca Mountain by Flint et al. (1996), as can be seen by comparing them to the rates shown for these locations in Appendix Figures D-4b and D-6b.

Pore-water data extracted from nonwelded tuffs are also available from this and other Yucca Mountain studies to apply the CMB method (Table 5-2). New data used in this table are the porewater Cl concentrations measured for samples from drillholes in the North Ramp. The apparent fluxes calculated for these porewater samples are as much as an order of magnitude higher than those calculated for the soil and alluvial samples discussed above, ranging from  $3$  to  $6 \text{ mm yr}^{-1}$ . These fluxes calculated for the porewaters again are consistent with those predicted for these locations by the numerical infiltration model of Flint et al. (1996) (Appendix Figure D-3b).

Table 5-1. Apparent infiltration rates calculated for soil and alluvial profiles > 2 m, based on the Cl mass balance (CMB) method<sup>1</sup>

Location	Maximum depth of profile (m)	Cumulative CMB age at bottom of profile <sup>2</sup> (yr)	Cumulative depth of water stored in profile <sup>3</sup> (mm)	Apparent infiltration rate at bottom of profile <sup>1</sup> (mm/yr)
Midway Valley soil pits				
MWV-P2	2.1	3074	210	0.07
MWV-P31	2.2	1292	220	0.17
Boreholes				
UZ-14	9.4	4244	940	0.22
UZ#16	9.2	9462	920	0.10
UZ-N37	12.6	2268	1260	0.56
UZ-N54	6.6	9500	660	0.07

Notes:

- <sup>1</sup> Results of calculations summarized from Tables 5-2 and 5-3 in Fabryka-Martin et al. (in press [b]). The approach calculates the total mass of Cl accumulated in the profile, from the surface to the sampled depth. The Cl mass balance (CMB) age is calculated by assuming a constant rate of Cl deposition at the top of the profile. This age is converted to an infiltration rate by calculating the cumulative depth of water stored in the profile, and dividing the cumulative depth of water by its cumulative age (i.e., column 4 divided by column 3 in the table above). See text for a discussion of the underlying assumptions and possible sources of error for this simple model.
- <sup>2</sup> Calculation of mass of Cl in the interval assumes a bulk density of 1700 kg m<sup>-3</sup> and an annual Cl accumulation rate of 106 mg m<sup>-2</sup> (Fabryka-Martin et al., in press [b]).
- <sup>3</sup> Calculation of cumulative depth of water stored in profile assumes an average volumetric water content of 0.1, estimated from moisture contents shown for deep alluvial profiles in neutron boreholes in Flint and Flint (1995, their Figures 8 to 106).

Table 5-2. Effective infiltration rates calculated from pore-water Cl concentrations by the Cl mass balance (CMB) method<sup>1</sup>

Borehole	Hydrogeologic unit <sup>2</sup>	# of samples	Data source <sup>3</sup>	Range of sample depths (m)	Cl concentrations, mg L <sup>-1</sup>		Effective infiltration rate <sup>4</sup> (mm yr <sup>-1</sup> )	
					Range	Geometric mean		
UZ#16	PTn	2	YA96	50 - 55	32 - 38	35	3.0	
	CHn (Tac)	19		368 - 440	14 - 82	28	3.7	
	CHn (Tcp)	5		453 - 503	27 - 71	49	2.2	
UZ-14	PTn	17	YA96	14 - 75	44 - 245	80	1.3	
	CHn (Tac)	14		430 - 511	10 - 75	20	5.3	
	CHn (Tcp)	3		517 - 529	12 - 39	21	4.9	
UZ-4	PTn	7	YA88 YA92	91 - 97	85 - 104	93	1.1	
UZ-5	PTn	6	YA88	29 - 37	34 - 47	42	2.5	
	PTn	3	YA90	94 - 97	51 - 89	72	1.5	
NRG-6	PTn	7	YA96	48 - 78	47 - 185	85	1.2	
NRG-7A	CHn (Tcp)	2	YA96	455 - 457	39 - 50	33	3.2	
North Ramp	Base of TCw to top of PTn	4	Table 4-15	~100	20-45	31	3.4	
	Top of PTn to top of TSw	6		~100-150	15-23	17	6.2	
Perched water						Midpoint		
	NRG-7A	CHn (Tac)	4	Table 460	8.9 - 10	9.5	11	
	SD-7	CHn (Tac)	13	4-16	480 - 488	4.0 - 5.0	4.5	23
	SD-9	TSw	1	and 454	7.0	7.0	15	
UZ-14	TSw	9	YA96	391	6.1 - 7.9	6.8	16	

Notes:

- <sup>1</sup> The CMB method estimates an apparent infiltration rate from the measured Cl concentration in the porewater, by assuming that infiltration as a proportion of precipitation is directly proportional to which the porewater Cl concentration has been enriched (by evapotranspiration) relative to its effective concentration (including both wet and dry Cl deposition) in precipitation. Expressed as a formula,  $I = P (C_p/C_o)$ , where I is the infiltration rate, P is the precipitation rate, and C<sub>o</sub> and C<sub>p</sub> are the Cl concentrations of precipitation and porewater, respectively.
- <sup>2</sup> Hydrogeologic and lithostratigraphic units are defined in Table 2-1.
- <sup>3</sup> Data sources: YA88, Yang et al., 1988; YA90, Yang et al., 1990; YA92, Yang et al., 1992; YA96, Yang et al., 1996 (their Tables 2-4 for porewaters extracted from core). Data for porewaters extracted from North Ramp cores are summarized from Table 4-15 in this report. Measurements for perched water are summarized from Table 4-16 in this report, and exclude bailed samples UZ-14A and UZ-14C; depths for perched-water samples are from Table 6 in Yang et al. (1996).
- <sup>4</sup> Calculation of effective infiltration rate assumes annual average precipitation rate of 170 mm yr<sup>-1</sup>, with a Cl concentration of 0.62 mg L<sup>-1</sup> (including dry fallout).

Many of the estimated fluxes in Table 5-2 exceed the saturated matrix hydraulic conductivity ( $k_{sat}$ ) of the overlying bedrock matrix. For example, the nonwelded PTn unit in UZ#16 is overlain by 30 m of the welded TCw unit, with an average matrix  $k_{sat}$  of 0.9 mm yr<sup>-1</sup>, and the nonwelded CHn unit in UZ-14 and UZ#16 is overlain by over 300 m of the welded TSw unit, with an average matrix  $k_{sat}$  of 1.9 mm yr<sup>-1</sup> (Flint and Flint, 1994). The 3-5 mm yr<sup>-1</sup> flux calculated by the CMB method for the nonwelded units at these particular locations thus provides evidence that the primary mechanism of water transport to these units cannot be via matrix flow through the overlying welded units. Alternative mechanisms are fracture transport or lateral transport. In contrast, for this data set, the lowest fluxes (about 1 mm yr<sup>-1</sup>) calculated by the CMB method are those for the nonwelded PTn unit intercepted by UZ#4 and UZ-14, which are located in large channel bottoms where the PTn is not overlain by any welded unit. The PTn has an average matrix  $k_{sat}$  of 13 cm yr<sup>-1</sup>, so this low flux estimated by the CMB method would indicate matrix flow alone, without a fracture component. This interpretation is also consistent with the Flint et al. (1996) conceptual model in which fracture flow is initiated beneath areas of thin soil overlying fractured welded rock. Additional support for this conceptual model is provided by the distribution of bomb-pulse <sup>36</sup>Cl in borehole profiles (section 5.2).

### 5.1.3 *Input to flow and transport models*

During the past year, flow and transport modelers have made significant advances in investigating the potential utility of simulating Cl transport in the unsaturated zone, as an additional means for evaluating alternative conceptual models and for establishing the validity of hydrologic parameter values (Sonnenthal and Bodvarsson, 1997; Robinson et al., 1997). Both modeling efforts assume that the map of spatially-distributed infiltration at the site (Flint et al., 1996) can be converted in a straightforward manner to a map of the spatial distribution of Cl concentrations in infiltrating water by solving for  $C_p$  in equation 5-1 above. An example of the resulting map is shown in Figure 8-19 and is discussed in section 8.7.1. Section 8 summarizes the results of the LANL simulations, with respect to the predicted distribution of Cl concentrations in the unsaturated zone. A major problem with this approach at the present time is the limited spatial coverage of the porewater Cl analyses available to compare against the simulated concentrations.

## 5.2 Penetration of bomb-pulse <sup>36</sup>Cl into soil profiles

Qualitative and bounding information on infiltration fluxes can be obtained from the shape and magnitude of the bomb-pulse profile and the depth to the center of mass of the <sup>36</sup>Cl bomb pulse in alluvium and deep soils. Infiltration rates in arid soils have been evaluated using bomb-pulse <sup>36</sup>Cl as a water tracer in several studies (Norris et al., 1987; Phillips et al., 1988; Scanlon et al., 1990; Walker et al., 1991). Only a negligible proportion of the <sup>36</sup>Cl measured in these studies was of cosmogenic origin; the isotopic composition of the samples was dominated by bomb-pulse <sup>36</sup>Cl injected into the atmosphere primarily from the series of high-yield nuclear-weapons

tests conducted at the surface of the Pacific Ocean between 1952 and 1958.

Interpretation of isotopic data relating to the distribution of bomb-pulse  $^{36}\text{Cl}$  in shallow samples is presented in Fabryka-Martin et al (in press [b]). The integrals of the bomb-pulse  $^{36}\text{Cl}$  peaks in the UZ-N37 and UZ-N54 profiles agreed with the expected integral for total global fallout at the site. Hence, there is no evidence for large-scale lateral transport of Cl into or out of these profiles, nor for contamination by  $^{36}\text{Cl}$  fallout from NTS activities. A net infiltration rate on the order of 1 mm/yr was calculated for these profiles based on the depth at which the  $^{36}\text{Cl}$  peak was found, but the authors concluded that this was an overestimate because the bomb-pulse signal still resided almost entirely within the zone of evapotranspiration and hence still retained the imprint of the root-zone velocity (e.g., see Figure 5-1) (Tyler and Walker, 1994).

Other than data for the NRSF-TP-19 soil profile, which were presented and discussed in section 4.3, no new data are available for this aspect.

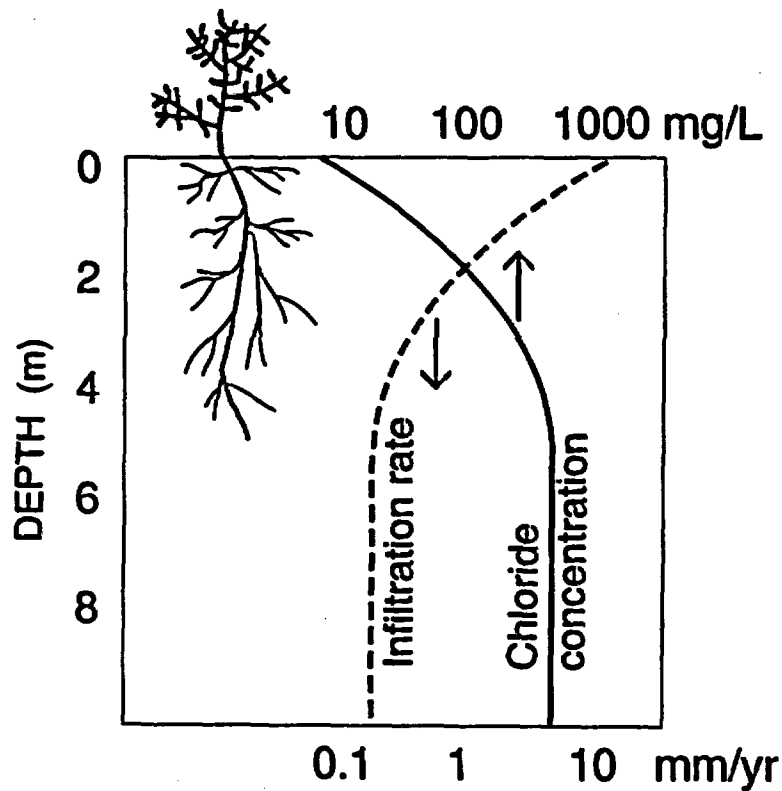


Figure 5-1. Schematic diagram illustrating the underlying basis of the chloride mass balance method. With increasing depth, porewater chloride concentrations increase, and apparent infiltration rates decrease, as water is extracted by evapotranspiration (ET). Net infiltration is the flux of water moving below the zone of ET, at which depth porewater chloride concentrations will be relatively constant, provided the underlying assumptions are met (see section 5.1).

## 6. SUBSURFACE FLOW PATHS AND TRAVEL TIMES

This section contains analyses and discussions relevant to the hydrologic interpretation of the  $^{36}\text{Cl}/\text{Cl}$  and  $\text{Cl}$  data. The  $^{36}\text{Cl}/\text{Cl}$  data are classified into categories with implications for ground-water ages. Assumptions and corrections required for data interpretation are described. Data from related isotopic and geochronologic studies are examined in the context of their relevance to the  $^{36}\text{Cl}$  investigations. Data and conceptual models of chloride redistribution at the surface and in the shallow subsurface are discussed. Evidence for the structural associations of fast paths is summarized. Finally, the conceptual model for the distribution of fast paths from the surface to the potential repository horizon is used as the basis for predicting the occurrence of bomb-pulse  $^{36}\text{Cl}$  in the planned East-West drift.

### 6.1 Subsurface distribution of $^{36}\text{Cl}$ at Yucca Mountain

#### 6.1.1 Samples with elevated $^{36}\text{Cl}/\text{Cl}$ ratios

An overview of the distribution of  $^{36}\text{Cl}$  in the unsaturated zone at Yucca Mountain is provided in Table 6-1. The table documents that many of the borehole and ESF samples have elevated  $^{36}\text{Cl}/\text{Cl}$  ratios relative to natural background values. Statistical analysis of the extensive ESF data set as well as other lines of evidence indicates that ratios above a threshold of  $1250 \times 10^{-15}$  are unambiguously above background values. These samples record the input of anthropogenic  $^{36}\text{Cl}$  (bomb-pulse  $^{36}\text{Cl}$ ) into the unsaturated-zone ground-water system to the depth of the potential repository horizon at several locations in the north part of the ESF (Figures 6-1 and 6-2). Alternative explanations for the elevated  $^{36}\text{Cl}/\text{Cl}$  ratios that have been examined and rejected include the following:

- subsurface production of  $^{36}\text{Cl}$  by the *in-situ* neutron flux (rejected because there is no basis for expecting a neutron flux of the magnitude required to account for the observed levels of  $^{36}\text{Cl}$ ),
- release of cosmogenic  $^{36}\text{Cl}$  from soil calcites (rejection based on mass balance calculations, section 3.4),
- laboratory contamination (minimized by the frequent analysis of blanks, section 4.1), and
- field contamination (considered highly unlikely in the absence of any known sources).

Thus, it is highly probable that these data that bomb-pulse  $^{36}\text{Cl}$  is actually present in most if not all of these samples. This conclusion is supported by the detection of other bomb-pulse nuclides at similar stratigraphic intervals (section 6.2).

The presence of bomb-pulse  $^{36}\text{Cl}$  in the ESF records travel of waters through the entire PTn at those locations in 50 years or less, indicating that some flow followed structural pathways and largely bypassed the PTn matrix (Fabryka-Martin et al., in press [a]). Based on cooperative USGS/LANL characterization of the sample localities, a conceptual model has been developed for the distribution of fast flow paths in the unsaturated zone at Yucca Mountain. The basis of the proposed model is that three conditions must be present for bomb-pulse  $^{36}\text{Cl}$  to reach the

Table 6-1. Overall distribution of <sup>36</sup>Cl in the unsaturated zone at Yucca Mountain

Location	Relevant sample sets	Observed <sup>36</sup> Cl distribution
Soil	Surface soils Surface runoff Soil profiles Alluvial profiles for UZ-N37, UZ-N39, UZ-N54, UZ-N61, UZ-14, UZ#16	In areas with sufficiently thick soil cover, bomb-pulse <sup>36</sup> Cl is almost completely retained within the uppermost 2-3 m of soil. For thinner soils, some fraction of the bomb-pulse signal has moved down into the underlying bedrock (see below). Elevated <sup>36</sup> Cl/Cl ratios in shallow soils and surface runoff suggest that residual bomb-pulse <sup>36</sup> Cl is still present on the surface.
TCw	Bomb-pulse in TCw: UZ-N11, UZ-N15, UZ-N16, UZ-N17, UZ-N27, UZ-N36, UZ-N38, UZ-N53, UZ-N55, UZ-N64 No bomb-pulse in TCw: UZ-N37, UZ-N54, UZ#16  ESF North Ramp ESF South Ramp	Based on borehole data, bomb-pulse <sup>36</sup> Cl appears to be widely present in the fractured welded TCw unit where it is overlain by thin soil cover (ridgetops and sideslopes) and absent where the soil thickness is at least 3 m. Fracture transport is also indicated by UZ-N53 neutron logging data which have shown changes in moisture content down to a depth of 12 m, well into the TCw (Flint and Flint, 1995). The North Ramp data provide evidence of transport of bomb-pulse <sup>36</sup> Cl through the TCw. However, the apparent absence thus far of bomb-pulse <sup>36</sup> Cl from TCw samples collected along the ESF South Ramp, where soil thickness is less than 3 m, is not yet understood (Figure 6-1).
PTn	Bomb-pulse in PTn: UZ-N11, UZ-N53; UZ-N55 ESF North Ramp	Evidence for fast transport of water into the PTn is shown by elevated <sup>36</sup> Cl/Cl ratios from this interval in boreholes with thin soil cover. Bomb-pulse <sup>36</sup> Cl has also been measured in the PTn unit in several ESF samples from the North Ramp.
	No bomb-pulse in PTn: most of PTn in UZ-N37, UZ-N53, UZ-N54, UZ#16, UZ-14 ESF North Ramp ESF South Ramp	No evidence of bomb-pulse <sup>36</sup> Cl is seen in the South Ramp despite infiltration rates and soil thicknesses that are similar to those over the North Ramp.
TSw	ESF Perched water: UZ-14, NRG-7A, SD-7, SD-9	Bomb-pulse <sup>36</sup> Cl has been observed at several locations in ESF, and appears to be associated with faults. No unambiguous levels of bomb-pulse <sup>36</sup> Cl are observed in any of the perched water bodies at the base of this unit or at the top of the CHn; values for these samples are at or slightly above present-day background. Borehole <sup>36</sup> Cl data are usually too diluted by rock Cl to provide a reliable indication of the presence or lack of bomb-pulse <sup>36</sup> Cl in samples from this unit.
CHn	UZ-14 UZ#16 SD-12	No unambiguous levels of bomb-pulse <sup>36</sup> Cl have been observed in the CHn. Measured <sup>36</sup> Cl/Cl ratios are generally at or somewhat above present-day background. The highest ratios have been measured in SD-12, to a maximum value of $843 \times 10^{-15}$ .
Saturated zone	C#3, G-2, SD-7, J-13, SD-9, WT-10, WT-12	The <sup>36</sup> Cl/Cl ratio is uniformly at present-day background in the aquifer underlying the site, independent of location or depth

sampled depth within 50 years (Fabryka-Martin et al., in press [a]; Levy et al., 1997; Sweetkind et al., 1997a; and this report):

1) *A continuous fracture path must extend from the surface to the sampled depth.* This condition is necessary because, based on transport modeling using the 1996 set of hydrologic parameters for the PTn, travel times through the matrix of even a thin interval of unfractured PTn bedrock were shown to exceed 50 years (Fabryka-Martin et al., in press [a]; Robinson et al., 1996). Continuous fracture paths exist in most of the welded portions of the Tiva Canyon and Topopah Spring Tuffs (Anna and Wallman, 1997; Anna, in press). However, the intervening PTn-equivalent lithologic units are mostly nonwelded and unfractured (Sweetkind et al., 1995a). Flow through the PTn is predicted to be predominantly through the matrix (Wittwer et al., 1995; Bodvarsson and Bandurraga, 1996; Robinson et al., 1996) on the basis of material properties and hydrologic parameters from Bodvarsson and Bandurraga (1996) and Robinson et al. (1996). Therefore, the presence of faults that cut the PTn and increase its fracture conductivity is required to satisfy the condition of a continuous fracture pathway (Fabryka-Martin et al., in press [a]).

2) *The magnitude of surface infiltration must be sufficiently high to initiate and sustain at least a small component of fracture flow along the connected fracture path.* Previously-published transport simulations indicated that a minimum infiltration rate of 1 mm/yr is required to satisfy this criterion (Robinson et al., 1996; Fabryka-Martin et al., in press [a]).

3) *The residence time of water in the alluvium must be less than 50 years.* Travel time through alluvial cover must be sufficiently rapid to allow infiltrating waters to reach the soil/bedrock interface before being lost through evapotranspiration (Flint and Flint, 1995). In general, the thickness of the alluvial layer must be less than about 3 meters (Flint and Flint, 1995; Flint et al., 1996).

The above is only a model, and as such is expected to oversimplify the true conditions at the site. However, the key issue is whether or not it is consistent with the majority of the observations. Appendix D presents a case-by-case evaluation of the extent to which the above three conditions are present for ESF samples containing bomb-pulse  $^{36}\text{Cl}$ . The appendix also identifies locations at which the model would predict bomb-pulse  $^{36}\text{Cl}$  but at which this tracer has not been detected. The results of this evaluation are summarized in sections 6.3 and 6.4.

#### 6.1.2 *Samples with low $^{36}\text{Cl}/\text{Cl}$ ratios*

The south part of the ESF includes several samples with  $^{36}\text{Cl}/\text{Cl}$  ratios less than  $350 \times 10^{-15}$ , well below the range of meteoric values during the past 50,000 years (50 ka). Several alternative hypotheses have been suggested to explain the data. An early hypothesis was that these low ratios represented stagnant zones where water travel time is sufficiently long for radioactive decay of  $^{36}\text{Cl}$  to have occurred (on the order of  $10^5$  years). Mineralogic data suggestive of

possible differences in hydrochemical and structural environments between the northern and southern parts of Yucca Mountain are discussed in section 7.5. However, the hypothesis of stagnant zones in the southern part of the ESF is not clearly supported by field evaluations of the sample settings (sections 6.3 and 6.4), nor by transport modeling simulations (section 8).

A more likely explanation is that the  $^{36}\text{Cl}/\text{Cl}$  ratios of these samples have been diluted by rock Cl released during sample preparation. The Br/Cl ratio is inadequate as an indicator of rock Cl in this case because of the presence of construction water traced with Br. Low  $\text{SO}_4/\text{Cl}$  ratios of leachates appear to support this hypothesis for some of the samples, particularly the two with the lowest  $^{36}\text{Cl}/\text{Cl}$  ratios (E255-1 at station 58+77 with a ratio of  $140 \times 10^{-15}$ , and E290-1 at station 59+98 with a ratio of  $205 \times 10^{-15}$ , Appendix B). However, variations in the  $\text{SO}_4/\text{Cl}$  ratio at Yucca Mountain are not yet sufficiently well understood to apply this method of detecting rock Cl with any confidence. Even if dilution of the signal by rock Cl can be shown to be the correct explanation for the low  $^{36}\text{Cl}/\text{Cl}$  ratios in the South Ramp samples, it remains to be answered why rocks from the southern part of the ESF seem to be more susceptible to release of rock Cl than rocks from the northern part.

A third hypothesis is that past variations in the meteoric input signal may have included lower values than estimated in the reconstructed signal in section 3.1. However, the number of fossil packrat samples used to reconstruct the past input appears sufficient to rule out this hypothesis.

### 6.1.3 *Samples with intermediate $^{36}\text{Cl}/\text{Cl}$ ratios*

Most of the ESF samples have  $^{36}\text{Cl}/\text{Cl}$  values between  $350 \times 10^{-15}$  and  $1250 \times 10^{-15}$ , the range of natural variation of the meteoric input (Figure 3-1) (Fabryka-Martin et al., in press [a]). Similarly, most of the borehole samples collected below the PTn have  $^{36}\text{Cl}/\text{Cl}$  ratios that are also well below a value of  $700 \times 10^{-15}$  although these results have not been corrected for dilution by rock Cl, an issue which is addressed in section 6.1.4. For these samples with ratios that do not indicate the clear presence of bomb-pulse  $^{36}\text{Cl}$ , five alternative scenarios are proposed to explain the measured  $^{36}\text{Cl}/\text{Cl}$  results on the basis of different initial  $^{36}\text{Cl}/\text{Cl}$  ratios for the percolating water. The first two scenarios are considered the most probable interpretations of the data, based on independent evidence (e.g., other geochemical and isotopic data, surface infiltration rates, and solute-transport simulations):

#### *Scenario 1: Travel times < 50 ka (Holocene to late Pleistocene water)*

Although a bomb-pulse component is undeniably present for specific locations in the unsaturated zone, the travel time for most water encountered below the PTn unit is assumed to be greater than 50 years (i.e., pre-bomb pulse). Under Scenario 1, travel times are assumed to be less than 50 ka, such that decay of  $^{36}\text{Cl}$  in the samples would be negligible. In this case, variations in the  $^{36}\text{Cl}/\text{Cl}$  signals simply reflect variations in the input function and mixing of water parcels with different input ratios. Reconstruction of the input function could be used to estimate apparent

travel times, e.g., a sample with a ratio of  $1200 \times 10^{-15}$  could only have recharged during limited periods of time when the input value was at least that high (e.g., either 15-22 ka or 38-50 ka according to Figure 3-2). Lower age limits between 0 ka and 15 ka can be established for each of the samples with ratios in the range of  $500 \times 10^{-15}$  and  $1200 \times 10^{-15}$ , by matching their measured ratios with the reconstructed ratios or measured ratios for packrat samples in this period in Figure 3-2b.

*Scenario 2: Modern water mixed with water < 10 ka*

According to this scenario, travel times for water in the potential repository horizon are assumed to be sufficiently fast that an initial ratio of  $500 \times 10^{-15}$  can be assumed (i.e., less than 10 ka, Figure 3-2). The Cl in any particular sample is assumed to represent a mixture of water parcels, each having different travel times as a result of traveling along different flow paths, and hence may include variable contributions of bomb-pulse  $^{36}\text{Cl}$ . Samples with  $^{36}\text{Cl}/\text{Cl}$  ratios significantly higher than  $500 \times 10^{-15}$  contain at least a small component of bomb-pulse water (e.g., the threshold ratio for detecting bomb-pulse  $^{36}\text{Cl}$  would be on the order of  $700 \times 10^{-15}$  although the actual value would have to be established on a sounder basis). Based on this scenario, a bomb-pulse  $^{36}\text{Cl}$  signal exists essentially everywhere in the north part of the ESF. The conceptual model presented in section 6.1.1 is still valid for this scenario, with the least diluted bomb-pulse  $^{36}\text{Cl}$  signals being those transmitted through the zones of increased fracturing through the PTn. However, additional emphasis is given to subsequent spreading of the signal as it enters the fractured TSw.

This scenario is consistent with the measured distribution of bomb-pulse tritium in YMP boreholes, assuming that the detection limit for tritium is 4 Tritium Units (T.U.). For example, under this assumption, bomb-pulse tritium was detected in half of the samples in UZ#16, including throughout the TSw (Yang et al., 1996, their Figure 11). To a lesser extent, a similar statement could be made for the UZ-14 profile (Yang et al., 1996, their Figure 13). However, if the detection limit is higher, e.g. at 20 T.U., then one would conclude from the tritium data that fast paths, while present, do not appear to be a widespread phenomenon at this site or else do not comprise significant fraction of the total flux through the TSw.

The scenario of pervasive modern water is inconsistent with the results of previously-reported solute-transport calculations (Fabryka-Martin et al., in press [a]) which showed that it is not possible to conduct a bomb-pulse signal through the PTn using reasonable values for hydrologic parameters (based on those of Bodvarsson and Bandurraga, 1996), except in restricted locations where the PTn fracture characteristics have been modified. However, it is consistent with the results of simulations using the most recent set of hydrologic parameters, at least for the north part of the ESF, as described in section 8.

*Scenario 3: Post-bomb water*

A variation of scenario 2 interprets  $^{36}\text{Cl}/\text{Cl}$  ratios at present-day background as being indicative of post-bomb-pulse water, i.e., it assumes that water has already flushed all bomb-pulse  $^{36}\text{Cl}$  in the rock column beyond the sampled horizon. By this scenario, water in the south part of the ESF which appears to be devoid of bomb-pulse  $^{36}\text{Cl}$ , would be younger than water in the north part of the ESF.

This scenario is not supported by other lines of evidence. Even though the  $^{36}\text{Cl}/\text{Cl}$  signal in rain has largely returned to its pre-bomb levels (Synal et al., 1990), water infiltrating into the bedrock today should still show a bomb-pulse component. This is expected because post-bomb water and bomb-pulse water are mixed along the subsurface pathways. A simple visualization demonstrates this concept. Picture infiltration occurring through a layered box model in which the  $^{36}\text{Cl}$ -bearing rain input to the top box is immediately mixed with the contents of that box (the top 0-5 cm of soil and the moisture it contains) before moving to the next box down (the 5-10 cm layer of soil), with its modified isotopic signal. The same mixing process repeats endlessly as the water moves downward, with progress often arrested during dry periods. The result is a modified  $^{36}\text{Cl}/\text{Cl}$  input signal (i.e., the isotopic signal as it enters the bedrock) in which the peak of the bomb-pulse is shifted to later time, with a slow reduction in the signal such that present-day values are still above pre-bomb background (Figure 3-3a). Data supporting this concept that even present-day infiltration has a bomb-pulse  $^{36}\text{Cl}$  component are: (1) bomb-pulse  $^{36}\text{Cl}/\text{Cl}$  ratios are endemic throughout the TCw in neutron holes in high-flux regions (e.g., Figure 4-8; Fabryka-Martin et al., in press [b]), even where neutron-probe monitoring shows that the water is post-bomb; (2) all surface runoff samples have shown bomb-pulse  $^{36}\text{Cl}/\text{Cl}$  ratios (Table 4-13); and (3) even the shallowest soil layers in most sampled profiles show bomb-pulse values (Table 4-6). However, additional sampling of surface soil and soil profiles to determine the  $^{36}\text{Cl}/\text{Cl}$  ratio in present-day infiltration, especially above the ESF, are recommended to test this hypothesis.

*Scenario 4: Travel times > 50 ka (mid- to late Pleistocene water)*

Again, although a bomb-pulse  $^{36}\text{Cl}$  component is present at specific locations in the unsaturated zone, the travel time for most water encountered in samples below the PTn is assumed by this scenario to range up to several hundred thousand years, so that the input  $^{36}\text{Cl}/\text{Cl}$  ratio for some or all of the percolating water is assumed to have been much higher than the present value. Most of the samples are assumed to reflect some reduction from their initial  $^{36}\text{Cl}$  content due to radioactive decay. Upper limits for water travel time can be calculated using equation (3-1) assuming a maximum initial  $^{36}\text{Cl}/\text{Cl}$  value of  $1250 \times 10^{-15}$ . Although at least a small component of bomb-pulse water has reached the TSw unit in the ESF via fault and fracture zones, the upper limits for water ages in the TSw rock matrix, breccia, and non-fast-path fractures average about 250 ka and range up to 630 ka (Fabryka-Martin et al., in press [a]).

This scenario is rejected because it is inconsistent with tritium and  $^{14}\text{C}$  measurements in deep boreholes (Yang et al., 1996, 1997). All ground-water ages based on  $^{14}\text{C}$  analyses of porewater extracted from unsaturated-zone samples at Yucca Mountain indicate travel times less than 10 ka, and usually substantially less than this value. Even younger age estimates result when the  $^{14}\text{C}$  measurements are corrected for dilution of the signal by isotopic exchange with carbonate minerals (Yang et al., 1997). Finally, none of transport simulations using any reasonable set of hydrologic parameters and boundary conditions result in average travel times on the order of  $10^5$  years.

#### *Scenario 5: Travel times indeterminate*

According to Scenario 5, the presence of cosmogenic  $^{36}\text{Cl}$  released from soil calcite renders travel times by the  $^{36}\text{Cl}$  method indeterminate. The rationale behind this scenario, and the arguments against soil calcite as a dominating influence on the  $^{36}\text{Cl}$  signal, are presented in section 3.4. The conclusion from that section, however, is that mass balance calculations comparing the contribution from this source to that from atmospheric deposition of Cl argue against soil calcite as a significant source of  $^{36}\text{Cl}$  at Yucca Mountain. The statistical analysis of the ESF  $^{36}\text{Cl}$  results in section 4.2.4 also argues against this scenario because one would otherwise expect a broader distribution of background  $^{36}\text{Cl}/\text{Cl}$  ratios.

#### *Conclusion*

The above five scenarios represent end-member cases. At present, scenarios 1 and 2 are most consistent with the data and with solute transport modeling simulations. The true travel times may reflect some combination of all five scenarios, but it would be difficult to distinguish a decrease in signal strength due to radioactive decay (Scenario 4), from a higher-than-present initial  $^{36}\text{Cl}/\text{Cl}$  ratio in old water that has subsequently been reduced by mixing with younger water (Scenario 1). In any case, true travel times are less than or equal to the upper limits calculated for Scenario 4, and probably considerably less.

This ambiguity in interpretation can best be resolved by continuing to pursue independent lines of evidence, such as alternative isotopic and geochemical methods for tracing and dating water movement (section 6.2) and by transport simulations, such as those presented in section 8, based on the most current hydrologic parameters, infiltration models, and geologic models. As the latter models are revised, the consistency between the results of the flow and transport simulations and the observed distribution of environmental tracer data should continued to be re-evaluated.

#### *6.1.4 Comparison of $^{36}\text{Cl}$ Results for ESF and Deep Borehole Samples*

Measured  $^{36}\text{Cl}/\text{Cl}$  ratios for the TSw unit in deep borehole samples are generally much lower than the values for ESF samples from this unit (Fabryka-Martin et al., in press [b]). This

apparent discrepancy is probably attributable to differences in the sample collection techniques. Borehole samples are obtained from ream cuttings. Rock Cl is released from the surface of the cuttings during drilling, and is leached together with the pore-water Cl during sample preparation for  $^{36}\text{Cl}$  analysis. The rock Cl has  $^{36}\text{Cl}/\text{Cl}$  ratios in the range of  $20 \times 10^{-15}$  to  $40 \times 10^{-15}$  (section 3.4.1). Correction of the measured  $^{36}\text{Cl}/\text{Cl}$  ratio for dilution by rock Cl, with its lower  $^{36}\text{Cl}$  content, is necessary in order to raise the  $^{36}\text{Cl}/\text{Cl}$  ratio back to the true value of the meteoric component of Cl in the borehole samples. This correction is analogous to that conducted for  $^{14}\text{C}$  analyses, although the method of correction for the  $^{36}\text{Cl}$  data is not as well developed as those for  $^{14}\text{C}$ . The ESF samples are generally not as affected by rock Cl release as are borehole samples because the manual and jackhammer methods of collection pulverize only very small amounts of the rock.

The proportion of rock Cl present in borehole samples and the magnitude of the  $^{36}\text{Cl}/\text{Cl}$  correction factor can be estimated from the Br/Cl ratio for the sample because this ratio is distinctly different for rock-derived and atmospheric halides (Fabryka-Martin et al., in press [b]), as follows.

*Br/Cl ratio in the rock end-member.* The Br/Cl ratio of rocks from Yucca Mountain was determined by a step-leaching method that involves repeated grinding and leaching of the rock sample, progressively decreasing the meteoric component and increasing the rock component of Br and Cl (presumably released from fluid inclusions, microcracks, and glass pyroclasts) with each step (Fabryka-Martin et al., in press [b]). These experiments provided narrow estimates for the rock Br/Cl ratios of moderately and densely welded units, averaging about  $1.8 \times 10^{-3}$  for TCw, and  $1.9 \times 10^{-3}$  for TSw, excluding its basal vitrophyre (Ttpv3) which had a higher value of  $2.8 \times 10^{-3}$ .

*Br/Cl ratios for the meteoric end-member.* Altogether, seven types of samples were analyzed to investigate the Br/Cl ratio for the meteoric component, with results presented in Fabryka-Martin et al. (in press [b]): precipitation, surface soils, soil within the root zone, soil below the root zone, cuttings from nonwelded tuff units, unsaturated-zone porewater, and perched water. The range of Br/Cl values is large, and a weak correlation with depth suggests that the meteoric halides may be fractionated by processes in the plant root zone. Because the geochemical behavior of these two halides during the infiltration process apparently is not identical, the choice of Br/Cl ratio to use in the age-correction model depends upon the nature of the infiltration process—e.g., the residence time of the infiltrating water in the root zone—as well as upon the extent of mixing between waters contributed by different pathways. It is proposed that the Br/Cl ratios measured for perched water or for porewater from the nonwelded units are the most appropriate to represent the meteoric component for water in the TSw.

*Application of the correction method to borehole data.* Table 6-2 applies the correction approach to cuttings samples from the TSw unit in UZ-14, UZ#16, NRG-4, NRG-6 and NRG-7A assuming that the Br/Cl ratio of infiltrating meteoric waters in this unit at these locations is

represented by the average Br/Cl ratio measured in perched water (0.010, Table 4-16). This value was chosen by assuming that the variability of the Br/Cl ratio in water exiting the shallow rock units is largely homogenized by mixing in the PTn. The chosen value is in good agreement with Br/Cl data obtained for PTn porewater samples extracted from drillholes in the North Ramp (section 4.15). The correction is a two-step process, presented below.

First, the fraction of Cl derived from meteoric sources ( $f_m$ ) is estimated from the measured Br/Cl ratio,  $(Br/Cl)_x$ , of the salts leached from the sample,

$$f_m = \frac{(Br/Cl)_x - (Br/Cl)_r}{(Br/Cl)_m - (Br/Cl)_r} \quad (6-1)$$

where  $(Br/Cl)_r$  and  $(Br/Cl)_m$  are the representative end-member ratios for the rock and meteoric salt sources. Once a value of  $f_m$  has been estimated for a given sample, the corrected  $^{36}Cl/Cl$  ratio,  $(^{36}Cl/Cl)_m$ , is calculated from:

$$(^{36}Cl/Cl)_m = \frac{(^{36}Cl/Cl)_x - (1-f_m) (^{36}Cl/Cl)_r}{f_m} \quad (6-2)$$

**Conclusion:** The corrected borehole  $^{36}Cl/Cl$  ratios are generally similar to  $^{36}Cl/Cl$  ratios obtained for ESF samples. None of the corrected ratios for the UZ-14 and UZ#16 samples are indicative of bomb-pulse  $^{36}Cl$  at the sampled locations. However, data corrected by this method support the occurrence of bomb-pulse  $^{36}Cl$  in the samples measured from NRG-4, NRG-6 and possibly NRG-7a, from intervals corresponding to the depth of the ESF. ESF samples collected from stations where NRG-4 passes near the ESF (~ Station 11+00), also contained bomb-pulse  $^{36}Cl$  (Appendix B contains the data, and Appendix Figure D-3a shows locations of NRG holes relative to the locations of the  $^{36}Cl$  samples from the ESF).

## 6.2 Comparison with other environmental tracers

### 6.2.1 Tritium, $^{14}C$ and Major Ion Geochemistry of Pore Waters

One of the best ways to corroborate the interpretation of elevated  $^{36}Cl$  signals as an indicator of recent water movement is to investigate the presence of other bomb-pulse nuclides. Altogether, three radiometric techniques are being used to estimate pore-water ages at Yucca Mountain: tritium,  $^{14}C$ , and  $^{36}Cl$ . Because of its short half-life (12.3 yr), tritium is used primarily as a screening technique to provide an indicator of recent water movement (i.e., presence of bomb-pulse concentrations), and not for developing quantitative travel-time estimates. The half-life of  $^{14}C$  (5.73 ka) is appropriate for travel-time estimates at Yucca Mountain, and vertical

Table 6-2. Measured  $^{36}\text{Cl}/\text{Cl}$  ratios for borehole cuttings from the TSw unit, adjusted for dilution by rock  $\text{Cl}^1$

.LANL ID	Depth (m)	Br/Cl x $10^{-3}$	Measured $^{36}\text{Cl}/\text{Cl}$ x $10^{-15}$	Meteoric fraction <sup>2</sup>	Corrected $^{36}\text{Cl}/\text{Cl}$ x $10^{-15}$
<i>UZ-14</i>					
R421-2	86	4.8	202 ± 6	0.35	524
R422-2	88	3.8	112 ± 3	0.23	396
R603-2	155	7.0	490 ± 21	0.63	764
R423-3	383	3.8	165 ± 5	0.24	610
R424-2	392	5.0	265 ± 18	0.39	647
<i>UZ#16</i>					
R205-2	204	4.8	145 ± 15	0.36	360
R206-2	216	9.1	351 ± 27	0.89	392
R210-2	255	5.7	192 ± 6	0.47	381
R214-2	290	4.3	275 ± 9	0.30	869
R219-2	332	4.4	123 ± 7	0.31	343
R221-2	342	5.2	150 ± 9	0.33	400
NRG-4	176	3.5	724 ± 26	0.20	3570
NRG-6	165	4.0	395 ± 15	0.26	1475
NRG-7A	208	5.1	486 ± 14	0.40	1177

Notes:

- <sup>1</sup> Data and calculations for UZ-14 and UZ#16 are summarized from Tables 6-2 and 6-3 in Fabryka-Martin et al. (in press [b]). Data for the NRG holes were reported in Appendix B of that same report. Samples for which the meteoric fraction is less than 0.2 have been omitted from this table because the uncertainties in the corrected  $^{36}\text{Cl}/\text{Cl}$  ratio are then excessively large. The approach is summarized in section 6.1.5 of this report.
- <sup>2</sup> Meteoric fraction: The meteoric fraction of Cl in each sample is calculated from the measured Br/Cl ratio of the salts leached from the rock cuttings, assuming that the Cl consists of a mixture of salts from two sources, meteoric water and rock salts, each assumed to have a known and constant Br/Cl ratio (equation 6-1 in the text). The rock end-member Br/Cl ratio is assumed to be  $1.9 \times 10^{-3}$  for all of these TSw samples except those from the TSw basal vitrophyre, for which a value of  $2.8 \times 10^{-3}$  is assumed (Fabryka-Martin et al., in press [b]). The meteoric end-member Br/Cl ratio is assumed to be represented by the average Br/Cl ratio measured for perched water, 0.010 (Table 4-16).
- <sup>3</sup> Corrected  $^{36}\text{Cl}/\text{Cl}$ : The measured  $^{36}\text{Cl}/\text{Cl}$  ratio is corrected for the effect of dilution by rock Cl using equation (6-2), assuming a  $^{36}\text{Cl}/\text{Cl}$  ratio of  $25 \times 10^{-15}$  for the rock end-member.

concentration profiles have been assembled for this nuclide in both the gas and liquid phases in several boreholes as part of a USGS study (e.g., Yang et al., 1996, 1997). USGS scientists have also been measuring pore-water chemistry in samples squeezed from bedded and nonwelded tuffs as well as perched waters from the unsaturated zone at Yucca Mountain (Yang et al., 1988, 1990, 1996, 1997). Vacuum distillation methods have been used to extract pore water from densely welded tuffs and to extract residual waters left in nonwelded tuffs, but these samples could only be used for tritium,  $^{14}\text{C}$ ,  $\delta\text{D}$ , and  $\delta^{18}\text{O}$  measurements. All these studies contribute to the investigation of hydrologic flow in the unsaturated zone of Yucca Mountain.

Ground-water ages in countless aquifer systems are estimated routinely based on the residual carbon-14 activity in the porewater. Prior to the advent of atmospheric testing of nuclear devices,  $^{14}\text{C}$  in the atmosphere was entirely derived from cosmic-ray bombardment of nitrogen nuclei. By definition, the specific activity of  $^{14}\text{C}$  in carbon that was in equilibrium with the atmosphere prior to the nuclear age is 100 percent modern carbon (pmc), corresponding to about 14 disintegrations per minute (dpm) per gram of carbon. Numerous lines of evidence indicate that this initial activity has been relatively constant for the past several tens of thousands of years, with fluctuations of about 10%. Copious quantities of  $^{14}\text{C}$  were produced in the atmosphere by nuclear testing in the 1950s and 1960s, and have also been released as a byproduct of the reprocessing of spent nuclear fuel. The peak activity occurred in 1963, at 200 pmc, with subsequent decrease due to exchange of  $^{14}\text{C}$  for nonradioactive carbon in the biosphere and hydrosphere, principally the ocean. In contrast with the present atmospheric signals for tritium and  $^{36}\text{Cl}$ , the present  $^{14}\text{C}$  value is still elevated about 20% above natural background due to the comparatively long residence time of carbon in the atmosphere.

In groundwater investigations,  $^{14}\text{C}$  measurements are made on inorganic carbon extracted from water and gas samples. For Yucca Mountain samples, typical volumes have been 100 mL for water, and 2 L for gas samples. In the absence of a bomb-pulse signal, an apparent age can be calculated based on the radioactive decay equation, using the  $^{14}\text{C}$  half-life of 5730 yr. However, this unadjusted age represents a maximum, and the true age can be substantially less. Because carbon-bearing chemical species are distributed among the solid, liquid and gas phases in unsaturated geologic systems, many geochemical reactions occur that dilute the initial signal (Yang et al., 1997). These include re-equilibration with soil-gas  $\text{CO}_2$ , which has lower  $^{14}\text{C}$  activity than that in the atmosphere; release from or isotopic exchange with carbonate and gypsum minerals along the flow path; oxidation of dissolved organic matter; and re-equilibration with  $\text{CO}_2$  in the vapor phase in the unsaturated zone. The many geochemical models available to correct the measured signal generally require the user to specify solution chemistry and carbonate speciation, relevant mineral-water reactions that control the carbonate chemistry of the system, stable carbon isotope signals and  $^{14}\text{C}$  activities of the various carbon sources and sinks in the system, and prevailing water temperature.

Some of the results reported by Yang et al. (1996) can be summarized as follows:

- (1) The remarkable similarity between pore-water chemistry high in the stratigraphic column

and that in specific deep locations indicates that faults and/or fractures may be acting as pathways for the rapid transport of young waters to deeper parts of the system at Yucca Mountain. This similarity shows that the TSw matrix is largely bypassed by infiltrating water, a point that should not be confused with evaluation of the extent to which flow may bypass the PTn matrix.

- (2) Observations of inversions and irregularities in tritium and  $^{14}\text{C}$  vertical profiles for several Yucca Mountain boreholes support the interpretation that fracture flow is a dominant flow mechanism in the welded units at Yucca Mountain. Samples with high tritium levels show that water has been transported to the CHn in UZ#16 in less than 50 years, a conclusion which is also supported by relatively high  $^{14}\text{C}$  activities (maximum, 98 pmc) at this depth.
- (3) Large  $^{14}\text{C}$  variations are recorded for fluids from the CHn in UZ#16 and UZ-14. These data indicate that waters as young as 400 to 2000 years may exist at these depths in UZ-14, with ages of 5000 to 9000 years in UZ#16.
- (4) Chemical and isotopic compositions of perched waters indicate ages of 5 to 7 ka (i.e. post-glacial). The lack of significant water-rock exchange of hydrogen and oxygen isotopes, as well as the low Cl concentrations in the waters, supports an interpretation of fast (fracture) percolation of the perched waters.

Conclusions from the tritium,  $^{14}\text{C}$ , and pore-water chemical data listed above are compatible with the evidence of fast infiltrating fluids recorded by the bomb-pulse signals in the  $^{36}\text{Cl}$  data set. These data provide important confirmation from independent geochemical systems that active fast flow paths exist at Yucca Mountain. However, both sets of data are also consistent with the expectation that the flux associated with the fast infiltrating water is small.

#### *6.2.2 Cesium-137, Plutonium and Technetium-99*

A prototype effort was undertaken by LANL to screen a small set of samples for the presence of bomb-pulse radionuclides other than  $^{36}\text{Cl}$  produced during atmospheric testing of nuclear weapons (Fabryka-Martin et al., in press [a]). These radionuclides are technetium-99 ( $^{99}\text{Tc}$ ), iodine-129 ( $^{129}\text{I}$ ), cesium-137 ( $^{137}\text{Cs}$ ), and plutonium (Pu) isotopes. The selection of these nuclides was based on the following considerations:

- they are produced in atmospheric tests of nuclear devices, resulting in the deposition of measurable quantities in surface outcrops and soils,
- established procedures exist for separating these nuclides from geologic matrices,
- analysis by radiochemical or mass spectrometric techniques is straightforward, and
- these radionuclides span the mobility range from highly immobile (Pu) to very mobile ( $^{99}\text{Tc}$  and  $^{129}\text{I}$ ).

The first suite of samples was selected to provide a proof-of-principle as the basis for expanding the effort to include other ESF samples. This suite included shallow soil samples from Midway Valley and from soil exposed at the NRG-5 drillpad, cuttings from UZ-N55 (depth 55 m), and gouge from the Bow Ridge fault exposed at ESF Station 2+00 (depth ~40 m). The latter two samples both had elevated  $^{36}\text{Cl}$  levels. A detailed review of these nuclides and analytical results for  $^{99}\text{Tc}$ ,  $^{137}\text{Cs}$ , and Pu isotopes are presented in Fabryka-Martin et al. (in press [a]) and summarized below: The  $^{99}\text{Tc}$  data for the two soil samples are new.

- Bomb-pulse  $^{99}\text{Tc}$  was detected in all four of the rock and soil samples, with the highest concentration measured in the soil from the NRG-5 drillpad. The association of bomb-pulse  $^{99}\text{Tc}$  with elevated  $^{36}\text{Cl}$  signals in these samples strongly supports the interpretation that the elevated  $^{36}\text{Cl}$  signals at these locations are of bomb-pulse origin. The Bow Ridge fault data from the ESF may not represent natural infiltration conditions because the presence of Trench 14A exposing the fault immediately above the ESF may have enhanced the infiltration rate at this location above its undisturbed levels due to removal of surficial deposits and ponding of surface runoff in the trench. However, these data at least demonstrate the technical feasibility of this approach, laying the groundwork for extending the method to samples from other locations in the ESF.
- Measurable levels of  $^{137}\text{Cs}$  and Pu were detected in the surface soils (0 to 5 cm depth) from Midway Valley; Pu was also detectable in the soil exposed at the NRG-5 drillpad (0 to 40 cm depth). Quantities of both elements were below detection limits in deeper samples from borehole UZ-N55 and from the Bow Ridge Fault at ESF Station 2+00. These data confirm the immobility of Pu and Cs in surface sediments at Yucca Mountain, and indicate that their usefulness as tracers of recent ground water movement is very limited except possibly as a method to detect colloidal transport of nuclides.
- The Pu content of Yucca Mountain soil ( $0.07 \text{ pCi g}^{-1}$ ) is higher than could be attributed to global fallout, and in fact derives from local Nevada Test Site nuclear testing. This conclusion is also supported by the Pu isotopic ratio.

In summary, multiple lines of evidence indicate that young waters (<50 yr) have traversed the welded TCw and nonwelded PTn units in areas of throughgoing fractures. Other data indicate that rainwater has infiltrated through the TCw and PTn into the underlying TSw at Yucca Mountain without undergoing significant chemical modification through water-rock interaction..

### 6.2.3 Strontium Isotopic Ratios

Strontium isotopic signatures of ground water are principally derived from water-rock interaction, and therefore these isotopic data are not directly comparable to data for cosmogenic or bomb-pulse isotopes such as  $^{36}\text{Cl}$ . Because the variations in strontium isotopic values of rock leachates reflect processes such as the interaction of water with rock whose isotopic signatures change very slowly as a result of *in situ* radioactive decay, strontium isotopic studies cannot be used to detect fast fluid flow. The data can, however, be used to test hypotheses about fluid

sources or pathways and fluid mixing.

Strontium isotopic data for drill core leachates from drill hole USW SD-7 (Paces et al., 1997) have been interpreted in fundamentally different ways with respect to water sources and water-rock interaction. The data show that, near the top of the core, the  $\delta^{87}\text{Sr}$  value is similar to the values found for calcite coatings on bedrock at the surface and to the perched water in the drill hole. Values of  $\delta^{87}\text{Sr}$  gradually increase with depth in the Tiva Canyon Tuff, but rise sharply in the nonwelded units of the Paintbrush Group (PTn-equivalent lithostratigraphic units). In the upper part of the Topopah Spring Tuff,  $\delta^{87}\text{Sr}$  is fairly constant with values similar to those found in thick calcite-rich soils at the surface. An absence of correlation between pore-water  $\delta^{87}\text{Sr}$  and rock  $\delta^{87}\text{Sr}$  is interpreted by Paces et al. (1997) to indicate that there is little or no rock influence on the pore-water strontium isotopic compositions.

One hypothesis to explain this data set, proposed by Paces et al. (1997), is that mixing of percolating waters with two distinct  $\delta^{87}\text{Sr}$  compositions takes place within the PTn-equivalent lithologic units. One end member, with low Sr concentrations, is obtained through dissolution of calcite coatings and eolian dust on ridge crests and side slopes lacking thick calcretes. The other end member contains a higher Sr concentration derived through interaction with thick calcite- and Sr-rich soils present on surfaces of lesser slope and in drainages. An isotopic distinction between these two Sr reservoirs has been documented by Marshall and Mahan (1994). Mixing of the two water types occurs in the PTn with the high-concentration member dominating the isotopic composition of the resulting mixed water. Slight increases in  $\delta^{87}\text{Sr}$  with depth in the welded units are probably due to a very limited amount of water-rock interaction.

Based on the SD-7 data (Paces et al., 1997), mixing of the two water types in the PTn would have to be accomplished in large part by lateral flow because the  $\delta^{87}\text{Sr}$  values in the Tiva Canyon Tuff in SD-7 are much lower than the values in the underlying PTn-equivalent lithologic units and the upper and middle portions of the Topopah Spring Tuff. This interpretation is not cited by Paces et al. (1997) as evidence for lateral flow in the PTn-equivalent lithologic units, although they present other data in favor of a flow model that includes down-dip diversion of percolation in the PTn.

The Sr isotopic data of Paces et al. (1997) are interpreted by Sonnenthal et al. (1997) in the context of a conceptual model involving substantial water-rock interaction within the PTn-equivalent lithologic units. Sonnenthal et al. (1997) have modeled the Sr isotopic data for SD-7 in terms of downward percolation of water within the unsaturated zone. There are some problems with this model because the downward transition from Tiva Canyon Tuff to PTn-equivalent lithologic units corresponds to increasing  $\delta^{87}\text{Sr}$  of leachates, but an opposite trend in the rocks themselves. A one-dimensional numerical model of percolation flux and rock reaction (dissolution) rate to simulate the vertical distribution of isotopic data adequately reproduces the observed data in the Tiva Canyon and Topopah Spring Tuffs but not in the PTn-equivalent units.

The existence of lateral diversion in the PTn- equivalent lithologic units could be investigated by closely spaced sampling around faults and subunit lithologic contacts, especially those in the ESF North Ramp where bomb-pulse values of  $^{36}\text{Cl}/\text{Cl}$  have been detected. Our present data set documents a few examples of isotopic differences associated with subunit contacts, but the distribution and number of sampling sites is insufficient to test for compatibility with lateral diversion.

If the interpretation of leached Sr isotopic data as representing the mixture of two end-member waters derived from infiltration through thick, calcite-rich soil calcretes and infiltration through areas lacking such deposits (Paces et al., 1997) is correct, it might provide a means to investigate the contribution of cosmogenic  $^{36}\text{Cl}$  released into infiltrating water by dissolution of surface calcite. This process has been evaluated and discounted as a significant contributor to the  $^{36}\text{Cl}$  of infiltrating water (section 3.4). If additional evidence should be required, samples of Tiva Canyon Tuff collected beneath areas of differing calcrete development could be analyzed for both  $^{36}\text{Cl}/\text{Cl}$  and  $\delta^{87}\text{Sr}$  to check for systematic and correlative differences in the two isotopic systems. By sampling in the densely welded portion of the Tiva Canyon Tuff, the effects of fluid mixing in the underlying PTn-equivalent lithologic units could be largely avoided.

#### *6.2.4 Uranium-Series Disequilibrium Studies of Fracture Mineral Ages in the ESF*

A parallel effort to the  $^{36}\text{Cl}$  sampling effort in the ESF was initiated by the USGS, based on the measurement of uranium series disequilibrium for secondary minerals deposited in fractures and lithophysal cavities in the ESF. These data provide the basis for estimating mineral formation ages which can then be used as surrogate indicators of past water movement through these features. The following summarizes the cogent conclusions from recent reports on the findings of this effort (Paces et al., 1996, 1997).

- Most of the secondary minerals (opal and calcite) have calculated U-series ages for outer mineral surfaces that range from 28 ky to >500 ky, with no distinct clustering of ages.
- Secondary minerals from lithophysal cavities as well as from fractures have similar deposition age distributions.
- A correlation is observed between sample size (milli- versus microgram sample quantities) and mineral deposition age. Larger sample sizes are associated with older ages as an artifact of the sampling process which leads to a homogenization of depositional growth zones and thus ages. Therefore, it is imperative that sampling be done on the smallest sample possible to give the most accurate age for the latest period of mineral deposition.
- Initial uranium isotope compositions of secondary minerals are variable throughout the unsaturated zone. Most notably, mineralization in the shallow portions of the ESF contains low  $^{234}\text{U}/^{238}\text{U}$  similar to values observed in surface waters and soils, whereas occurrences deeper in the TSw have elevated  $^{234}\text{U}/^{238}\text{U}$ . Therefore,  $^{234}\text{U}$ -enrichment is a function of the percolation process and contains information related to the history and mechanisms of unsaturated-zone flow.

- The  $^{234}\text{U}/^{238}\text{U}$  composition of percolating solutions will represent a mixture of the  $^{238}\text{U}$  that was acquired mostly at the surface through reaction with soil materials and the excess  $^{234}\text{U}$  that is available along flow pathways. Large amounts of water with normal U concentrations (0.5 to 3  $\mu\text{g}/\text{l}$ ) will contain enough  $^{238}\text{U}$  to overwhelm recoil  $^{234}\text{U}$ , resulting in waters with low  $^{234}\text{U}/^{238}\text{U}$ . If the infiltrating waters have very dilute U concentrations, higher  $^{234}\text{U}/^{238}\text{U}$  ratios may be obtained for the same amount of flux. Small amounts of flux that wash pathway surfaces continuously will remove gradually accumulating  $^{234}\text{U}$  and also inhibit  $^{234}\text{U}/^{238}\text{U}$  from reaching elevated values. However, if only a small amount of intermittent flux is present in fractures,  $^{234}\text{U}$  will gradually accumulate on surfaces to a level that will not be overwhelmed by the  $^{238}\text{U}$  in migrating solutions. Under the latter conditions,  $^{234}\text{U}/^{238}\text{U}$  ratios would become elevated to the high values that are typically observed in minerals throughout most of the ESF main drift and north and south bends. Quantitative analysis of isotope mass balance between  $^{238}\text{U}$  and  $^{234}\text{U}$  are required to place limits on the effectiveness of using  $^{234}\text{U}/^{238}\text{U}$  as a proxy for percolation volume.
- Boundaries between zones of low versus high  $^{234}\text{U}/^{238}\text{U}$  values observed in the ESF correspond to shallower stratigraphic levels within the TSw or with areas of increased structural disruption of the PTn. These two conditions are broadly coincident in the ESF, complicating attempts to resolve the dominating influence.

Most of the  $^{36}\text{Cl}/\text{Cl}$  data for salts extracted from the pore space of the bulk rock matrix, breccias, and non-fast-path fractures in borehole cuttings and ESF samples have values between  $500 \times 10^{-15}$  and  $1200 \times 10^{-15}$ . Five possible interpretations for these data are given in section 6.1.3 of this report. Of these, a combination of Scenarios 1 and 4 would result in an age distribution for  $^{36}\text{Cl}$  in these rocks in general agreement with the interpretations of the U-series data summarized above. A strong correlation between the distribution of outer-surface mineral ages and calculated maximum water ages based on  $^{36}\text{Cl}/\text{Cl}$  data need not be expected, but water ages should not be substantially older than mineral ages, at least in areas where mineral deposits are common.

A more appropriate comparison would be the  $^{36}\text{Cl}$ -based age of salts trapped in secondary minerals at the time of their formation, analogous to the U-series technique. A preliminary set of  $^{36}\text{Cl}$  results obtained for calcite and opal fracture minerals is reported in Fabryka-Martin et al. (In press [a]; their Table 5-5). Three of the four mineral samples have  $^{36}\text{Cl}/\text{Cl}$  ratios that are indistinguishable from the equilibrium  $^{36}\text{Cl}/\text{Cl}$  ratio for the rock, i.e., the Cl in these minerals is so old (at least 1 My) as to have reached equilibrium with the prevailing neutron flux. One mineral sample has a ratio ( $268 \times 10^{-15}$ ) well above the equilibrium value but still lower than most of the values obtained for the ESF rocks, and represents an apparent average mineral age  $> 700$  ka. It is conceivable that the opal-calcite mineral separates used for the  $^{36}\text{Cl}$  analysis were not altogether pure and that other, older, mineral phases may have been present, such that the isotopic result may be biased somewhat on the low side. This possibility can be assessed by XRD analyses of the analyzed fractions.

Recent interpretation of the U-series data indicates that mineral deposition may be occurring on

scales finer than can be mechanically separated for analysis (Peterman and Paces, 1996) such that all U-series ages may be a mixture of younger mineral layers with older ones. In this case, the true mineral formation ages for the outermost layer would be variably younger than the ones calculated from the U-series analyses. This interpretation of the U-series data would be consistent with both Scenarios 1 and 4 in section 6.1.3 in which the  $^{36}\text{Cl}$  extracted from rock samples is assumed to reflect a complex combination of radioactive decay and a variable meteoric  $^{36}\text{Cl}$  input. Under these scenarios, the ages of most water in the deep unsaturated zone ranges from modern to 600 ka.

The U-series data and associated mineral deposition ages do not capture evidence of the fast infiltrating fluids being recorded by the bomb-pulse signals seen in the  $^{36}\text{Cl}$  data. Several plausible explanations can be advanced for this apparent discrepancy.

- The two data sets may be sampling different flow networks. Despite intentions of LANL and the USGS to coordinate their ESF sampling efforts and collect as many samples as possible from the same locations, in reality, practical constraints on sample size requirements greatly limited the number of cases in which sampling for multiple isotopic analyses was actually feasible. Chlorine-36 samples were often collected from features where little or no secondary mineralization was visible; conversely, samples for U-series analysis were often collected as narrow fracture linings which could not provide the 1-kg sample size needed for  $^{36}\text{Cl}$  analysis.
- As a corollary to the above hypothesis, the U-series sample set may be biased toward older fluids if young fluids such as those transporting bomb-pulse  $^{36}\text{Cl}$  are not actively depositing secondary minerals phases that can be measured by U-series disequilibrium methods. These faster-moving fracture fluids may be undersaturated with respect to calcite and silica, or the kinetics of mineral precipitation may be too slow relative to the flow rate to allow measurable deposition. Geochemical analyses of the PTn porewaters from the drillholes in the North and South Ramp should help to assess this hypothesis.
- In some cases at least, the mineral formation ages determined by the U-series analyses may actually record the time at which a the sampled section of a fracture became closed to active water movement.
- Calculated average long-term mineral growth rates of 0.001 to 0.004 mm/ka (Paces et al., 1997) would result in 0.05 to 0.2 mm of deposition on the outer surface of a crystal in 50 ka. The difficulty of sampling such thin layers means that evidence of mineral deposition even by non-fast-path fluids would be unobtainable from many or most mineral samples.

### 6.3 Surface infiltration controls on subsurface distribution of Cl and $^{36}\text{Cl}$

The relationship between surface infiltration rates and the  $^{36}\text{Cl}/\text{Cl}$  ratios measured in ESF rock samples is shown in Figure 6-3. The relationship between the infiltration rate and the distribution of  $^{36}\text{Cl}$  is obviously not a simple one. This section examines the  $^{36}\text{Cl}$  data from the perspective of evaluating how infiltration and percolation processes control its distribution in the subsurface, with an emphasis on the use of the  $^{36}\text{Cl}$  results as an indicator of fast paths. An analogous evaluation from the perspective of geologic structures is summarized in section 6.4 Supporting discussion of individual sample results from the perspective of surface geology, structure and infiltration rates is provided in Appendix D.

#### 6.3.1 Surface infiltration controls on the subsurface distribution of Cl

A common simplistic assumption in the interpretation of Cl and  $^{36}\text{Cl}$  concentrations is that the deposition of these environmental tracers from the atmosphere is uniformly distributed across the site, and that these tracers then move vertically downward to enter the underlying bedrock. These assumptions of a known source term and one-dimensional transport underlie the application of Cl porewater concentrations as a proxy indicator for infiltration rates. However, the subsurface distribution of Cl is controlled not only by the distribution of net infiltration but also by its subsequent redistribution in the unsaturated zone (discussed in the following section). This section examines the extent to which these processes affect the validity of the underlying assumptions.

*Cl deposition rate.* Cl enters the hydrologic system both as wet fallout (with precipitation) as well as an approximately equal amount as dry fallout. The spatial distribution of Cl deposited from the atmosphere is not well-known on the local scale but is assumed to approximate the spatial distribution of the average annual precipitation, which is known (Hevesi et al., 1994). Precipitation averages 170 mm/yr over Yucca Mountain but ranges from less than 130 mm/yr at the lower elevations to over 280 mm/yr at higher elevations. These ratios could be used to provide an initial estimate of the ratio of the spatial distribution of Cl attributed to precipitation. In general, however, the spatial distribution directly over the repository is fairly uniform with high precipitation over the crest (170 mm/yr) decreasing to 160 or 150 mm/yr in the lower washes. Consequently, the assumption of a relatively uniform Cl deposition rate is probably reasonable for the site.

*Redistribution of Cl by surface runoff.* Two major mechanisms for redistribution of water and Cl at the surface are surface runoff and lateral subsurface flow such as along the tuff-alluvium contact. In general, runoff occurs 2 to 3 times in ten years and varies from wash to wash (Flint et al., 1996). Even for major runoff events, water usually infiltrates into the downstream deep alluvial channel without ever leaving the site (Flint et al., 1996). Thus, although redistributed, the bulk of the Cl remains on site but may be more concentrated in the deep alluvial channels. Few runoff events in the washes over the potential repository ever penetrate more than 6 m. The

Cl brought into these channels by runoff likely remains in the root zone and is not a significant factor in redistribution of Cl in the subsurface. An exception may be in upslope washes with less than 6 m of alluvium. In this case, Cl may accumulate to a greater extent and there may be more of an accumulation of Cl and more influence on the subsurface distribution of Cl. A concern is that this increased Cl concentration in the channels may lead to higher Cl concentrations in the porewater, thereby leading to severe underestimates of the infiltration rate at those locations (because high Cl concentrations are interpreted as low infiltration rates). However, not only is Cl imported into the channels by runoff, but so is water at the same time, such that the Cl concentration in infiltrating water under channels is not necessarily increased as a result of runoff. Work is currently underway to determine the significance of Cl in runoff entering channels.

*Redistribution of Cl by subsurface lateral flow.* In most years, subsurface lateral flow is negligible due to low precipitation. In wetter years, when higher saturations are attained at the tuff-alluvium contact, lateral flow is initiated and Cl may be redistributed down slope. The lateral transport distance is unknown for any given event but probably does not exceed 40 m during even the wettest years, and likely is limited to 10 m. During lateral redistribution, water also continues to infiltrate vertically into the bedrock, thereby maintaining a spatially distributed input. Recurrent lateral flow events, however, could increase Cl concentrations in alluvial-filled valleys. Further down slope, migration is reduced considerably when the alluvial thickness increases with a corresponding increase in storage capacity. Subsurface flow entering the thick alluvium is quickly imbibed into the drier alluvium and can actually imbibe upward into the drier overlying soil. Neutron probe data support this hypothesis and indicate that lateral flow from sideslopes entering the deeper alluvial-filled washes can penetrate laterally 5 to 10 m but that the flow has never exceeded 15 m in lateral distance (Flint and Flint, 1995; Flint et al., 1996). Under these conditions, <sup>36</sup>Cl deposited over the site may have moved downslope about 30 m every ten years, and less than 150 m since deposition of the peak fallout in the mid-1950s. Any bomb-pulse <sup>36</sup>Cl that has reached the deeper alluvium in the washes is likely still in storage in the alluvium. This simple analysis is not conclusive but suggests that redistribution of bomb-pulse <sup>36</sup>Cl in kilometer-wide watersheds may be minimal. Additional field work and numerical modeling are needed to test this hypothesis.

With the above arguments in mind and an assumption that, as a first approximation, Cl deposition is uniformly distributed, then the spatial distribution of Cl entering the unsaturated zone is approximately directly proportional to the spatial distribution of net infiltration presented by Flint et al. (1996); Cl concentrations, however, are inversely proportional. The analysis by Flint et al. (1996) accounts for the spatial distribution of precipitation, soil thickness, fracture densities and permeabilities of the underlying bedrock and adds an enhancement factor for alluvial channels. They do not account for the lateral redistribution of Cl which is still under investigation. Overall, the largest influx of net infiltration and, therefore, of the lowest Cl concentrations in infiltrating water occurs under thin soils (low storage capacity) at higher elevations (increased precipitation) where the more permeable bedrock is found (higher infiltration to lower evapotranspiration rates). The soil thickness along the ESF is highly

variable (Figure 6-4). The relatively quick transition from thin to thick and the potential for subsurface redistribution make interpretations using soil thickness alone very questionable.

### *6.3.2 Surface infiltration controls on the subsurface distribution of bomb-pulse $^{36}\text{Cl}$*

Sources of  $^{36}\text{Cl}$  transported with infiltrating waters in the unsaturated zone were previously discussed at a general level (section 3); the primary sources of interest are cosmogenic  $^{36}\text{Cl}$  and global fallout of bomb-pulse  $^{36}\text{Cl}$  from the atmosphere. Similar to the case for Cl, it is generally assumed that cosmogenic and bomb-pulse  $^{36}\text{Cl}$  are uniformly deposited across a site, and that this tracer then moves vertically downward to enter the underlying bedrock. Arguments made for Cl in the previous section are also valid for  $^{36}\text{Cl}$ ; in any event, the two tracers travel together so that processes leading to the concentration of one will equally cause the concentration of the other, maintaining the initial ratio. The exception to this case is where waters of different ages mix together, particularly if one parcel of water contains bomb-pulse  $^{36}\text{Cl}$  while the other does not.

As is the case for Cl, two major mechanisms for redistribution of bomb-pulse  $^{36}\text{Cl}$  at the surface are surface runoff and lateral subsurface flow. Evidence that such redistribution occurs is readily observed in cases where vertical profiles of bomb-pulse  $^{36}\text{Cl}$  contain considerably more, or considerably less, than the amount expected for global fallout. For example, a soil profile from Yucca Wash measured by Norris et al. (1987) contained only a very small proportion of the  $^{36}\text{Cl}$  expected for global fallout, which was interpreted as indication of its removal by subsurface lateral transport. Similarly, soil profiles exposed at the NRG-5 drillpad contained more  $^{36}\text{Cl}$  than expected from accumulation of global fallout in a one-dimensional column, suggesting introduction of additional bomb-pulse  $^{36}\text{Cl}$  by downslope transport (Fabryka-Martin et al., in press [b]). However, in the deep alluvial profiles measured at UZ-N37 and UZ-N54, the amount of bomb-pulse  $^{36}\text{Cl}$  present was as expected for global fallout, indicating the absence of significant lateral transport into or out of this part of these profiles.

As for the case with Cl, in most years, subsurface lateral flow is negligible due to low precipitation. In wetter years, lateral flow is initiated and  $^{36}\text{Cl}$  may be redistributed down slope about 30 m every ten years, for a total transport distance less than 150 m since deposition of the peak fallout in the mid-1950s. Any bomb-pulse  $^{36}\text{Cl}$  that has reached the deeper alluvium in the washes is likely still in storage in the alluvium. This analysis suggests that redistribution of bomb-pulse  $^{36}\text{Cl}$  in kilometer-wide watersheds may be minimal. Additional field work and numerical modeling are needed to test this hypothesis.

A case-by-case analysis of the distribution of  $^{36}\text{Cl}$  in the ESF is presented in Appendix D. This analysis supports the conceptual model for fast paths, i.e., that the occurrence of bomb-pulse  $^{36}\text{Cl}$  in the subsurface (below the PTn) is mostly controlled by the distribution of faults, alluvial thicknesses and infiltration rates and only related secondarily, if at all, to redistribution of bomb-pulse  $^{36}\text{Cl}$  in surficial materials. The analysis in that appendix relates the geologic conditions at the surface and subsurface, the modeled infiltration rate and soil thickness. The analysis assumes

that the presence of bomb-pulse  $^{36}\text{Cl}$  is related to the presence of a fault, infiltration rates  $> 2$  mm/yr, and alluvial thickness less than 3 m. A further assumption is that there is enough bomb-pulse  $^{36}\text{Cl}$  present over the entire surface of Yucca Mountain, regardless of redistribution by lateral flow and runoff, that its presence in the subsurface is an indication of a fast path and that  $^{36}\text{Cl}/\text{Cl}$  ratios  $< 500 \times 10^{-15}$  indicate the absence of bomb-pulse  $^{36}\text{Cl}$ .

#### 6.4 Structural controls on subsurface distribution of $^{36}\text{Cl}$

##### 6.4.1 Structural characterization of ESF sample sites

The structural setting of the ESF sample localities was established in order to evaluate the structural significance and distribution of possible hydrologic pathways exploited by water that has transmitted bomb-pulse  $^{36}\text{Cl}$  to sample locations in the ESF. Each sampling location in the ESF has been described in terms of 1) attributes of the sampled feature (orientation, length, aperture, interpreted origin); 2) local structural setting (fracture set interpretation, location with respect to known faults); and 3) interpreted connection to other features. Additional data on the orientation, length, and amount of offset of structural features sampled in the ESF were obtained from the full-periphery mapping and detailed line survey (DLS) data from the ESF.

The described ESF sample localities were placed in a broader structural setting by locating each sample site with respect to structural features mapped at the surface and subsurface. Geologic cross sections were used in correlating surface and subsurface structures. Interpretations of local structural controls on the distribution of bomb-pulse  $^{36}\text{Cl}$  were made using knowledge of fracture characteristics and vertical connectivity of the fracture network(s) in rocks equivalent to the TCw (welded part of the Tiva Canyon Tuff), the PTn, and TSw (welded part of the Topopah Spring Tuff) hydrogeologic units.

##### 6.4.2 Recognition of Syngenetic Features

The identification of transmissive features of syngenetic origin is an important aspect of sampling site characterization. Syngenetic features are formed during the cooling of a newly emplaced ash flow. A syngenetic origin of fractures or breccia zones carries useful implications of age and spatial continuity. Cooling joints, in particular, do not extend beyond the boundaries of an ash flow into underlying or overlying units. Their extent may be further limited by changes in syngenetic textural zonation; for example, cooling joints may be well developed in densely welded, nonlithophysal tuff but die out across a transition into lithophysal tuff where thermal contraction was accommodated by mechanisms other than tensile fracturing. These limitations of spatial continuity imply that transmissive features of purely syngenetic origin can be fast pathways only if they are connected to throughgoing pathways such as faults. In some cases, post-emplacement tectonic deformation can exploit the pre-existing fractures and breccias, creating pathways of hybrid origin (Potter et al., 1996b; Sweetkind et al., 1996b).

Significant syngenetic features for the study of fast paths include vapor-phase partings, cooling

joints, syngenetic fractures, and syngenetic breccias. Vapor-phase partings are discontinuous, incipient fractures with fillings of mostly high-temperature silica minerals and feldspar. The partings commonly formed subparallel to flattening foliation. Cooling joints typically have low surface roughness and are planar to arcuate. Distinctive light-colored margins as much as a few millimeters thick, also known as "bleached margins," are common attributes of cooling joints. Breccias and fractures other than cooling joints may be identifiable as syngenetic by the presence of certain mineral cements and fracture fillings. Tridymite, cristobalite, and alkali feldspar deposits are highly reliable indicators that fractures or breccias formed early in the cooling history of an ash flow; euhedral quartz and chalcedony are deposited later in the cooling history at near-ambient temperatures (Levy, 1993; Levy and O'Neil, 1989).

#### 6.4.3 Fault characteristics

*Presence of faults.* Areas along the North Ramp and northern part of the Main Drift of the ESF in which multiple samples show indications of bomb-pulse  $^{36}\text{Cl}$  are not randomly distributed. The multiple samples are almost always feature-based samples; generally it is only when specific structural features are targeted that elevated levels of  $^{36}\text{Cl}$  are detected. Further, intervals of multiple bomb-pulse  $^{36}\text{Cl}$  samples are associated with faults mapped at the surface and in the ESF (Figures 6-1 and 6-2). These intervals include the Bow Ridge fault, the faulted interval at the east end of Azreal Ridge, the Drill Hole Wash fault, the projected location of the Diabolus Ridge fault, and the Sundance fault. Of these, only the block-bounding Bow Ridge fault has a vertical separation that is greater than the thickness of the PTn unit (thickness greater than 30 m along the North Ramp of the ESF; Moyer et al., 1996) and thus creates a complete discontinuity in the PTn. The other faults are intrablock faults with less than 20 m of offset (Day et al., in press). These faults do not completely offset the PTn; the PTn unit (albeit different lithostratigraphic units) would occur in both the hanging wall and footwall of these faults. The general spatial correspondence with structural features is consistent with model results that indicate that the presence of a fault is required to allow transport of small amounts of bomb-pulse  $^{36}\text{Cl}$  to the ESF level in fifty years or less (Fabryka-Martin et al., in press [a]; Robinson et al., 1996). Simulations utilizing the material properties and hydrologic parameters from Bodvarsson and Bandurraga (1996) and Robinson et al. (1996) for the PTn-equivalent rock units with no faulting or increased fracturing do not result in the arrival of bomb-pulse  $^{36}\text{Cl}$  at the ESF within the necessary time interval, even for infiltration rates as high as 50 mm/yr (Robinson et al., 1996; Fabryka-Martin et al., in press [a]). Faults in the PTn were then simulated by increasing fracture frequency and apertures above the original values; with this increased bulk permeability for the PTn, infiltration rates of 1 to 5 mm/yr were found to be sufficient to transport small amounts of bomb-pulse  $^{36}\text{Cl}$  to the ESF level within the requisite time period (Fabryka-Martin et al., in press [a]; Robinson et al., 1996).

In contrast to the general association of samples having elevated levels of  $^{36}\text{Cl}$  with structures in the North Ramp and northern part of the Main Drift of the ESF, no bomb-pulse  $^{36}\text{Cl}$  has been observed in samples collected from the vicinity of faults in the southern end of the Main Drift or

in the South Ramp of the ESF (Figure 6-1). Samples from this part of the ESF that lack elevated levels of  $^{36}\text{Cl}$  include those taken from the Ghost Dance fault, the Dune Wash fault, and major intrablock faults in the Boundary Ridge area. In this portion of the ESF, the block-bounding Dune Wash fault and the large intrablock fault exposed in the ESF around Station 70+56 have vertical separations that are greater than the thickness of the PTn unit (thickness less than 30 m along the South Ramp of the ESF; Moyer et al., 1996) and thus create a complete discontinuity in the PTn. The other faults (including the Ghost Dance fault) are intrablock faults with less than 20 m of offset (Day et al., in press). These faults do not completely offset the PTn. The lack of elevated levels of  $^{36}\text{Cl}$  in these faulted areas indicates that the presence of faults is not the only controlling factor in the distribution of  $^{36}\text{Cl}$  in the ESF. The areas near faults in the southern end of the Main Drift and the South Ramp of the ESF underlie topographically low areas with generally low surface infiltration (Appendix Figure D-7b). Further, the southern splay of the Ghost Dance fault and the Dune Wash fault underlie washes where alluvium is estimated to be 3 m thick or greater (Figure D-7c), resulting in travel times through the alluvial cover longer than 50 years. The distribution of  $^{36}\text{Cl}$  in the ESF depends upon multiple interrelated controls; the presence of faults does not result in bomb-pulse  $^{36}\text{Cl}$  in the ESF without sufficient net infiltration and sufficiently fast travel times through the alluvial cover.

*Frequency of faults and magnitude of fault offset.* Faults (defined here as structural discontinuities that display offset, regardless of magnitude) sampled for  $^{36}\text{Cl}$  analysis have offsets ranging over four orders of magnitude, from 0.1 m to 100 m. Bomb-pulse  $^{36}\text{Cl}$  values are associated with a variety of fault types, including a block-bounding fault (the Bow Ridge fault), a probable strike-slip fault (the Drill Hole Wash fault), and smaller, intrablock faults, such as the Sundance fault and the Diabolus Ridge fault. Samples show no apparent correlation between the magnitude of fault offset and the occurrence of elevated  $^{36}\text{Cl}/\text{Cl}$  ratios. In fact, the majority of the samples with elevated  $^{36}\text{Cl}/\text{Cl}$  ratios are from cooling joints and unit contacts where no offset was measured (Sweetkind et al., 1997a).

The frequency of faults in the ESF, reported as number of faults per 100 m, was derived from full periphery geologic maps through Station 75+00 by counting the number of mapped features labeled as having any amount of offset (including "shears", a term used by the U.S. Bureau of Reclamation to denote faults having less than 10 cm of offset). Areas with a relatively high frequency of faults (such as the area north of the Ghost Dance fault between ESF Station 53+00 and 57+00, or the area east of the Dune Wash fault between ESF Station 70+00 and 72+00) do not correspond to intervals where bomb-pulse  $^{36}\text{Cl}$  is observed (Figure 6-5). Conversely, intervals along the ESF in which multiple samples show indications of bomb-pulse  $^{36}\text{Cl}$ , such as around the Sundance fault, or around the Drill Hole Wash fault, do not correspond to areas having greater numbers of faults (Figure 6-5). In fact, intervals along the ESF in which multiple samples show indications of bomb-pulse  $^{36}\text{Cl}$  tend to correspond to intervals where relatively few faults are present (Figure 6-5). Many of the faults tabulated from the full periphery geologic maps are short trace length, small (10's of cm) displacement faults that are not necessarily throughgoing features; a number of these faults are not large enough to be recorded on both ribs of the ESF. It is possible that the distribution of bomb-pulse  $^{36}\text{Cl}$  in the ESF may be controlled in some way by

the absence of numerous small faults. However, given the spatial correspondence between the samples having elevated  $^{36}\text{Cl}/\text{Cl}$  ratios and the larger faults (Figure 6-1), it is likely that the presence of a fast pathway depends upon faults with offset greater than 1m, even if these are isolated, discrete features, rather than upon the frequency of faults having smaller displacements. The interval between Station 9+00 and 11+00 is the only location in which a group of samples with elevated  $^{36}\text{Cl}/\text{Cl}$  ratios is associated with a zone of high fault density (Figure 6-5). The PTn unit is exposed in this interval of the ESF, and the samples analyzed for  $^{36}\text{Cl}$  from this interval were all collected from subunit contacts.

#### 6.4.4 Fracture characteristics

*Fracture frequency* derived from the ESF detailed line survey data through Station 75+00 is shown in Figure 6-6. Fracture frequency is portrayed as the number of 1 m or longer fractures per 10-m interval. In general, the distribution of samples containing a component of bomb-pulse  $^{36}\text{Cl}$  does not correspond to intervals of high fracture frequency, with the exception of three bomb-pulse samples that occur within the intensely fractured zone between Station 42+00 to 51+50 (Figure 6-6). In fact, intervals along the ESF in which multiple samples show indications of bomb-pulse  $^{36}\text{Cl}$  tend to correspond to minima in the frequency of fracturing, or at least to intervals where fracture frequency remains relatively constant.

Although the fracture network certainly would be expected to play a role in the distribution of bomb-pulse  $^{36}\text{Cl}$  at the local scale (discussed below), it is unlikely that the overall distribution of bomb-pulse  $^{36}\text{Cl}$  in the ESF is directly controlled by fracture frequency, whether high or low. The character of the fracture network—including the number of sets, orientation distribution, length distribution, density of fracturing, and network connectivity—are in general specific to particular lithostratigraphic intervals (Throckmorton and Verbeek, 1995; Sweetkind and Williams-Stroud, 1996; Sweetkind et al., 1997b). The overall variability in fracture frequency is primarily a function of lithology (Sweetkind and Williams-Stroud, 1996; Sweetkind et al., 1997b). Fracture frequency is generally highest in densely welded, nonlithophysal rock, and lower in lithophysal units and nonwelded to partially welded tuffs. Structural controls on fracture frequency are secondary to primary, lithologic controls (Sweetkind and Williams-Stroud, 1996; Sweetkind et al., 1997b). For 1 m or longer fractures averaged over 10-m intervals, faults have no apparent effect on fracture intensity; there are no sharp increases in the number of fractures larger than 1 m that are related to proximity to faults (Sweetkind et al., 1997b).

In general, the vertical extent of joint networks for specific lithostratigraphic intervals tends to be limited. Cooling joints, in particular, do not extend beyond the boundaries of an ash flow into underlying or overlying units. The vertical extent of cooling joints may be further limited by textural zonation within the pyroclastic flow. Cooling joints may be well developed in densely welded, nonlithophysal tuff but die out across a transition into lithophysal tuff where thermal contraction was accommodated by mechanisms other than tensile fracturing. For example, fractures within the middle nonlithophysal zone of the Topopah Spring Tuff, including those of

the intensely fractured zone, appear to be dominantly stratabound (Albin et al., 1997). The presence of higher fracture frequency within a particular lithostratigraphic interval does not by itself constitute a fast pathway. The limitations of spatial and especially vertical continuity imply that transmissive features within a fracture network dominated by cooling joints can be fast pathways only if they are connected to throughgoing pathways such as faults.

*Fracture orientation.* The distribution of orientations of faults and fractures sampled for  $^{36}\text{Cl}$  analysis includes steeply-dipping northwest-, north- and northeast-striking features and gently-to moderately dipping fractures and faults that generally have northwest strikes and that dip to the northeast (Sweetkind et al., 1997a). The orientation distribution of the sampled features is generally representative of the overall distribution of orientations in the ESF (Barr et al., 1996, Albin et al., 1997, Sweetkind et al., 1997b). Each of the principal joint sets defined for the ESF were sampled, as were a variety of fault orientations. There is no apparent correlation between orientation, of either faults or fractures, and samples with elevated  $^{36}\text{Cl}/\text{Cl}$  ratios. There does not appear to be a preferred orientation of structural feature responsible for the distribution of elevated  $^{36}\text{Cl}/\text{Cl}$  ratios in the ESF.

#### *6.4.5 Local Structural Control*

The general spatial correspondence of multiple samples having elevated  $^{36}\text{Cl}/\text{Cl}$  ratios with large offset faults in the ESF (Figure 6-1) is consistent with previously-reported flow and transport model results that require the presence of a fault through the PTn units in order to transport small amounts of bomb-pulse  $^{36}\text{Cl}$  to the ESF level within fifty years (Robinson et al., 1996; Fabryka-Martin et al., in press [a]). Although samples from some fault planes have elevated  $^{36}\text{Cl}/\text{Cl}$  ratios, samples with elevated  $^{36}\text{Cl}/\text{Cl}$  ratios are more commonly observed along minor structures, such as cooling joints or local faults with small displacements. The most prominent example is the vicinity of the Sundance fault where samples with bomb-pulse  $^{36}\text{Cl}$  comprise a 300-m zone along the ESF (Fabryka-Martin et al., in press [a]) (Figure D-5a). The Sundance fault is the only structure mapped in this vicinity (Potter et al., 1995; Day et al., in press) that could serve as the pathway through rocks equivalent to the PTn hydrogeologic unit. The broad zone of elevated  $^{36}\text{Cl}/\text{Cl}$  values north of the fault thus appears to represent lateral flow away from the plane of the fault and implies a connection between the fault and other structures, either small subsidiary faults or interconnected joints, in the rock mass surrounding the fault.

A connected pathway through a joint network is most likely where joints are long, where fracture intensity is high, and where fracture intersections are plentiful. Longer fractures have greater chances of intersecting, and there is a much higher probability of forming a connected pathway from a small number of intersecting long fractures than from a large number of short fractures (Odling, 1995). Also, the likelihood of fracture interaction increases as both fracture intensity and the number of fracture intersections increase (LaPointe and Hudson, 1985). The middle nonlithophysal zone of the Topopah Spring Tuff has significantly different fracture network properties (including fracture intensity, length distribution, and fracture connectivity) from the overlying portion of the Topopah Spring Tuff, especially the immediately overlying upper

lithophysal zone (Barr et al., 1996; Sweetkind et al., 1997b). Fracture data collected by detailed line survey in the ESF show a roughly three-fold increase in the fracture frequency (in fractures per ten m interval) between the upper lithophysal and middle nonlithophysal zones. Simulated fracture networks based on these ESF data indicate that the middle nonlithophysal zone has about 10 times the number of fracture intersections per meter and about 3 times the number of fractures per square meter as the overlying upper lithophysal zone (Anna, in press). In the ESF, the average fracture trace length is only slightly higher in the middle nonlithophysal zone than the upper lithophysal zone, but the number of very long fractures (10 m or longer) is much higher in the middle nonlithophysal zone. Lateral flow away from the Sundance fault is very unlikely within the upper lithophysal zone of the Topopah Spring Tuff, which has a poorly connected fracture network and few throughgoing discontinuities (Sweetkind et al., 1995b; Anna, in press). Lateral spreading of flow away from fault planes below the level of the PTn hydrogeologic unit is most likely within the middle nonlithophysal zone of the Topopah Spring Tuff where large, relatively closely spaced cooling joints and the common presence of gently dipping cooling joints promote network connectivity and the chances of a connected pathway in the rock mass surrounding the fault (Sweetkind et al., 1997a).

In the vicinity of the Sundance fault in the ESF, the distribution of samples having a component of bomb-pulse  $^{36}\text{Cl}$  depends on the presence of connected fracture pathways that are governed by the relative expression and spatial distribution of cooling joint sets and the degree of connection between the cooling joint sets and the fault. Cooling joints in the middle nonlithophysal zone of the Topopah Spring Tuff generally consist of two subvertical sets, having northwest and northeast strike directions, and a subhorizontal set (Sweetkind et al., 1995b; Albin et al., 1997). In the ESF there is also a well-developed set of cooling joints that generally strike to the northwest, dip between 20 and 50 degrees to the northeast, and are restricted to the area north of approximately Station 37+00 (Sweetkind et al., 1997b). Gently and moderately dipping joints are not well represented in the detailed line survey data because of the bias inherent in sampling the subhorizontal joints with a horizontal trace line, but these joint sets are prominent on the full-periphery geologic maps north of Station 37+00. The moderately dipping joints are often very large, continuous features crossing the entire diameter of the tunnel and extending along the tunnel for 20 m or more; these joints act as important connectors between steeply dipping cooling joints. The Sundance fault cuts the middle nonlithophysal zone of the Topopah Spring Tuff near Station 36+00, within the area where the moderately dipping joint set is well developed. The zone of bomb-pulse occurrences in the ESF that extends northward for 300-m from the Sundance fault appears to represent flow away from the plane of the fault along connected fracture paths within the middle nonlithophysal zone of the Topopah Spring Tuff. The width of the zone may be enhanced by flow along moderately north-dipping cooling joints that happen to be prominent in the vicinity of the Sundance fault.

#### *6.4.6 Summary of Structural Controls*

Fast pathways at Yucca Mountain appear distinctive in terms of their structural settings and the associated hydrologic properties of those structures. Previous work proposed that the primary

controls on their distribution in the ESF are: 1) the presence of faults that cut rocks equivalent to the PTn hydrogeologic unit; 2) the magnitude of surface infiltration; and 3) the thickness of alluvial cover. In agreement with this conceptual model, rock samples from the North Ramp and northern part of the Main Drift of the ESF that have elevated levels of  $^{36}\text{Cl}$  show a general spatial correspondence to faults mapped at the surface and in the ESF. In the northern part of the ESF, bomb-pulse  $^{36}\text{Cl}$  values are spatially associated with a variety of fault types, including a block-bounding fault, a probable strike-slip fault, and smaller, intrablock faults. Samples show no apparent correlation between elevated  $^{36}\text{Cl}/\text{Cl}$  ratios and either the magnitude of fault offset or feature orientation. In general, the distribution of samples containing a component of bomb-pulse  $^{36}\text{Cl}$  does not correspond to intervals of high fracture frequency or fault density.

At a more detailed scale, on the order of tens of meters to a few hundred meters, the presence or absence of specific joint sets, and the spacing and size of joints, appear to control the geometry of flow and the magnitude of lateral flow away from the fault. The Sundance fault exemplifies a transmissive structural feature in which flow is apparently spread away from the plane of the fault. Lateral spreading of flow away from a fault plane is most likely within the middle nonlithophysal zone of the Topopah Spring Tuff where large, closely spaced cooling joints and the presence of gently dipping cooling joints promote fracture network connectivity in the rock mass surrounding the fault. Locally variable  $^{36}\text{Cl}/\text{Cl}$  ratios in the vicinity of the fast path may reflect the distribution of connected fracture paths within a particular lithostratigraphic unit, or may be the result of local primary lithologic controls and secondary structural controls that operate at the scale of a few meters to a few tens of meters.

#### **6.5 Predicted distribution of fast paths containing bomb-pulse $^{36}\text{Cl}$ in the planned East-West Drift**

Predicting the occurrence or nonoccurrence of bomb-pulse  $^{36}\text{Cl}$  can be fairly straight forward once a conceptual or numerical model is available. The complexities come at an earlier stage, with the development and testing of alternative conceptual models and with the incorporation of the adopted conceptual model into an adequate numerical model. The numerical model may be required to account for specific features, such as faults, that may be only of limited local extent. Accounting for all features with the potential to act as fast paths may be a near impossible task numerically. Prediction of fast paths using only a conceptual model may be preferable in its capability to account for numerous known large or small features. This section uses known site information and a simple conceptual model to predict the occurrence of bomb-pulse  $^{36}\text{Cl}$  in the planned East-West drift. In addition, because of the simplicity of the model, predictions are made for the entire site.

The conceptual model was developed by Hudson and Flint (1996) and Flint et al. (1996) and subsequently refined by Fabryka-Martin et al. (in press [b]), Levy et al. (1997), and Sweetkind et al. (1997a) and, simultaneously, by this work. The conceptual model is straight forward and only requires 3 conditions to be met in order for bomb-pulse  $^{36}\text{Cl}$  to be transmitted below the PTn: 1)

shallow soils, 2) adequate net infiltration (>1 to 2 mm/yr) and 3) a continuous fracture pathway through the PTn. Shallow soils allow for conditions of saturation or near saturation to occur at the tuff/alluvium contact, which initiates fracture flow in the TCw. Adequate net infiltration is required to maintain fracture flow and to offset imbibition into the rock matrix along the flow pathway. These two conditions are widely satisfied throughout most of the site area. However, the most important aspect—and the most constraining one—is a continuous fracture pathway through the PTn in order to offset its high matrix permeability and, therefore, its high imbibition capacity and high storage capacity. The prediction of the nonoccurrence of bomb-pulse  $^{36}\text{Cl}$  requires that one or more of these conditions be missing.

Three cases are presented as predictions of the presence of bomb-pulse  $^{36}\text{Cl}$  in the planned East-West drift as well as a much larger part of the study area. Using a GIS system, a fault map (Day et al., in press) was overlain by an infiltration map (Flint et al., 1996) to produce estimates of locations at which infiltration was adequate (>2 mm/yr) and at which a fault existed that would provide a continuous pathway through the PTn. In this exercise, the condition of shallow soil thickness is accounted for only in post analysis of the mapped results for the other two conditions. In the model, faults were assigned a somewhat arbitrary zone of influence of 30 m in width. Infiltration calculations were also done on 30 m grid cells (Flint et al., 1996). The two maps are overlain, and the intersection of these two features (a fault and >2 mm/yr infiltration) is plotted as dots on the map (Figure 6-7). Strictly speaking, these dots would indicate locations where bomb-pulse  $^{36}\text{Cl}$  would be able to penetrate the PTn and enter the TSw. Where they coincide with the planned East-West drift comprises a preliminary prediction of the occurrence of bomb-pulse  $^{36}\text{Cl}$  in that excavation, and where the dots do not occur is a prediction of where bomb-pulse  $^{36}\text{Cl}$  will not be found. Additional maps were produced which require infiltration rates of 5 mm/yr and 10 mm/yr in order to show the sensitivity of the model to infiltration rates (Figures 6-8 and 6-9). In some locations, high infiltration rates occur over faulted areas but no bomb-pulse  $^{36}\text{Cl}$  would be predicted to penetrate the PTn. These situations occur when deep alluvium exists (>6 m, Appendix Figure D-4c) that would delay the entry of the pulse into the bedrock for more than 50 years, for example in lower Drill Hole Wash (N 4079000 m, E 545000m, Figure 6-7).

Although some inadequacies of this predictive technique are apparent when it is tested against known bomb-pulse  $^{36}\text{Cl}$  locations in the ESF, the comparison also leads to some useful correlations. The predictions are reasonably consistent with measurements in the north ramp (Figure D-3a) and with the main drift near the Sundance Fault (Figure D-5a) but predict bomb-pulse  $^{36}\text{Cl}$  in the south ramp where no bomb-pulse  $^{36}\text{Cl}$  has yet been detected (Figure D-8a). Several observations can be made in comparing the predictions in Figures 6-7 and 6-8 against the measured values in Figures D-3 through D-8. These observations require specific causation to be added to the simple predictive model. First, surface expression of a fault is not necessarily related to the location at which the fault breaks the PTn (Figure 6-3). Gently-dipping faults may break through the PTn away from the surface expressions of the faults. Therefore, the first modification to this simple model would be to use the location of the fault where it penetrates the PTn as the relevant condition for transmitting bomb-pulse, as opposed to its exposure at the

surface. Second, it appears at several locations in the ESF, such as the Sundance fault, that the bomb-pulse  $^{36}\text{Cl}$  may move a considerable distance down dip following lithostratigraphy and cooling features. Therefore the next modification would be to increase the buffer zone around the fault in the PTn toward the down dip side of the TSw lithostratigraphic units. A third modification would be to remove the deep alluvial valleys from consideration. Finally, improved estimates are needed of the infiltration rates required to maintain fracture flow through the PTn. If the threshold for infiltration to transmit bomb-pulse  $^{36}\text{Cl}$  through the PTn were increased to 5 mm/yr or even 10 mm/yr (Figures 6-8 and 6-9), then the conceptual model would predict the virtual absence of bomb-pulse  $^{36}\text{Cl}$  in the south ramp, or indeed in most other locations in the ESF. An infiltration rate between 2 and 5 mm/yr may allow bomb-pulse  $^{36}\text{Cl}$  to be transmitted to the level of the ESF in the north while eliminating it from the south. However, one would then need to provide a rational explanation why 2 mm/yr would be an adequate condition for arrival of bomb-pulse  $^{36}\text{Cl}$  in the north ramp, while requiring 5 mm/yr in the south ramp. Further analysis of this and other considerations will be developed in FY98 and included in the FY98 milestone.

Regardless of these caveats, it is fairly clear that there are two major locations where the presence of bomb-pulse  $^{36}\text{Cl}$  is predicted in the planned East-West drift (Figure 6-7). Again, there are subtleties that must be addressed to enhance the prediction. A wider zone of influence of the fault would lead to a prediction of bomb-pulse  $^{36}\text{Cl}$  along the eastern side of both the Sundance Fault (N4078800 m, E548500 m, Figure 6-7) as well as the eastern splay of the Solitario fault (N4078100 m, E547500 m, Figure 6-7). For the central part of the East-West Drift, the model predicts the absence of bomb-pulse  $^{36}\text{Cl}$  because this area is virtually unaffected by faults (excluding hidden faults that have no surface expression), even though soils are shallow and the infiltration rate exceeds 5 mm/yr in this area.

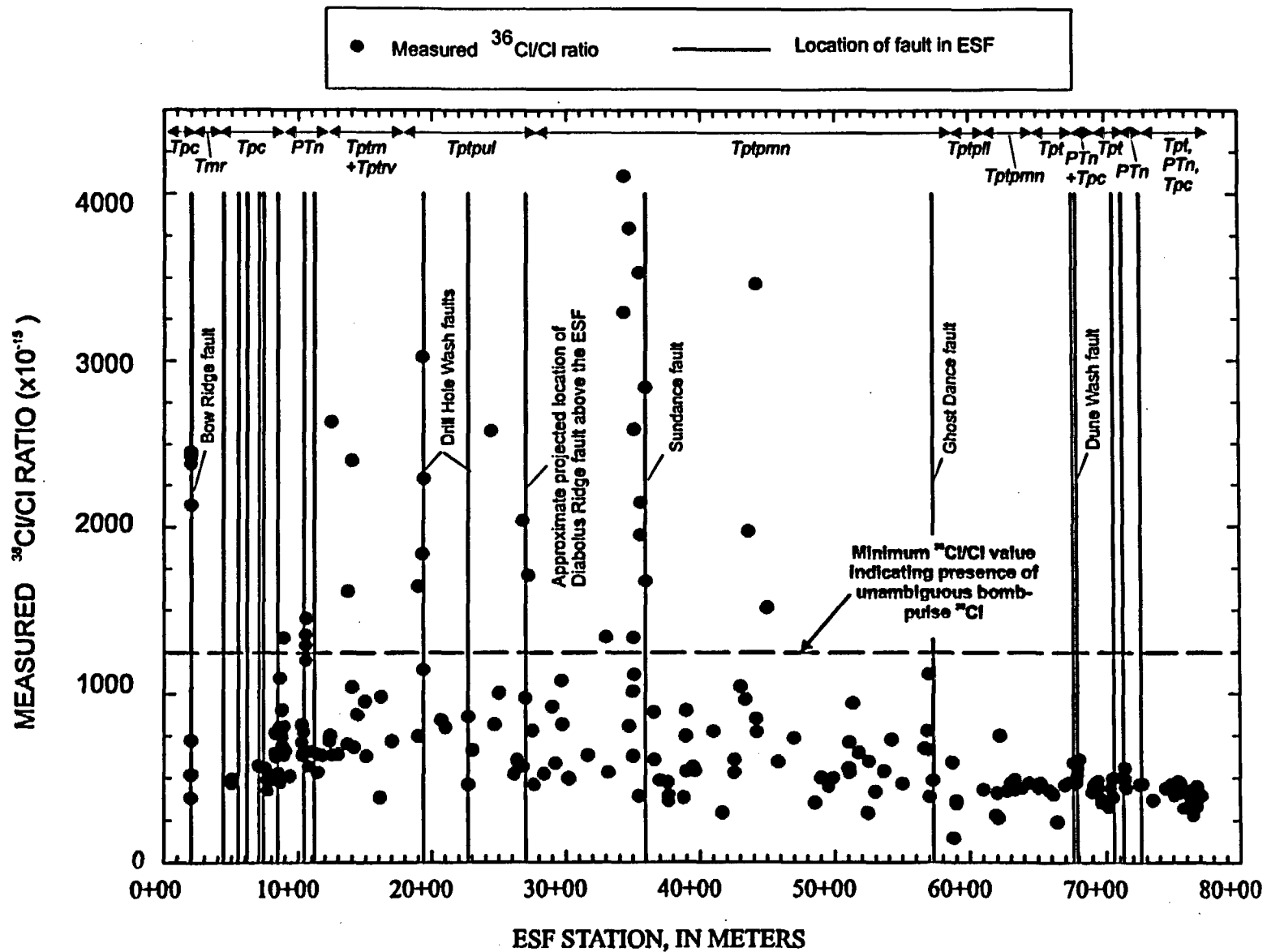


Figure 6-1. Faults and distribution of  $^{36}\text{Cl}/\text{Cl}$  ratios measured for rock samples in the ESF. Faults in the ESF that correlate with mapped faults at surface are shown. General location of lithostratigraphic units exposed in the ESF is shown along upper axis. Stratigraphic abbreviations are given in Table 2-1.

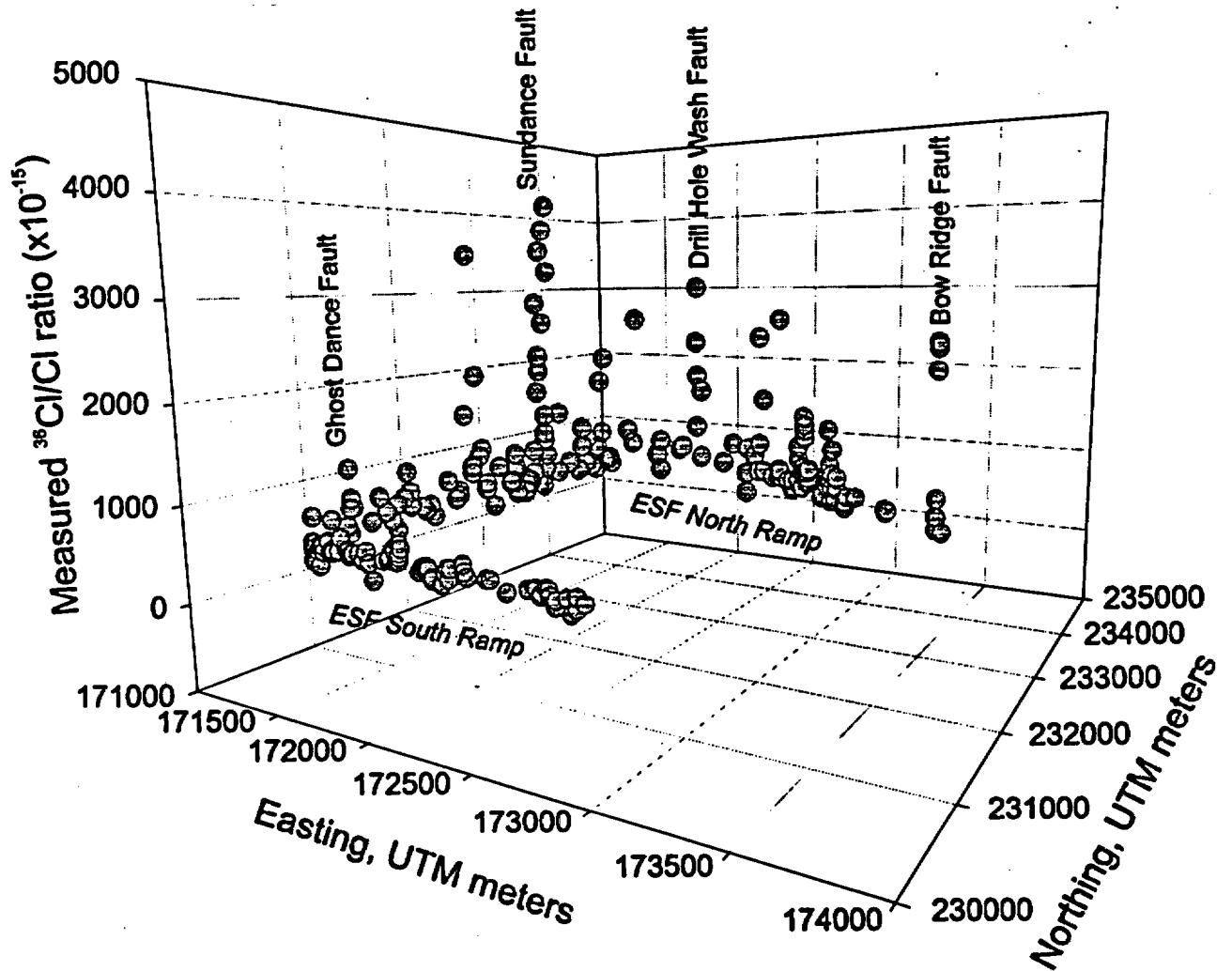


Figure 6-2. Perspective view showing distribution of  $^{36}\text{Cl}/\text{Cl}$  ratios measured for rock samples in the ESF. View is to the northwest.

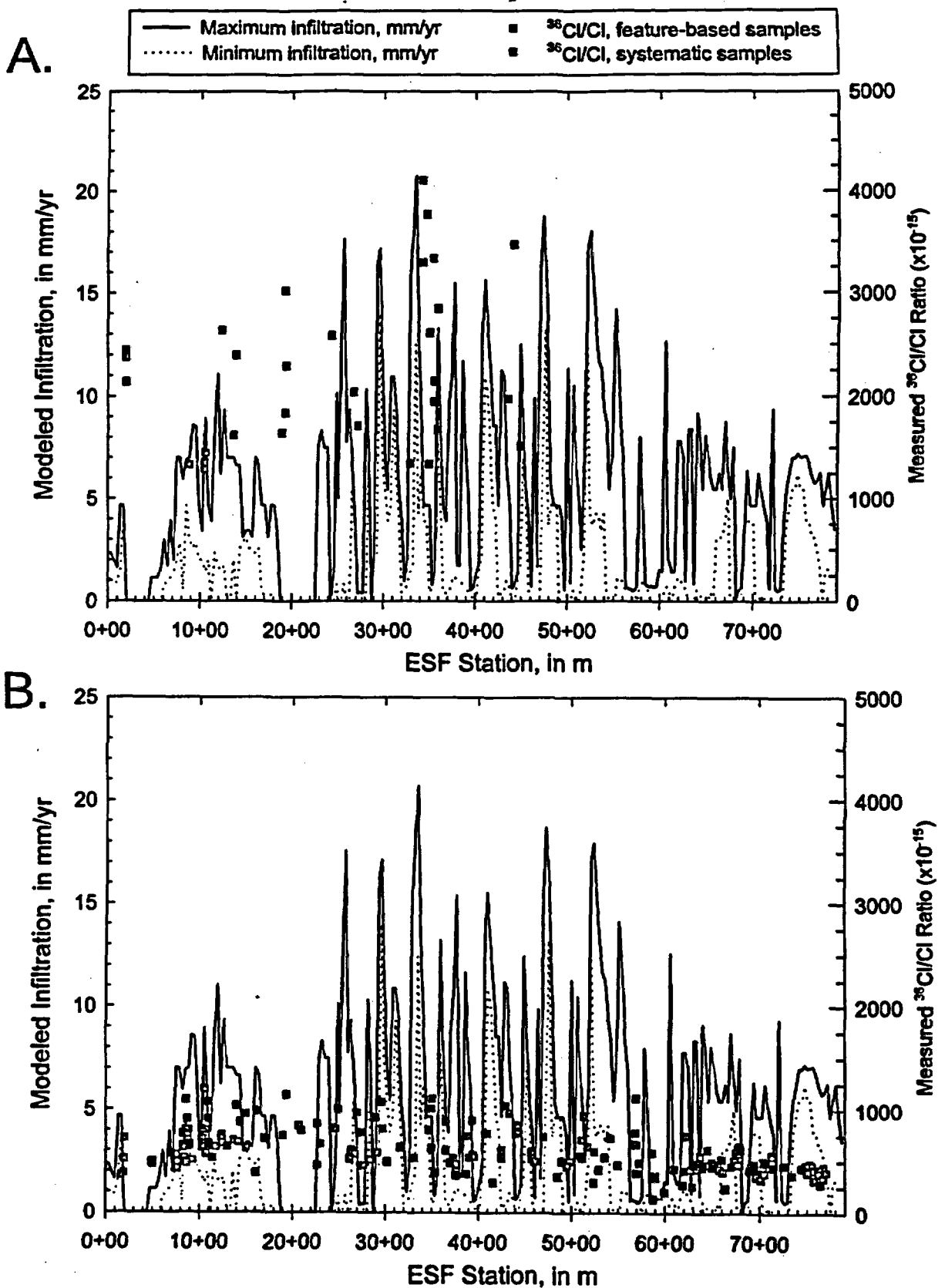


Figure 6-3. Modeled surface infiltration rates above the ESF and measured  $^{36}\text{Cl}/\text{Cl}$  ratios for rock samples in the ESF. A. Samples with an elevated  $^{36}\text{Cl}/\text{Cl}$  ratio indicative of the presence of bomb-pulse  $^{36}\text{Cl}$ . B. Samples with  $^{36}\text{Cl}/\text{Cl}$  ratios less than  $1250 \times 10^{-15}$ . Surface infiltration rate, using average annual precipitation, from the numerical model of Flint et al. (1996). Maximum and minimum infiltration rates are derived by selecting modeled values from within a 150 m-wide swath centered over the surface trace of the ESF.

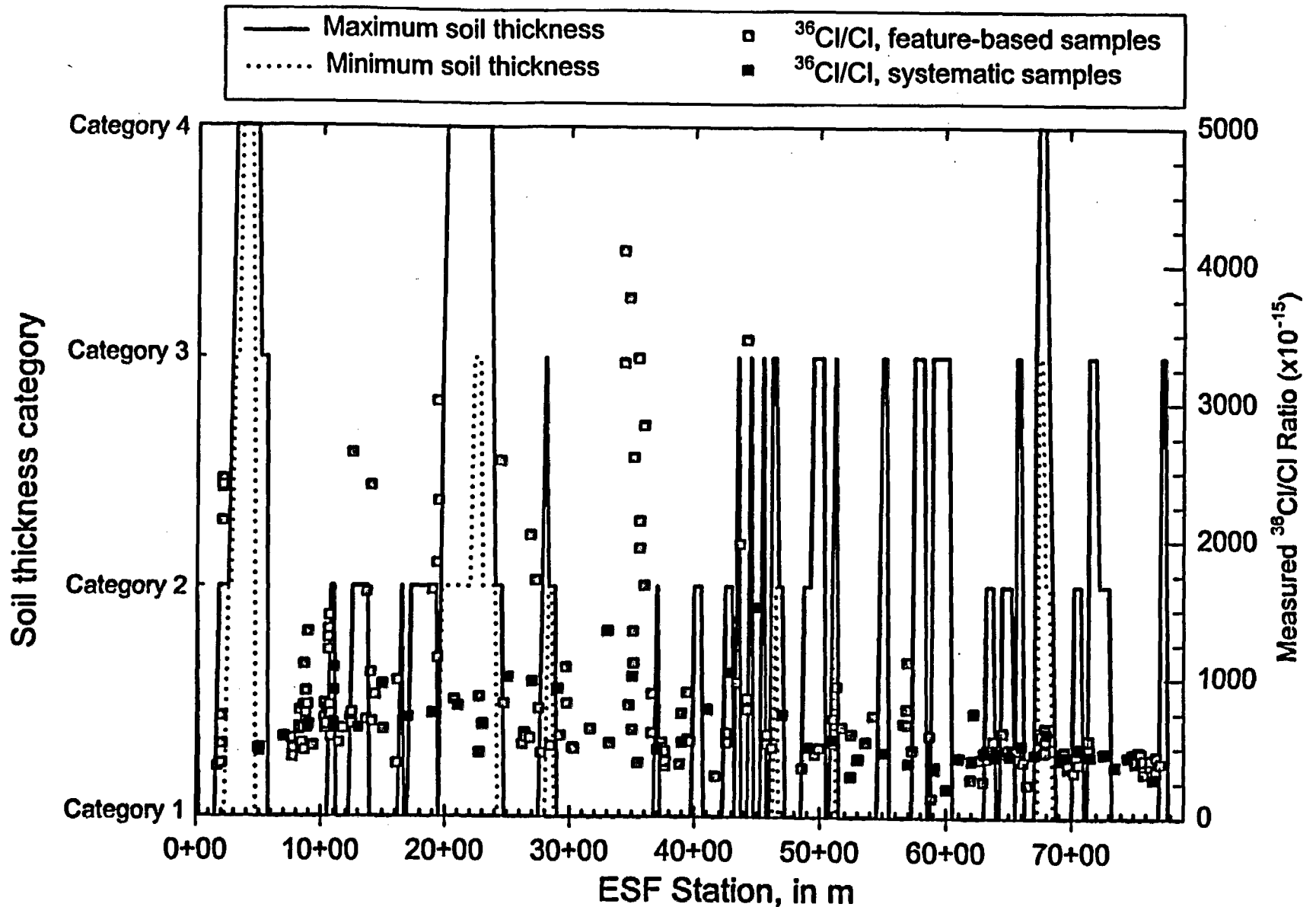


Figure 6-4. Soil thickness categories and distribution of  $^{36}\text{Cl}/\text{Cl}$  ratios measured for rock samples in the ESF. Soil thickness is reported in four categories: 1, <0.5 m; 2, 0.5 m to <3 m; 3, 3 m to <6 m; and 4, >6 m. Maximum and minimum soil thickness categories are derived by selecting modeled values (from Flint et al., 1996) within a 150 m-wide swath centered over the surface trace of the ESF.

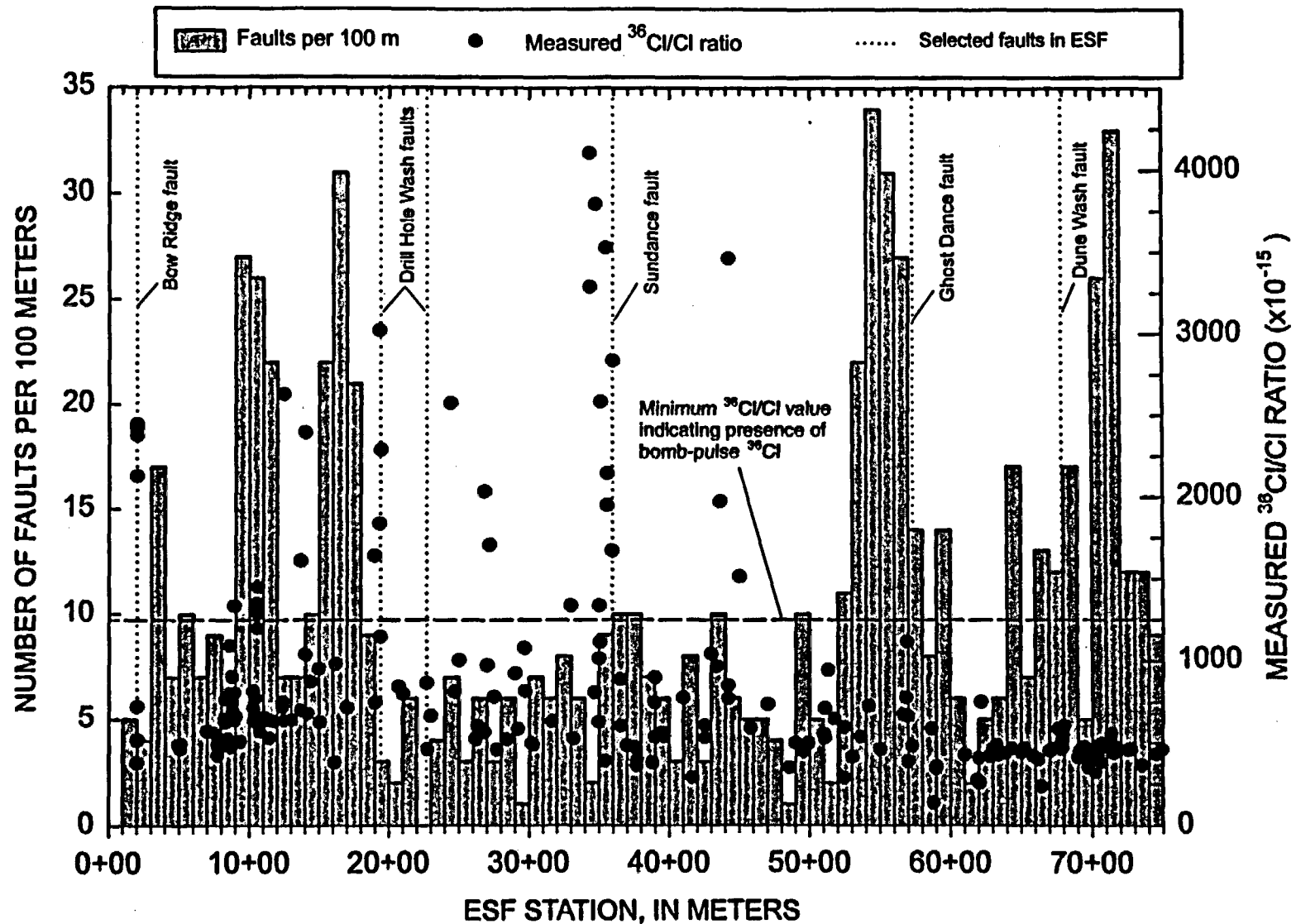


Figure 6-5. Fault density and measured  $^{36}\text{Cl}/\text{Cl}$  ratios for rock samples in the ESF (Sweetkind et al., 1997a). ESF stations are marked in 100-m increments, so that station 10+00 is 1000 m from the north portal. The number of faults (defined as structural features having any amount of offset) are summed for each 100-m segment of the ESF from the full-periphery geologic maps of the ESF.

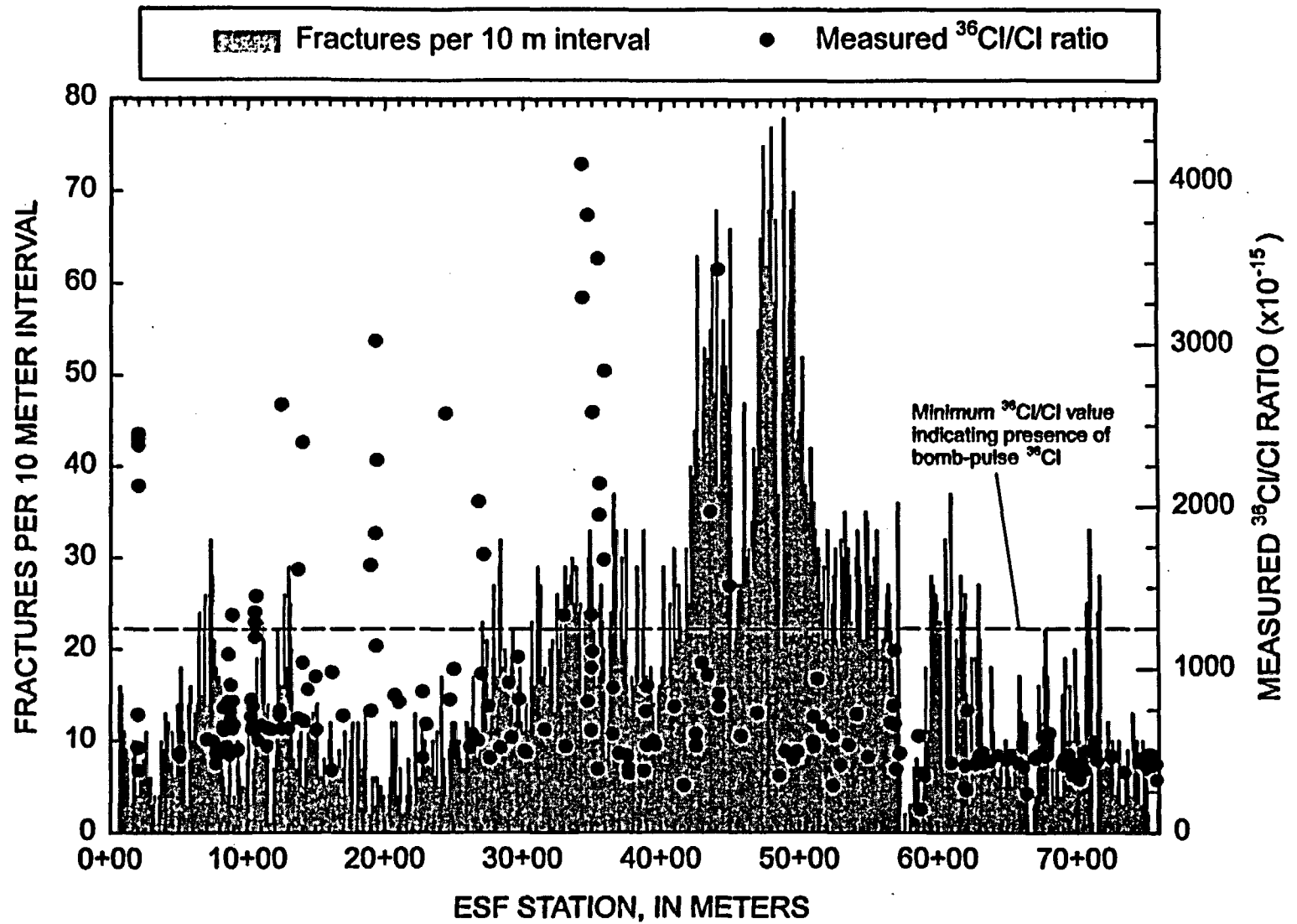
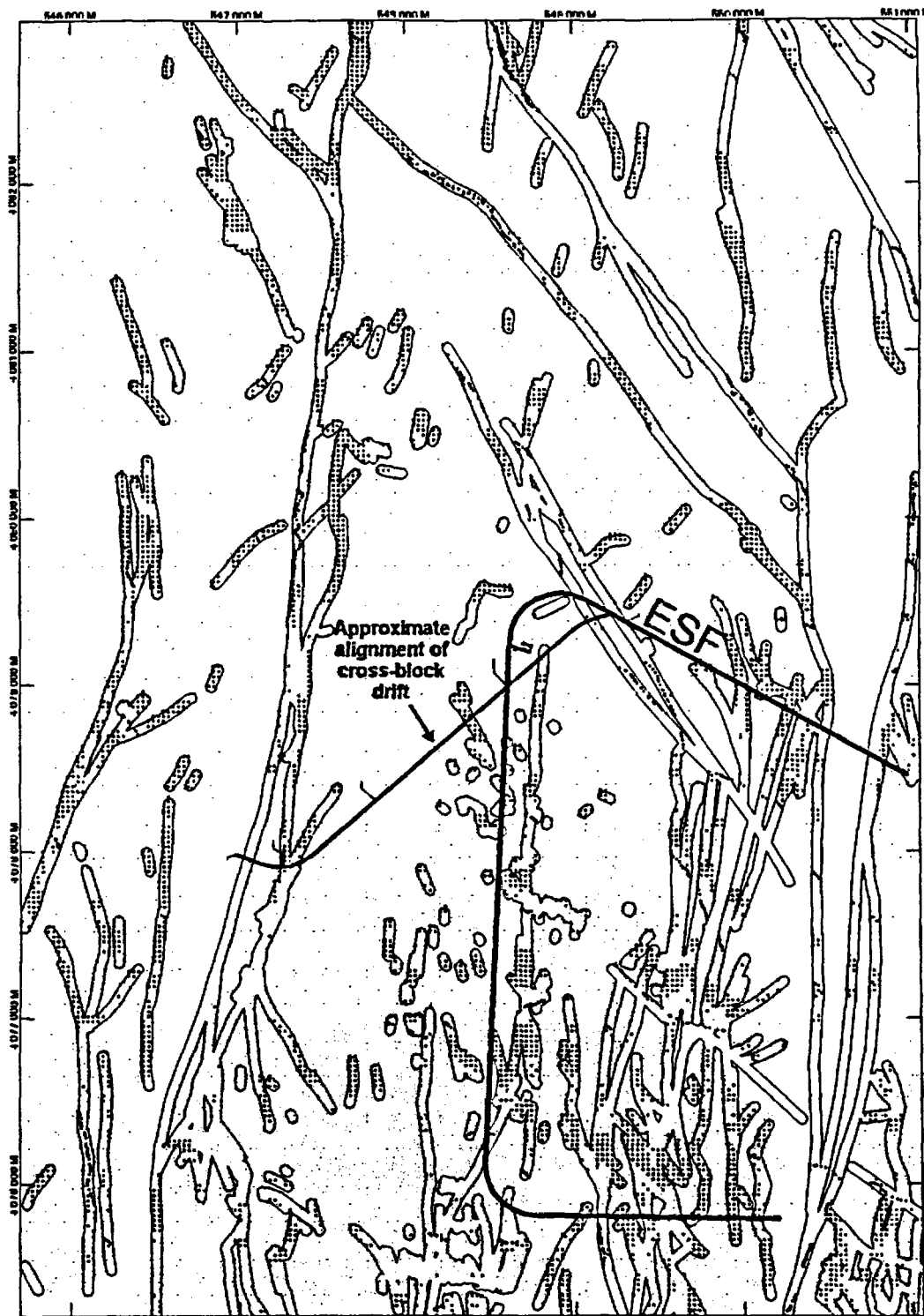


Figure 6-6. Fracture frequency and measured  $^{36}\text{Cl}/\text{Cl}$  ratios for rock samples in the ESF (Sweetkind et al., 1997a). ESF stations are marked in 100-m increments, so that station 10+00 is 1000 m from the north portal. The number of fractures collected by detailed line survey is summed for each 10-m segment of the ESF.



**Figure 6-7.** Areas (shown as dots) for which the infiltration rate exceeds 2 mm/yr above a mapped fault at the surface. Surface fault traces, from the Day et al. (in press) 1:6,000-scale map, are bounded on each side by a 30 m-wide envelope. Surface infiltration rate, using average annual precipitation, from the numerical model of Flint et al. (1996).

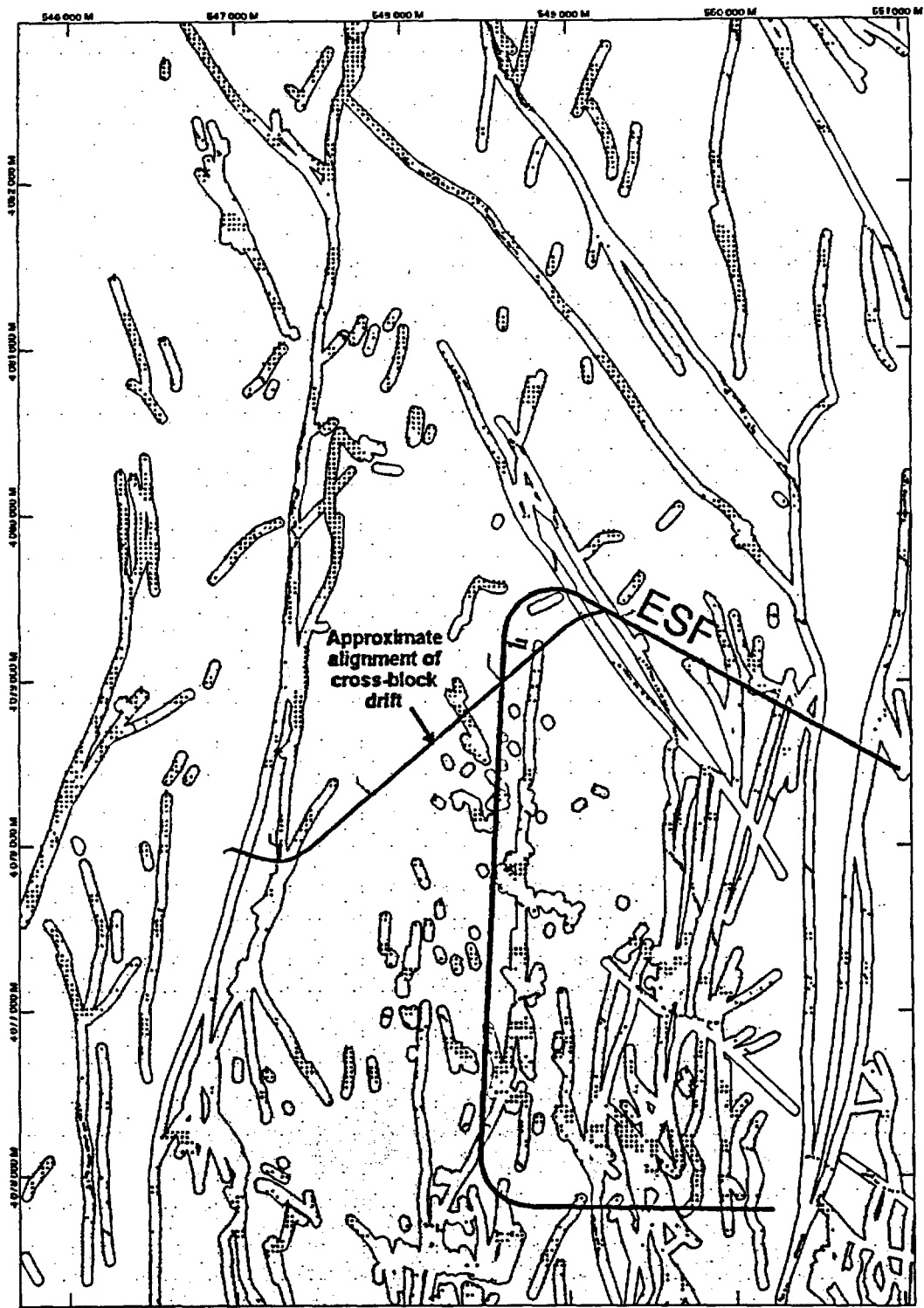
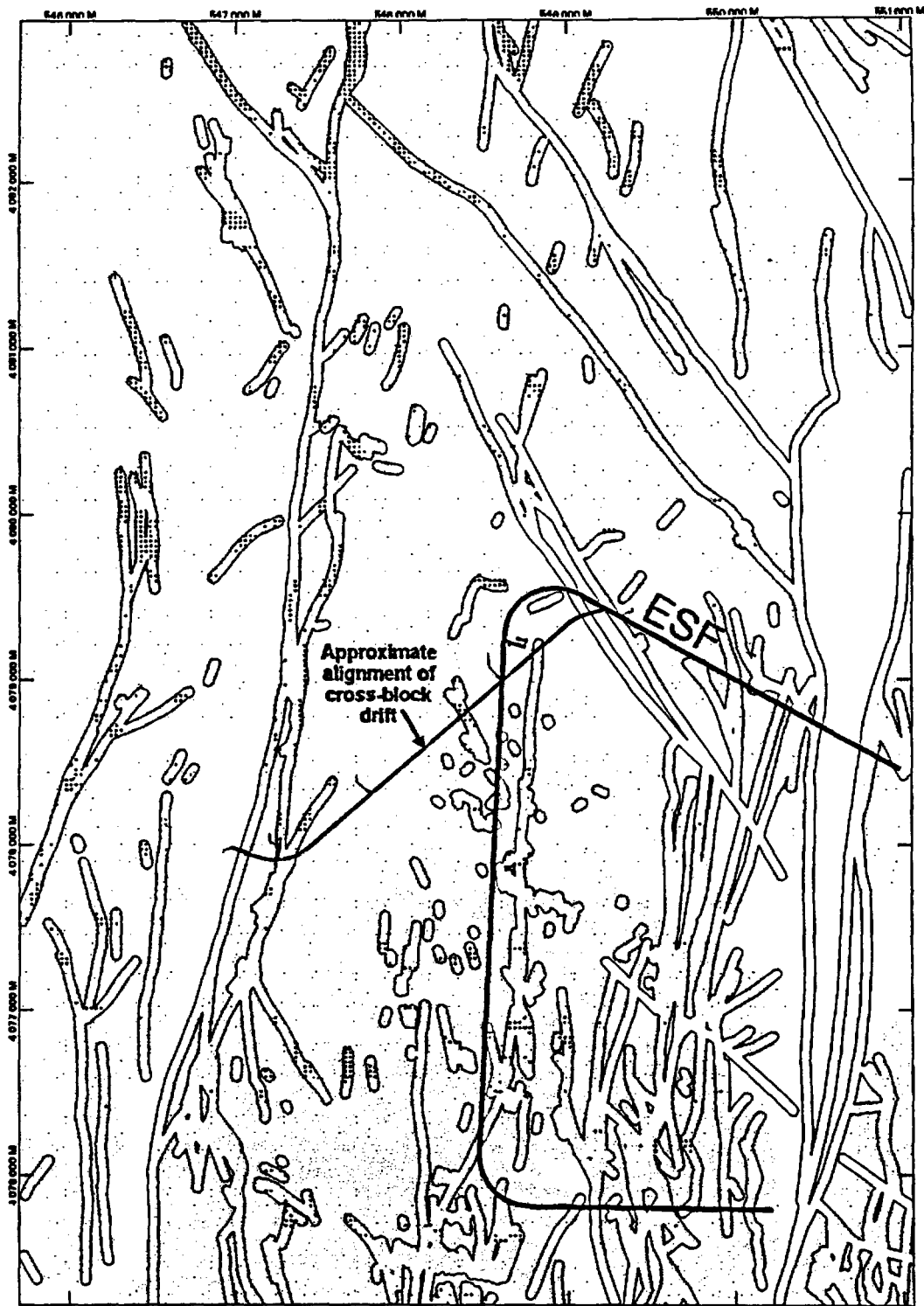


Figure 6-8. Areas (shown as dots) for which the infiltration rate exceeds 5 mm/yr above a mapped fault at the surface. Surface fault traces, from the Day et al. (in press) 1:6,000-scale map, are bounded on each side by a 30 m-wide envelope. Surface infiltration rate, using average annual precipitation, from the numerical model of Flint et al. (1996).



**Figure 6-9.** Areas (shown as dots) for which the infiltration rate exceeds 10 mm/yr above a mapped fault at the surface. Surface fault traces, from the Day et al. (in press) 1:6,000-scale map, are bounded on each side by a 30 m-wide envelope. Surface infiltration rate, using average annual precipitation, from the numerical model of Flint et al. (1996).

## 7. PETROLOGIC AND MINERALOGIC CHARACTERISTICS OF FLOW PATHS

### 7.1 Rationale for petrologic characterization

The discussion in sections 6-3 and 6-4 suggests that fast pathways are distinctive in terms of structural settings, their associated hydrologic properties, and surficial factors affecting infiltration. Another aspect of the investigation is testing whether the attributes of fast pathways contribute to the formation of distinctive secondary mineral assemblages. Mineralogic studies of samples collected for isotopic analysis will help establish whether there is a distinctive geochemical context for fast fluid pathways. It would be cost-effective to develop predictive tools based on infiltration, structure, and mineralogy to guide sampling efforts, particularly during the repository construction phase when a more focused investigation of percolation would be appropriate. Equally important is the insight about small-scale *in situ* differences in infiltration pathways and fracture-matrix interaction to be gained from studies of mineral distributions around fast flow paths.

The mineralogic attributes of zones that might have longer than usual water residence times are also under investigation. Most of the samples that may possibly represent such zones are from the ESF South Ramp (section 6.1). The number of such samples that have been studied in detail is small enough at present that the results are not discussed here on a mineral-by-mineral basis, as has been done for the fast-path samples, but rather are simply summarized in section 7.5.

Studies of void-filling minerals in surficial pedogenic deposits and in the subsurface (e.g., Vaniman et al., 1995; Paces et al., 1996) suggest that the most common secondary minerals deposited during the last few hundred thousand years are calcite, opal, and clays. In subsurface fractures, manganese minerals are widespread and locally abundant, as well. Syngenetic minerals, such as the high-temperature silicates, have not been deposited in the Quaternary, but documentation of their distribution aids in reconstructing the origins of fast pathways.

In addition to minerals deposited from solution, secondary deposits in the ESF rock also include accumulations of transported particulate material. Deposits of clays and coarser-grained materials can be some of the best indicators of saturated versus unsaturated conditions in the fractures and other void spaces at the time of deposition, even though the rock section in question lies in the unsaturated zone. Particulate deposits can also document multiple episodes of fracture aperture dilation to identify zones where fracture continuity and connectivity have been enhanced by rock deformation.

Thus far, the detailed mineralogy and petrology have been described for 57 of the  $^{36}\text{Cl}$  samples, as summarized in this section and in Table 7-1, based on detailed descriptions in Appendix C. These 57 samples include 10 systematic samples plus 47 feature-based ones. Highest priority has been given to the study of samples from known fast paths insofar as they contain unambiguous levels of bomb-pulse  $^{36}\text{Cl}$  (i.e.,  $^{36}\text{Cl}/\text{Cl}$  ratios above  $1250 \times 10^{-15}$ ). Twenty-three of

**TABLE 7-1**  
**Lithostratigraphic and Structural Settings, <sup>36</sup>Cl/Cl Values, and Secondary Mineralogy of ESF Sample Sites**

Sample <sup>1</sup>	Station	Lithostrati- graphic unit	Sampled feature <sup>2</sup>	Corrected <sup>36</sup> Cl/Cl ×10 <sup>-15</sup>	Calcite	Opal <sup>3</sup>	Clay/Mord. <sup>4</sup>	Clay/Mord. 2 or more <sup>5</sup>	Feldspar±Cr. Silica±Fe-Ti oxides <sup>6</sup>	Transported Particulates <sup>7</sup>	Mn minerals	Other mineral(s) <sup>8</sup>
E001	1+98	Tpcpl1?	fault breccia	518 <sup>9</sup>	-	-	●	-	●	●	●	-
E008	1+99.8	Tpcp	fault breccia	2138 <sup>10</sup>	●	-	●	-	●	●	●	-
E010	1+99.8	Tpcp	fault breccia	720	-	-	●	-	?	●	●	-
E011	1+99.8	Tpcp	fault breccia	2378	●	●	?	?	?	●	●	-
E007	2+03	Tmbt1	bedrock	519	-	-	-	-	-	-	-	-
E073	5+04	Tpcpul	fracture	468	-	-	●	-	-	-	●	-
E244	8+38	Tpbt3	fault	488	-	-	-	-	-	-	●	-
E171	8+90	Tpp	below contact	1335	-	-	●	-	-	-	-	●
E172	8+90	Tpbt3/Tpp	contact	637	-	-	●	-	-	-	-	●
E173	8+90	Tpbt3	above contact	806	-	-	?	-	-	-	●	●
E027	11+00	Tptrv1	bedrock	1076	-	-	●	-	●	-	●	-
E028	12+44	Tptrn	cooling jts.	2637	-	-	-	-	●	●	-	●
E029	13+00	Tptrn	bedrock	640	-	-	-	-	●	-	-	-
E030	13+67	Tptrn	cooling jts.	1621	-	-	-	-	●	-	-	-
E031	14+00	Tptrn	shear zone	2398	-	-	-	-	●	-	-	-
E033	14+41	Tptrn	fault breccia	876	●	●	-	-	●	-	-	-
E035	15+05	Tptrn	fracture	628	●	●	●	-	●	-	●	-
E036	16+12	Tptrn	cooling jt.	382	●	●	-	-	●	-	-	●
E037	16+19	Tptrn	fracture	982	-	-	●	-	-	●	-	-
E038	17+00	Tptrn	bedrock	714	-	-	-	-	●	-	●	-
E040	18+96	Tptpul	broken rock	1642	●	-	●	-	●	-	-	-
E041	19+00	Tptpul	bedrock	746	-	-	-	-	●	-	●	-
E042	19+31	Tptpul	breccia	3019	●	-	-	-	-	-	-	-
E044	19+42	Tptpul	breccia	2290	●	-	-	-	●	-	-	-
E045	21+00	Tptpul	bedrock	799	-	-	-	-	●	-	-	-
E046	22+71	Tptpul	fractures	862	●	-	-	-	●	-	-	-
E047	23+00	Tptpul	bedrock	663	-	-	-	-	-	-	-	-
E050	24+40	Tptpul	fault breccia	2579	●	-	-	-	●	-	-	-
E020	24+68	Tptpul	fracture	814	●	●	-	-	●	-	-	-
E052	26+79	Tptpul/tpmn	shear zone	2036	●	-	-	-	●	-	-	-
E058	27+66	Tptpmn	fault breccia	458	-	-	-	-	●	●	●	-
E141	29+00	Tptpmn	bedrock	922	-	-	-	-	●	-	-	-

**TABLE 7-1 (cont.)**  
**Lithostratigraphic and Structural Settings, <sup>36</sup>Cl/Cl Values, and Secondary Mineralogy of ESF Sample Sites**

Sample <sup>1</sup>	Station	Lithostratigraphic unit	Sampled feature <sup>2</sup>	Corrected <sup>36</sup> Cl/Cl ×10 <sup>-15</sup>	Calcite	Opal <sup>3</sup>	Clay/Mord. <sup>4</sup>	Clay/Mord. 2 or more <sup>5</sup>	Feldspar±Cr. Silica±Fe-Ti oxides <sup>6</sup>	Transported particulates <sup>7</sup>	Mn minerals	Other mineral(s) <sup>8</sup>
E142	29+21	Tptpmn	fracture	583	●	-	-	-	-	-	-	-
E144	29+73	Tptpmn	cooling jt.	815	●	-	-	-	-	-	-	-
E149	31+64	Tptpmn	cooling jt.	631	●	-	●	-	-	-	●	-
E150	33+00	Tptpmn	fr. bedrock	1341	-	-	-	-	-	-	●	-
E151	33+16	Tptpmn	lith. cavity	529	●	●	-	-	●	-	-	-
E152	34+28	Tptpmn	fr. bedrock	4105	●	-	-	●	●	-	●	-
E153	34+32	Tptpmn	cooling jts.	3291	●	-	●	-	-	●	●	-
E154	34+71	Tptpmn	cooling jts.	3767	(●) <sup>11</sup>	-	-	●	-	-	●	-
E154	34+71	Tptpmn	breccia	803	(●) <sup>11</sup>	-	-	●	-	●	●	-
E155	35+00	Tptpmn	syst./bedrock	1013	-	-	●	-	●	●	●	-
E156	35+00	Tptpmn	broken rock	626	-	-	-	-	●	-	-	-
E157	35+03	Tptpmn	cooling jts.	(1339)	●	-	-	-	-	-	●	-
E158	35+08	Tptpmn	cooling jts.	(2605)	●	-	-	●	-	-	●	-
E160	35+45	Tptpmn	cooling jts.	3329	(●) <sup>11</sup>	-	-	●	●	●	●	-
E161	35+58	Tptpmn	cooling jt.	(2141)	●	-	-	●	●	-	●	-
E175	35+93	Tptpmn	fault breccia	(2840)	(●) <sup>11</sup>	-	-	●	●	●	●	-
E201	43+63	Tptpmn	cooling jts.	1974	-	-	-	-	●	-	●	-
E202	44+20	Tptpmn	cooling jts.	3463	-	-	●	-	●	-	●	-
E205	45+00	Tptpmn	syst./cool. jts.	1514	-	-	-	-	●	-	●	-
E255	58+77	Tptpmn	below frcts.	140 <sup>12</sup>	-	-	-	-	●	-	●	-
E258	61+92	Tptpmn	fractures	276	-	-	-	●	●	-	●	-
E260	62+05	Tptpmn	fault	261	-	?	-	-	●	-	●	-
E280	66+40	Tptm	fault breccia	238	●	●	-	-	●	-	●	-
E283	67+27	Tpcpv2/1	thin bed	470	-	-	●	-	●	-	-	-
E286	67+87	Tpcpv	fault/graben	475	●	-	-	●	●	-	●	●

See footnotes on following page

TABLE 7-1 (cont.)

<sup>1</sup>Samples were divided into separate splits for isotopic and mineralogic analysis. Mineralogic data were also recorded for the sample sites. In cases where more than one split of a sample was measured for chlorine isotopic ratios, there are separate entries for each analyzed split or the value reported in this table is the highest value obtained.

<sup>2</sup>Abbreviations: cooling jt., cool. jt. = cooling joint; fr. bedrock = fractured bedrock; frcts. = fractures; syst. = systematic sample.

<sup>3</sup>As used here, opal is transparent, colorless to light-colored, and typically fluoresces yellow-green in short-wave UV light. X-ray diffraction analysis of selected samples indicates opal-A.

<sup>4</sup>This category includes clay and/or mordenite. The clay is predominantly smectite, but may include palygorskite.

<sup>5</sup>An entry in this column indicates the presence of two or more distinct deposits of different colors, as identified by binocular microscopy.

<sup>6</sup>This category includes minerals inferred to be of early to late syngenetic origin. Reported occurrences in this category are limited to minerals in growth position on the rock surfaces. Cr. Silica = crystalline silica, including quartz, chalcedony, cristobalite, tridymite, opal-CT.

<sup>7</sup>This category includes physically transported particulates, mostly silt- and sand-size material. Deposits of clay-size material are not included here even though some clays are transported.

<sup>8</sup>This category includes fluorite, zeolite, and unidentified minerals.

<sup>9</sup>Data from Appendix B.

<sup>10</sup>Values in boldface denote samples containing a component of bomb-pulse chlorine ( $^{36}\text{Cl}/\text{Cl}$  values  $> 1250 \times 10^{-15}$ ) inferred to be less than 50 years old.

<sup>11</sup>Calcite was not present in the aliquot for mineralogic characterization but was observed in fractures at the collection site (E154, E160) or in fractures adjacent to the fault (E175).

<sup>12</sup>Italicized values are below  $350 \times 10^{-15}$  and may denote samples with longer water residence times than elsewhere.

the samples in Table 7-1 meet this criterion. Samples whose low  $^{36}\text{Cl}/\text{Cl}$  ratios raise the possibility that water residence times may be longer than at most sites also were assigned a higher priority, and four of the samples in the table are from such sites. The data set that forms the basis for mineralogic interpretation therefore over-represents fast-path and possibly long water-residence samples, a fact that limits our ability to draw conclusions from the mineralogy at this time. Lithostratigraphic terminology in Table 7-1 follows the usage of Yucca Mountain Project Reference Information Base, Chapter 1, Section 1.12, Item a (1995).

## 7.2 History of Secondary Mineral Deposition

Deposition of secondary minerals in and adjacent to fractures and other void spaces began very soon after the ash flows were deposited and has continued in the Quaternary. The general chronology of secondary-mineral deposition has been established by many studies and continues to be refined (e.g., Levy and O'Neil, 1989; Cowan et al., 1993; Levy et al., 1996; Whelan et al., 1996; Paces et al., 1996). The brief summary given here emphasizes aspects of mineral deposition that are helpful for documenting the origins and longevity of transmissive features.

Vapor-phase crystallization in fractures and lithophysal cavities (gas pockets) is a high-temperature process that occurs early in the cooling history of an ash flow deposit. The vapor-phase mineral products are most prominent in the upper portions of the Tiva Canyon and Topopah Spring Tuffs. Late-stage syngenetic minerals that formed at ambient or near-ambient temperature include quartz, chalcedony, opal-CT, and opal-C. Some calcite and opal-A also formed under these conditions (Whelan et al., 1996; Levy, 1993). Many other minerals likely crystallized during the late stages of cooling; among these are smectite, mordenite, heulandite-clinoptilolite, potassium feldspar, apatite, and zircon (Levy et al., 1996).

For the past 11 million years or so since the decline of major volcanic activity near Yucca Mountain, the rocks of the ESF have remained in the unsaturated zone (Levy, 1991). The rocks did not experience the pervasive diagenetic or hydrothermal alteration that affected rocks at greater depth. During at least the last few hundred thousand years, secondary-mineral deposition of calcite, opal, and clay represents the main mineralogic modification in the shallow unsaturated zone (e.g., Vaniman et al., 1995; Paces et al., 1996). Many geochemical attributes of the calcites reflect soil-zone processes and interactions with infiltrating water (Whelan and Stuckless, 1992). The extent to which clays in the unsaturated zone, particularly in the PTn, are the products of late-syngenetic alteration versus localized diagenetic alteration related to perched water is under investigation (Levy and Chipera, 1997).

### 7.3 Distributions of secondary minerals

#### 7.3.1 Calcite

Examination of the subset of analyzed samples for which mineralogic data are available shows that calcite is commonly present at sample sites that have received infiltration during the last 50 years (Table 7-1), with 15 of 23 bomb-pulse values obtained for samples containing calcite. By comparison, calcite is present in 11 of the 34 samples in which no discernible bomb-pulse signal is present, or 11 out of 27 if systematic bedrock samples are excluded. Between Sta. 17+00 and 36+00, calcite is present at 20 of the 23 feature-based sample sites, but 14 of the feature-based sites in this interval are also bomb-pulse sites. Thus, in intervals where calcite is not common, bomb-pulse sites are somewhat more likely to contain calcite; the interval where calcite is common also contains a relatively large number of bomb-pulse sites. These associations certainly do not by themselves provide a highly reliable basis to predict the locations of fast paths. The data base of mineralogic data is not yet large enough for statistical analysis, but a few interesting observations arise from a comparison with the line-survey data on calcite distribution in the ESF (Paces et al., 1996). The line survey has identified an interval between Stations 12+00 and 17+00 in which calcite is relatively common and an interval between Stations 17+00 and 22+00 in which it is rare. Three  $^{36}\text{Cl}$  samples collected between Stations 14+00 and 17+00 do contain calcite, but four samples collected between Stations 12+00 and 14+00, including three bomb-pulse samples, contain no calcite. The six samples from Stations 17+00 through 22+00 include three bomb-pulse samples, all of which contain calcite. These comparisons are far from conclusive, but they suggest the possibility that in some intervals the mineralogy of fast paths shows trends contrary to general patterns of mineral distribution. A more recent report on the distribution of calcite and opal in fractures (Paces et al., 1997) does not depict the two minerals separately, so we cannot make comparisons of line-survey data and calcite occurrences in  $^{36}\text{Cl}$  samples beyond Station 30+00.

We have observed in a qualitative sense that calcite deposits in many of the bomb-pulse samples have thicknesses less than about a millimeter. In some cases, this reflects the size of the aperture in which the calcite grew. At least some examples exist of thin calcite coatings in samples with sufficient pore spaces for thicker coatings to have grown; sample E008, a Bow Ridge fault breccia, is one example. These calcite deposits are much thinner than the several-cm-thick aggregates from which multiple layers have been dated by  $^{230}\text{Th}/\text{U}$  methods (Paces et al., 1996). The thin calcite coatings may record shorter segments of depositional history, or the depositional layers may be thinner due to slower deposition rates than those calculated for other ESF sites (Paces et al., 1996). Either explanation would have significant, though different, implications for differences between bomb-pulse transmissive features and other calcite deposition sites. For example, if fast-path calcites record a shorter and mostly more recent depositional history, then geochronologic data from these samples could help elucidate the initiation and longevity of the fast-path function.

### 7.3.2 Opal

Amorphous opal (opal-A) is much less common than calcite in the samples and is associated with only one of the bomb-pulse samples from the Bow Ridge fault zone (E011). Furthermore, only seven of the 42 fractured or brecciated samples (16%) contain opal, always with calcite. This finding was unexpected because the line-survey data of Paces et al. (1996) suggest that opal, although less abundant and less widely distributed than calcite, is still a very common secondary mineral in the ESF, at least as far as Sta. 30+00 (the fracture mineral abundance data set of Paces et al., 1997, extends to Sta. 70+00 but does not give separate abundance data for calcite and opal). Because opal, where present, generally occurs only with calcite (Whelan et al., 1996), the apparently low abundance of opal in our sample set could be partly linked to processes responsible for the lesser thicknesses of calcite deposits in fast pathways.

### 7.3.3 Clays

Clays, predominantly smectites, are nearly ubiquitous in the major rock units of the ESF. Bulk samples of the devitrified Tiva Canyon and Topopah Spring Tuffs have smectite contents of about 1 to 10 wt %, although values less than 3 wt % are most common (Bish and Chipera, 1989; Chipera et al., 1995; Chipera et al., 1996). The clay represented by the bulk analyses of these rocks is disseminated throughout the matrix. As the result of *in situ* alteration, the matrix clay content of the PTn can be as high as ~95 wt % (Levy et al., 1996).

Except for the samples of various Tpbt and Tpp bedrock (PTn hydrogeologic unit), the clays reported in Table 7-1 are all fracture or breccia clast coatings or fault fillings, rather than matrix components. The presence of these deposits is assumed to result from aqueous transport of fine clay particles within the fracture network because clays would not be readily released from the local densely welded rock matrix. The actual sources of the clays and the distances of transport have not been determined. Multiple clay deposits are distinguishable by color and, in some cases, by differences in distribution on the rock surfaces. These distinctive deposits were derived from different source materials and may have been transported and deposited at different times.

The potential implications of clay deposits coating fractures or breccia clasts are twofold. First, the constituents of these clay deposits were transported as particulates rather than as solutes and are unlikely to have been derived directly from the adjacent rock matrix. Such transport requires a significant component of fluid flow in the fractures that was distinct from any influx that might be received from the matrix. Second, the heterogeneity of clay deposits in a sample indicates that the sample site has received aqueous input from rocks that experienced different alteration processes. We hypothesize that input from multiple sources is somewhat more likely to occur along fluid pathways offering the greatest continuity of fracture transport, possibly across lithologic unit boundaries, and therefore the greatest accessibility to different clay sources. The existence of a component of fluid traveling almost exclusively through fractures, with a high interunit continuity of flow path, is a predicted attribute of fast pathways. This attribute is also

important for the subsidiary fractures that distribute fast flow away from the primary transmissive feature, usually a fault. Further observations related to the significance of clay coatings are contained in section 7.4.

For the samples included in Table 7-1, clay/mordenite is present in 23 out of 54 samples (excluding matrix clays in bedded tuffs) or 43%. Eleven of the 22 bomb-pulse samples (excluding one PTn sample), or 50%, contain clay/mordenite. The mineralogic data set, taken as a whole, does not indicate an association between fast paths (defined by the presence of bomb-pulse  $^{36}\text{Cl}$ ) and the presence of clay/mordenite. However, in the interval from Sta. 34+28 to Sta. 35+93 (Sundance fault) there is a high incidence of both bomb-pulse  $^{36}\text{Cl}/\text{Cl}$  values and clay/mordenite. Eight out of 11 samples (73%) have the bomb-pulse signature, nine out of 11 samples contain clay/mordenite, and seven of the eight bomb-pulse samples (88%) contain clay/mordenite. When the thicknesses of the clay coatings on fractures are taken into account (from the descriptions in Appendix C), the coatings in the Sta. 34+28 to 35+93 interval stand out as tending to be thicker than elsewhere. Further details of the clay coatings near the Sundance fault are given in section 7.4.

#### *7.3.4 Transported Particulates*

For particulates larger than clay particles, it is possible in many cases to determine whether they are different from the local bedrock and have therefore been transported to their present location from elsewhere in the geologic section. It is relatively easy to recognize samples in which the fine particulates are highly enriched in vapor-phase or hydrothermal minerals relative to their abundance in the local bedrock, and this is a good preliminary criterion for documenting evidence of particulate transport. Vapor-phase particulates are typically mixtures of very well formed <1-mm crystals of tridymite, cristobalite, alkali feldspar, quartz, biotite, Fe-Ti oxides, and hematite. Compared to a devitrified bedrock, vapor-phase materials may also contain a higher proportion of silica minerals (tridymite, cristobalite, and quartz) relative to alkali feldspar. Table 7-2 shows the mineralogy of two textural constituents of the Bow Ridge fault breccia in ESF sample E008. The data suggest that the powdery white material that acts as a weak cement has a higher ratio of silica minerals to feldspar than do the calcite-cemented bedrock breccia clasts. However, a high uncertainty associated with the feldspar content of the white material renders the comparison statistically insignificant. The errors of measurement could be reduced by the use of longer counting times for the X-ray diffraction analysis. At this site within the lower lithophysal zone of the Tiva Canyon Tuff, local sources exist for the vapor-phase particulates and therefore they need not have been transported very far. However, a substantial amount of vapor-phase particulates had to be transported, probably from overlying rocks rich in vapor-phase material, to form the ubiquitous white coatings on the bedrock breccia clasts in the fault zone. The presence of translocated particulates within a flow path attests to the existence of connected pore spaces with apertures large enough to permit the passage of the particulates.

Sample E037-2, from Sta. 16+19 in the Topopah Spring Tuff, offers a dramatic example of

**TABLE 7-2**  
**Quantitative and Qualitative X-Ray Powder Diffraction Results for Mineralogy Samples from the ESF**

Sample	Smectite	Clinoptil- olite	Mord- enite	Glass <sup>1</sup>	Opal-A <sup>1</sup>	Opal-CT	Tridymite	Cristo- ballite	Feldspar	Quartz	Calcite	Total
<i>Bow Ridge Fault</i>												
E008 breccia	4±2 <sup>2</sup>	— <sup>3</sup>	—	—	—	—	3±1	6±1	23±4	4±1	60±6	100±7
E008 <150µm white coating	16±6	—	—	—	—	—	10±2	9±4	46±10	11±2	7±2	100±13 <sup>4</sup>
E008 calcite-opal cement	—	—	—	—	present	—	—	—	—	—	present	—
<i>PTn, North Ramp</i>												
E171 Tpbt3	7±2	—	—	72±4	—	—	—	1±1	18±3	1±1	—	100±4 <sup>5</sup>
E172 Tpbt3/Tpp	18±5	—	—	59±6	—	—	—	1±1	19±3	2±1	—	100±6 <sup>5</sup>
<i>Tsw, Main Drift</i>												
E158 coating on cooling joints	43±13	—	42±21	—	—	—	—	8±1	—	—	—	93±25

<sup>1</sup>The identities of glass and opal-A, indistinguishable by standard X-ray diffraction analysis, were resolved by petrographic examination.

<sup>2</sup>Errors are conservative 2-sigma values.

<sup>3</sup>— " = not detected, or, for total of semi-quantitative analysis, not applicable.

<sup>4</sup>Includes 1±1 weight % hematite.

<sup>5</sup>Includes 1±1 weight % mica.

particulate transport. The wall rock is densely welded, devitrified tuff, but the fracture filling consists of devitrified rock fragments in a fine-grained matrix of glass pyroclasts. Several sequences of graded bedding are preserved within the fillings. Graded bedding is produced by settling of particles in a water-filled fracture. The glassy constituents came from tens of meters higher in the stratigraphic section.

Despite the evidence of fluid flow sufficient to transport silt-size particulates tens of meters in the fracture, this sample does not have a bomb-pulse  $^{36}\text{Cl}/\text{Cl}$  signature. A number of factors unrelated to the hydrologic properties of this specific fracture may be responsible. The most likely explanation is that the particulate fillings were deposited before the PTn nonwelded tuffs were emplaced on top of the Topopah Spring Tuff. In numerical simulations of infiltration, the PTn dampens out the effects of episodic high-infiltration events (Fabryka-Martin et al., in press [a]) so that particulate-laden flow sufficient to saturate a fracture in an underlying unit would be unlikely to occur. Remobilization of nonwelded pyroclasts would also have been more feasible before the tuffs were compacted by the addition of new overburden. This one-time fast path may have been isolated from the surface by later pyroclastic deposition, and a throughgoing connection may never have been re-established.

The significance of transported particulates is similar to that of clay deposits, described above, but possibly less valuable as a fast-path recognition criterion. As in the E037-2 example, particulate deposits may relate more to former than to present fast pathways as far as the Topopah Spring Tuff is concerned.

### *7.3.5 Feldspar, Crystalline Silicas, and Fe-Ti oxides*

This category of syngenetic minerals includes alkali feldspar, tridymite, cristobalite, quartz, opal-CT (opal with short-range cristobalite and tridymite ordering), opal-C (opal with short-range cristobalite ordering), chalcedony (fibrous microcrystalline quartz), hematite, and other Fe-Ti oxides. Each of the tuff units exposed in the ESF contains some or all of these phases that formed as it cooled. In particular, feldspar, tridymite, cristobalite, and the Fe-Ti-oxides are known as vapor-phase minerals deposited at high temperatures very early in the cooling history of a tuff (e.g., Carlos, 1985). The main significance of syngenetic minerals is that their presence in growth position on fracture walls, breccia fragments, or other secondary pore surfaces establishes the early origins of these transmissive features. For example, the vapor-phase-altered breccias at Sta. 35+93 (sample E175) document the early intraformational origin of this zone of deformation which is now part of the Sundance fault.

### *7.3.6 Manganese Minerals*

No definitive mineral identifications have been made for the generally <1-mm deposits of Mn minerals present in many of the samples collected for this study. X-ray diffraction and scanning-electron microscopic studies of drill core of the Tiva Canyon and Topopah Spring Tuffs in the

unsaturated zone have identified rancieite (Ca-bearing hydrous Mn oxide) and lithiophorite (Li-, Al-bearing hydrous Mn oxide) as the dominant Mn phases (Carlos et al., 1993). Notations of the presence of Mn minerals, as used in Appendix C and Table 7-1, refer only to Mn minerals on the surfaces of rock materials. Manganese minerals within the rock matrix cannot be detected by stereomicroscopy.

For samples from the Topopah Spring Tuff (Sta. 12+44 through 35+93, Table 7-1), a transition from uncommon to nearly ubiquitous Mn minerals corresponds very approximately to the boundary between the upper lithophysal and middle nonlithophysal zones. This boundary marks a downsection change from less frequent and shorter fractures to more frequent and longer ones. This observation is consistent with core-based observations of Carlos et al. (1993) that Mn coatings are especially abundant on smooth-surfaced cooling joints, which are most common in the middle nonlithophysal zone.

The link between Mn mineral occurrence and fracture characteristics associated with syngenetic zonation implies that these minerals are very old and therefore unlikely to be good predictors of present fast pathways in the unsaturated zone. There is a possibility, however, that Mn minerals can be indicators of fracture-matrix interactions, colloid transport in fractures, and the role of aqueous emulsions on fracture surfaces in unsaturated-zone transport. For example, some manganese deposits on fracture surfaces surround or radiate from mafic minerals or Fe-Ti oxides in the rock matrix within a few mm of the fracture, indicating local derivation and short-range transport of Mn during water-rock interaction adjacent to fractures.

#### 7.4 Textural studies of breccia/wall rock paired samples

The kilogram-size samples required for isotopic analysis preclude our investigating the fine-scale spatial distribution of bomb-pulse  $^{36}\text{Cl}$  within samples. We have made preliminary attempts to detect variations in isotopic ratios for texturally distinct materials collected at a single site (Table 7-3). The goal is to detect differences related to fragment size in breccia samples or differences between breccia and adjacent wall rock as possible indicators of local factors that affect water flow. Six breccia samples from Sta. 13+00 to 36+00 which had been collected into single sample bags were manually sifted in the laboratory into separates with particle sizes either larger or smaller than ~0.5 cm. One sample from Sta. 56+93 was separated into fractions with particle sizes larger or smaller than 2 mm. The finer fractions were processed for analysis without further size reduction. For the coarser fractions, the larger rock fragments were individually crushed with a steel plate and hammer to a maximum size of ~2 cm, then processed for analysis. Eleven additional sample pairs from ~Sta. 34+00 to 77+00 represent a variety of texturally distinct materials, such as breccia and the adjacent rock or cooling joint surface or separate generations of fault fillings, collected into separate bags. The texturally distinct materials of each pair were processed and analyzed separately.

Table 7-3. Paired anion and chlorine-36 analyses of ESF rock samples

Sample ID	Approx ESF station	Feature	Analyzed aliquot	Leached mg Cl kg <sup>-1</sup> (Note 1)	Br/Cl x 10 <sup>-3</sup>	SO <sub>4</sub> /Cl	% Cl from construction water (Note 2)	Corrected <sup>36</sup> Cl/Cl x 10 <sup>-15</sup> (Note 3)
E030-1 E030-2	13+67	Cooling joints	Breccia < 0.5 cm Breccia > 0.5 cm	1.02 0.54	261 561	0.8 1.8	8 18	697 ± 35 1634 ± 85
E031-1 E031-3	14+00	Shear zone	Breccia > 1 cm Breccia < 1 cm	0.60 0.72	51 38	1.8 1.7	1 1	1038 ± 35 2398 ± 191
E042-2 E042-3	19+31	Fault zone	Breccia > 0.5 cm Breccia < 0.5 cm	0.62 0.63	142 100	1.7 1.8	4 3	3023 ± 94 1837 ± 65
E154-1 E154-3	34+71	Cooling joints	Breccia Wall rock	0.33 0.23	177 156	1.9 1.3	6 5	803 ± 42 3794 ± 120
E158-1 E158-3	35+08	Cooling joints	Breccia < 0.5 cm Breccia > 0.5 cm	0.74 0.46	865 1009	2.4 2.3	29 33	1113 ± 58 2671 ± 158
E161-1 E161-3	35+58	Cooling joint	Breccia < 0.5 cm Breccia > 0.5 cm	0.79 0.54	457 509	1.3 1.1	15 17	1951 ± 103 2169 ± 80
E175-1 E175-3	35+93	Fault	Breccia > 0.5 cm Breccia < 0.5 cm	0.27 0.27	1130 1189	1.5 1.7	37 39	2840 ± 231 1674 ± 141
E176-1 E176-3	36+55	Fault	Breccia > 0.5 cm Breccia < 0.5 cm	0.88 1.04	150 179	1.1 1.1	5 6	887 ± 27 604 ± 24
E179-1 E179-3	37+68	Cooling joint	Breccia Wall rock	1.46 1.51	395 206	1.7 0.9	13 7	363 ± 22 397 ± 13
E222-1 E222-2	42+55	Shear sets	Gouge Wall rock	3.80 2.90	116 138	1.4 1.3	4 4	605 ± 18 531 ± 16
E226-1 E226-2	49+56	Cooling joint	Breccia Wall rock	1.13 1.05	272 160	1.4 1.2	9 5	451 ± 20 456 ± 20
E231-1 E231-2	51+07	Cooling joints	Wall rock Breccia	0.50 0.50	304 364	1.3 1.3	10 12	709 ± 30 530 ± 26
E242-1 E242-2	56+93	Cooling joint	Breccia > 2 mm Breccia < 2 mm	0.70 0.93	269 252	1.5 1.5	9 8	664 ± 30 1117 ± 49
E256-1 E256-3	59+00	Systematic	Breccia Wall rock	0.52 1.65	1186 584	2.3 1.4	39 19	347 ± 41 361 ± 22
E286-1 E286-4	67+87	Fault zone	Clay frac fill Wall rock	2.19 0.67	38 167	3.0 6.9	1 5	475 ± 22 645 ± 29

Sample ID	Approx ESF station	Feature	Analyzed aliquot	Leached mg Cl kg <sup>-1</sup> (Note 1)	Br/Cl x 10 <sup>-3</sup>	SO <sub>4</sub> /Cl	% Cl from construction water (Note 2)	Corrected <sup>36</sup> Cl/Cl x 10 <sup>-15</sup> (Note 3)
E323-1 E323-3	75+54	Cooling joints	Breccia Wall rock	3.37 4.40	119 34	1.3 0.9	4 1	465 ± 17 413 ± 19
E324-1 E324-3	75+78	Fault	Breccia Wall rock	5.42 4.46	25 38	2.1 1.2	1 1	418 ± 31 322 ± 13
E325-1 E326-1	76+30	Fault	Breccia Wall rock	2.34 4.65	72 62	1.0 1.4	2 2	380 ± 20 423 ± 9
E328-1 E328-3	76+76	Fault	Breccia < 1 cm Breccia > 1 cm	1.28 0.62	160 68	2.5 2.5	5 2	334 ± 15 445 ± 20

Notes:

1. Analytical data from Appendix B.
2. The concentration of Cl leached from the sample is only a qualitative indicator of the sample's Cl content. Rock samples were leached for 48 hours in deionized water using a water:rock weight ratio of 1:1. Because the focus of this activity is generally on determining anion ratios and isotopic ratios, no attempt is made to maximize the yield of the leaching process, which is probably quite variable.
3. The Br/Cl ratio of the leached salts is used to estimate the proportion of Cl derived from construction water, assuming that meteoric salts and construction water are the only two significant sources of Cl in a sample (see Appendix B footnotes).
4. <sup>36</sup>Cl/Cl ratios reported in this table have been adjusted for the assumed presence of construction water (see Appendix B footnotes).

Several factors may potentially complicate the comparison of isotopic results for paired samples. Even weakly cemented fine breccia fragments can end up in the coarse breccia fraction during the size separation process, obscuring any existing isotopic differences between size separates. Differences between paired samples in the amount of size reduction (i.e., fragment breakage) required to prepare a sample for leaching may lead to a systematic difference in the proportion of rock chloride to infiltration-derived chloride in the leachate. Fine-grained samples would require little or no size reduction, minimizing the creation of newly exposed rock surface, whereas coarser material would require the most reduction and consequently would have more new rock surface and associated rock chloride exposed for leaching. The sulfate content of sample leachates – expressed as the ratio  $\text{SO}_4/\text{Cl}$  – may serve as a guide to differences in the amount of rock chloride released into the leachates. We are currently exploring the value of sulfate as an indicator of rock chloride contamination (section 4.2.5 and 4.4.3).

Our attempts to investigate differences in the bomb-pulse  $^{36}\text{Cl}$  content of fracture zones or breccias and adjacent wall rock are still in the developmental stage, in terms of both sample preparation and data interpretation. The choice of 0.5 cm as the criterion for separating breccia samples into coarse and fine fractions does not result in the production of separates with any true genetic significance because it does not consistently separate "wall rock" from "fault gouge," or "broken but intact rock" from "mineralogically altered gouge," or "bedrock fragments" from "cement." Despite this cautionary note, the paired analyses of coarse and fine fractions or of broken wall rock and adjacent breccia from Stations 13+67 through 35+93 show a consistent pattern of higher  $^{36}\text{Cl}/\text{Cl}$  values in the coarse fractions (Fig. 7-1 and Table 7-3). All of the coarse-fraction values and about half the fine-fraction values in this interval have  $^{36}\text{Cl}/\text{Cl}$  ratios above  $1250 \times 10^{-15}$ , which is the threshold value indicating the unambiguous presence of bomb-pulse  $^{36}\text{Cl}$ . Samples from Sta. 36+55 and beyond have lower values and generally smaller differences between the ratios measured for the different size separates.

Petrologic and mineralogic examination of the analyzed separates are in progress, but a few generalized observations may be relevant to the isotopic results. The baseline interpretation supported by the results from Stations 13+67 through 35+93 is that the fluids occupying accessible pore spaces of the fast fluid pathways were not in equilibrium with respect to the  $^{36}\text{Cl}$  isotopic signal. Because these samples all represent active fast pathways that have apparently received infiltration from the surface within the past 50 years, and because the isotopic composition of the infiltration they receive has changed significantly over this short period due to input of bomb-pulse  $^{36}\text{Cl}$ , isotopic disequilibrium within the fluid pathway is readily detectable. In areas of the ESF that have received no detectable bomb-pulse  $^{36}\text{Cl}$  input and where ground-water travel times may have been significantly longer, as indicated by lower  $^{36}\text{Cl}/\text{Cl}$  ratios, the changes of isotopic composition in the infiltrating water moving through these rocks probably occurred so gradually over this period that a lack of isotopic equilibrium between matrix and fracture porewater would not be detectable by a comparison of their  $^{36}\text{Cl}$  signals.

The wall rock and breccia subsamples E154-3 and E154-1, with  $^{36}\text{Cl}/\text{Cl}$  values of  $3767 \times 10^{-15}$  and  $803 \times 10^{-15}$ , respectively (Figure 7-1), differ substantially with regard to rock fragment sizes.

Pervasive multidirectional fracturing of the bedrock has broken it into intact rock domains of ~10 cm dimensions. The breccia deposit, bounded by two cooling joint faces oriented 031/86W, consists of ~1 cm to <0.1 mm fragments and contains additional translocated silt- and clay-size material (<~0.1 mm) near the outer edges of the deposit. With a relatively fine grain size and a porous clastic texture, the breccia should have hydrologic properties approaching those of a nonwelded tuff in which slower matrix flow predominates over fracture flow. Fluids entering the breccia deposit may travel through tortuous intergranular pathways.

The nature of the interfaces between the rock fracture surfaces and the breccia deposit provides indications of the long-term importance of these features as fluid pathways. The 1 mm-thick clay coating on the outer surfaces of the breccia deposit is several times thicker than the similar coatings on breccia clasts and wall-rock blocks. The clay coatings did not originate *in situ*, but rather had to be transported to their present locations by water. The greater thickness of the clay coating on the breccia deposit could reflect a larger aperture between the wall rock and the breccia deposit than between either wall-rock blocks or breccia clasts, allowing the interface to accommodate a thicker clay coat. In addition, the interface may have received more fluid input than the breccia deposit or the unmodified fractures within the bedrock. Clearly, these two potential factors are not mutually independent because a fluid pathway with larger aperture and greater continuity would likely receive more influx.

The existence of finer-grained translocated material in the outermost few mm of the breccia deposit indicates that the fracture or fractures hosting the deposit experienced mm-scale dilation after the main portion of the deposit was formed. Through the processes of compaction and clay deposition, the breccia gradually developed sufficient cohesion to prevent the component clasts from totally collapsing into newly opened space as the fracture dilated. Later dilation provided space for transport and deposition of the 1-mm clay coating on the outer surfaces of the breccia deposit.

In summary, it appears that repeated dilation occurred as this fracture/breccia system accommodated tectonic extension. By means of this process, a fracture pathway could be maintained along the interface between the bedrock and the breccia that allows at least some percolating water to bypass the breccia. The possible role of the clay coatings in restricting access of fracture fluids to either the breccia or the wall rock is uncertain, and no special attempt was made to separate the coatings from either subsample. It may be feasible to investigate these factors in detail in the region of the proposed E-W drift north of the Sundance fault, comparable to the E154 location.

## **7.5 Discussion and conclusions about petrologic and mineralogic trends**

The mineralogic and textural data collected so far have not defined generally applicable, distinctive characteristics of either fast-path or long water-residence sites in the ESF. These special infiltration cases apparently represent relatively minor variations in the hydrologic and

geochemical environment of the unsaturated zone, especially when the effects of infiltration, as represented by the mineralogy, are averaged over very long periods of time. Specific examples of fast-path systems, however, may be distinguished by characteristic differences in mineral abundance. The Sundance fault and associated subsidiary flow paths constitute the best example of distinctive mineralogy. The two mineralogic characteristics are the presence of calcite and thick clay/mordenite fracture coatings. Both of these attest to the particularly high fracture connectivity in the Sta. 34+28 to 35+93 interval north of the Sundance fault. The thicknesses and textures of the clay coatings suggest that the apertures of cooling joints were increased by minor tectonic movement shortly after the Topopah Spring Tuff was deposited. The widespread occurrence of calcite precipitates in this interval also indicates excellent inter-fracture and fracture-fault connectivity. These findings support the conclusions from the structural analysis of the Sundance fault zone in section 6.4: the vicinity of the Sundance fault is distinguished, not only by the presence of an additional local fracture set, but also by the mineralogic evidence for multiple episodes of fracture dilation and extension.

The secondary mineralogy of samples with  $^{36}\text{Cl}/\text{Cl}$  ratios less than  $350 \times 10^{-15}$ , based on four feature-based South Ramp samples, is generally similar to that of samples with higher ratios. Syngenetic minerals (feldspar, crystalline silica, Fe-Ti oxides) and Mn minerals are present in these samples just as they are in other samples from the same lithostratigraphic subunits. One of the four samples contains calcite, which is comparable to or slightly less than the calcite abundance in samples in which bomb-pulse  $^{36}\text{Cl}$  has not been detected. Such comparisons will be more meaningful when mineralogic data are available for a larger proportion of the full sample set.

Mineralogic data collected from ESF South Ramp samples by Levy and Chipera (1997), including some sites sampled in parallel with the  $^{36}\text{Cl}$  studies, may help identify some of the fundamental reasons why zones of possibly longer-than-usual water residence time exist and why they are most common in the South Ramp. The unstable minerals kenyaite (hydrous sodium silicate) and moganite (monoclinic crystalline silica) were documented along fractures and faults in the Tpcpv (equivalent to the uppermost PTn hydrogeologic unit) at Stations 75+07 and 75+20 (E320, Appendix A). Kenyaite has been tentatively identified in drill hole USW GU-3 (Carlos et al., 1995), and moganite has not been previously identified at Yucca Mountain. High activities of alkalis, sulfates, or both may play a role in the crystallization of both minerals (Eugster, 1967; Heaney and Post, 1992). At Yucca Mountain, these minerals are associated with other secondary minerals that probably formed by water-rock interaction during the cooling of the Tiva Canyon Tuff, an alteration episode that affected the tuff in the southern part of the mountain. In this part of the mountain, there was local development of pore fluids with extremely saline, alkaline compositions. These fluids must have evolved in a rock-fracture system that inhibited the intermixing of pore fluids traveling along different pathways through the rock unit. We do not know the specifics of how this system might have differed from conditions further north, other than structural and mineralogic evidence that the southern parts of Yucca Mountain and Busted Butte experienced faulting and fracturing during the cooling of the Tiva Canyon Tuff.

Kenyaite and moganite almost certainly are not in equilibrium with present pore-fluid chemistry in the PTn unit, based on pore-fluid composition data for the ESF North Ramp (Table 4-15) or the chloride contents of rock leachates for South Ramp samples (Appendix B). The survival of these minerals may be partly attributable to arid conditions, as suggested by Heaney and Post (1992). The distributed infiltration model of Flint et al. (1996) generally assigns lower net infiltration values to the ESF south ramp and GU-3 areas than to more northerly areas (Appendix D). This relative aridity could be a factor contributing to the survival of unstable minerals, but there is no evidence that it has existed for the last 12 million years. The occurrences of the unstable minerals with coatings or intergrowths of quartz may have offered some protection from mineral/water interaction.

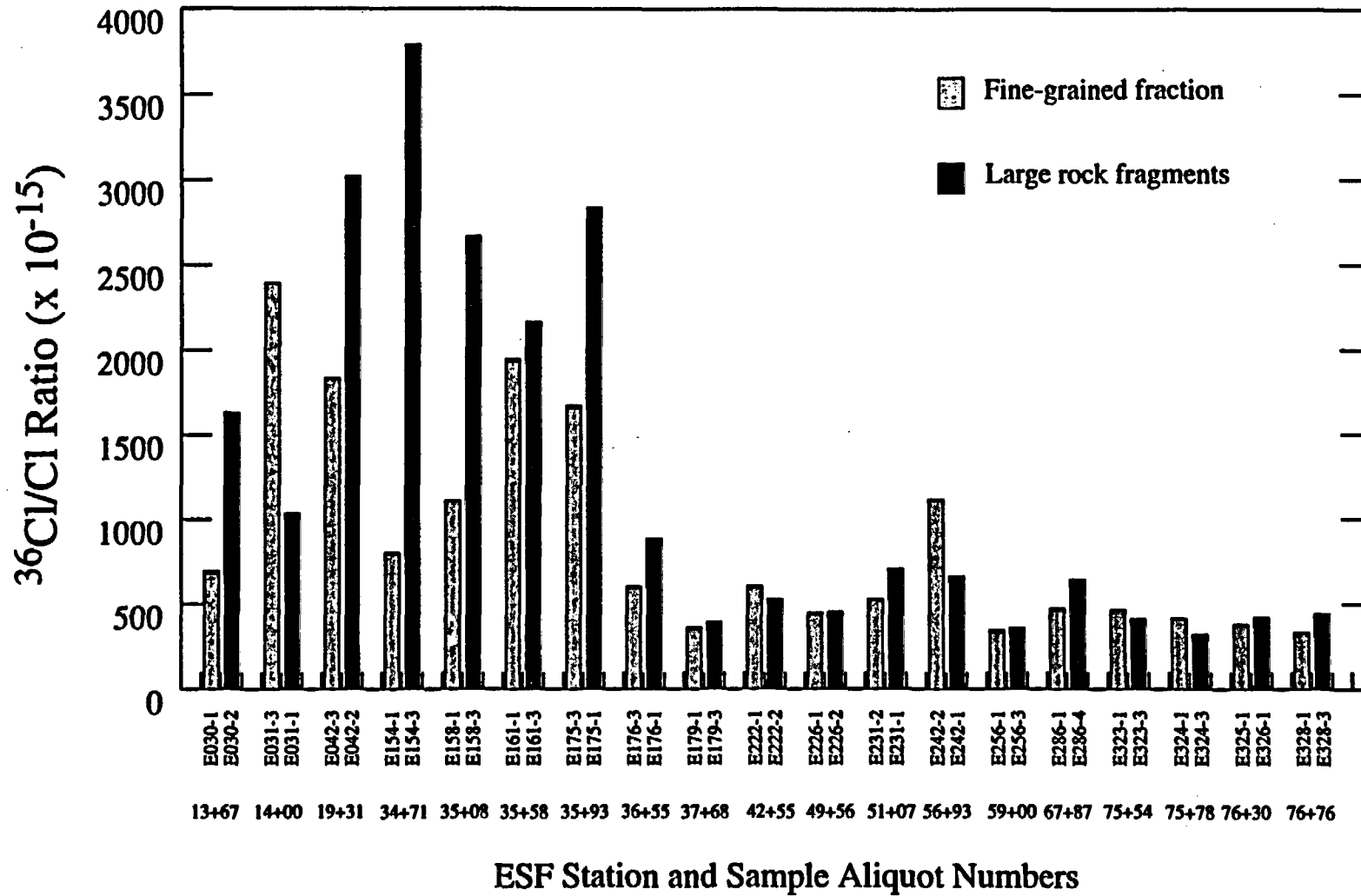


Figure 7-1. Analytical results for paired size separates. Each pair was collected at a single location. At some locations, a single sample was collected and manually separated in the laboratory into coarse and fine subsamples. Elsewhere, the different size separates were collected separately in the field to be representative of the fault or fracture infilling and of the adjacent wallrock. Detailed site descriptions in Appendix C, and data from Appendix B.

## 8. SOLUTE TRANSPORT SIMULATIONS OF $^{36}\text{Cl}$ MIGRATION AND DISTRIBUTION TO TEST ALTERNATIVE CONCEPTUAL MODELS

### 8.1 Introduction

In this section, the role of studies coupling environmental isotope data and numerical modeling in identifying flow and transport processes as well as constraining the property sets used to model them are discussed. This section primarily summarizes Chapter 6 of Robinson et al. (1997), which is a detailed analysis of environmental isotope modeling. This section also contains additional analyses on the relationship of PTn thickness, estimated infiltration rate, and hydrologic model parameters to the prediction of fast paths from the surface to the potential repository horizon. Additional analyses on the propagation of episodic infiltration events to depth are also provided here to augment the results presented in Robinson et al. (1997).

Starting with various hydrologic property sets from LBNL, which are all based on fits matching matrix fluid saturation and capillary pressure (Bodvarsson et al., 1997), we perform a series of transport studies were performed with one-, two-, and three-dimensional transport models and examine how well the simulated distributions of  $^{14}\text{C}$  and  $^{36}\text{Cl}$  were examined to determine how well they match those of the measured data. The most significant finding in this study is that minor changes in hydrologic parameters lead to different flow distributions in the PTn matrix and fractures that, in turn, affect the predictions of the locations at which fast paths exist between the surface and potential repository horizon. Since multiple property sets were developed by Bodvarsson et al. (1997), reducing the uncertainty in property set choice based on environmental tracer observations and tracer transport modeling may have significant implications for repository design and performance modeling. For example, if the parameter set that is shown to be most consistent with the tracer data is also one that predicts ubiquitous fracture flow through the PTn, then repository design may need to account for periodic high fluxes resulting from transient infiltration events that are not damped in the PTn matrix. Also, such sustained PTn fracture flow leads to a greater incidence of predicted bomb-pulse  $^{36}\text{Cl}/\text{Cl}$  ratios in the TSw and CHn, even away from fault zones. With current material property estimates, episodic infiltration events (precipitation-related infiltration events lasting on the order of days) are more likely to be damped in regions of thicker PTn. The direct correlation of the PTn's damping potential to the magnitude of the infiltration rate is not straightforward. Fully assessing whether episodic infiltration is a significant concern for repository design and performance assessment requires a better understanding of the hydrologic properties and fracture flow potential of the PTn.

A new analysis in this section that was not covered in Robinson et al. (1997), is an investigation with the site-scale, three-dimensional transport model of the relationship between estimated surface infiltration rate, the PTn thickness, and predicted arrivals of bomb-pulse  $^{36}\text{Cl}$  at the potential repository horizon, even away from fault zones. The investigation of this relationship serves as an initial methodology for providing predictions of the distribution of fast paths in the planned East-West Drift as well as a sensitivity analysis of the hydrologic property sets.

The environmental isotope data coupled with transport modeling, also provide a basis for evaluating alternative conceptual models and the infiltration estimates that which the hydrologic parameters are calibrated to. One alternative conceptual model suggests that all  $^{36}\text{Cl}/\text{Cl}$  ratios found in the ESF that are significantly above the present-day background value of  $500 \times 10^{-15}$  represent very recent (bomb-pulse) water. The current LBNL hydrologic properties tend to support this particular conceptual model to a greater extent than did simulations with previous property sets (e.g., Fabryka-Martin et al., in press [a]) insofar as simulated fracture flow in the PTn is more readily initiated and sustained with the current properties. Using the current infiltration map and the corresponding material properties, tracer simulations in this section predict that transport rates from ground surface to the ESF should be more rapid in the southern portion of the ESF than in the northern portion. To the contrary, however, the  $^{36}\text{Cl}$  measurements suggest that early arrivals containing bomb-pulse  $^{36}\text{Cl}$  are more prevalent in the northern half, particularly in faulted regions. In fact, there is virtually no geochemical or isotopic evidence for fast travel to the ESF beyond station 45+00.

## 8.2 Implications

Direct measurement of unsaturated-zone percolation flux is difficult if not impossible, especially at depths greater than a few meters. To date, no such measurement has been made at Yucca Mountain. Inferring unsaturated-zone flux from physical measurements of saturation and water potential is also extremely difficult, especially in multiporosity systems such as fractured volcanic tuff. Likewise, controlled measurements of dissolved solute migration have not been made in the unsaturated zone at Yucca Mountain, although an unsaturated-zone transport test is now being planned. In saturated-zone studies, tracer tests are often used to help quantify physical and chemical attributes of the system as well as the groundwater flux. However, performing liquid-phase tracer tests in fractured, unsaturated porous media is not a simple task, especially at the scales of interest in the site-scale characterization program of Yucca Mountain. Fortunately, measurements of naturally-occurring environmental tracers such as Cl,  $^{36}\text{Cl}$  and  $^{14}\text{C}$ , if considered properly, can provide important insights into the system characteristics. Further, these tracers capture a time scale that cannot be addressed with conventional tracer tests. An additional utility in evaluation of environmental tracer tests is the man-made signal associated predominantly with the atmospheric testing of more than 70 nuclear weapons in the Pacific Proving Grounds between 1952 and 1958 which is generally referred to as the bomb pulse. The presence of bomb-pulse  $^{36}\text{Cl}$ ,  $^{14}\text{C}$ , tritium and other fallout radionuclides in a subsurface sample indicates that a component of the fluid traveled from the ground surface to the sample location in less than 50 yrs.

Recent efforts to characterize the hydrologic properties of the various units at Yucca Mountain have involved laboratory measurements of porosity, permeability, and characteristic curves by Flint (1996), air permeability tests (Bodvarsson and Bandurraga, 1996; Le Cain and Patterson, 1996), and numerical modeling to match measured saturations and gas-phase pressure response (Bodvarsson and Bandurraga, 1996; Bodvarsson et al., 1997). Although extremely beneficial in characterizing matrix material properties, these studies do not capture the "bulk response" of the system, particularly the combined influence of fracture-matrix interactions on transport processes in the

liquid phase. For that reason, the environmental tracer studies described herein serve to validate and enhance the conceptual and numerical model of flow and transport in Yucca Mountain.

This study demonstrates that different hydrologic properties which yield similar simulations of saturation may lead to significantly different predictions of transport rates. Simulated transport times for solutes through the PTn range from several tens of yrs to tens of thousand yrs, with differences in the percent of solute traveling along the fastest pathways depending on which parameter set is used. Environmental isotopes and conservative ions help identify both whether fast pathways exist and the age of sampled porewaters away from fast pathways, thus providing a useful tool for narrowing the field of possible parameter sets for hydrologic characterization, particularly when the difference in parameter sets is the method of representing fracture-matrix interactions. In conjunction with transport modeling, these data also prove useful in evaluating the accuracy of infiltration estimates.

### 8.3 Background

#### 8.3.1 Previous $^{36}\text{Cl}$ Modeling Studies at Yucca Mountain

Investigations of the significance of  $^{36}\text{Cl}$  data for identifying appropriate numerical model formulations for flow and transport processes in the unsaturated zone at Yucca Mountain were initially reported by Robinson et al. (1995). That report showed that only with the dual permeability model formulation could the observed rapid transport of bomb-pulse  $^{36}\text{Cl}$  to the PTn be simulated. With the equivalent continuum model, all of the bomb-pulse  $^{36}\text{Cl}$  stayed in the upper TCw. Also, Robinson et al. (1995) demonstrated that infiltration rates closer to those estimated by Flint et al. (1996), that average about 5 mm/yr over the site-scale model domain, could be used with the dual permeability model and still simulate matrix saturations consistent with those achieved by Wittwer et al. (1995) using an equivalent continuum formulation and infiltration rates on the order of 0.1 mm/yr.

The first implications of the  $^{36}\text{Cl}$  studies coupling Exploratory Studies Facility (ESF) sample analysis with flow and transport modeling were reported by Fabryka-Martin et al. (1996). These studies were later elaborated on by Fabryka-Martin et al. (in press [a]) and Robinson et al. (1996). These reports demonstrate that fracture flow must play a role in the Yucca Mountain unsaturated-zone flow and transport system and that infiltration rates close to those estimated by Flint et al. (1996), at least over the ESF, are required to generate the  $^{36}\text{Cl}/\text{Cl}$  signals that have been measured in the ESF (both bomb pulse and non-bomb pulse signals). The most recent site-scale hydrologic model of Bodvarsson et al. (1997) primarily adopts the estimates of Flint et al. (1996) and a dual permeability model in the parameter calibration activity.

Bodvarsson and Bandurraga (1996) and Bodvarsson et al. (1997) investigate, through numerical simulation, some issues associated with bomb-pulse isotopes measured at the ESF. These

simulations focus only on "fast-path processes." The 1996 report examines processes in a single fault using a continuum model to specify different properties in the fault zone and host rock bounding the fault zone (Fairley and Sonnenthal, 1996). The 1997 report examines transport from the surface to the ESF over the last 50 yrs using a two-dimensional dual-permeability model that extends along the main drift of the ESF, and has modified PTn material properties at certain faults and hypothesized faults (undetected at the surface or at depth) (Fairley and Wu, 1997). Although the modification of fracture properties is not described in the 1997 report, it is assumed to be similar to, or based on, the approach of Robinson et al. (1996), where fracture permeabilities in fault zones are increased consistent with either more fractures or larger fracture apertures that result from tectonic activity. In transport simulations, Fairley and Wu (1997) use an input signal to their model that incorporates bomb-pulse  $^{36}\text{Cl}/\text{Cl}$  ratios that range up to  $1.6 \times 10^{-10}$ . The simulated  $^{36}\text{Cl}/\text{Cl}$  ratios at depth in some locations are identified as containing bomb-pulse  $^{36}\text{Cl}$ , although these ratios are less than the ratio for present-day background (which is approximately  $500 \times 10^{-15}$ ). In any event, these simulations show, consistent with previous simulations by Robinson et al. (1996), that in zones with properties modified to represent faulted conditions, solutes entering the mountain at the surface can arrive at the ESF in less than 50 yrs. Issues regarding different numerical model formulations and constraints when simulating transport in a dual permeability framework are discussed in Robinson et al. (1997).

A final concern regarding processes affecting arrivals of bomb-pulse  $^{36}\text{Cl}$  at the ESF is the significance of transient infiltration events that occur on the scale of days. Robinson et al. (1996) used a synthetic 100-yr record of daily infiltration for which the infiltration rate on any given day was either zero or 0.06 mm/day with an average of 30 days/yr having non-zero infiltration. The annual average was 2 mm/yr and the simulations showed no significant difference in transport rates between those obtained for the transient case and those for the uniform infiltration rate case. In the simulations of transient effects by Bodvarsson et al. (1997), a pulse of 3.5 mm/day for 7 days is applied once, and the effects are examined over the next 10 yrs. The large pulse apparently has an effect on the maximum depth of penetration, especially in faults. This study further investigated the role and significance of transient infiltration events by varying the length, magnitude, and frequency of recurring transient events in and away from faults.

### 8.3.2 Significant Previous Findings

Fabryka-Martin et al. (in press [a]) and Robinson et al. (1996) reported on a detailed study that modified base-case PTn properties were in accordance with the increased fracturing that is expected to occur as a result of tectonic activity. In those studies, using base-case hydrologic properties from the Project's most recent analyses at the time (Bodvarsson and Bandurraga, 1996; Robinson et al., 1995), infiltration rates were found in the range of 1 to 5 mm/yr led to simulations consistent both with the observed occurrence of bomb-pulse  $^{36}\text{Cl}$  signals near fault zones as well as with the non-bomb pulse signals found away from fault zones in the ESF. Specifically, in regions away from faults where the fracture characteristics of the PTn were not expected to be modified, simulated travel times of Cl to the ESF were on the order of 5,000 to 20,000 yrs and yielded  $^{36}\text{Cl}/\text{Cl}$  ratios in

the 600 to 900  $\times 10^{15}$  range (Figure 3-2), matching the levels that have been measured in ESF samples from the North Ramp. If infiltration rates less than 1 mm/yr were used, then simulated travel times often exceeded 100,000 yrs and decay of  $^{36}\text{Cl}$  resulted in predictions of  $^{36}\text{Cl}/\text{Cl}$  ratios significantly less than the measured values. With infiltration rates greater than 5 mm/yr, all simulated travel times to the ESF were less than 10,000 yrs, and the resulting signal reflected a Holocene source with a nearly constant  $^{36}\text{Cl}/\text{Cl}$  ratio of  $500 \times 10^{15}$ .

For simulations in which the PTn fracture permeability was increased to reflect greater fracturing in fault zones, arrivals of bomb-pulse  $^{36}\text{Cl}$  at the ESF were predicted for infiltration rates greater than 1 mm/yr (Fabryka-Martin et al., in press [a]). Thus, the transport simulations both into and away from fault zones in the ESF yielded consistent results for the same range of infiltration rates.

## 8.4 Flow and Transport Model

### 8.4.1 Numerical Flow and Transport Model: FEHM

The numerical simulations are conducted using FEHM (Finite Element Heat and Mass transfer) (Zyvoloski et al., 1992). The mathematical models and numerical methods are summarized in Zyvoloski et al. (1992, 1995a, b), Robinson et al. (1996) and Viswanathan (1996). Solute transport in FEHM can be performed either with the particle tracking module or with the finite-element, reactive transport module. Both modules are coupled to the flow module, allowing simulation of transport for steady state or transient flow conditions. The particle tracker accommodates advection, dispersion, matrix diffusion, linear sorption, and radioactive decay. With the finite-element solver, the additional process of multi-species reactions such as complexation, competitive sorption, and precipitation/dissolution can be simulated (Viswanathan et al., 1997; Robinson et al., 1997). Here, since only aqueous chloride transport is considered, the particle tracker is adequate and substantially more efficient than the finite element solver. A large part of the efficiency associated with the particle tracker results from its ability to yield accurate solutions, even when fluid velocities are large. In fractured tuff, the velocities in fractures are substantially greater than in the rock matrix and resolution of solute movement would require very small time steps or unrealistic grid resolution with standard finite-element or finite-difference techniques. However, the particle tracker is based entirely on the already computed flux into and out of each element and its computational limitation is only dependent on the number of particles used (see Chapter 4 of Robinson et al., 1997). With modern computers, transport of millions of particles can be simulated efficiently.

### 8.4.2 $^{36}\text{Cl}$ input

Fabryka-Martin et al. (in press [a]) and Plummer et al. (1997) developed the reconstructed  $^{36}\text{Cl}/\text{Cl}$  function shown in Figure 8-1 that is used as an input to the numerical simulations in this study.

The infiltration estimates of Flint et al. (1996) are generally on the order of 1 to 10 mm/yr above the ESF sample locations. Such infiltration rates correspond to simulated groundwater ages on the order of 1,000 to 20,000 yrs. These travel times are entirely consistent with the sample ratios found in the ESF. The radioactive-decay dating method using  $^{36}\text{Cl}$  loses its applicability for such short travel times, but the elevated  $^{36}\text{Cl}/\text{Cl}$  ratio at the end of the Pleistocene provides a valuable tracer for groundwater age determination.

#### *8.4.3 Simulated Systems*

One-, two-, and three-dimensional numerical models are used to interpret the  $^{36}\text{Cl}/\text{Cl}$  observations and the general hydrologic behavior of the system above the potential repository to aid in the prediction of migration rates of other radionuclides from the potential repository to the accessible environment. A schematic of the locations of the various models used in this section is given in Figure 8-2.

Two and three-dimensional models are used to study the site-scale behavior including the effects of dipping strata of variable thickness and extent, spatially-distributed infiltration rates, and spatially-distributed material attributes. The one-dimensional models are used to examine specific fracture-matrix interactions associated with flow and transport in and away from fault zones. Also, transport under transient and steady-state flow conditions is evaluated with the one-dimensional models in order to assess whether or not time scales associated with episodic infiltration events (days) need to be addressed in the model when simulations of tens of thousands of years in two and three dimensions are required for radionuclide migration studies.

The layers in the numerical models are derived from the three-dimensional, site-scale stratigraphic framework model (Zelinski and Clayton, 1996). The GEOMESH software package (Gable et al., 1996) is used to extract the region of interest from the geologic model and to generate unstructured finite element grids. Material properties and parameters for the different layers are obtained from Bodvarsson et al. (1997) and are listed in Table 8-2 and Robinson et al. (1997, their Appendix 1).

#### *8.4.4 Domain and Boundary Conditions*

Migration and distribution of  $^{36}\text{Cl}$  are simulated on the east-west cross section two-dimensional model and in the site-scale three-dimensional model. Carbon-14, Cl, and other chemical tracers are simulated on the two-dimensional cross section. The two-dimensional model domain is located at Nevada State Plane Northing coordinate 232100 m and crosses several faults between Easting coordinates 168275 m and 174175 m. This domain (Figure 8-3) includes the Solitario Canyon Fault, the Ghost Dance Fault, and the Bow Ridge Fault. The infiltration map of Flint et al. (1996) (the I map) and a version of that map where are set at one-third of the Flint et al. values (the I/3 map) are used as the top boundary conditions for the two-dimensional model (see Table 8-1). These

maps are shown in Figure 8-4 for the two-dimensional cross section. The areal domain of the three-dimensional model is shown on top of the I infiltration map of Flint et al. (1996) in Figure 8-5. The extent of faults and general structure of the three-dimensional model are described in Chapter 3 of Robinson et al. (1997). A saturation boundary condition is prescribed at the water table for all models.

**Table 8-1. Infiltration Maps Used In Environmental Isotope Simulations**

Infiltration Map Name	Source	Modification
I	Flint et al. (1996)	None
I/3	Flint et al. (1996)	Scaled everywhere by 1/3

#### 8.4.5 Material Properties

The hydrologic properties used in this study are either taken directly from, or are based on, the hydrologic properties of Bodvarsson et al. (1997), that were developed through calibration to measured matrix saturations. Table 8-2 lists the property sets used in the environmental tracer models and the source and modifications associated with each set. The input parameters to FEHM are provided in Appendix 1 of Robinson et al. (1997). The major difference in property sets is the modification of set 6541a to 6541b, in which the fracture/matrix reduction factors in the PTn were eliminated.

**Table 8-2. Parameter Sets for Environmental Isotope Simulations**

Property Set name used in this report	LBNL set on which properties are based (tables cited below are in Bodvarsson et al., 1997)	Location in LBNL report of property set (page number)	Modification of LBNL properties from those reported in Bodvarsson et al. (1997)
6541a	Table 6.5.4-1	A-28	None
6541b	Table 6.5.4-1	A-28	No reduction factor for fracture/ matrix interaction in PTn
6541fit	Table 6.5.4-1	A-28	PTn fracture permeability increased by one order of magnitude
6541perched	Table 6.5.4-1	A-28	Basal vitrophyre fracture permeability reduced and fault zone fracture permeability reduced. Leads to perched water on top of the basal vitrophyre with fault as "dams".
6412b	Table 6.4.1-2b	6-12	None

## 8.5 Two-Dimensional $^{36}\text{Cl}$ Simulation Results

The transport of chloride and resulting  $^{36}\text{Cl}/\text{Cl}$  ratios throughout the two-dimensional cross section are simulated for a variety of different conditions and described in detail in Robinson et al. (1997). The results are evaluated both in terms of the overall resulting distributions and the temporal breakthrough curves at selected locations. Figure 8-6 to Figure 8-10 show the simulated  $^{36}\text{Cl}/\text{Cl}$  ratios and simulated saturations for two different parameter sets. The 6541a property set is taken directly from Bodvarsson et al. (1997) while the 6541b property set does not utilize the reduced fracture-matrix interaction model in the PTn. The primary difference is that bomb-pulse  $^{36}\text{Cl}$  signals completely penetrate the PTn at all locations between the Solitario Canyon fault and the Ghost Dance fault for the simulation using the 6541a set but that bomb-pulse  $^{36}\text{Cl}$  does not penetrate the PTn when the 6541b set is used. This effect is evident from the presence of the bomb-pulse  $^{36}\text{Cl}$  signal in the CHn matrix for the first set, but its absence from this unit for the second set. The following summary describes the implications of the simulations.

Two parameter sets that yield virtually identical saturation fields (Figure 8-8 to Figure 8-10) lead to very different predictions regarding whether or not significant amounts of bomb-pulse  $^{36}\text{Cl}$  penetrate the PTn above the potential repository. The assumption that has been made by Bodvarsson et al. (1997) and by Robinson et al., (1996) in the past is that the PTn fully damps the signal and hence episodic events need not be considered in simulations spanning thousands of yrs. However, if travel times through the PTn are less than 50 yrs, then this assumption may be reconsidered.

Breakthrough curves, which also represent the cumulative age distribution of a sample at a location in the model domain, were used by Robinson et al. (1997) to further investigate the differences that result from what appears to be a minor property change. These results show that the proportion of water flowing through the potential repository horizon, that traveled primarily in PTn fractures differs substantially depending on what property set is used. The difference is greatest where the PTn is thinnest. Less of the water that enters the PTn in fractures is able to imbibe into the PTn matrix when the 6541a property set is used, due to the use of a reduction factor that limits the rate of imbibition.

Whereas the choice of property sets has a significant impact on the amount of bomb-pulse  $^{36}\text{Cl}$  that completely penetrates the PTn in fractures, the median travel times, or water ages, from the surface to the potential repository horizon vary little between the two sets examined. However, the infiltration rate boundary condition has a large impact on the median travel time through the PTn and to the potential repository. Robinson et al (1997) ran simulations with the Flint et al. (1996) I infiltration map and the scaled I/3 map. For the current LBNL matrix property values (Bodvarsson et al., 1997), median simulated travel times increased approximately 5000 yrs when the scaled infiltration map was used. Further, the simulated average travel times for the oldest ten percent of the water at the potential repository horizon increased approximately 20,000 yrs. At the location where the east-west cross section intersects the ESF, the simulated travel times using the I/3 map may be more consistent with the measured  $^{36}\text{Cl}/\text{Cl}$  ratios in ESF samples. With the I map

simulations and the LBNL properties, only seven percent of the water flowing past the ESF is older than 10,000 yrs whereas with the I/3 map, that fraction is closer to twenty percent.

## 8.6 Three-Dimensional $^{36}\text{Cl}$ Simulation Results

### 8.6.1 Simulated $^{36}\text{Cl}/\text{Cl}$ Ratios

Chloride transport and  $^{36}\text{Cl}/\text{Cl}$  ratio distributions are simulated on the 143,000 node site-scale transport model. The grids for these simulations are described in detail in Chapter 3 of Robinson et al. (1997). Figure 8-11 shows north-south and east-west slices through a three-dimensional simulation of  $^{36}\text{Cl}/\text{Cl}$  ratios. The simulated bomb-pulse  $^{36}\text{Cl}$  signal reached the top of the PTn, where its downward migration velocity has been retarded as the flow partitions from the TCw fractures into the PTn matrix. Figure 8-12 shows the results from the three-dimensional simulation at the ESF horizon (plane at elevation 1090 m). The distribution of simulated  $^{36}\text{Cl}/\text{Cl}$  ratios reflects the spatial distribution of infiltration used in the simulation. To the east, where infiltration rates are lowest, travel times are long and decay of  $^{36}\text{Cl}$  reduces the ratio to values lower than  $500 \times 10^{-15}$ . However, the bomb-pulse  $^{36}\text{Cl}$  signature is seen in the Bow Ridge fault zone, the north-south trending fault that crosses the ESF near its north and south portals. The possible role of such block-bounding faults in transporting bomb-pulse  $^{36}\text{Cl}$  signatures to depth is also seen in the Solitario Canyon Fault zone west of the ESF main drift. In the central portion of the domain, where infiltration rates are relatively high, simulated travel times to the potential repository horizon range between 1000 and 30,000 yrs. Thus the simulated signal at this depth captures the variability of the input  $^{36}\text{Cl}/\text{Cl}$  ratio as based on the reconstructed signal, especially the values of about  $800 \times 10^{-15}$  that are predicted for the Pleistocene period.

Finally, travel times from the surface to the potential repository horizon were simulated using the I and I/3 infiltration maps. With the I/3 map, a greater percentage of a fluid sample is predicted to be greater than 10 ka old. One interpretation of the  $^{36}\text{Cl}/\text{Cl}$  ratios measured for the northern half of the ESF samples is that they indicate ages greater than 10,000 yrs because the ratios are similar in magnitude to those calculated for the end of the Pleistocene. As with the two-dimensional simulation described above, a key question is the extent that the  $^{36}\text{Cl}/\text{Cl}$  measurements of ESF rocks are representative of the water flowing past a sample location (i.e., are the measured signals more representative of the matrix fluids than of the fracture fluids). Part of the effort to address this issue has involved sampling in and away from fractures as well as collecting gouge material from fractures and comparing the results with those for adjacent matrix samples (section 7.4). To date, there is no indication that the water age increases with greater distance away from fractures. This issue may be resolved in the future if the new inhouse capability to extract pore water using an ultracentrifuge or high-pressure extraction system can be applied to welded TSw samples. If enough water can be extracted for  $^{36}\text{Cl}/\text{Cl}$  analysis by either of these techniques, then direct analyses of pore-water  $^{36}\text{Cl}/\text{Cl}$  ratios can be compared with those obtained by leaching rock samples at the same or nearby location.

### 8.6.2 *Travel Time Summary*

As with the two-dimensional model, Robinson et al. (1997) used the three-dimensional model to look at breakthrough curves (age distributions) at various locations in the site model. Twelve locations in the ESF between stations 8+00 and 77+00 and eight locations at the potential repository horizon along a north-south transect located at Easting coordinate 107,600 m were investigated. The LBNL and modified LBNL properties, parameter sets 6541a and 6541b, were used in conjunction with the I and I/3 infiltration maps.

Between stations 12+00 and 35+00, very little bomb-pulse  $^{36}\text{Cl}$  arrival is simulated in the ESF for either parameter set. There is significant bomb-pulse  $^{36}\text{Cl}$  arrival at station 8+00 because there is no PTn overlying that location in the ESF. Between stations 40+00 and 70+00, the percentage of fluid of bomb pulse age increases from 4% to almost 30% for simulations using the 6541a parameter set and the I infiltration map. With the 6541b parameter set and the I infiltration map, the percent of early arrival in the southern stations is greater than in the northern stations, but it is never greater than 4%. With the I/3 map and the 6541b set, the maximum percent of bomb-pulse  $^{36}\text{Cl}$  arrivals is less than 1% of the simulated particles.

A similar trend is simulated along the north-south transect with the three-dimensional transport model. The percentage of bomb-pulse travel times at the potential repository increases to the south. The simulated percent decreases significantly when the simulation uses a modification of the properties representing fracture-matrix coupling in the PTn.

### 8.6.3 *PTn Thickness/ Flux/ Bomb-Pulse $^{36}\text{Cl}$ Arrival Study*

In both the ESF and north-south transect studies, the percentage of bomb-pulse age water reaching the potential repository horizon increases with thinning PTn. Because the PTn thickness and estimated infiltration rate vary spatially, an additional study was performed to investigate the relationship between PTn thickness, estimated infiltration rate, and simulated travel times from the surface to the potential repository horizon. A set of locations at the potential repository horizon were selected for this study. Each location is approximately 500 m from its neighbors and is at an elevation of approximately 1080 m above sea level. The study is performed between Easting coordinates 169,000 and 173,000 and Northing coordinates 230,000 and 235,000. Figure 8-13 shows the monitoring locations at elevation 1080 m and the PTn thickness contoured over this domain. Figure 8-14 shows the infiltration map over the same domain. A series of transport simulations were conducted where simulated travel times from the surface to the various locations at the potential repository horizon were monitored. One million particles were applied uniformly over the surface as an instantaneous pulse and breakthrough curves at each location were then computed. If one percent of the particles arriving at any monitored location had travel times of 50 yrs or less, then that location was designated as having a bomb-pulse  $^{36}\text{Cl}$  signal. Figure 8-15 and Figure 8-16 show the bomb-pulse and non bomb-pulse locations for simulations using the I

infiltration map and the LBNL and modified LBNL property sets (6541a and 6541b).

In these simulations, bomb-pulse  $^{36}\text{Cl}$  arrivals were simulated in most of the two western columns of the grid because there is no overlying PTn at these locations. In the northwest portion of the grid, the PTn is present and the incidence of bomb-pulse  $^{36}\text{Cl}$  signatures decreases for both cases. At the remaining locations, the bomb-pulse  $^{36}\text{Cl}$  arrivals are well correlated with the thinning of the PTn to the south. With the modified PTn properties, significantly fewer locations experience arrivals of bomb-pulse  $^{36}\text{Cl}$ . For either property set, these results appear inconsistent with the ESF data, which indicate no clear-cut bomb-pulse  $^{36}\text{Cl}$  signature in the ESF samples south of 232,000 m. Likewise, these predictions indicate no bomb-pulse  $^{36}\text{Cl}$  signatures in the northern ESF stations, yet these are where most of the elevated  $^{36}\text{Cl}/\text{Cl}$  ratios have been found. However, the present analysis does not address fast paths in fault zones. Therefore, if fault zones are necessary conduits in order for bomb-pulse  $^{36}\text{Cl}$  to penetrate the PTn, then these simulations are consistent with the non-fault zone related measurements in the northern ESF.

Based on these simulations, an attempt was made to establish the correlation between flux, PTn thickness, and simulated bomb-pulse  $^{36}\text{Cl}$  travel times to the horizon of the potential repository. Figure 8-17 shows a scatter plot of bomb-pulse  $^{36}\text{Cl}$  arrivals for infiltration rate vs. PTn thickness using the 6541a parameter set. A general trend shown in this figure is that for PTn thicknesses less than 40 m, bomb-pulse  $^{36}\text{Cl}$  arrivals tend to be simulated regardless of the infiltration rate. Figure 8-18 shows a similar scatter plot for the 6541b parameters. Although the trends are similar, the 5 locations with PTn thicknesses greater than 40 m that had bomb-pulse  $^{36}\text{Cl}$  with the 6541a parameter set have none when the 6541b parameter set is used. Also, substantially fewer locations with overlying PTn thicknesses less than 40 m have bomb-pulse  $^{36}\text{Cl}$  signals when the modified PTn properties are used. However, the relationship between flux and PTn thickness is not obvious when the PTn thickness is less than 40 m. For both parameter sets, bomb-pulse  $^{36}\text{Cl}$  was absent at one location that had a high infiltration rate and thin PTn. Further investigations will serve to identify why this particular location (in the northwest corner) does not have the expected bomb-pulse  $^{36}\text{Cl}$  signal. Likewise, for PTn thicknesses between 20 and 50 m and using the 6541a parameter set, bomb-pulse indicators associated with the highest infiltration rates switched to no bomb-pulse indicators when the 6541b set was used. The initial expectation would be that the switch would occur for low infiltration rates but that bomb-pulse indicators associated with high infiltration rates would be less sensitive to the parameter set.

## 8.7 Carbon-14, Chloride, and Other Conservative Tracers

### 8.7.1 Chloride and Other Conservative Tracers

In Chapters 6 and 7 of Robinson et al. (1997), transport simulations of carbon-14, Cl, Br, and sulfate were performed. In those simulations, the concentration of dissolved species such as Cl are assumed to be inversely proportional to the infiltration rate (section 5.1). Therefore, water entering

at a high infiltration rate is assumed to have a low Cl concentration whereas water from low infiltration zones has a high chloride concentration.

The input chloride concentrations to the three-dimensional model are shown in the left-hand side of Figure 8-19, with a spatial pattern that mimics that of the infiltration map. The simulated Cl concentrations at an elevation of 900 m are shown in Figure 8-19. This depth approximately coincides with the top of the CHn. At depth, the concentration patterns are more uniform than at the surface due to mixing. The concentration values at depth are generally lower due to mixing with the high-flux, low-concentration water. This simulation supports the conceptual model that water entering the system where the infiltration rates are highest has the greatest influence on geochemical concentrations at depth, at least for conservative species (for example in perched water). Low-flux water percolating vertically through zones where the PTn pore water has high chloride concentrations has only a minor contribution to the chemical composition of the deeper system due to dilution with large volumes of low-Cl water entering in higher flux regions such as the Yucca Crest region. This effect is further demonstrated by Robinson et al. (1997) when they modify the basal vitrophyre fracture properties and fault-zone properties of the model such that perched water bodies form adjacent to faults. The simulated Cl concentration of the perched water is more representative of dilute water entering the system in high-infiltration zones than the high Cl, low-flux water entering directly above.

### 8.7.2 Carbon-14

The  $^{14}\text{C}$  simulations performed by Robinson et al. (1997) utilize the 6541a and 6541b parameter sets that were used in the  $^{36}\text{Cl}/\text{Cl}$  ratio comparisons. They also use the parameter set with modified basal vitrophyre and fault zone properties that lead to simulated perched water as described above for the Cl simulations. The  $^{14}\text{C}$  input function is uniform in space and time and decay occurs with a 5730 year half life. Although  $^{14}\text{C}$  may not be a conservative aqueous tracer due to reactions with the solid and gas phase, it is assumed that it remains in the liquid phase.

One of the utilities of the  $^{14}\text{C}$  data is the independent corroboration it provides for our conceptual model of  $^{36}\text{Cl}$ . Figure 8-20 shows the decay with time of the input signals for both  $^{36}\text{Cl}/\text{Cl}$  and  $^{14}\text{C}$ . Over the past 50,000 yrs, there is very little decay of  $^{36}\text{Cl}$  due to its 301,000 yr half life. Thus the reconstructed signal is well preserved. The  $^{14}\text{C}$ , on the other hand, shows significant decay from the input function of unity. Values from both of these plots taken at the same times are then used to create the meteoric water curve (gray line) in Figure 8-21, which is shown along with measured  $^{14}\text{C}$  and  $^{36}\text{Cl}/\text{Cl}$  ratios from perched water samples. Samples with lower  $^{14}\text{C}$  activity have higher  $^{36}\text{Cl}/\text{Cl}$  ratios, especially samples with  $^{14}\text{C}$  ages greater than 10,000 yrs. Thus, the data provide independent support for the use of the reconstructed  $^{36}\text{Cl}/\text{Cl}$  input function to age-date fluid samples for which  $^{14}\text{C}$  ages are unavailable.

In the numerical simulations of  $^{14}\text{C}$  transport and distribution (Robinson et al., 1997), there is no bomb-pulse signal in the input function. Thus, the differences between simulations using property

sets 6541a and 6541b are virtually undetectable. The simulated apparent ages of 400 to 5,000 yrs in the CHn matrix between the Solitario Canyon Fault and Ghost Dance Fault are consistent with the breakthrough curves at the repository horizon (Figures 6-15 to 6-18 in Robinson et al., 1997). To the west of the Ghost Dance Fault, the apparent ages increase with decreasing estimated infiltration rate.

For the perched water model (low fracture permeability in the TSw basal vitrophyre), apparent ages in the perched water near the Ghost Dance Fault are about 1000 yrs when the I infiltration map is used and 2000 yrs when the I/3 map is used. These ages are not indicative of the vertical travel times at the sample location; rather, they indicate the travel time of water entering near the crest and moving laterally along the basal vitrophyre.

## 8.8 One-Dimensional Process Level Modeling

A series of one-dimensional column modeling studies were performed to provide greater sensitivity analysis of significant processes and model parameters. Three columns were selected as representative of the different regimes encountered at Yucca Mountain. Two are coincident with ESF stations 35 and 57 and one falls in the middle of the potential repository block.

### 8.8.1 Column Descriptions

#### ESF Station 35

Station 35 is a location where the three-dimensional simulation did not predict significant early arrivals. It is also a location near which both bomb-pulse  $^{36}\text{Cl}/\text{Cl}$  ratios and ratios possibly indicative of 10,000+ year old water have been found by Fabryka-Martin et al. (in press [a]). The bomb-pulse signal has been correlated with structural features by Levy et al. (1997). The infiltration rate above Station 35, according to Flint et al. (1996) is about 3 mm/yr. This is also a location at which the consistency between fault-zone and base-case model results as compared with field data and infiltration estimates was demonstrated (Robinson et al., 1996). The location of the Station 35 column in NSP coordinates is (171277, 233393) and the PTn thickness is 42 m.

#### Repository Column

The repository column is located in a zone of high estimated infiltration in the middle of the potential repository block. The estimated infiltration rate is about 13 mm/yr. The PTn is 58 m thick, significantly greater than over the ESF at stations 35 or 57. The location of the repository column in NSP coordinates is (170600, 234000).

### ESF Station 57

Station 57 represents a unique location both in terms of the geology and the measurements that were made on samples from that location. The geology above station 57 is characterized by thinner PTn than is found further north and west (c.f. Rautman and Engstrom, 1996). This location is also near where the Ghost Dance fault crosses the ESF. However, unlike Station 35 where bomb-pulse  $^{36}\text{Cl}/\text{Cl}$  levels were found and attributed to a fault, no unambiguous bomb-pulse signal has been found at or near this ESF station (one isolated peak signal at Station 56+93 may be suggestive of bomb-pulse  $^{36}\text{Cl}$ ). Station 57 poses a high potential for recording a bomb-pulse signal in that the PTn is only 30 m thick. However, the infiltration rates estimated by Flint et al. (1996) are significantly lower (about 1 mm/yr) than above other ESF stations where bomb-pulse  $^{36}\text{Cl}/\text{Cl}$  has been found. The Station 57 column is located at NSP coordinates (171160, 231200).

### *8.8.2 One-Dimensional Modeling Approach*

The systematic modeling approach taken for each of the three columns serves to investigate process sensitivity to parameter variations and flux variations. For each parameter set investigated, simulations of flow and transport are run with mean infiltration rates ranging between 1 and 50 mm/yr. The parameter sets we look at include: the base and modified set, 6541a and 6541b respectively; the base-case set, 6412b, as reported by Bodvarsson et al. (1997); and a fault-zone set, 6541ft, that is based on the 6541a set but with increased fracture permeability in the PTn. The basis for increasing the permeability in the PTn as a result of tectonic activity is discussed in detail in Robinson et al. (1996). The principle behind this parameter set lies with the fact that nonwelded units tend to have very low bulk fracture permeability relative to the welded units. In fault zones, however, increased fracture permeability in the PTn occurs either as a result of more fractures or greater fracture apertures. Increased permeability in fault zones, up to two orders of magnitude in nonwelded units, has been inferred from the field air permeability testing (Rousseau et al., 1996).

### *8.8.3 One-Dimensional Modeling Results*

#### Steady-State Flow

Robinson et al. (1997) describe the flow and transport simulations on each column with uniform annual infiltration rates of 1, 5, 10, 20, and 50 mm/yr. With these steady-state flow fields, particles are inserted into the fractures of the TCw and their breakthrough at the potential repository horizon is monitored. The simulations shown in Figure 6-36 of Robinson et al. (1997) demonstrate the role of infiltration rate and PTn thickness. Supporting the analysis with the three-dimensional model presented earlier in this chapter, the results of Robinson et al. (1997) show that for a thinner PTn (Station 57), the potential for sustained fracture flow in the PTn is greater and hence leads to the arrival of a bomb-pulse signal at the ESF. Decreasing the infiltration rate leads to greater median

travel times to the potential repository horizon and a greater proportion of ages greater than 10,000 yrs.

Multiple property sets were compared with these steady-state column studies. One very strong difference worth highlighting is between property sets 6412b and either 6541a or 6541b. The 6412b set uses a uniform scaling of the fracture-matrix interaction term in all units, resulting in significantly less flow from fractures into matrix than is simulated with the 6541a set. In fact, with 5 mm/yr flux in the Station 35 column, the minimum percent of the total simulated flow in the PTn fractures is fifty percent. More than twenty-five percent of simulated solute arrivals at the ESF are less than 50 yrs with the 6412b property set. This result predicts the presence of bomb-pulse signatures everywhere in the system. Thus, in order for the 6412b properties to be representative of the system, it would have to be assumed that the non-bomb pulse signatures (away from a fault zone) are not representative of most of the flow, and that the bomb-pulse signatures associated with faults represent some anomaly. The first part of this assumption is currently under investigation. Namely, one alternative conceptual model is that PTn fracture flow is ubiquitous and the ESF  $^{36}\text{Cl}/\text{Cl}$  analyses either demonstrate some component of bomb pulse (but below the threshold  $^{36}\text{Cl}/\text{Cl}$  value of  $1250 \times 10^{-15}$  used to indicate an unambiguous bomb-pulse signal) or else are just not representative of the flow system since they are performed on comparatively large quantities (1-5 kg) of leached rock samples rather than directly on pore-water salts. There are no immediate explanations for the second part of the assumption regarding the bomb-pulse signals that are found and their correlation with faults. Substantiation of the assumption will be difficult unless ubiquitous bomb-pulse signatures are found at depth. Therefore, we do not pursue this line of reasoning was not pursued further with these analyses.

The column studies of Robinson et al. (1997) also compare the 6541a and 6541b parameter sets in terms of predicted bomb-pulse arrivals at the potential repository horizon of each column for 10 mm/yr flux. The 6541a set show a greater propensity than the 6541b, but the differences are subtle. The fault zone properties, on the other hand, clearly show a greater potential for rapid transport to depth than do the other sets. The general conclusion that can be drawn from the steady-state simulations is that bomb-pulse travel times to the potential repository horizon are readily simulated with a reasonable model of fault zone properties in the PTn. Away from fault zones, simulated travel times are sensitive to the choice of parameter set and to the thickness of the PTn.

### Transient Flow

Both the UZ flow model (Bodvarsson et al., 1997) and the UZ transport model (Robinson et al., 1997) operate on the assumption that episodic transient infiltration events that occur on the scale of days, are damped in the PTn and that the flux leaving the PTn and entering the TSw is constant over time. This does not include large transient events that occur over the scale of thousands or tens of thousands of yrs. The occurrence of bomb-pulse at depth in the PTn highlights the question whether episodic events are actually damped. Therefore, in addition to the studies that use steady-state flow fields, the migration of solutes from the surface to depth under transient cases were also examine.

Neutron moisture meter logging in subsurface boreholes indicates that significant infiltration does not occur after every storm, but rather only every several yrs (Flint et al., 1996). Therefore, a set of simulations of transient infiltration events were implemented to examine if very large pulses of water recurring only every 5 yrs can create sustained fracture flow in the PTn. In these simulations, all the water associated with a given period of time is applied to the system over a specified short episode. The base-case transient model applies all of the water associated with a given infiltration rate (1, 5, 10, 20, and 50 mm/yr) for 10 days every 5 yrs. Modifications of this approach include 90-day instead of 10-day application periods and infiltration events occurring every year rather than every 5 yrs. Table 8-3 shows the transient infiltration models that have been used in this analysis. With these models, the total infiltrating volume, the duration of application, and the frequency of application can be examined in terms of response fluxes at the potential repository and in the PTn. The property sets used in this study include 6541a, 6541b, and 6541ft. The 6412b set showed substantial PTn fracture flow under steady-state conditions and is, therefore, not examined further for transient flow.

Figure 8-22 shows the different responses for the three different property sets considered in this section (6541a, 6541b, and 6541ft) when 10-5-10 and 50-5-10 models of transient infiltration (see table 8-3) are specified. These simulations were performed for the repository column model where the PTn thickness is 58 m. Based on current infiltration rate estimates, the 10-5-10 model represents a reasonable total flux with a very short duration of application. The 50-5-10 model represents nearly extreme total flux with a very short duration of application. For both infiltration rate models, the fluxes calculated using property sets 6541a and 6541b show almost complete damping at the potential repository, whereas fluxes for the fault-zone property set, 6541ft, display only partial damping after each infiltration event. For the 50-5-10 model, the flux response for the 6541ft property set is considerably larger than that for the 10-5-10 model. This observation is expected due to the larger volume of water being applied every 5 yrs. The flux is virtually

**Table 8-3: Transient Infiltration Rate Models**

Model Name	Avg. Annual Infiltration Rate (mm/yr)	Frequency of Infiltration Events (yrs)	Duration of Infiltration Events (days)	Daily Infiltration Rate During Event (mm/day)
10-5-10	10	5	10	5
50-5-10	50	5	10	25
50-1-10	50	1	10	5
10-5-90	10	5	90	0.55
50-5-90	50	5	90	2.78

completely damped for both the 6541a and 6541b sets. Also, with all three property sets, large oscillations in mean flux occur over multiple episodic events and appear to be caused by the change from initial steady-state to transient flow conditions, and then again from transient to steady-state flow after 300 yrs (extension of Figure 8-22 to 700 yrs shows all lines converging). The exact reason for this behavior is not immediately known, but further investigation will determine whether it highlights a time scale of wetting and drying in the PTn during changes between transient and steady-state flow, is suspected, or whether it is a numerical artifact. Finally, the average annual rate of infiltration in the 10-5-10 model is actually about 9.2 mm/yr, hence the mean decrease from the steady state input flux of 10 mm/yr.

Figure 8-23 shows the flux responses to the 10-5-10 and 50-5-10 transient infiltration models in the Station 57 model. The thickness of the PTn in the Station 57 model is 30 m compared to 58 m in the repository column model. This decrease in PTn thickness produces less damping for all three property sets for both 10-5-10 and 50-5-10 models. However, the flux for property sets 6541a and 6541b are still essentially damped at the ESF and the assumption of steady state flow when not in a fault zone is probably warranted, even where the PTn is only 30 m.

Figure 8-24 compares the damping of the flux responses at the potential repository horizon in the repository column model and the Station 57 model for property set 6451ft. Where the PTn is thicker (repository column), less fracture flow is sustained and the flux variations at the ESF are damped to a greater extent. Likewise, at either location, larger pulses of water lead to more sustained PTn fracture flow and thus are less damped than are smaller pulses.

The effect of decreasing the recurrence interval of episodic events from 5 yrs to 1 year is examined in Figure 8-25 for the repository column model and for the Station 57 model using property set 6541ft. The transient model comparison is between model 50-5-10 and 50-1-10 (see Table 8-3). The magnitude of the flux response decreases by about a factor of three (repository column) or four (Station 57). This represents a nearly linear relationship between the change in input pulse magnitude and the change in response with, perhaps, an indication of some additional damping as the magnitude increases.

#### Comparison between property sets 6541a and 6541b

Robinson et al. (1997) found that more bomb-pulse arrival at the ESF in the Station 57 model is simulated for property set 6541a than property set 6541b. In this study both sets have shown almost completely damped flux responses (see Figure 8-23. Simulated). Therefore, the percent of fracture flow versus matrix flow in the PTn for simulations using these two parameter sets was next examined. Figure 8-26 shows the simulated distribution of PTn flux between matrix and fractures in the repository column model and the Station 57 model for property sets 6541a and 6541b. The times awhen these flux distributions are plotted are just before a pulse and 45 days after a pulse during the transient infiltration simulation. This figure shows that as the pulse moves through the

PTn, the fracture flow component increases. Where the PTn is thin at Station 57, fracture flow, albeit a small amount, is sustained completely for property set 6541a. At the repository column, the PTn fracture flow increases as the pulse moves through, but then damps out due to the thickness of the PTn. Complete fracture flow through the PTn is never sustained in that column for either property set. Thus, the difference in solute arrival times at the ESF in the Station 57 model for the two parameter sets appears to be due to small differences in the amount of sustained fracture flow in the PTn during the transient event. The total fraction of PTn fracture flow, however, is so small that it has very little effect on the flux rate at the ESF. In the Repository Column, the simulated breakthrough curves for the two property sets differ little due to the large component of total PTn matrix flow for either case.

### 8.9 Conclusions

This study reconfirmed that modified, fault-zone PTn properties lead to simulations of bomb-pulse age solutes arriving at the potential repository horizon. Away from fault zones, the prediction of bomb-pulse age solutes arriving at depth is sensitive to the hydrologic parameter set (namely the model for fracture-matrix interaction), the PTn thickness, and the flow rate. Transport models were used to investigate relationships of these three controlling factors in order to develop a methodology for predicting fast paths at unsampled locations.

The fracture-matrix interaction model for the PTn plays a significant role in predictions of whether bomb-pulse signals penetrate the PTn completely. Varying the model has little effect on simulated saturations, but has a large effect on the depth that bomb-pulse solutes can travel. Of the parameter sets investigated (see Table 8-2), set 6412b led to substantial amounts of PTn fracture flow. Sets 6541a and 6541b show similar characteristics in terms of the very small amount of PTn fracture flow that is simulated. However, the small difference between the two sets is the difference between simulations of bomb-pulse signals arriving at depth or not. Therefore, this study indicates that incorporating subsurface geochemistry data into the calibration process may serve to reduce the number of possible parameter sets that realistically characterize the flow system.

The relationship between PTn thickness and infiltration rate on bomb-pulse signal predictions at the potential repository horizon was investigated with the site-scale three-dimensional transport model. As the PTn thins to the south, the prediction of bomb-pulse arrivals at the potential repository horizon increases. With the 6541a parameter set, the bomb-pulse predictions extended further north (under thicker PTn) than for the 6541b parameter set. The 6541a parameter set also leads to predictions of more bomb-pulse travel times to the ESF than the 6541b set. However, there is a strong inconsistency between the simulated distribution of bomb-pulse  $^{36}\text{Cl}$  with either model parameter set, as compared to the measured distribution. Whereas the incidence of bomb-pulse predictions with the model is highest in the south ramp of the ESF due to thin overlying PTn, the data indicate virtually no bomb-pulse signals in this area. ESF stations where bomb-pulse has been found are all further north, where the model predicts less bomb-pulse travel to the ESF. However, the locations where bomb-pulse signals have been measured in the northern part are mostly well-correlated with faults. The site-scale model does not resolve any of the faults associated with the

ESF bomb-pulse predictions. Because of the lack of faults in the two- and three-dimensional models, one-dimensional models are used to investigate flow and transport processes and hydrologic parameters for fault zones. As described above, modification of PTn properties to represent increased fracturing in faults leads to predictions of bomb-pulse  $^{36}\text{Cl}$  in the ESF, even where the PTn is relatively thick.

The transport model was also used to investigate the role of episodic infiltration in transport of bomb-pulse  $^{36}\text{Cl}$  and in flux variations at the potential repository horizon. Differences between simulations with parameter sets 6541a and 6541b were minor as the PTn damps the pulsed input almost completely for both cases. The difference in predicted bomb-pulse transport between these two sets remains due to slight differences in the small amount of sustained fracture flow in the PTn. The difference is greatest where the PTn is thinnest because fracture flow with set 6541a is sustained through the entire PTn. As the PTn thickens, fracture flow through the entire unit is not sustained with either set. In fault zones, on the other hand, fracture flow is sustained and the pulses are not damped completely. Where the PTn is thinnest, simulated pulses at the potential repository are greatest, an issue of potential significance to repository design and performance assessment.

With the new geologic model (Zelinski and Clayton, 1996), the new hydrologic parameters (Bodvarsson et al., 1997), and the spatially distributed infiltration map (Flint et al., 1996), simulated transport times through the PTn matrix are quicker than with previous models (Fabryka-Martin et al., in press [a]). Whereas most of the solutes arriving at the ESF or the potential repository horizon in transport simulations had travel times on the order of 10,000 yrs in earlier studies, the median simulated travel times are now between 1,000 and 7,000 yrs. There still is a component of simulated solute arrival times (or water ages) that are greater than 10,000 yrs, but it represents only 5 to 20% of a sample. Thus, there may be a discrepancy in the interpretation of elevated  $^{36}\text{Cl}/\text{Cl}$  signals away from fault zones. Previously, the interpretation was that these signals indicated water that entered the system during the Pleistocene with a higher  $^{36}\text{Cl}/\text{Cl}$  ratio than is found in modern water. We also interpreted these signals as being representative of the water flowing past the sample location. If, however, most of the water flowing past a sample location is really Holocene in origin (e.g. less than 10,000 yrs old) as the current simulations suggest, then the ESF samples may not be representative of most of the water flowing through the TSw. In other words, the  $^{36}\text{Cl}/\text{Cl}$  ratio measured for an ESF sample may, in fact, indicate the presence of matrix water older than 10,000 yrs, but the ratio of Cl extracted from the rock sample may be insensitive to the age of water flowing in the TSw fractures. A closer examination of the ESF sampling locations and data should be able to evaluate this hypothesis. The other conceptual model is that all of the ESF samples elevated above present-day background (e.g., samples with  $^{36}\text{Cl}/\text{Cl}$  ratios above  $600-800 \times 10^{-15}$ ) may contain a small bomb-pulse component. Whereas the recent PTn model of fracture-matrix interaction supports this conceptual model, the TSw fracture-matrix interaction model would need revision to prevent all simulated bomb-pulse signals from completely bypassing the TSw matrix. Such a conceptual model also leaves questions about the apparent present-day signal under thin PTn and higher signals in fault zones and away from fault zones under thicker PTn. It is expected that further closure on these apparent discrepancies will be reached with additional geochemical analyses such as the pore-water Cl concentrations measured for the PTn in the North Ramp (section 4.5).

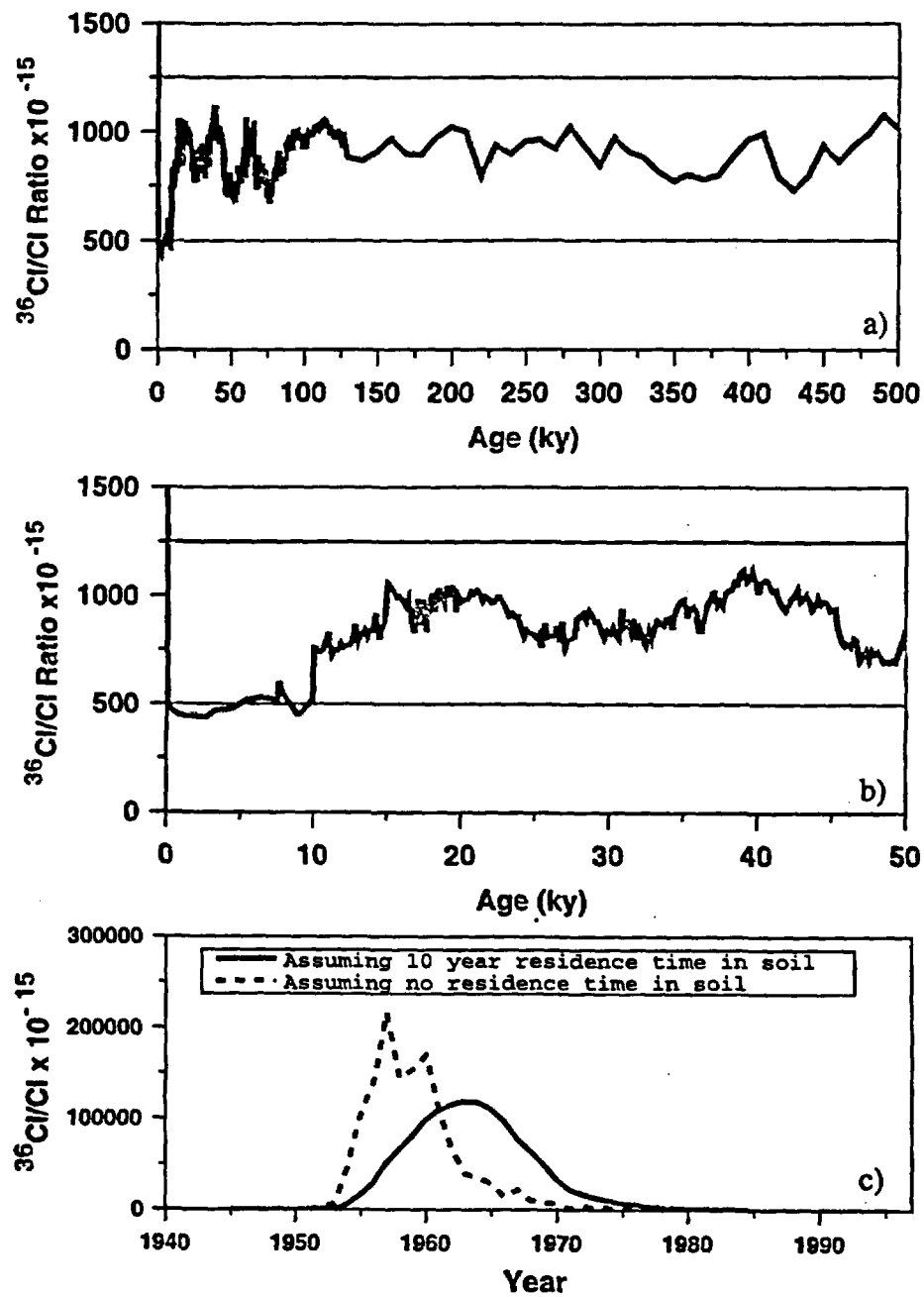


Figure 8-1. Reconstructed  $^{36}\text{Cl}/\text{Cl}$  ratio in infiltrating water (Section 3.1 of this report), a) last 500,000 years, b) last 50,000 years, c) last 50 years.

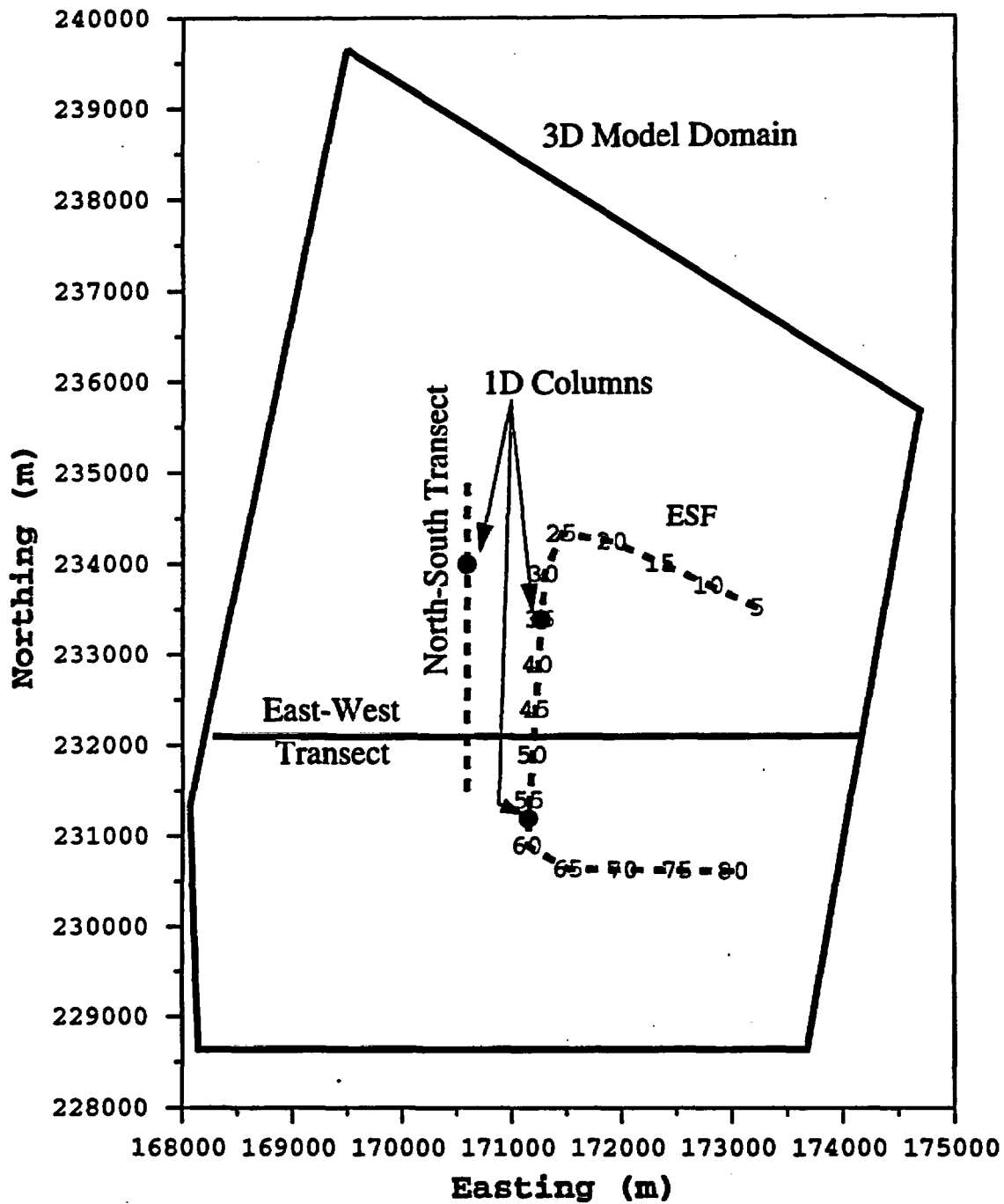


Figure 8-2. Plan view of three-dimensional model domain with locations of ESF, ESF stations, two-dimensional east-west model transect, north-south transect, and one-dimensional vertical column studies.

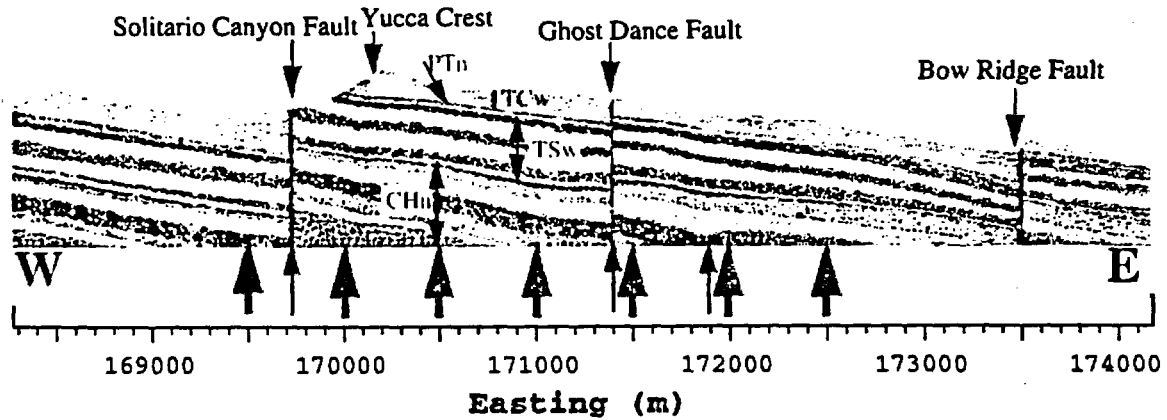


Figure 8-3. Finite-element grid for the two-dimensional cross section at Antler Ridge. Northing location in NSP coordinates is 232100 m. Red arrows show easting location for potential repository horizon breakthrough study.

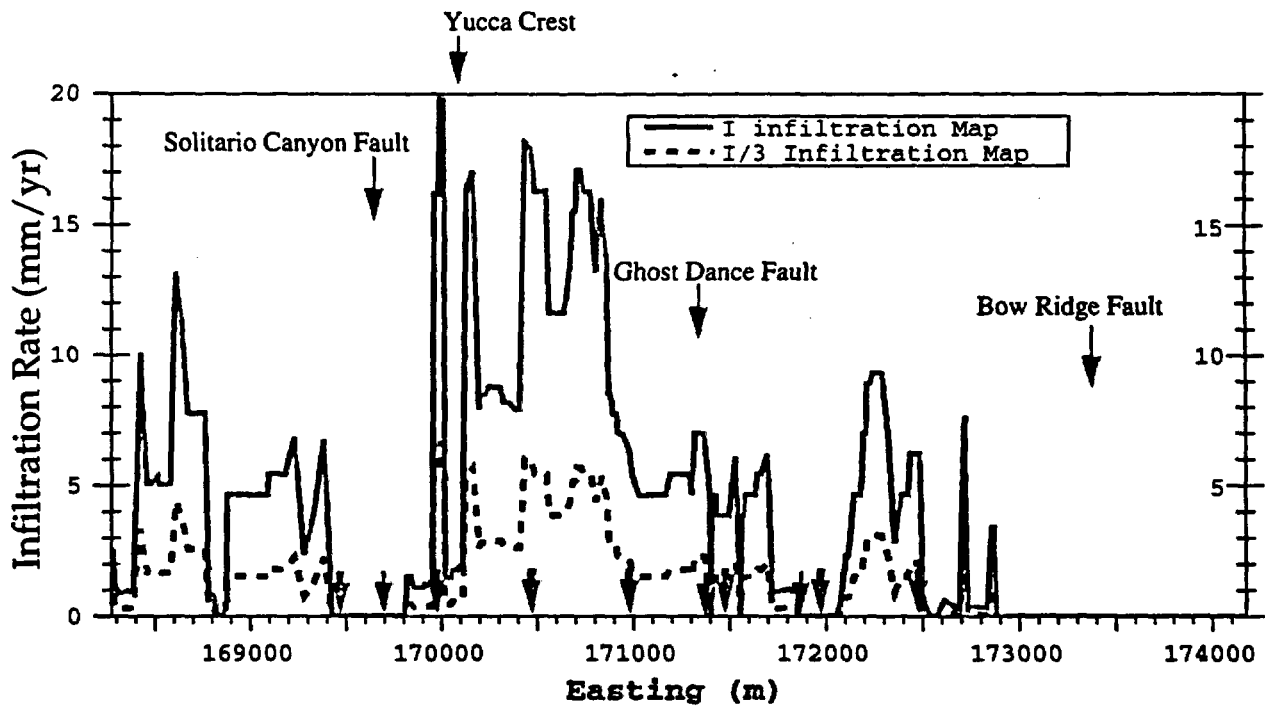


Figure 8-4. Infiltration rates extracted from Flint et al. (1996) map along Antler Ridge cross section. I map is directly extracted, I/3 map is the I map scaled by 3. Green arrows show easting location for potential repository horizon breakthrough study.

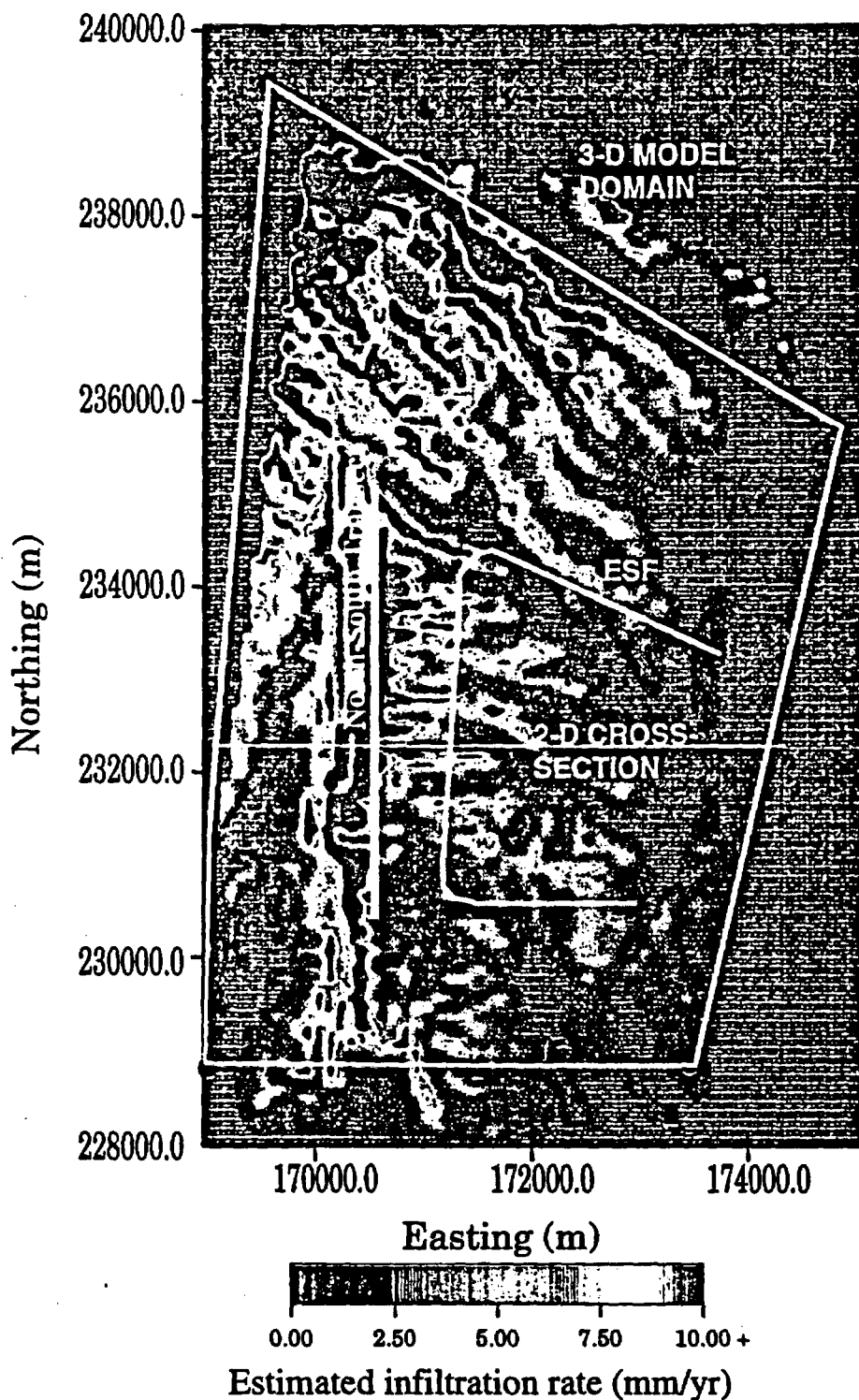


Figure 8-5. Plan view of three-dimensional domain outline on top of Flint et al. (1996) infiltration map. Also shown for reference are the ESF, the east-west two-dimensional cross section and the north-south transect (used to interpret the three-dimensional model results).

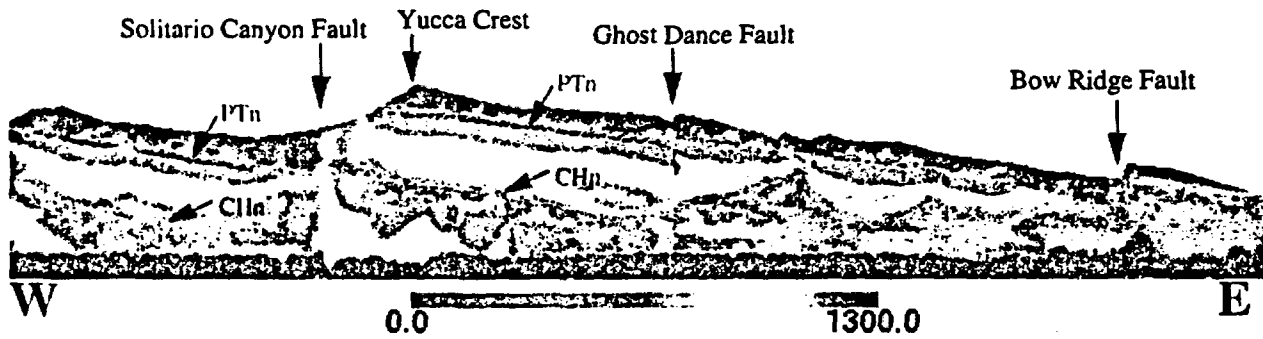


Figure 8-6. Simulated  $^{36}\text{Cl}/\text{Cl}$  ratios ( $\times 10^{-15}$ ) in Antler Ridge 2-D cross section with 6541a material property set and Flint et al. (1996) infiltration map.

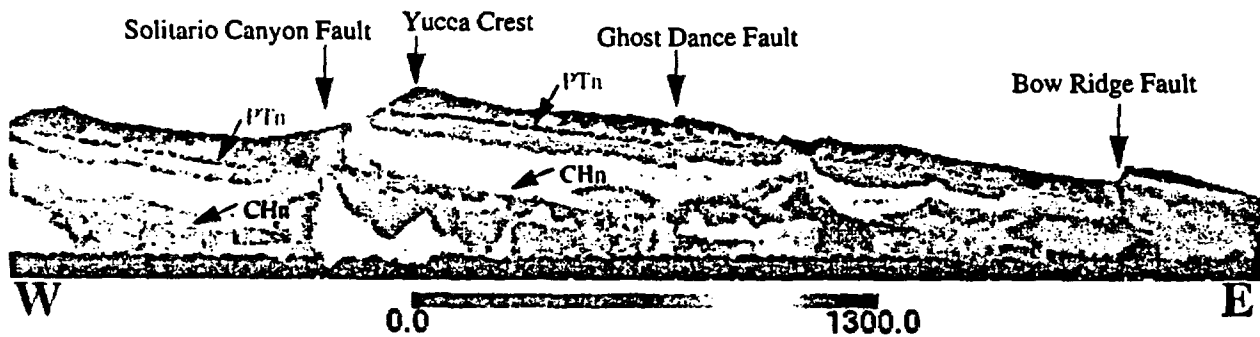


Figure 8-7. Simulated  $^{36}\text{Cl}/\text{Cl}$  ratios ( $\times 10^{-15}$ ) in Antler Ridge 2-D cross section with 6541b material property set (*no weighting of fracture-matrix connection in PTn*) and Flint et al. (1996) infiltration map. Note the reduced amount of bomb-pulse  $^{36}\text{Cl}$  arriving at the top of the CHn.

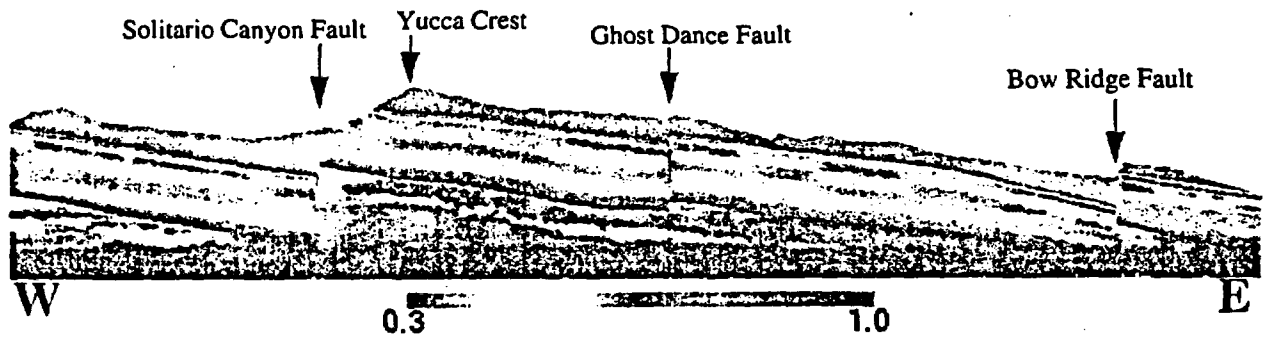


Figure 8-8. Simulated saturations in Antler Ridge 2-D cross section with 6541a material property set and Flint et al. (1996) infiltration map.

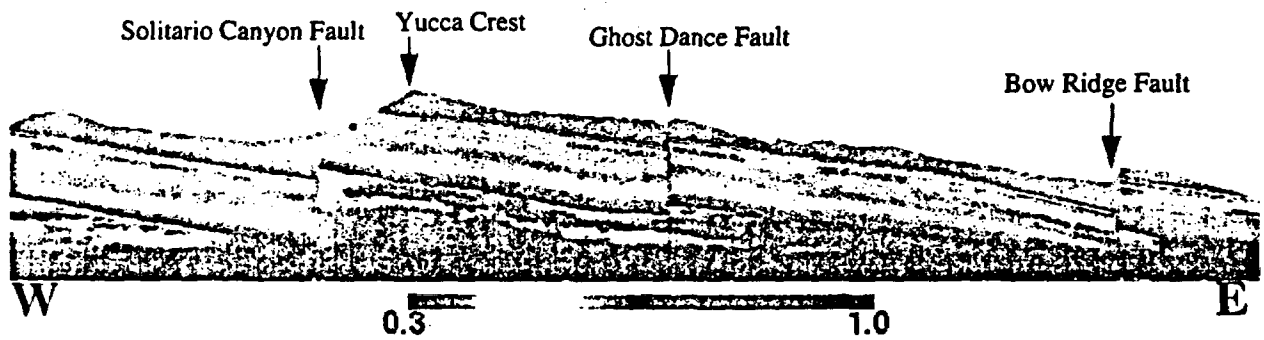


Figure 8-9. Simulated saturations in Antler Ridge 2-D cross section with 6541b material property set and Flint et al. (1996) infiltration map.

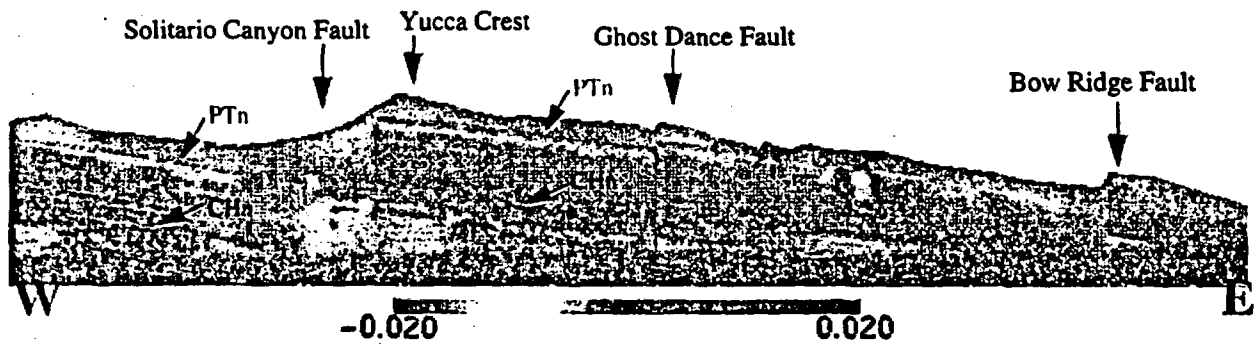


Figure 8-10. Difference in simulated saturations for property sets 6541a and 6541b.

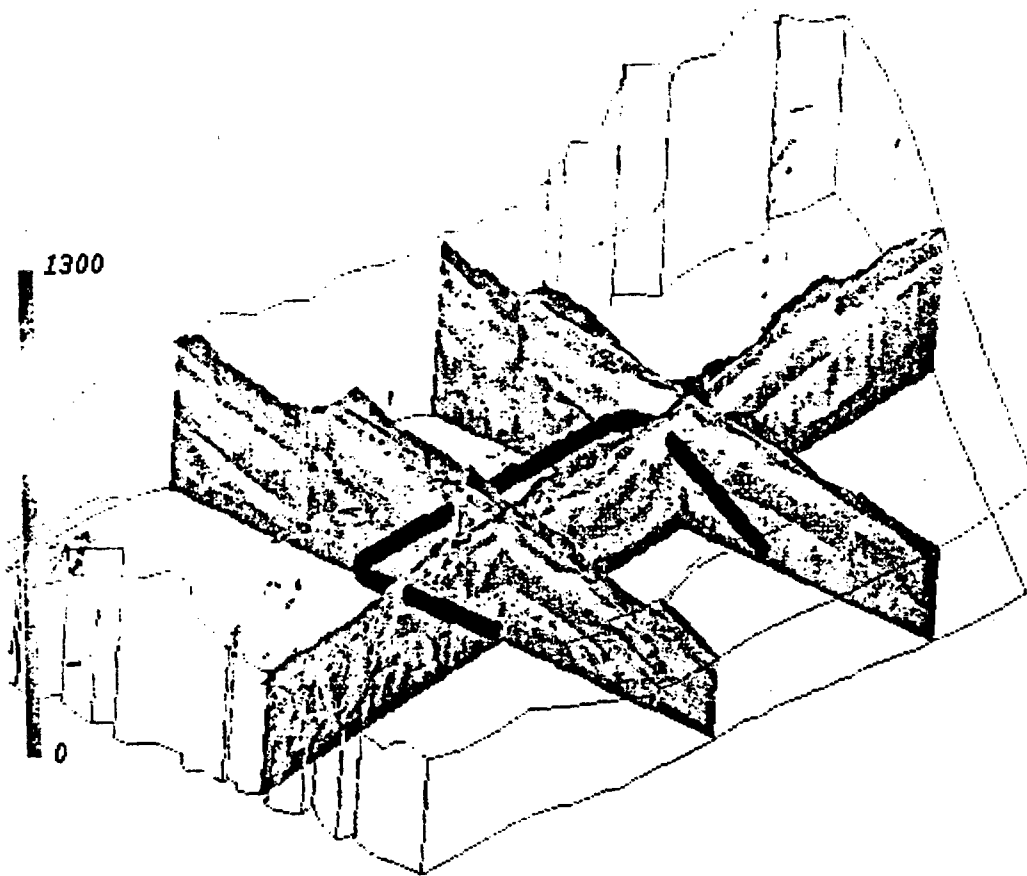


Figure 8-11. Three-dimensional simulation of  $^{36}\text{Cl}/\text{Cl}$  ratios (x  $10^{-15}$ ) using property set 6541a and infiltration map of Flint et al. (1996).

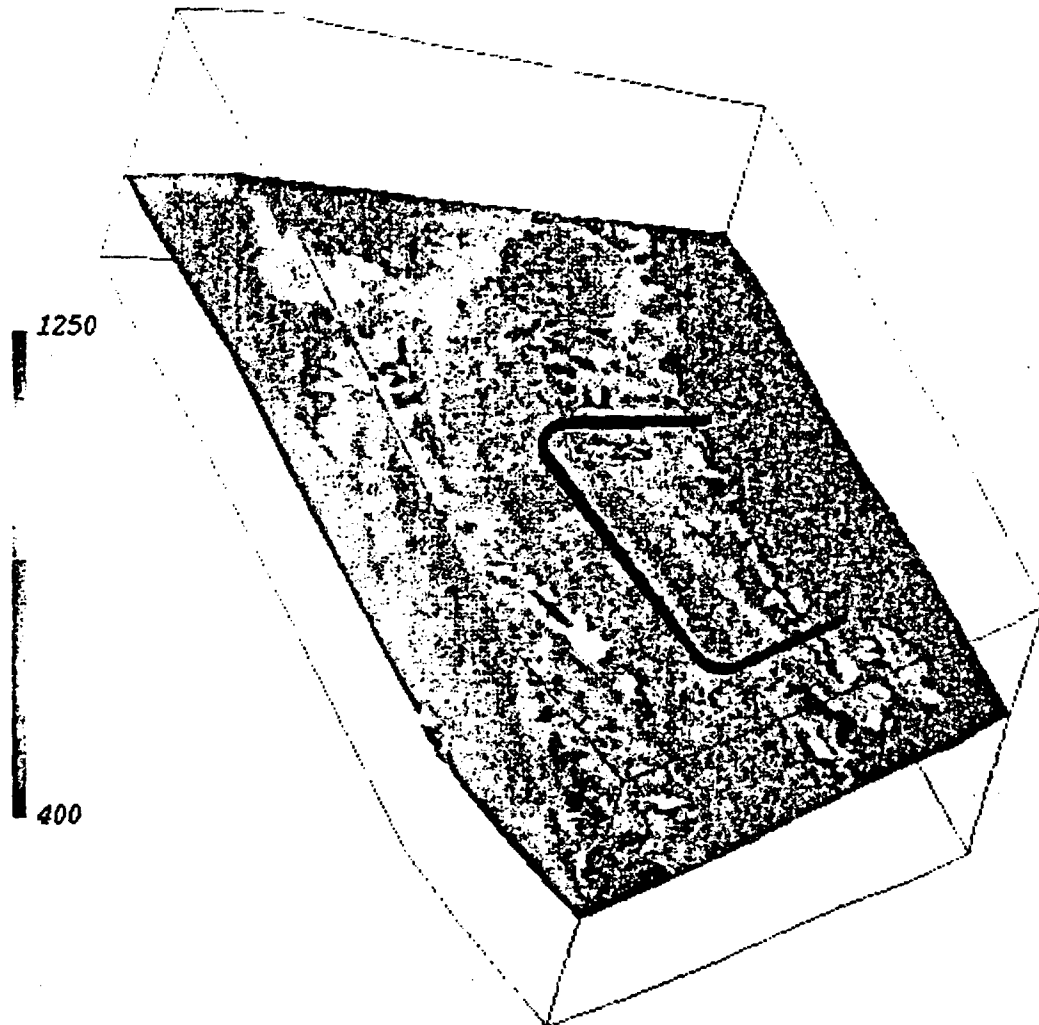


Figure 8-12. Simulated  $^{36}\text{Cl}/\text{Cl}$  ratios ( $\times 10^{-15}$ ) at ESF horizon with three-dimensional transport model. Uses material property set 6541a and infiltration map from Flint et al. (1996).

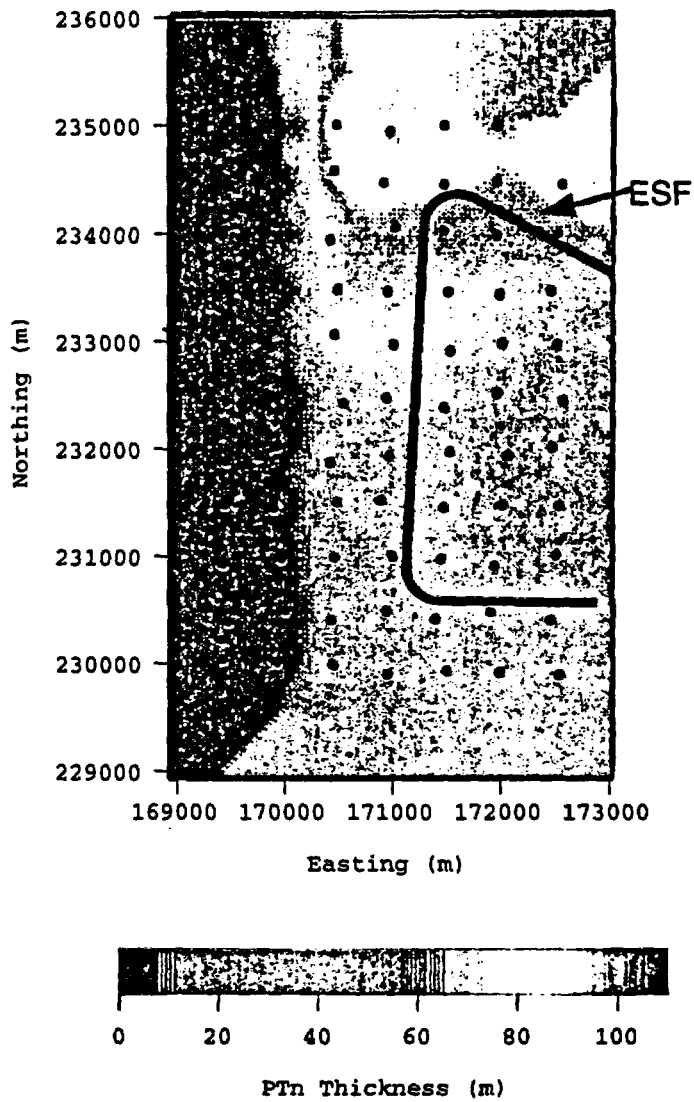


Figure 8-13. PTn thickness in the area included in the study simulating the arrival of bomb-pulse <sup>36</sup>Cl at the potential repository horizon.

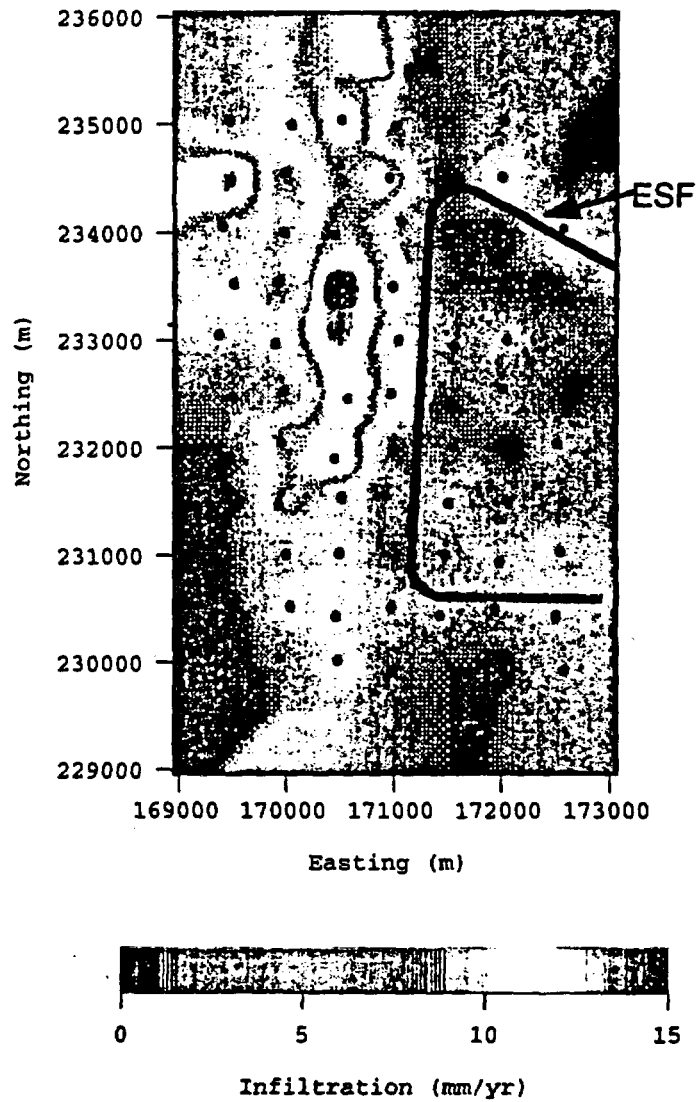


Figure 8-14. Estimated infiltration rate in the area included in the study simulating the arrival of bomb-pulse  $^{36}\text{Cl}$  at the potential repository horizon.

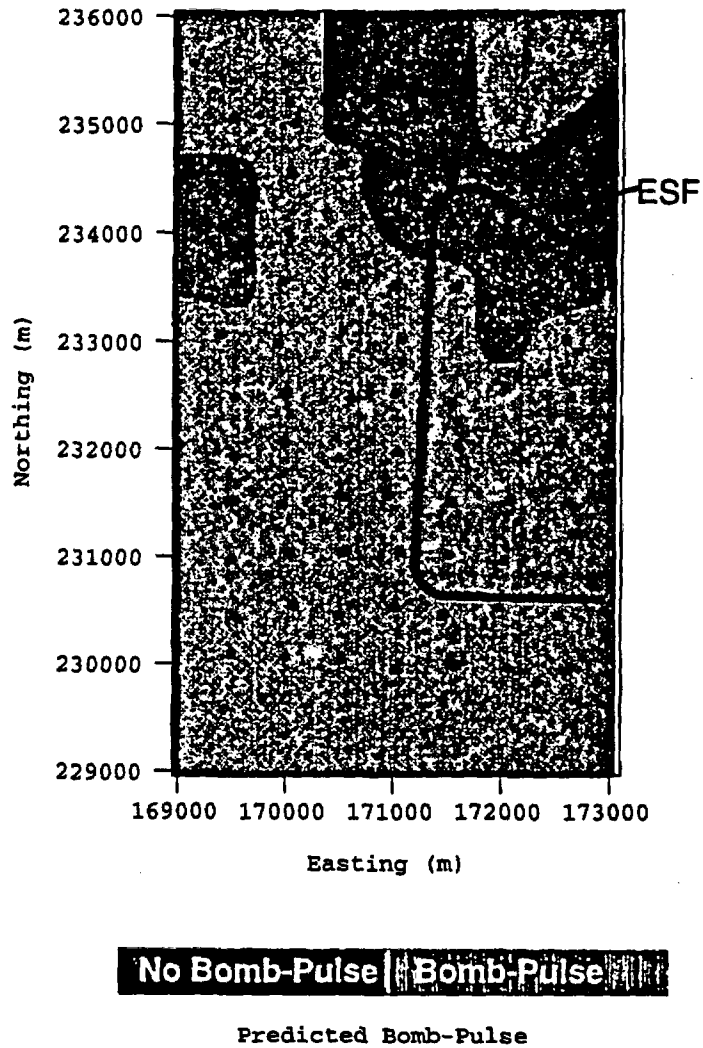


Figure 8-15. Predicted arrivals of bomb-pulse  $^{36}\text{Cl}$  at the potential repository horizon using property set 6541a. Locations at which more than 1% of the particle travel times are less than 50 years are designated as a bomb-pulse zone.

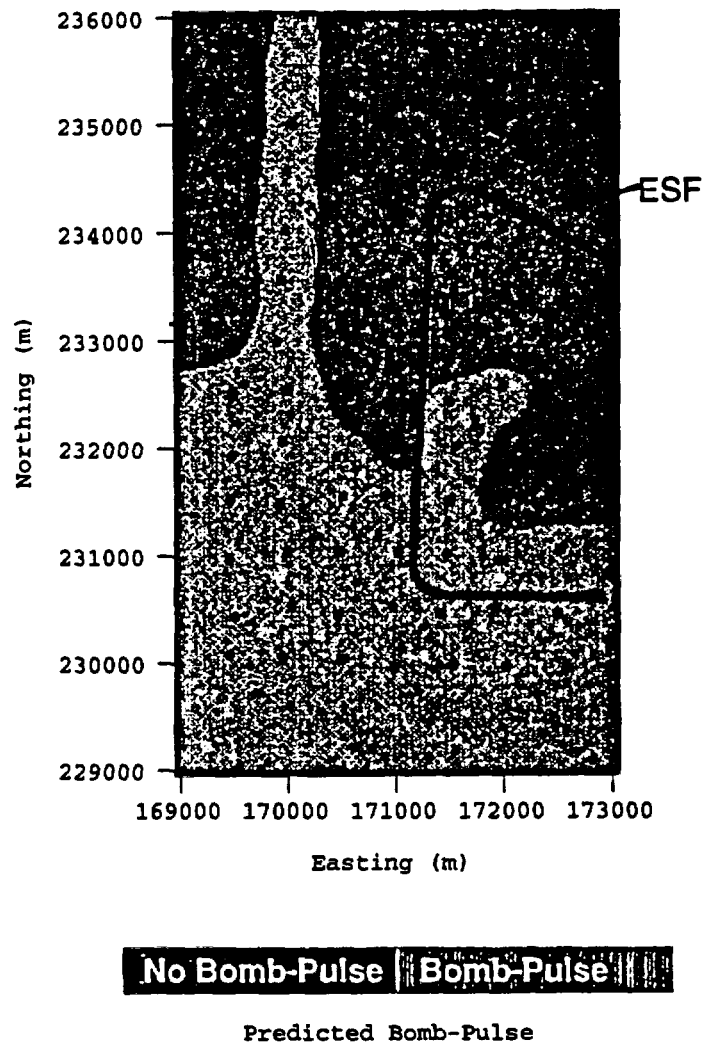


Figure 8-16. Predicted arrivals of bomb-pulse  $^{36}\text{Cl}$  at the potential repository horizon using property set 6541b. Locations at which more than 1% of the particle travel times are less than 50 years are designated as a bomb-pulse zone.

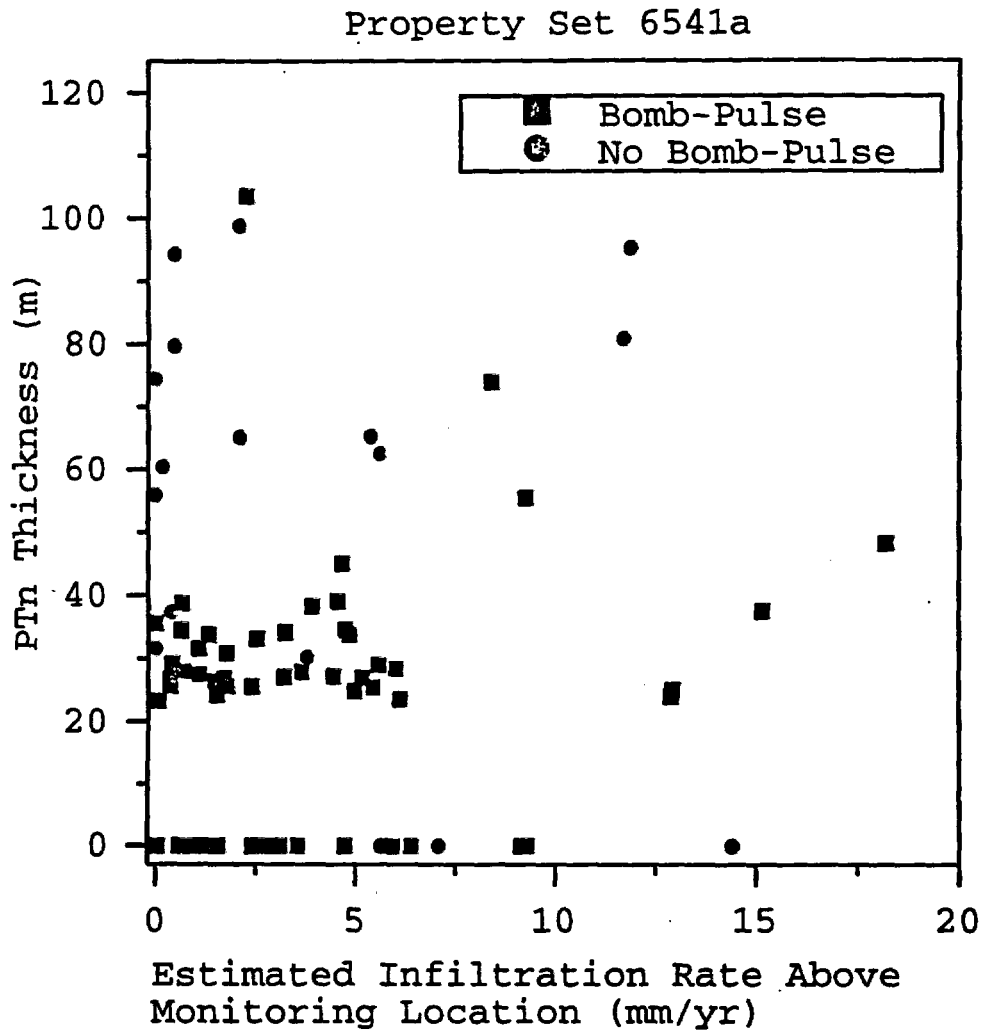


Figure 8-17. Scatter plot of bomb-pulse  $^{36}\text{Cl}$  indicators for infiltration rate vs. PTn thickness above monitoring locations, for simulations using property set 6541a.

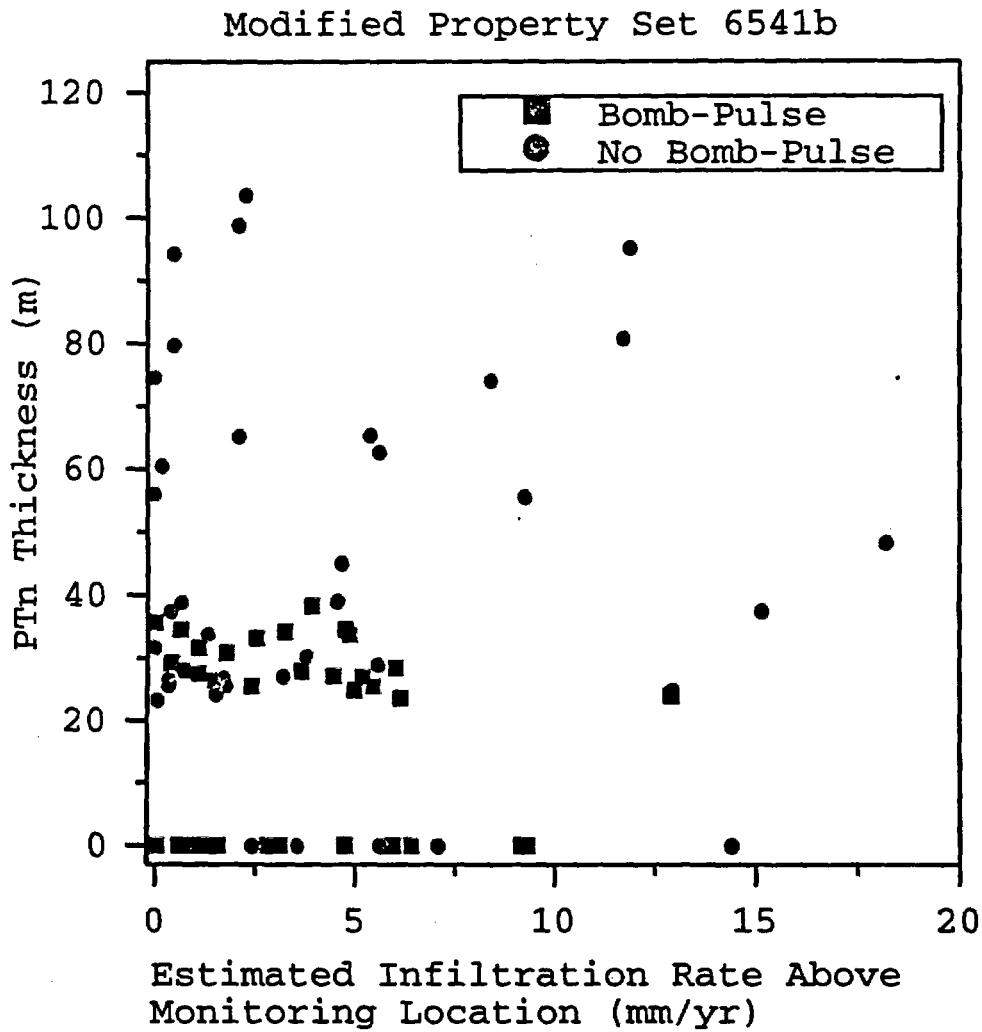
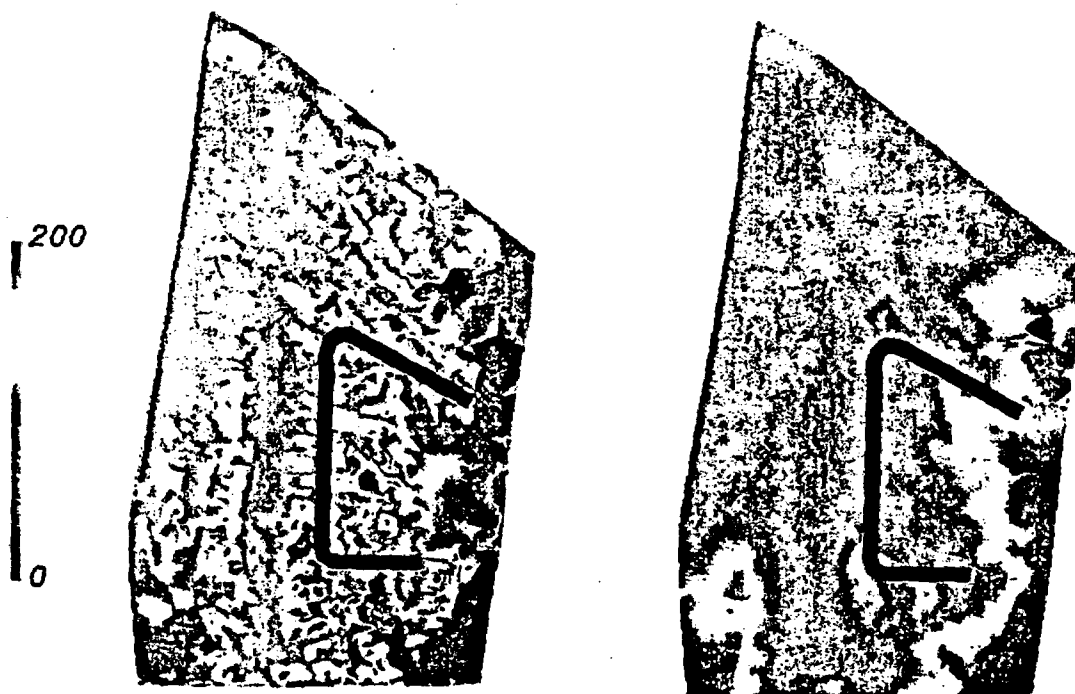


Figure 8-18. Scatter plot of bomb-pulse  $^{36}\text{Cl}$  indicators for infiltration rate vs. PTn thickness above monitoring locations, for simulations using property set 6541b.



**Figure 8-19. Chloride concentration (mg/L) predicted in the three-dimensional model. Left figure: map of estimated chloride concentrations at the surface. Right figure: simulated chloride concentrations at an elevation of 900 m. Top of page is North.**

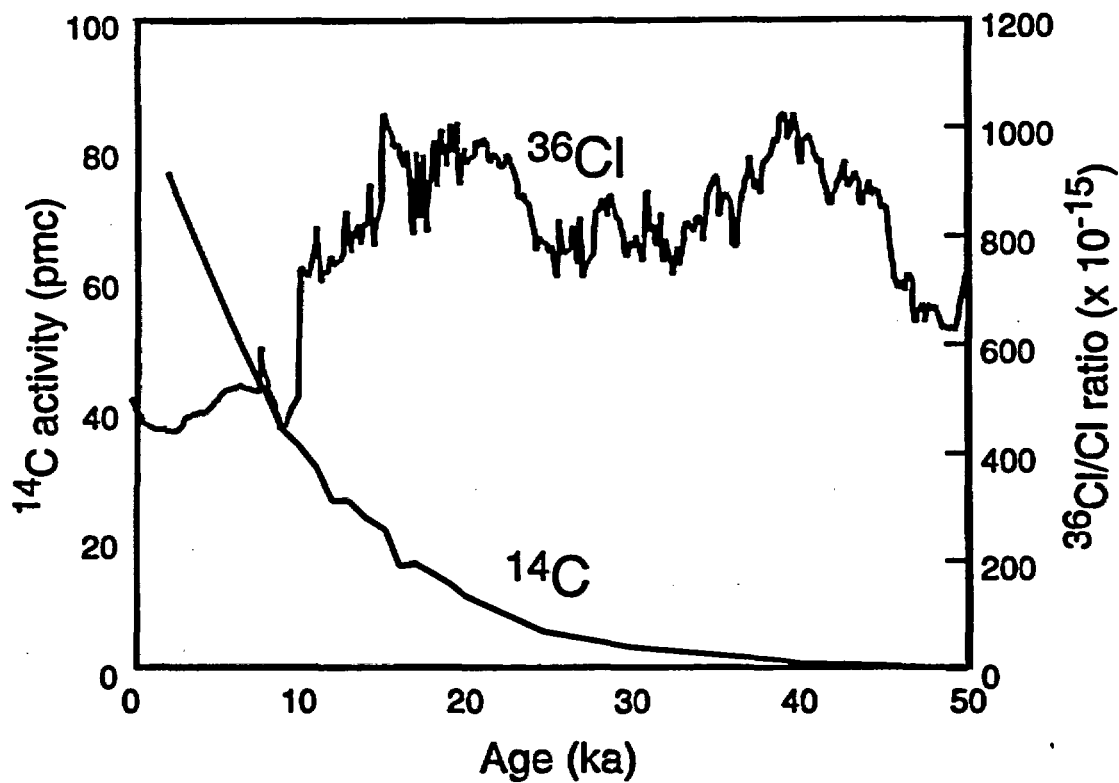


Figure 8-20. Reconstructed <sup>14</sup>C and <sup>36</sup>Cl activities for the last 50 ka. From Fabryka-Martin et al. (in press [b]).

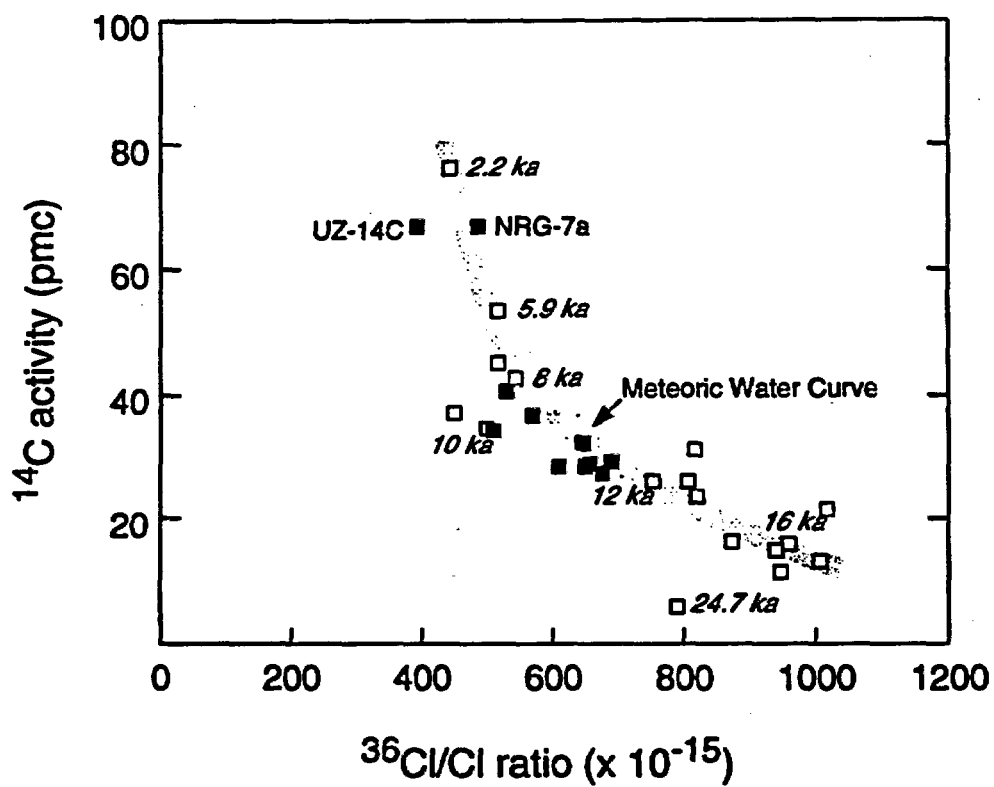


Figure 8-21. Reconstructed  $^{14}\text{C}$  and  $^{36}\text{Cl}$  activities in the atmosphere for the last 20 ka, from Fabryka-Martin et al. (in press [b]). Perched water data from UZ-14, SD-7 and NGR-7/7a.

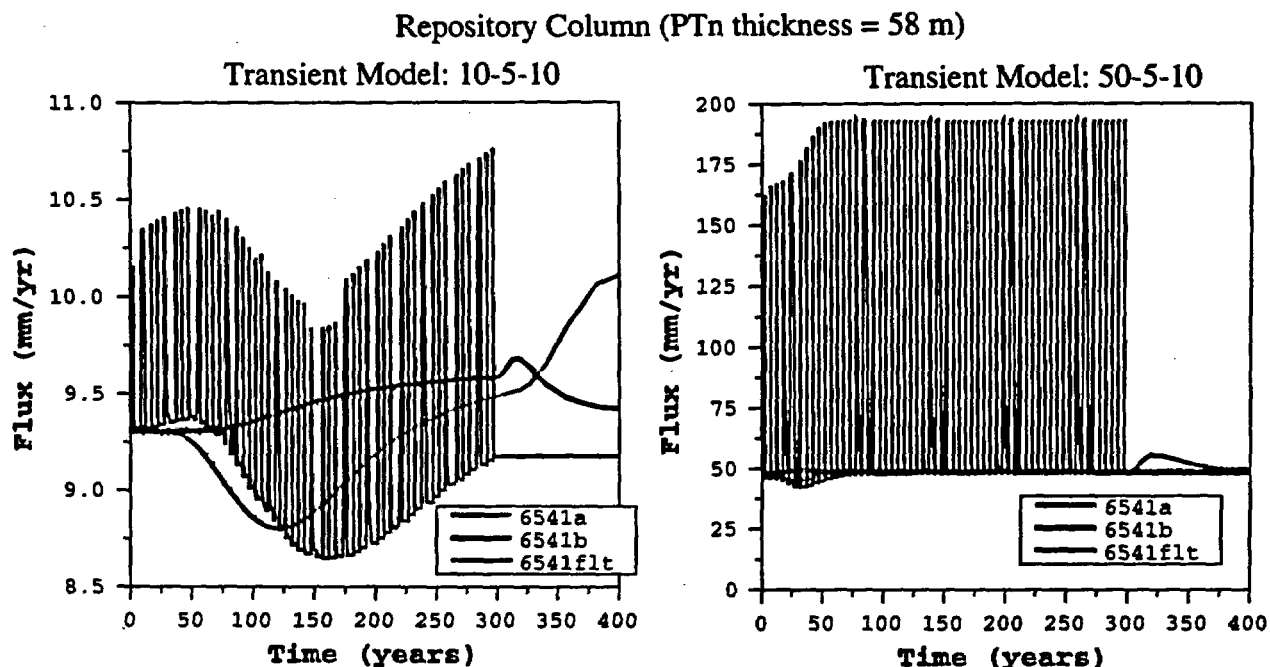


Figure 8-22. Simulated flux variation responses at potential repository in repository column model for 10-5-10 and 50-5-10 transient infiltration models. Model input involves 300 years of transient infiltration followed by 100 years of uniform infiltration.

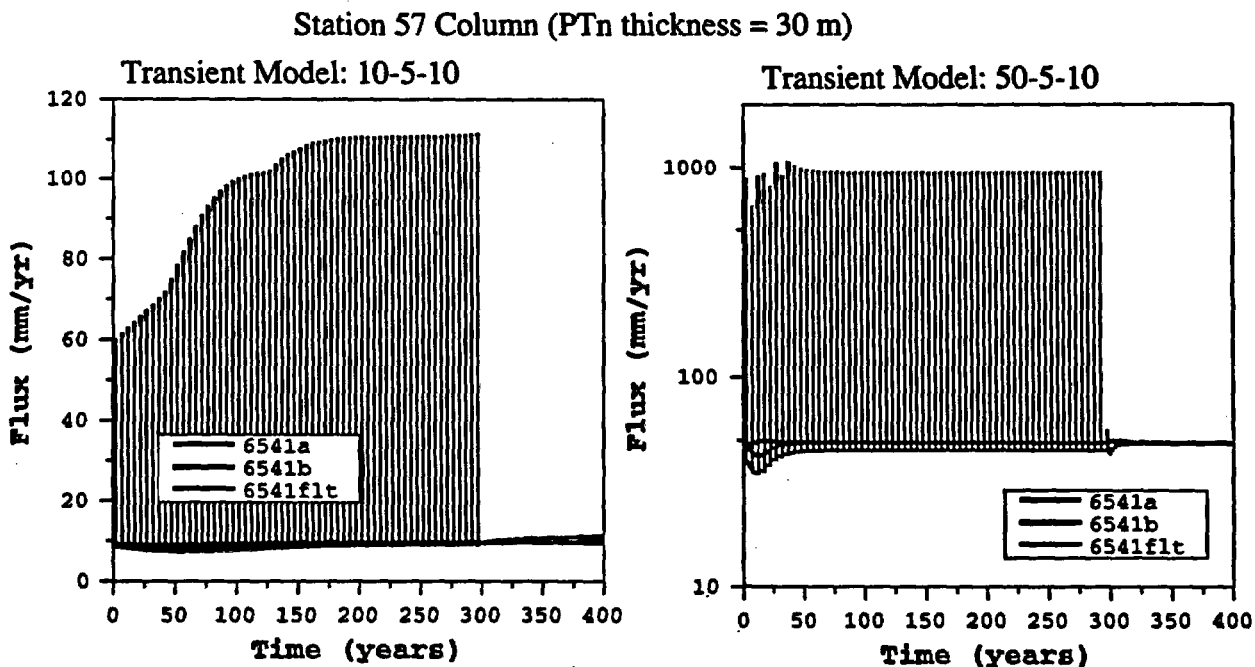


Figure 8-23. Simulated flux variation responses at ESF in Station 57 model for 10-5-10 and 50-5-10 transient infiltration models. Figures show 200 years of transient infiltration.

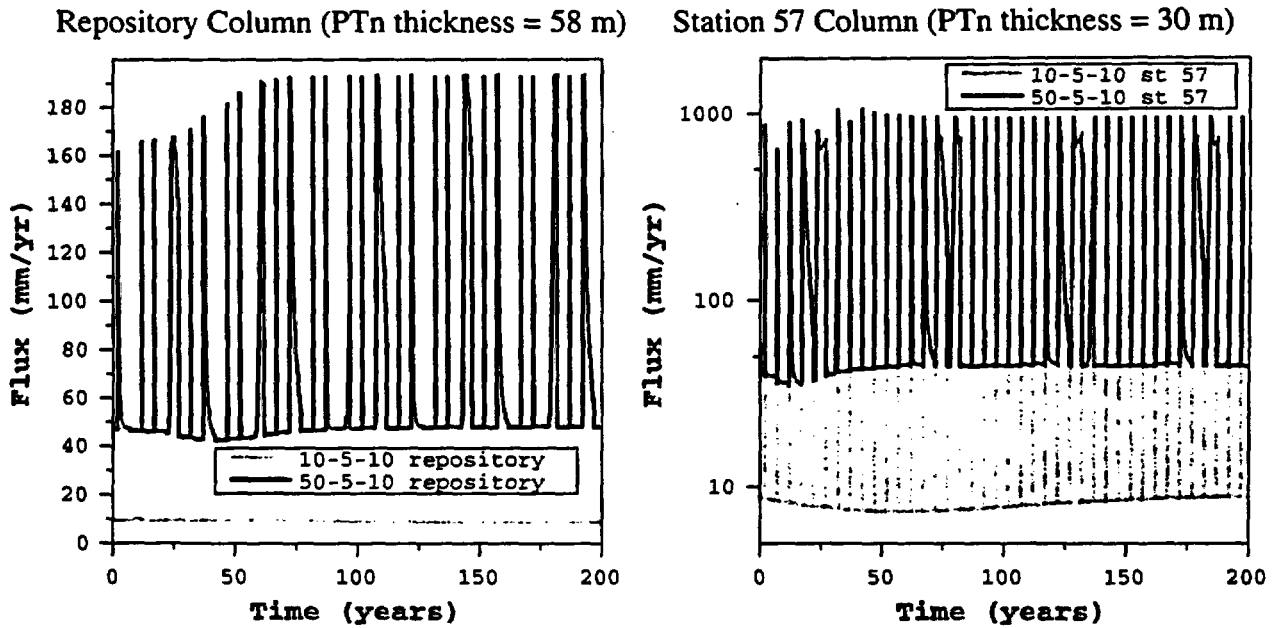


Figure 8-24. Simulated flux variation responses in fault zones at potential repository elevation with the Repository Column model and the Station 57 model for 10-5-10 and 50-5-10 transient infiltration rate models. The first 200 years of transient is shown for property set 6541ft.

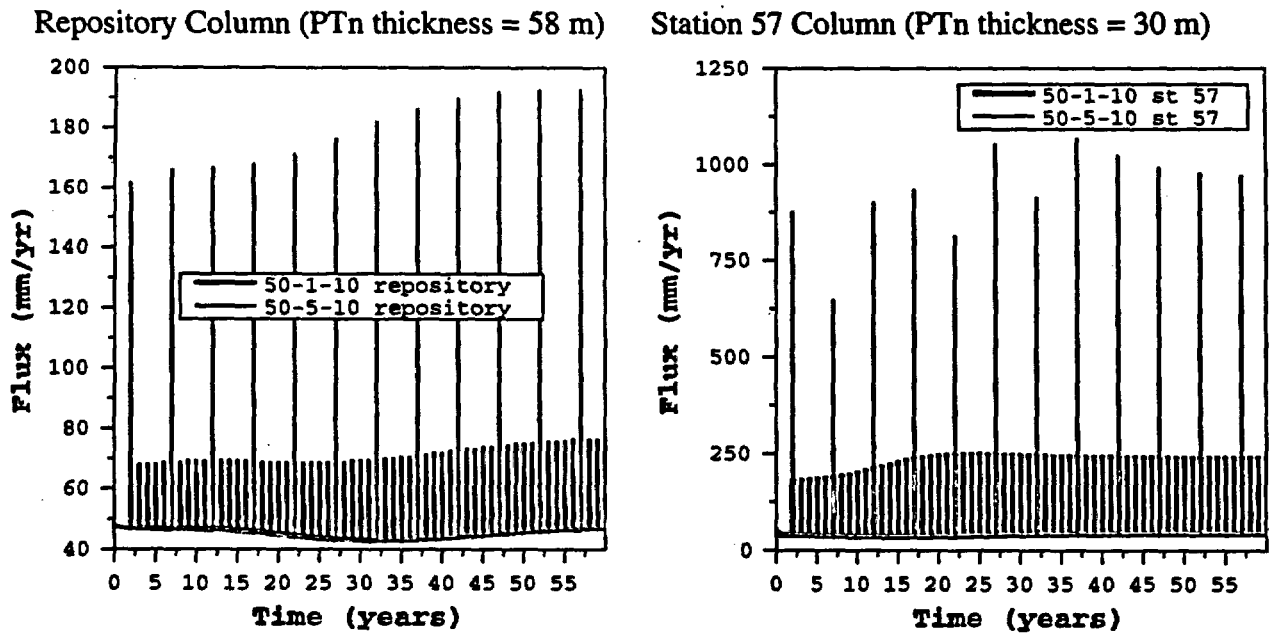
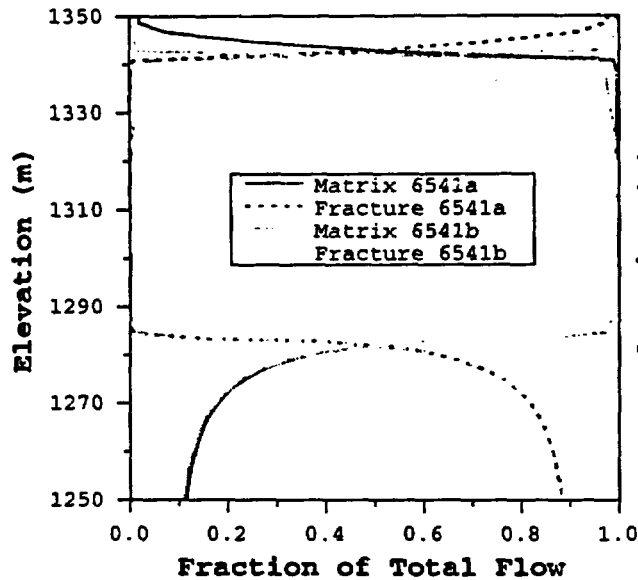
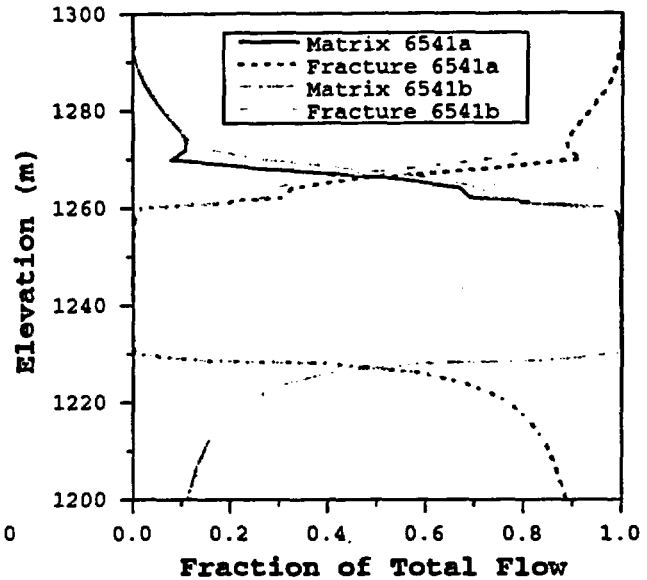


Figure 8-25. Simulated flux variation responses in faults at potential repository horizon with the Repository Column model and the Station 57 model for 50-1-10 and 50-5-10 transient infiltration rate models. The first 60 years of transient is shown for property set 6541ft

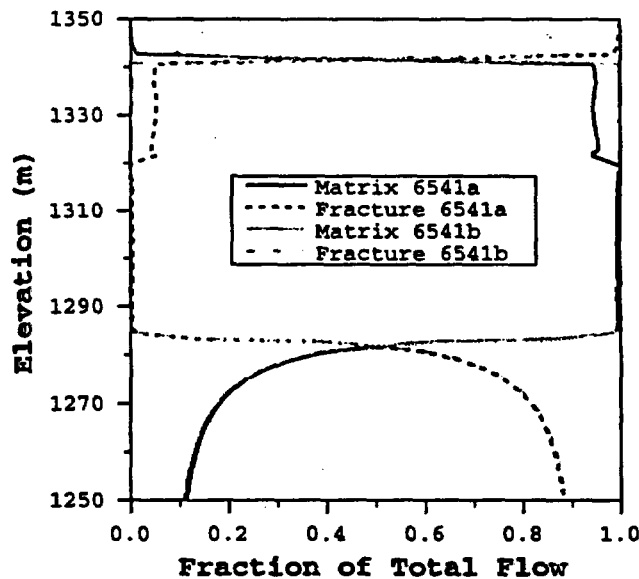
Repository Column (PTn thickness = 58 m)  
Just before pulse



Station 57 Column (PTn thickness = 30 m)  
Just before pulse



Repository Column (PTn thickness = 58 m)  
45 days after pulse



Station 57 Column (PTn thickness = 30 m)  
45 days after pulse

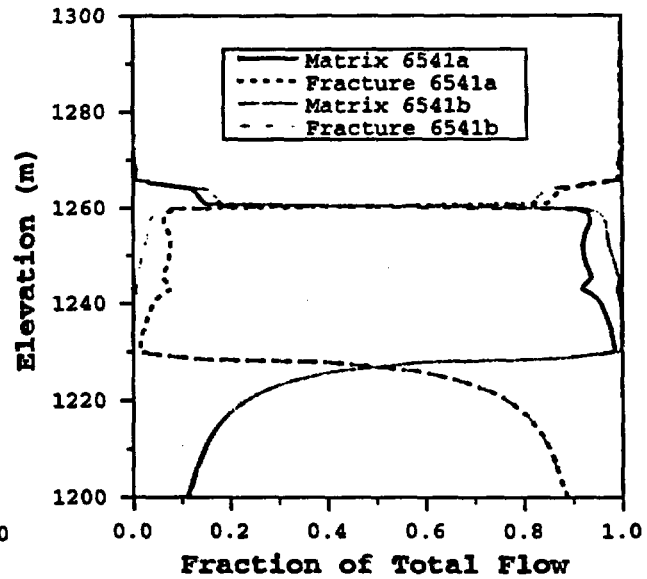


Figure 8-26. Simulated flux distributions in Repository Column model and Station 57 model for parameter sets 6541a and 6541b during 10-5-50 transient infiltration simulation. Figures show flux distribution between matrix and fractures in PTn just before a pulse of water is applied and 45 days after a pulse is applied. Pulses are applied every 5 years for 10 days at a rate of 25 mm/day

## 9. CONCLUSIONS

The objective of the Water Movement Test activity is to acquire geochemical and isotopic data relevant to the development and testing of conceptual flow and transport models for the unsaturated zone at Yucca Mountain. Over the past ten years, more than 600 samples have been analyzed for  $^{36}\text{Cl}$  from deep and shallow boreholes, soil profiles, ground water, and the ESF. These data have been used to establish lower bounds on infiltration rates, estimate ground water ages, establish bounding values for hydrologic flow parameters governing fracture transport, and develop a conceptual model for the distribution of fast flow paths. Under wetter climatic conditions fast flow pathways will respond quickly to increase in infiltration and have the potential to become seeps.

### 9.1 Data collection and analysis

The most extensive set of  $^{36}\text{Cl}$  data for Yucca Mountain is for rock samples from the ESF. Thus far, 237 analyses are available from 234 sample locations. The  $^{36}\text{Cl}$  signals in the northern part of the ESF are highly variable and elevated above present background levels. At several locations, the measured signals are high enough to be unambiguous indicators of at least a small component of bomb-pulse  $^{36}\text{Cl}$ , implying that some fraction of the water at the ESF level arrived there during the past 50 years. In the southern part of the ESF, the  $^{36}\text{Cl}$  signals are less variable and at levels equal to or slightly below the present-day background value. The following findings and accomplishments highlight the significance of the data collected to-date, as well as important considerations and directions for further analysis:

- The ESF sample results show a wide distribution of  $^{36}\text{Cl}/\text{Cl}$  ratios. These range from a few samples with low ratios significantly below the present-day meteoric background ratio of  $500 \times 10^{-15}$  to several samples with high values considered to be unambiguous indicators of the presence of bomb-pulse  $^{36}\text{Cl}$  in the ESF pore fluids. These bomb-pulse samples have  $^{36}\text{Cl}/\text{Cl}$  ratios that are greater than  $1250 \times 10^{-15}$ , ranging up to  $4100 \times 10^{-15}$ .
- Even the highest  $^{36}\text{Cl}/\text{Cl}$  ratios observed thus far in the ESF are low when compared to some of the ratios measured for samples from surface-based boreholes. Ratios for the latter category exceed  $20,000 \times 10^{-15}$  for one of the samples from the TCw unit in borehole UZ-N55 and over  $30,000 \times 10^{-15}$  for one from the PTn.
- The ESF samples exhibit a sharp contrast in the  $^{36}\text{Cl}$  signals, with respect to their magnitude and variability, when comparing those for the north part of the ESF to those from the south part.
- Cl concentrations measured in porewater from the PTn in the North Ramp range from 15 to 45 mg/L and, based on their low Br/Cl ratios, have not been influenced by ESF construction water. These low Cl concentrations are consistent with the Flint et al. (1996) infiltration model. Their uniformity suggests that the flux through the PTn matrix is on the order of 5 mm/yr at this location. Also, because the values approach those measured in perched water at Yucca Mountain, these results support a conceptual model that does not require fracture

- The low  $^{36}\text{Cl}/\text{Cl}$  ratios measured for several of the samples from the southern part of the ESF highlight the need to identify a geochemical indicator suitable for quantifying the extent to which these low  $^{36}\text{Cl}$  results may have been diluted by rock Cl. Sulfate concentrations have been measured for precipitation, ground water, soil and rock samples from Yucca Mountain in order to evaluate the applicability of  $\text{SO}_4/\text{Cl}$  ratios for this purpose.

## 9.2 Conceptual model of flow and transport

A conceptual flow and transport model for the unsaturated zone at Yucca Mountain must meet several criteria in that it must account for, or at least be consistent with, all of the following data sets:

- observed distribution of  $^{36}\text{Cl}/\text{Cl}$  ratios in the ESF, e.g., the absence of bomb-pulse  $^{36}\text{Cl}$  in some locations and its presence in others, provides a significant challenge for our conceptual and numerical models,
- observed distribution of  $^{36}\text{Cl}/\text{Cl}$  ratios in shallow and deep boreholes,
- observed distributions of other travel-time indicators, such as tritium and  $^{14}\text{C}$ ,
- observed distribution of other environmental tracers such as Cl,
- spatial distribution of surface infiltration,
- surface and subsurface distribution of structural features, and their degree of connectivity within and between lithologic units, and
- hydrological flow and transport parameters for matrix and fracture flow.

Our conceptual model for flow in the unsaturated zone at Yucca Mountain, which appears to meet most of the above criteria, includes the following components:

- Surface infiltration percolates downward through the TCw via rapid fracture flow.
- A transition from fracture- to matrix-dominated flow occurs at the TCw/ PTn boundary. Fracture flow in the PTn is expected to represent only a small portion of the total flow if it exists at all. However, under the zones with the highest infiltration rates, PTn fracture flow may be more predominant.
- Due to the matrix-dominated flow in the PTn, most climatic variability should be damped out in this unit. However, the PTn is not expected to completely smooth all spatial variability in infiltration rates.
- At the PTn/TSw interface, there is a return to fracture-dominated flow, due to the low matrix permeabilities of the TSw. Therefore, transport times for  $^{36}\text{Cl}$  and other solutes through the TSw (as with the TCw) are expected to be very short, such that the "fast" part of fast pathways identified with bomb-pulse nuclides actually resides in the PTn. Thus, for any samples collected in the TSw, any indications of travel times reflect the PTn's control on the upper hydrologic flow system of Yucca Mountain.
- Complex flow patterns in the unsaturated zone below the potential repository may be associated with features such as the TSw basal vitrophyre and the heterogenous secondary mineral distribution in the CHn. Lateral flow above the basal vitrophyre could serve as a converging mechanism bringing dilute fluid from high infiltration zones to perched water bodies which have been encountered beneath low infiltration zones. Similarly, low-

permeability zeolitic zones in the CHn may divert the lateral flow the downward flow of water beneath high infiltration zones laterally to locations below the perched water.

Uncertainties associated with the flow system above the potential repository horizon are generally associated with the quantification of the proportion of the PTn flux in the fractures as well as the bulk hydrologic properties used in large-scale simulations. Other uncertainties in the upper part of the system include the potential for lateral diversion at the TCw/PTn and PTn/TSw interfaces. In the lower part of the unsaturated zone, below the potential repository, the age and source of the perched water remains uncertain. Also, the degree of fracturing in the zeolitized CHn is not well characterized, leading to inexact predictions of fluid flow partitioning between fractures and matrix in that unit.

The conceptual model of unsaturated-zone flow also includes fault zones. The primary characteristic of fault zones is the predicted increased fracture permeability of nonwelded units. This increased fracture permeability generates a greater potential for fast flow and transport through the PTn. However, due to the high matrix permeability, most flow, even in fault zones, will remain in the matrix. The portion of flow that occurs in fractures will feed young water from the base of TCw to the top of the TSw. Thus, water traveling along this path and measured in pore fluids from the ESF or in perched water bodies should have the signature of young water insofar as it is not retarded in the PTn matrix. A fast path detected by high levels of  $^{36}\text{Cl}$  in the TSw does not need to be directly in a fault zone. Rather, the water that arrives at the sample location need only have traveled in the fault zone through the PTn. The ubiquitous cooling fractures in the TSw may provide more opportune pathways than the fault, particularly where the fault is not vertical. This part of the conceptual model is supported by the presence of bomb-pulse  $^{36}\text{Cl}$  in samples that may be a large distance away from faults but that almost always appear to be associated with faults.

The apparent lack of bomb-pulse  $^{36}\text{Cl}$  in most of the ESF samples suggests that the PTn, at least away from a fault zone, significantly damps the timing and magnitude of fluxes that increase due to climate change. If this concept holds true through further analysis, then it would suggest that repository design and performance assessment (PA) efforts can be based on fluxes that are uniform in time, even near fault zones. Although the  $^{36}\text{Cl}$  data cannot be used to quantify fluxes directly, they do at least identify the type of fast path for which it may not be acceptable to assume damping of high fluxes. Further analysis is required to determine the significance of the data set from this perspective. However, if additional analysis shows that  $^{36}\text{Cl}/\text{Cl}$  ratios much below  $800 \times 10^{-15}$  also indicate the presence of bomb-pulse  $^{36}\text{Cl}$ , then this finding may invalidate the assumption that long-term average fluxes can be used for repository design and PA calculations, and that episodic fluxes at the potential repository horizon still need to be considered for these applications.

Finally, the  $^{36}\text{Cl}$  data are consistent with  $^{14}\text{C}$  data and with the results of solute-transport simulations suggesting that groundwater travel times are less than 10,000 years everywhere in the unsaturated zone at Yucca Mountain. Low  $^{36}\text{Cl}/\text{Cl}$  ratios measured for some ESF samples

require further evaluation in order to assess whether or not these ratios provide evidence for "stagnant" zones of older water.

### 9.3 Conceptual model for fast paths

Considerable attention has been focused on understanding the distribution of elevated  $^{36}\text{Cl}/\text{Cl}$  ratios that indicate the presence of bomb-pulse  $^{36}\text{Cl}$  at the sampled depths, i.e., a component of travel time less than 50 years. Independent corroborative evidence for this interpretation includes bomb-pulse tritium in the TSw from surface-based boreholes as well as in samples from the ESF.

Detailed characterization of the structural settings of the  $^{36}\text{Cl}$  sample locations and of their relationships to structural features and infiltration rates has provided the basis for a proposed conceptual model for fast pathways at Yucca Mountain. Although the presence of bomb-pulse isotopes in the unsaturated zone at Yucca Mountain was known prior to the construction of the ESF, little significant information was known about the structural settings in the vicinity of the samples collected from boreholes. In addition, determination of horizontal variability in the concentrations of bomb-pulse isotopes in a single stratigraphic unit was not possible. The conceptual model, which can now be corroborated by data from surface-based boreholes, states that three conditions must be present in order to transmit bomb-pulse  $^{36}\text{Cl}$  to the sampled depth within 50 years:

- A continuous fracture path must extend from the surface to the sampled depth. This condition is necessary because travel times through the matrix of unfractured rock is expected to exceed 50 years. The condition of a continuous fracture path is easily satisfied in most of the welded portions of the Tiva Canyon and Topopah Spring units. The limiting hydrologic unit for controlling transport rates is the nonwelded PTn unit which is usually relatively unfractured. Hence, satisfying the condition of a continuous fracture pathway requires the presence of faults that cut the PTn unit and increase its fracture conductivity.
- The magnitude of surface infiltration must be sufficiently high to initiate and sustain at least a small component of fracture flow along the connected fracture path. Transport simulations indicate that the threshold rate may be on the order of 1-2 mm/yr.
- The residence time of water in the soil cover must be less than 50 years, i.e., the soil thickness must be less than 3 meters.

Evaluation of this fast-path model using field observations, and current structural and infiltration models, are presented in the report. The model was used to predict the distribution of bomb-pulse  $^{36}\text{Cl}$  for the study area, including the planned East-West drift. The model was evaluated by a case-by-case examination of the ESF data against the model's prediction of the presence or absence of bomb-pulse  $^{36}\text{Cl}$ . The evaluation concluded that the model successfully predicted the presence of bomb-pulse  $^{36}\text{Cl}$  in most cases. However, in some cases, the conceptual model did not adequately account for the observed  $^{36}\text{Cl}$  data. In the southern part of the ESF, such as along the south ramp, the PTn thins and faults are encountered but nonetheless no bomb-pulse  $^{36}\text{Cl}$  has been detected here. Although this finding supports a hypothesis that the infiltration rates in the northern part of the ESF may have been over-estimated, porewater chloride concentrations from

the North Ramp boreholes in the PTn actually support the infiltration estimates. If the true infiltration rates were lower in the north, then mean travel times to the ESF (based on transport simulations) would be about 10,000 years, leading to consistency between the site-scale transport model and the observed  $^{36}\text{Cl}$  and  $^{14}\text{C}$  data sets. Then, as the PTn thins to the south, average simulated travel times to the ESF increase, and the model predicts a modern (pre-bomb)  $^{36}\text{Cl}$  signal just as is observed. On the other hand, if the present estimates for the infiltration rates to the north can be shown to be correct, then the PTn hydrologic properties may be in error. These properties have been determined by an inversion procedure, in which the infiltration rate is assumed to be known, and the hydrologic properties are varied until the flow model achieves an acceptable match with measured saturation profiles for boreholes. A modification of the inversion procedure to incorporate checks against porewater chloride concentrations measured in samples from surface-based boreholes as well as from ESF drillholes, along with analysis of the detailed hydrologic properties, may be required to resolve this issue. Finally, it is also critical to evaluate the  $^{36}\text{Cl}$  sampling locations and data for the South Ramp samples in order to corroborate those results.

Further refinements to the conceptual model have been suggested by the analysis and are currently underway. Data supporting the occurrence of fast paths associated only with fault zones are the unambiguous bomb-pulse signals found in the ESF. Data supporting the assumption of longer travel times to the ESF at locations away from fault zones, are the  $^{36}\text{Cl}/\text{Cl}$  ratios in the range of  $700 \times 10^{-15}$  to  $1200 \times 10^{-15}$  because these signals match the higher background values expected to have been present prior to the Holocene (10,000 years ago). However, an alternative conceptual model which cannot be ruled out identifies many of these signals as also containing a small component of bomb-pulse  $^{36}\text{Cl}$ . The distribution of locations containing bomb-pulse  $^{36}\text{Cl}$  would not change markedly if the detection threshold for a bomb-pulse signal were to be dropped from a  $^{36}\text{Cl}/\text{Cl}$  ratio of  $1250 \times 10^{-15}$ , to a ratio of  $800 \times 10^{-15}$ , i.e., the conceptual model would not need to be changed to adjust to this re-interpretation of the  $^{36}\text{Cl}$  data. However, the zones over which the bomb-pulse signals occur would broaden considerably if the threshold were to be dropped to even lower values. A broader distribution of lower signals could result from spreading of the more concentrated bomb-pulse  $^{36}\text{Cl}$  signal as it enters the top of the fractured TSw.

#### 9.4 Numerical modeling results

The numerical model results provide insight into several important issues associated with isotopic data:

- evaluation of the validity of alternative hydrologic parameter sets,
- estimates of groundwater travel times,
- applicability of environmental data sets for evaluating alternative conceptual models (particularly the utility of  $^{36}\text{Cl}$ ,  $^{14}\text{C}$ , and Cl concentrations for this purpose).

The results of transport simulations in this study reconfirm previous findings that modified PTn properties in fault zones lead to simulations of the arrival of bomb-pulse  $^{36}\text{Cl}$  at the potential

repository horizon. Away from fault zones, the prediction of bomb-pulse  $^{36}\text{Cl}$  at depth is sensitive to the hydrologic parameter set (namely, the model for fracture-matrix interaction), PTn thickness, and flow rate. Transport models were used to investigate relationships of these three controlling factors in order to develop a methodology for predicting fast paths at locations for which data do not exist. The fracture-matrix interaction model for the PTn plays a significant role in predictions of whether or not bomb-pulse  $^{36}\text{Cl}$  signals completely penetrate the PTn and reach the potential repository horizon. Varying this aspect of the model has little effect on simulated saturations, but has a large effect on the depth to which bomb-pulse solutes can travel. The differences in PTn parameters affect what proportion of the total flow occurs in PTn fractures. For some of the parameter sets investigated, the simulations predicted a large component of PTn fracture flow; for others, the predicted PTn fracture flow was small or negligible. Fracture-dominated flow in the PTn resulted in the prediction of a ubiquitous distribution of bomb-pulse  $^{36}\text{Cl}$  at the potential repository horizon. Simulations using parameter sets that predicted only a small fraction of the fracture flow in the PTn were more sensitive in predicting penetration of bomb-pulse  $^{36}\text{Cl}$  at the potential repository horizon. These simulations illustrate how the incorporation of geochemical or isotopic data, such as bomb-pulse  $^{36}\text{Cl}$ , into the calibration (inversion) process serves to reduce the number of possible parameter sets that characterize the flow system.

The influence of PTn thickness and infiltration rate on the prediction of a bomb-pulse  $^{36}\text{Cl}$  signal reaching the potential repository horizon was investigated using the site-scale transport model. As the PTn thins to the south, the frequency of arrivals of bomb-pulse  $^{36}\text{Cl}$  at the potential repository horizon is predicted to increase. Again, these predictions are sensitive to which hydrologic parameter set is used. With parameters that yield a higher proportion of fracture flow in the PTn, the area in which bomb-pulse  $^{36}\text{Cl}$  is predicted to reach the potential repository horizon extends further north (under thicker PTn) than for the parameter sets which favor matrix-dominated flow in the PTn. The distribution of bomb-pulse  $^{36}\text{Cl}$  that is simulated with each model parameter set is inconsistent with the measured distribution of this environmental tracer. The incidence of bomb-pulse  $^{36}\text{Cl}$  is predicted to be highest in the south ramp of the ESF due to a thin overlying PTn; however, the measured data indicate virtually no bomb-pulse  $^{36}\text{Cl}$  signals in this area. The locations at which bomb-pulse  $^{36}\text{Cl}$  signals have been measured in the northern part are mostly well-correlated with faults. The site-scale model does not incorporate any of the faults associated with the ESF bomb-pulse  $^{36}\text{Cl}$  locations. Because of the lack of such faults in the two- and three-dimensional models, one-dimensional models are used to investigate flow and transport processes and hydrologic parameters for fault zones. As described above, modification of PTn properties to represent increased fracturing in faults leads to predictions of bomb-pulse  $^{36}\text{Cl}$  in the ESF, even where the PTn is relatively thick.

The transport model was also used to investigate the role of episodic infiltration on transport of bomb-pulse  $^{36}\text{Cl}$  and flux variations at the potential repository horizon. Simulations using two different hydrologic parameter sets both predicted almost complete damping of the pulsed input in the PTn. The difference in predicted arrivals of bomb-pulse  $^{36}\text{Cl}$  using these two sets remains due to slight differences in the small amount of sustained fracture flow in the PTn. The

difference between the results is greatest where the PTn is thinnest because fracture flow with one of the parameter sets is sustained through the entire PTn. As the PTn thickens, fracture flow through the entire unit is not sustained with either set. In contrast, fracture flow is sustained in fault zones under all cases, and the episodic pulses are not completely damped at these locations. The amplitude of the simulated pulses at the potential repository are greatest where the PTn is thinnest, posing an issue of potential significance to repository design and performance assessment.

With the new geologic model (Zelinski and Clayton, 1996), the new hydrologic parameters (Bodvarsson et al., 1997), and the spatially distributed infiltration map (Flint et al., 1996), simulated transport times through the PTn matrix are shorter than were obtained with previously reported models (Fabryka-Martin et al., in press [a]). Whereas most of the solutes arriving at the ESF or the potential repository horizon in transport simulations had travel times on the order of 10,000 years in earlier studies, the median simulated travel times in the present simulations are between 1,000 and 7,000 years. A component of simulated solute arrival times (or water ages) that are greater than 10,000 years is still present, but represent only 5 to 20% of the particle travel times.

This shift to younger travel time estimates in the simulations contradicts an earlier interpretation of the elevated  $^{36}\text{Cl}/\text{Cl}$  signals (those greater than  $600 \times 10^{-15}$  but less than  $1250 \times 10^{-15}$ ) which have been observed away from fault zones. This interpretation proposed that these signals reflected water that entered the flow system during the Pleistocene, with  $^{36}\text{Cl}/\text{Cl}$  ratios about twice that of the present-day background value. The measured signals were also assumed to be representative of the isotopic composition of water flowing past the sample location. If, however, most of the water flowing past a sample location is actually Holocene in origin (i.e., less than 10,000 years old) as the current simulations suggest, then one hypothesis to resolve the discrepancy with the data is that the measured  $^{36}\text{Cl}/\text{Cl}$  ratios are representative of matrix fluids, which are probably older than 10,000 years, and are relatively insensitive to the composition of TSw fracture fluids, which are younger than 10,000 years. A closer examination of the ESF sampling locations and  $^{36}\text{Cl}$  data and the preparation of samples by direction extraction of porewaters instead of leaching rocks should be able to evaluate this hypothesis.

An alternative conceptual model is that all of the ESF samples with  $^{36}\text{Cl}/\text{Cl}$  ratios elevated above present-day background (e.g., samples with  $^{36}\text{Cl}/\text{Cl}$  ratios above  $\sim 700 \times 10^{-15}$ ) may contain a small component of bomb-pulse  $^{36}\text{Cl}$ . Whereas simulations using the recent PTn model of fracture-matrix interaction supports this conceptual model, the TSw fracture-matrix interaction model would need to be revised in order to prevent all simulated bomb-pulse signals from bypassing the TSw matrix altogether. Such a conceptual model also raises the question as to the apparent absence of bomb-pulse  $^{36}\text{Cl}$  in areas of the ESF under thin PTn, but its widespread presence in zones under thicker PTn. These apparent discrepancies will be addressed with additional isotopic and geochemical analyses such as pore-water chloride concentrations measured for the PTn in the North and South Ramps.

## 9.5 Mineralogic characteristics of flow paths

The mineralogic and textural data collected so far have not defined generally applicable, distinctive characteristics of either fast-path or long water-residence sites in the ESF. These special infiltration cases apparently represent relatively minor variations in the hydrologic and geochemical environment of the unsaturated zone, especially when the effects of infiltration, as represented by the mineralogy, are averaged over very long periods of time. Specific examples of fast-path systems, however, may be distinguished by characteristic differences in mineral abundance. The Sundance fault and associated subsidiary flow paths constitute the best example of distinctive mineralogy. The two mineralogic characteristics are the presence of calcite and thick clay/mordenite fracture coatings. Both of these attest to the particularly high fracture connectivity in the interval north of the Sundance fault. The thicknesses and textures of the clay coatings suggest that the apertures of cooling joints were increased by minor tectonic movement shortly after the Topopah Spring Tuff was deposited. The widespread occurrence of calcite precipitates in this interval also indicates excellent inter-fracture and fracture-fault connectivity. These findings support the conclusions from the structural analysis of the Sundance fault zone: the vicinity of the Sundance fault is distinguished, not only by the presence of an additional local fracture set, but also by the mineralogic evidence for multiple episodes of fracture dilation and extension.

The secondary mineralogy of samples with  $^{36}\text{Cl}/\text{Cl}$  ratios below  $350 \times 10^{-15}$ , based on characterization of four samples from the South Ramp, is generally similar to that of samples with higher ratios. Syngenetic minerals (feldspar, crystalline silica, Fe-Ti oxides) and Mn minerals are present in these samples just as they are in other samples from the same lithostratigraphic subunits. Mineralogic data collected from the ESF South Ramp samples may help identify some of the fundamental reasons why zones of possibly longer-than-usual water residence time exist and why these zones are more common in the South Ramp. The unstable minerals kenyaite (hydrous sodium silicate) and moganite (monoclinic crystalline silica) were documented along fractures and faults in the Tpcpv (equivalent to the uppermost PTn hydrogeologic unit). High activities of alkalis, sulfates, or both may play a role in the crystallization of both minerals. At Yucca Mountain, these minerals are associated with other secondary minerals that probably formed by water-rock interaction during the cooling of the Tiva Canyon Tuff, an alteration episode that affected the tuff in the southern part of the mountain. In this part of the mountain, there was local development of pore fluids with extremely saline, alkaline compositions. These fluids must have evolved in a rock-fracture system that inhibited the intermixing of pore fluids traveling along different pathways through the rock unit.

The mineralogic data set collected to date over-represents fast-path samples and samples from sites that may represent ground water with long travel times because the characterization of these sites was assigned a higher priority. In the absence of major mineralogic differences between samples with very different  $^{36}\text{Cl}/\text{Cl}$  values, this bias increases the difficulty of detecting more subtle mineral or textural features associated with different kinds of flow paths. The associations described above must be regarded as preliminary until a larger proportion of the ESF sample set

has been characterized.

#### **9.6 Open issues and the need for additional work**

Suggestions for further work have been made throughout the report. In general, a more thorough development and testing of alternative conceptual models that are consistent with the hydrologic conditions as well as with the geochemical and isotopic data is required. The potential role of the PTn in delaying or diverting increased flux under wetter future climatic condition needs to be explored. Independent confirmation of the infiltration model should be obtained by building an extensive data base of porewater Cl concentrations of samples from the underground excavation. These data can then be incorporated into the calibration process to produce improved estimates for PTn hydrologic properties.

Other important and perplexing issues to resolve are the differences in the magnitude and variability observed in the  $^{36}\text{Cl}$  signals between the northern half of the ESF to those from the southern half. Additional sampling should be conducted to test the reproducibility of the high and variable  $^{36}\text{Cl}$  signals in the north, supplemented by analyses for other bomb-pulse nuclides such as  $^{99}\text{Tc}$  and  $^{129}\text{I}$ . A careful assessment of the structural settings of the south set of samples should be conducted to determine whether sampling in this area may have been biased against sites with bomb-pulse  $^{36}\text{Cl}$ . A transect of soil samples across the surface above the ESF could address the question of the magnitude of the  $^{36}\text{Cl}$  signal entering the bedrock at present. The applicability of  $\text{SO}_4/\text{Cl}$  ratios for quantifying dilution of samples with rock Cl should continue to be assessed, particularly to address the low  $^{36}\text{Cl}$  signals in some of the south ESF samples.

These concerns are not new and are being addressed within the current workscope of the Water Movement Test in the ESF. Continued collection of  $^{36}\text{Cl}$  data in conjunction with analysis of Cl pore water, detailed hydrologic property analysis of the PTn, and investigation of the role of structural features in controlling flow will help resolve many of the issues.

---

## ACKNOWLEDGMENTS

This work was supported and managed by the U.S. Department of Energy, Yucca Mountain Site Characterization Office (YMP) as part of the Civilian Radioactive Waste Management Program. Data acquired as part of this activity and presented in this report were developed under YMP quality assurance procedures; their QA status and traceability to data tracking numbers or YMP notebooks are given in Appendix E.

The YMP Test Coordination Office, particularly A. Mitchell, supported field sample collection in the ESF tunnel. We are grateful for sampling advice from S. Beason. Paul Dixon supervised ESF sample collection and processing in 1996 and early 1997. Assisting in this aspect of the activity were D. Brenner, Q. Snead, J.C. Watt, and S. Winters. D. Elmore, P. Sharma, S. Vogt and T. Miller at PRIME Laboratory worked assiduously to ensure timely and accurate isotopic analyses. G. Woldegabriel assisted in the mineralogic characterization of the ESF rock samples.

Technical review comments on an early draft were provided by R. Patterson, W. Scott, B. Mukhopadhyah, and B. Robinson. A later draft was reviewed by J. Boak, P. Reimus, and D. Vaniman. We thank all of these reviewers for their useful suggestions.

## 10. REFERENCES

- Albin, A.L., Singleton, W.L., Moyer, T.C., Lee, A.C., Lung, R.C., Eatman, G.L.W., and Barr, D.L. (1997). "Geology of the main drift - station 28+00 to 55+00, Exploratory Studies Facility, Yucca Mountain Project, Yucca Mountain, Nevada," Rep. to the U.S. Department of Energy, DTN GS970208314224.005.
- Allison, G.B., Gee, G.W., and Tyler, S.W. (1994). "Vadose-zone techniques for estimating groundwater recharge in arid and semiarid regions," *Soil Sci. Soc. Amer. J.*, Vol. 58, 6-14.
- Allison, G. B., and Hughes, M.W. (1978). "The use of environmental chloride and tritium to estimate total recharge to an unconfined aquifer," *Austr. J. Soil Res.*, Vol. 16, 181-195.
- Anna, L.O. (in press). "Preliminary three-dimensional discrete fracture model of the Topopah Spring Tuff in the Exploratory Studies Facility, Yucca Mountain area, Nye County, Nevada," U.S. Geol. Surv. Open-File Rep., p. 75.
- Anna, L., and Wallman, P. (1997). "Characterizing the fracture network in the unsaturated zone at Yucca Mountain, Nevada, Part 2. Numerical simulation of flow based in a three-dimensional discrete fracture network, in fractured reservoirs: characterization and modeling," *In Rocky Mountain Geologists 1997 Guidebook*, Hoak, T.E., Klawitter, A.L., and Blomquist, P.K., (Eds.), pp. 199-208.
- Bandurraga, M. (1996). Lawrence Berkeley Lab., Berkeley, CA, personal communication.
- Barr, D.L., Moyer, T.C., Singleton, W.L., Albin, A.L., Lung, R.C., Lee, A.C., Beason, S.C., and Eatman, G.L.W. (1996). "Geology of the North Ramp - Stations 4+00 to 28+00, Exploratory Studies Facility, Yucca Mountain Project, Yucca Mountain, Nevada," Summary Rep. by the U.S. Bur. of Reclam. to the U.S. Department of Energy, p. 258.
- Beason, S.C., Turlington, G.A., Lung, R.C., Eatman, G.L.W., Ryter, D., and Barr, D.L. (1996). "Geology of the North Ramp - Station 0+60 to 4+00, Exploratory Studies Facility, Yucca Mountain Project, Yucca Mountain, Nevada," Summary Rep. by the U.S. Bur. of Reclam. to the U.S. Department of Energy, DTN GS690908314224.019.
- Bentley, H.W., Phillips, F.M., and Davis, S.N. (1986). "Chlorine-36 in the terrestrial environment," *In Hand. of Environ. Isotope Geochem.*, Fontes, J.C., and Fritz, P., (Eds.), Vol. IIB, pp. 427-480.
- Bevington, P.R., and Robinson, D.K. (1992). "Data reduction and error analysis for the physical sciences," McGraw-Hill, Inc., New York, p. 328.
- Bish, D.L., and Chipera, S.J. (1989). "Revised mineralogic summary of Yucca Mountain,

Nevada," Los Alamos National Lab. Rept. LA-11497-MS, p. 68.

Blinov, A. (1988). "The dependence of cosmogenic isotope production rate on solar activity and geomagnetic field variations," *In Secular Solar and Geomagnetic Variations in the Last 10,000 years*, Stephenson, F.R., and Wolfendale, A.W., (Eds.), pp. 329-340.

Bodvarsson, G.S., and Bandurraga, T.M. (1996). "Development and calibration of the three-dimensional site-scale unsaturated zone model of Yucca Mountain, Nevada," Lawrence Berkeley National Lab. Rep. 39315, p. 539.

Bodvarsson, G.S., Bandurraga, T.M., and Wu, Y.S. (1997). "The site-scale unsaturated zone model of Yucca Mountain, Nevada, for the viability assessment," Lawrence Berkeley National Lab. Rep. 40378 (June 1997).

Braun, C.A., Spengler, R.W., Martin, L.G., and Blackburn, R.L. (1996). "Detailed geologic mapping along the Ghost Dance fault, Yucca Mountain, Nevada," U.S. Geol. Surv. Admin. Rep. to the U.S. Department of Energy. DTN GS940108314221.001

Broxton, D.E., Warren, R.G., Hagan, R.C., and Luedemann, G. (1986). "Chemistry of diagenetically altered tuffs at a potential waste repository, Yucca Mountain, Nye County, Nevada," Los Alamos National Lab. Rep. LA-10802-MS.

Buesch, D.C., Spengler, R.W., Moyer, T.C., and Geslin, J.K. (1996). "Proposed stratigraphic nomenclature and macroscopic identification of lithostratigraphic units of the Paintbrush Group exposed at Yucca Mountain, Nevada: U.S. Geol. Surv. Open File Rep. 94-469, p. 52.

Buesch, D.C., Dickerson, R.P., Drake, R.M., and Spengler, R.W. (1994). "Integrated geology and preliminary cross section along the north ramp of the Exploratory Studies Facility, Yucca Mountain," *In Procs. Fifth Annual Intern. Conf. on High Level Radioactive Waste Management*, Las Vegas, NV, May 22-26, 1994, pp. 1055-1065.

Byers, F.M., Jr., Carr, W.J., Orkild, P.P., Quinlivan, W.D., and Sargent, K.A. (1976). "Volcanic suites and related cauldrons of Timber Mountain-Oasis Valley caldera complex, southern Nevada," U.S. Geol. Surv. Prof. Paper 919, p. 69.

Carlos, B.A. (1985). "Minerals in fractures of the unsaturated zone from drill core USW G-4, Yucca Mountain, Nye County, Nevada," Los Alamos National Lab. Rep. LA-10415-MS, p. 55.

Carlos, B.A., Chipera, S.J., and Bish, D.L. (1995). "Distribution and chemistry of fracture-lining minerals at Yucca Mountain, Nevada," Los Alamos National Lab. Rep. LA-12977-MS, p. 92.

Carlos, B.A., Chipera, S.J., Bish, D.L., and Craven, S.J. (1993). "Fracture-lining manganese oxide minerals in silicic tuff, Yucca Mountain, Nevada, U.S.A.," *Chem. Geol.*, Vol. 107, 47-69.

Carr, W.J. (1986). "Volcano-tectonic setting of Yucca Mountain and Crater Flat, southwestern Nevada," *In Geologic and Hydrologic Investigations of a Potential Nuclear Waste Disposal at Yucca Mountain, Southern Nevada*, Carr, D., and Yount, J.C., (Eds.), U.S. Geol. Surv. Bull., Vol. 1790, 35-49.

Chipera, S.J., Vaniman, D.T., and Bish, D.L. (1996). "Zeolite abundances and the vitric-to-zeolitic transition in drill holes USW SD-7, 9, and 12, Yucca Mountain, Nevada," Los Alamos National Lab. Yucca Mountain Milestone Rept. LA4240.

Chipera, S.J., Vaniman, D.T., Carlos, B.A., and Bish D.L. (1995). "Mineralogic variation in drill core UE-25 UZ#16, Yucca Mountain, Nevada," Los Alamos National Lab. Rept. LA-12810-MS, p. 39.

Christiansen, R.L., and Lipman, P.W. (1965). "Geologic map of the Topopah Spring Northwest Quadrangle, Nye County, Nevada," U.S. Geol. Surv. Geologic Quad. Map GQ-444, 1:24,000-scale.

Claassen, H.C. (1983). "Sources and mechanisms of recharge for ground water in the west-central Amargosa Desert, Nevada -- a geochemical interpretation," U.S. Geol. Surv. Open-File Rep. 83-542, p. 61.

Cowan, D.L., Priest, V., and Levy, S.S. (1993). "ESR dating of quartz from Exile Hill, Nevada," Appl. Radiat. Isot. Vol. 44, 1035-1039.

Davis, S.N., and Murphy, E. (1987). "Dating ground water and the evaluation of repositories for radioactive waste," Wash. D.C., U.S. Gov. Printing Off., Rep. NUREG/CR-4912, p. 181.

Day, W.C., Potter, C.J., Sweetkind, D.S., Dickerson, R.P., and San Juan, C.J. (in press). "Bedrock geologic map of the central block area, Yucca Mountain, Nye County, Nevada," U.S. Geol. Surv. Misc. Invest. Ser. I-2601, 1:6000 scale, 2 plates with text.

Engstrom, D.A., and Rautman, C.A. (1996). "Geology of the USW SD-9 drill hole, Yucca Mountain, Nevada," Sandia Report, Sandia National Lab., SAND-96-2030, p. 128.

Eugster, H.P. (1967). "Hydrous sodium silicates from Lake Magadi, Kenya: precursors of bedded chert," Science. Vol. 157, 1177-1180.

Fabryka-Martin, J.T., and Liu, B. (1995). "Distribution of chlorine-36 in UZ-14, UZ#16, perched water, and the ESF North Ramp, Yucca Mountain, Nevada," Los Alamos National Lab., Yucca Mountain Project Milestone Rep. M3431 (draft approved by Yucca Mountain Project Office, being revised for publication).

Fabryka-Martin, J.T., Wightman, S.J., Murphy, W.J., Wickham, M.P., Caffee, M.W., Nimz, G.J.,

Southon, J.R., and Sharma, P. (1993). "Distribution of chlorine-36 in the unsaturated zone at Yucca Mountain: an indicator of fast transport paths," *In Proc., FOCUS '93: Site Characterization and Model Validation*, Amer. Nucl. Soc., La Grange Park, IL, pp. 58-68.

Fabryka-Martin, J.T., Dixon, P.R., Levy, S.S., Liu, B., Turin, H.J., and Wolfsberg, A.V. (1996). "Summary report of chlorine-36 studies: systematic sampling for chlorine-36 in the Exploratory Studies Facility," Los Alamos National Lab., Yucca Mountain Project Milestone Report 3783AD, (Submitted to Yucca Mountain Project Office on Mar. 31, 1996). LA-UR-96-1384.

Fabryka-Martin, J.T., Wolfsberg, A.V., Dixon, P.R., Levy, S.S., Musgrave, J., and Turin, H.J. (in press [a]). "Summary report of chlorine-36 studies: systematic sampling for chlorine-36 in the Exploratory Studies Facility," Los Alamos National Lab., Yucca Mountain Project Milestone Report 3783M. Draft dated 8-30-96, submitted to DOE on 8-30-96, approved by DOE on 01-16-97. Resubmitted corrected Rep. on 7-16-97, awaiting DOE approval.

Fabryka-Martin, J.T., Turin, H.J., Brenner, D., Dixon, P.R., Liu, B., Musgrave, J., and Wolfsberg A.V. (in press [b]). "Summary report of chlorine-36 studies," Los Alamos National Lab. Yucca Mountain Project Milestone Report 3782M, approved by Yucca Mountain Project Office for publication on Jan. 16, 1997.

Fairley, J.P., and Sonnenthal, E. (1996). "Preliminary conceptual model of flow pathways based on <sup>36</sup>Cl and other environmental isotopes," *In Development and Calibration of the Three-dimensional Site-scale Unsaturated Zone Model of Yucca Mountain, Nevada*, Bodvarsson, G.S. and Bandurraga, T.M. (Eds.), Lawrence Berkeley National Lab. Rep. 39315, pp. 380-415.

Fairley, J.P., and Wu, Y.S. (1997). "Modeling of fast flow and transport pathways in the unsaturated zone using environmental isotopic tracers," *In The Site-scale Unsaturated Zone Model of Yucca Mountain, Nevada, for the Viability Assessment*, Bodvarsson, G.S., Bandurraga, T.M. and Wu, Y.S. (Eds.), Lawrence Berkeley National Lab. Report 40378 (June 1997). pp. 16-1 to 16-16.

Flint, L.E., Matrix properties of hydrogeologic units at Yucca Mountain Nevada, U.S. Geological Survey Open File Report, MOL 19970324.0046, GS950308312231.002, (in preparation), 1996.

Flint, A.L., and Flint, L.E. (1994). "Spatial distribution of potential near-surface moisture flux at Yucca Mountain, Nevada," *In Procs. Fourth Internat. Conf., High Level Radioactive Waste Management*, Amer. Nucl. Soc., La Grange Park, IL., pp. 2352-2358.

Flint, A.L., Hevesi, J.A., and Flint, L.E. (1996). "Conceptual and numerical model of infiltration for the Yucca Mountain Area, Nevada," U.S. Geol. Surv. Yucca Mountain Project Milestone Rep. 3GUI623M, U.S. Geol. Surv. Water Resour. Invest. Rep. USGS WRIR MOL 19970409.0087, GS960908312211.003 DOE Milestone 3GUI623M, U.S. Geol. Surv.

Flint, L.E., and Flint, A.L. (1995). "Shallow infiltration processes at Yucca Mountain, Nevada - neutron logging data 1984-93," U.S. Geol. Surv Water Resour. Invest. Rep. 95-4035, p. 46.

Gable, C. W., Trease, H., and Cherry, T. (1996). "Geological applications of automatic grid generation tools for finite elements applied to porous flow modeling, Numerical Grid Generation in Computational Fluid Dynamics and Related Fields," Soni, B.K., Thompson, J.F., Hausser, H., and Eiseman, P.R., (Eds.), Engin. Res. Center, Mississippi State Univ. Press.

Gardner, W. R. (1967). "Water uptake and salt distribution pattern in saline soil," *In Proc. Symp. on Isotope and Radiation Techniq. on Soil Phys. and Irrig. Studies*, pp. 335-340.

Hay, R.L., Pexton, R.E., Teague, T.T., and Kyser, T.K. (1986). "Spring-related carbonate rocks, Mg clays, and associated minerals in Pliocene deposits of the Amargosa Desert, Nevada and California," Geol. Soc. Amer. Bull. Vol. 97, 1488-1503.

Heaney, P.J., and Post, L.E. (1992). "The widespread distribution of a novel silica polymorph in microcrystalline quartz varieties," Science, Vol. 255, 441-443.

Hevesi, J.A., Flint, A.L. and Flint, L.E. (1994). "Verification of a 1-dimensional model for predicting shallow infiltration at Yucca Mountain," *In Procs. Fifth Intern. Conf. on High Level Radioactive Waste Management*, Amer. Nucl. Soc., La Grange Park, IL, pp. 2323-2332.

Hevesi, J.A., Flint, A.L., and Flint, L.E. (1996). "The effect of bedrock properties on the spatial variability of infiltration at Yucca Mountain, Nevada," Geol. Soc. Amer. Abstr. with Prog., Vol. 28, p. A-522.

Hevesi J.A., Flint, A.L., and Istok, J.D. (1992). "Precipitation estimation in mountainous terrain using multivariate statistics. Part II: isohyetal maps," J. Appl. Meteor., Vol. 31, 677-688.

Hudson, D.B. and Flint, A.L. (1996). "Estimation of shallow infiltration and presence of potential fast pathways for shallow infiltration in the Yucca Mountain area, Nevada," U.S. Geol. Surv. Level 3 Milestone 3GUI611M.

Kwicklis, E.M., Bodvarsson, G.S. and Flint, A.L. (1997) "A conceptual model of unsaturated zone flow and transport," U.S. Geol. Surv. Level 3 Milestone 3GUM612M.

La Pointe, P.R., and Hudson, J.A. (1985). "Characterization and interpretation of rock mass joint patterns," Geol. Soc. of Amer. Spec. Pap., Vol. 199, p. 37.

LeCain, G.D. and Patterson, G. (1996). "Technical analysis/interpretation, air permeability and hydrochemistry data through January 31, 1997," Yucca Mountain Project level 4 milestone SPH35EM4, U.S Geol. Surv.

- Levy, S.S. (1991). "Mineralogic alteration history and paleohydrology at Yucca Mountain, Nevada," *In Proc. Second Annual Intern. Conf. on High-Level Radioactive Waste Management, Las Vegas, Nevada, Amer. Nucl. Soc. and Amer. Soc. Civil Engin., La Grange, IL and New York, NY, pp. 477-485.*
- Levy, S.S. (1993). "Surface-discharging hydrothermal systems at Yucca Mountain - examining the evidence," *In Scientific Basis for Nuclear Waste Management XVI, Interrante, C.G. and Pabalan, R.T. (Eds.), MRS Sympos. Procs., Vol 294, Mat. Res. Soc., Pittsburgh, PA, pp. 543-548.*
- Levy, S.S., and Chipera, S.J. (1997). "Mineralogy, alteration, and hydrologic properties of the PTn hydrologic unit, Yucca Mountain, Nevada," *Los Alamos National Lab. Yucca Mountain Project Level 4 Milestone Rep. SP344DM4.*  
p. 42.
- Levy, S.S., Norman, D.I., and Chipera, S.J. (1996). "Alteration history studies in the Exploratory Studies Facility, Yucca Mountain, Nevada, USA," *In Scientific Basis for Nuclear Waste Management XIX, Murphy, W.M. and Knecht, D.A. (Eds.), MRS Sympos. Procs. Vol. 412, Mat. Res. Soc., Pittsburgh, PA pp. 783-790.*
- Levy, S.S., and O'Neil, J.R. (1989). "Moderate-temperature zeolitic alteration in a cooling pyroclastic deposit," *Chem. Geol., Vol. 76, 321-326.*
- Levy, S.S., Sweetkind, D.S., Fabryka-Martin, J.T., Dixon, P.R., Roach, J.L., Wolfsberg, L.E., Elmore, D., and Sharma, P. (1997). "Investigations of structural controls and mineralogic associations of chlorine-36 fast pathways in the ESF," *Los Alamos National Lab. Yucca Mountain Project milestone SP2301M4.*
- Liu, B., Fabryka-Martin, J.T., Wolfsberg, A.V., Robinson, B.A., and Sharma, P. (1995). "Significance of Apparent Discrepancies in Water Ages Derived from Atmospheric Radionuclides at Yucca Mountain, Nevada," *In Water Resources at Risk, Hotchkiss, W.R., Downey, J.S., Gutentag, E.D., and Moore, J.E., (Eds.), Amer. Inst. Hydrol., Minneapolis, MN, NH-52 - NH-62.*
- Lundstrom, S.C., McDaniel, S.M. Guertal, W., Nash, M.H., Wesling, J.R., Cidziel, J., Cox, S., and Coe, J. (1995). "Characteristics and development of alluvial soils of Yucca Mountain," *Yucca Mountain Project Branch Milestone 1995 Milestone Report 3GCH510M.*
- Marshall, B.D., and Mahan, S.A. (1994) "Strontium isotope geochemistry of soil and playa deposits near Yucca Mountain, Nevada," *In Procs. Fifth Intern. Conf. on High Level Radioactive Waste Management, Amer. Nucl. Soc., La Grange Park, IL, pp. 2685-2691.*
- Matthias A.D., Hassan, H.M., Hu, Y.Q., Watson, J.E., and Warrick, A.W. (1986).

"Evapotranspiration estimates derived from subsoil salinity data," J. Hydrol., Vol. 85, 209-223.

McKinley, P.W., and Oliver, T.A. (1994). "Meteorological, stream-discharge, and water-quality data for 1986 through 1991 from two small basins in Central Nevada," U.S. Geol. Surv. Open-File Rep. 93-651.

McKinley, P.W., and Oliver, T.A. (1995). "Meteorological, stream-discharge, and water-quality data for 1986 through 1992 from two small basins in Central Nevada," U.S. Geol. Surv. Open-File Rep. 94-456.

Montazer, P., and Wilson, W.E. (1984). "Conceptual hydrologic model of flow in the unsaturated zone, Yucca Mountain, Nevada," U.S. Geol. Surv. Water Resour. Invest. Rep. 84-4345, p. 55.

Moyer, T.C., and Geslin, J.K. (1995). "Lithostratigraphy of the Calico Hills Formation and the Prow Pass Tuff (Crater Flat Group) at Yucca Mountain, Nevada: U.S. Geol. Surv. Open File Rep. 94-460, p. 59.

Moyer, T.C., Geslin, J.K., and Flint, L.E. (1996). "Stratigraphic relations and hydrologic properties of the Paintbrush Tuff nonwelded (PTn) hydrologic unit, Yucca Mountain, Nevada," U.S. Geol. Surv. Open File Rep. 95-397, p. 151.

Mower, T.E., Higgins, J.D., Yang, In.C., and Peters, C.A. (1994). Pore-water extraction from unsaturated tuff by triaxial and one-dimensional compression methods, Nevada Test Site, Nevada. U.S. Geol. Surv. Water Resour. Invest. Rep. 93-4144.

NADP (National Atmospheric Deposition Program), (NRSP-3/National Trends Network (1997). NADP/NTN Coordination Office, Natural Resource Ecology Laboratory, Colorado State University, Fort Collins, CO 80523.

Norris, A.E., Bentley, H.W., Cheng, S., Kubik, P.W., Sharma, P., and Gove, H.E. (1990). "<sup>36</sup>Cl studies of water movements deep within unsaturated tuffs," Nucl. Instrum. Meth. Phys. Res., Vol. B52, 455-460.

Norris A.E., Wolfsberg, K., Gifford, S.K., Bentley, H.W., and Elmore, D. (1987). "Infiltration at Yucca Mountain, Nevada, traced by <sup>36</sup>Cl," Nucl. Instrum. Meth. Phys. Res., Vol. B29, 376-379.

Odling, N. (1995). "The development of network properties in natural fracture patterns: an example from the Devonian sandstones of western Norway," *In Procs. Conf. on Fractured and Jointed Rock Masses*, Myer, L.R., Tsang, C.F., Cooks, N.W.G., and Goodman, R.E., (Eds.), A.A. Balkema Pubs., Rotterdam, The Netherlands, pp. 35-41.

Ortiz, T.S., Williams, R.L., Nimick, F.B., and South, D.L. (1985). "A three-dimensional model of reference thermal/mechanical and hydrological stratigraphy at Yucca Mountain, southern

Nevada," Sandia National Labs. Rep. SAND 84-1076, Albuquerque, NM.

Paces, J.B., Mahan, S.A., Ludwig, K.R., Kwak, L.M., Neymark, L.A., Simmons, K.R., Nealey, L.D., Marshall, B.D., and Walker, A. (1995). "Progress report on dating Quaternary surficial deposits," U.S. Geol. Surv., Yucca Mountain Project Branch Milestone 1995 Milestone Report 3GCH510M.

Paces, J.B., Marshall, B.D., Whelan, J.F., and Neymark, L.A. (1997). "Progress report on unsaturated zone stable and radiogenic isotope studies," U.S. Geol. Surv. Yucca Mountain Project Branch Level 4 Milestone Rep. SPC23FM4, p. 6.

Paces, J.B., Neymark, L.A., Marshall, B.D., Whelan, J.F., and Peterman Z.E. (1996). "Ages and origins of subsurface secondary minerals in the Exploratory Studies Facility (ESF)," U.S. Geol. Surv. Yucca Mountain Project Branch 1996 Milestone Rept. 3GQH450M.

Peterman, Z.E., and Paces J.B. (1996). "Paleohydrology - age control from U-Series and <sup>14</sup>C dating of calcite and opal in the ESF," Nucl. Waste Tech. Rev. Bd. meeting, July 9-10, 1996, Denver, CO.

Phillips, F.M. (1994). "Environmental tracers for water movement in desert soils of the American southwest," Soil Sci. Soc. Am. J., Vol. 58, 15-24.

Phillips, F.M., Mattick, J.L., Duval, T.A., Elmore, D., and Kubik, P.W. (1988). "Chlorine-36 and tritium from nuclear weapons fallout as tracers for long-term liquid and vapor movement in desert soils," Water Resour. Res., Vol: 24, 1877-1891.

Plummer, M.A., Phillips, F.M., Fabryka-Martin, J.T., Turin, H.J., Wigand, P.E., and Sharma, P. (1997). "Chlorine-36 in fossil rat urine: an archive of cosmogenic nuclide deposition during the past 40,000 years," Science, Vol. 277, 538-541.

Potter, C.J., Day, W.C., Sweetkind, D.S., and Dickerson, R.P. (1996). "Fault styles and strain accommodation in the Tiva Canyon Tuff, Yucca Mountain, Nevada," EOS Trans. Amer. Geophys. Un., Vol. 77, p. S265.

Potter, C.J., Dickerson, R.P., and Day, W.C. (1995). "Nature and continuity of the Sundance fault, Yucca Mountain, Nevada," U.S. Geol. Surv. Admin. Rep. to the U.S. Department of Energy, p. 26.

Rautman, C.A., and Engstrom, D.A. (1996). "Geology of the USW SD-7 drill hole, Yucca Mountain, NV," Sandia National Labs. SAND 96-1474.

Reheis, M.C. and Kihl, R. (1995). "Dust deposition in southern Nevada and California, 1984-1989: relations to climate, source area, and source lithology," J. Geophys. Res., Vol. 100, 8893-

8918.

Robinson, B.A., and Henderson, S.E. (1997, submitted). "A cell-based particle tracking technique for solute transport in porous media," Water Resour. Res.

Robinson, B.A., Wolfsberg, A.V., Gable, C.W., and Zyvoloski, G.A. (1995). "An unsaturated zone flow and transport model of Yucca Mountain," Los Alamos National Lab. Yucca Mountain Project Milestone Rep. 3468.

Robinson, B.A., Wolfsberg, A.V., Viswanathan, H.S., Gable, C.W., Zyvoloski, G.A., and Turin, H.J. (1996). "Modeling of flow, radionuclide migration, and environmental isotope distributions at Yucca Mountain," Los Alamos National Lab. YMP Milestone 3672.

Robinson, B.A., Wolfsberg, A.V., Viswanathan, H.S., Bussod, G.Y., Gable, C.W., and Meijer, A. (1997). "The site-scale unsaturated zone transport model of Yucca Mountain," Los Alamos National Lab. Yucca Mountain Project Milestone SP25BM3.

Rock Color Chart Committee, "Rock-color chart," Geol. Soc. Amer. (1980).

Rousseau, J.P., Kwicklis, E.M., and Gillies, D.C., Eds. (1996). "Hydrogeology of the unsaturated zone, north ramp area of the Exploratory Studies Facility, Yucca Mountain, Nevada," U.S. Geol. Surv., Water Res. Invest. Rep. (Draft submitted to Yucca Mountain Project Office in Sept. 1996).

Sawyer, D.A., Fleck, R.J., Lamphere, M.A., Warren, R.G., Broxton, D.E., and Hudson, R. (1994). "Episodic caldera volcanism in the Miocene southwestern Nevada volcanic field: Revised stratigraphic framework,  $^{40}\text{Ar}/^{39}\text{Ar}$  geochronology, and implications for magmatism and extension," Geol. Soc. Amer. Bull., Vol. 106, 1304-1318.

Scanlon, B.R. (1991). "Evaluation of moisture flux from chloride data in desert soils," J. Hydrol., Vol. 128, 137-156.

Scanlon, B.R. (1992). "Moisture and solute flux along preferred pathways characterized by fissured sediments in desert soils," J. Contam. Hydrol., Vol. 10, 19-46.

Scanlon, B.R., Kubik, P.W., Sharma, P., Richter, B.C., and Gove, H.E. (1990). "Bomb chlorine-36 analysis in the characterization of unsaturated flow at a proposed radioactive waste disposal facility, Chihuahuan Desert, Texas," Nucl. Instrum. Meth. Phys. Res., Vol. B52, 489-492.

Scott, R.B. (1990). "Tectonic setting of Yucca Mountain, southwest Nevada," *In Basin and Range Extensional Tectonics Near the Latitude of Las Vegas, Nevada: Boulder, Colorado*, Wernicke, B.P., (Ed.), Geol. Soc. Amer. Memoir, Vol. 76, 251-282.

Scott, R.B., and Bonk, J. (1984). "Preliminary geologic map of Yucca Mountain, Nye County,

Nevada, with geologic sections," U.S. Geol. Surv. Open File Rep. 84-494, scale-1:12,000.

Scott, R.B., Spengler, R.W., Diehl, S., Lappin, A.R., and Chornack, M.P. (1983). "Geologic character of tuffs in the unsaturated zone at Yucca Mountain, southern Nevada," *In* Role of the Unsaturated Zone in Radioactive and Hazardous Waste Disposal, Mercer, J.W., Rao, P.S.C. and Marine, I.W. (Eds.), Ann Arbor Sci., Ann Arbor, MI., p. 289-335.

Sharma M.L., and Hughes, M.W. (1985). "Groundwater recharge estimation using chloride, deuterium and oxygen-18 profiles in the deep coastal sands of Western Australia," J. Hydrol. Vol. 81, 93-109.

Sharma, P., Kubik, P.W., Fehn, U., and Gove, H.E. (1990). "Development of <sup>36</sup>Cl standards for AMS," Nucl. Instrum. Meth. Phys. Res., Vol. B52, 410-415.

Simonds, F.W., Whitney, J.W., Fox, K.F., Ramelli, A.R., Yount, J.C., Carr, M.D., Menges, C.M., Dickerson, R.P., and Scott, R.B. (1995). "Map showing fault activity in the Yucca Mountain area, Nye County, Nevada," U.S. Geol. Surv. Misc. Invest. Ser. I-2520, 1:24,000 scale, 1 sheet.

Smith, D.B., Zielinski, R.A., and Taylor, H.E. (1982). "Leaching characteristics of ash from the May 18, 1980, eruption of Mount St. Helens volcano, Washington," U.S. Geol. Surv. Open-File Rep. 82-987, p. 22.

Sonnenthal, E.L., and Bodvarsson, G.S. (1997). "Modeling the chloride geochemistry in the unsaturated zone," *In* The Site-Scale Unsaturated Zone Model of Yucca Mountain, Nevada, for the Viability Assessment, Bodvarsson, G.S., Bandurraga, T.M. and Wu, Y.S., (Eds.), Lawrence Berkeley National Lab. Rep. 40378, pp. 15-1 to 15-39.

Sonnenthal, E.L., DePaolo, D.J., and Bodvarsson, G.S. (1997). "Modeling the strontium geochemistry and isotopic ratio in the unsaturated zone," *In* The Site-Scale Unsaturated Zone Model of Yucca Mountain, Nevada, for the Viability Assessment, Bodvarsson, G.S., Bandurraga, T.M. and Wu, Y.S., (Eds.), Lawrence Berkeley National Lab. Report LBNL-40376, p. 17-1-17-14.

Spengler, R.W., and Rosenbaum, J.G. (1980). "Preliminary interpretations of geologic results obtained from boreholes UE25a-4, -5, -6, and -7, Yucca Mountain, Nevada Test Site," U.S. Geol. Surv. Open-File Rep. 80-929, 33 p.

Stone, J.O., Allan, G.L., Fifield, L.K., and Cresswell, R.G. (1996). "Cosmogenic chlorine-36 from calcium spallation," Geochim. Cosmochim. Acta, Vol. 60, 679-692.

Stone, W. J. (1984). "Research in the Salt Lake coal field based on chloride in the unsaturated zone," New Mexico Bur. of Mines and Min. Resour. Open-File Rep. No. 214.

Swadley, W.C., Hoover, D.L., and Rosholt, J.N. (1984). "Preliminary report on Late Cenozoic faulting and stratigraphy in the vicinity of Yucca Mountain, Nye County, Nevada," U.S. Geol. Surv. Open-File Rep. 84-788, p. 42.

Sweetkind, D.S., Verbeek, E.R., Geslin, J.K., and Moyer, T.C. (1995a). "Fracture character of the Paintbrush Tuff nonwelded hydrologic unit, Yucca Mountain, Nevada," U.S. Geol. Surv. Admin. Rep. to the U.S. Department of Energy, 202 p.

Sweetkind, D.S., Verbeek, E.R., Singer, F.R., Byers, F.M., Jr., and Martin, L.G. (1995b). "Surface fracture network at pavement P2001, Fran Ridge, near Yucca Mountain, Nye County, Nevada," U.S. Geol. Surv. Admin. Rep. to the U.S. Department of Energy, p. 130.

Sweetkind, D.S., Potter, C.J., and Verbeek, E.R. (1996a). "Interaction between faults and the fracture network at Yucca Mountain, Nevada," EOS Trans., Amer. Geophys. Un., Vol. 77, p. S266.

Sweetkind, D.S., Beason, S.C., Potter, C.J., Lung, R., Day, W.C., and Barr, D. (1996b). "Correlation between surface and subsurface features at Yucca Mountain, Nevada," Geol. Soc. Amer. Abstr. with Prog., Vol. 28, A-521.

Sweetkind, D.S., and Williams-Stroud, S. (1996). "Characteristics of fractures at Yucca Mountain, Nevada," Synthesis Rep. U.S. Geol. Surv. Admin. Rep. to the U.S. Department of Energy, p. 124.

Sweetkind, D.S., Fabryka-Martin, J.T., Flint, A., Potter, C., and Levy, S.S. (1997a). "Evaluation of the structural significance of bomb-pulse  $^{36}\text{Cl}$  at sample locations in the Exploratory Studies Facility, Yucca Mountain, Nevada," U.S. Geol. Surv. memorandum transmitting Level 4 milestone SPG33M4 to R. Craig, Yucca Mountain Project Branch, 29 Aug., 1997.

Sweetkind, D.S., Barr, D.L., Polacsek, D.K., and Anna, L.O. (1997b). "Integrated fracture data in support of process models, Yucca Mountain, Nevada," U.S. Geol. Surv. Admin. Rep. to the U.S. Department of Energy, p. 145.

Synal, H.A., Beer, J., Bonani, G., Suter, M., and Wolfli, W. (1990). "Atmospheric transport of bomb-produced  $^{36}\text{Cl}$ ," Nucl. Instrum. Meth. Phys. Res., Vol. B52, 483-488.

Throckmorton, C.K., and Verbeek, E.R. (1995). "Joint networks in the Tiva Canyon and Topopah Spring Tuffs of the Paintbrush Group, southwestern Nevada," U.S. Geol. Surv. Open File Rep. 95-2, p. 179.

Tyler, S.W., Chapman, J.B., Conrad, S.H., Hammermeister, D.P., Blout, D., Miller, J., and Ginanni, J.M. (1996). "Soil water flux on the Nevada Test Site: spatial and temporal variations over the last 120,000 years," Water Resour. Res., Vol. 32, 1481-1499.

Tyler S.W. and Walker, G.R. (1994). "Root zone effects on tracer migration in arid zones," Soil Sci. Soc. Amer. J., Vol. 58, 25-31.

Vaniman, D.T., Chipera, S.J., and Bish D.L. (1995). "Petrography, mineralogy, and chemistry of calcite-silica deposits at Exile Hill, Nevada, compared with local spring deposits," Los Alamos National Lab. Rep. LA-13096-MS, 70 p.

Viswanathan, H. S. (1996). "Modification of the Finite Element Heat and Mass Transfer Code (FEHMN) to model multicomponent reactive transport," M.S. Thesis, Univ. of Illinois, Champaign-Urbana, IL, 1995, Tech. Rep. LA-13167-T, Los Alamos National Lab.

Viswanathan, H., Robinson, B.A., Valocchi, A.J., and Triay, I. (submitted, 1997). "A reactive transport model of neptunium migration from the potential repository at Yucca Mountain," J. Hydrol.

Walker, G.R., Jolly, I.D., Stadler, M.H., Leaney, F.W., Davie, R.F., Fifield, L.K., Ophel, T.R., and Bird, J.R. (1991). "Evaluation of the use of chlorine-36 in recharge studies," *In* Intl. Symp. on the Use of Isotope Techniq. in Water Resour. Devel., Vienna, Austria, Paper No. IAEA-SM-319/2.

Whelan, J.F., Moscati, R.J., Allerton, S.B.M., and Marshall, B.D. (1996). "Applications of isotope geochemistry to the reconstruction of Yucca Mountain paleohydrology," U.S. Geol. Surv. Yucca Mountain Project Branch milestone 3GQH257M, p. 17.

Whelan, J.F., and Stuckless, J.S. (1992). "Paleohydrologic implications of the stable isotopic composition of secondary calcite within the tertiary volcanic rocks of Yucca Mountain, Nevada," *In* Proc. Third Annual Intern. Conf. on High Level Radioactive Waste Management, Amer. Nucl. Soc. and Amer. Soc. Civil Engin., La Grange, IL, and New York, NY, pp. 1572-1581.

Winograd, I.J. (1981). "Radioactive waste disposal in thick unsaturated zone flow and transport," Science, Vol. 212, 1457-1646.

Wittwer, C.G., Chen, G., Bodvarsson, G.S., Chormack, M.P., Flint, A.L., Flint, L.E., Kwicklis, E., and Spengler, R. W. (1995). "Preliminary development of the LBL/USGS three-dimensional site-scale model of Yucca Mountain," Nevada: Rep. LBL-37356, UC-814, Lawrence Berkeley National Lab., Berkeley, CA.

Yang, I.C., Turner, A.K., Sayer, T.M., and Montazer, P. (1988). "Triaxial-compression extraction of pore water from unsaturated tuff, Yucca Mountain, Nevada," U.S. Geol. Surv. Water Resour. Invest. Rep. 88-4189.

Yang, I.C., Davis, G.S., and Sayer, T.M. (1990). "Comparison of pore-water extraction by triaxial compression and high-speed centrifugation method," *In* Minimizing Risk to the Hydrologic

---

Environment, Dubuque, Iowa, Kendall /Hunt Publ. Co, p. 250-259.

Yang, I.C., Rattray, G.W., and Yu, P. (1996). "Interpretations of chemical and isotopic data from boreholes in the unsaturated zone at Yucca Mountain, Nevada," U.S. Geol. Surv. Water Resour. Invest. Rep. WRIR 96-4058.

Yang, I.C., Yu, P., Rattray, G.W., and Thorstenson, D.C. (1997, in press) Hydrogeochemical investigations and geochemical modeling in characterizing the unsaturated zone at Yucca Mountain, Nevada," U.S. Geol. Surv., Water Resour. Invest. Rep.

Yucca Mountain Project Reference Information Base (1995). "Stratigraphy: geologic/lithologic stratigraphy," S.R. Bodnar, compiler, Chapter 1, Sect. 1.12, Item a, RIB Cont. No. MO9510RIB00002.004, p. 48.

Zelinski, W.P., and Clayton, R.W. (1996). "A 3D geologic framework and integrated site model if Yucca Mountain," vs. ISIM 1.0: Civilian Radioactive Waste Management System Management and Operating Contr. Doc. B00000000-01717-5700-00002, TRW Environ. Safety Syst. Inc., Las Vegas, Nevada.

Zreda, M.G., Phillips, F.M., Elmore, D., Kubik, P.W., Sharma, P., and Dorn, R.I. (1991). "Cosmogenic chlorine-36 production rates in terrestrial rocks," Earth Planet. Sci. Lett., Vol. 105, 94-109.

Zyvoloski, G.A., Dash, Z.V., and Kelkar, S. (1992). "FEHMN 1.0: Finite element heat and mass transfer code", Los Alamos National Lab. Rep., LA-12062-MS, Rev.1.

Zyvoloski, G.A., Robinson, B.A., Dash, Z.V., and Trease, L.L. (1995a). "Users manual for the FEHMN application," Tech. Rep. LA-UR-94-3788, Rev. 1, Los Alamos National Lab.

Zyvoloski, G.A., Robinson, B.A., Dash, Z.V., and Trease, L.L. (1995b). "Models and methods summary for the FEHMN application," Tech. Rep. LA-UR-94-3787, Rev. 1, Los Alamos National Lab.

APPENDIX A

ESF SAMPLES COLLECTED FOR <sup>36</sup>Cl ANALYSIS,  
FEBRUARY 1995 TO AUGUST 1997

LANL ID	Approx. ESF station	SMF barcode	Analytical status for <sup>36</sup> Cl (see footnote 1)	Sampled feature (Preliminary)	Preliminary field description (see footnote 2)
E001	1+98	507923	App. B	Fault zone	Bow Ridge Fault, Tiva Canyon tuff wallrock, ~1 m into footwall (collected by U.S. Bureau of Reclamation)
E007	2+03	507924	App. B	Fault zone	Bow Ridge Fault, pre-Rainier Mesa tuff wall rock, zeolitic, ~1 m into hanging wall (collected by U.S. Bureau of Reclamation)
E008	2+00	509016	App. B (High ratio)	Fault zone	Bow Ridge Fault, fault gouge (collected by U.S. Bureau of Reclamation)
E009	2+00	509017	App. B (High ratio)	Fault zone	Bow Ridge Fault, fault gouge (collected by U.S. Bureau of Reclamation)
E010	2+00	509018	App. B	Fault zone	Bow Ridge Fault, fault gouge (collected by U.S. Bureau of Reclamation)
E011	2+00	509019	App. B (High ratio)	Fault zone	Bow Ridge Fault, rubble/fault gouge (collected by U.S. Bureau of Reclamation)
E012	2+00	509020	App. B (High ratio)	Fault zone	Bow Ridge Fault, fault gouge (collected by U.S. Bureau of Reclamation)
E020	24+68	509220	App. B	Fracture	Partly syngenetic rubbly breccia in TSw, fracture surfaces coated with vapor-phase silica
E027	11+00	503935	App. B	Systematic	Systematic sampling of TSw bedrock
E028	12+44	503934	App. B (High ratio)	Cooling joints	Vertical cooling joints and intervening horizontal cooling joints
E029	13+00	503932	App. B	Systematic	Systematic sampling of TSw bedrock
E030	13+67	503931	App. B (High ratio)	Cooling joints	Weakly cemented rubble from shear zone at intersection with another shear zone
E031	14+00	503930	App. B (High ratio)	Shear zone	Broken rock from shear zone
E032	14+14	503929	App. B	Shear zone	Broken rock from shear zone
E033	14+41	503928	App. B	Fault	Calcite-cemented breccia from fault at intersection with fracture
E034	15+00	503926	App. B	Systematic	Systematic sampling of TSw bedrock
E035	15+05	503925	App. B	Fracture	Calcite lining fracture; calcite-cemented breccia
E036	16+12	509242	App. B	Cooling joint	Separated cooling joint with calcite infilling
E037	16+19	509241	App. B	Fracture	Clay-rich fracture fill
E038	17+00	503924	App. B	Systematic	Systematic sampling of TSw bedrock
E040	18+96	503922	App. B (High ratio)	Broken rock	Bedrock cut by many short-segment, high-angle cooling cracks
E041	19+00	503921	App. B	Systematic	Systematic sampling of TSw bedrock
E042	19+31	503920	App. B (High ratio)	Breccia zone	Bulk broken rock and breccia
E043	19+37	503919	App. B	Fault zone	Bulk broken rock and breccia
E044	19+42	503918	App. B (High ratio)	Breccia zone	3-m wide syngenetic rubbly zone, bounded by vertical fractures, with widespread calcite cement
E045	21+00	503917	App. B	Systematic	Systematic sampling of TSw bedrock

LANL ID	Approx. ESF station	SMF barcode	Analytical status for <sup>36</sup> Cl (see footnote 1)	Sampled feature (Preliminary)	Preliminary field description (see footnote 2)
E046	22+71	503916	App. B	Fracture zone	Near-vertical fracture zone about 6-m wide; 40% of rock is lithophysal cavities
E047	23+00	509247	App. B	Systematic	Systematic sampling of TSw bedrock
E050	24+40	509240	App. B (High ratio)	Fault zone	Uncemented fault gouge from a near-vertical fault following an old cooling crack
E051	25+00	509259	App. B	Systematic	Systematic sampling of TSw bedrock
E052	26+79	509244	App. B (High ratio)	Shear zone?	Broken rock from 1-meter wide cooling joint zone
E054	27+00	509257	App. B	Systematic	Systematic sampling of TSw bedrock
E056	27+18	509243	App. B (High ratio)	Fault	Broken rock from fault separating TSw1 and TSw2
E057	27+50	509238	App. B	Fracture	Breccia from fracture, with weak calcite veinlets throughout
E058	27+66	509237	App. B	Fault	Fault gouge consisting of clay and breccia with trace of calcite
E059	28+40	509236	App. B	Fault	Fault zone with carbonate-cemented breccia
E073	5+04	504280	App. B	Fracture	Breccia from fracture oriented 165/71 (U.S. Bureau of Reclamation)
E074	5+05	503866	App. B	Fracture	Breccia from fracture oriented 185/69 (U.S. Bureau of Reclamation)
E086	11+43	510583	App. B	Bedrock	Unaltered TSw (U.S. Bureau of Reclamation, 1995)
E126	10+34	509155	App. B	Fault	Altered tuff bisected by fault oriented at 156/75 (collected by U.S. Bureau of Reclamation)
E128	10+40	509147	App. B	Fault	Tuff within 2 m of fault (collected by U.S. Bureau of Reclamation)
E130	10+41	509150	App. B	Fault	Tuff bisected by fault plane; fault oriented at 038/64 (collected by U.S. Bureau of Reclamation)
E134	10+66	510506	App. B	Fault	Fault material (collected by U.S. Bureau of Reclamation)
E136	10+67	510505	App. B	Fault	Fault material (collected by U.S. Bureau of Reclamation)
E139	10+74	510510	App. B	Fault	Fault material (collected by U.S. Bureau of Reclamation)
E141	29+00	503947	App. B	Systematic	Systematic sampling of TSw bedrock
E142	29+21	503983	App. B	Fracture	Subhorizontal fracture zone with calcite
E143	29+65	503948	App. B	Fault	Fault breccia following syngenetic alteration zone
E144	29+73	503949	App. B	Cooling joints	Bulk rock above lithophysal cavity at intersection of cooling joints
E146	30+18	503987	App. B	Lith. cavity	Calcite from lithophysal cavity
E147	30+27	503976	App. B	Cooling joints	Broken rock between two cooling joints
E149	31+64	503973	App. B	Cooling joint	Breccia along cooling joint
E150	33+00	503939	App. B (High ratio)	Systematic	Systematic sampling of TSw bedrock
E151	33+16	503990	App. B	Lith cavity	Cavity with calcite/opal, intersected by vertical cooling joint
E152	34+28	503993	App. B (High ratio)	Fractures	Cooling joints and rubble rock
E153	34+32	503938	App. B (High ratio)	Cooling joints	Broken rock at the intersection of offset cooling joints

LANL ID	Approx. ESF station	SMF barcode	Analytical status for <sup>36</sup> Cl (see footnote 1)	Sampled feature (Preliminary)	Preliminary field description (see footnote 2)
E154	34+71	503937	App. B (High ratio)	Cooling joints	Breccia in offset cooling joint
E155	35+00	503980	App. B	Systematic	Systematic sampling of TSw bedrock
E156	35+00	503969	App. B	Cooling joints	Broken rock with throughgoing cooling joints
E157	35+03	503994	App. B (High ratio)	Cooling joints	Calcite breccia cement in separated cooling joints
E158	35+08	503995	App. B (High ratio)	Cooling joints	Breccia bounded by high-angle cooling joints
E160	35+45	503979	App. B (High ratio)	Cooling joints	Broken rock from a zone of vertical cooling joints
E161	35+58	503999	App. B (High ratio)	Cooling joints	Breccia zone bounded by high-angle cooling joint
E163	4+94	512551	App. B	Systematic	Systematic sampling of TCw bedrock
E164	7+00	512550	App. B	Systematic	Systematic sampling of TCw bedrock
E165	7+70	512549	App. B	TCw contact	Tpcpln/Tpcpv contact, ~ 1 m above contact
E166	7+70	512548	App. B	TCw contact	Tpcpln/Tpcpv contact
E167	7+70	512547	App. B	TCw contact	Tpcpln/Tpcpv contact, ~ 1 m below contact
E168	8+59	512546	App. B	PTn contact	Tpcpv/Tpbt4 contact, ~ 1 m above contact
E169	8+59	512545	App. B	PTn contact	Tpcpv/Tpbt4 contact
E170	8+59	512544	App. B	PTn contact	Tpcpv/Tpbt4 contact, ~ 1 m below contact
E171	8+90	512554	App. B (High ratio)	PTn contact	Tpbt3/Tpp contact, ~ 1 m below contact
E172	8+90	512553	App. B	PTn contact	Tpbt3/Tpp contact
E173	8+90	512552	App. B	PTn contact	Tpbt3/Tpp contact, ~ 0.5 m above contact
E174	9+00	512543	App. B	Systematic	Systematic sampling of PTn bedrock
E175	35+93	512511	App. B (High ratio)	Fault	Breccia (possibly Sundance Fault)
E176	36+55	512506	App. B	Fault	Fault gouge
E177	37+00	512510	App. B	Systematic	Systematic sampling of TSw bedrock
E178	37+60	512504	App. B	Cooling joint	Fault gouge within modified cooling joint
E179	37+68	512509	App. B	Cooling joint	Wallrock and breccia adjacent to cooling joint
E180	38+47	512513	NA	Fracture	Fracture and fracture fill minerals
E181	38+62	512515	NA	Lith cavity	Bulk rock and lithophysal cavity
E182	38+79	512502	App. B	Fracture	Fracture material/gouge
E183	38+95	512517	App. B	Cooling joint	Fracture fill/gouge
E184	39+00	512508	App. B	Systematic	Systematic sampling of TSw bedrock (fractured rock)
E185	39+39	503944	App. B	Fracture/lith. cavity	Lithophysal cavity with calcite
E186	39+47	503943	App. B	Cooling joint	Gouge within offset cooling joint
E187	39+61	503946	App. B	Cooling joint	Gouge within offset cooling joint
E188	8+26	515100	App. B	PTn contact with fracture	Tpcpv1/Tpbt4 contact, ~1 m above contact, with fracture/fault crossing contact
E189	8+26	515101	App. B	PTn contact	Tpcpv1/Tpbt4 contact, just above contact
E190	8+26	515102	App. B	PTn contact	Tpcpv1/Tpbt4 contact, ~1 m below contact
E191	8+75	515104	App. B	PTn contact	Tpbt3, ~ 1 m above contact between coarse and fine subunits
E192	8+75	515105	App. B	PTn contact	Tpbt3, at contact between coarse and fine subunits

LANL ID	Approx. ESF station	SMF barcode	Analytical status for <sup>36</sup> Cl (see footnote 1)	Sampled feature (Preliminary)	Preliminary field description (see footnote 2)
E193	8+75	515106	App. B	PTn contact	Tpbt3, ~ 1 m below contact between coarse and fine subunits
E194	10+56	512586	App. B (High ratio)	PTn contact	Tprv2/Tprv1 contact, ~ 2 m above contact, adjacent to NRG-4
E195	10+56	512587	App. B (High ratio)	PTn contact	Tprv2/Tprv1 contact, ~ 1 m above contact, adjacent to NRG-4
E196	10+56	512588	App. B	PTn contact	Tprv2/Tprv1 contact, at contact, adjacent to NRG-4
E197	10+62	512585	App. B (High ratio)	PTn contact	Tprv2/Tprv1 contact, ~ 1 m below contact, adjacent to NRG-4; vitric tuff
E198	41+65	510700	App. B (Low ratio)	Cooling joint	Broken rock with cooling joints
E199	43+00	512590	App. B	Systematic	Systematic sampling of TSw bedrock
E200	43+39	512589	App. B	Fault	Gouge zone with minor offset bounded by cooling joints
E201	43+63	512591	App. B (High ratio)	Cooling joint	Hard rock cut by cooling joints
E202	44+20	512592	App. B (High ratio)	Cooling joints	Multiple cooling joint sets
E203	44+21	512593	App. B	Cooling joints	Multiple cooling joint sets
E204	44+22	512594	App. B	Cooling joint	Thin breccia layer along cooling joint
E205	45+00	512595	App. B (High ratio)	Systematic	Systematic sampling of TSw bedrock
E206	45+78	512596	App. B	Cooling joints	Calcite along cooling joints
E207	45+79	512597	App. B	Cooling joints	Multiple cooling joint sets
E208	46+18	515103	App. B	Fault	Clayey gouge
E209	46+18	512598	NA	Fault	Calcite cement
E210	Alcove #4	515109	App. B	PTn contact	Station 0+51.58, ~2.3 m above red argillic horizon
E211	Alcove #4	515107	App. B	PTn contact	Station 0+51.58, in red argillic horizon
E212	Alcove #4	515108	App. B	PTn contact	Station 0+51.58, below red argillic horizon
E213	12+36	510792	App. B	Fracture	0.5 to 1-m wide fracture-breccia zone
E214	12+44	510790	App. B	Cooling joints	Resampling of sample E028
E215	12+49	510791	App. B	Cooling joints	Broken rock adjacent to cooling joints
E216	20+71	510788	App. B	Fault zone	Broken rock, little secondary mineralization
E217	26+19	510716	App. B	Fracture	
E218	26+36	510714	App. B	Fracture	Several closely-spaced fractures with secondary mineralization
E219	26+46	510713	App. B	Fracture	High-angle fracture with secondary mineralization
E220	26+79	510719	App. B	Fracture/fault	Fracture/fault zone in lithophysal tuff
E221	41+00	510710	App. B	Systematic	Systematic sampling of TSw bedrock
E222	42+55	510724	App. B	Shear	Intersecting shear sets: host rock (1 bag); gouge (1 bag)
E223	47+00	510728	App. B	Systematic	Systematic sampling of TSw bedrock
E224	49+00	510734	App. B	Systematic	Systematic sampling of TSw bedrock
E225	48+56	510731	App. B	Cooling joints	Breccia zone bounded by cooling joints
E226	49+56	510737	App. B	Cooling joint	Breccia along cooling joint
E227	49+89	510705	App. B	Cooling joints	Breccia zone bounded by cooling joints

LANL ID	Approx. ESF station	SMF barcode	Analytical status for <sup>36</sup> Cl (see footnote 1)	Sampled feature (Preliminary)	Preliminary field description (see footnote 2)
E228	Alcove #2	510795	App. B	Bulk rock, drill and blast construction	Station 0+25.5 in alcove; objective is to evaluate effects of drill and blast construction on <sup>36</sup> Cl and halide signals
E229	Alcove #3	510702	App. B	Monitoring	Adjacent to USGS moisture probe site. Station 0+14.5 in alcove; objective is to compare <sup>36</sup> Cl signal to flux measurements at this location
E230	51+00	510739	App. B	Systematic	Bedrock cut by several sets of cooling joints
E231	51+07	510740	App. B	Cooling joints	Broken rock/breccia at intersection of cooling joints
E232	51+33	510741	App. B	Cooling joints	Intersection of cooling joints with calcite joint filling
E233	51+73	510742	App. B	Fracture	Broken rock zone bounded by fracture
E234	52+43	510743	App. B (Low ratio)	Cooling joint	Joint surfaces with calcite and fluorite
E235	52+46	510744	App. B	Cooling joint	Joint surfaces and adjacent bedrock
E236	53+00	510745	App. B	Systematic	Bedrock cut by rare vertical cooling joint
E237	53+61	510746	App. B	Cooling joints	Broken rock between cooling joints
E238	54+20	510747	App. B	Cooling joints	Breccia at intersection of cooling joints
E239	55+00	510748	App. B	Systematic	Fractured bedrock
E240	56+63	510756	App. B	Cooling joints	Breccia zone bounded by cooling joints
E241	56+85	510754	App. B	Cooling joints	Breccia/shear zone between cooling joints
E242	56+93	510750	App. B	Cooling joints	Breccia/shear zone between cooling joints
E243	1+99	509751	App. B	Fault zone	Bow Ridge Fault, gouge (resampled in vicinity of E012)
E244	8+38	515135	App. B	Fault	Fault in TCw with 1 m offset
E245	8+44	515136	App. B	Fracture	Fe-stained fracture at base of TCw ( only Fe-stained frax in ESF)
E246	8+66	515137	App. B	Fault	Fault at top of PTn with 1 m offset
E247	9+32	515138	App. B	Fault	Fault in PTn
E248	10+75	515139	App. B	Fault	Fault in TSw, dies out about 3 m into PTn; associated calcite
E249	11+00	515142	App. B	Systematic	Resample of E027
E250	11+43	515140	App. B	Fault	Through-going fault at TSw/PTn contact
E251	11+77	515141	App. B	Fault	TSw/PTn fault with 7-8 m offset
E252	57+00	515143	App. B	Systematic	Systematic sample
E253	57+27	515144	App. B	Fault	Ghost Dance Fault
E254	58+66	515145	App. B	Fault	Fault zone gouge, ~0.5-m wide
E255	58+77	515146	App. B (Low ratio)	Unit contact	Nonfractured lower lithophysal zone overlain by fractured middle nonlithophysal zone
E256	59+00	515147	App. B (Low ratio)	Systematic	Systematic sample (1 bag); fracture with gouge (1 bag)
E257	61+00	515148	App. B	Systematic	Systematic sample
E258	61+92	515149	App. B (Low ratio)	Fracture	Large vertical fracture set
E259	62+00	515150	App. B	Systematic	Systematic sample, ~5 m N of fault trace at E260
E260	62+05	515151	App. B (Low ratio)	Fault	Fault ~10 cm wide
E261	62+18	515152	App. B	Fault	Footwall of Ghost Dance Fault, highly fractured, large apertures
E262	62+71	515153	App. B	Shear	Intersecting shear/cooling joint sets

LANL ID	Approx. ESF station	SMF barcode	Analytical status for <sup>36</sup> Cl (see footnote 1)	Sampled feature (Preliminary)	Preliminary field description (see footnote 2)
E263	63+00	515154	App. B	Systematic	Systematic sample
E264	63+06	515155	App. B	Fracture	156/84 fracture, ~ 10 cm wide; calcite-cemented breccia (1 bag); adjacent matrix (1 bag)
E265	63+21	515156	App. B	Fracture	Intersecting fractures with breccia
E266	63+26	515157	App. B	Fracture	Fracture/breccia zone, ~ 1 m wide, very broken up
E267	63+30	515158	App. B	Fault	Intersection of fault (30-cm offset) with vapor-phase parting
E268	65+20	515180	App. B	Fracture	Fracture zone
E269	63+73	515188	App. B	Fracture	Fracture ~ 1m wide, with calcite filling
E270	63+81	515187	App. B	Fracture	Large fracture
E271	64+00	515186	App. B	Systematic	Systematic sample with 2 intersecting fractures
E272	64+34	515185	App. B	Broken rock	Broken rock, no obvious structure
E273	64+50	515184	App. B	Broken zone	Representative sample from broken zone ~ 35 m wide
E274	64+93	515182	App. B	Fracture	Calcite in fracture below lithophysal cavity
E275	65+00	515181	App. B	Systematic	Systematic sample
E276	65+56	515179	App. B	Fracture	Large fracture zone ~ 1.5 m wide
E277	65+80	515178	App. B	Fracture	Large 2-m wide fracture zone
E278	66+00	515177	App. B	Systematic	Systematic sample with 2 intersecting fractures
E279	66+15	515176	App. B	Fault	Calcite-cemented fault breccia
E280	66+40	515175	App. B (Low ratio)	Fault hanging wall	Fault zone in TSw with about 0.5-m offset
E281	67+00	515174	App. B	Systematic	Systematic sample in nonfaulted, nonwelded unit
E282	67+20	515183	NA	Damp zone	Large wetted zone in poorly to nonwelded tuff
E283	67+27	515172	App. B	Fault	Fault in high-porosity zone of nonwelded tuff, wetted appearance
E284	67+35	515173	App. B	Unit contact	Welded/nonwelded contact
E285	67+73	515171	App. B	Damp zone	Damp sandy zone (nonhorizontal) in PTn
E286	67+87	515133	App. B	Fault	About 3-m wide fault in Tsw: fault gouge (1 bag); calcite-cemented gouge (1 bag)
E287	67+87	515134	App. B	Fault	Sandy fault breccia
E288	67+90	515132	App. B	Fault	Footwall east of fault zone sampled by E286 and E287
E289	67+61	515170	App. B	Fault	Fault breccia/gouge (sandy to clay consistency)
E290	59+98	521128	App. B (Low ratio)	Systematic	Note limited availability of air hose prevented sampling exactly at Station 60
E292	69+00	521123	App. B	Systematic	Systematic sampling of TSw bedrock
E293	69+14	521122	App. B	Fault	Fault gouge zone, ~0.3-m wide
E294	69+32	521121	APP. B	Fracture	Fracture, ~10-cm wide, containing gouge
E295	69+42	521120	App. B	Fracture zone	Fracture zone, ~0.5-cm wide, with calcite + opal
E296	Alcove #6	521129	App. B	Fault zone	Sta 0+95 in alcove, ~3 m from Sundance Fault
E297	Alcove #6	521130	App. B	Fault zone	Sta 0+99 in alcove, approx. at Sundance Fault
E298	68+00	521127	App. B	Systematic	Systematic sampling of TSw bedrock
E299	69+47	522221	App. B	Systematic	Systematic sample; 2 subparallel features in Tptrn
E300	69+68	522220	App. B	Fault (?)	3-m wide broken zone, possible fault in Tptrn
E301	69+95.8	522219	NA	Fault	E-side down fault with 0.9 m offset in Tptrv3 (vitrophyre)

LANL ID	Approx. ESF station	SMF barcode	Analytical status for <sup>36</sup> Cl (see footnote 1)	Sampled feature (Preliminary)	Preliminary field description (see footnote 2)
E302	70+19	522218	App. B (Low ratio)	Fault	W-side down fault with 1.6 m offset in Tptrv1
E303	70+36	522217	App. B	Fault	Down-to-E fault in Tpbt2 with 0.55 m displacement
E304	70+50	522216	App. B	Systematic	Systematic, unfractured rock in Tpbt2
E305	70+55.5	522215	App. B	Fault	Fault breccia; PTn (bt2) down against Tptpmn.
E306	70+66	522214	App. B	Fault	Intersection of 2 small faults in Tptpmn
E307	71+34	522212	App. B	Fault	Brecciated/fractured Tptpmn in hanging wall of fault.
E308	71+39	522213	App. B	Fault	Rubble in Tptpmn in fault zone
E309	71+41	522211	App. B	Fault	Brecciated rock in hanging wall of fault in Tptpmn
E310	71+50	522210	App. B	Systematic	Systematic sample near top of Tptpmn
E311	72+50	522209	App. B	Systematic	Systematic sample in relatively unbroken Tptpul
E312	72+69	522208	App. B	Fault	Fault in Tptpul, offset unknown
E313	73+48	522207	App. B	Systematic	Systematic sample, single large cooling joint intersecting sample
E314	74+43	522206	NA	Fault	Broken rock from shear/fault zone that offsets the top of the TS <sub>w</sub>
E315	74+49	522205	App. B	Systematic	Systematic sample near top of Tptrv1 or rv2
E316	74+89	522202	App. B	Fault	Fault in PTn (Tpbt3) with 0.93 m offset
E317	75+09	522201	App. B	Contact	Below Tpcpv2/pv1 contact, downdip from moist zone along this contact
E318	75+09.5	522203	App. B	Contact	In lithic-rich horizon separating Tpcpv2/pv1, downdip of moist zone along this contact
E319	75+10	522204	App. B	Contact	Above Tpcpv2/pv1 contact, downdip from moist zone along this contact
E320	75+20	522200	NA	Contact	At Tpclnc/cpv contact
E321	75+34	521287	App. B	Fault	Breccia/gouge fill on 2 subparallel joints/faults
E322	75+47.5	521288	NA	Systematic	Systematic sample; intersection of 2 cooling joints
E323	75+53.5	521289	App. B	Cooling joints	Broken rock at intersection of cooling joints, ~10-cm wide sandy gouge
E324	75+78	521290	App. B (Low ratio)	Fault	Fault with 0.21 m offset, filled with 4-5 cm clay
E325	76+30	521291	App. B	Fault	Fault zone ~0.5 m wide, rubbly zone; offset unknown
E326	76+31	521292	App. B	Fault	Hanging wall of fault @76+30
E327	76+50	521295	App. B (Low ratio)	Systematic	Systematic sample, minor brecciation; 1-m long fracture in almost completely unbroken rock
E328	76+76	521294	App. B (Low ratio)	Fault	Fault 0.2-m down to W, rubbly breccia zone
E329	77+10	521293	App. B	Fault	Fault with 0.24 m offset, down to W
E330	Niche #1	524999	NA	Breccia zone	Wet zone intercepted in back of niche @ Sta 0+13.5
E331	Niche #1	524998	NA	Breccia zone	Wet zone intercepted in back of niche @ Sta 0+13.5
E332	Niche #1	524999	NA	Breccia zone	Wet zone intercepted in back of niche @ Sta 0+13.5
E333	Alcove 6	524960	NA	Fault	Breccia and wall rock from Ghost Dance Fault
E334	Alcove 7	524959	NA	Fracture	Fracture intersection @ Sta 1+37.9
E335	77+19	524901	NA	Fracture	Fracture/rubble zone

Footnotes for Appendix A:

<sup>1</sup> Definition of codes for analytical status:

NA—No analysis yet available but sample is in queue for measurement;

App. B—Sample results are reported in Appendix B;

High ratio—corrected  $^{36}\text{Cl}/\text{Cl}$  ratio exceeds  $1250 \times 10^{-15}$ , probably indicating presence of bomb-pulse  $^{36}\text{Cl}$ ;

Low ratio—corrected  $^{36}\text{Cl}/\text{Cl}$  ratio is less than  $350 \times 10^{-15}$ . These sample results are currently being investigated to determine whether or not they are indicative of water travel times sufficiently long to show effects of radioactive decay of its meteoric  $^{36}\text{Cl}$  signal (i.e., on order of  $10^5$  years).

<sup>2</sup> Field descriptions: Samples were collected by LANL staff unless this column indicates collection by the U.S. Bureau of Reclamation staff. Sample locations and descriptions are taken from documentation in field notebooks or on sample collection reports. This information is preliminary. USGS and LANL field geologists are systematically revisiting each site to develop fuller descriptions of the sampled features and to verify locations (e.g., see Appendix C).

## Appendix B

### Halide, sulfate and $^{36}\text{Cl}$ analyses of ESF rock samples, sorted by ESF station

#### Notes on column headings in Appendix B:

1. **Leached salts:** The mass of sample processed was generally on the scale of 1-5 kg. Each sample was leached for 48 hours in deionized water using a water:rock weight ratio of 1:1. Because the focus of this task was on the determination of anion ratios and isotopic ratios, no attempt was made to maximize the yield of the leaching process, which is not only quite variable but also probably quite low for welded samples that consist of pieces with cm-scale dimensions. Consequently, the concentrations of salts leached from the rock samples provide only a qualitative indicator of each sample's actual salt content and generally cannot be used to estimate the porewater concentrations.
2. **% CW:** Percent Cl derived from construction water. Construction water is used for numerous routine operations in the ESF, including wetting the Tunnel Boring Machine cutter head, wet-drilling for installation of rock bolts, providing dust control on the muck belt, and spraying tunnel ribs to facilitate fracture mapping. It is prepared from UE25 J#13 wellwater traced with lithium bromide salt to a bromide concentration of 20 mg/L, about 400 times its background level. The proportion of construction-water chloride ( $f_c$ ) present in each sample processed for  $^{36}\text{Cl}$  is estimated from the measured Br/Cl (halide) ratio ( $\text{HR}_x$ ), using a two-component mixing equation,  $f_c = (\text{HR}_x - \text{HR}_m) / (\text{HR}_c - \text{HR}_m)$ , where  $\text{HR}_m$  is the Br/Cl ratio of meteoric water (0.009) and  $\text{HR}_c$  is the Br/Cl ratio of the construction water (3.0) (section 4.2.2).
3. The  $^{36}\text{Cl}/\text{Cl}$  ratios ( $R_m$ ) reported in this appendix have been corrected for the presence of chloride from construction water, using the following equation:  $R_m = (R_x - f_c R_c) / (1 - f_c)$ , where  $R_x$  is the measured  $^{36}\text{Cl}/\text{Cl}$  ratio,  $f_c$  is the proportion of chloride in the sample that is attributable to the construction water, and  $R_c$  is the  $^{36}\text{Cl}/\text{Cl}$  ratio of the construction water ( $500 \times 10^{-15}$ ) (section 4.2.2).

Appendix B. Halide, sulfate and chlorine-36 analyses of RSF rock samples, sorted by ESF station  
(See notes about column headings on page B-1)

LANL ID	SMF barcode	Approx ESF station	Sampled feature	Description of analyzed aliquot	Leached salts (Note 1)					% CW (Note 2)	Corrected $^{36}\text{Cl}/\text{Cl} \times 10^{-15}$ (Note 3)	
					Cl mg/kg	Br $\mu\text{g}/\text{kg}$	$\text{SO}_4$ mg/kg	Br/Cl	$\text{SO}_4/\text{Cl}$			
E228-1	510795	Alc 2, 0+25	Drill & blast	Representative bulk material	0.71	818	6.88	1152	9.7	38	359 ±	42
E001-1	507923	1+98	Fault zone	Wall rock	1.95	554	---	284	---	9	518 ±	20
E010-2	509018	1+99.8	Fault zone	Rubble	2.29	22	---	9	---	0	720 ±	49
E008-2	509016	1+99.8	Fault zone	Breccia	2.62	23	---	9	---	0	2138 ±	137
E243-1	509751	1+99.8	Fault zone	Breccia	4.42	49	---	11	---	0	381 ±	16
E009-2	509017	1+99.8	Fault zone	Breccia	1.96	15	---	8	---	0	2444 ±	169
E011-2	509019	1+99.8	Fault zone	Rubble	2.02	19	---	9	---	0	2378 ±	153
E012-2	509020	1+99.8	Fault zone	Breccia	2.12	19	---	9	---	0	2398 ±	154
E007-2	507924	2+03	Fault zone	Wall rock	3.42	221	---	65	---	2	519 ±	13
E163-3	512551	4+94	Systematic	Representative bulk material	2.35	126	---	54	---	1	485 ±	12
E073-1	504280	5+04	Fracture	Breccia	5.63	364	---	65	---	2	468 ±	19
E074-1	503866	5+5.5	Fracture	Breccia	11.82	858	---	73	---	2	493 ±	17
E164-3	512550	7+00	Systematic	Representative bulk material	0.61	13	---	21	---	0	571 ±	35
E229-1	510702	Alc 3, 0+14	Intact bedrock	Representative bulk material	3.41	77	---	22	---	0	558 ±	19
E167-3	512547	7+70	Subunit contact	Representative bulk material	24.1	218	---	9	---	0	427 ±	13
E166-3	512548	7+70	Subunit contact	Representative bulk material	12.2	109	---	9	---	0	484 ±	15
E165-3	512549	7+70	Subunit contact	Representative bulk material	2.94	22	---	8	---	0	496 ±	14
E189-2	515101	8+26.5	Subunit contact	Representative bulk material	4.28	92	---	22	---	0	625 ±	17
E188-2	515100	8+26.5	Subunit contact	Representative bulk material	2.24	66	---	29	---	1	766 ±	24
E190-2	515102	8+26.5	Subunit contact	Representative bulk material	6.33	110	---	17	---	0	647 ±	14
E244-1	515135	8+38	Fault	Representative bulk material	1.48	443	3.20	299	2.2	10	488 ±	17
E245-1	515136	8+44	Fracture	Representative bulk material	1.71	295	3.73	173	2.2	5	530 ±	21
E169-3	512545	8+59	Subunit contact	Representative bulk material	0.55	44	1.03	79	1.9	2	1096 ±	40

LANL ID	SMF barcode	Approx ESF station	Sampled feature	Description of analyzed aliquot	Leached salts (Note 1)					% CW (Note 2)	Corrected $^{36}\text{Cl}/\text{Cl} \times 10^{-15}$ (Note 3)	
					Cl mg/kg	Br $\mu\text{g}/\text{kg}$	$\text{SO}_4$ mg/kg	Br/Cl	$\text{SO}_4/\text{Cl}$			
E170-3	512544	8+59	Subunit contact	Representative bulk material	1.11	38	---	34	---	1	635 $\pm$	23
E168-3	512546	8+59	Subunit contact	Representative bulk material	0.80	72	---	89	---	3	802 $\pm$	29
E246-1	515137	8+66	Fault	Representative bulk material	0.79	40	1.59	50	2.0	1	475 $\pm$	17
E191-2	515104	8+75	Subunit contact	Representative bulk material	0.86	99	---	115	---	4	904 $\pm$	28
E192-2	515105	8+75	Subunit contact	Representative bulk material	0.81	141	---	174	---	6	698 $\pm$	20
E193-2	515106	8+75	Subunit contact	Representative bulk material	1.54	33	---	21	---	0	748 $\pm$	21
E173-3	512552	8+90	Subunit contact	Representative bulk material	0.70	51	---	73	---	2	806 $\pm$	33
E171-1	512554	8+90	Subunit contact	Representative bulk material	0.68	64	---	94	---	3	1335 $\pm$	56
E172-3	512553	8+90	Subunit contact	Representative bulk material	0.57	45	---	79	---	2	637 $\pm$	26
E174-3	512543	9+00	Systematic	Representative bulk material	0.61	87	---	143	---	4	660 $\pm$	29
E247-1	515138	9+32	Fault	Representative bulk material	0.55	176	1.85	321	3.4	10	509 $\pm$	22
E211-2	515107	Alc. 4, 51.58	Subunit contact	Representative bulk material	2.06	31	---	15	---	0	810 $\pm$	24
E210-2	515109	Alc. 4, 51.58	Subunit contact	Representative bulk material	4.26	67	---	16	---	0	712 $\pm$	31
E212-2	515108	Alc. 4, 51.58	Subunit contact	Representative bulk material	2.94	60	---	20	---	0	815 $\pm$	18
E126-1	509155	10+34	Fault zone	Representative bulk material	0.76	328	2.46	431	3.2	14	633 $\pm$	41
E128-1	509147	10+40	Fault zone	Representative bulk material	1.53	28	3.91	18	2.6	0	662 $\pm$	27
E130-1	509150	10+41	Fault zone	Representative bulk material	0.70	119	1.78	170	2.5	5	773 $\pm$	40
E196-2	512588	10+56	Subunit contact	Representative bulk material	0.39	33	---	85	---	3	1202 $\pm$	27
E194-2	512586	10+56	Subunit contact	Representative bulk material	0.69	65	---	94	---	3	1354 $\pm$	45
E195-2	512587	10+56	Subunit contact	Representative bulk material	0.81	123	---	152	---	5	1292 $\pm$	37

LANL ID	SMF barcode	Approx ESF station	Sampled feature	Description of analyzed aliquot	Leached salts (Note 1)					% CW (Note 2)	Corrected $^{36}\text{Cl}/\text{Cl} \times 10^{-15}$ (Note 3)	
					Cl mg/kg	Br $\mu\text{g}/\text{kg}$	$\text{SO}_4$ mg/kg	Br/Cl	$\text{SO}_4/\text{Cl}$			
E197-2	512585	10+62.5	Subunit contact	Representative bulk material	0.11	21	---	191	---	6	1452 $\pm$	72
E134-1	510506	10+66	Fault	Representative bulk material	1.80	935	2.97	519	1.7	17	747 $\pm$	41
E136-1	510505	10+66.8	Fault	Representative bulk material	2.53	1103	5.15	436	2.0	14	801 $\pm$	33
E139-1	510510	10+74.2	Fault	Representative bulk material	1.38	1577	3.49	1143	2.5	38	738 $\pm$	52
E248-1	515139	10+75	Fault	Representative bulk material	0.48	415	1.83	865	3.8	29	571 $\pm$	38
E249-3	515142	11+00	Systematic	Representative bulk material	0.35	281	0.74	803	2.1	27	674 $\pm$	47
E027-3	503935	11+00	Systematic	Representative bulk material	0.32	195	0.66	609	2.1	20	1076 $\pm$	52
E249-1	515142	11+00	Systematic	Representative bulk material	0.48	375	1.11	781	2.3	26	655 $\pm$	37
E249-4	515142	11+00	Systematic	Representative bulk material	0.95	735	3.06	774	3.2	26	910 $\pm$	58
E250-1	515140	11+43	Fault	Representative bulk material	0.41	323	1.75	788	4.3	26	532 $\pm$	35
E086-1	510583	11+43	Bedrock	Representative bulk material	0.73	175	---	239	---	8	640 $\pm$	29
E251-1	515141	11+77	Fault	Representative bulk material	0.50	28	1.50	57	3.0	2	633 $\pm$	38
E213-1	510792	12+36.5	Fracture	Breccia	0.33	323	---	980	---	32	719 $\pm$	68
E028-1	503934	12+44	Cooling joints	Representative bulk material	0.21	16	0.51	78	2.4	2	2637 $\pm$	106
E214-1	510790	12+44	Cooling joints	Representative bulk material	0.45	104	---	231	---	7	750 $\pm$	28
E215-1	510791	12+49	Cooling joints	Representative bulk material	0.38	105	---	275	---	9	668 $\pm$	54
E029-1	503932	13+00	Systematic	Representative bulk material	0.60	10	---	17	---	0	640 $\pm$	28
E030-2	503931	13+67	Cooling joints	Breccia > 0.5 cm	0.54	303	0.99	561	1.8	18	1634 $\pm$	85
E030-1	503931	13+67	Cooling joints	Breccia < 0.5 cm	1.02	261	0.86	255	0.8	8	697 $\pm$	35
E031-1	503930	14+00	Shear zone	Breccia > 1 cm	0.60	30	1.10	51	1.8	1	1038 $\pm$	35
E031-3	503930	14+00	Shear zone	Breccia < 1 cm	0.72	28	1.21	38	1.7	1	2398 $\pm$	191
E032-2	503929	14+14	Shear zone	Representative bulk material	0.77	35	---	45	---	1	680 $\pm$	45

LANL ID	SMF barcode	Approx ESF station	Sampled feature	Description of analyzed aliquot	Leached salts (Note 1)					% CW (Note 2)	Corrected $^{36}\text{Cl}/\text{Cl} \times 10^{-15}$ (Note 3)	
					Cl mg/kg	Br $\mu\text{g}/\text{kg}$	$\text{SO}_4$ mg/kg	Br/Cl	$\text{SO}_4/\text{Cl}$			
E033-1	503928	14+41	Fault	Gouge	0.33	49	---	149	---	5	876 $\pm$	42
E034-1	503926	15+00	Systematic	Representative bulk material	0.31	33	---	107	---	3	954 $\pm$	51
E035-1	503925	15+05	Fracture	Breccia	0.99	1376	---	1390	---	46	628 $\pm$	61
E036-1	509242	16+12	Cooling joint	Representative bulk material	1.39	544	---	391	---	13	382 $\pm$	56
E037-2	509241	16+19	Fracture	Representative bulk material	0.51	81	---	160	---	5	982 $\pm$	42
E038-1	503924	17+00	Systematic	Representative bulk material	0.39	35	---	89	---	3	714 $\pm$	38
E040-1	503922	18+96	Broken rock	Representative bulk material	0.59	172	---	291	---	9	1642 $\pm$	59
E041-1	503921	19+00	Systematic	Representative bulk material	0.63	237	---	376	---	12	746 $\pm$	27
E042-3	503920	19+31	Fault zone	Breccia < ~0.5 cm	0.63	63	1.13	100	1.8	3	1837 $\pm$	65
E042-2	503920	19+31	Fault zone	Breccia > ~0.5 cm	0.62	88	1.03	142	1.7	4	3023 $\pm$	94
E043-2	503919	19+37	Fault zone	Representative bulk material	0.77	68	---	88	---	3	1144 $\pm$	36
E044-2	503918	19+42	Breccia zone	Representative bulk material	0.56	155	---	277	---	9	2290 $\pm$	74
E216-1	510788	20+71	Fracture	Representative bulk material	1.23	438	---	356	---	12	842 $\pm$	38
E045-1	503917	21+00	Systematic	Representative bulk material	0.59	137	---	233	---	7	799 $\pm$	29
E046-1	503916	22+71	Fracture zone	Representative bulk material	0.99	568	1.35	574	1.4	19	862 $\pm$	43
E046-4	503916	22+71	Fracture zone	Representative bulk material, crushed and ground (PRIME)	1.05	292	4.93	278	4.7	9	458 $\pm$	24
E047-1	509247	23+00	Systematic	Representative bulk material	0.81	84	---	103	---	3	663 $\pm$	37
E050-2	509240	24+40	Fault zone	Breccia	0.41	74	---	181	---	6	2579 $\pm$	94
E020-1	509220	24+68	Fracture	Representative bulk material	0.55	486	---	884	---	29	814 $\pm$	56
E051-1	509259	25+00	Systematic	Representative bulk material	0.53	270	---	509	---	17	1003 $\pm$	49

LANL ID	SMF barcode	Approx ESF station	Sampled feature	Description of analyzed aliquot	Leached salts (Note 1)					% CW (Note 2)	Corrected $^{36}\text{Cl}/\text{Cl} \times 10^{-15}$ (Note 3)
					Cl mg/kg	Br $\mu\text{g}/\text{kg}$	$\text{SO}_4$ mg/kg	Br/Cl	$\text{SO}_4/\text{Cl}$		
E217-1	510716	26+19	Cooling joints	Representative bulk material	0.66	57	---	87	---	3	522 $\pm$ 21
E218-1	510714	26+36	Fracture	Representative bulk material	1.18	164	---	139	---	4	603 $\pm$ 20
E219-1	510713	26+46	Fracture	Representative bulk material	0.42	144	---	343	---	11	578 $\pm$ 38
E220-1	510719	26+79	Fracture	Representative bulk material	1.33	786	---	591	---	19	565 $\pm$ 25
E052-1	509244	26+79	Shear zone	Representative bulk material	0.44	138	---	313	---	10	2036 $\pm$ 68
E054-1	509257	27+00	Systematic	Representative bulk material	0.42	30	---	72	---	2	973 $\pm$ 29
E056-1	509243	27+18	Fault	Representative bulk material	0.39	17	---	44	---	1	1709 $\pm$ 53
E057-2	509238	27+50	Fracture	Breccia	1.30	282	---	217	---	7	779 $\pm$ 23
E058-2	509237	27+66	Fault	Breccia	1.44	22	---	15	---	0	458 $\pm$ 19
E059-2	509236	28+40	Fault	Breccia	2.08	128	---	62	---	2	512 $\pm$ 21
E141-1	503947	29+00	Systematic	Representative bulk material	0.43	70	---	162	---	5	922 $\pm$ 36
E142-1	503983	29+21	Fracture	Representative bulk material	0.54	446	---	826	---	27	583 $\pm$ 28
E143-1	503948	29+65	Fault	Representative bulk material	0.43	290	---	673	---	22	1077 $\pm$ 162
E144-1	503949	29+73	Cooling joint	Representative bulk material	0.22	66	---	301	---	10	815 $\pm$ 34
E146-4	503987	30+18	Lith cavity	Representative bulk material, crushed and ground (PRIME)	1.80	31	1.48	17	0.8	0	496 $\pm$ 24
E147-1	503976	30+27	Cooling joints	Representative bulk material	1.65	528	---	320	---	10	490 $\pm$ 15
E149-1	503973	31+64	Cooling joint	Representative bulk material	0.71	454	---	640	---	21	631 $\pm$ 29
E150-1	503939	33+00	Systematic	Representative bulk material	0.29	3	---	11	---	0	1341 $\pm$ 56
E151-4	503990	33+16	Lith cavity	Representative bulk material, crushed and ground (PRIME)	2.31	470	2.92	203	1.3	7	529 $\pm$ 24

LANL ID	SMF barcode	Approx ESF station	Sampled feature	Description of analyzed aliquot	Leached salts (Note 1)					% CW (Note 2)	Corrected $^{36}\text{Cl}/\text{Cl} \times 10^{-15}$ (Note 3)	
					Cl mg/kg	Br $\mu\text{g}/\text{kg}$	$\text{SO}_4$ mg/kg	Br/Cl	$\text{SO}_4/\text{Cl}$			
E152-1	503993	34+28	Fractures	Representative bulk material	0.25	260	---	1041	---	35	4105 $\pm$ 310	
E153-3	503938	34+32	Cooling joints	Representative bulk material	0.22	131	---	594	---	20	3261 $\pm$ 160	
E154-1	503937	34+71	Cooling joints	Breccia	0.33	59	0.62	177	1.9	6	803 $\pm$ 42	
E154-3	503937	34+71	Cooling joints	Wall rock	0.23	36	0.31	156	1.3	5	3794 $\pm$ 120	
E155-1	503980	35+00	Systematic	Representative bulk material	0.52	218	---	419	---	14	1013 $\pm$ 60	
E156-1	503969	35+00	Cooling joints	Representative bulk material	1.00	298	---	298	---	10	626 $\pm$ 29	
E157-3	503994	35+03	Cooling joints	Representative bulk material	0.49	305	---	622	---	20	1339 $\pm$ 83	
E158-3	503995	35+08	Cooling joints	Breccia > ~0.5 cm	0.46	464	1.09	1009	2.4	33	2671 $\pm$ 158	
E158-1	503995	35+08	Cooling joints	Breccia < ~0.5 cm	0.74	640	1.65	865	2.3	29	1113 $\pm$ 58	
E160-4	503979	35+45	Cooling joints	Representative bulk material, crushed and ground (PRIME)	1.77	114	1.74	64	1.0	2	388 $\pm$ 17	
E160-1	503979	35+45	Cooling joints	Representative bulk material	0.25	201	0.45	802	1.8	27	3529 $\pm$ 205	
E161-3	503999	35+58	Cooling joint	Breccia > ~0.5 cm	0.54	275	0.62	509	1.1	17	2169 $\pm$ 80	
E161-1	503999	35+58	Cooling joint	Breccia < ~0.5 cm	0.79	361	1.06	457	1.3	15	1951 $\pm$ 103	
E175-3	512511	35+93	Fault	Breccia < ~0.5 cm	0.27	321	0.45	1189	1.7	39	1674 $\pm$ 141	
E175-1	512511	35+93	Fault	Breccia > ~0.5 cm	0.27	305	0.42	1130	1.5	37	2840 $\pm$ 231	
E176-3	512506	36+55	Fault	Breccia < ~0.5 cm	1.04	187	1.18	179	1.1	6	604 $\pm$ 24	
E176-1	512506	36+55	Fault	Breccia > ~0.5 cm	0.88	132	1.01	150	1.1	5	887 $\pm$ 27	
E177-1	512510	37+00	Systematic	Representative bulk material	0.91	8	---	8	---	0	484 $\pm$ 15	
E297-1	521130	Alc 6, 0+98	Fault	Representative bulk material	1.75	875	3.26	500	1.9	16	499 $\pm$ 29	
E296-1	521129	Alc 6, 0+95	Fault	Representative bulk material	1.59	1599	4.70	1006	3.0	33	533 $\pm$ 52	

LANL ID	SMF barcode	Approx ESF station	Sampled feature	Description of analyzed aliquot	Leached salts (Note 1)					% CW (Note 2)	Corrected $^{36}\text{Cl}/\text{Cl} \times 10^{-15}$ (Note 3)	
					Cl mg/kg	Br $\mu\text{g}/\text{kg}$	$\text{SO}_4$ mg/kg	Br/Cl	$\text{SO}_4/\text{Cl}$			
E178-1	512504	37+60	Cooling joint	Gouge	1.76	160	---	91	---	3	471 $\pm$	26
E179-3	512509	37+68	Cooling joint	Wall rock	1.51	311	1.34	206	0.9	7	397 $\pm$	13
E179-1	512509	37+68	Cooling joint	Breccia	1.46	577	2.46	395	1.7	13	363 $\pm$	22
E182-1	512502	38+79	Fracture	Breccia	0.43	374	---	869	---	29	379 $\pm$	38
E183-1	512517	38+95	Cooling joint	Breccia	0.39	295	---	757	---	25	745 $\pm$	39
E184-1	512508	39+00	Systematic	Representative bulk material	0.24	21	---	89	---	3	536 $\pm$	29
E185-1	503944	39+39	Frac/lith cavity	Representative bulk material	0.30	187	---	622	---	20	897 $\pm$	46
E186-1	503943	39+47	Cooling joint	Breccia/gouge	0.45	340	---	754	---	25	561 $\pm$	34
E187-1	503946	39+61	Cooling joint	Breccia/gouge	0.92	204	---	222	---	7	540 $\pm$	33
E221-1	510710	41+00	Systematic	Representative bulk material	0.61	27	---	44	---	1	773 $\pm$	24
E198-2	510700	41+65	Cooling joint	Representative bulk material	1.92	301	---	157	---	5	291 $\pm$	12
E222-1	510724	42+55	Shear sets	Gouge	3.80	441	5.18	116	1.4	4	605 $\pm$	18
E222-2	510724	42+55	Shear sets	Wall rock	2.90	400	3.74	138	1.3	4	531 $\pm$	16
E199-2	512590	43+00	Systematic	Representative bulk material	0.28	126	---	448	---	15	1042 $\pm$	53
E200-2	512589	43+39	Fault	Gouge	0.27	312	---	1156	---	38	967 $\pm$	66
E201-2	512591	43+63	Cooling joint	Representative bulk material	0.40	47	---	118	---	4	1974 $\pm$	65
E202-2	512592	44+20	Cooling joint	Representative bulk material	0.59	34	---	58	---	2	3463 $\pm$	97
E203-2	512593	44+21	Cooling joint	Representative bulk material	0.43	40	---	93	---	3	849 $\pm$	34
E204-2	512594	44+22	Cooling joint	Representative bulk material	0.61	59	---	96	---	3	772 $\pm$	31
E205-2	512595	45+00	Systematic	Representative bulk material	0.25	157	---	628	---	21	1514 $\pm$	69
E206-1	512596	45+78	Fracture zone	Representative bulk material	1.64	259	1.76	158	1.1	5	525 $\pm$	29
E207-2	512597	45+79	Cooling joint	Representative bulk material	1.60	20	---	13	---	0	593 $\pm$	15
E208-1	515103	46+18	Fault	Breccia	1.85	417	3.92	225	2.1	7	497 $\pm$	26
E223-1	510728	47+00	Systematic	Representative bulk material	0.32	75	---	234	---	8	734 $\pm$	37
E225-1	510731	48+56	Cooling joints	Breccia	1.22	420	---	344	---	11	351 $\pm$	14
E224-1	510734	49+00	Systematic	Representative bulk material	1.65	36	---	22	---	0	499 $\pm$	16

LANL ID	SMF barcode	Approx ESF station	Sampled feature	Description of analyzed aliquot	Leached salts (Note 1)					% CW (Note 2)	Corrected <sup>36</sup> Cl/Cl x 10 <sup>-15</sup> (Note 3)
					Cl mg/kg	Br µg/kg	SO <sub>4</sub> mg/kg	Br/Cl	SO <sub>4</sub> /Cl		
E226-2	510737	49+56	Cooling joint	Wall rock	1.05	168	1.26	160	1.2	5	456 ± 20
E226-1	510737	49+56	Cooling joint	Breccia	1.13	307	1.55	272	1.4	9	451 ± 20
E227-1	510705	49+89	Cooling joints	Breccia	0.54	399	---	739	---	24	497 ± 32
E230-1	510739	51+00	Systematic	Representative bulk material	0.50	68	---	136	---	4	555 ± 23
E231-2	510740	51+07	Cooling joints	Breccia	0.50	182	0.65	364	1.3	12	530 ± 26
E231-1	510740	51+07	Cooling joints	Wall rock	0.50	152	0.64	304	1.3	10	709 ± 30
E232-1	510741	51+33	Cooling joints	Representative bulk material	0.35	31	---	87	---	3	942 ± 42
E233-1	510742	51+73	Fracture	Representative bulk material	0.34	165	---	485	---	16	647 ± 30
E234-1	510743	52+43	Cooling joint	Representative bulk material	0.49	247	0.50	504	1.0	17	291 ± 26
E235-1	510744	52+46	Cooling joint	Representative bulk material	0.27	140	---	519	---	17	596 ± 43
E236-1	510745	53+00	Systematic	Representative bulk material	0.71	94	---	133	---	4	417 ± 17
E237-1	510746	53+61	Cooling joint	Representative bulk material	0.44	95	---	216	---	7	539 ± 27
E238-1	510747	54+20	Cooling joint	Breccia	1.34	128	---	96	---	3	727 ± 37
E239-1	510748	55+00	Systematic	Representative bulk material	0.30	24	---	79	---	2	464 ± 23
E240-1	510756	56+63	Cooling joint	Breccia	0.29	112	---	386	---	13	673 ± 42
E241-1	510754	56+85	Cooling joint	Breccia	0.73	446	1.31	611	1.8	20	778 ± 39
E242-2	510750	56+93	Cooling joint	Breccia <2mm	0.93	234	1.44	252	1.5	8	1117 ± 49
E242-1	510750	56+93	Cooling joint	Breccia >2mm	0.70	188	1.04	269	1.5	9	664 ± 30
E252-1	515143	57+00	Systematic	Representative bulk material	0.69	74	1.03	108	1.5	3	388 ± 23
E253-1	515144	57+27	Fault	Representative bulk material	1.72	64	3.30	37	1.9	1	483 ± 14
E254-1	515145	58+66	Fault	Breccia	0.47	552	1.15	1175	2.4	39	588 ± 58
E255-1	515146	58+77	Subunit contact	Representative bulk material	2.98	873	2.20	293	0.7	9	140 ± 9
E256-3	515147	59+00	Systematic	Wall rock	1.65	964	2.34	584	1.4	19	361 ± 22
E256-1	515147	59+00	Systematic	Breccia	0.52	617	1.18	1186	2.3	39	347 ± 41
E290-1	521128	59+98	Systematic	Representative bulk material	0.58	41	0.33	71	0.6	2	205 ± 14
E257-1	515148	61+00	Systematic	Representative bulk material	1.19	305	1.76	256	1.5	8	428 ± 26

LANL ID	SMF barcode	Approx ESF station	Sampled feature	Description of analyzed aliquot	Leached salts (Note 1)					% CW (Note 2)	Corrected $^{36}\text{Cl}/\text{Cl} \times 10^{-15}$ (Note 3)	
					Cl mg/kg	Br $\mu\text{g}/\text{kg}$	$\text{SO}_4$ mg/kg	Br/Cl	$\text{SO}_4/\text{Cl}$			
E258-1	515149	61+92	Fracture	Representative bulk material	0.82	327	0.89	398	1.1	13	276 ±	21
E259-1	515150	62+00	Systematic	Representative bulk material	0.49	87	0.80	177	1.6	6	409 ±	28
E260-1	515151	62+05	Fault	Representative bulk material	1.15	111	1.21	97	1.1	3	261 ±	13
E261-1	515152	62+18	Fault	Representative bulk material	0.47	270	0.96	574	2.0	19	749 ±	39
E262-1	515153	62+71	Shear	Representative bulk material	0.42	227	0.80	540	1.9	18	420 ±	28
E263-1	515154	63+00	Systematic	Representative bulk material	3.03	220	3.58	72	1.2	2	465 ±	14
E264-1	515155	63+06	Fracture	Representative bulk material	1.71	278	2.77	162	1.6	5	458 ±	13
E265-1	515156	63+21	Fracture	Representative bulk material	3.31	128	6.04	39	1.8	1	452 ±	12
E266-1	515157	63+26	Fracture	Representative bulk material	3.73	175	6.64	47	1.8	1	486 ±	16
E267-1	515158	63+30	Fault	Representative bulk material	3.74	427	5.98	114	1.6	4	427 ±	14
E269-1	515188	63+73	Fracture	Representative bulk material	2.51	479	3.85	191	1.5	6	551 ±	14
E270-1	515187	63+81	Fracture	Representative bulk material	3.64	692	5.65	190	1.6	6	439 ±	14
E271-ID	515186	64+00	Systematic	Representative bulk material	3.15	392	3.95	124	1.3	4	438 ±	19
E271-1	515186	64+00	Systematic	Representative bulk material	3.15	392	3.95	124	1.3	4	467 ±	20
E272-1	515185	64+34	Broken rock	Representative bulk material	1.38	36	1.74	26	1.3	1	467 ±	22
E273-1	515184	64+50	Broken rock	Representative bulk material	1.42	474	2.14	334	1.5	11	612 ±	23
E274-1	515182	64+93	Fracture	Representative bulk material	2.90	1300	3.50	448	1.2	15	491 ±	27
E275-1	515181	65+00	Systematic	Representative bulk material	1.79	167	2.56	93	1.4	3	443 ±	19
E268-1	515180	65+20	Fracture zone	Breccia	1.73	91	2.37	53	1.4	1	468 ±	18
E276-1	515179	65+56	Fracture zone	Breccia	1.61	423	2.41	263	1.5	8	479 ±	14
E277-1	515178	65+80	Fracture zone	Representative bulk material	1.97	545	2.66	277	1.4	9	424 ±	33

LANL ID	SMF barcode	Approx ESF station	Sampled feature	Description of analyzed aliquot	Leached salts (Note 1)					% CW (Note 2)	Corrected $^{36}\text{Cl}/\text{Cl} \times 10^{-15}$ (Note 3)
					Cl mg/kg	Br $\mu\text{g}/\text{kg}$	$\text{SO}_4$ mg/kg	Br/Cl	$\text{SO}_4/\text{Cl}$		
E278-1	515177	66+00	Systematic	Representative bulk material	1.50	88	1.56	59	1.0	2	520 ± 61
E279-1	515176	66+15	Fault	Breccia	1.32	1335	2.24	1011	1.7	34	402 ± 40
E280-1	515175	66+40	Fault hanging wall	Representative bulk material	0.30	197	0.74	657	2.5	22	238 ± 30
E281-1	515174	67+00	Systematic	Representative bulk material	2.28	66	3.80	29	1.7	1	453 ± 18
E283-1	515172	67+27	Fault	Representative bulk material	3.04	64	4.63	21	1.5	0	470 ± 21
E284-1	515173	67+35	Subunit contact	Representative bulk material (welded)	1.77	30	2.80	17	1.6	0	502 ± 20
E284-3	515173	67+35	Subunit contact	Representative bulk material (nonwelded)	1.28	6	1.93	4	1.5	0	509 ± 19
E289-1	515170	67+61	Fault	Gouge	4.36	228	9.44	52	2.2	1	589 ± 23
E285-1	515171	67+73	Damp zone	Representative bulk material	4.75	57	12.05	12	2.5	0	468 ± 23
E287-1	515134	67+87	Fault	Breccia	2.26	45	4.35	20	1.9	0	517 ± 19
E286-1	515133	67+87	Fault zone	Clay fracture filling	2.19	83	6.64	38	3.0	1	475 ± 22
E286-4	515133	67+87	Fault zone	Wall rock	0.67	112	4.60	167	6.9	5	645 ± 29
E288-1	515132	67+90	Fault footwall	Wall rock	1.09	278	2.58	255	2.4	8	557 ± 31
E298-1	521127	68+00	Systematic	Representative bulk material	1.42	143	2.67	101	1.9	3	606 ± 17
E292-1	521123	69+00	Systematic	Representative bulk material	3.11	144	3.58	46	1.2	1	414 ± 17
E293-1	521122	69+14.5	Fault zone	Breccia	2.66	82	2.08	31	0.8	1	454 ± 35
E294-1	521121	69+32.5	Fracture	Breccia	1.73	547	3.52	316	2.0	10	473 ± 22
E295-1	521120	69+41.7	Fracture zone	Representative bulk material	1.86	52	1.46	28	0.8	1	476 ± 21
E299-1	522221	69+47	Systematic	Representative bulk material	2.10	64	1.36	31	0.6	1	441 ± 20
E300-1	522220	69+68	Fault (?)	Representative bulk material	2.49	437	2.74	176	1.1	6	354 ± 13
E300-3	522220	69+68	Fault (?)	Representative bulk material	2.27	412	2.38	181	1.0	6	376 ± 16
E302-1	522218	70+19	Fault	Representative bulk material	5.75	518	6.89	90	1.2	3	327 ± 13

LANL ID	SMF barcode	Approx ESF station	Sampled feature	Description of analyzed aliquot	Leached salts (Note 1)					% CW (Note 2)	Corrected $^{36}\text{Cl}/\text{Cl} \times 10^{-15}$ (Note 3)
					Cl mg/kg	Br $\mu\text{g}/\text{kg}$	$\text{SO}_4$ mg/kg	Br/Cl	$\text{SO}_4/\text{Cl}$		
E303-1	522217	70+36	Fault	Representative bulk material	2.29	96	3.77	42	1.6	1	439 ± 17
E304-1	522216	70+50	Systematic	Representative bulk material	5.07	313	6.09	62	1.2	2	491 ± 21
E305-1	522215	70+55	Fault	Breccia	4.37	236	5.49	54	1.3	2	386 ± 12
E306-1	522214	70+66	Fault	Breccia	3.25	477	5.84	147	1.8	5	499 ± 19
E307-1	522212	71+34	Fault	Representative bulk material	0.73	31	1.19	42	1.6	1	557 ± 29
E308-1	522213	71+39	Fault	Representative bulk material	1.07	40	1.74	37	1.6	1	492 ± 13
E309-1	522211	71+41	Fault	Representative bulk material	1.03	51	1.28	49	1.2	1	445 ± 21
E310-1	522210	71+50	Systematic	Representative bulk material	1.01	191	1.56	189	1.5	6	441 ± 21
E311-1	522209	72+50	Systematic	Representative bulk material	2.43	664	3.06	273	1.3	9	459 ± 11
E312-1	522208	72+69	Fault	Representative bulk material	1.61	280	2.40	174	1.5	6	463 ± 18
E313-1	522207	73+48	Systematic	Representative bulk material	3.78	80	4.48	21	1.2	0	367 ± 14
E315-1A	522205	74+49	Systematic	Representative bulk material	11.49	413	12.43	36	1.1	1	435 ± 16
E316-1	522202	74+89	Fault	Representative bulk material	5.92	66	7.13	11	1.2	0	459 ± 11
E317-1	522201	75+09	Subunit contact	Representative bulk material	1.80	1297	3.66	721	2.0	24	402 ± 30
E318-1	522203	75+09.5	Subunit contact	Representative bulk material	2.27	1785	4.08	786	1.8	26	395 ± 16
E319-1	522204	75+10	Subunit contact	Representative bulk material	3.62	462	4.94	128	1.4	4	414 ± 16
E321-1	521287	75+34	Fault	Breccia	6.08	175	8.38	29	1.4	1	476 ± 12
E323-3	521289	75+53.5	Cooling joints	Wall rock	4.40	151	3.99	34	0.9	1	413 ± 19
E323-1	521289	75+53.5	Cooling joints	Breccia	3.37	400	4.43	119	1.3	4	465 ± 17
E324-3	521290	75+78	Fault	Wall rock	4.46	169	5.19	38	1.2	1	322 ± 13
E324-1	521290	75+78	Fault	Breccia	5.42	136	11.19	25	2.1	1	418 ± 31
E325-1	521291	76+30	Fault	Breccia	2.34	169	2.42	72	1.0	2	380 ± 20
E326-3	521292	76+31	Fault	Wall rock	3.35	98	3.06	29	0.9	1	419 ± 11
E326-1	521292	76+31	Fault	Wall rock	4.65	288	6.71	62	1.4	2	423 ± 9
E327-1	521295	76+50	Systematic	Representative bulk material	2.42	226	2.37	93	1.0	3	281 ± 12

LANL ID	SMF barcode	Approx ESF station	Sampled feature	Description of analyzed aliquot	Leached salts (Note 1)					% CW (Note 2)	Corrected $^{36}\text{Cl}/\text{Cl} \times 10^{-15}$ (Note 3)
					Cl mg/kg	Br $\mu\text{g}/\text{kg}$	SO <sub>4</sub> mg/kg	Br/Cl	SO <sub>4</sub> /Cl		
E328-3	521294	76+76	Fault	Breccia > ~1 cm	0.62	42	1.58	68	2.5	2	445 ± 20
E328-1	521294	76+76	Fault	Breccia < ~1 cm	1.28	205	3.14	160	2.5	5	334 ± 15
E329-1	521293	77+10	Fault	Representative bulk material	0.50	76	0.95	152	1.9	5	394 ± 19

## APPENDIX C

### STRUCTURAL AND PETROLOGIC CHARACTERIZATION OF ESF SAMPLING SITES

Detailed descriptions are provided in this appendix for a subset of the full listing of ESF samples listed in Appendices A and B. The samples selected for inclusion in this appendix are (a) those that contain bomb-pulse  $^{36}\text{Cl}$ , based on measured  $^{36}\text{Cl}/\text{Cl}$  ratios greater than  $1250 \times 10^{-15}$  (Appendix C-1), (b) those with  $^{36}\text{Cl}/\text{Cl}$  ratios significantly lower than present-day background and which may possibly indicate zones of comparatively stagnant water (Appendix C-2), and (c) additional samples for which petrologic descriptions are available at the present time (Appendix C-3). Chlorine-36 data for each of the samples in this appendix are from Appendix B. Sampling objectives are described in section 4.2.

**Structural analysis.** The orientation, length, and amount of offset of structural features sampled in the ESF were obtained from the full-periphery mapping and detailed line survey (DLS) data from the ESF. These data were augmented by field observations and interpretations made at each sample locality, including:

- a description of the sampled feature, such as interpreted joint origin, degree and character of brecciation, and description of features too small to be portrayed on the full-periphery maps (which portray features with lengths greater than 2 m) or in the DLS data (which are limited to fracture lengths greater than 0.3 m to Sta. 37+80, greater than 1 m thereafter);
- description of the local structural setting, such as a description of the relative expression of fracture sets, location of the sampled feature with respect to known faults, and changes in fracture intensity near fault zones; and
- interpreted connection to other features, including termination relations with other fracture sets.

**Petrologic analysis.** Subsamples designated for mineralogic and petrologic study were examined by binocular microscope. Mineral identifications are based on color, morphology, hardness, comparison to known materials, limited X-ray diffraction analysis, and evidence of fluorescence under ultraviolet light. Some ambiguities of mineral identification are unresolved; for example, clay and mordenite (a zeolite) in minute deposits cannot be distinguished without electron microscopy or similar techniques. Standard color charts were not used to determine color names because they are a potential source of Cl cross-contamination. X-ray powder diffraction data for selected samples were obtained on an automated Siemens D-500 diffractometer using Cu-K $\alpha$  radiation, incident- and diffracted-beam Soller slits, and a Kevex (SiLi) solid-state detector. Data were collected from 2 to 50° 2 $\theta$  and count times  $\geq 2.0$  s per step. Quantitative analyses used 1.0- $\mu\text{m}$  corundum as the internal standard.

**Abbreviations and terms used in this appendix:** DLS, detailed line survey; FPGM, full-periphery geologic map; IFZ, intensely fractured zone. The term spring line refers to the midpoint location on the tunnel wall that is halfway between the crown and the floor of the ESF. Abbreviations for lithostratigraphic units follow the usage of Buesch and others (1996) and are explained in Table 2-1.

## APPENDIX C-1

### CHARACTERIZATION OF SAMPLE SITES WITH ELEVATED $^{36}\text{Cl}/\text{Cl}$ RATIOS

This section of Appendix C contains structural and petrologic descriptions for samples with  $^{36}\text{Cl}/\text{Cl}$  ratios greater than  $1250 \times 10^{-15}$ , which is above the estimated range over which the ratio has varied in the atmosphere over the past 40 ka (section 3.1.2), and which is the threshold above which a sample is interpreted as having an unambiguous component of bomb-pulse fluid present (section 4.2.4).

Sample results with  $^{36}\text{Cl}/\text{Cl}$  ratios less than  $1250 \times 10^{-15}$  have also been included in this section when the samples are closely associated with others that have ratios above  $1250 \times 10^{-15}$ . One example is sample E010, one of several collected within the Bow Ridge fault zone, but the only one with a ratio less than  $1250 \times 10^{-15}$ . In many cases, two aliquots of a given sample are reported with one aliquot having a ratio greater than  $1250 \times 10^{-15}$ , and the other less than this value.

LANL ID:	SMF barcode:	Station location:
E008	509016	2+00
E009	509017	2+00
E010	509018	2+00
E011	509019	2+00
E012	509020	2+00

**Measured  $^{36}\text{Cl}/\text{Cl}$  ratio ( $\times 10^{-15}$ ) and description of analyzed aliquot:**

E008-2	2138 $\pm$ 137	Breccia
E009-2	2444 $\pm$ 169	Breccia
E010-2	720 $\pm$ 49	Rubble
E011-2	2378 $\pm$ 153	Rubble
E012-2	2398 $\pm$ 154	Breccia

**Sampled feature:** Bow Ridge fault

**Sampling Objective:** Role of faults

**Lithology:** Tpcpll in footwall, Tmbt1 (pre-Rainier Mesa bedded tuff) in hanging wall.

**Structural setting of sampled feature:**

These samples were collected from within the Bow Ridge fault. The Bow Ridge fault has an orientation of 190/70, with about 100 m of normal, west-side down, displacement. Fault rock associated with the Bow Ridge fault is an approximately 3 m-wide zone of dominantly matrix-supported breccia. The fault breccia is rubbly material that is uncemented to weakly consolidated. Macroscopic breccia clasts consist of rotated angular to subangular clasts of Tpcpll (and a small number of clasts of pre-Rainier Mesa bedded tuff) that range in size from less than 5 mm to greater than 25 cm. Breccia matrix is composed of clayey, tuffaceous material derived from the pre-Rainier Mesa bedded tuff.

**Mineralogy and petrology of sampled feature:**

**E008 (Sta. 1+99.8)**

The fault gouge is composed of fragments of densely welded, devitrified Tiva Canyon Tuff. Individual breccia clasts range from more than 5 cm across to less than 150  $\mu\text{m}$ . There are local segregations of the fine-grained material. Larger clasts are somewhat rounded.

Some of the larger clasts have dendritic coatings of manganese minerals. All clasts are coated with a less than 1 mm thick powdery white layer composed of feldspar, smectite, quartz, tridymite, cristobalite, calcite, and hematite, in order of decreasing abundance (see Table 7-2). Most of this may be material of vapor-phase and lower-temperature hydrothermal origin redistributed onto the surfaces of the breccia clasts. There is local tight cementation of the fine-grained breccia and adjacent coarser clasts by less than 1 mm thick coatings of less than 0.2 mm calcite crystals whose overall abundance is undetermined. The calcite is also covered with white powder. No UV-fluorescent or otherwise visually identifiable silica is present.

E010 (Sta. 1+99.8)

This sample from the Bow Ridge fault zone consists of ~2- to 5-cm rubble. The rubble clasts are subangular to subrounded and are either intact densely welded, devitrified Tiva Canyon bedrock or loosely cemented Tiva Canyon breccia, in about equal proportions. The brecciated tuff consists of 1-cm fragments of fractured tuff cemented by gray-white, slightly clayey, <<1-mm material. Rubble clasts of intact rock commonly have 1 mm-thick coatings of powdery gray-white material.

Most rock fragments have scattered surficial patches of dendritic manganese minerals. On newly broken breccia clast fracture surfaces, a few of the manganese patches surround highly weathered mafic minerals. No calcite or UV-fluorescent silica was observed.

E011 (Sta. 1+99.8)

This sample consists of mostly coarse (>1 cm) rubble and minor fine-grained breccia from the Bow Ridge fault zone. The rubble clasts are all densely welded, devitrified Tiva Canyon Tuff and are mostly subequant and subangular.

About 95% of the brecciated rock surfaces are coated with a <1 mm-thick layer of pale pink to buff powdery material. In a few places where the coating is thin or absent, discontinuous coatings of dendritic manganese minerals cover less than 5% of the rock surfaces. In the fine-grained breccia and on a few coarse clast surfaces, there are <<1 mm-thick coatings of <0.5 mm calcite crystals with probably rhombohedral morphology. Most of the calcite shows little fluorescence, except for a few 1 to 2 mm wide patches that fluoresce white (more strongly in long- than in short-wave UV light). Some calcite may have a very thin, visually undetectable, coating of opal because it shows weak yellow-green fluorescence in short-wave UV light. The calcite does not form a dense cement, and there are small cavities <1 mm within the fine-grained breccia that lack calcite or powdery coatings.

LANL ID: SMF barcode: Station location:  
E028 503934 12+44

**Measured  $^{36}\text{Cl}/\text{Cl}$  ratio ( $\times 10^{-15}$ ) and description of analyzed aliquot:**

E028-1 2637  $\pm$  106 Representative bulk material

**Sampled feature:** Cooling joints

**Sampling Objective:** Role of fractures in percolation

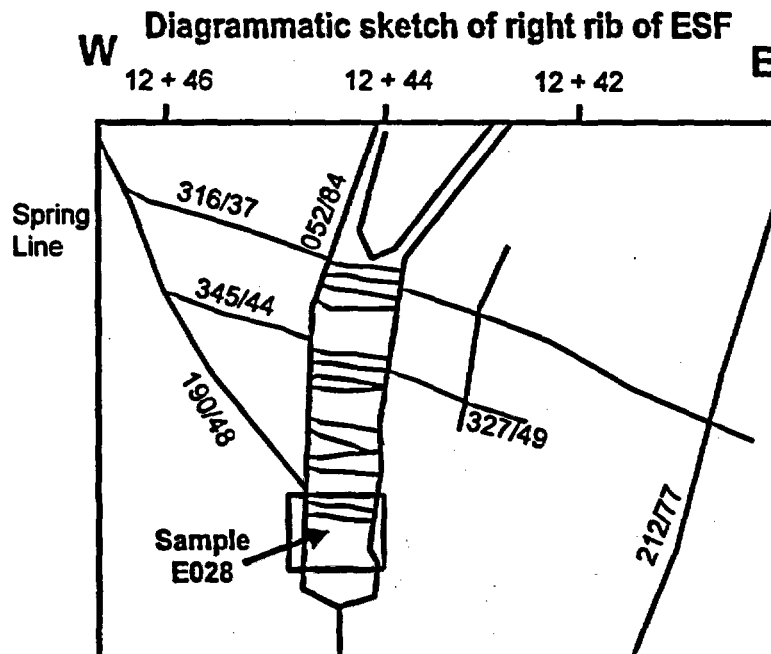
**Lithology:** Tptrn3, (pumice-poor subzone)

**Structural setting of sampled feature:**

The host bedrock is densely welded, devitrified, nonlithophysal, crystal-rich Topopah Spring Tuff. The sampled structure is a pair of two near-vertical cooling joints 30 cm to 1 m apart, with the intervening rock cut by a second set of ladderlike sub-horizontal fractures perpendicular to the main fractures. This feature is traceable from invert to crown on both ribs of the tunnel. Similar features are spaced laterally about 10 to 20 m apart.

**Mineralogy and petrology of sampled feature:**

The sampled rock contains about 10-15% phenocrysts of mostly alkali feldspar. Pumice lapilli constitute about 10% and commonly contain vapor-phase alteration cavities up to 2 cm across. The main secondary mineral in the vapor-phase cavities is clear to white crystalline silica. The prominent cooling cracks have widespread but incomplete coatings, less than 1 mm thick, of mostly white, granular to arborescent, non-UV-fluorescent silica, probably a vapor-phase product. Some cooling cracks and other, more irregular cracks, have 1 to 2 mm thick veneers of less than 1 mm tuff detritus cemented in place by UV-fluorescent botryoidal silica, mostly blue-gray and slightly translucent. Locally, the botryoidal texture grades into surface-conformal aggregates of subparallel 1 to 2 mm drusy quartz crystals. This cement locally overlies the vapor-phase silica. Isolated aggregates of drusy quartz are perched along fractures, especially fracture intersections. The dominant botryoidal silica cement also contains some white and nearly opaque silica. A small amount of clear sub-botryoidal opal overlies the rest of the silica cement, especially in depressions. No calcite was observed.



LANL ID: E030      SMF barcode: 503931      Station location: 13+68

**Measured  $^{36}\text{Cl}/\text{Cl}$  ratio ( $\times 10^{-15}$ ) and description of analyzed aliquot:**

E030-1	697 ± 35	Breccia (< ~0.5 cm)
E030-2	1621 ± 83	Breccia (> ~0.5 cm)

**Sampled feature:** Weakly consolidated rubble/breccia along intersection of possible cooling joint with a shear zone

**Sampling Objective:** Role of fractures in percolation

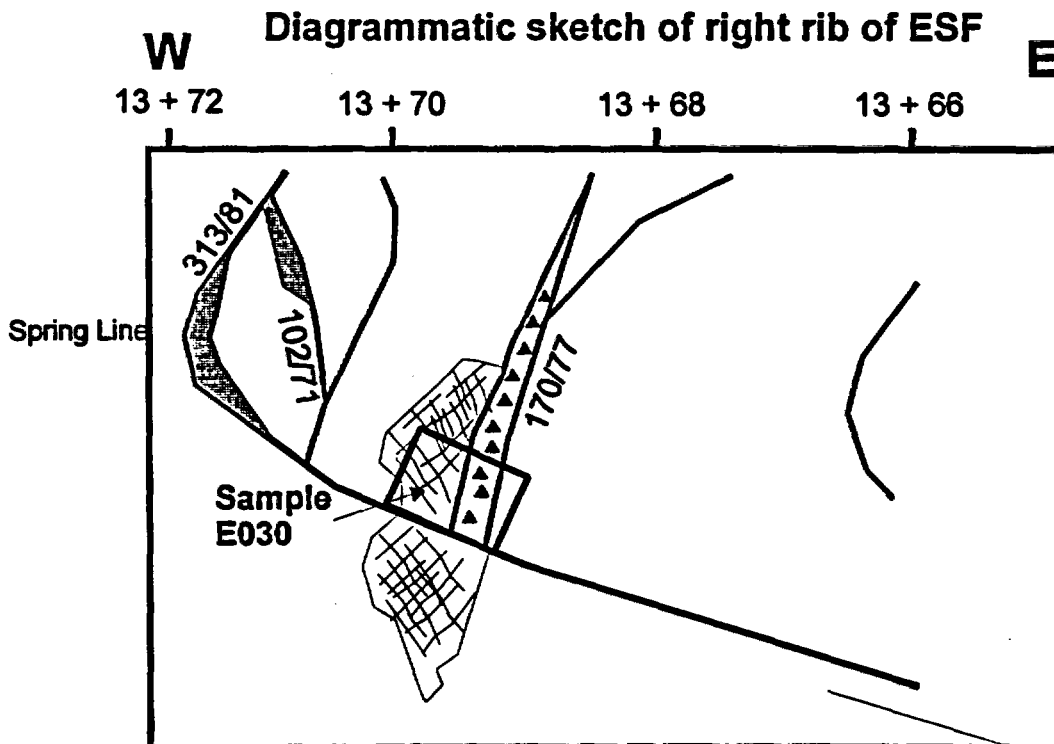
**Lithology:** Tptm2, mixed pumice subzone

**Structural setting of sampled feature:**

The sample is from weakly consolidated rubble/breccia along a fracture. The fracture is oriented 170/77 and, although breccia-filled, does not show evidence of offset. There is a complicated age relationship between fractures in the vicinity of the sampled feature. The breccia-filled fracture appears to terminate against a joint oriented at 313/81. There is minor rubble, broken rock below, but no discrete breccia-filled fracture. However, the 313/81 joint terminates at the upper end (or is offset by) the breccia-filled fracture (not shown on sketch). The breccia-filled fracture extends to the left rib.

**Mineralogy and petrology of sampled feature:**

The sampled material is rubble composed of subangular to subrounded clasts of densely welded, devitrified crystal-rich Topopah Spring Tuff. The rock is slightly crumbly due to pervasive vapor-phase alteration of the pumice lapilli to feldspar, crystalline silica, and Fe-Ti oxides. The surfaces of some of the larger rubble clasts exhibit domains of <1 mm rock fragments cemented by vapor-phase minerals, and some areas of the rubble surfaces have coatings of vapor-phase minerals extending beyond the boundaries of altered pumices. These textural relations suggest that brecciation was at least partly syngenetic. No calcite or UV-fluorescent silica was observed.



LANL ID: E031-1      SMF barcode: 503930      Station location: 14+00

Measured  $^{36}\text{Cl}/\text{Cl}$  ratio ( $\times 10^{-15}$ ) and description of analyzed aliquot:

E031-1	1038 $\pm$ 35	Breccia (> ~1 cm)
E031-3	2398 $\pm$ 191	Breccia (< ~1 cm)

Sampled feature: Broken rock along fault

Sampling Objective: Role of faults

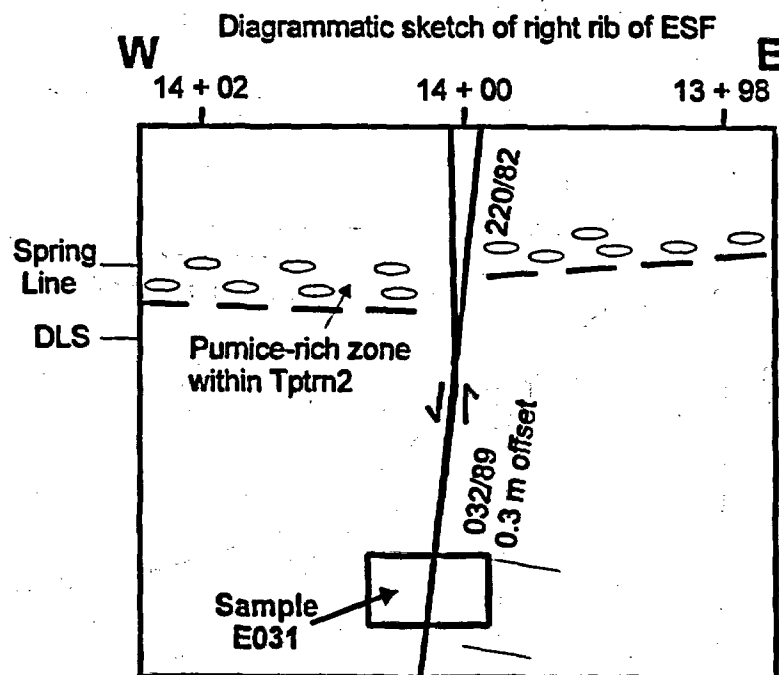
Lithology: Tptrn2, mixed pumice subzone

Structural setting of sampled feature:

The feature sampled is a northeast-striking fault, oriented at 032/89. The fault has about 0.3 m down-to-west offset, based on the offset of the pumice horizon at springline. The fault has up to 3 cm wall separation and open space along the fault plane below the DLS. This opening goes back into the wall at least 2 m. This is a single feature cutting the Tptr; the nearest mapped fracture is approximately 5 m to the east or west. No connections to other features are apparent.

Mineralogy and petrology of sampled feature:

This sample is composed of moderately to densely welded, devitrified Topopah Spring Tuff. Flattened, elongate pumice lapilli are up to 5 cm long and have been highly modified by vapor-phase crystallization. The pumices now have a cellular "bubble" texture, with individual cells from <1 mm to ~1 cm across. The mineralogy of the <1-mm vapor-phase crystals is mostly alkali feldspar and silica (forming the walls of the cells), with lesser amounts of biotite, Fe-Ti oxides, amphibole, and hematite. No UV-fluorescent mineral phases were observed. The sample is unfractured, although the flattened pumices may provide partings in the rock.



LANL ID: SMF barcode: Station location:  
E040 503922 18+96

**Measured  $^{36}\text{Cl}/\text{Cl}$  ratio ( $\times 10^{-15}$ ) and description of analyzed aliquot:**

E040-1 1642  $\pm$  59 Representative bulk material

**Sampled feature:** Lower boundary of rubble zone

**Sampling Objective:** Representative sample of rubbly, broken rock

**Lithology:** Tptpul

**Structural setting of sampled feature:**

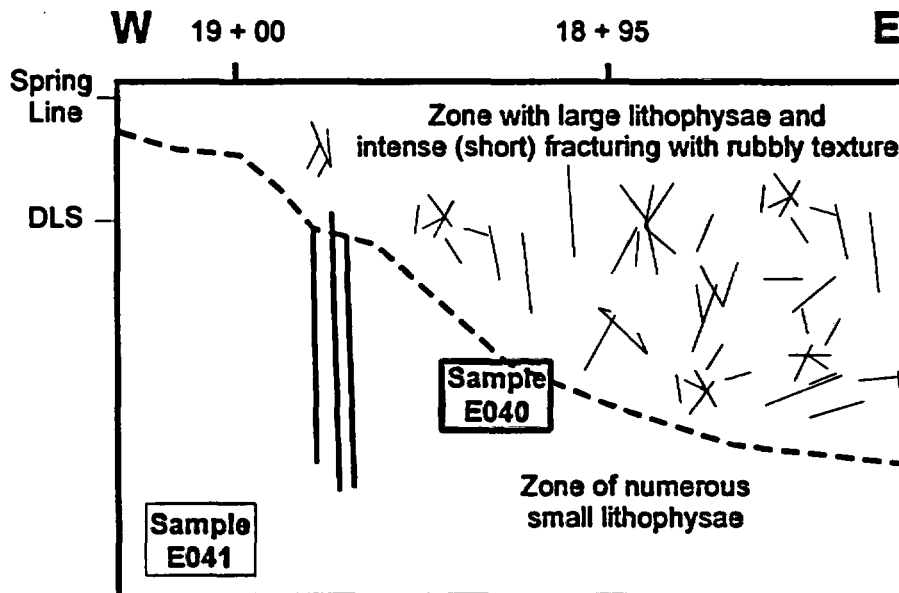
The sample is at the boundary between lithophysal rock and rubbly-textured rock. The block size in the upper zone is 5-10 cm. Most fractures are 30 cm or less. The Drill Hole Wash fault extends to station location 19 + 00 on the left rib; samples are approximately 8 m from the fault plane. It is possible that the rubbly-textured rock has local importance here as a zone of enhanced permeability in the general vicinity of the Drill Hole Wash fault.

**Mineralogy and petrology of sampled feature:**

The bedrock at the sampling site is lithophysal, densely welded, devitrified Topopah Spring Tuff. The lithophysal cavities are up to 0.5 m wide, and lithophysal fractures with vapor-phase mineral coatings are common. The rock is cut by many short-segment (<1 m), high-angle cooling cracks. Small amounts of calcite are present in the exposed rock, but not in the sampled material.

Rock fragments in the sampled material are mostly 5 to 10 cm across, angular, and equant to elongate. The smaller lithophysal cavities and partings, coated with vapor-phase minerals, are elongate parallel to the rock layering caused by flow and welding. The vapor-phase altered borders on the cavities and partings are up to about 1 cm thick. The <1 mm crystals lining the cavities and partings are feldspar, crystalline silica, and minor Fe-Ti oxides. Away from the central lithophysal cavities, the vapor-phase crystals are finer grained, <0.1 mm. Most rock fragment surfaces, especially those that are smoother and more planar (probable cooling cracks), have <<1 mm translucent to transparent coatings of probable cryptocrystalline silica. Locally, the silica has an equally thin overcoat of pale blue-gray clay. There is a dusting of loose to somewhat adhesive vapor-phase material on all rock surfaces. No calcite or UV-fluorescent silica was observed in the sampled material.

**Diagrammatic sketch of right rib of ESF**



LANL ID: SMF barcode: Station location:  
E042 503920 19+31

Measured  $^{36}\text{Cl}/\text{Cl}$  ratio ( $\times 10^{-15}$ ) and description of analyzed aliquot:

E042-2	3019 $\pm$ 93	Breccia ( $>\sim 0.5$ cm)
E042-3	1837 $\pm$ 65	Breccia ( $<\sim 0.5$ cm)

Sampled feature: Immediate hanging wall of eastern splay of the Drill Hole Wash fault

Sampling Objective: Role of faults

Lithology: Tptpul

Structural setting of sampled feature:

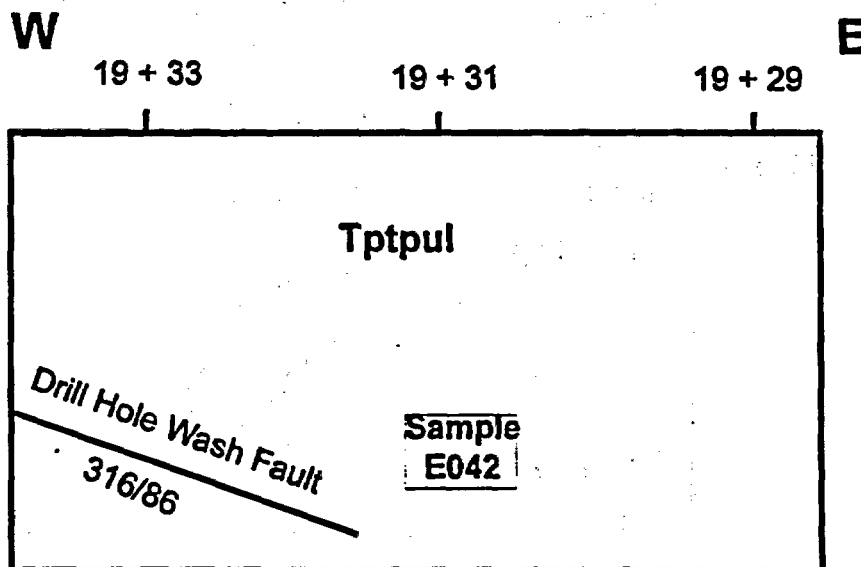
The sample at station 19+31 (E042) is in unfractured lithophysal rock, about 1 m east of the fault plane. The fault passes almost directly overhead on the crown. No other faults are nearby, and there does not appear to be any evidence of abundant short fractures in this sampling interval.

Mineralogy and petrology of sampled feature:

The sampled bedrock is lithophysal, densely welded, devitrified Topopah Spring Tuff. The abundant lithophysal cavities are less than 20 cm across. The rock is generally broken into mostly  $<10$  cm fragments. Orientation and extent of the broken rock zone are unknown. There are no obvious throughgoing fractures, but a possible adjacent fracture zone parallel to the tunnel axis may have been mostly removed during mining. Calcite fillings in a cluster of lithophysal cavities about 1 m above and to the right of the collection site suggest a possible flow pathway.

There is preferential breakage and comminution of the vapor-phase altered margins of lithophysal cavities and vapor-phase altered pumice lapilli. This soft material is composed of  $<0.1$  mm crystals of feldspar and crystalline silica. Networks of fine ( $\ll 1$  mm apertures) fractures within the breccia clasts are filled with poikilitic calcite, and the surfaces of the clasts have  $<1$  mm-thick coatings of poikilitic calcite with a variety of surface terminations. The pore spaces between the larger clasts, i.e., larger than a few millimeters, are not completely filled with calcite although the surface coatings are sufficient to form a tight cement. The calcite is not UV-fluorescent, and no fluorescent silica was observed.

Diagrammatic sketch of 19 + 31 locality



LANL ID: SMF barcode: Station location:  
E044 503918 19+42

Measured  $^{36}\text{Cl}/\text{Cl}$  ratio ( $\times 10^{-15}$ ) and description of analyzed aliquot:

E044-2 2290  $\pm$  74 Representative bulk material

Sampled feature: Fractured rock in hanging wall of the Drill Hole Wash fault

Sampling Objective: Sampling of faults

Lithology: Tptpul

Structural setting of sampled feature:

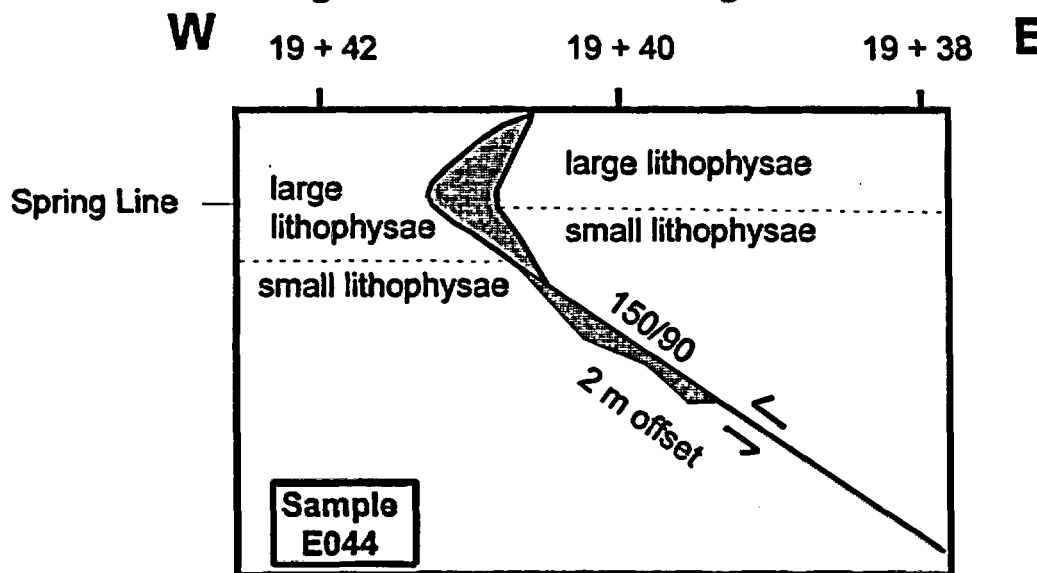
The sampled feature corresponds to the northeast fault of the Drill Hole Wash structure along the base of the slope along the NE side of Drill Hole Wash. The sample itself is about 1 m into the hanging wall of the Drill Hole Wash fault, in the Tptpul. The rock here is reddish with numerous 1-cm lithophysae and spots. The second Drill Hole Wash fault splay is approximately 3 m to the east. Rock between the faults is generally unfractured.

Mineralogy and petrology of sampled feature:

The sample site is a crackle breccia zone in lithophysal, densely welded, devitrified Topopah Spring Tuff. The breccia zone is about 3 m wide and laterally bounded by discrete fractures. The breccia is fairly tight, with little or no realignment of the blocks. The breccia zone extends from the invert about halfway up the right rib, but the opposite rib shows more upward continuity.

Lithophysal cavities are up to about 3 cm across and lined with <1 mm crystals of feldspar, silica, and Fe-Ti oxides. The angular fragments are locally coated with <<1 mm crystals of vapor-phase minerals, suggesting that the fragmentation of the rock is at least partly syngenetic. A ubiquitous white powder on the rock surfaces contains vapor-phase minerals that may have been redistributed from lithophysae. UV-fluorescent calcite cement is widespread but not abundant. Coatings of <1 mm calcite crystals are located in some lithophysal cavities and adjacent surfaces of intersecting fractures. No UV-fluorescent silica was detected in the sample.

Diagrammatic sketch of right rib of ESF



LANL ID: SMF barcode: Station location:  
E050 509240 24+40

Measured  $^{36}\text{Cl}/\text{Cl}$  ratio ( $\times 10^{-15}$ ) and description of analyzed aliquot:

E050-2 2579  $\pm$  94 Breccia

Sampled feature: Fault zone

Sampling Objective: Sampling of faults

Lithology: Tptpul

Structural setting of sampled feature:

The sampled material is taken from a 5-8 cm-wide zone of fault gouge along a fault with an orientation of 195/83. The fault offsets a large cooling joint (orientation 039/78; joint appears on left rib at Sta. 24+58) with about 1.5 m west side down apparent dip separation. Fault zone is filled with poorly cemented gouge in places, in other places it is cavernous. At sample location, there is a hole that extends downward about 1 m below invert. On left rib is a cavern about 3m high by 1 m wide along fault.

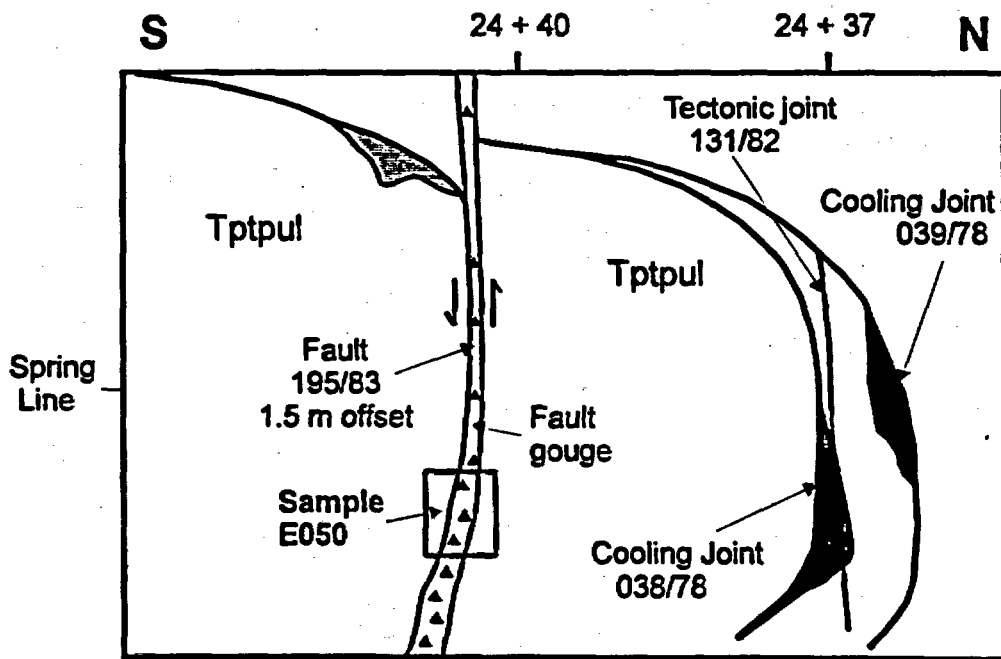
The bedrock in this vicinity is virtually unfractured rock except for the fault and the large cooling joint at Sta. 24+37. This fault does not correlate with any fault mapped at the surface (Day and others, in press).

Mineralogy and petrology of sampled feature:

The sampled material is fault gouge and calcite from a near-vertical fault in lithophysal, densely welded, devitrified Topopah Spring Tuff. Some large lithophysal cavities are intersected by the fault trace, and many have calcite overlying the 1 cm-thick vapor-phase mineral coatings.

The gouge itself, as sampled, is uncemented and contains no detectable UV-fluorescent silica. A local deposit of calcite, separated for  $^{36}\text{Cl}/\text{Cl}$  analysis, was the only calcite observed within the fault. Centimeter-scale clasts are subangular to subrounded and have scattered thin coatings of vapor-phase minerals, mostly feldspar and crystalline silica, typical of the smaller lithophysal cavities. Most clasts, including those <1 mm, are coated with light buff powdery material.

Diagrammatic sketch of right rib of ESF



LANL ID: SMF barcode: Station location:  
E052 509244 26+79  
E220 510719

Measured  $^{36}\text{Cl}/\text{Cl}$  ratio ( $\times 10^{-15}$ ) and description of analyzed aliquot:

E052-1	2036 ± 68	Representative bulk material
E220-1	564 ± 25	Representative bulk material

Sampled feature: Large lithophysal cavity at intersection of two small fractures

Sampling objective: The original bomb-pulse sample (E052) was resampled (E220) with no bomb-pulse results. The Br/Cl ratio of the second sample, E220, indicates that it was contaminated to a greater extent by construction water than was E052. Some walls in ESF were lightly sprayed/washed, which could have altered the  $^{36}\text{Cl}$  signal.

Lithology: At Tptpul/Tptpmn contact

Structural setting of sampled feature:

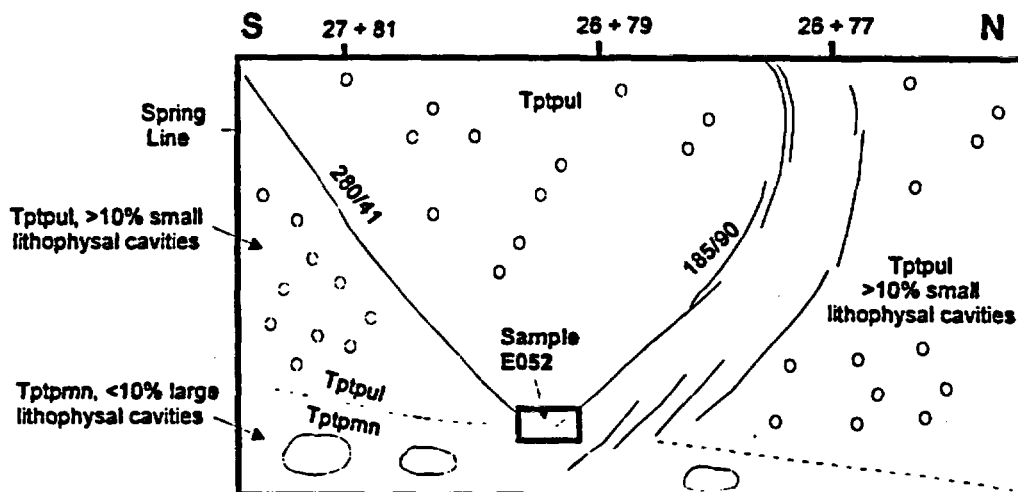
Sampling site is a single large (0.7 m diameter) lithophysal cavity at intersection of a probable cooling joint oriented 280/41 and discontinuous, probable tectonic joint oriented 185/80. The latter is discontinuous, appears as an en-echelon series of fractures within a 1 m-wide zone, and is traceable about 3/4 of the distance from invert to crown. In this vicinity a set of probable cooling joints exists with strikes of 280-290; true spacings of 2-5 m. Three joints of this set have mapped offset between Sta. 26+45 and 26+75.

Mineralogy and petrology of sampled feature:

The bedrock is densely welded, devitrified Topopah Spring Tuff with >10% lithophysal cavities up to 0.5 m across. Some cavities are aligned parallel to adjacent or intersecting fractures, some of which are cooling cracks. The sampling site includes a near-vertical, probable cooling crack with multiple traces within a 1 m-wide zone, traceable about 3/4 of the distance from invert to crown. Fracture apertures are generally 1 mm. Fractures like this occur at about a 3- to 4-m spacing along the tunnel wall. There are no obvious coatings of calcite or manganese minerals on the fracture walls, but most of the larger lithophysae have 2- to 3-cm-thick crusts of 1 to 2 mm calcite crystals on the bottoms and sides of the cavities.

Smaller lithophysal cavities, a few centimeters across, have <1 mm-thick coatings of <1 mm crystals of feldspar, crystalline silica, and Fe-Ti oxides. Examination of one cooling joint surface revealed scattered 1 to 2-mm patches of very thin and very fine-grained blue-gray silica. None of the silica fluoresces in UV light. No calcite was observed in the small cavities or on the fracture surface.

Diagrammatic sketch of right rib of ESF



LANL ID: SMF barcode: Station location:  
E056 509243 27+18

Measured  $^{36}\text{Cl}/\text{Cl}$  ratio ( $\times 10^{-15}$ ) and description of analyzed aliquot:  
E056-1 1709  $\pm$  53 Representative bulk material

Sampled feature: Broken rock in the fault near the Ttpul/Ttpmn contact

Sampling Objective: Role of faults

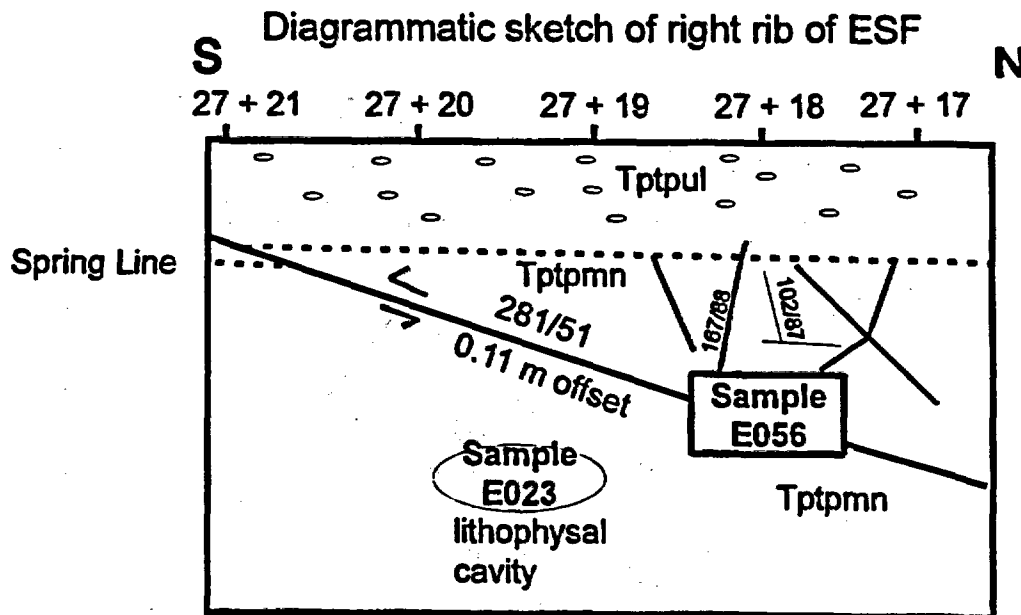
Lithology: Top of the Ttpmn approximately 1.5 m below the contact

**Structural setting of sampled feature:**

The sampled feature is an 8-10 cm wide rubble zone along a faulted joint. The full-periphery geologic map (FPGM) shows an orientation of 292/41 at the crown, 281/51 at the sample location. The fault is shown with 0.11 m offset on the right rib. Numerous small tight fractures shown on the FPGM are obscured with dust. Many joints in the Ttpmn terminate at the contact with the overlying Ttpul. This fault is very smooth and planar; no fault breccia is observed along this plane, although dust obscures viewing. This fault is probably a reactivated cooling joint, based upon the following: 1) similar orientation to a large moderately dipping cooling joint farther south in the tunnel; and 2) this faulted joint on the left rib has an obvious bleached rim along the fault surface. This faulted joint is the largest fracture for at least 20 m in either direction, with no apparent connections to other structures.

**Mineralogy and petrology of sampled feature:**

No detailed description available.



LANL ID: SMF barcode: Station location:  
E150 503939 33+00

Measured  $^{36}\text{Cl}/\text{Cl}$  ratio ( $\times 10^{-15}$ ) and description of analyzed aliquot:

E150-1 1341  $\pm$  56 Representative bulk material

Sampled feature: Intact rock

Sampling Objective: Systematic

Lithology: Tptpmn

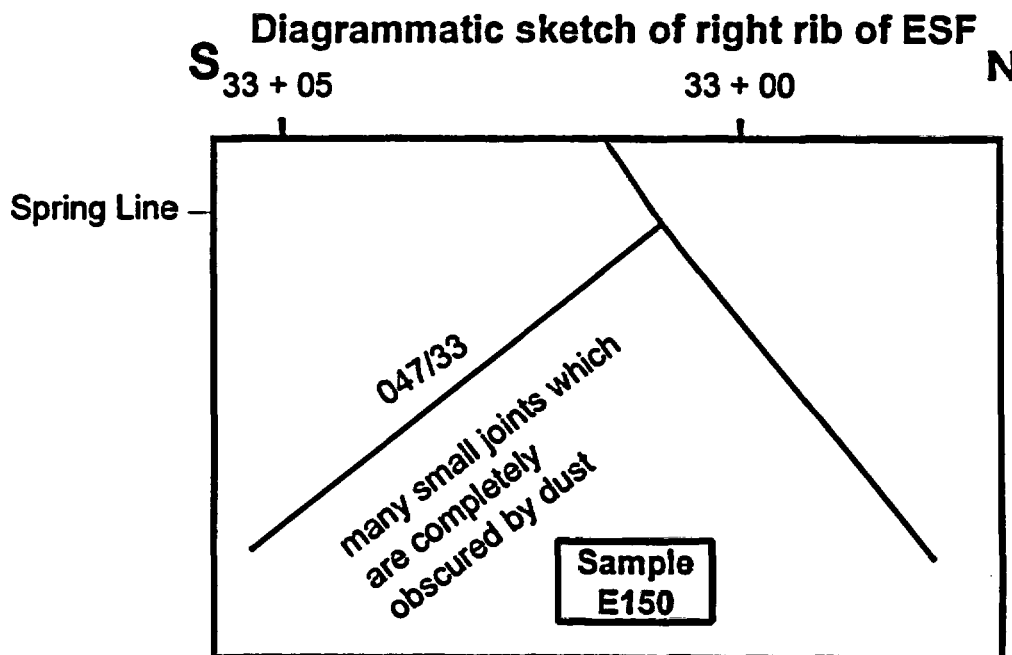
Structural setting of sampled feature:

A large number of small tight fractures, obscured by dust, are present here but are barely visible on the tunnel wall. Most have thin calcite filling. The fracture above the sample location is a relatively large joint (047/33) exposed at the invert at Station 33+05. It intersects a second joint at the springline at Station 33+01, although this is difficult to observe through the dust covering the wall. The nearest fracture to the sample location that is shown on the FPGM is a short fracture with orientation of 127/87. This fracture terminates at its lower end near the invert at Sta. 33+00. The DLS has a 9-m gap (from about Sta. 32+96 to about 33+05) in which no fracture data were collected. However, at least 19 fractures are shown on the FPGM in this interval.

This interval of tunnel is characterized by very large, gently dipping cooling joints. The nearest such joint to the sample site is oriented 215/23 and crosses the crown of the ESF at about Sta. 32+81. This joint dips toward the sample site and terminates above springline on the right rib at about Sta. 32+97. It is labelled on the FPGM as 215/23 but must be 035/23 because it is south-dipping (a similar joint at the crown at station 32+60 is 030/20).

Mineralogy and petrology of sampled feature:

This systematic sample of densely welded, devitrified Topopah Spring Tuff is gray-red with  $\leq 5$  mm pumices and several cm-long, highly flattened red-orange pumice fiammi. Spherulitic devitrification and rare vapor-phase cavities are localized in relict pumice clasts. There are a few planar, slightly rough fractures parallel to the alignment of flattened pumice clasts. Rare deposits of  $< 1$  mm patches of Mn minerals are present on the fracture surfaces. No short-wave UV-fluorescent phases were observed.



LANL ID: SMF barcode: Station location:  
E152 503993 34+28

Measured  $^{36}\text{Cl}/\text{Cl}$  ratio ( $\times 10^{-15}$ ) and description of analyzed aliquot:

E152-1 4105  $\pm$  310 Representative bulk material

Sampled feature: Fractured rock at intersection of several joints

Sampling Objective: Role of fractures in percolation

Lithology: Ttpmn

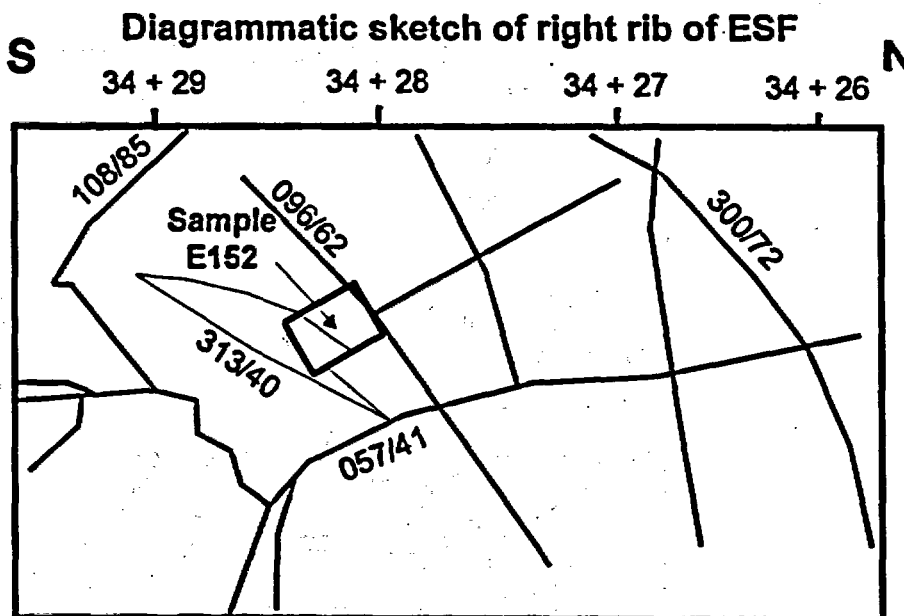
Structural setting of sampled feature:

The sample is taken about 2 m up the wall (approximately at the DLS) in a zone of complicated fracture intersections. The sample is from a mineralized vug about 8 cm wide between two fracture faces. The largest feature in the immediate vicinity of the sample site is a fracture (probable cooling joint) that extends across the tunnel. This feature is shown on the FPGM with orientations of 300/72 on the right rib and 282/57 on the left rib. This large joint is disrupted on the right rib near Sta. 34+29 by a small fault oriented 108/85. The DLS has a 10.5-m gap (from about Sta. 34+24.5 to about 34+35) in which no fracture data were collected.

Mineralogy and petrology of sampled feature:

The rock is densely welded, devitrified tuff, grayish red (5 R 4/2), with ~2% phenocrysts of mostly feldspar and lesser biotite and Fe-Ti oxides. The rock is broken into angular fragments bounded by a combination of cooling joints and tectonic fractures. The cooling joints have bleached margins and vapor-phase mineral coatings. The majority of fractures are slightly planar and rough to smooth; these may be cooling related. A few rough, irregular fractures are probably of tectonic origin.

The majority of fracture surfaces have calcite coatings ranging in thickness from 0.1 to 5 mm. Calcite morphology includes aggregates of flat prismatic crystals, individual freestanding crystals, and 0.5 to 3 mm-thick coatings of calcite in cm-scale domains of near syntaxial alignment, with flat rhombohedral terminations. Other minor coatings, directly on the rock surfaces, include <1 mm manganese mineral spots and mm-scale patches, <<1 mm thick, of waxy, soft, blue white clay/mordenite and white clay/mordenite. Coverage by these minerals is <1%. The calcite shows moderate purple white fluorescence in short-wave UV light. No other fluorescent phases were observed, except for weak red fluorescence by vapor-phase coatings.



LANL ID: SMF barcode: Station location:  
E153 503938 34+32

**Measured  $^{36}\text{Cl}/\text{Cl}$  ratio ( $\times 10^{-15}$ ) and description of analyzed aliquot:**

E153-3 3291  $\pm$  165 Representative bulk material

**Sampled feature:** Breccia/fractured zone at intersection of two cooling joints

**Sampling Objective:** Role of fractures in percolation

**Lithology:** Tptpmn

**Structural setting of sampled feature:**

The sampled feature is a large cooling joint, oriented 283/72 that extends across the tunnel. A north-striking fracture (orientation about 160/82; strike reported from 152 to 165 on FPGM) curves into (terminates against) the sampled feature. Some slickenlines are visible locally at the sampled feature. Most of the fractures in this vicinity are tight; little aperture or brecciation.

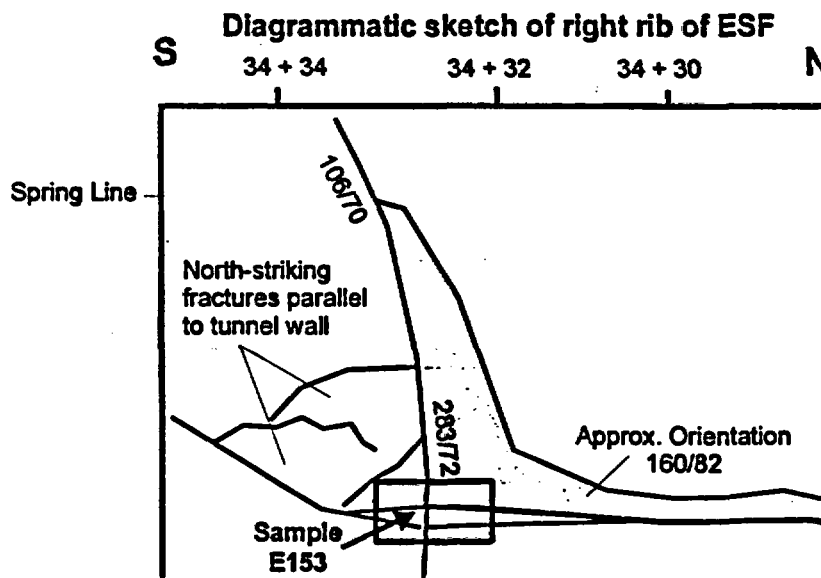
There are several large, gently dipping joints (orientations of about 300/35) mapped on the FPGM between about Sta. 34+20 and 34+40. These are intersected by a second set of large cooling joints that strike roughly east-west. The sampled joint crosses (with no offset) the 300/72 cooling joint shown on the FPGM near Sta. 34+28.

**Mineralogy and petrology of sampled feature:**

This breccia sample was collected from a cooling joint with variable brecciation and about 1 to 2 cm of offset. The joint is within densely welded, devitrified Topopah Spring Tuff. Minor calcite is present within the joint, but the examination subsample does not contain calcite.

The examination subsample consists of one 9-mm thick piece of breccia fracture filling. The thickness of the filling is very uniform, and the outer surfaces are planar and fairly smooth. The filling is moderately cohesive, with less than ~5% porosity. Constituents include ~80% angular and subangular, mostly equant fragments of mottled orange and pink-gray, densely welded, devitrified tuff. The fragments are 1 to 10 mm across, and many contain incipient cracks. About 10% of the breccia consists of white aggregates,  $\leq 1$  mm across, of  $< 1$  mm vapor-phase crystals. Gray detritus  $\ll 1$  mm, rich in vapor-phase crystals, slightly clayey, and molded around rock fragments comprises about 10%.

The outermost  $< 0.5$ -mm-thick portions of the deposit consist of a variably distinct gray layer of loosely cohesive  $< 0.1$  mm vapor-phase crystals. There are minor black or brown  $\leq 1$  mm patches of Mn minerals on rock fragment surfaces and on the outer surfaces of the breccia filling. In a few places, there are indications of a coating underlying the outer vapor-phase granular layer. No long- or short-wave UV-fluorescent phases were observed.



LANL ID: SMF barcode: Station location:  
 E154 503937 34+71

Measured  $^{36}\text{Cl}/\text{Cl}$  ratio ( $\times 10^{-15}$ ) and description of analyzed aliquot:

E154-1	803 ± 42	Breccia
E154-3	3767 ± 118	Wall rock

Sampled feature: Breccia along large cooling joint

Sampling Objective: Role of fractures in percolation

Lithology: Tptpmn

Structural setting of sampled feature:

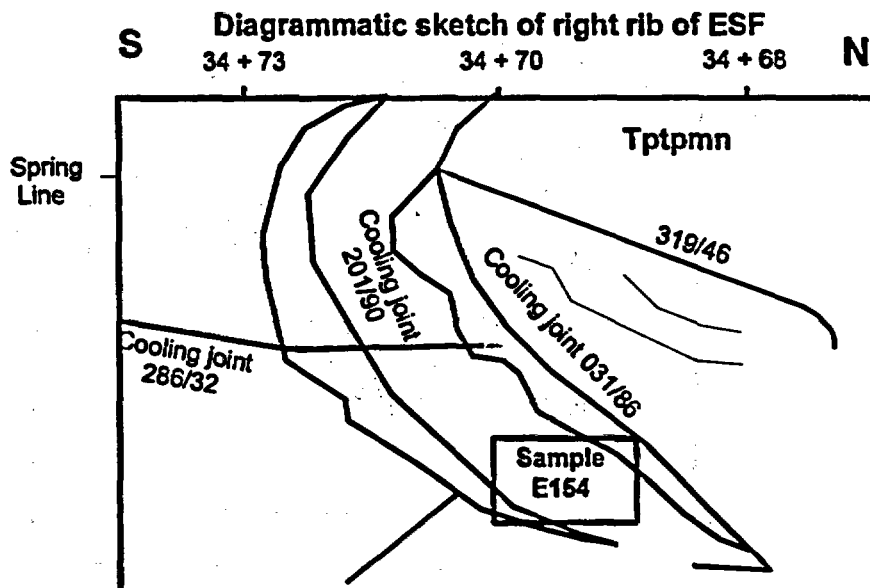
Sample was collected about 1 m above the invert from between two large northeast-striking cooling joints (orientations of 201/90 and 031/86). Wall rock is generally intact between the joints, minor 2 cm-wide breccia occurs along the 031/86 joint. Two additional northeast-striking joints (orientation of 188/89) occur around 34+80. These joints form a local set, all within 10 m of each other, as measured perpendicular to the joint surfaces. The northeast-striking cooling joints that bound the sample locality are large, extending to at least the crown of the ESF. The 031/86 joint is approximately 21 m-long as shown on the FPGM.

Mineralogy and petrology of sampled feature:

Breccia and adjacent wall rock of densely welded, devitrified Topopah Spring Tuff were collected from a high-angle ~NNE cooling joint with cm-scale offset. There is discontinuous brecciation along the joint trace. Minor calcite deposits are located on the joint surfaces. Subsamples of the slightly clayey breccia and the adjacent rock, including fracture surfaces, were collected.

A 1- to 5-cm-thick breccia filling from between cooling crack surfaces is moderately cohesive but friable. The angular to subangular fragments vary from ~1 cm to <0.1 mm. Many mm-scale fragments are easily crumbled. The rock fragments are mostly orange with lesser gray-brown mottling. Fragments larger than ~1 mm have <<1-mm-thick, discontinuous coatings of white clay. The outermost few mm of the breccia filling contain additional tan clayey-silty material, and the outer surfaces of the breccia filling are coated with white-tan clay, slightly less than 1 mm thick and without silt. In some places, this coating has cracked cleanly away from the adjacent breccia.

Common, but not abundant, <1 mm dendritic patches of brown submetallic Mn minerals are present on rock fragment surfaces. Some patches surround primary or syngenetic metallic oxide grains. In a few places, the Mn coatings adhere to the clayey matrix separated from a rock fragment. No short-wave UV-fluorescent phases were observed.



LANL ID: SMF barcode: Station location:  
E157 503994 35+03

Measured  $^{36}\text{Cl}/\text{Cl}$  ratio ( $\times 10^{-15}$ ) and description of analyzed aliquot:

E157-3 1339  $\pm$  83 Representative bulk material

Sampled feature: Faulted cooling joint

Sampling Objective: Role of fractures in percolation.

Lithology: Near top of Tptpmn

Structural setting of sampled feature:

Sample is taken above a large, undulatory cooling joint. The joint has an orientation of 314/33 where measured along the DLS, but flattens near sampling site before dipping steeply again near invert. The joint is mapped as having 0.25 m offset, but does not extend to crown of ESF. There is no obvious connection with steeply dipping cooling joint sets.

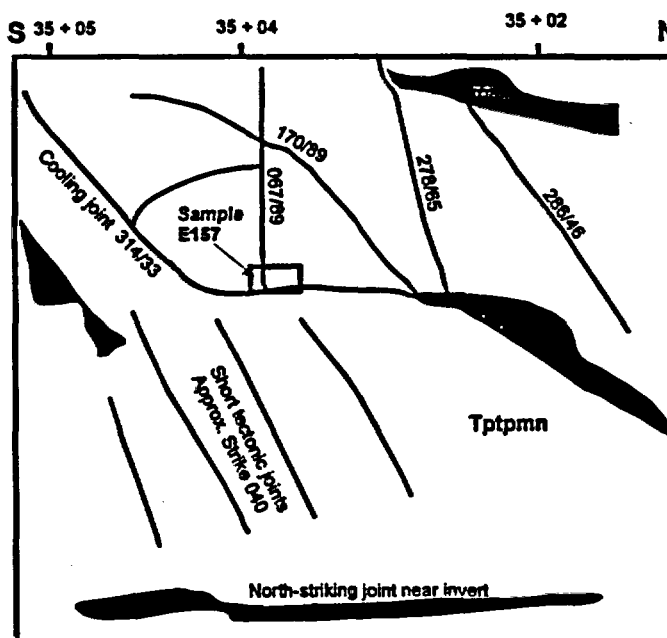
Sample is taken in hollow a hollow created by intersection of smaller tectonic joints with the 314/33 cooling joint. North striking tectonic fractures clearly terminate against the cooling joints here. Small northeast tectonic joints terminate against the north striking joints.

Mineralogy and petrology of sampled feature:

This sample is from a zone of broken rock and cooling joints in nonlithophysal densely welded, devitrified Topopah Spring Tuff. A cooling joint forms the lower boundary of the collection area. The open-textured breccia consists mostly of angular thin to equant fragments  $\leq 4$  cm across. There are some domains of finer grained, mostly  $\leq 2$  mm fragments, locally clayey. The breccia also includes  $< 2\%$  fragments of white very fine-grained vapor-phase material, mostly feldspar.

The breccia is cemented by calcite that fluoresces blue-white in short-wave UV light. The calcite is mostly in networks of thin flat, pearly crystals. Crystal sizes vary from  $< 1$  mm to  $\sim 5$  mm. The larger crystals appear compound, possibly twinned, and occur in segregated rosettes. They fluoresce more strongly than the smaller crystals. The smaller crystals occur in finer grained breccia and along what may be surfaces that faced fracture walls bounding the breccia. In a few areas, the smaller crystals have tapering, knobby, rounded surfaces suggestive of dissolution. There are also rare dendritic manganese deposits on tuff clast surfaces. No UV-fluorescent silica deposits were detected.

Diagrammatic sketch of right rib of ESF



LANL ID: SMF barcode: Station location:  
E158 503995 35+08

**Measured  $^{36}\text{Cl}/\text{Cl}$  ratio ( $\times 10^{-15}$ ) and description of analyzed aliquot:**

E158-1	1109 ± 58	Breccia (< ~ 0.5 cm)
E158-3	2605 ± 172	Breccia (> ~ 0.5 cm)

**Sampled feature:** Cooling joint.  
**Sampling Objective:** Role of fractures in percolation  
**Lithology:** Tptpmn

**Structural setting of sampled feature:**

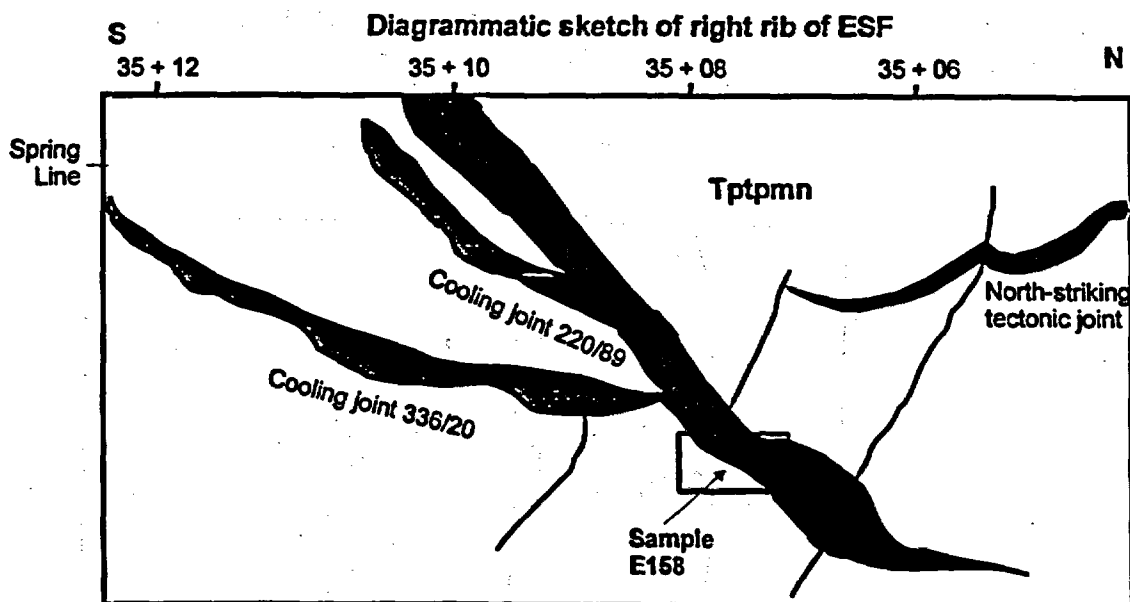
The sample site is a 6 cm-wide breccia zone bounded by steeply-dipping, subparallel cooling joints. The steeply dipping joints, oriented 220/89, are a series of 5 m-long, subparallel cooling joints (shown as shaded open faces on sketch) that coalesce near sample site. A gently dipping cooling joint, oriented 336/20, appears to truncate against these joints near the sample site. The 336/20 joint extends almost 5 m southward to where it is obscured behind the steel supports. Spacing of large cooling joints in this vicinity is approximately 2 m. Smaller tectonic fractures are also present near the sample site, including north-striking and northwest-striking joints.

**Mineralogy and petrology of sampled feature:**

The sample site is a breccia zone about 6 cm wide between two parallel cooling joints. Both joint surfaces adjacent to the breccia are polished and have minor coatings of waxy-texture calcite. The very loose crushed-tuff breccia and the adjacent fracture surfaces and bedrock were collected as subsamples.

The densely welded, devitrified Topopah Spring Tuff is mottled gray brown and lesser orange. The rock is broken into cm-scale or smaller fragments, with broken zones bounded in part by subparallel smooth planar fracture surfaces with no sign of vapor-phase minerals or bleached margins. Other fracture surfaces are rougher and more irregular. Disintegrated white phenocrysts, ~1 mm across, are prominent and comprise ~1%. Other phenocrysts are less altered.

Brown patches of Mn minerals,  $\leq 2$  mm across, are present on the rock fragment surfaces. The overall abundance is ~1%; local coverage is as much as 10%. Coatings of white (transparent where very thin), tan, and pink-gray-brown clay, <1 mm thick, are common and locally abundant, with overall coverage of about 10-15%. The coatings are most noticeable on smooth fracture surfaces, but are also present on some rougher surfaces. No short-wave UV-fluorescent minerals were observed.



LANL ID: SMF barcode: Station location:  
 E160 503979 35+45.4

**Measured  $^{36}\text{Cl}/\text{Cl}$  ratio ( $\times 10^{-15}$ ) and description of analyzed aliquot:**

E160-1 3329  $\pm$  166 Representative bulk material

**Sampled feature:** Cooling joints

**Sampling Objective:** Role of fractures in percolation

**Lithology:** Tptpmn

**Structural setting of sampled feature:**

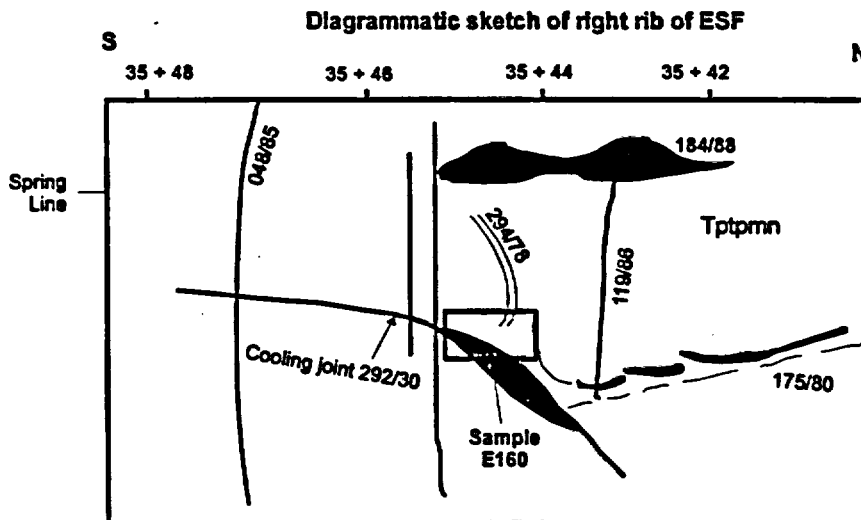
The sample site contains two nearly perpendicular sets of subvertical fractures, striking approximately north-south and east-west, with dm-scale spacing. Sample is of broken rock from a zone of subvertical cooling joints subparallel to tunnel wall. Near Sta. 35+42, these north-striking joints dip steeply to west (orientation of 175/80 where measured by the DLS), are very smooth and undulatory with an approximate wavelength of 10 cm. To the south (Sta. 35+44), the north-striking joints are a complicated series of en-echelon segments. The joints terminate against a large prominent curved joint at sample site. This joint is a gently northeast dipping cooling joint (orientation 292/30). This joint terminates at its south end south of a northeast-striking cooling joint oriented 218/84 near Sta. 35+47, and extends north to invert. In general, cooling joints are the predominant joint type in this vicinity. Most of them are long (up to 5 m). Fracture connectivity is through cooling joints terminating against each other.

**Mineralogy and petrology of sampled feature:**

This sample was collected from a zone of perpendicular sets of near-vertical cooling joints with bleached margins, backed by a very well developed ~N-S fracture subparallel to the tunnel wall. Fractures in the set perpendicular to the N-S fracture contain calcite, but the examination subsample contains no calcite.

The examination subsample is orange-brown, densely welded, devitrified Topopah Spring Tuff, including one smooth planar fracture with a ~1 mm bleached margin. On the fracture surface is a  $\leq 1$ -mm-thick compact deposit of <0.5 mm white vapor-phase crystals. Manganese minerals lie on top of the vapor-phase deposit.

Other rock surfaces are rough and irregular, with minor surface deposits including a variety of white to blue-white, waxy to powdery deposits of clay  $\pm$  mordenite, with ~1% overall coverage, but locally as much as 50% coverage. The deposits are <1 mm thick and may have slightly ropy textures. Similar but separate deposits of pale orange-pink color are also present. White to pale orange, slightly cohesive, <0.5 mm thick powdery deposits have an overall abundance of <1% on rock fragment surfaces but achieve 50% coverage. This material may be a mixture of translocated vapor-phase minerals and minor clay. There are also isolated <1 mm dendrites of Mn minerals, with overall coverage <1%. Some of the Mn dendrites overlie fine-grained particulate layers, confirming that the particulates are not construction dust. No short-wave UV-fluorescent phases were observed.



LANL ID: SMF barcode: Station location:  
 E161 503999 35+57.78

**Measured  $^{36}\text{Cl}/\text{Cl}$  ratio ( $\times 10^{-15}$ ) and description of analyzed aliquot:**

E161-1	1944 $\pm$ 102	Breccia (< ~ 0.5 cm)
E161-3	2141 $\pm$ 75	Breccia (> ~ 0.5 cm)

**Sampled feature:** Calcite-coated fracture along a small fault.

**Sampling Objective:** Role of fractures in percolation

**Lithology:** Tptpmn

**Structural setting of sampled feature:**

Sample is along a subhorizontal cooling joint where it is intersected by a small west/northwest striking fault (orientation 210/83) with 0.08 m offset, as shown by offset subhorizontal cooling joints. Fault plane itself has a minor amount of breccia near springline. Elsewhere the fault plane has calcite along it. Otherwise, it is a discrete plane with minimal wall separation. Two joint sets are common in this vicinity: one is a set with strikes ranging from 210 to 230; subhorizontal cooling joints form a systematic set of large joints. One joint extends south and is at crown level by about Sta. 35+63.

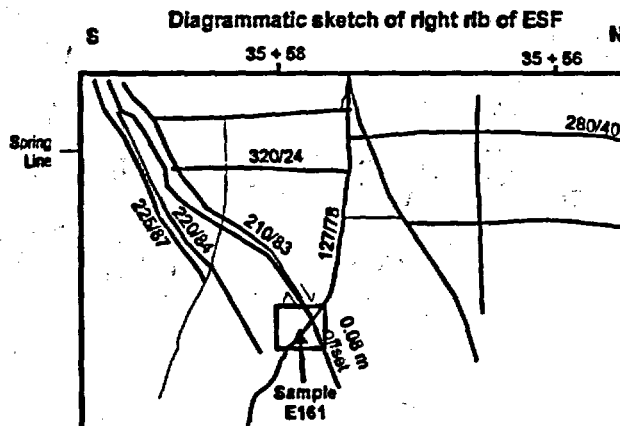
**Mineralogy and petrology of sampled feature:**

The sample site is a low-angle cooling joint intersected by two sets of high-angle fractures. The sampled fracture and the intersecting fractures form a boundary between a ~15-m interval of highly broken rock to the north and unbrecciated rock extending tens of meters to the south. Brecciated rock immediately below the low-angle joint is cemented by calcite.

The cm-scale fragments of densely welded, devitrified Topopah Spring Tuff are mostly flat and elongate. About half the fragment surfaces are smooth and planar, half to two-thirds of the surfaces have vapor phase coatings, and a few have bleached margins. All of these characteristics are indicative of syngenetic fracturing. The vapor phase coatings, up to ~1 mm thick, are composed of silica, feldspar, and Fe-Ti oxides. Some coatings are made up of crystals  $\leq 1$  mm, while other coatings are powdery looking and made up of ~0.1 mm crystals. The finer grained coatings are more loosely adhering to the rock surfaces but are somewhat cohesive.

Calcite, weakly fluorescent in short-wave UV light, occurs as coatings, ~0.5 mm to 1 cm thick, on rock fragment surfaces and cements smaller clasts. Most calcite crystals are flat, prismatic, and slightly pearly, in thin coatings consisting of several mm-scale monocrystalline domains, usually on bare rock surfaces. Dog-tooth calcite crystals <1 mm across occur in lithophysal joints. Calcite overlies vapor-phase coatings and bare rock.

Blue-gray translucent clay forms localized coatings, <1 mm thick on rock surfaces and calcite, with <2% to about 5% coverage. White to pale yellow-white, chalky clayey material locally encrusts calcite crystals. Some rock surfaces and calcite aggregates are partially coated with <1-mm-thick, loosely adhering sand-size material and white to reddish-brown clay. Widespread, but not ubiquitous or abundant,  $\leq 1$ -mm spots and diffuse stains of black to yellow-brown manganese minerals are present on rock surfaces, on powdery vapor-phase deposits, and rarely on calcite. No fluorescent silica was observed.



LANL ID: E171      SMF barcode: 512554      Station location: 8+90

**Measured  $^{36}\text{Cl}/\text{Cl}$  ratio ( $\times 10^{-15}$ ) and description of analyzed aliquot:**

E171-1       $1335 \pm 56$       Representative bulk material

**Sampled feature:**      Top of the Tpp

**Sampling Objective:**      Unit contact

**Lithology:**      Tpp/Tpbt3 contact

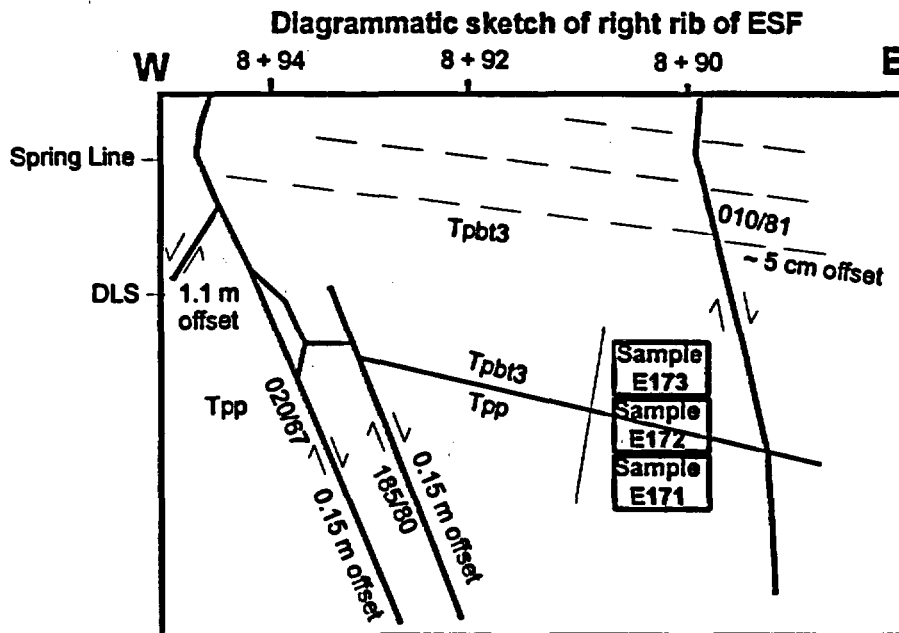
**Structural setting of sampled feature:**

Samples are from unfractured rock at the Tpp/Tpbt3 contact. There is no structural feature at the sample locality; these are representative bulk material from the vicinity of the unit contact. The samples collected at Sta. 8+90 are approximately 5 m east of a complicated series of faults which have offsets ranging from 0.15 m to 1.45 m. One fault has between 0.4 and 0.8 m of west-side down offset and occurs at the ESF crown at Sta. 8+90 and at Sta. 8+93 on the left springline. A second nearby fault occurs at 8+94 on the left springline and has 0.15 m east-side down offset (shown on left part of sketch). These two faults are part of a faulted interval that extends from Sta. 8+90 to Sta. 9+40. In this 50-m interval, there is at least 5.5 m of aggregate west-side down offset; total offset would be even higher except for the effect of antithetic offsets on east-side down faults in this interval.

**Mineralogy and petrology of sampled feature:**

The sample is a moderately cohesive, vitric nonwelded tuff. About 70% of the rock is matrix of fine-grained (<0.5 mm) pale orange pink (5 YR 8/2) ash. 5% of the rock consists of pumice clasts, mostly silky textured and with length:width ratios  $\leq 3:1$ . Minor colorless bubbly pumices  $\leq 3$  mm across are also present. Most pumice clasts are pinkish gray (5 YR 8/1), and some have faint <1mm haloes of moderate orange pink (5 YR 8/4) within the adjacent matrix. The pumices are 2 to 20 mm long. Phenocrysts, mostly  $\leq 1$  mm feldspar crystals plus lesser amounts of  $\leq 1$  mm biotite crystals that are minimally altered, comprise ~20%. The rock contains ~2% lithic grains, including 0.5 to 4 mm clasts of fine-grained, mostly red brown crystalline igneous rocks, as well as colorless, gray, black, and red glass chunks.

Visible matrix alteration, apart from the pumice haloes described above, consists of <1% irregular  $\leq 3$  mm reddish orange (10 R 6/6) haloes, some with biotite nuclei, staining the matrix. Smectite content of ~7% was detected by X-ray diffraction. No fractures were observed. No short-wave UV-fluorescent phases were present.



LANL ID: SMF barcode: Station location:  
E175 512511 35+93

**Measured  $^{36}\text{Cl}/\text{Cl}$  ratio ( $\times 10^{-15}$ ) and description of analyzed aliquot:**

E175-1	2840 ± 231	Breccia (> ~ 0.5 cm)
E175-3	1674 ± 141	Breccia (< ~ 0.5 cm)

**Sampled feature:** Fault rock and gouge from the Sundance fault

**Sampling Objective:** Role of faults

**Lithology:** Tptpmn

**Structural setting of sampled feature:**

This fault is the probable subsurface equivalent of the southern end of the Sundance fault zone. The fault has an orientation of 155/84 and an indeterminate amount of offset. The fault plane occurs as a polished slickensided fault surface, both on the right rib at 35+93 and on the left rib at 36+25. The fault on left rib at 36+25 also has horizontal mullions with amplitudes of about 10 cm and appears to have had little dip-slip motion. Although visible on both right rib and the left rib, the fault is very difficult to pick out at the crown. There is a second faulted surface to the south of the main trace (at 35+96) that intersects the main trace of the Sundance fault near invert. The fault at 35+96 also appears to be truncated by the Sundance fault at the crown; it cannot be traced across the Sundance fault at the crown. This smaller fault may have originally been a joint that has accommodated some slip as it was offset by the Sundance fault. The probable offset part of this joint on the east side of the Sundance fault occurs at Sta. 35+90 on the left rib as a prominent joint oriented 211/87. If this is an offset joint, the two segments would imply a 4 m strike separation on Sundance fault. There is a weak, gently west dipping fracture fabric, between the 2 faults. Otherwise, there are few systematic fractures in the immediate vicinity of the Sundance fault.

**Mineralogy and petrology of sampled feature:**

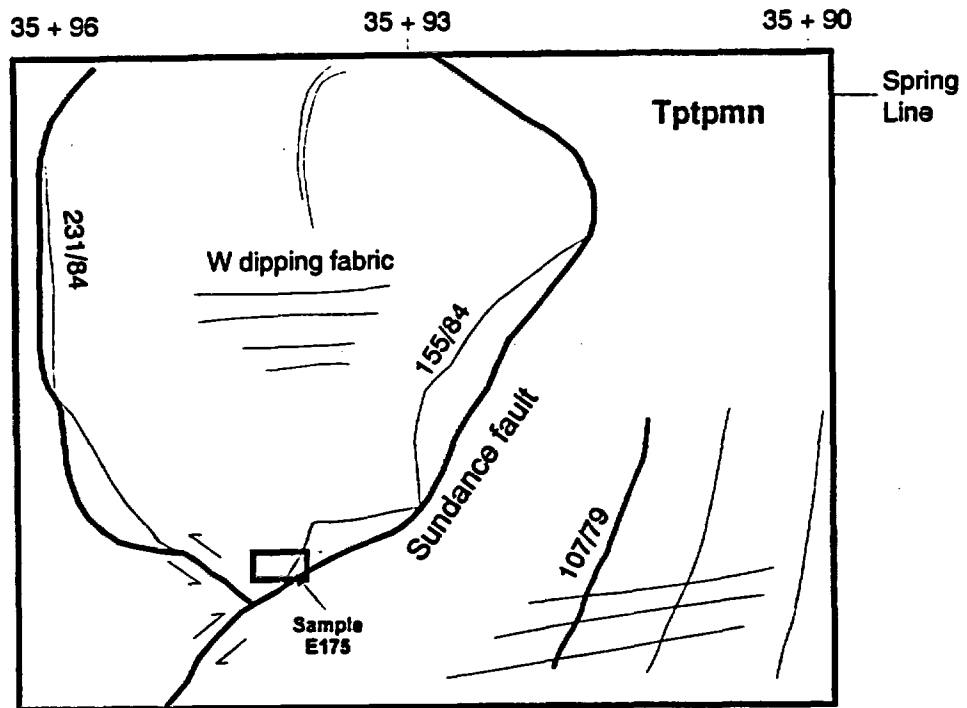
This sample was collected along a trace of the Sundance fault. The fault at this location consists of two intersecting traces. Both traces include cm-scale zones of fine- to medium-grained, slightly clayey breccia marked by horizontal slickensides. The densely welded, devitrified Topopah Spring bedrock has an overall fabric of short-trace (cm- to dm-scale), subhorizontal fractures with moderately rare calcite deposits.

E175-2: The breccia clasts are composed of red-brown, densely welded, devitrified Topopah Spring Tuff. The clasts, varying from ~7 cm to <0.1 mm, are angular and equant to elongate. Round patches, ≤0.5 cm across, of vapor-phase minerals are present on clast surfaces. The finest material, <0.1 mm, is commonly more whitish than the larger fragments, reflecting a high content of vapor-phase-derived material. The fine material also contains euhedral vapor-phase mafic and oxide crystals.

There is very little clay in the finest material, as shown by an absence of plasticity or cohesion when wetted. On a few newly separated fracture surfaces of breccia clasts, there are orange-brown clay skins <<1 mm thick or lobes of whitish particulates projecting inward from the fragment boundaries. Coatings of blue-white clay±mordenite, <0.1 mm thick, are also present though rare on the newly broken-apart fracture surfaces.

The breccia has less than ~5% porosity. There are 6- to 7-cm domains of much more cohesive breccia, disaggregated with a hammer, showing evidence of tuff fragment cementation by vapor-phase minerals. No long- or short-wave UV-fluorescent phases were observed.

Diagrammatic sketch of right rib of ESF



**LANL ID:** SMF barcode: Station location:  
E194 512586 10+56

**Measured  $^{36}\text{Cl}/\text{Cl}$  ratio ( $\times 10^{-15}$ ) and description of analyzed aliquot:**

E194-2 1354  $\pm$  45 Representative bulk material

**Sampled feature:** Subunit contact

**Sampling Objective:** Unit contact, role of the PTn

**Lithology:** ~2 m above Tptrv2/Tptrv1 contact

**LANL ID:** SMF barcode: Station location:  
E195 512587 10+56

**Measured  $^{36}\text{Cl}/\text{Cl}$  ratio ( $\times 10^{-15}$ ) and description of analyzed aliquot:**

E195-2 1292  $\pm$  37 Representative bulk material

**Sampled feature:** Subunit contact

**Sampling Objective:** Unit contact, role of the PTn

**Lithology:** ~1 m above Tptrv2/Tptrv1 contact

**LANL ID:** SMF barcode: Station location:  
E197 512585 10+62

**Measured  $^{36}\text{Cl}/\text{Cl}$  ratio ( $\times 10^{-15}$ ) and description of analyzed aliquot:**

E197-2 1452  $\pm$  72 Representative bulk material

**Sampled feature:** Subunit contact

**Sampling Objective:** Unit contact, role of the PTn

**Lithology:** ~1 m below Tptrv2/Tptrv1 contact

LANL ID: E201      SMF barcode: 512591      Station location: 43+63

**Measured  $^{36}\text{Cl}/\text{Cl}$  ratio ( $\times 10^{-15}$ ) and description of analyzed aliquot:**

E201-2      1974  $\pm$  65      Representative bulk material

**Sampled feature:**      Cooling joints, just north of the Intensely Fractured Zone (IFZ)

**Sampling Objective:**      Role of fractures in percolation

**Lithology:**      Tptpmn

**Structural setting of sampled feature:**

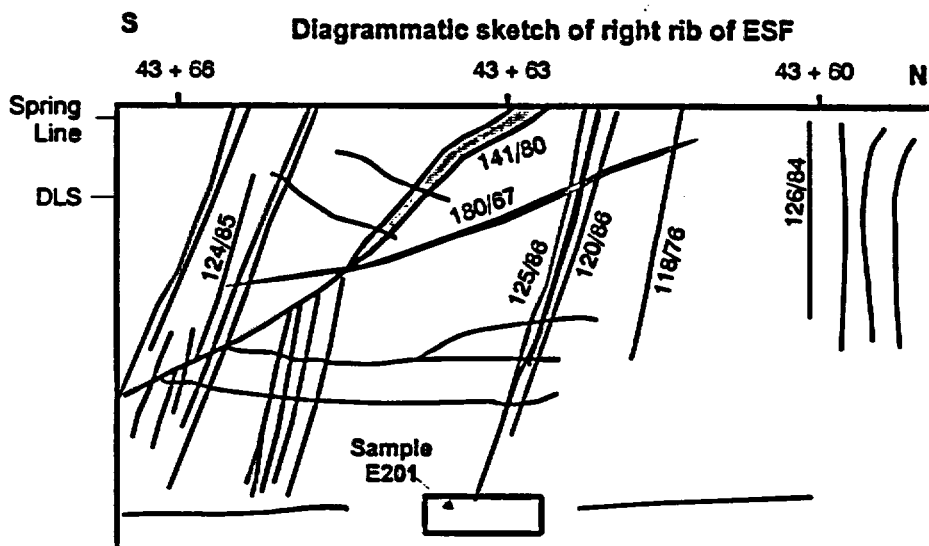
The sampled area is located in a zone of fractures with spacing and orientation similar to the IFZ; a zone with similar spacing is present near 43+66. These fractures are long, with strikes of 120-125 and are very tight, some with vapor phase alteration rinds. The 120-125 set is the most common systematic set in this vicinity. Also present is a poorly-expressed north-striking set. Joints of this set are 2-3 m long and irregular, and commonly terminate against the 120-125 set. Transecting the exposure above and left of the sample site is a large fracture with an orientation of 141/80. Offset on this fracture is indeterminate: some members of the 120-125 set terminate at this feature, although a number of the joints cross it without offset. It appears to terminate near the crown on the right rib, and two mineral-filled joints may cross it there.

**Mineralogy and petrology of sampled feature:**

The densely welded, devitrified tuff is grayish orange pink (5 YR 6.5/2) and contains ~2% phenocrysts of  $\leq 1$  mm feldspar, biotite, and Fe-Ti oxides. Light pinkish gray (5 YR 8/0.5) pumice clasts,  $\leq 2$  cm long, with dense spherulitic devitrification into  $\leq 1$  mm crystals, comprise 5 to 10 %.

The sample contains parallel smooth, planar to slightly planar fractures with ~4-cm spacing. Although bleached margins are faint or absent, these fractures are probably cooling joints. There are two or more directions of fracturing at high angles to the cooling joints. The surfaces of these fractures are slightly planar to slightly irregular and smooth to rough. On some fracture surfaces, particularly the smoother ones, there are cm-scale crushed zones  $< 1$  mm thick, many of them developed upon pumice clasts. Coverage of crushed zones on the fracture surfaces is  $\leq 15\%$ . Some bare fracture surfaces are locally polished, with a discontinuous clear glassy surface. Maximum local coverage by such features is ~20%.

There is highly variable coverage, from  $< 1\%$  to ~20%, of fracture surfaces by  $< 1$  mm spots and slightly dendritic patches,  $\ll 1$  mm thick, of dark brown Mn minerals. The more abundant deposits occur on smooth fracture surfaces and some deposits are concentrated adjacent to crush zones. No short-wave UV-fluorescent phases were observed.



LANL ID:	SMF barcode:	Station location:
E202	512592	44+20
E203	512593	44+21
E204	512594	44+22

**Measured  $^{36}\text{Cl}/\text{Cl}$  ratio ( $\times 10^{-15}$ ) and description of analyzed aliquot:**

E202-2	3463 $\pm$ 97	Representative bulk material
E203-2	849 $\pm$ 34	Representative bulk material
E204-2	772 $\pm$ 31	Representative bulk material

**Sampled feature:** Multiple joints at each location. Sample E204 has a thin breccia layer along joint striking northeast

**Sampling Objective:** Role of fractures in percolation: broken ground associated with cooling joints in the Intensely Fractured Zone (IFZ)

**Lithology:** Tptpmn

**Structural setting of sampled feature:**

The right rib is almost completely lagged over in this interval. The predominant joint set at all three locations is the IFZ set oriented at 115-125/85. The spacing on this set is 5 to 10 cm at all three sample sites. There are rare 180/90 and subhorizontal fractures.

There is a fault about 10 m north of the sample sites at ~44+11. The mapped fault is oriented 153/78. In the same area, two of the IFZ joints (orientations of 122/88 and 125/83) have horizontal slickenlines developed on a colorless mineral coating.

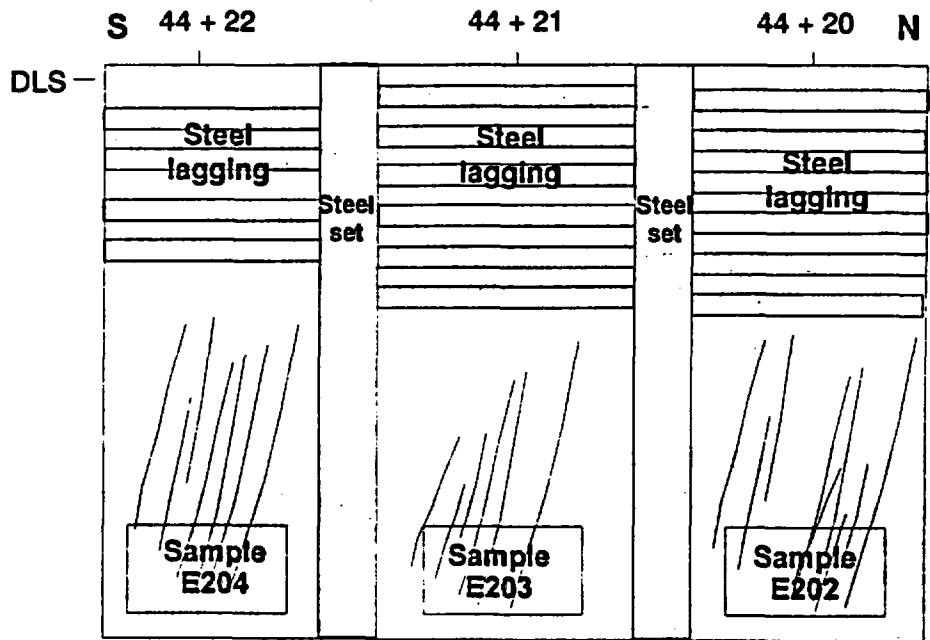
**Mineralogy and petrology of sampled feature:**

The sampled rock is densely welded, devitrified Tptpmn tuff containing ~3% phenocrysts,  $\leq 2$  mm across, predominantly of feldspar with lesser biotite. The rock also contains 3 to 5% elongate pumice clasts  $\leq 2$  mm across, with indistinct boundaries and 2 to 3% fine-grained lithic clasts  $\leq 1$  cm across. The overall rock color is pale red (10 R 6/2).

Rock surfaces include one smooth planar fracture face with a faint bleached margin, indicative of a cooling joint. Surface coatings on the cooling joint include  $\leq 1$  mm-thick white dense aggregates of  $\leq 0.1$  mm crystals of silica and feldspar. The exposed surfaces of these deposits are harder and denser than the interior, locally. Some of the less dense material has a brownish stain. Much of the coating has cracked off naturally, leaving a residual coverage of ~50%. The variously denuded coating and rock surface have overall ~20% coverage by  $< 0.5$  mm black-brown Mn spots.

A fracture surface subparallel to the one described above has no bleached margin, and a  $< 0.5$  mm-thick coating of  $< 0.1$  mm crystalline silica and feldspar. There is overall coverage of ~20% by  $\leq 1$  mm black-brown Mn spots. This fracture is planar and slightly rough. Other fracture surfaces are smooth and slightly planar, with 10-15% overall coverage by  $< 1$  mm black Mn spots, locally in cm-scale elongate aggregates. A few cm-scale patches of  $< 1$  mm thick, slightly cohesive aggregates of  $< 0.1$  mm whitish crystals, probably vapor-phase material, are stained brown by Mn coatings. The patches may be slightly pulverized relict pumice clasts. Rough, irregular fracture surfaces have  $\ll 1\%$  coverage by  $< 1$  mm Mn patches and white powdery to slightly waxy,  $< 1$  mm thick,  $< 1$  cm across patches of probable clay/mordenite. No long- or short-wave UV-fluorescent phases were observed.

Diagrammatic sketch of right rib of ESF



LANL ID: E205      SMF barcode: 512595      Station location: 45+00

**Measured  $^{36}\text{Cl}/\text{Cl}$  ratio ( $\times 10^{-15}$ ) and description of analyzed aliquot:**

E205-2      1514  $\pm$  69      Representative bulk material

**Sampled feature:**      Fractures in Tptpmn, almost exclusively 120-130 orientation

**Sampling Objective:**      Systematic sample in Intensely Fractured Zone (IFZ).

**Lithology:**      Tptpmn

**Structural setting of sampled feature:**

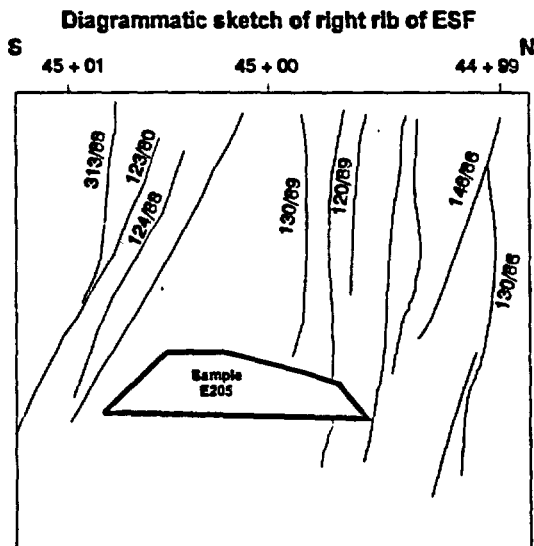
For systematic sampling, this is highly fractured; characterized by northwest-striking near vertical cooling joints that are smooth, and planar to gently curved. These joints, with typical orientations of 125-135/80-90, form virtually the only set present. These fractures are large, typically continuous for 5 m or more. Low-angle intersections are common. Most fractures are tight, with apertures only up to 1-2 mm. The typical joint spacing may be 10 cm and varies from 5-40 cm. About 20% of the cooling joints have bleached borders. At around Sta. 45+4, there is a ~3 m-wide domain of less fractured rock.

**Mineralogy and petrology of sampled feature:**

The rock is densely welded, devitrified Tptpmn tuff, grayish orange pink (5 YR 7/2). The tuff contains 1 to 3 % phenocrysts,  $\leq 2$  mm across, of feldspar, biotite, and rare mafic minerals, and ~10% pumice clasts  $\leq 2$  cm long, with spherulitic devitrification and dense vapor-phase crystallization. The remainder of the rock is a matrix of shards and ash.

Smooth, planar cooling joints are spaced parallel, 4 to 5 cm apart. about half the surfaces have faint bleached margins and  $< 1$  mm-thick dense coatings of crystalline silica  $\pm$  feldspar. Overlying the silica, with  $\leq 10$  % overall coverage, are  $\leq 1$  mm black Mn spots. Other cooling joint surfaces lack the bleached margins and crystalline silica coatings, but have overall coverage of  $\leq 15\%$  by  $\leq 3$  mm slightly dendritic black Mn spots.

On all cooling joint surfaces, there are cm-scale crush zones,  $< 1$  mm thick, where either the rock or the fracture coating is reduced to flat-surfaces powdery deposits of  $\leq 0.1$  mm grains and the Mn coatings are smeared out. Two to three orientations of rough, irregular fractures exist perpendicular to the smooth cooling joints. Dendritic black Mn spots,  $\leq 4$  mm across, are present with overall coverage ranging from  $< < 1\%$  to ~3%. Crush zones also occur on some of these surfaces. No long- or short-wave UV-fluorescent phases were observed.



## APPENDIX C-2

### CHARACTERIZATION OF SAMPLE SITES WITH LOW $^{36}\text{Cl}/\text{Cl}$ RATIOS

This section of Appendix C contains structural and petrologic descriptions of samples with  $^{36}\text{Cl}/\text{Cl}$  ratios less than  $350 \times 10^{-15}$ , well below the range over which the ratio has varied in the atmosphere over the past 40 ka or more (section 3.1.2).

**LANL ID:** E198      **SMF barcode:** 510700      **Station location:** 41+65

**Measured  $^{36}\text{Cl}/\text{Cl}$  ratio ( $\times 10^{-15}$ ) and description of analyzed aliquot:**

E198-2      291  $\pm$  12      Representative bulk material

**Sampled feature:** Cooling joint

**Sampling Objective:** Role of fractures in percolation

**Lithology:** Ttpmn

**Structural setting of sampled feature:**

Sample is from a cooling joint with an orientation of 135/87. The largest feature in the vicinity is a fault, oriented 304/89, with 0.25 m of offset. The fault is at Sta. 41+64 at the left springline and Sta. 41+76 at the right springline. On the right rib from the fault plane northward to around Sta. 41+60 is a fracture zone with many near vertical cooling joints. These joints have typical orientations of 155-130/85, similar to the sampled feature. Some of these joints have bleached margins, Mn coatings are prominent and horizontal slickensides are visible locally.

**Mineralogy and petrology of sampled feature:**

Detailed description not available.

**LANL ID:** E225      **SMF barcode:** 510731      **Station location:** 48+56

**Measured  $^{36}\text{Cl}/\text{Cl}$  ratio ( $\times 10^{-15}$ ) and description of analyzed aliquot:**

E225-1      350  $\pm$  14      Representative bulk material

**Sampled feature:** Cooling joints

**Sampling Objective:** Role of fractures in percolation

**Lithology:** Ttpmn

**Structural setting of sampled feature:**

Sample is of brecciated rock from a zone around 0.5 m wide, generally bounded by northwest-striking cooling joints, many of which have bleached margins. Two small faults (orientation 240/86, amount of offset unknown) occur between Sta. 48+57 and 48+58. A similarly oriented fracture (orientation 240/86) is present in the vicinity of the sample location.

**Mineralogy and petrology of sampled feature:**

Detailed description not available.

LANL ID: E234      SMF barcode: 510743      Station location: 52+43

Measured  $^{36}\text{Cl}/\text{Cl}$  ratio ( $\times 10^{-15}$ ) and description of analyzed aliquot:

E234-1       $293 \pm 25$       Representative bulk material

Sampled feature: Cooling joint

Sampling Objective: Role of fractures in percolation

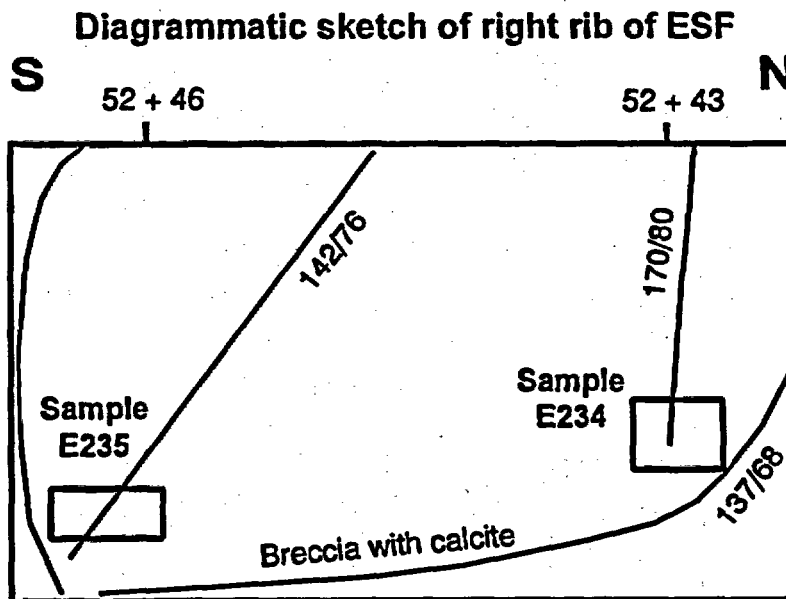
Lithology: Tptpmn

Structural setting of sampled feature:

Sample is from a large, smooth, curvilinear fracture (interpreted as a cooling joint) that extends across the ESF to the left rib. The sample fracture, oriented 170/80, is subparallel to a cooling joint with an orientation of 137/68; the cooling joint has bleached margins and calcite cementation.

Mineralogy and petrology of sampled feature:

The sampled fracture has cm-scale patches of purple fluorite, locally coated by calcite. The fracture has local cm-scale apertures, loosely filled by breccia. Fluorite also observed on intersecting cooling joints that have bleached margins and smooth planar surfaces. Fluorite infillings are noted frequently on the FPGM between Sta. 52+00 and 53+00.



LANL ID: E255                      SMF barcode: 515146                      Station location: 58+77

**Measured  $^{36}\text{Cl}/\text{Cl}$  ratio ( $\times 10^{-15}$ ) and description of analyzed aliquot:**

E255-1    140  $\pm$  9                      Representative bulk material

**Sampled feature:**                      Unfractured Tptpll

**Sampling Objective:**                      Role of fractures (and lack of fractures) in percolation: Sample Tptpll underneath a location where several fractures in Tptpmn terminate abruptly at contact.

**Lithology:**                                      Tptpll ~4 m below contact with Tptpmn.

**Structural setting of sampled feature:**

Sample collected in unfractured lithophysal rock. There is one very rough fracture in Tptpll at ~58+78 (041/86) that projects behind the sampled area. Lithophysae up to 15 cm. Mineral coatings appear to line all of cavity (top and bottom). Also, abundant "stringers" of vapor phase alteration are present along minor, foliation-parallel fractures (less than 20 cm long). There is a consistent set of anastomosing vapor phase partings that mark the Tptpll/Tptpmn contact.

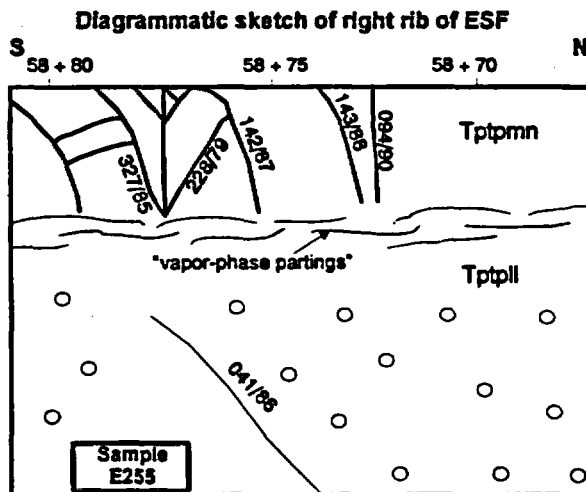
Several large fractures with strikes of 140 to 150 are present in the Tptpmn some 4 m above the sampling locality. All terminate abruptly at contact; there is no apparent connection to the underlying unfractured Tptpll.

**Mineralogy and petrology of sampled feature:**

The densely welded, devitrified tuff is mottled orange brown to red brown. Rock fragments are angular and highly irregular, with at least six orientations of short-segment (2 to 3 cm) fractures responsible for the shapes of the fragments. Less than 5% of fracture surfaces are vapor-phase partings, with ~0.5 cm-thick beige rinds of powdery light minerals and Fe-Ti oxides, overlain by ~1 mm-thick coatings of  $\leq 1$  mm tridymite crystals and other crystalline silica. Locally common are <0.5 mm-wide irregular fractures, at high angles to vapor-phase partings, filled with crystalline silica. The irregular fractures have a variable cm-scale spacing.

A majority of the surfaces of newly broken-apart fractures have variable coverage by powdery ( $\ll 0.1$  mm grain size) but hard white pink to pale blue white material, probably vapor-phase or other syngenetic minerals, some in dense to lacy aggregates, loose to moderately cohesive. Some aggregates also include Fe-Ti oxides, and some include patches or scattered crystals of <0.5 mm silica. There are rare Mn deposits on the powdery material. The Mn spots, with an overall abundance on rock surfaces of  $\ll 1\%$ , are locally  $\leq 10\%$ . The deposits are round, brown black, <0.5 mm across, and locally in linear arrays, some coalescing.

Many of the sub-centimeter rock fragments are at least 50% bounded by slightly vuggy areas (vugs <1mm) with crystalline silica or powdery white material with Fe-Ti oxides. No short-wave UV-fluorescent phases were observed other than feldspar phenocrysts that fluoresce weakly red.



LANL ID: E256      SMF barcode: 515147      Station location: 59+00

Measured  $^{36}\text{Cl}/\text{Cl}$  ratio ( $\times 10^{-15}$ ) and description of analyzed aliquot:

E256-1	347 ± 41	Breccia
E256-3	361 ± 22	Wall rock

Sampled feature: Systematic

Sampling Objective: Role of fractures in percolation

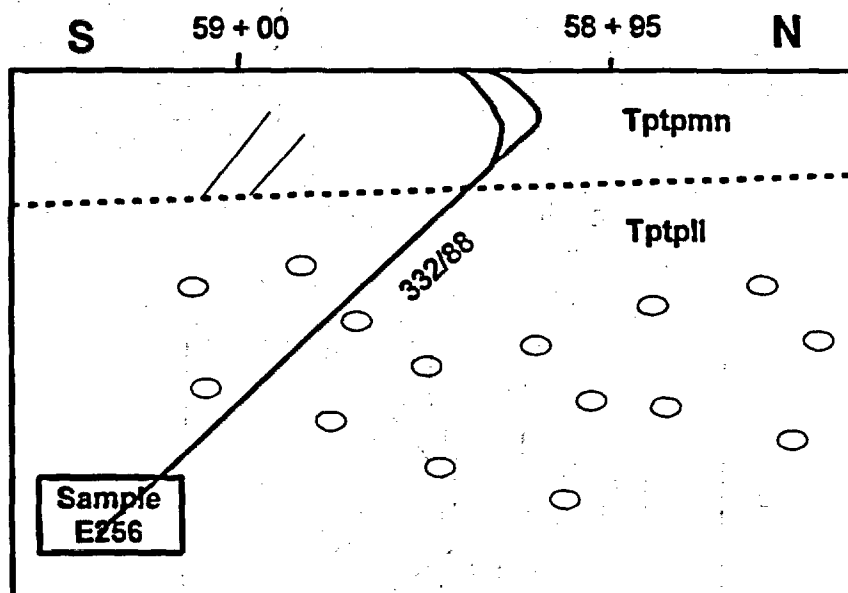
Lithology: Tptpll

Structural setting of sampled feature:

The sample site includes a single large fracture (oriented 332/88) that does not offset Tpmn/Tptpll contact but extends downward to invert. This feature connects the fracture network of the Tptpmn with the underlying Tptpll. Tpmn/Tptpll contact is ~10 m below springline. This fracture is part of the well-expressed set with strikes around 150 (or 330, for east-dipping fractures) that dominates Tptpmn from at least 59+50 to 58+50. The average fracture spacing is ~1 fracture per meter, and extends from Tptpmn/Tptpll contact to the crown. The fracture network in Tptpmn almost universally terminates at the Tptpmn/Tptpll contact. Here at 59+00 is one of the few places where a feature penetrates down into Tptpll.

Mineralogy and petrology of sampled feature:

Diagrammatic sketch of right rib of ESF



LANL ID: E258      SMF barcode: 515149      Station location: 61+92

Measured  $^{36}\text{Cl}/\text{Cl}$  ratio ( $\times 10^{-15}$ ) and description of analyzed aliquot:

E258-1      276  $\pm$  21      Representative bulk material

Sampled feature: Intersection zone of 3 fracture sets

Sampling Objective: Role of fractures in percolation

Lithology: Tptpmn

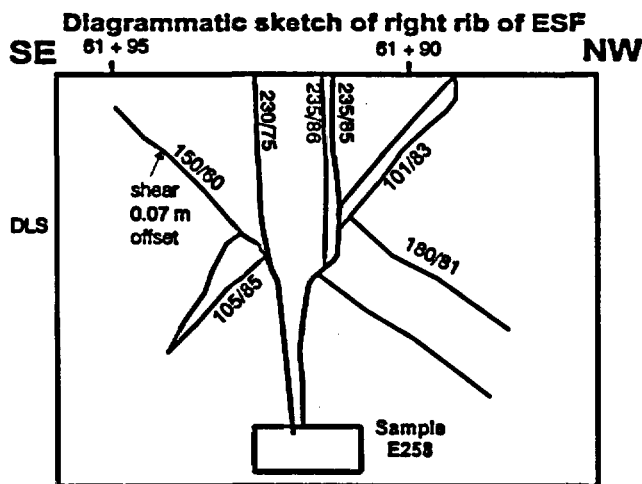
Structural setting of sampled feature:

Sample is taken below an area of intersection between three fracture sets; the intersection forms an open, rubbelized zone. The 1 m wide open zone at the level of the Detailed Line Survey narrows to ~4 cm near the invert. At invert, where sample was collected, the rock is almost unfractured. The three systematic fracture sets in this vicinity are: 1) a set with strikes of around 230; 2) a set with strikes around 100; and 3) a set with strikes between 130 and 150. The 230 set is very prominent between 61+92 and 61+00. Members of this set are steeply dipping and appear to terminate against 130-150 set. At the crown, the fracture network in Tptpmn forms a network of steep joints created by the 100 set and 150 set, which breaks rocks up into 2 m blocks. The sampled feature is along the line of intersection of these two sets. Near invert on left rib, getting close to base of Tptpmn, fracture spacing decreases and becomes almost columnar looking.

Mineralogy and petrology of sampled feature:

The rock is nonlithophysal, moderately to densely welded devitrified tuff. Overall color is grayish orange pink, with pale grayish red purple spots. The 2 to 3% phenocryst content consists of feldspar, biotite and other mafic minerals, and Fe-Ti oxides. Rare rounded, glassy quartz xenocrysts are also present. There is no evidence of crushed phenocrysts within the rock matrix. Pumice lapilli  $\leq 1$  cm long, comprising 10 to 15% of the rock, are somewhat indistinct, with spherulitic devitrification. The rock also contains ~2%  $\leq 7$  mm lithic inclusions, including very fine-grained gray inclusions and red brown inclusions with phenocrysts.

The fracture surfaces bounding the three largest rock fragments are variable from rough and irregular to smooth and planar (uncommon). One fracture surface has a partial coating,  $\leq 1$  mm thick, of microbreccia, cohesive but soft in places. The surface of the microbreccia has a shiny luster but no distinct slickensides. This is similar to the glassy-looking surface coatings in E260-2, but less glassy. Resting on top of the microbreccia are rare  $< 1$  mm patches,  $< 0.5$  mm thick, of pale blue white and pale pink clay/mordenite. Two  $< 1$  cm pieces have fracture surfaces that are smooth and planar, with  $\leq 1$  mm-thick, light-colored microbreccia zones, with 2 to 20% coverage by manganese mineral spots. Less than 10% of the fragment surfaces have a slightly rusty appearance, some of which is attributable to biotite alteration. There is ~1% overall coverage by mostly  $< 0.5$  mm manganese spots, some associated with lithic inclusions or mafic phenocrysts. In addition, there is less than 2% coverage of surfaces by white vapor-phase coatings  $\leq 1$  mm thick containing  $\leq 1$  mm crystals of silica. The deposits are mostly associated with patches of vapor-phase crystallization within the rock, including former pumice clasts. No short-wave UV-fluorescent phases were observed.



LANL ID: SMF barcode: Station location:  
E260 515151 62+05

Measured  $^{36}\text{Cl}/\text{Cl}$  ratio ( $\times 10^{-15}$ ) and description of analyzed aliquot:

E260-1 261  $\pm$  13 Representative bulk material

Sampled feature: A fault with 0.2 m offset

Sampling Objective: Role of faults

Lithology: Tptpmn - nonlithophysal

**Structural setting of sampled feature:**

The sampled area is of a fault that is a single, discrete plane oriented 160/78, with 0.2 m down to west displacement. The fault surface is moderately smooth with a 3 cm gouge zone along it. There is calcite on fractures that connect to this fault. Rock in immediate foot wall and hanging wall of sample site is basically unfractured. The fault is subparallel to tunnel alignment here, and it is difficult to trace it to the left rib. Locally, very few fractures. This is a single fault through relatively intact rock.

**Mineralogy and petrology of sampled feature:**

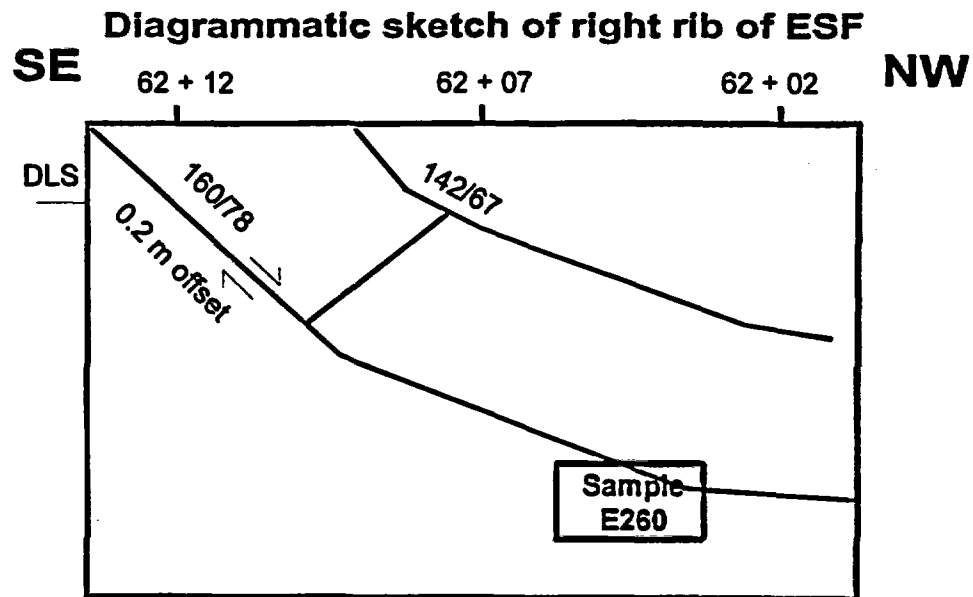
The rock is nonlithophysal, moderately to densely welded, devitrified tuff adjacent to a fault. The overall color is grayish orange pink, with pale grayish red purple spots. Phenocrysts comprise 2 to 3% and consist of feldspar, biotite and other mafic minerals, and Fe-Ti oxides. There are rare rounded, glassy quartz xenocrysts. The feldspar phenocrysts,  $\leq 2$  mm across, are commonly partly crushed. The crushed material is sized  $< 0.01$  mm and comprises 10 to 20% of the volume of the feldspar phenocrysts. The material is white, in contrast to the clear intact phenocrysts. This phenomenon exists up to at least 10 cm from the fault plane.

Pumice lapilli are 1 to 3 cm long, with highly variable length:width ratios probably unrelated to welding. They comprise 3 to 5% of the rock and are commonly crystallized to rounded aggregates of  $< 0.10$  mm crystalline silica and Fe-Ti oxides. The aggregates are  $\leq 1$  mm. The surfaces of vapor-phase deposits in relict pumices commonly coincide with the surfaces of rough, irregular fractures. Lithic inclusions of  $\leq 0.5$  cm fine- to medium-grained igneous rocks, comprise 5 to 10% of the rock.

The fracture that serves as a fault plane is planar and flat, with no bleached margins, but probably is a former cooling joint. There is a  $\leq 1$  mm-thick crushed zone variably developed below the fracture surface. There is  $\leq 80\%$  coverage of the fracture surface by  $< 0.5$  mm-thick spots, dendritic patches, and dense patches of manganese minerals. Locally, the deposits extend into fractures of  $\leq 0.1$  mm apertures within the crushed zone, usually at high angles to the main fracture.

The  $\leq 15$  cm rock fragments that comprise the sample are angular, equant to flat and elongate, bounded by rough, irregular fracture surfaces, many with cm-scale continuity. Coverage of fragment surfaces by fine particulates is locally 60 to 80% with deposits  $\leq 1$  mm thick. The particulates are of heterogeneous color and texture, falling into two general categories: 1) white, slightly to moderately cohesive, dense to lacy aggregates of vapor-phase constituents, commonly associated with vapor-phase features in the rock, 2) pinkish to yellowish gray, highly variable abundances and thicknesses, possibly excavation-induced. Some very irregular, indistinct crushed zones serve as local boundaries of rock fragments. The zones are  $< 1$  mm thick, continuous at less than cm scale, and contain some  $< 0.1$  mm particulates.

The overall abundance of manganese minerals is  $\ll 1\%$ , but they are locally common on rock surfaces as  $\leq 0.5$  mm spots surrounding lithic inclusions, biotite, and Fe-Ti oxides. They also fill radiating mm-long fractures surrounding mafic grains. Rare overall, but locally common in cm-scale areas of the rock surfaces, are  $< 0.01$  mm-thick deposits,  $< 1$  mm across, of colorless material with a vitreous luster. The deposits are located near, but not at, the edges of angular rock fragments. Locally, the deposits are overlain by multi-color, very fine-grained particulate and clayey "point-of-contact" deposits with irregular ring-like shapes formed where areas of adjacent rock fragments were in contact. No short-wave UV-fluorescent phases were observed.



LANL ID: E280                      SMF barcode: 515175                      Station location: 66+40

Measured  $^{36}\text{Cl}/\text{Cl}$  ratio ( $\times 10^{-15}$ ) and description of analyzed aliquot:  
 E280-1                      238  $\pm$  30                      Representative bulk material

Sampled feature: Bulk rock below Topopah vitrophyre

Sampling Objective: Representative background

Lithology: Tptrn2

**Structural setting of sampled feature:**

Sample is of bulk rock of the crystal-rich member of the Topopah Spring Tuff, about 4 m below the vitrophyre. This section is relatively unfractured, with no systematic joint sets. The nearest fault to the sampled location is at 66+45. This fault displaces top of Topopah by ~0.5 m down to the east. This fault zone appears to be very tight; a single plane at level of the Detailed Line Survey. Near invert, it appears as a diffuse zone of small features in solid rock. This fault is a throughgoing feature and is seen on the left rib. This fault is immediately west of the "fumarole" at 66+50. The fault is ~5 m west of fumarole on the right rib, but within it on the left.

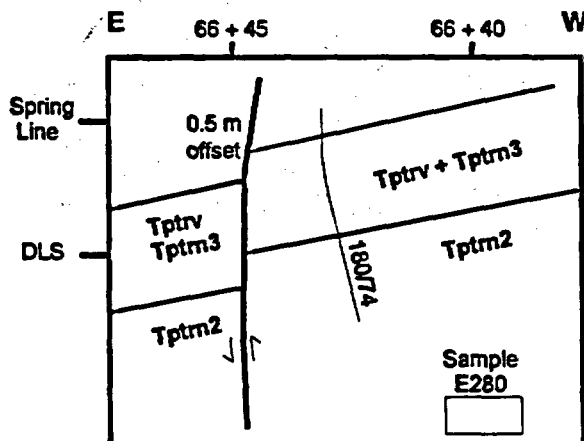
**Mineralogy and petrology of sampled feature:**

The sample consists of brecciated densely welded, devitrified grayish red (10 R 4/2) tuff. The rock contains 10-15%  $\leq$  mm phenocrysts of feldspar, coppery biotite, mafic grains, sphene, and Fe-Ti oxides, and ~5% round, vesicular pumice clasts  $\leq$  cm across. The clasts are vapor-phase altered, and about 20% of them contain  $\leq$  5 mm cavities. The rock also contains  $<$ 2% reddish and gray fine-grained lithic clasts  $\leq$  5 mm across.

The breccia clasts range from cm-scale to  $<$ 0.5 mm. The surfaces of larger clasts are rough and irregular; the fragments tend to be slightly flat and elongate. There are  $\leq$  1 cm-wide planar zones and irregular domains of  $\leq$  2 mm breccia clasts cemented by non-fluorescent crystalline silica. These domains have a hard flinty texture and uniform dark reddish brown (10 R 3/4) color due to preferential comminution or removal of white feldspar phenocrysts. These domains are cut by  $<$ 0.1 mm-aperture fractures filled with calcite and/or opal which is clear and fluoresces green in short-wave UV light. One such breccia zone has a roughly slickensided surface. A few breccia clast surfaces are coated with  $<$ 1 mm-thick layers of botryoidal opal, clear and fluorescent.

Some fine-grained breccia domains and surfaces of larger clasts are cemented or coated by 0.1 to 1 mm-thick calcite. The thinnest coatings are mm-scale patches, polycrystalline and discontinuous. The thicker coatings have  $\leq$  1 cm domains of common crystallographic orientation. Locally,  $\leq$  2 mm twinned equant crystals overlie opal and are partly coated by opal. Massive to lacy aggregates of white powder, slightly cohesive, are present on a few opal or calcite-coated surfaces and may be mostly calcite. All the calcite fluoresces faint purple in short-wave UV light. There are also sub-mm to cm-scale domains of uncemented breccia, cohesive but crumbly. Feldspar crystals are deformed and biotites are smeared apart. Overall coverage by calcite is  $<$ 5%, and coverage by opal is  $<$ 2%. There is overall  $<$ 1% coverage by isolated  $<$ 0.5 mm spots or rims of black Mn minerals, most associated with Fe-Ti oxide phenocrysts.

**Diagrammatic sketch of right rib of ESF**



LANL ID: E290      SMF barcode: 521128      Station location: 59+98

**Measured  $^{36}\text{Cl}/\text{Cl}$  ratio ( $\times 10^{-15}$ ) and description of analyzed aliquot:**

E290-1      205  $\pm$  14      Representative bulk material

**Sampled feature:** Representative fractured rock

**Sampling Objective:** Systematic

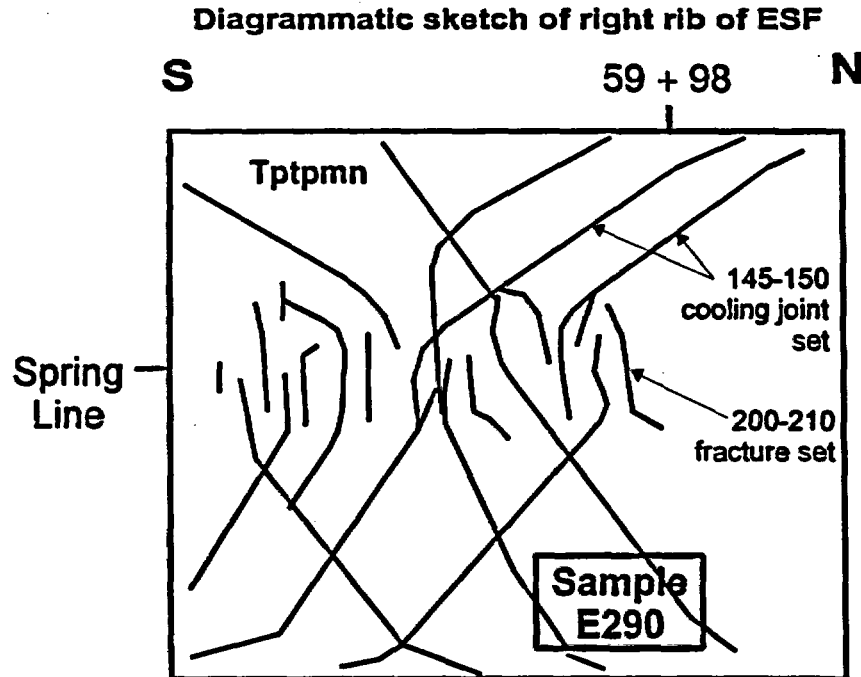
**Lithology:** Tptpmn

**Structural setting of sampled feature:**

This systematic sample was taken in an interval of the ESF where at least two joint sets are well-developed. The best expressed joints are a set of cooling joints with general orientations of 145-150/75-85. These joints are large, commonly extending from invert to crown, and where best developed have a spacing of around 1 m. A second set of joints with general orientations of 200-210/80-85 is present as well. These joints are shorter and less continuous, often terminating against the cooling joint set.

**Mineralogy and petrology of sampled feature:**

Detailed description not available.



LANL ID: E302      SMF barcode: 522218      Station location: 70+19

Measured  $^{36}\text{Cl}/\text{Cl}$  ratio ( $\times 10^{-15}$ ) and description of analyzed aliquot:

E302-1      327  $\pm$  13      Representative bulk material

Sampled feature: West-side down fault with 1.6 m offset

Sampling Objective: Role of faults

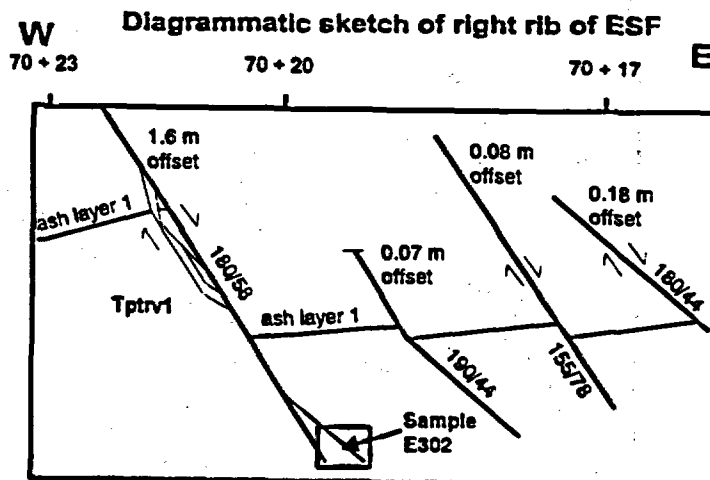
Lithology: Nonwelded Tptrv1 or Tpb2 (probably Tptrv1, it is below ash layer 1)

**Structural setting of sampled feature:**

Sample is from largest of a series of small west-side down faults that displace pumiceous, nonwelded tuff a few meters above the contact with the TSw. Sampled fault has orientation 180/60, smaller subsidiary faults have generally similar orientations (see sketch). The fault is in part anastomosing, exposed as raised ribs within the pumiceous unit. The sample is in orange-brown, pumiceous, nonwelded tuff with no evidence of fault plane at the sample site. The fault may be just east of the sample, with sample in hanging wall. No fractures seen in the bedrock except for the faults. These faults probably extend down to the top of the TSw, which is only a few meters below.

**Mineralogy and petrology of sampled feature:**

No detailed description available.



LANL ID: E324      SMF barcode: 521290      Station location: 75+78

Measured  $^{36}\text{Cl}/\text{Cl}$  ratio ( $\times 10^{-15}$ ) and description of analyzed aliquot:

E324-1	418 ± 31	Breccia
E324-3	322 ± 13	Wall rock

Sampled feature: A fault with 0.21 m offset, filled with 4-5 cm clay

Sampling Objective: Role of faults

Lithology: Tpcplnc

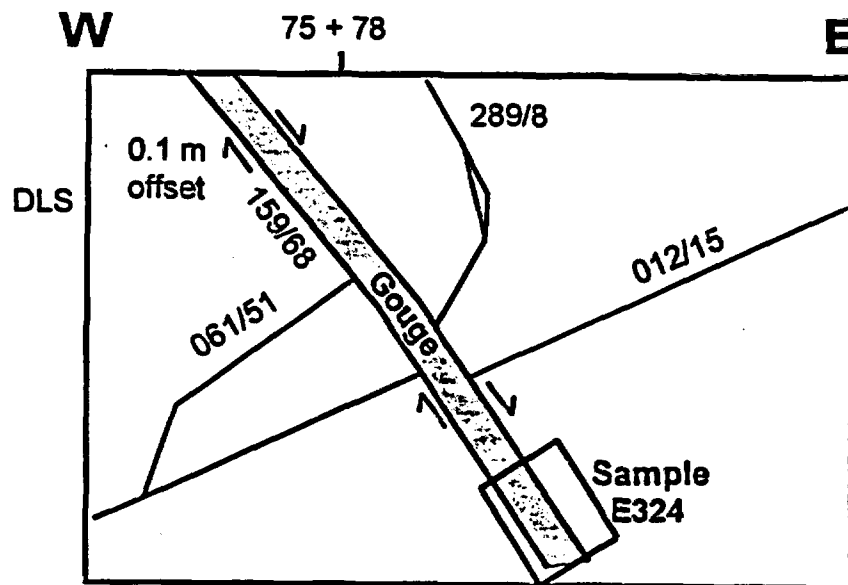
Structural setting of sampled feature:

The sample is from a 4-5 cm-wide gouge zone along a fault plane (gouge widens to 10-15 cm on the left rib). The fault is oriented 159/68 and offsets the Tpcplnc (columnar subzone of crystal-poor Tiva Canyon Tuff) by about 0.1 m. In this portion of the tunnel, certain cooling joints open up and become gouge or sediment-filled. The sampled gouge zone happens to be along a fault, but there are other cases where there is no fault, but sediment or gouge still occurs sporadically. The 180-190 joint set is common here.

Mineralogy and petrology of sampled feature:

No detailed description available.

Diagrammatic sketch of right rib of ESF



LANL ID: E327      SMF barcode: 521295      Station location: 76+50

Measured  $^{36}\text{Cl}/\text{Cl}$  ratio ( $\times 10^{-15}$ ) and description of analyzed aliquot:

E327-1       $281 \pm 12$       Representative bulk material

Sampled feature: A 1 meter long fracture in almost completely unbroken rock

Sampling Objective: Systematic sample

Lithology: Tpcpln

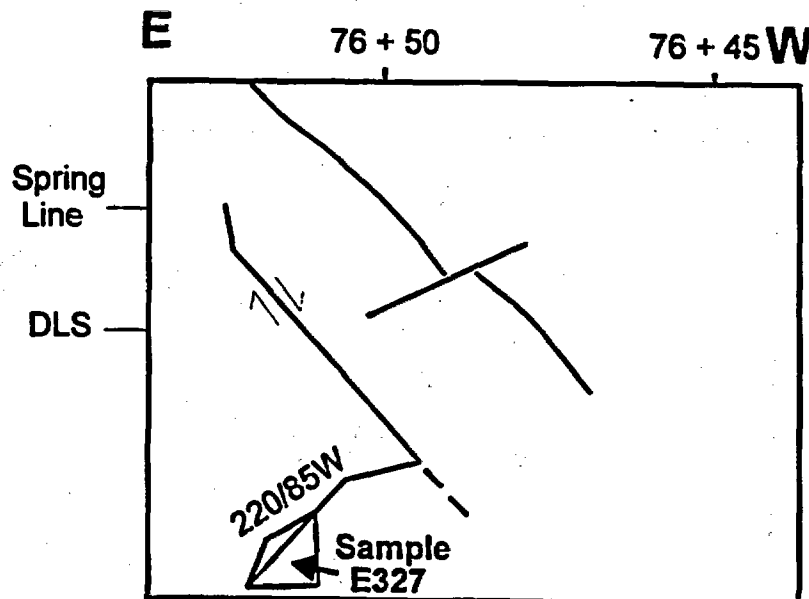
Structural setting of sampled feature:

This systematic sample includes a small fracture oriented 220/95. A number of 1-2 m long joints occur in the vicinity, and typically have blind terminations at each end. The largest joints are probably cooling joints; these are curved, 4-5 m long, and have orientations in the range of 105-120/70-85. The smaller joints are 1-2 m long and are probably tectonic joints, with orientations of 172/89, 136/66, 003/89. The rock has "hackly" fracturing.

Mineralogy and petrology of sampled feature:

No detailed description available.

Diagrammatic sketch of right rib of ESF



LANL ID: E328      SMF barcode: 521294      Station location: 76+76

Measured  $^{36}\text{Cl}/\text{Cl}$  ratio ( $\times 10^{-15}$ ) and description of analyzed aliquot:

E328-1	334 ± 15	Breccia (<~1 cm)
E328-3	445 ± 20	Breccia (>~1 cm)

Sampled feature: Fault, 0.2 m down to west (minimum)

Sampling Objective: Role of faults

Lithology: Tpcpln

Structural setting of sampled feature:

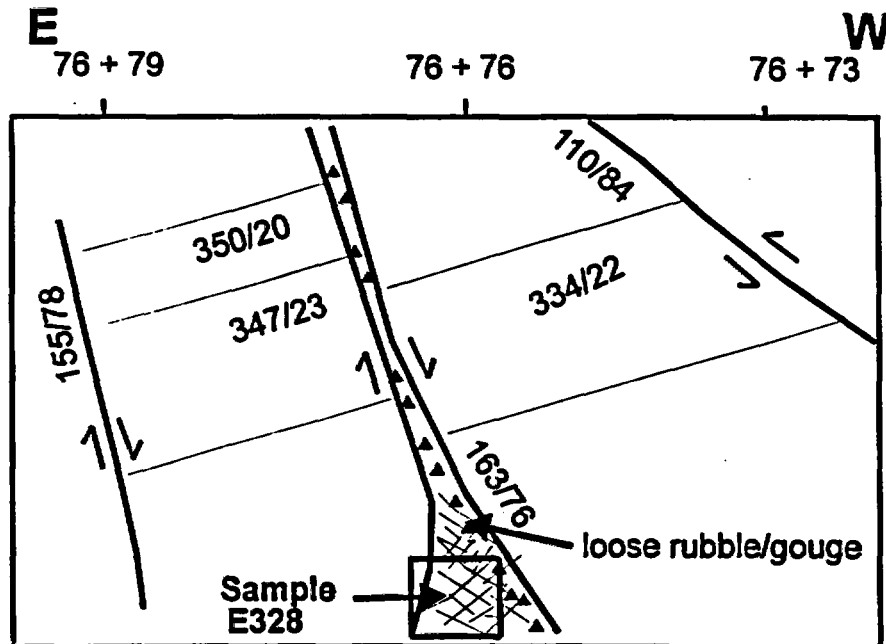
The sample is of loose rubble from a small fault that offsets Tpcpln. The fault has an orientation of 163/76, with 0.2 m down to west offset (minimum). Breccia in the fault occurs as 2-5 cm angular clasts; the walls of fault are smooth. The fault occurs on the left rib as a 1-m wide cavernous (lagged) rubble zone, surrounded by a 1-m wide zone of small (10-20 cm) fractures on either side of the fault.

The rock is not hackly here; this may be upper Tpcpln. The vapor phase parting is the only systematic joint set, cut by northwest-trending small faults. Vapor phase partings are oriented 330-350/20-25, with a spacing of about 0.5 m. Another small fault occurs at 76+79 with a 0.2 m down to west offset.

Mineralogy and petrology of sampled feature:

No detailed description available.

Diagrammatic sketch of right rib of ESF



## APPENDIX C-3

### PETROLOGIC CHARACTERIZATION OF OTHER SAMPLE SITES

This section of Appendix C contains petrologic and mineralogic descriptions of samples with  $^{36}\text{Cl}/\text{Cl} \times 10^{-15}$  values below 1250 and greater than 350. Some of the samples have not yet been analyzed for  $^{36}\text{Cl}$ . The purpose of these descriptions is to document the nature of the bedrock, the presence of field-scale structures such as faults, fractures, breccia zones, and other features that affect rock permeability, and the existence of secondary mineral deposits indicating that water has moved through the rocks. The descriptive process is in progress and many of the descriptions remain to be done or are incomplete, lacking either site or sample information. The descriptions given here include systematic sampling sites and sites that were chosen for the existence of a possible flow path, water-laid mineral deposit, or representative bedrock.

Particular attention has been devoted to features with implications for continuity of flow paths. In the context of Yucca Mountain geology, the term "syngenetic" refers to features that formed during the deposition or cooling of a pyroclastic unit. Syngenetic features such as cooling joints and some fracture zones could serve as fluid conduits, but do not normally extend beyond the boundaries of the host unit. For example, a cooling joint in the Topopah Spring Tuff with geochemical evidence of recent flow must have received its fluid input from a different conductive feature in the overlying nonwelded tuff. In contrast, a fault with evidence of repeated movement could by itself be a direct flow path from the surface to the Topopah Spring Tuff.

E001 (Sta. 1+98)

The bedrock is densely welded, devitrified lithophysal Tiva Canyon Tuff from the eastern wall of the Bow Ridge fault zone. The Bow Ridge fault is a westward-dipping normal fault with displacement downward to the west. The rock is fractured and fragmental. Individual fragments are more than 2 cm across, very irregular due to the lithophysae, and mostly angular to subangular.

The rock contains about 10% lithophysal cavities up to 3 cm across. The cavities have bleached borders up to 1 cm thick. Vapor-phase minerals in the cavities are feldspar, crystalline silica, and Fe-Ti oxides, all less than 1 mm. There may be some clay as well. Less than 5% of the cavities contain sprays of weakly UV-fluorescent drusy quartz overlying the vapor-phase minerals. Rock surfaces have less than 1% coverage of dendritic to diffuse spots of manganese minerals and a more widespread overcoating of powdery white material. The existence of these coatings suggests that the bedrock is highly fractured even beyond the boundary of the fault zone.

E007 (Sta. 2+3)

This bedrock sample is medium-grained nonwelded pre-Rainier Mesa tuff from the downthrown western wall of the Bow Ridge fault. There is no evidence of fracturing or fracture-filling minerals. The original glassy components of the rock have been completely replaced by zeolites, probably clinoptilolite. The pyroclastic constituents included about 30 to 50% of mostly white pumice clasts less than 1 cm across, 10 to 20% dark lithic grains less than 3 mm across, less than 5% phenocrysts of mostly feldspar and lesser bleached biotite, and the remainder of fine ash. No calcite or UV-fluorescent silica is present.

E020 (Sta. 24+68)

The sample site is a partly syngenetic rubbly breccia in sparsely lithophysal densely welded, devitrified Topopah Spring Tuff. Individual breccia clasts, up to at least 10 cm across, are coated on most surfaces with vapor-phase feldspar and silica. Feldspar is more common in the lithophysae and silica is more common on the fracture surfaces. The lithophysae are up to 2 cm across, with bleached borders.

The clasts have less than 1% coverage of surface-conformal crusts less than 1 mm thick of semi-aligned quartz crystals. There are also isolated patches of <1 mm drusy quartz crystals and associated rare botryoids of silica with granular surfaces (probable opal-CT). None of this silica is UV-fluorescent. All of this silica is partly overgrown by calcite. The calcite, in <1 mm equant crystals or <1 cm blades, fills some lithophysae (blades) and covers broken rock surfaces with or without underlying vapor-phase coatings (equant and blades). UV-fluorescent opal, in not quite clear <1 mm botryoids, are locally associated with calcite and have an overall abundance of 1 to 2%. The opal exists as overgrowths and intergrowths or inclusions in calcite. There are also <1 mm spheres of powdery white, possibly fluorescent silica preserved only as inclusions in calcite.

E027-1 (Sta. 11+00)

This systematic sample consists of moderately to densely welded, devitrified Topopah Spring Tuff. The rock is red-brown, with ~10% phenocrysts of feldspar, biotite, Fe-Ti oxides, other mafic minerals, and quartz. Pumice lapilli  $\leq 2$  cm across comprise ~25% and are vapor-phase altered to feldspar, crystalline silica, biotite, and other mafic phases. There are no obvious fractures in the sample, but local irregular, discontinuous breaks exist and are identifiable by uncommon Mn mineral coatings in  $\leq 1$  mm patches.

Rusty oxidation of mafic minerals is common, but not all grains are affected. Within the vapor-phase altered pumice lapilli are common but not ubiquitous <1 mm deposits of white translucent clay. Many of the deposits have forms that are reduced shape of the cavities in which they occur. Clay deposits are present in cavities newly exposed by breaking the sample. These relations suggest that the clays are of *in situ* origin. No short-wave UV-fluorescent phases were observed.

E029-1 (Sta. 13+00)

The sample is densely welded, devitrified Topopah Spring Tuff with moderately to densely welded, mm- to cm-scale pumice lapilli. Vapor-phase alteration is ubiquitous in the pumice lapilli. Lithophysal cavities contain mm-scale vapor-phase crystals of feldspar, hematite, and rare fibrous amphibole. No UV-fluorescent minerals were observed.

E033-1 (Sta. 14+41)

The sample consists of fragments, from <0.1 mm up to 3 cm across, of mostly densely welded, devitrified, crystal-rich Topopah Spring Tuff. Phenocrysts, ~15% of the rock, are feldspar, Fe-Ti oxides, and rare biotite. Local pumice-like areas are moderately welded and devitrified, but with well preserved glassy filament forms. Whitish pumices contain abundant vapor-phase minerals, mostly tridymite, feldspar, hematite, and amphibole.

There are a few mm- to cm-scale, ~1 to 2 mm thick crusts of ~1 mm drusy quartz crystals that do not fluoresce in UV light. The quartz is locally overgrown by ~1 mm flat prismatic calcite crystals. The base of one quartz crusts contains relict botryoidal silica that fluoresces green in short-wave UV light. There are cm-scale domains of ~1 mm rock fragments cemented by subpoikilitic equant to flat prismatic calcite crystals that fluoresce blue-white weakly in short-wave UV light.

Round, not botryoidal, flat blobs of blue-gray translucent silica <1 mm across occur as isolated deposits on calcite and less commonly on quartz. In several places, the calcite crystals have grown after silica deposition, partly to completely engulfing the silica deposits. These growth additions are commonly bounded by crystal faces surrounding the silica deposits. Less common deposits on calcite are <1 mm aggregates of transparent, slightly yellow silica. Both types of silica fluoresce green in short-wave UV light.

E035 (Sta. 15+05)

The sampled rock is a calcite-cemented, mostly syngenetic breccia of densely welded, devitrified Topopah Spring Tuff. The maximum clast size is about 2 cm. Most fragments are coated with <1 mm vapor phase minerals, mostly feldspar, silica, and minor Fe-Ti oxides. Slightly disaggregated vapor-phase minerals also serve as breccia matrix. A few clasts may have smectite-zeolite-silica alteration. A newly separated fracture surface shows the clay-rich clasts and pink-gray clay fracture coatings.

The breccia is tightly cemented by poikilitic calcite that comprises about 30% of the rock. In rare cavities within the cement, <1 mm across, the calcite has flat rhombohedral terminations. A prominent irregular fracture surface has a 0 to 2 mm-thick coating of flat rhombohedral calcite crystals <2 mm across. Overlying this calcite are <1 mm spots of silica that are mostly whitish, waxy, and subopaque, rarely clear. The silica, with an overall abundance on the fracture surface of <2%, fluoresces green in short-wave UV light. There are very rare manganese mineral coatings, mostly on tuff fragments, but also possibly on adjacent calcite crystals.

E036, E036-1 (Sta. 16+12)

This sample consists of broken rock and a separated cooling joint in densely welded, devitrified crystal-rich Topopah Spring Tuff, with calcite infilling. One rock fragment has a smooth surface coated with loosely adhering powdery vapor-phase material. Vapor-phase cavities in pumice lapilli are coated with feldspar, silica, and Fe-Ti oxides. Most cavities have infillings of calcite over the vapor-phase minerals.

The separated cooling joint was initially filled with botryoidal chalcedony overlain by drusy quartz. The chalcedony and quartz separated from the joint wall and the intervening space was almost completely filled with dense mosaic calcite consisting of <1 mm crystals with flat rhombohedral terminations on free surfaces. The calcite shows faint laminations parallel to the joint surface, especially under short-wave UV light, perhaps related to variable content of very-fine-grained tuffaceous impurities. The laminations may indicate progressive opening and infilling of the joint. There are also calcite overgrowths on the drusy quartz away from the joint surface. Rare pale yellow <1 mm aggregates of silica occur with calcite in the interstices of the drusy quartz crystals. The surfaces of the mosaic calcite deposits are locally covered with thin patches 1 to 3 mm across of water-clear botryoidal silica with blocky surfaces, probably opal-CT. An unidentified rose-lavender very fine-grained mineral on fractured surfaces of the mosaic calcite is rare but locally prominent.

E037-2 (Sta. 16+19)

The sample consists of mm- to cm-scale angular rock fragments in a matrix of sand-, silt-, and clay-size material that constitute a fracture filling. The smallest fragments are ≤0.1 mm. The rock fragments are densely welded, devitrified Topopah Spring Tuff, mostly orange-brown and gray, with vapor-phase alteration in the pumice clasts. Phenocryst content is ~15 to 25%, mostly feldspar. No UV-fluorescent phases were observed in any part of the sample.

E037-2 (Sta. 16+19) (continued)

The fine-grained matrix is composed mostly of chunks and elongate striated pieces of white to orange undeformed, translucent to chalky glass. Individual biotite crystals comprise ~5% of the sand-silt fraction. The crystals are heterogeneous, including greenish, brown, orange-brown, "tarnished" examples. Many dark crystals have partly resorbed textures. Other mafic minerals include pyroxene, hornblende, and Fe-Ti oxides.

The abundance of clay-size material is ~10-20%. Centimeter-scale domains of the finest-grained material, without coarser components, show graded bedding from very fine sand to silt, capped with  $\leq 1$ -mm thick layers of red-brown clay. The deposits are deformed and surrounded by coarser material.

The lithic fragments are derived from local bedrock, but the vitric material is derived from higher in the Topopah Spring section and must have moved tens of meters downward through an open fracture. The layered, fine-grained deposits formed by particle settling in water-filled spaces. The biotite content of the matrix is probably enriched relative to its abundance in overlying rock (Buesch et al., in press), suggesting concentration by aqueous suspended transport.

E038-1 (Sta. 17+00)

This systematic sample consists of red-brown, densely welded, devitrified Topopah Spring Tuff in irregular rough-surfaced fragments. The tuff contains ~10% phenocrysts of  $\leq 1$  mm feldspar, Fe-Ti oxides, biotite, and sphene. There are also ~10% 1-2 mm elongate vapor-phase patches in former pumice clasts, containing  $< 1$  mm cavities and  $< 1$  mm crystals of silica and feldspar.

The subsample includes one irregular incipient fracture with vapor-phase minerals and a  $< 1$  mm rock fragment cemented by vapor-phase minerals. There is  $< 1$  % overall coverage of the rock surfaces by isolated  $< 1$  mm Mn mineral spots, many adjacent to lithic grains or mafic phenocrysts. The presence of the Mn coatings indicates that the rock fragment surfaces are natural and not caused by the air hammer during sample collection. No UV-fluorescent phases were observed.

E041-1 (Sta. 19+00)

This systematic sample is mottled orange-brown and gray-pink, densely welded, devitrified Topopah Spring Tuff. The gray-pink areas are concentrations of mostly white,  $< 1$  mm vapor-phase crystals. The rock is broken into rough-surface, irregular fragments. A few tight, planar fractures, with original apertures  $< 1$  mm, are filled with vapor-phase white minerals and show no evidence of subsequent breakage or separation.

There is very slight development of  $< 0.5$  mm Mn patches adjacent to small lithic inclusions or phenocrysts. No short-wave UV-fluorescent phases were observed.

E045-1 (Sta. 21+00)

This is a systematic sample of densely welded, devitrified Topopah Spring Tuff. The mottled orange and pink-gray rock is in angular fragments with common  $< 1$  mm thick coatings of vapor-phase minerals (tridymite, other silicates, and mafic phases). No short-wave UV-fluorescent minerals were observed.

E046 (Sta. 22+71)

The site is a near-vertical fracture zone about 6 m wide that extends about 2/3 of the distance from the invert to the crown. The bedrock is lithophysal, densely welded, devitrified Topopah Spring Tuff. Lithophysal cavities, mostly  $< 30$  cm, comprise about 40% of the rock, and there are numerous lithophysal fractures. Some of the fractures have calcite coatings, but no calcite was observed in the lithophysae.

The lithophysal cavities and fractures are commonly coated by  $< 1$  mm vapor-phase crystals of feldspar and Fe-Ti oxides. The highly irregular surfaces of the lithophysal fractures are also variably coated with at least three varieties of silica, as well as calcite. The least abundant variety is a combination of clear botryoidal and irregular lacy masses of UV-fluorescent opal. This material is overlain by drusy quartz crystals in a dense coating or open network, about 1 mm thick. Some quartz lies directly on the rock surface on or the vapor-phase feldspar. Some crystals are skeletal or hollow or form surface-conformal crusts, up to several cm across, of semi-aligned crystals with prism faces parallel to the rock surface. Examples exist in which the outer margins of quartz crusts are nonfluorescent and have a fairly sharp boundary with the fluorescent quartz, although no obvious morphological boundary is visible.

E046 (Sta. 22+71) (continued)

Sparry calcite forms <1 mm-thick, discontinuous coatings on the quartz, especially filling the interstices of the network and the centers of hollow crystals. A minor amount of calcite also occurs as film-like crystal aggregates directly on the rock surface. Domains of fine-grained bedrock breccia, cemented by calcite and possibly by quartz, also exist.

E047-1 (Sta. 23+00)

This systematic sample is red-brown, densely welded, devitrified Topopah Spring Tuff. The rock contains ~1% elongate, <1 cm vapor-phase patches, pockets, and spherulites of white, <1 mm crystals of silica and feldspar, plus minor biotite. There are no Mn minerals or long- or short-wave UV fluorescent phases.

E058 (Sta. 27+66)

The sample is orange brown, densely welded, devitrified Topopah Spring Tuff, nonlithophysal at the sample scale. The rock contains cm-scale or smaller purple gray relict pumice clasts with local spherulitic devitrification. Uncommon vapor-phase partings or cooling joints have  $\leq 1$  mm-thick white to clear fillings or coatings of crystalline silica in  $\leq 0.5$  mm crystals. There is <1% coverage by  $\leq 1$  mm Mn mineral spots on rock surfaces, less commonly on or within silica coatings or white beige particulate deposits (see below). Rarely, there are linear aggregates of black Mn minerals radiating away from mafic minerals within the rock. Manganese deposits on granular material are dark brown.

Most rock surfaces are coated with rock dust of uncertain origin, either natural or mining-derived. Newly washed rock surfaces have  $\leq 60$  coverage by <1 mm-thick coatings of <1 mm rock fragments (larger fragments orange brown, smaller ones white beige) that are slightly cohesive and locally coated or cemented by Mn deposits. The surfaces of freshly broken-apart tight fractures have <5% coverage by lacy to filiform <1 mm aggregates of whitish beige <0.1 mm uncemented particulates. No short-wave UV-fluorescent phases were observed.

E073-1 (Sta. 5+04)

This sample consists of angular to subangular  $\leq 4$ -cm fragments of densely welded, devitrified Tiva Canyon Tuff. The fragments are mottled red-brown and gray. Patches and less common dendrites of red-brown Mn minerals,  $\leq 1$  mm across, rest directly on the rock fragment surfaces. The overall abundance of the Mn minerals is ~1%, but the material is locally more abundant. There are also local <<1-mm-thick coatings of white clay. The fragments have loose coatings, up to 1 mm thick, of white powdery material. No short-wave UV-fluorescent phases were observed.

E141-2 (Sta. 29+00)

The sample is densely welded, devitrified Topopah Spring Tuff. Cavity surfaces and fractures have <1-mm thick coatings of <1-mm white crystals of feldspar and minor black Fe-Ti oxides. No UV-fluorescent phases were observed.

E142-2 (Sta. 29+21)

The examination subsample is red-brown, densely welded, devitrified Topopah Spring Tuff with 1 to 2% phenocrysts. Spherulitic devitrification, with <1 mm spherules, is associated with relict pumice clasts.

One fracture surface in the sample is subplanar but irregular due to vapor-phase alteration of the rock. The surface has a  $\leq 1$ -mm deposit of <1 mm silica crystals, including tridymite, and 2-3% euhedral, skeletal crystals of hematite. A bleached margin is locally developed adjacent to the fracture surface. Another fracture, perpendicular to the first, is irregular and subplanar with a vague ~1 mm bleached margin. Patchy <1-mm-thick white coatings of  $\leq 0.2$  mm vapor-phase crystals are mostly silica. No Mn coatings or short-wave UV-fluorescent phases were observed. Particulates are of uniform color and are considered to be products of mining.

E145-2 (Sta. 29+80)

The sample was collected from two lithophysal/devitrification cavities about 2 m apart along a low-angle cooling joint of about 10-m extent. The cooling joint has been modified by brecciation.

The examination subsample consists of  $\leq 1$ -cm-thick elongate fragments of densely welded, devitrified and vapor-phase devitrified Topopah Spring Tuff. There are also a few subequant cm-scale fragments; most are almost completely covered by  $\leq 1$ -mm-thick white coatings of  $< 1$  mm vapor-phase crystals. The rock fragments are coated by calcite and less abundant opal in coatings up to  $\sim 3$  cm thick. Opal is more restricted in occurrence than calcite.

The calcite fluoresces weakly white in short-wave UV light. Most of the calcite is in dense ( $< 5\%$  porosity) intergrowths of irregular flat rhombohedral crystals,  $\leq 1$  cm across, in groups of subparallel crystals. The crystals, many with short dimensions perpendicular to rock surfaces, are gray with glassy to slightly pearly luster. About 50% of the calcite has  $< 1$ -mm-thick overgrowths of clear opal with bumpy, rounded surfaces. The opal fluoresces strongly yellow-green in short-wave UV light. There are also opal layers and patches within the calcite coatings.

Calcite coatings on opposite sites of flat rock fragments are noticeably different. The original orientations of the samples have not been preserved, but it is probable that underside coatings have thinner, more porous calcite layers. The calcite is glassier and in smaller, better formed crystals, some  $< 1$  mm, with both flat rhombohedra and prismatic forms. The smallest crystals are in localized lacy aggregates. There is no associated opal.

The rock fragments contain incipient fractures with  $< 1$  mm apertures, subparallel to the flat rock surfaces. Many fractures are filled with mostly monocrystalline calcite. There is also some poikilitic cementation of vapor-phase altered rock by calcite. No Mn minerals were observed.

E146 (Sta. 30+18)

The analyzed mineral separate is from a lithophysal-devitrification cavity about 1 m across in densely welded, devitrified Topopah Spring Tuff with  $< 5\%$  lithophysae in an area of few throughgoing fractures. The cavity is intersected by at least one cooling crack with smooth surfaces and bleached margins.

Resting on the bottom of the cavity are loose crusts of platy, pearly calcite aggregates up to  $\sim 2$  cm thick. There are many local textural varieties of calcite. Common forms, all less than 1 mm long, include steep rhombohedra grouped on the surfaces of larger crystals, tapering hairlike crystals, and beadlike strings of crystals. Many of these forms have textural features suggestive of both deposition and dissolution. In some places, extremely thin, ribbonlike calcite aggregates have grown as much as several centimeters upward from the crystalline crusts. Clear opal-A occurs locally with calcite as intergrowths and, more abundantly, as thin overgrowths. Both the calcite and the opal fluoresce in short-wave UV light.

E148-2 (Sta. 31+61)

The sample consists of densely welded, devitrified Topopah Spring rock and vapor-phase fragments cemented by calcite, from an incipient lithophysal cavity intersected by a cooling joint subparallel to the tunnel wall and another cooling joint dipping  $\sim 30^\circ$  to the north. Where the calcite cements tuff fragments, it occurs locally in cm-scale poikilitic crystals. The presence of lacy crystal surfaces and  $< 1$  mm tapered narrow crystals may be evidence of dissolution.

The calcite crust from the cavity is  $\sim 1$  cm thick. Crystals on the upper part of the crust are 1-mm to 1-cm short prismatic forms of variable orientation. There are local cm-scale areas of lesser deposition or, more rarely, of nondeposition. The calcite is slightly fluorescent under short-wave UV light. No fluorescent silica was observed.

E149-2 (Sta. 31+63)

The sampled material is crushed tuff breccia along a cooling joint in densely welded, devitrified Topopah Spring Tuff. The joint is traceable from invert to crown, and at least one joint surface is coated with calcite.

The mm- to cm-scale breccia fragments are equant to flat and elongate, and have some smooth, planar faces and irregular rounded faces, both with bleached margins. One cooling joint surface of a fragment has a  $< 1$ -mm-thick coating of  $< 1$  mm feldspar and silica crystals. One smooth fragment surface, without a bleached margin, has a  $\sim 1$ -mm-thick coating of laminated white to pale yellow, translucent clay overlying a  $< 1$ -mm-thick layer of  $< 1$ -mm tuff fragments. Most fragments have very thin dustings of powdery material and scattered  $< 1$ -mm spots of manganese minerals. No UV-fluorescent minerals were observed in the examination aliquot.

E151-2 (Sta. 33+16)

The sampling site is a 0.5-m lithophysal cavity with fillings of calcite and opal. The cavity is intersected by at least one vertical cooling joint. The cavity is lined with ~1-mm-thick coatings of <1-mm feldspar, silica, and Fe-Ti oxide crystals.

Calcite crystals immediately overlying the vapor-phase linings are equant and ~1 mm across. Where the calcite is separated from the vapor-phase linings, there are a few <1-mm crystals of prismatic or dog-tooth calcite crystals that grew downward from the main mass of calcite. Overlying crystals, in fairly dense aggregates, are platy and up to 1 cm across. Most platy crystals are oriented with thin dimensions horizontal. Fragments of vapor-phase linings are imbedded in the upper parts of the calcite aggregates. The calcite fluoresces purple in short-wave UV light.

Three textural varieties of silica, all of which fluoresce in short-wave UV light, are present. Coatings, <<1 mm thick, of clear opal with round protuberances cover ~50% of the calcite surfaces in cm-scale patches. Similar material may be included in the interiors of some calcite crystals as well. Patches of individual <1-mm hollow yellowish silica spheroids form deposits on calcite. The overall abundance of this silica variety is <1%. The spheroids are slightly granular on the outer surfaces and have a powdery appearance on the hollow inner surfaces. Some spheroids are partly overgrown by calcite. In addition, there are rare 1-2 mm aggregates of translucent, gray-white botryoidal silica. Individual botryoids are <1 mm across. The surfaces of the botryoids are covered with clear opal. The textural relations of this silica variety with calcite are uncertain.

E155-2 (Sta. 35+00)

This is a systematic sample of densely welded, devitrified, nonlithophysal Topopah Spring Tuff. The site is within a zone of broken rock with throughgoing, subvertical cooling joints. The cooling joints are common, with several orientations, and have smooth, planar surfaces. Some fracture traces are discontinuous on a 4- to -5cm scale and abut fractures of slightly different orientation.

The tuff is gray-brown, with local spherulitic devitrification and very slight development of ~1 cm lithophysal cavities. Cooling joints have slight development of bleached margins. All planar fracture in the examination subsample have vapor-phase coatings up to 1 mm thick. The constituents are feldspar, silica, and very minor Fe-Ti oxides. The coatings are powdery to hard. Other more irregular fractures are mostly without vapor-phase deposits.

There is much less than 1% coverage by yellow-brown and red-brown Mn minerals on cooling joints and other fractures. The minerals are in patches up to 2 mm and in discontinuous elongate, dendritic patches following the texture of the vapor-phase substrate. Several of the rougher-surfaced fractures have minor scattered <1 mm deposits, <<1 mm thick, of blue-white translucent clay. Discontinuous deposits <<1 mm thick of tan silty material, some together with clay, are common on rough fracture surfaces. No short-wave UV-fluorescent phases were observed.

E244-2 (Sta. 8+38)

This sample of Tpbt3 consists of predominantly vitric nonwelded, bedded tuff. The three basic varieties of bedded tuff are: 1) fine-grained (<1 mm) partly to moderately cohesive tuff of 98-99% glass pyroclasts, mostly colorless and pale brown. Larger pyroclasts are mostly bubble fragments and minor long-tube fragments. Phenocryst content of about 1% includes biotite, Fe-Ti oxides, and feldspar. There is ≤1% pale orange clasts of altered pumiceous glass; 2) like (1) but with ~10% of 2-3 mm white to beige, equant to elongate pumice clasts; 3) tuff composed of about 90% 2-3 m clasts of pumiceous glass and round perlitic fragments and 10% <0.5 mm glass particles, with no bubble shards. The trace content of phenocrysts has mineralogy as above. This tuff is moderately cohesive and well consolidated, with ≤20% intergranular porosity. There are some incipient irregular fractures along clast margins with 3 to 5% coverage by black to brown Mn spots, <0.5 mm across. The overall color is pale gray orange.

There is overall <1% coverage of clasts by brown black, <1 mm Mn spots, some as black coatings on larger glass particles. No short-wave UV-fluorescent phases were observed.

E286 (Sta. 67+87)

This fault filling consists of two or more distinctive clay fillings and admixed rock fragments. The clay fillings contain from almost no rock fragments to about a 50/50 mixture of clay and rock fragments. This variability and the existence of nearly pure clay as deposits within the fault zone indicate that these are translocated clays. The two most common clay fillings are 1) reddish brown (10 R 3/6), locally very pure fracture filling, slickensided, 2) grayish brown (5 YR 3/2) clay, more commonly mixed with rock fragments but in places clearly a coating on fragment surfaces. A portion of the sample was decanted to remove loose clay. The 1- to 5-mm fraction of the remaining material is composed of a mixture of rock fragments and former lithic inclusions, plus a few phenocrysts of mostly feldspar. The following rock fragment varieties were observed: 1) moderate orange pink (5 YR 8/4) mostly zeolitized moderately welded tuff in  $\leq 3$  mm rounded soft fragments containing ~2% feldspar phenocrysts  $\leq 1$  mm across. This is tentatively identified as Tpcpv2; 2) angular fragments of reddish orange (10 R 6/5) densely welded, devitrified tuff  $\leq 3$  mm across. The fragments contain 5-15% phenocrysts,  $\leq 2$  mm across, of feldspar, biotite, and other mafic minerals. Some fragments contain patches of white vapor-phase/lithophysal material and rare  $\leq 1$  mm gray lithic grains. A few fragments are angular slivers cemented by  $\leq 0.4$  mm-thick chalcedony/opal-CT that fluoresces green in short-wave UV light; 3) pale red (10R 6/2) to pale reddish brown (10 R 5/4) angular fragments  $\leq 5$  mm across, with a subvitic luster. The fragments have a densely welded shard texture and contain ~2% phenocrysts, mostly feldspar; 4) a variety of pink, gray, red orange, red brown, and whitish smectite-zeolite-altered crystal-poor tuffs and lithic-rich tuffs.

Local calcite cementation of the fault filling in  $\leq 1$  mm-thick drusy crusts of  $\leq 0.2$  mm crystals has resulted in the formation of an 8-cm nodule. The calcite fluoresces weakly purple in short-wave UV light. Patches of milky to translucent white chalcedony/opal-CT, 0.1 to 0.5 mm thick, coat fragments of devitrified and altered vitric tuff. The silica is also present as fragments mixed in with brecciated rock and clay. The overall abundance of the silica is  $< 1\%$ . The silica fluoresces green in short-wave UV light. It is unclear whether the silica is of *in situ* origin. Many rock fragments and lithic grains have  $< 10\%$  coverage by  $< 0.5$  mm black-gray Mn mineral spots. One clast has a coating consisting of a few delicate zeolite prisms  $< 0.5$  mm long.

## Appendix D

### Descriptions of Surface and Subsurface Geology and Modeled Infiltration Rates above the ESF

#### D1. Scope of Appendix D

Appendix D focuses on providing a detailed characterization of surface geology, structural features, surface infiltration rates, and soil thicknesses above the ESF and at nearby borehole locations. This level of detail is useful for developing and evaluating alternative conceptual models of flow and transport, some of which are summarized in section 6 of the main text. For example, the conceptual model for fast paths containing a component of bomb-pulse  $^{36}\text{Cl}$  states that three simple conditions must be present (section 6.1):

- 1) A continuous fracture path must extend from the surface to the sampled depth, which requires the presence of faults that cut the PTn and increase its fracture conductivity.
- 2) The magnitude of surface infiltration must be sufficiently high to initiate and sustain at least a small component of fracture flow along the connected fracture path. Although intuitively one would expect the threshold infiltration value to be a function of PTn thickness, for the purpose of discussion, we are assuming that the minimum rate is 2 mm/yr.
- 3) The residence time of water in the overlying alluvium must be less than 50 years, which means that the thickness of the alluvial layer must be less than about 3 meters.

The first two conditions were used to produce a map of the study area predicting locations at which bomb-pulse  $^{36}\text{Cl}$  would penetrate to the depth of the potential repository and proposed East-West drift (Figure 6-7). The detailed maps and discussion in this appendix allow a test of these predictions through a case-by-case evaluation of ESF samples containing unambiguous levels of bomb-pulse  $^{36}\text{Cl}$  ( $^{36}\text{Cl}/\text{Cl}$  ratios above  $1250 \times 10^{-15}$ ), as well as an evaluation of locations where it was predicted in Figure 6-7 but not found. These evaluations provide the basis for the overall findings presented in section 6 about the validity of the conceptual model for fast paths, and the identification of some aspects that remain inconclusive in our understanding of flow and transport at Yucca Mountain.

#### D2. Geological setting and coverage of detailed maps

The central part of Yucca Mountain that includes the potential repository occupies a relatively undeformed block, called the central block, bounded by major, or block-bounding, faults (Figure D-1). Block-bounding faults within the vicinity of this central block of Yucca Mountain include the Solitario Canyon, Bow Ridge, and Dune Wash faults. All of these major faults dip  $60^\circ$ - $70^\circ$  to the west and commonly have experienced hundreds of meters of Tertiary displacement of

Miocene Paintbrush Group tuffs, with subordinate amounts of strike-slip motion (Scott and Bonk, 1984; Day et al., in press). In some places, Quaternary offset has been documented on these faults (Simonds et al., 1995). Faults that lie entirely within the structural blocks defined by the block-bounding faults may be described as intrablock faults. Intrablock faults are nearly vertical, have 1-30 m of displacement, and typical mapped lengths of less than 1 km (Day et al., in press). The largest intrablock fault, the Ghost Dance fault (Figure D-1), has up to 25 m of stratigraphic offset. Other important intrablock faults include the Sundance fault, faults in the hanging-wall of the Bow Ridge fault (part of the "imbricate fault zone" of Scott, 1990), and the Drill Hole Wash fault (Figure D-1).

Concurrent geologic mapping activities in the central block at the surface and within the ESF have defined a number of areas where the correlation of structural features between the surface and the subsurface is almost one-to-one. Correlation is best for faults with a meter or more of apparent vertical separation, particularly within the Tiva Canyon Tuff, where uncertainties in surface-to-ESF projections are minimal (Barr et al., 1996). Numerous very small (less than 1-m offset) faults identified within the ESF are generally not resolvable at the surface due to lack of exposure or lack of suitable stratigraphic markers. Recent mapping in the vicinity of the potential repository block documents that many small faults (those with trace lengths of about 200 m or less and 1 to 10 m of displacement) are vertically and laterally discontinuous (Scott and Bonk, 1984; Potter et al., 1995; Braun et al., 1996; Day et al., in press). These minor intrablock faults are marked by breccia zones that are commonly 0.1-1.0 m in width, and many of them are parallel to the dominant orientations of cooling joints in the Tiva Canyon Tuff, of which the two most prominent sets have orthogonal northeasterly and northwesterly strikes (Sweetkind and Williams-Stroud, 1996). These faults likely have reactivated pre-existing cooling joints, a conclusion that is supported by the presence of thin (1 cm thickness) tabular tectonic breccia bodies along cooling joints (Sweetkind, Verbeek, Singer et al., 1995). Strain between the discrete fault strands appears to be accommodated either by distributed brecciation, or by incremental movements along numerous pre-existing cooling joints (Potter et al., 1995; Potter et al., 1996; Sweetkind et al., 1996).

The following maps of surface geology, infiltration, and soil thickness (Figures D-3 through D-8) depict the structural setting of the samples collected in the ESF for  $^{36}\text{Cl}$  analysis by placing them in the context of mapped surface and subsurface geology and the modeled spatial distribution of surface infiltration. Chlorine-36 sample locations in the ESF are plotted as symbols on these maps, and the  $^{36}\text{Cl}/\text{Cl}$  ratios are classified qualitatively in the following categories:

- water containing bomb-pulse  $^{36}\text{Cl}$ :  $^{36}\text{Cl}/\text{Cl}$  ratios greater than  $1250 \times 10^{-15}$ , shown by solid blue triangles plotted on the side corresponding to the left rib of the ESF trace;
- possibly old "stagnant" water, as indicated by samples with ratios less than  $350 \times 10^{-15}$ , shown by gray diamonds plotted on the left rib of the ESF trace; and
- intermediate values: all other ratios, plotted as open triangles on the right rib of the ESF trace.

Surface geology is from 1:6000 scale mapping of Day et al. (in press). Faults with one meter or more of displacement are shown on the surface maps. Subsurface geologic mapping of the exploratory studies facility (ESF), was carried out between 1993 and 1997 at a scale of 1:125. In the ESF, structural features with offset of 10 cm or more are classified as faults. Features with less than 10 cm offset are referred to as shears.

The following subsections focus on providing a more detailed overview of the structural features in and above the ESF, and modeled spatial distribution of surface infiltration in specific areas corresponding to the spatial coverage of each of the geologic maps in figures D-3 through D-8:

Figure D-3. Azreal Ridge area	ESF Stations 0+00 to 18+00
Figure D-4. Drill Hole Wash/Diabolus Ridge area	ESF Stations 18+00 to 30+00
Figure D-5. Sundance Fault area	ESF Stations 30+00 to 40+00
Figure D-6. Antler Ridge/Whale Back Ridge area	ESF Stations 40+00 to 54+00
Figure D-7. Ghost Dance Wash area	ESF Stations 54+00 to 69+00
Figure D-8. Boundary Ridge area	ESF Stations 69+00 to 78+77

An explanation of stratigraphic units and map symbols used on all of the maps in figures D-3 through D-8 is provided in figure D-2.

### D3. Azreal Ridge area (Station 0+00 to 18+00)

The principal structural features along the first 1800 m of the North Ramp of the ESF include the block-bounding Bow Ridge fault at Station 2+00 and a series of steeply dipping faults at the eastern end of Azreal Ridge, approximately between stations 5+50 and 8+00 (Figure D-3a). The Bow Ridge fault is a major down-to-the-west normal fault having approximately 100 m displacement. In the ESF (40 m beneath the surface), the fault is a 2-m wide zone that dips approximately 60 degrees to the west and contains sand to gravel-size fault gouge (Beason et al., 1996). West of the Bow Ridge fault are north- and northwest-striking faults, which have normal displacement both down-to-the-west and down-to-the east. These faults are the result of hanging-wall deformation associated with the Bow Ridge fault (Day et al., in press). The eastern-most faults exposed in this zone are east-dipping down-to-the-east normal faults that form a graben or series of grabens, in the hanging-wall of the Bow Ridge fault buried beneath the alluvial cover to the west of Exile Hill. Faults in the western part of this zone, between boreholes USW NRG-3 and USW NRG-4 (Figure D-3a), have northeast-, north- and northwest strikes. Many of these faults are characterized by wide zones of rock breakage with numerous fault splays at the surface that merge into more discrete, narrower fault zones at depth (Day et al., in press). Nearly all of the faults with offset greater than 4 m may be correlated with a fault mapped in the ESF (Barr et al., 1996). In contrast to the relatively high density of faulting at the eastern end of Azreal Ridge (Figure D-3a), the western portion of Azreal Ridge is cut by only a few minor northeast-trending faults that are dominantly downthrown to the west (Figure D-4a).

Between the north portal of the ESF (at Station 0+00) and Station 18+00, 67 samples have been collected for  $^{36}\text{Cl}$  analysis (Appendix A), for which 71 analyses are available (Appendix B). Of

the analyses, 10 were systematic samples, 22 were from samples of subunit contacts, 36 were from samples of specific features, and 3 were from samples collected for other objectives. Of the analyzed samples, 12 samples have  $^{36}\text{Cl}/\text{Cl}$  ratios above  $1250 \times 10^{-15}$  and are interpreted to contain bomb-pulse  $^{36}\text{Cl}$ , 4 samples have slightly lower ratios that range between  $1000 \times 10^{-15}$  and  $1250 \times 10^{-15}$ , and the remaining samples have  $^{36}\text{Cl}/\text{Cl}$  ratios that range between  $350 \times 10^{-15}$  and  $1000 \times 10^{-15}$ . The samples collected along the North Ramp of the ESF that have elevated  $^{36}\text{Cl}/\text{Cl}$  ratios indicating a component of bomb-pulse  $^{36}\text{Cl}$  have a general spatial association with the numerous faults that cut the east end of Azreal Ridge (Figure D-3a). In detail, however, local control on the distribution of bomb-pulse  $^{36}\text{Cl}$  from samples in PTn-equivalent rock units appears to be controlled by stratigraphy, not structural features. Nine faults have been sampled within the interval where PTn-equivalent rock units are exposed in the North Ramp between ESF stations 7+70 to about 12+00. Fault offset ranges from 0.1 m to 18 m. None of the sampled features have unambiguous bomb-pulse levels of  $^{36}\text{Cl}$ . The only samples in this interval that have elevated  $^{36}\text{Cl}/\text{Cl}$  ratios indicating a component of bomb-pulse  $^{36}\text{Cl}$  are samples collected at unit contacts; three samples are from the welding transition near the top of the crystal-rich vitric zone of the Topopah Spring Tuff at about Station 10+56, and one is from the base of the Pah Canyon Tuff at about Station 8+90 (Fabryka-Martin et al., in review). Bomb-pulse  $^{36}\text{Cl}$  may be present in other samples from this zone, but the  $^{36}\text{Cl}/\text{Cl}$  ratios are less than the threshold value of  $1250 \times 10^{-15}$  that has been used to indicate the unambiguous presence of bomb-pulse  $^{36}\text{Cl}$ .

The closest faults to the bomb-pulse sample collected at Station 8+90 are about 3 m away. One fault has between 0.4 and 0.8 m of west-side down offset and occurs at the ESF crown at Station 8+90 and at Station 8+93 on the left springline. A second nearby fault occurs at 8+94 on the left springline and has 0.15 m east-side down offset. These two faults are part of a faulted interval that extends from Station 8+90 to Station 9+40. In this 50-m interval, there is at least 5.5 m of aggregate west-side down offset; total offset would be even higher except for the effect of antithetic offsets on east-side down faults in this interval. This offset is not portrayed on the North Ramp cross section (Drawing OA-46-195 in Barr et al., 1996), but is shown in figure 5 of Barr et al. (1996) as an increased frequency of faults with less than 4 meters offset in the interval from Station 8+20 to Station 11+20. The nearest fault to the samples at Station 8+90 that correlates with a fault mapped at the surface is at ESF station 8+45. This fault has an orientation of N.  $29^\circ$  E./ $86^\circ$  W. (N.  $40^\circ$  E./ $84^\circ$  W. on the cross section) and a down-to-the-west displacement of 4 m. The closest fault to the bomb-pulse samples collected at Station 10+56 is around Station 10+41. This small fault has between 0.9 and 1 m of offset. This fault does not appear to correlate to any fault mapped at the surface; it differs by almost 90 degrees in strike direction from the nearest mapped surface fault, the upward-splaying fault east of USW NRG-4 (Figure D-3a).

All bomb-pulse sample locations are under zones of relatively high infiltration (Figure D-3b) and shallow soils (figure D-3c). Using the simple conceptual model presented in section 6.1, bomb-pulse  $^{36}\text{Cl}$  would be predicted at all these locations. The presence of bomb-pulse  $^{36}\text{Cl}$  would also have been predicted at approximately ESF stations 7+00 and 11+00. The measured  $^{36}\text{Cl}/\text{Cl}$  ratio

at Station 11+00 was greater than  $1000 \times 10^{-15}$ . If the conceptual model applies, this observation would suggest that a bomb-pulse component exists in samples with  $^{36}\text{Cl}/\text{Cl}$  ratios of less than  $1250 \times 10^{-15}$ . The ratio for the sample from Station 7+00 was slightly under  $600 \times 10^{-15}$ , a level at which any mixing of the bomb-pulse component is largely uncertain.

#### D4. Drill Hole Wash and Diabolus Ridge area (Station 18+00 to 30+00)

The Drill Hole Wash fault consists of two principal strands, one along the northeast edge of Drill Hole Wash, the other beneath the center of the wash (Figure D-4a). The northeastern trace of the fault was intersected in borehole UE25a#4 (Spengler and Rosenbaum, 1980), and probable related faults are mapped at the surface at the base of the south-facing slope of Azreal Ridge near the USW NRG-5 drill pad (Figure D-3a) (Day et al., in press). In the ESF, the northeastern trace of the fault is observed as two subparallel northwest-striking faults between ESF stations 19+01 and 19+42 (Barr et al., 1996). These faults produce a total west-side down offset of about 4 m in the ESF and also have subhorizontal slickensides that indicate a dextral sense of offset. The southwestern strand of the Drill Hole Wash fault runs beneath the center of the wash along most of its length; it is exposed in bedrock northwest of borehole USW H-1 (Figure D-5a) (Day et al., in press). At this location, the Tiva Canyon Tuff is displaced 15 m down-to-the-southeast by several discontinuous fault splays (Figure D-5a); the amount of stratigraphic throw decreases abruptly in both directions from these outcrops. The southwestern strand of the Drill Hole Wash fault is exposed in the ESF at Station 22+65, 400 m to the southeast of the bedrock exposures. As exposed in the ESF, this fault is an open, uncemented breccia zone about 2-m wide that contains rotated blocks as much as 1-m long. In the ESF, the fault has an average strike of N.  $10^\circ$  W. and dips  $80^\circ$  to the southwest. Apparent offset across the zone is about 2 m down-to-the-southwest (Barr et al., 1996).

For the ESF interval between Station 18+00 and Station 30+00, 26 samples have been collected for  $^{36}\text{Cl}$  analysis (Appendix A), of which 28 analyses are available (Appendix B). Of the analyses, 6 were systematic samples and the remaining 22 were from specific features. Of the analyzed samples, 7 samples have  $^{36}\text{Cl}/\text{Cl}$  ratios above  $1250 \times 10^{-15}$  and are interpreted to contain bomb-pulse  $^{36}\text{Cl}$ , 3 samples have slightly lower ratios that range between  $1000 \times 10^{-15}$  and  $1250 \times 10^{-15}$ , and the remaining samples have  $^{36}\text{Cl}/\text{Cl}$  ratios that range between  $350 \times 10^{-15}$  and  $1000 \times 10^{-15}$ . Samples with elevated  $^{36}\text{Cl}$  ratios coincide with the northeastern splay of the Drill Hole Wash fault, but not the southwestern splay (Figure D-4a). The southwestern splay underlies deep alluvium in the center of Drill Hole Wash, where net infiltration is probably negligible (Figure D-4b) (Flint and Flint, 1995). In contrast, the northeastern splay underlies shallow soils at the base of the sideslope of Azreal Ridge, a location considered more favorable to net infiltration than the wash bottom (Flint and Flint, 1995). In detail, the pattern of  $^{36}\text{Cl}/\text{Cl}$  results from samples near the northeastern splay of the Drill Hole Wash fault is complicated, alternating between high and low values in the vicinity of the fault. The variation in  $^{36}\text{Cl}$  levels results from local controls that are not well understood, although abundant short-trace length fractures (less than 0.3 m) in the upper lithophysal zone of the Topopah Spring Tuff in this vicinity (Barr et al.,

1996; Sweetkind et al., 1997) may play a role in diverting flow away from the fault to the sample location showing bomb-pulse  $^{36}\text{Cl}$  at Station 18+96. Bomb-pulse  $^{36}\text{Cl}$  was not predicted to exist between ESF stations 19+00 and 20+00 (Figure 6-7). The modeled infiltration rate is too low (Figure D-4b) to meet the 2 mm/yr criterion for initiating and sustaining fracture flow through the PTn (Figure 6-7) even though the soil thickness was modeled to be between 0.5 and 3 m (Figure D-4c). However, lateral subsurface flow, which was not accounted for in the numerical infiltration model by Flint et al. (1996), would be likely to increase the infiltration at the margin of the wash directly over the fault (figure D-4a), thereby leading to the presence of bomb-pulse  $^{36}\text{Cl}$  at this location in the ESF.

The Diabolus Ridge fault is a locally prominent intrablock fault that produces about 7 m of west-side-down displacement of the base of the crystal-rich member of the Tiva Canyon Tuff at the crest of Diabolus Ridge about 250 m west of the projected trace of the ESF at the surface (Figure D-4a). Because the hanging wall has been translated upward relative to the footwall along the entire mapped trace, the Diabolus Ridge fault is a thrust fault (Day et al., in press). In cross section, the Diabolus Ridge fault has a 30 degree dip to the southeast (Figure 6-3). This gentle fault dip is based on: (1) three-point calculations from the mapped trace of the fault as it crosses Wren Wash; (2) the attitude of breccia zones observed along the trace of the fault at the surface; and (3) the intersection of a gently dipping fault by borehole USW SD-9 within poorly welded Yucca Mountain Tuff (Engstrom and Rautman, 1996). The dip may be even shallower where the trace of the fault hooks to the east-southeast on the northeast slope of Diabolus Ridge (Figure D-4a). The Diabolus Ridge fault crosses the topographically high ridge top that is capped by crystal-rich member of the Tiva Canyon Tuff, a setting considered to be favorable for high net infiltration (Flint and Flint, 1995; Flint et al., 1996). The projected location in the subsurface where this fault transects the PTn hydrogeologic unit lies almost directly above the ESF, where bomb-pulse  $^{36}\text{Cl}$  was detected in samples from Station 26+79 and Station 27+18. Bomb-pulse  $^{36}\text{Cl}$  at these locations may be the result of percolating waters moving eastward, down the plane of the Diabolus Ridge fault, through the PTn-equivalent rock units, and then percolating downward to the fracture network in the vicinity of the ESF. Again, local controls may be the cause of alternating high and low  $^{36}\text{Cl}$  values beneath the area where the fault transects the PTn hydrogeologic unit (Figure 6-3). Although modeled infiltration rates are high where the fault is exposed at the surface, rates are also high directly over the ESF (figure D-4b) where the soils are shallow (figure D-4c). Water percolating directly downward would reach the PTn in the faulted zone and percolate through the TSw in the vicinity of the ESF. Bomb-pulse  $^{36}\text{Cl}$  was not predicted at this location (figure 6-7) because the conceptual model assumes that faults exposed at the surface are vertical or near vertical (section 6.5).

At a nearby sample site (Station 24+40), a fault with 1.5 to 2 m of offset cuts the upper lithophysal zone of the Topopah Spring Tuff (Figure D-4a). No corresponding fault is mapped at the surface (Day et al., in press). Although it is unknown how far upsection the Station 24+40 fault extends, it does not offset the lower lithophysal zone of the Tiva Canyon Tuff at the surface (Day et al., in press). There are several examples of mapped faults that can be documented to be

pre-Tiva Canyon Tuff in age because fault displacement dies out within lithostratigraphic units equivalent to the PTn hydrogeologic unit or within the lower portions of the Tiva Canyon Tuff (Day et al., in press). Given the presence of bomb-pulse  $^{36}\text{Cl}$  along the fault plane, the fault at Station 24+40 may be a pre-Tiva Canyon Tuff fault that offsets the base of the section equivalent to the PTn hydrogeologic unit.

#### **D5. Vicinity of the Sundance fault (Station 30+00 to 40+00)**

The northwest-striking Sundance Fault zone can be traced for about 750 m in the northern part of the central block, from Dead Yucca Ridge to Live Yucca Ridge (Figure D-5a). The vertical to steeply east-dipping faults in this zone are almost exclusively characterized by northeast-side-down displacement. The maximum width of the Sundance Fault zone in surface exposures is about 75 meters and the cumulative northeast-side-down vertical displacement across the fault zone does not exceed 11 m (Potter et al., 1995). Even though some horizontal slickensides have been observed, significant strike-slip displacement along the Sundance Fault zone is not suggested by the field relations (Potter et al., 1995). Individual fault strands within the Sundance fault zone are discontinuous and stratigraphically controlled (Potter et al., 1995). On Purgatory Ridge and Dead Yucca Ridge (Figure D-5a), several strands of the Sundance Fault comprise a 25- to 70-m-wide zone at the top of the middle nonlithophysal zone of the Tiva Canyon Tuff (Tcpmn, Figure D-5a), low on the south-facing slopes (Potter et al., 1995). On both ridges, only one fault strand continues up into the crystal-rich member of the Tiva Canyon Tuff at the top of the ridge, with the displacement accomplished by this single strand being subequal to the cumulative displacement across the broader fault zone that cuts the top of the middle nonlithophysal zone. Potter et al. (1995) related the stratigraphically controlled faulting style within the Sundance fault zone to the relative frequency of cooling joints in various lithostratigraphic zones of the Tiva Canyon Tuff, with broader areas of deformation occurring in lithostratigraphic zones where cooling joints were more numerous. The lack of vertical continuity of individual fault strands through the different stratigraphic levels requires strain between the discrete fault strands be accommodated, probably either by distributed brecciation, or by incremental movements along numerous pre-existing cooling joints (Potter et al., 1996; Sweetkind et al., 1996).

The ESF passes beneath the southeastern end of the Sundance Fault zone as mapped by Potter et al. (1995), where displacement is minimal on the south flank of Live Yucca Ridge. The discontinuous northwest-striking fault identified as the Sundance Fault in the ESF is located near Station 36+00 (Albin et al., 1997). This fault has a strike of N. 25° W. and dips 84 degrees to the west. The amount and sense of offset along this fault is unknown, and there are subhorizontal mullion structures and slickenlines developed on the polished fault surface. This specific fault is part of the distributed faulting that characterizes the northwest-striking Sundance fault zone (Potter et al., 1995), but is probably not directly correlative with the principal strand of the Sundance Fault as mapped at the surface because: (1) the fault observed in the ESF occurs approximately 50 m north of where the main trace of the Sundance Fault would project to the

ESF; and (2) the fault observed in the ESF dips to the west. In the North Ghost Dance Test Alcove (labeled as Alcove 6, Figure D-5a), the Sundance Fault is identified within a broad zone of discontinuous minor northwest-striking faults and joints in the middle nonlithophysal zone of the Topopah Spring Tuff, similar in character to the fault zone mapped at the surface near its southeastern termination on the south-facing slope of Live Yucca Ridge (Potter et al., 1995; Day et al., in press).

For the ESF interval between Station 30+00 and Station 40+00, 33 samples have been collected for  $^{36}\text{Cl}$  analysis (Appendix A), for which 34 analyses are available (Appendix B). Of the analyses, 4 were systematic samples and the remaining 30 were from specific features. Of the analyzed samples, 11 samples have  $^{36}\text{Cl}/\text{Cl}$  ratios above  $1250 \times 10^{-15}$  and are interpreted to contain bomb-pulse  $^{36}\text{Cl}$ , 2 samples have slightly lower ratios that range between  $1000 \times 10^{-15}$  and  $1250 \times 10^{-15}$ , and the remaining samples have  $^{36}\text{Cl}/\text{Cl}$  ratios that range between  $350 \times 10^{-15}$  and  $1000 \times 10^{-15}$ . Sample locations in the ESF that show evidence of bomb-pulse  $^{36}\text{Cl}$  in the general vicinity of the Sundance fault comprise a 300-m zone along the ESF (Figure D-5a). The Sundance fault is the only structure mapped at the surface in this vicinity (Potter et al., 1995; Day et al., in press) that could provide a continuous structural pathway through the PTn hydrogeologic unit. Thus, the broad zone of elevated  $^{36}\text{Cl}/\text{Cl}$  values north of Station 36+00 in the ESF may represent lateral flow away from the plane of the fault (Levy et al., 1997). The Sundance fault is one of the few faults in the northern part of the central block that crosses topographically high ridgetops (Purgatory Ridge and Dead Yucca Ridge) capped by the crystal-rich member of the Tiva Canyon Tuff, a setting projected to be favorable for high net infiltration (Flint and Flint, 1995, Flint et al., 1996).

Generally high infiltration rates are modeled at the surface in the location of the Sundance fault and over much of the ESF in the vicinity of the samples with measured bomb-pulse  $^{36}\text{Cl}$  locations (figure D-5b). Low infiltration rates are predicted near station 35+50 because of the exposure of the low-permeability Tcpll (figure D-5a) even though the soils are thin throughout this zone (figure D-5c). The infiltration rate in the general area is sufficiently high to expect bomb-pulse  $^{36}\text{Cl}$  between station 34+00 and station 36+00 (figure 6-7). The occurrence of  $^{36}\text{Cl}$  away from the fault would support a change to enhance the down slope component to the conceptual predictive model (section 6.5) if the bomb-pulse  $^{36}\text{Cl}$  entered the TSw directly in the Sundance fault zone and then flowed laterally through the fracture network.

#### **D6. Antler Ridge-Whale Back Ridge area (Station 40+00 to 54+00)**

Where the ESF traverses the portion of the central block between Antler Ridge and Whale Back Ridge (Figure D-6a), there are no major faults that have been mapped at the surface or in the subsurface that cross the trace of the ESF. Except for the Ghost Dance fault, the faults in this area have maximum trace lengths of about 200 m, and commonly much less.

In the ESF, there is an intensely fractured zone that extends from approximately Station 42+00 to 51+50 where the overall fracture frequency within the middle nonlithophysal zone of the crystal-poor member of the Topopah Spring Tuff is more than double the frequency observed elsewhere in the ESF (Albin et al., 1997). Within this intensely fractured zone, a northwest striking set, oriented N. 67° W. to N. 34° W., dominates all other joint sets. These joints are smooth, with manganese-oxide coatings and some vapor-phase mineralization, indicating that they originated at least in part as cooling joints (Albin et al., 1997).

For the ESF interval between Station 40+00 and Station 54+00, 27 samples have been collected for  $^{36}\text{Cl}$  analysis (Appendix A), for which 29 analyses are available (Appendix B). Of the analyses, 7 were systematic samples and the remaining 22 were from specific features. Of the analyzed samples, 3 samples have  $^{36}\text{Cl}/\text{Cl}$  ratios above  $1250 \times 10^{-15}$  and are interpreted to contain bomb-pulse  $^{36}\text{Cl}$ , 1 sample has a slightly lower ratio within the range between  $1000 \times 10^{-15}$  and  $1250 \times 10^{-15}$ , 23 samples have  $^{36}\text{Cl}/\text{Cl}$  ratios that range between  $350 \times 10^{-15}$  and  $1000 \times 10^{-15}$ , and the remaining 2 samples have low  $^{36}\text{Cl}/\text{Cl}$  ratios below  $350 \times 10^{-15}$ . These low ratios are being investigated to evaluate whether or not they are valid indications that the average water travel times to these locations may be sufficiently long to show effects of radioactive decay of its meteoric  $^{36}\text{Cl}$  signal (i.e., on order of  $10^5$  years).

Three samples (between Stations 43+00 and 45+00) analyzed for  $^{36}\text{Cl}$  from near the beginning of the intensely fractured zone have elevated  $^{36}\text{Cl}/\text{Cl}$  ratios that indicate a component of bomb-pulse  $^{36}\text{Cl}$  (Figure D-6a). None of the three sample localities correspond to mapped faults in the surface or subsurface, nor does fracture frequency vary significantly from other highly fractured portions of this zone (Albin et al., 1997). If the fault inferred to underlie Antler Wash southeast of borehole USW H-4 (Day et al., in press) were projected about 850 m to the northwest, the three samples would lie in the general vicinity of where the fault would be projected to cross the ESF. However, no northwest-striking fault is mapped in the ESF between about Station 42+00 and 45+00, and map relations suggest that offset along this inferred structure decreases to zero northwest of borehole USW H-4 (Figure D-6a; Day et al., in press). Infiltration is low (figure D-6b), except near ESF station 45+00, and the soils are thin (figure D-6c). In the absence of a fault, no bomb-pulse  $^{36}\text{Cl}$  would be predicted in this area (figure 6-7). As yet, the presence of elevated  $^{36}\text{Cl}$  at these three localities remains unexplained.

#### **D7. Ghost Dance Wash-Dune Wash area (Station 54+00 to 69+00)**

The Ghost Dance fault bifurcates south of Broken Limb Ridge (Figure D-7a). Although there are two principal fault splays, the fault zone in detail is made up of numerous fault splays that both parallel the main north-striking trace of the zone and branch off the main fault laterally and vertically (Day et al., in press). The Ghost Dance fault in the vicinity of Highway Ridge and in the Ghost Dance Wash area (Figure D-7a) dips steeply to the west and has a west-side down displacement of less than 3 m, both on the surface (Day et al., in press) and in the ESF (Albin et

al., 1997). The zone of fracturing and brecciation associated with the fault in the ESF at about Station 57+30 is about 2 m wide (Sweetkind et al., 1997).

The Dune Wash Fault is exposed in the ESF near Station 67+88. Offset on the Dune Wash Fault is 65 m at this latitude, although offset increases to the south (Day et al., in press). The zone of increased fracture frequency in the vicinity of the fault is 6-7 m wide (Sweetkind et al., 1997). The area around the southern turn of the ESF is characterized by numerous closely spaced minor faults that coalesce and gain displacement to the south (Figure D-7a).

For the ESF interval between Station 54+00 and Station 69+00, 46 samples have been collected for  $^{36}\text{Cl}$  analysis (Appendix A), for which 50 analyses are available (Appendix B). Of the analyses, 15 were systematic samples, 3 were from samples of subunit contacts, 31 were from samples of specific features, and 1 was collected for other objectives. Of the analyzed samples, there are no samples that have  $^{36}\text{Cl}/\text{Cl}$  ratios above  $1250 \times 10^{-15}$  and only one sample has a slightly lower ratio that falls within the range between  $1000 \times 10^{-15}$  and  $1250 \times 10^{-15}$ , 43 samples have  $^{36}\text{Cl}/\text{Cl}$  ratios that range between  $350 \times 10^{-15}$  and  $1000 \times 10^{-15}$ , and there are 6 samples with low  $^{36}\text{Cl}/\text{Cl}$  ratios below  $350 \times 10^{-15}$ . These low ratios are being investigated to evaluate whether or not they are valid indications that the average water travel times to these locations may be sufficiently long to show effects of radioactive decay of its meteoric  $^{36}\text{Cl}$  signal (i.e., on order of  $10^5$  years). None of the samples analyzed for  $^{36}\text{Cl}$  from this interval of the ESF have elevated  $^{36}\text{Cl}/\text{Cl}$  ratios that would unambiguously indicate a component of bomb-pulse  $^{36}\text{Cl}$ , although a distinct peak in the  $^{36}\text{Cl}/\text{Cl}$  profile at station 56+93 is suggestive of its possible presence here (Figure 6-1). Two damp zones were sampled within the PTn interval, one along a small fault that cuts the PTn-equivalent rock units, the other a moist zone parallel to a welding transition near the base of the crystal-poor vitric zone of the Tiva Canyon Tuff. None of the samples analyzed from the damp zones had elevated  $^{36}\text{Cl}/\text{Cl}$  ratios.

The physiographic character of this area is one of subdued ridges, broad, alluvium-filled washes, and very limited exposure of the crystal-rich member of the Tiva Canyon Tuff. In the vicinity where they are exposed in the ESF, both the Ghost Dance and Dune Wash faults underlie washes filled with alluvium of unknown thickness. However, the thickness of alluvium farther south in Dune Wash varies from 6 m to 15 m in boreholes USW UZ-N67, USW UZ-N68, and USW UZ-N69, all between 700 and 900 m south of the ESF South Ramp (Flint and Flint, 1995, Flint et al., 1996) (figure D-7c). In general, faults that underlie alluvium-filled washes are a location considered unfavorable for significant net infiltration (Flint and Flint, 1995, Flint et al., 1996) (figure D-7b) and, as a consequence, bomb-pulse  $^{36}\text{Cl}$  was not predicted throughout much of this area (Figure 6-7). The major exception is in the vicinity of ESF station 67+00. The reason for lack of bomb-pulse  $^{36}\text{Cl}$  in this vicinity is unclear and will be discussed in the next section.

#### D8. Boundary Ridge area (Station 69+00 to 78+77)

The Boundary Ridge area lies between the Dune Wash fault on the west and the Bow Ridge fault on the east (Figure D-8a). This area is characterized by an increased frequency of intrablock faulting, complex deformation in the hanging-wall of the Bow Ridge Fault, and northwest-trending structures resulting from the interaction of the two block-bounding faults (Day et al., in press). Faults in this area have trace lengths greater than 1 km, dip steeply, have north- and northwest-strikes, and have normal displacement both down-to-the-west and down-to-the east (Day et al., in press). There are several narrow (100 m wide), steep-walled, northwest-striking *en echelon* grabens in the Boundary Ridge area (Figure D-8a; Day et al., in press; Scott and Bonk, 1984). Within these grabens, stratigraphic units are locally displaced downward by as much as 30 m, although there is minimal aggregate offset of stratigraphic units on either side of the graben (Scott, 1990; Day et al., in press). Comparison of surface mapping (Day et al., in press) with geologic mapping in the ESF shows that these grabens are bounded by faults that dip toward the center of the graben.

For the ESF interval between Station 69+00 and Station 77+10, 35 samples have been collected for  $^{36}\text{Cl}$  analysis (Appendix A), for which 35 analyses are available (Appendix B). Of the analyses, 7 were systematic samples, 3 were from samples of subunit contacts, and the remaining 25 were from samples of specific features. Of the analyzed samples, there are no samples that have  $^{36}\text{Cl}/\text{Cl}$  ratios above  $1250 \times 10^{-15}$ ; in fact, there are no samples that have  $^{36}\text{Cl}/\text{Cl}$  ratios above  $600 \times 10^{-15}$ . Thirty-one samples have  $^{36}\text{Cl}/\text{Cl}$  ratios that range between  $350 \times 10^{-15}$  and  $600 \times 10^{-15}$ , and 4 samples have low  $^{36}\text{Cl}/\text{Cl}$  ratios below  $350 \times 10^{-15}$ . These low ratios are being investigated to evaluate whether or not they are valid indications that the average water travel times to these locations may be sufficiently long to show effects of radioactive decay of its meteoric  $^{36}\text{Cl}$  signal (i.e., on order of  $10^5$  years).

Despite the structural complexity in this part of Yucca Mountain, no analyzed samples from the ESF in this area appear to contain bomb-pulse  $^{36}\text{Cl}$ . The structures encountered in the ESF, however, mostly underlie a topographically low, alluvium-filled wash (left of center, Figure D-8c), a location considered unfavorable for significant net infiltration (Flint and Flint, 1995, Flint et al., 1996) (left of center, Figure D-8b). There are several locations where bomb-pulse  $^{36}\text{Cl}$  is predicted (figure 6-7) but was not detected (Figures D-8a and D-8b). On close observation (Figure D-8b), it appears that the few samples were collected hydrostratigraphically down-dip from the fault near ESF station 76+00 but that no samples were collected down-dip from the fault near station 77+40, two faults in higher infiltration zones. The lack of bomb-pulse  $^{36}\text{Cl}$  in zones predicted to contain bomb-pulse  $^{36}\text{Cl}$  cannot, at present, be explained, although it would appear that unfortuitous sampling may have missed the down-dip zones where bomb-pulse  $^{36}\text{Cl}$  may exist.

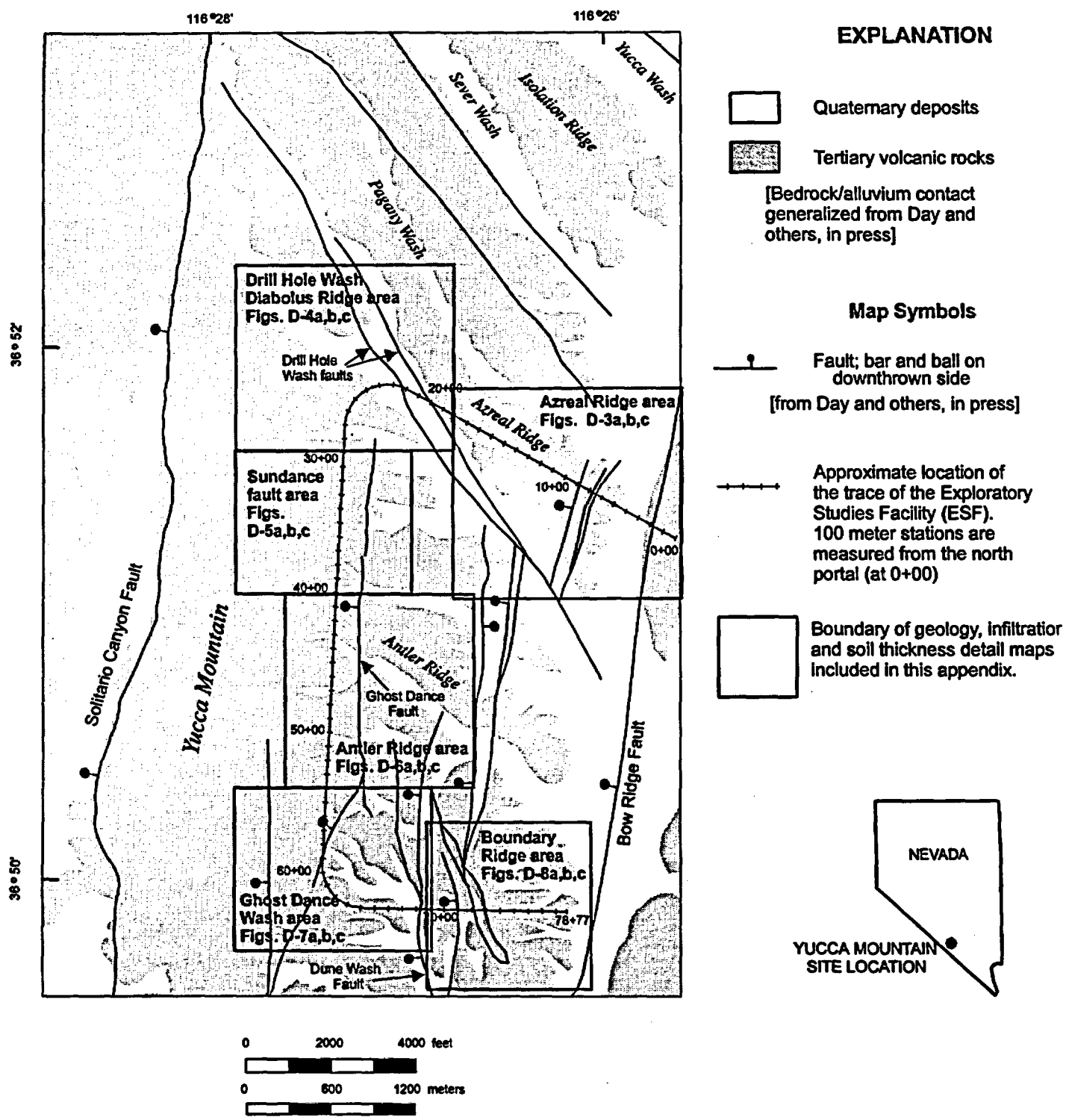


Figure D-1. Index map of central Yucca Mountain. Outlines of the detail maps in Appendix D are shown.

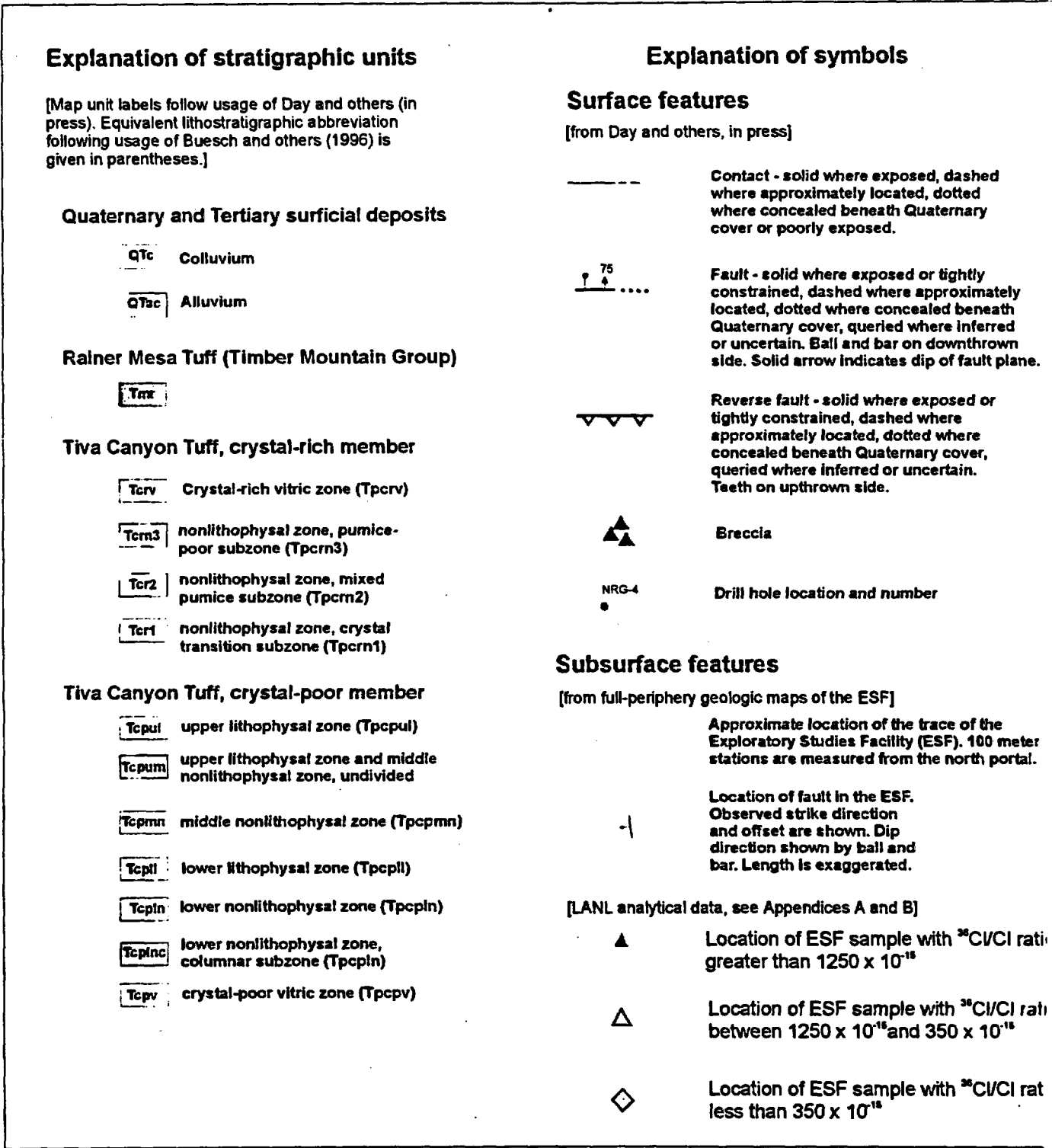


Figure D-2. Explanation of stratigraphic units and map symbols.



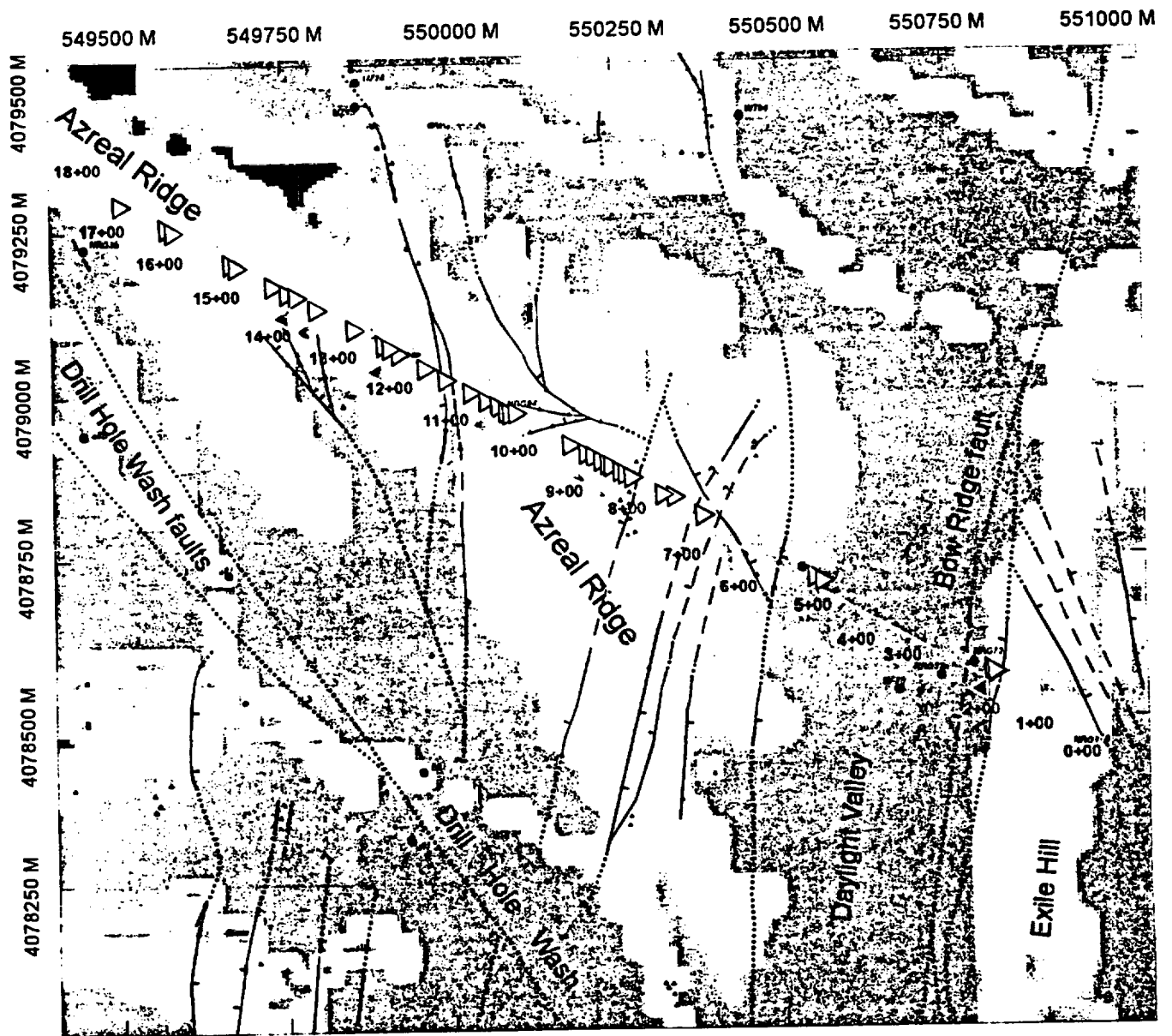


Figure D-3b. Conceptual model of infiltration in the Azreal Ridge area. Numerical model of infiltration, using average annual precipitation, from Flint and others (1996). Explanation of map symbols is given in figure D-2. Black areas have infiltration rates greater than 10 mm/yr.

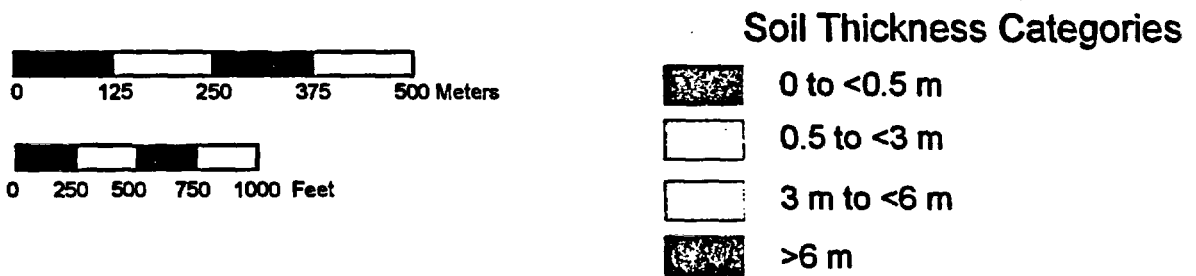
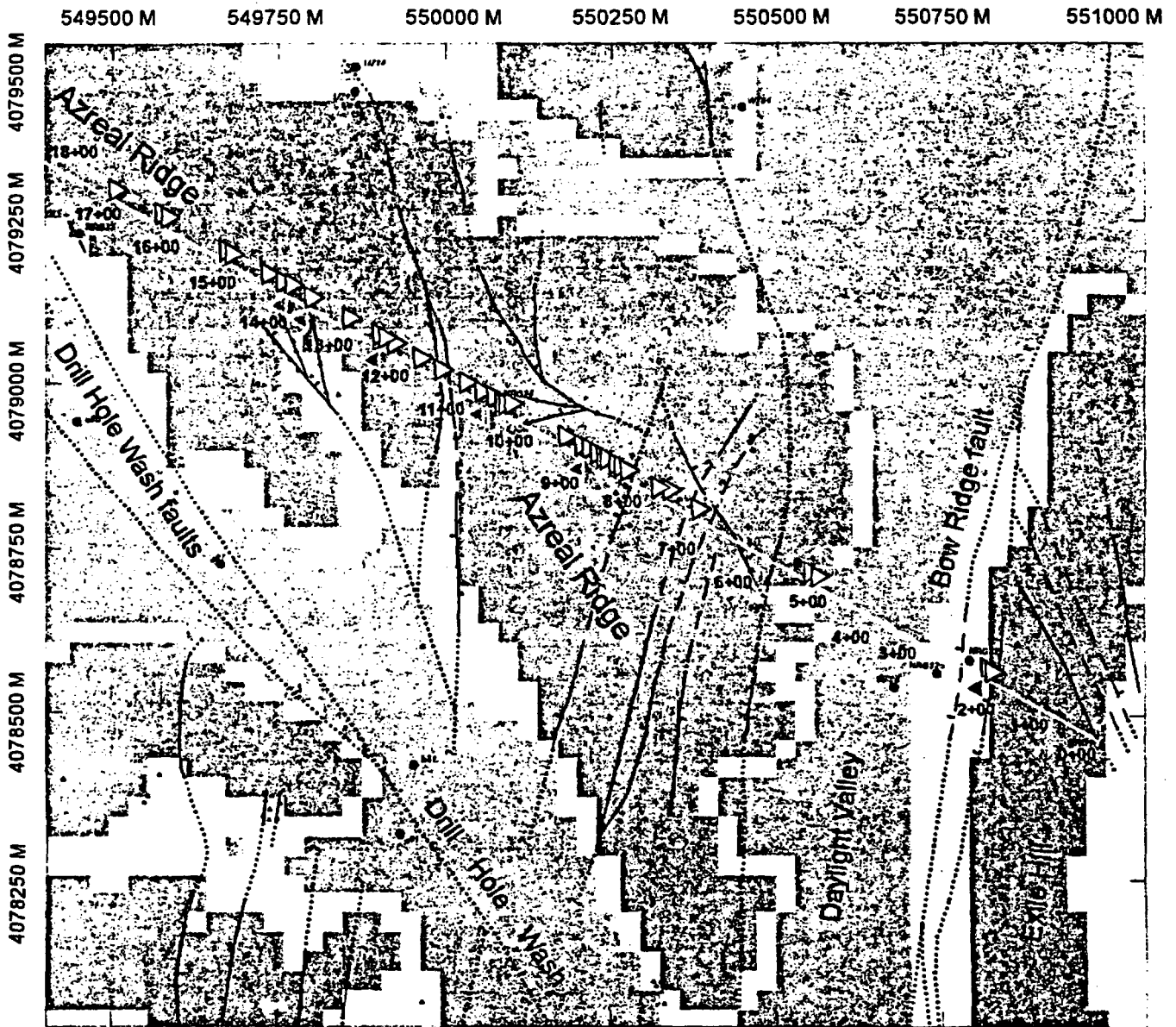


Figure D-3c. Map of soil thickness in the Azreal Ridge area. Soil thickness data as reported in Flint et al. (1996).



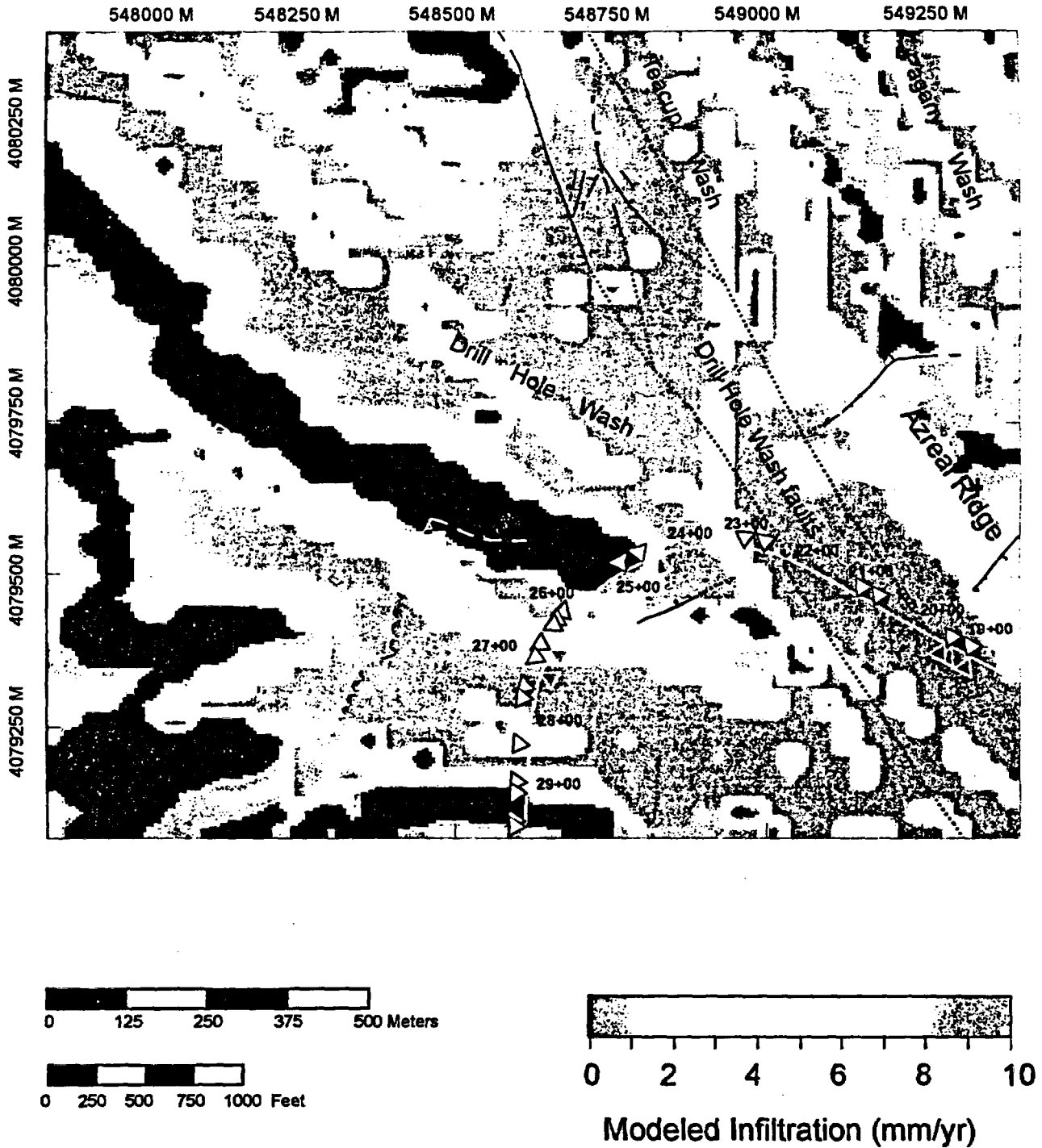
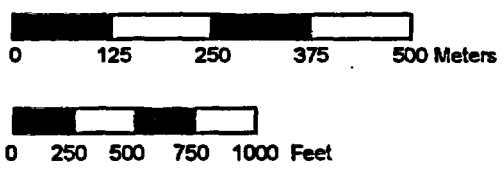
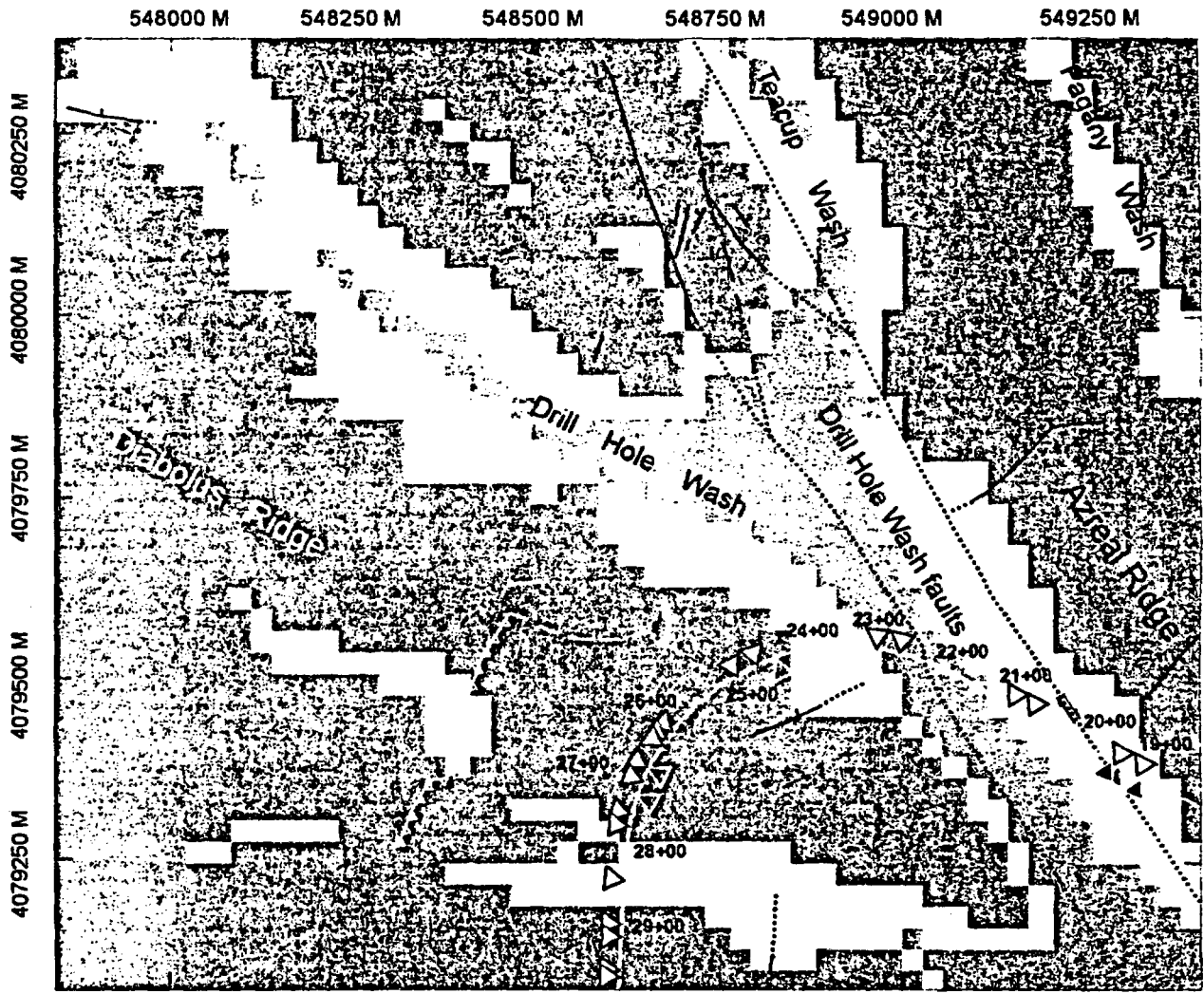


Figure D-4b. Conceptual model of infiltration for Drill Hole wash/Diabolus Ridge area. Numerical model of infiltration, using average annual precipitation, from Flint and others (1996). Explanation of map symbols is given in figure D-2. Black areas have infiltration rates greater than 10 mm/yr.



**Soil Thickness Categories**

-  0 to <0.5 m
-  0.5 to <3 m
-  3 m to <6 m
-  >6 m

Figure D-4c. Map of soil thickness in the Diabolus Ridge/Drill Hole Wash area. Soil thickness data as reported in Flint et al. (1996).

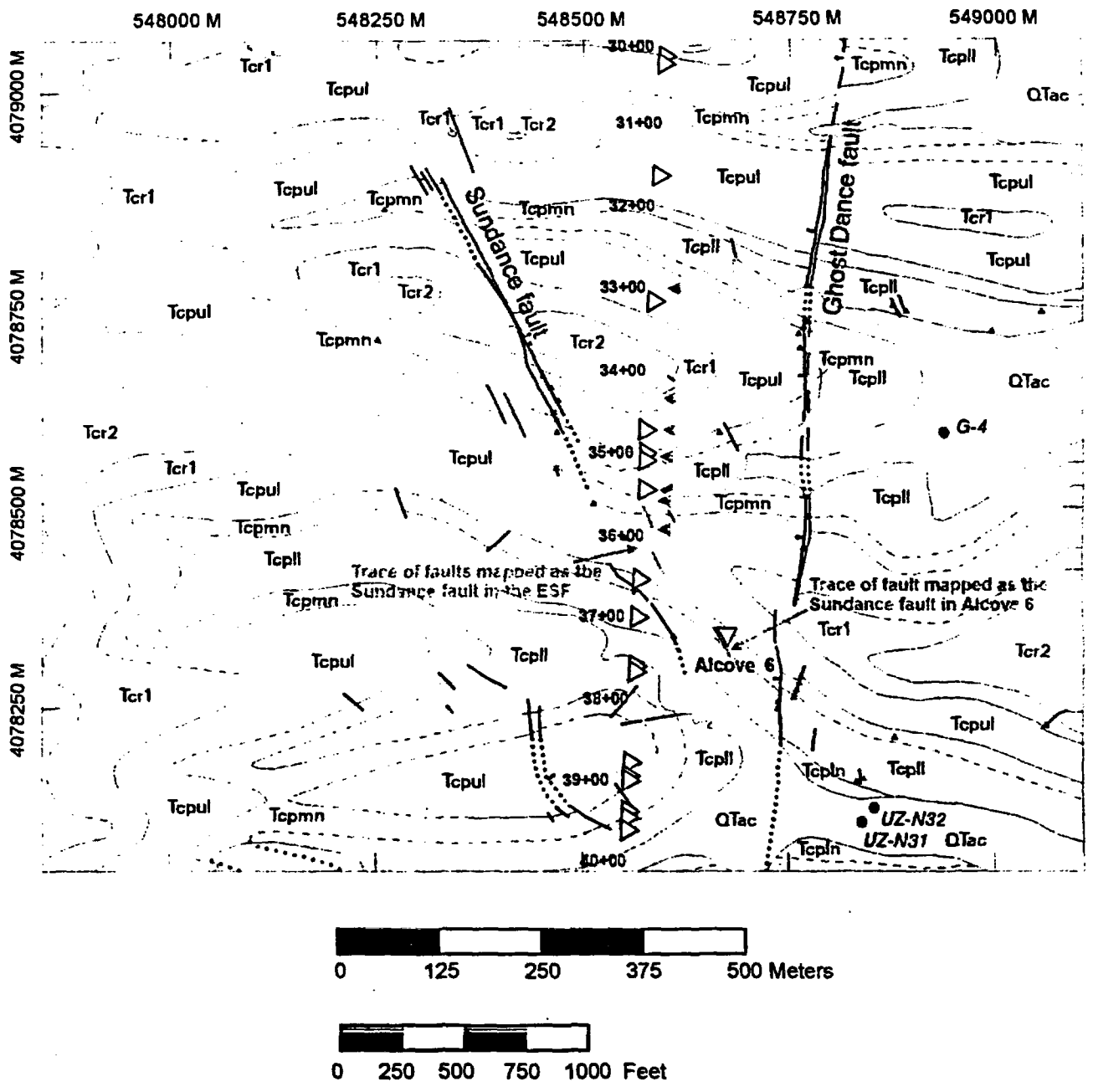
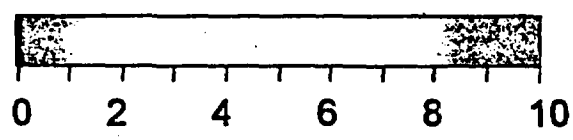
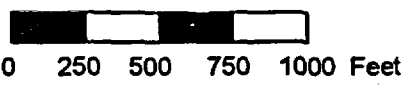
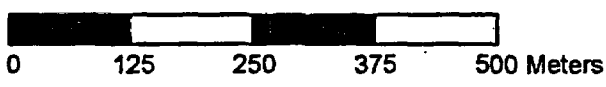
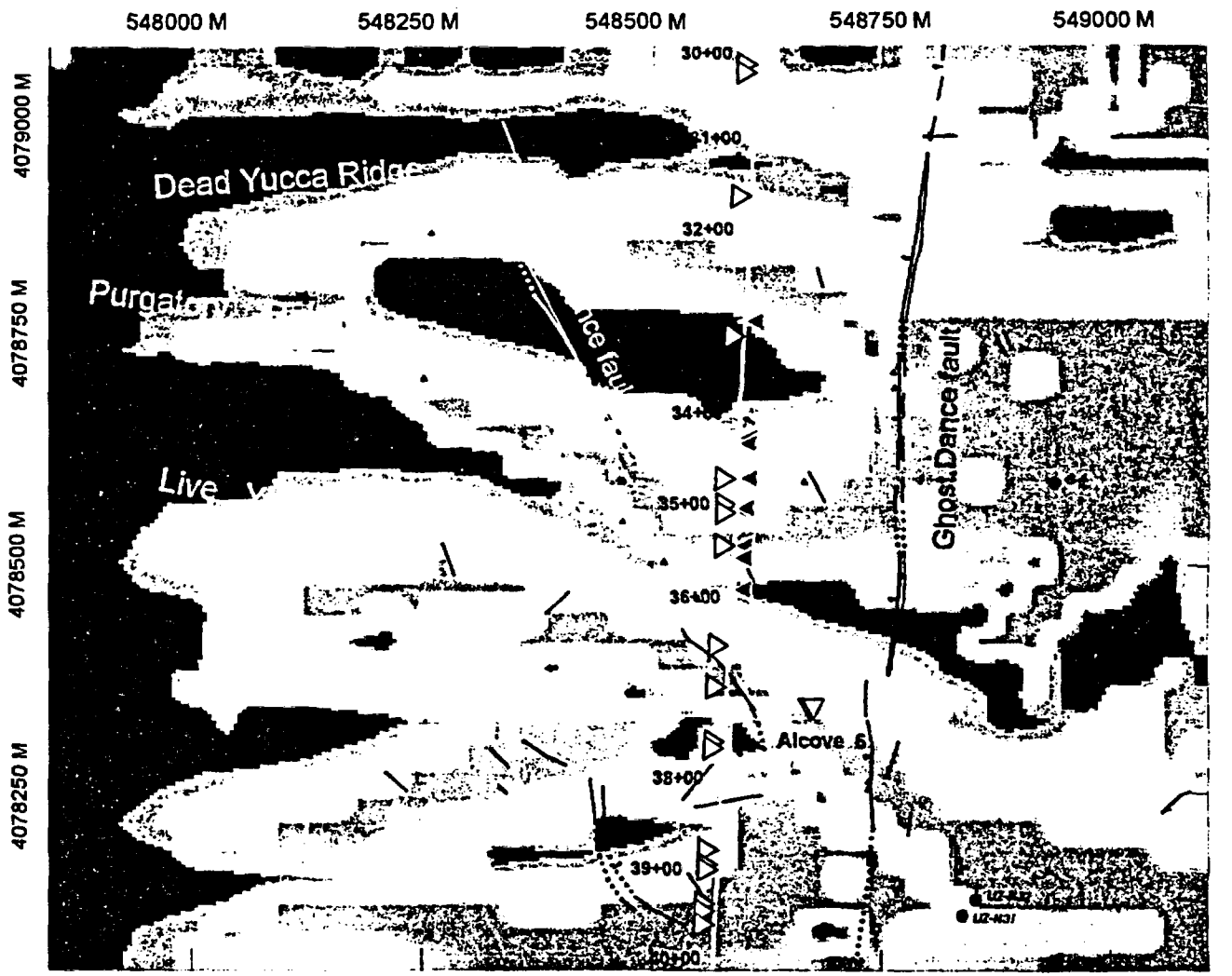
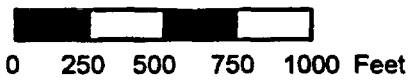
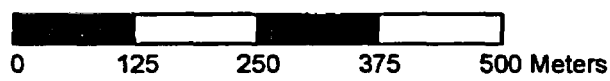
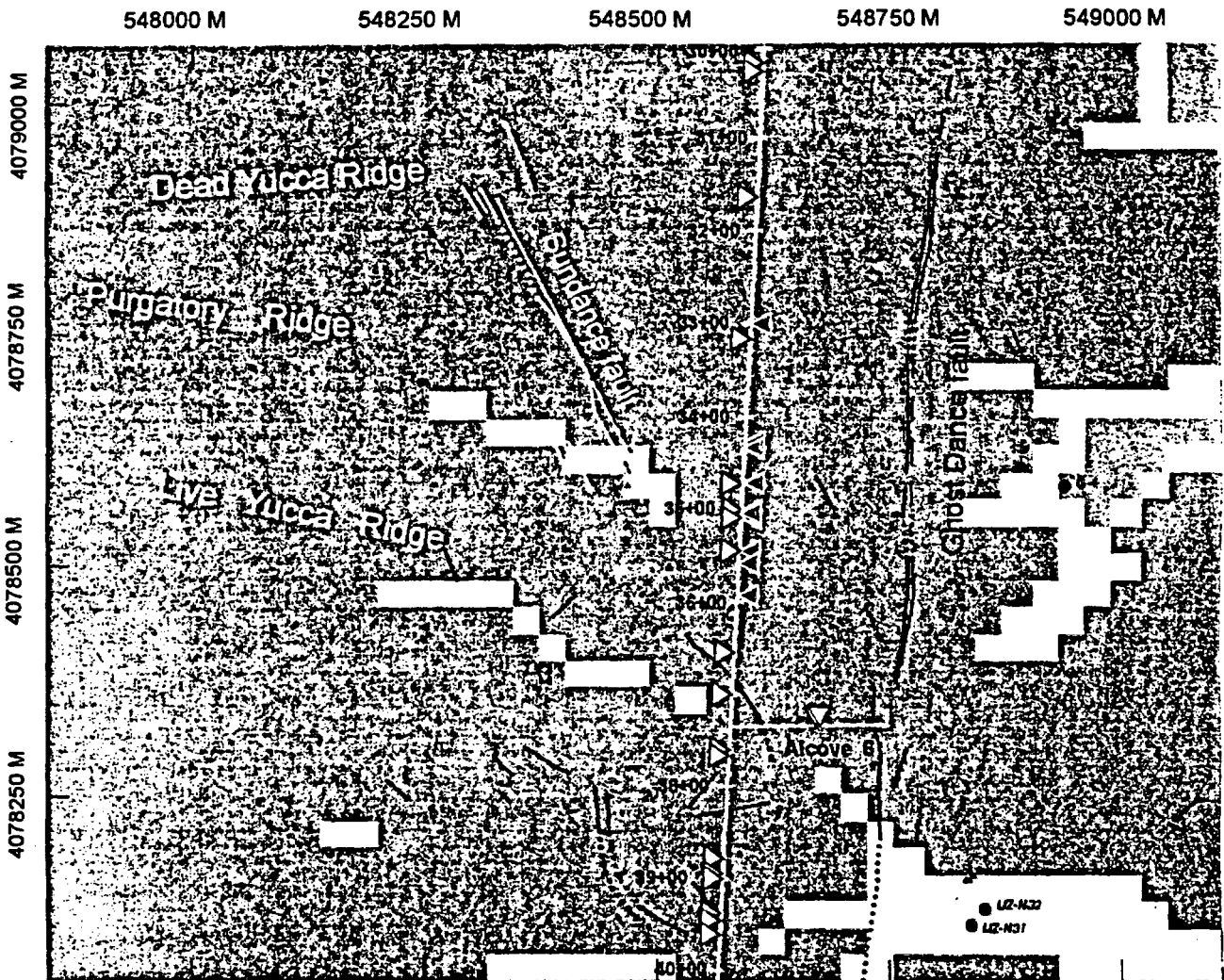


Figure D-5a. Geologic map in the vicinity of the Sundance fault. Explanation of stratigraphic units and map symbols is given in figure D-2.



Modeled Infiltration (mm/yr)

Figure D-5b. Conceptual model of infiltration in the vicinity of the Sundance fault. Numerical model of infiltration, using average annual precipitation, from Flint and others (1996). Explanation of map symbols is given in figure D-2. Black areas have infiltration rates greater than 10 mm/yr.



**Soil Thickness Categories**

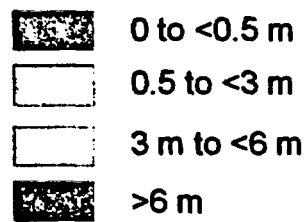


Figure D-5c. Map of soil thickness in the vicinity of the Sundance fault. Soil thickness data as reported in Flint et al. (1996).



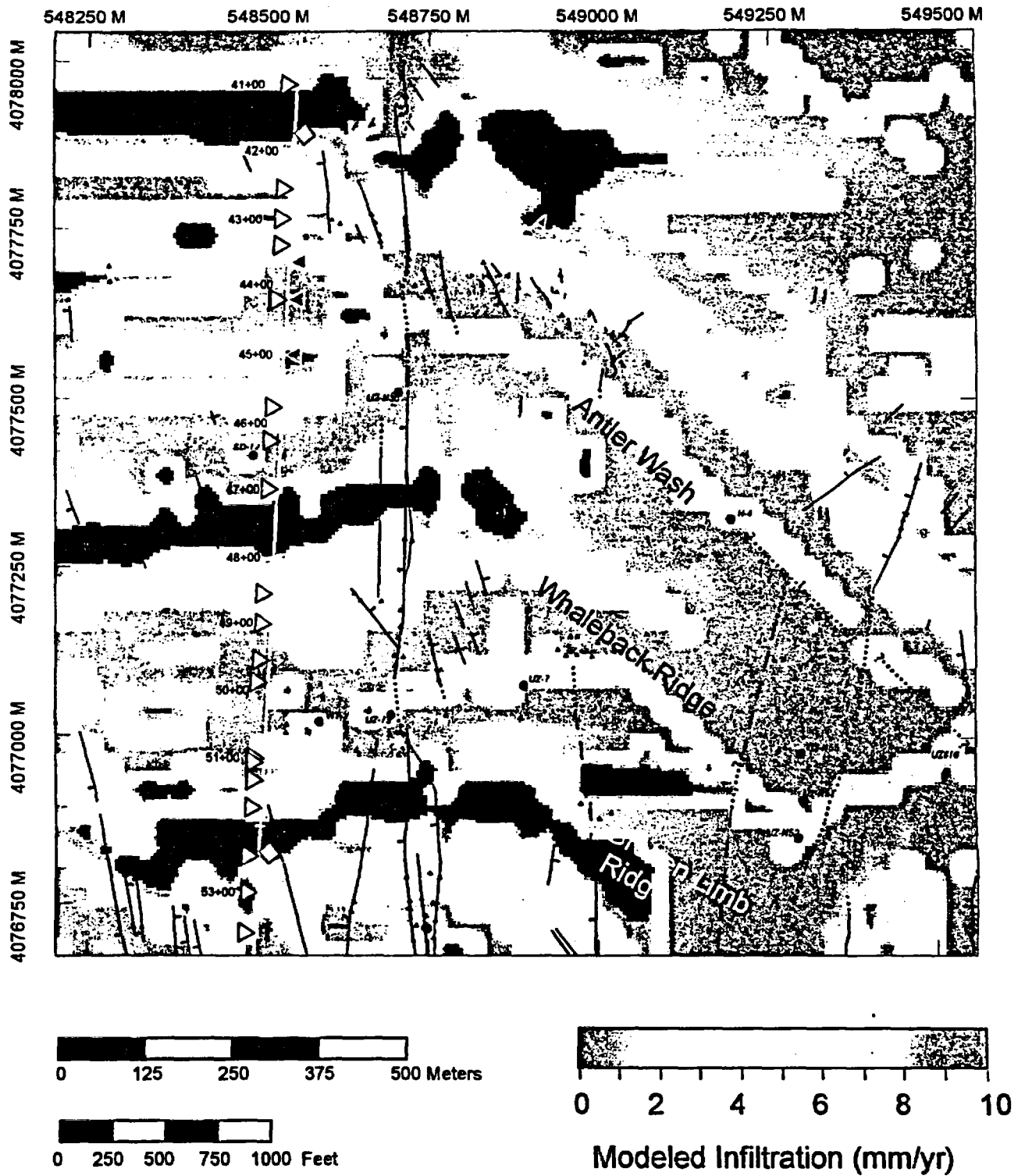


Figure D-6b. Conceptual model of infiltration in the Antler Ridge/Whale Back Ridge area. Numerical model of infiltration, using average annual precipitation, from Flint et al. (1996). Explanation of map symbols is given in figure D-2. Black areas have infiltration rates greater than 10 mm/yr.

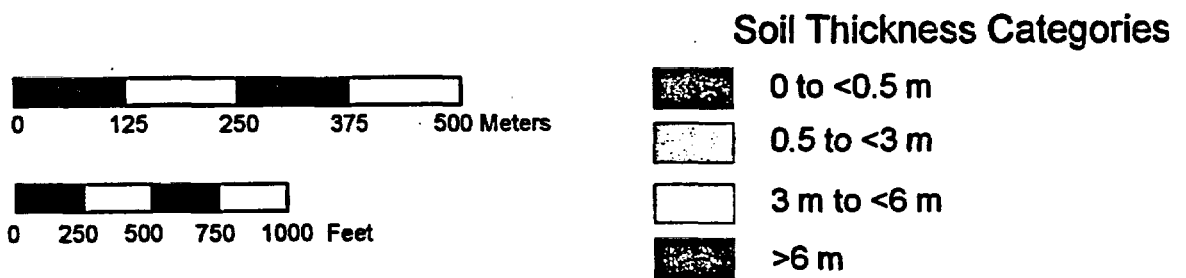
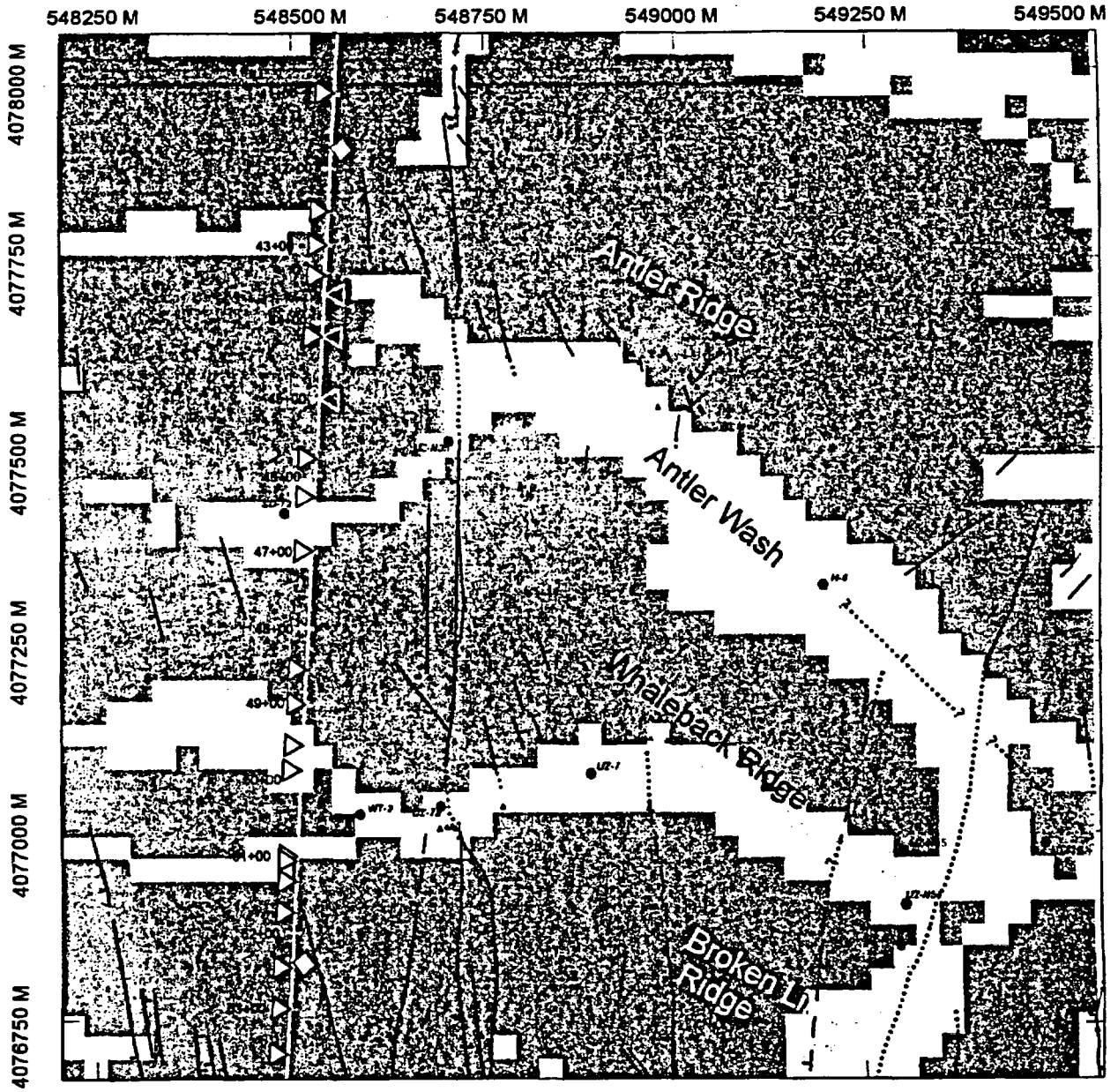


Figure D-6c. Map of soil thickness in the Antler Ridge area. Soil thickness data as reported in Flint et al. (1996).



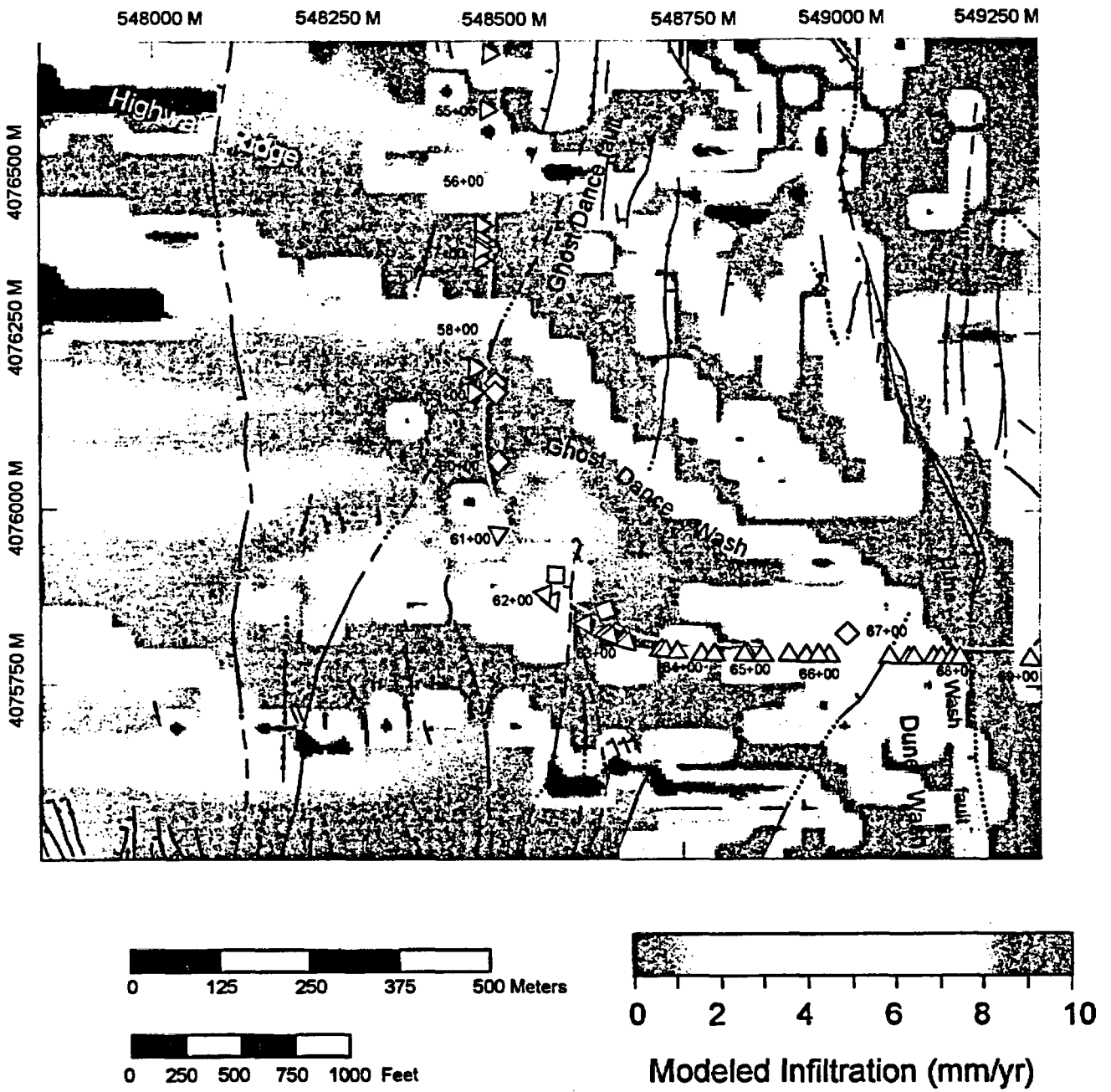
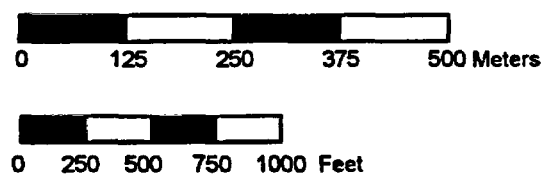
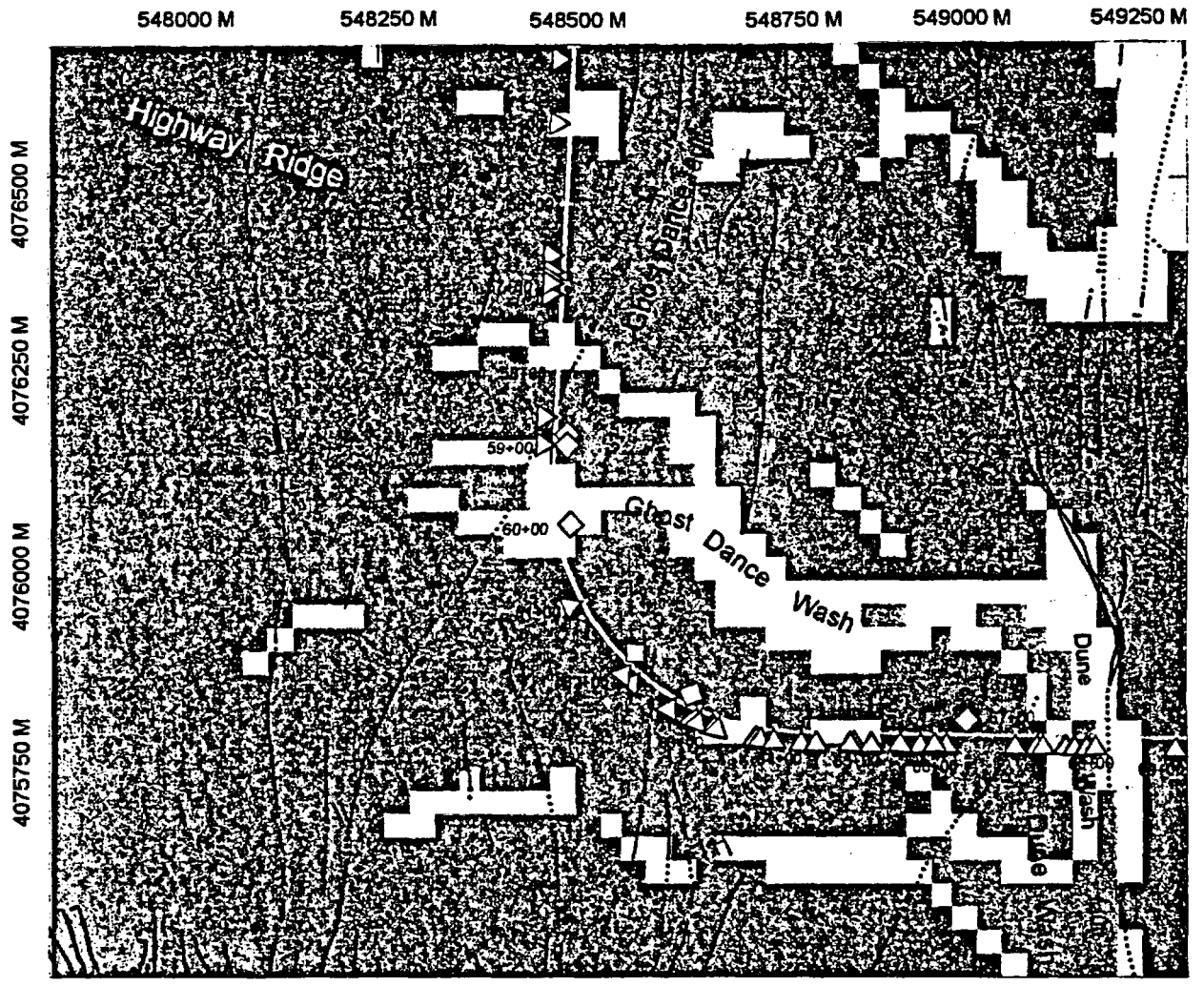


Figure D-7b. Conceptual model of infiltration in the vicinity of Ghost Dance Wash. Numerical model of infiltration, using average annual precipitation, from Flint et al. (1996). Explanation of map symbols is given in Figure D-2. Black areas indicate infiltration rates greater than 10 mm/yr.



**Soil Thickness Categories**

-  0 to <0.5 m
-  0.5 to <3 m
-  3 m to <6 m
-  >6 m

Figure D-7c. Map of soil thickness in the Ghost Dance Wash area. Soil thickness data as reported in Flint et al. (1996).



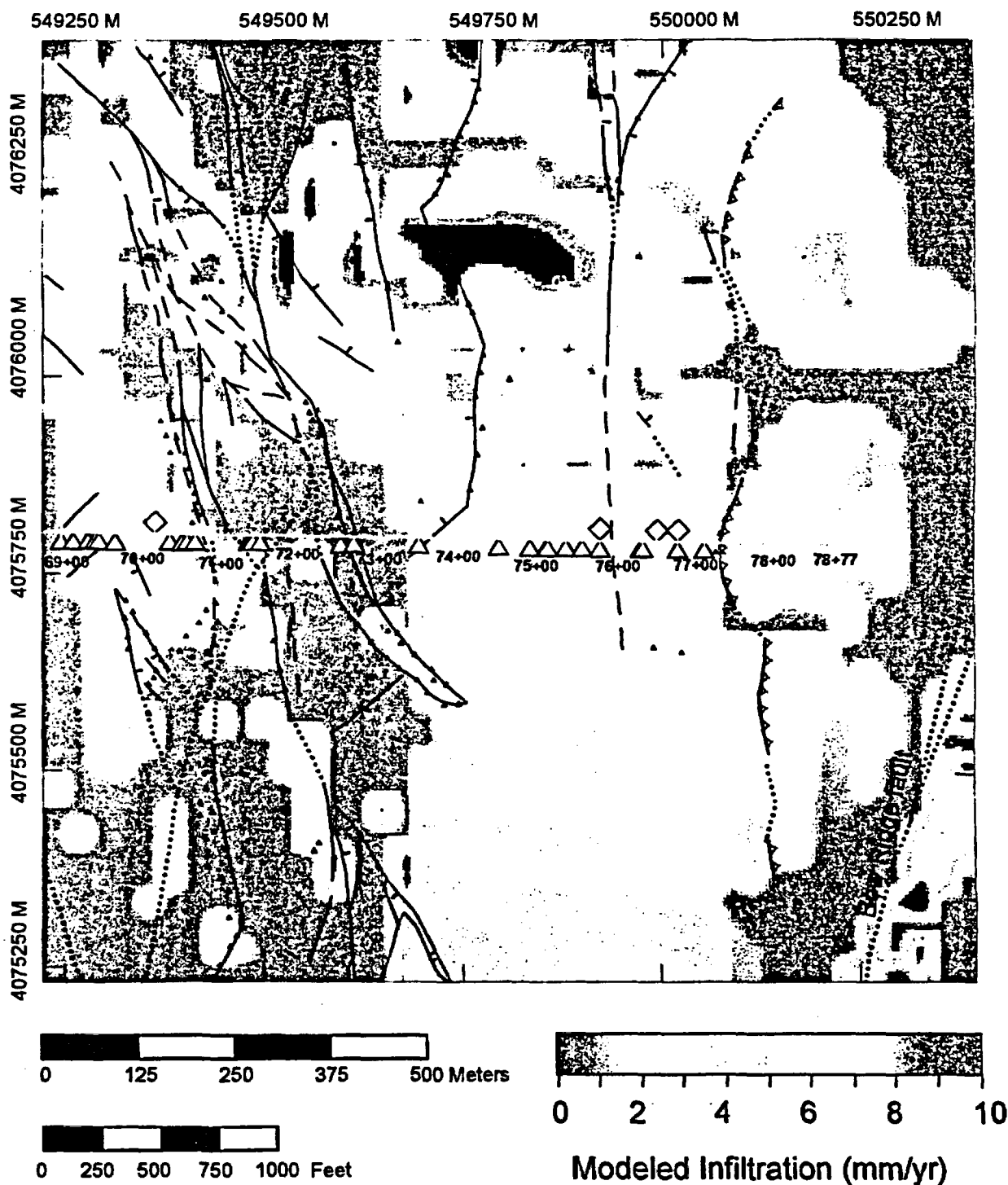


Figure D-8b. Conceptual model of infiltration in the Boundary Ridge area. Numerical model of infiltration, using average annual precipitation, from Flint et al. (1996). Explanation of map symbols is given in figure D-2. Black areas indicate infiltration rates greater than 10 mm/yr.

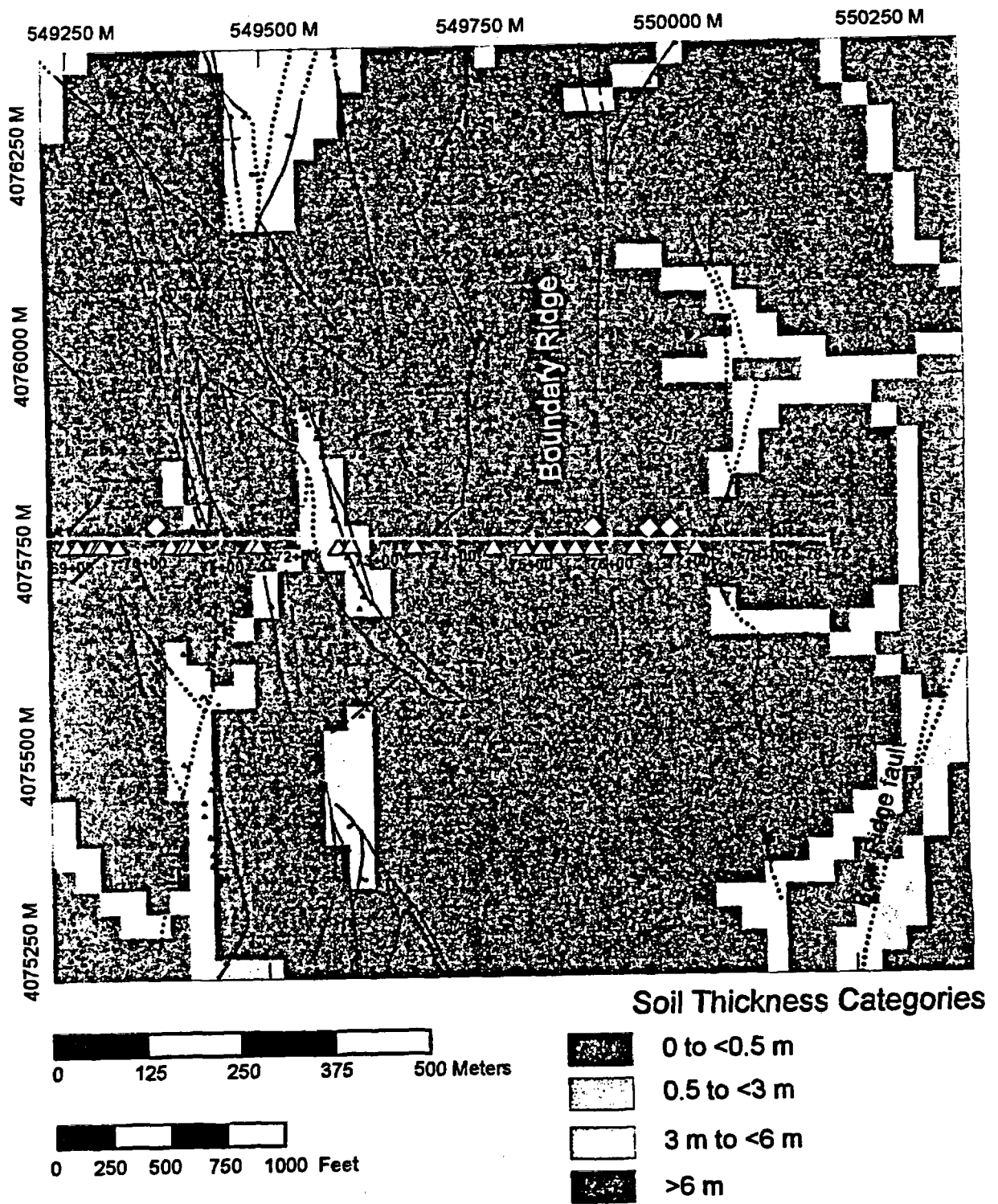


Figure D-8c. Map of soil thickness in the Boundary Ridge area. Soil thickness data as reported in Flint et al. (1996).

## Appendix E

### QA Status and Data Traceability of New or Revised Data Cited in this Report

**E1. Traceability of Analytical and Field Data**

DTN or YMP Notebook Identifier	Description of data	QA status
DTN LAJF831222AQ97.002	Chlorine-36 analyses of packrat urine	QA
DTN LAJF831222AQ97.003	Halide, sulfate and chlorine-36 analyses of ESF construction water	QA
DTN LAJF831222AQ97.004	Halide, sulfate and chlorine-36 analyses of ESF rock samples	QA
DTN LAJF831222AQ97.005	Sulfate analyses of surface soils collected in the Yucca Mountain Controlled Area	QA
DTN LAJF831222AQ97.006	Halide, sulfate and chlorine-36 analyses of soils from Midway Valley soil pits MWV-P31 and NRSF-TP-19	QA
DTN LAJF831222AQ97.007	Halide, sulfate and chlorine-36 analyses of cuttings from borehole SD-12	QA
DTN LAJF831222AN97.008	Halide, sulfate and chlorine-36 analyses of cuttings from borehole ONC#1	NQA
DTN LAJF831222AQ97.009	Sulfate analyses of Yucca Mountain precipitation	QA
DTN LAJF831222AQ97.010	Halide and sulfate analyses of Paintbrush tuffs from Yucca Mountain	QA
DTN LAJF831222AQ97.011	Halide, sulfate and chlorine-36 analyses of porewaters, groundwaters and surface runoff from the Yucca Mountain vicinity	QA
DTN LAJF831222AN97.012	Halide, sulfate and chlorine-36 analyses of surface soils	NQA
DTN LAJF831222AQ97.013	Halide, sulfate and chlorine-36 analyses of ESF porewaters,	QA
LA-EES-1-NBK-96-002	Petrologic descriptions of soil calcites (laboratory notebook)	QA
LA-EES-1-NBK-96-001 LA-EES-1-NBK-96-008	Descriptions of soil calcites and ESF rock sampling locations (field notebooks)	QA
LA-CST-NBK-96-004	Chlorine-36 analyses of calcites and technetium-99 analyses of ESF, soil and borehole samples (laboratory notebook)	QA
LA-EES-1-NBK-96-001 LA-EES-1-NBK-96-002 LA-EES-1-NBK-96-008 SN-0103 (USGS) GS970608314222.004	Structural settings of ESF sampling localities (laboratory notebooks and data package)	QA
LASL831222AQ97.001	Petrologic and mineralogic descriptions of ESF samples (laboratory notebook)	QA

QA Data were generated following YMP QA procedures, have been technically reviewed, and are in the process of being submitted to the Records Processing Center (RPC).

**NQA** Non-QA: ONC#1 data were generated following YMP QA procedures but are considered non-QA for YMP purposes because this borehole was not drilled under YMP/QA procedures.

## **E2. Traceability of the Solute Transport Code, FEHM**

The code (FEHM) used to perform the transport calculations in section 8 has been certified in accordance with LANL YMP procedures. The Los Alamos software QA program is a rigorous, life-cycle-based approach in which QA and user documents are reviewed during each of the phases of development, including the requirements phase, the design phase, and the implementation phase. The following documents are available:

- ... Software Requirements Specifications;
- ... Models and Methods Summary;
- ... Software Design Document;
- ... Verification and Validation Plan and Procedures;
- ... Verification and Validation Report; and
- ... User's Manual.

**E3. Description of milestone completion criteria and a summary of their location for the U.S. Department of Energy**

<b>CRITERIA</b>	<b>TEXT LOCATION</b>
This deliverable will consist of a report that will supercede all previous level 3 and 4 milestones and will summarize the results of analyses of cuttings, minerals, and water samples from boreholes and the ESF.	The report summarizes relevant data from previous milestones and reports new data for samples from the ESF (section 4.2), soils (section 4.3), boreholes (section 4.4), and waters (section 4.5).
Data will be interpreted with respect to the following:	
a) Identification of preferential flow and transport pathways ("fast paths") from the surface to depth	Section 4.2.4 Section 6 Appendices C and D
b) Estimation of the average residence time of infiltrating water as a function of depth	Sections 2, 6, 8, 9
c) Application of results to the verification of site-scale hydrologic and solute-transport modeling scenarios being developed for PA	Section 8, 9
This report will support preparation of Level 3 Milestone No. SP23KM3, "Distribution and analyses of geochronological age determinations," and Level 3 Milestone, "UZ site transport model."	Data in this report have been used to support the UZ site transport model (Robinson et al., in review; their chapters 6 and 7; c.f. our section 8).